Tectonothermal Evolution of the southwestern Central Zone, Damara Belt, Namibia

Luke Longridge

A dissertation submitted to the Faculty of Science, University of the Witwatersrand, Johannesburg, in fulfilment of the requirements for the degree of Doctor of Philosophy.
Johannesburg, 2012

DECLARATION

I declare that this thesis is my own, unaided work. It is being submitted for the degree of Doctor of Philosophy at the University of the Witwatersrand, Johannesburg. It has not been submitted before for any degree or examination in any other university.

_____

Luke Longridge

13 of July, 2012

DEDICATION

To my parents.
With love and thanks.

ABSTRACT

This is an integrated study of the stratigraphy, deformation, magmatism, and metamorphism in the vicinity of the Ida and Palmenhorst Domes, an area in the southwestern Central Zone of the Damara Orogen, Namibia. The principal aim is to understand the timing of tectonic events through high-precision U-Pb dating of structurally constrained intrusions and anatectic rocks, and link these tectonic events across the Damara Orogen and Pan-African Orogeny. A secondary aim is to compare the Central Zone and Damara Orogen to other collisional orogens.

The stratigraphy of the study area is similar to that noted elsewhere in the Central Zone, but the mapped distribution of lithologies differs slightly from previous work. Specifically, Damara Supergroup rocks have been found infolded with the Abbabis Complex, and the stratigraphic positions of certain units in have been locally reclassified. The mapped distribution of lithologies suggests a Type-2 fold interference pattern across the study area.

This Type-2 fold interference is confirmed by structural analysis. A D2 deformation event formed strongly S- to SE-verging km-scale recumbent to shallow NW-dipping folds with smaller-scale parasitic folds. The long limbs of these folds are extended, and a number of shear zones are found on these extending limbs, as well as near the contact between the Abbabis Complex and the Damara Supergroup. NE-SW extension is associated with the late stages of D2, and forms a conjugate set of shear bands and a shallow NE-plunging mineral stretching lineation. This D2 event was overprinted by upright to steeply WNW-dipping km-scale D3 folds to form the domes in the study area. Mesoscale fold interference structures are rare, but D2 structures are shown to be consistently reoriented by D3 structures. D3 deformation does not have a strong vergence, and mesoscale D3 folds are rare. D2 and D3 were preceded by a D1 fabric forming event locally observed as rootless isoclinal intrafolial folds, and followed by brittle deformation. The Ida Dome is a fairly simple domal structure formed by the km-scale interference between a shallow NNW-dipping D2 anticline and an upright to steeply WNW-dipping D3 anticline. East of the Ida Dome, NE-trending D3 structures predominate, but are seen to overprint earlier D2 structures. The Palmenhorst Dome is a larger area where Damara Supergroup rocks have been infolded into the Abbabis Complex during D2 deformation. These isoclinal, N- to NW-dipping D2 folds have been refolded by upright D3 folds to form a Type-2 fold interference pattern. D2 structures along the southern margin of the Palmenhorst Dome dip steeply towards the south, in contrast to D2 structures elsewhere. This is interpreted to be the result of a lower-intensity km-scale D2 fold.

The orogen-parallel extension and orogen-perpendicular recumbent folding that took place during D2 cannot be explained by previous structural models for the Central Zone and a new model is suggested where these structures form as the result of coeval irrotational NE-SW extension and S- to SE-verging simple shear during extensional collapse of the orogen.

A number of intrusive rock types are found in the study area and have been dated using SHRIMP U-Pb. Amphibolite dykes have a chemical affinity to mafic rocks of the Goas Suite, and are suggested to be either pre-Damaran or early Damaran intrusives as they cut the gneisses of the Abbabis Complex, and are affected by D2. They have been dated at 2026.9 ± 2.3 Ma (zircon) or 557.2 ± 7.4 Ma (zircon) with metamorphic overgrowths in this sample giving 520 ± 6.9 Ma. Red, potassic granites emplaced near the contact with the Abbabis Complex and Damara Supergroup contain a D2 gneissic fabric and give ages of 536 ± 7.2 Ma (monazite), and zircons have lower intercept ages of 539 ± 17 Ma and upper intercept ages of 1013 ± 21 Ma. Grey granites are abundant in the study area, and form a continuum from dark grey granites (which are tonalitic to dioritic in composition and contain hornblende and abundant biotite) to light grey granites (which are leucogranitic and contain abundant K-feldspar and minor biotite). These grey granites show a fractionation trend from dark to light varieties, and cross-cutting relationships indicate that the lighter variety is younger than the darker variety. The grey granites show syn-D2 structural relationships and contain a fabric subparallel to the S2 fabric, and which is more pronounced in the darker varieties. They show similarities with granites described by earlier workers, and two samples have been dated at 519.1 ± 4.2 Ma and 520.4 ± 4.2 Ma (zircon). A variety of sheeted granites are found – quartz-feldspar-magnetite pegmatitic granites are associated with grey granites, occur axial-planar to F2 folds, and have metamict zircons which are dated at 530-525 Ma. Garnet (± cordierite) granites are leucocratic, have garnet poikiloblasts, are emplaced axial planar to F2 folds and are also folded and boudinaged by D2. They are associated with pelitic units in the Damara Supergroup and are dated at 520.3 ± 4.6 Ma (zircon) and 514.1 ± 3.1 Ma (monazite). Uraniferous leucogranites found are similar to those widely described in the Central Zone, but metamict zircons give imprecise ages of between 515 and 506 Ma. Pink pegmatitic leucogranites comprise pink perthitic feldspar and milky quartz, are emplaced into more brittle structures and gives an age of 434.4 ± 2 Ma (zircon). Almost all granites analysed appear to be crustal-melt granitoids, with the exception of the darker grey granites, which show a calc-alkaline affinity. No Salem-type granites are found in the study area. In addition, SHRIMP U-Pb analyses of zircons from three Abbabis Complex gneisses give ages of 2056 $^{+11}/_{-10}$ Ma, 2044 $^{+32}/_{-27}$ Ma and 2044 $^{+17}/_{-14}$ Ma, and titanites from an amphibolite sample give ages of 493.4 ± 6.4 Ma. Two anatectic leucosomes from D2 shear zones and shear bands give zircon ages of 511 ± 18 Ma and 508.4 ± 8.7 Ma in spite of high-U zircons.

Lu-Hf data on zircons from an Abbabis Complex gneiss gives model ages of *ca*. 3 Ga, whilst similar data for a grey granite gives a model age of *ca*. 2 Ga. Zircons from the Abbabis Complex gneiss have variable O-isotopic values, whilst the grey granite gives O-isotopic values of *ca*. 7‰. These geochonological and isotopic data show that the Abbabis Complex is part of the Congo Craton, and that some amphibolites are pre-Damaran, whilst others may be related to the Goas Intrusive Suite, and represent a phase of early Damaran magmatism. In contrast to the chronology previously presented for the Central Zone, M1 in the study area appears to have occurred at 535-540 Ma, with M2 coeval with D2 deformation at 510-520 Ma. Elsewhere in the Central Zone, NW-verging D2 deformation is dated at 540-560 Ma, and the Central Zone appears to have a diachronous tectonometamorphic evolution along strike. It is suggested here that this represents the preservation of two separate tectonic events in the Central Zone at different crustal levels, one at 540-560 Ma and the other at 520-510 Ma. D3 deformation is suggested to have taken place at 508 Ma, immediately after D2 extension. The Central Zone began to cool following D2, and the 495 Ma titanite age reflects this cooling. Isotopic evidence from this and other studies shows that Damaran granitoids (with 1.5-2.2 Ga model ages) cannot be derived from the Abbabis Complex (with 3 Ga model ages) but must come from an alternative source, suggested here to be Kalahari Craton material subducted below the Congo Craton.

Textural studies of a number of pelitic samples indicate syn-D2 low-pressure, high-temperature metamorphism. Differences in observed assemblages between various sample types are due to compositional differences, and samples appear to have reached similar conditions across the study area. Mineral compositional profiles show no prograde zoning, indicating mineral re-equilibration. Orthopyroxene is locally observed, suggesting lower-granulite conditions. This is confirmed by pseudosection modelling of a number of samples, which gives peak conditions of 750-850 °C and 4.5-5 kbar. This modelling shows lower-granulite facies conditions with higher temperatures than previous estimates based on mineral compositional geothermometers, which are affected by re-equilibration. These conditions are sufficiently high for fluid-absent biotite breakdown to form the voluminous anatectic leucosomes and granitoids in the southwestern Central Zone. Pseudosection modelling and phase relationships indicates a low-pressure (*ca*. 4 kbar) clockwise heating path, with slight decompression at the thermal peak. All metamorphism noted is 520-510 Ma M2 metamorphism, and no petrographic evidence exists for earlier 540-535 M1 metamorphism. This cryptic M1 is suggested to be related to the emplacement of the Goas Intrusive Suite and Salem-type granites early in the orogenic history, whilst M2 may be related to thermal relaxation following crustal thickening early in the orogenic history, but requires an additional heat source. The difference in ages for deformation and metamorphism between the study area and elsewhere in the lower

grade portions of the Central Zone is suggested to be related to the preservation of different portions of the orogenic history in different areas.

The results of this study together with previous work details a multi-stage evolution for the Central Zone involving subduction, continent-continent collision, crustal thickening, slab breakoff, magmatism, granulite-facies metamorphism and exhumation of the mid-crust. This multistage evolution explains the multiple ages for deformation and metamorphism in the Central Zone. NW-folding and thrusting documented in the Karibib area at 560-540 Ma is related to an early phase of crustal thickening owing to continent-continent collision following a brief period of subduction. Slab breakoff led to asthenospheric upwelling and heating of the lower crust, and produced the Goas Intrusive Suite and Salem-type granites, as well as providing heat for 540-535 Ma M1 metamorphism and the melting of the crust to produce anatectic red granites. SE-verging deformation, extension and granulite facies metamorphism recorded in this study is related to orogenic collapse following crustal thickening, and the heat source for low-P, high-T metamorphism may be highly radiogenic crust that was thickened , which is suggested to be either burial of crust enriched in heat-producing elements, or asthenospheric upwelling owing to delamination of the Congo Craton lithospheric mantle or asthenospheric upwelling owing to the position of the southwestern Central Zone on a major orocline.

The events recorded for the Central Zone have been correlated across the entire Damara Orogen, and the timing of events can be correlated along strike into the Zambezi Belt. Events in the Kaoko Belt appear to predate those in the Damara Belt, which appears to also show a similar collisional timing to the Gariep Belt. It is therefore proposed that the Gariep and Damara Belts formed part of a younger orogenic episode to that which formed the Kaoko and Dom Feliciano orogenic belts. The Damara Belt shows similarities to both Alpine-style and Himalayan-style orogens. An evaluation is provided of a channel flow model for the Central Zone, but there are currently insufficient data for the Damara Belt to confirm or repudiate this model. Nonetheless, this study has identified a more complex tectonic history for the Central Zone than previously, with chronological and lithogeochemical evidence for two episodes of deformation and metamorphism that have been linked to the collisional history of the entire Damara Belt and have been correlated with events in other Pan-African belts.

ACKNOWLEDGEMENTS

The help, support and encouragement of a vast number of people have contributed to the success of this project. Without them, the project would not have been possible. Firstly, I owe a huge thanks to Judith Kinnaird and Roger Gibson for their outstanding supervision. They provided support, guidance and encouragement where it was needed, whilst still allowing me the freedom to lead this project to where it is. I also owe Paul Nex for first introducing me to the beauty of Namibia and the wonders of the Central Zone, and for getting me hooked on Damaran geology.

Without funding provided by the National Research Foundation, the REI fund of the GSSA, and the Jim and Gladys Taylor Trust Fund, this project would not have been possible. I am also lucky to have received a Merit Award Scholarship from Wits Univeristy for a number of years, and thank CCIC for help with funding early in the project. I am also extremely grateful for sponsorships to vaious conferences, including the Yorsget conference, the EURISPET series of conferences and short courses, the Granulites and Granulites Conference, and an SEG field trip to Chile.

In the field I was lucky to have the company of Guy Freemantle, without whom marching around the desert would have been much more tedious, and with whom I discussed my findings over many a cold Hansa draught in Swakopmund. In Namibia, logistical support from both Extract Resources and Bannerman Resources also made for much more pleasant fieldwork, and the exploration teams from both these companies are thanked for being so accommodating. I hope some of my results will be of use to them.

Advice and assistance I received on the variety of analytical techniques employed in this thesis was essential. At Wits, Alex Mathebula prepared excellent thin sections in record time, and Joe Aphane taught me the art of zircon, monazite and titanite separation. At ANU, Richard Armstrong and Greg Yaxley helped with SHRIMP dating, O-isotope analyses and Lu-Hf data, and I owe them for their helpfulness and efficiency. Without their help many of the most interesting results of this project would not have been possible. At

Pretoria University, Peter Graser always made time for me and was a great help with getting quality mineral chemistry. At the University of Cape Town, Anton Le Roux and Fayrooza Rawoot helped with ICP-MS trace element analyses. Paula Ogilvie, Johann Diener and Richard White were invaluable in helping with various THERMOCALC niggles, and I especially owe Paula for always being patient with my questions.

The postgrad students and staff at the Wits School of Geosciences made the school the home it has been for many years. In particular, the company and friendship of Guy Freemantle, Anika Solanki, Louise Coney, Paula Ogilvie, Grant Bybee, and Trishya Owen-Smith made coming to varsity a pleasure. This project has benefited greatly from discussions with (amongst others) Ian Buick, Chris Clarke, Rob Ward, Celal Sengor, Stefan Büttner, Paul Dirks, Lew Ashwal, Sharad Master, Guy Charlesworth, Lorenzo Milani, Kalin Naydenov, Kerstin Saalmann and Jeremie Lehmann.

Along the course of this project I have been fortunate enough to attend a number of conferences and short courses both in South Africa and abroad, and although they are too numerous to list, I'd like to thank everyone who has contributed to discussions around my project.

To Louise Coney, a massive thanks for helping with the final proofing, which was a task not for the faint of heart.

To my kayak friends, thanks for keeping me sane.

To my parents, thank you for everything – for getting me started, for your love and support, and especially for treading lightly near the end.

And most of all, thanks to my lovely wife Phia, for always being positive and encouraging, for putting up with the late nights and non-existent weekends over the last couple of years, and for generally being awesome. Your support has been invaluable, and you can have me back now!

TABLE OF CONTENTS

DECLARATION **ii**

DEDICATION **iii**

ABSTRACT **iv**

ACKNOWLEDGEMENTS **viii**

TABLE OF CONTENTS **x**

LIST OF FIGURES **xix**

LIST OF TABLES **xxxiv**

LIST OF ABBREVIATIONS **xxxvi**

CHAPTER 1 – INTRODUCTION **1**

1.1 An Introduction to the Damara Orogen **3**

1.2 Zones of the Damara Orogen **7**

1.3 A Review of Previous Work on the Central Zone **14**

1.3.1 The Stratigraphy of the Central Zone **14**

1.3.1.1 Abbabis Complex **15**

1.3.1.2 Nosib Group **17**

1.3.1.3 Swakop Group **18**

1.3.1.4 Stratigraphy used in this study **19**

1.3.2 Metamorphism in the Central Zone **20**

1.3.3 Lithological Mapping in the Central Zone **23**

1.3.4 Deformation in the Central Zone **26**

1.3.4.1 Formation of Domes in the southern Central Zone of the Damara Orogen **26**

1.3.4.2 The Structural History of the Central Zone **27**

1.3.5 Granites of the Central Zone **31**

1.3.5.1 The Goas Intrusive Suite **33**

1.3.5.2 Salem-type granites **33**

1.3.5.3 Red granites **34**

1.3.5.4 Homogeneous syn-tectonic granites **35**

1.3.5.5 Post-tectonic leucogranites **36**

1.3.5.6 Post-tectonic alaskites, leucogranites and pegmatites **36**

1.3.6 Geochronology and the timing of events in the Central Zone **37**

1.4 Aims of the Project **40**

1.5 Location of the Study Area **42**

1.6 Approach and Thesis Outline **43**

CHAPTER 2 – STRATIGRAPHY **45**

2.1 The Abbabis Complex **48**

2.2 The Damara Supergroup **60**

2.2.1 The Nosib Group **61**

2.2.1.1 The Etusis Formation **62**

2.2.1.2 The Khan Formation **65**

2.2.2 The Swakop Group **76**

2.2.2.1 The Rössing Formation **76**

2.2.2.2 The Chuos Formation **83**

2.2.2.3 The Arandis, Ghaub, Karibib and Kuiseb Formations **89**

2.3 Implications of Lithological Mapping **90**

2.4 Summary **95**

CHAPTER 3 – STRUCTURE **100**

3.1 Results from Lithological Mapping **111**

3.2 Pre-Damaran Deformation in the Abbabis Complex **114**

3.3 D1 Deformation **118**

3.4 Non-Coaxial, S- to SE-Verging Deformation and NE-SW Extension **120**

3.4.1 S- to SE- verging folding in the southwestern Central Zone **121**

3.4.2 High-strain zones in the study area **129**

3.4.3 NE-SW extension in the study area **139**

3.5 Upright Folding in the Study Area **145**

3.5.1 Mesoscale upright folding **145**

3.5.2 The Arcadia Syncline **148**

3.5.3 Eastern margin of the Ida Dome **151**

3.6 Fold Interference in the Study Area **153**

3.6.1 The Ida Dome **154**

3.6.2 Structural synthesis of the Ida Dome **156**

3.6.3 Southern margin of the Palmenhorst Dome **157**

3.6.4 Structural synthesis of the Palmenhorst Dome **165**

3.7 Post-D3 Deformation in the Study Area **168**

3.8 Dome Formation and the Structural Evolution of the Southwestern Central Zone **169**

CHAPTER 4 – INTRUSIVE ROCKS **185**

4.1 Amphibolites **188**

4.2 Red Granites **194**

4.3 Grey Granites **201**

4.4 Sheeted Granites **215**

4.4.1 Quartz-feldspar-magnetite pegmatitic granite **217**

4.4.2 Garnet (±cordierite)-bearing Leucogranites **218**

4.4.3 Uraniferous leucogranites **221**

4.4.4 Pink pegmatitic leucogranites **224**

4.4.5 Geochemistry of the sheeted granites **225**

4.6 Comparison of granite chemistry with the classification of McDermott (1986) **228**

4.7 Discussion **231**

4.8 Implications for the tectonometamorphic evolution of the Central Zone **238**

CHAPTER 5 – GEOCHRONOLOGY AND ISOTOPE GEOCHEMISTRY **240**

5.1 – SHRIMP U-Pb Geochronology **244**

5.1.1 Abbabis Complex gneisses **244**

5.1.1.1 Descriptions of samples and zircons analysed **245**

5.1.1.2 Results of SHRIMP U-Pb geochronology **248**

5.1.1.3 Discussion of results **250**

5.1.2 Amphibolites **250**

5.1.2.1 Descriptions of samples and zircons analysed **251**

5.1.2.2 Results of SHRIMP U-Pb geochronology **253**

5.1.2.3 Discussion of results **255**

5.1.3 Red granites **256**

5.1.3.1 Descriptions of sample and zircons analysed **256**

5.1.3.2 Results of SHRIMP U-Pb geochronology **257**

5.1.3.3 Discussion of results **258**

5.1.4 Grey granites **259**

5.1.4.1 Descriptions of sample and zircons analysed **260**

5.1.4.2 Results of SHRIMP U-Pb geochronology **262**

5.1.4.3 Discussion of results **263**

5.1.5 Quartz-feldspar-magnetite pegmatitic granites **264**

5.1.5.1 Descriptions of sample and zircons analysed **264**

5.1.5.2 Results of SHRIMP U-Pb geochronology **264**

5.1.5.3 Discussion of results **265**

5.1.6 Garnet-bearing leucogranites **266**

5.1.6.1 Descriptions of sample and zircons analysed **266**

5.1.6.2 Results of SHRIMP U-Pb geochronology **268**

5.1.6.3 Discussion of results **268**

5.1.7 Uraniferous leucogranites **269**

5.1.7.1 Descriptions of samples and zircons analysed **271**

5.1.7.2 Results of SHRIMP U-Pb geochronology **272**

5.1.7.3 Discussion of results **274**

5.1.8 Pink pegmatitic leucogranites **275**

5.1.8.1 Descriptions of samples and zircons analysed **275**

5.1.8.2 Results of SHRIMP U-Pb geochronology **275**

5.1.8.3 Discussion of results **276**

5.1.9 Anatectic leucosomes **277**

5.1.9.1 Descriptions of sample and zircons analysed **278**

5.1.9.2 Results of SHRIMP U-Pb geochronology **278**

5.1.9.3 Discussion of results **279**

5.2 Hf - and O-isotope Analyses **280**

5.2.1 Hf-isotopes **282**

5.2.2 O-isotopes **286**

5.2.3 Discussion of results **288**

5.3. Summary and Discussion **290**

CHAPTER 6 – METAMORPHISM **299**

6.1 Previous Studies of Metamorphism in the Central Zone **299**

6.2 Aims of this Study **304**

6.3 Approach of this Study **306**

6.4 Field Relationships **309**

6.5 Petrography **312**

6.5.1 Garnet-cordierite-biotite schists **312**

6.5.2 Cordierite-biotite schists **318**

6.5.3 Garnet-sillimanite-cordierite schists **324**

6.5.4 Interpretation of petrographic results **328**

6.6 Mineral and Whole-rock Chemical Data **334**
6.6.1 Garnet **334**
6.6.2 Biotite **340**
6.6.3 Cordierite **343**
6.6.4 Spinel **344**
6.6.5 Feldspars **345**
6.6.6 Orthopyroxene and gedrite **346**
6.6.7 Garnet-cordierite-biotite schists **349**
6.6.8 Cordierite-biotite schists **351**
6.6.9 Garnet-cordierite-sillimanite schists **353**
6.6.10 Compositional controls on mineral assemblages **355**

6.7 Qualitative Petrogenetic Grids **357**

6.8. Cation Exchange Thermometry **362**

6.9 Average P-T calculations using THERMOCALC **369**

6.10 Pseudosection Modelling (Quantitative Petrogenetic Grids)
using THERMOCALC **375**
6.10.1 Pseudosections in the system NCKFMASH **377**
6.10.1.1 Sample CZRL19 (sillimanite-cordierite schist) **377**
6.10.1.2 Sample LID039 (garnet-biotite schist) **379**
6.10.1.3 Sample LKR013 (garnet-biotite schist) **383**
6.10.1.4 Sample LHA006 (cordierite-biotite schist) **385**
6.10.2 Pseudosections in the system NCKFMASHTO **391**
6.10.2.1 Sample CZRL19 (sillimanite-cordierite schist) **392**
6.10.2.2 Sample LID039 – garnet cordierite schist **399**
6.10.2.3 Sample LKR013 – garnet cordierite schist **405**

6.11 Discussion **409**

6.11.1 Overall P-T path **409**

6.11.2 Evidence for polymetamorphism? **411**

6.11.3 The relationship between melting and deformation, timing of metamorphism and the P-T-d-t path of the Central Zone **412**

6.11.4 Implications for partial melting in the Central Zone **416**

6.11.5 Possible heat sources for metamorphism **417**

6.11.6 The relationship between metamorphism in the study area and the geodynamics of the Central Zone and the Damara Orogen. **418**

CHAPTER 7 – DISCUSSION AND CONCLUSIONS **420**

7.1 Introduction **420**

7.2 A Tectonic Model for the Central Zone, and the Evolution of the Damara Orogen **423**

7.2.1 Heat sources for metamorphism **434**

7.2.2 Preservation of different domains in the Central Zone **440**

7.3 The Timing of Events in the Other Zones of the Damara Orogen **441**

7.4 The Damara Orogen in the Context of the Pan-African Orogeny **450**

7.4.1 The Kaoko Belt **451**

7.4.2 The Gariep Belt **453**

7.4.3 The Zambezi Belt **454**

7.5 The Damara Orogen and the Assembly of Gondwana **456**

7.6 Comparison with Other Collisional Orogens **458**

7.6.1 A comparison with Himalayan-type and Alpine-type orogens **459**

7.6.2 Channel flow as a potential mechanism for the exhumation of the Central Zone **464**

7.6.3 Comparison with the Variscan and Caledonian Orogens **470**

7.6.3.1 Slab breakoff vs. lithospheric delamination in the Damara **473**

7.6.4 The exhumation of the Central Zone **474**

7.7 Conclusions and Recommendations for Future Studies of the Damara Orogen **477**

REFERENCES **483**

LIST OF APPENDICES **525**

APPENDICES PAGE1 TO APPENDICES PAGE 68

LIST OF FIGURES

Fig. 1.1 – Distribution of Neoproterozoic (Pan-African) mobile belts (grey) on the world's continents, as they were configured prior to the breakup of the Gondwana Supercontinent. **2**

Fig. 1.2 – Cratons involved in Pan-African collision, and the resultant orogenic belts formed during the Pan-African. **4**

Fig. 1.3 – Map of the Damara Orogen, showing the subdivision of the Damara Belt into a number of tectonometamorphic zones, major lineaments, and the location of the study area. **6**

Fig. 1.4 – Lithostratigraphic correlations across the Damara Orogen, with approximate ages of deposition for the Damaran Stratigraphy. **9**

Fig. 1.5 – Detailed geological map of the Central Zone south of the Namibfontein-Vergenoeg Dome. **11**

Fig. 1.6 – Cross section through the Damara Orogen, showing the location of various zones of the orogen. **13**

Fig. 1.7 – Stratigraphic column for the study area in the Central Zone. **15**

Fig. 1.8 – Simplified map of peak metamorphic assemblages in the Damara Orogen. **22**

Fig. 1.9 – Distributions of Abbabis Complex and Damara Supergroup rocks in the Palmenhorst Dome along the Khan River. **24**

Fig. 2.1 – Geological map of the study area produced from this study, showing the distribution of the Abbabis Complex and Damara Supergroup rocks. **46**

Fig. 2.2 – A: Quartzofeldspathic augen gneiss from the study. B: Complex refolding of a pale green L-tectonite in the Abbabis Complex. C: Crenulated quartzofeldspathic augen gneisses from the Palmenhorst Dome. D: Banded (para) gneisses from the Palmenhorst Dome, cut by Damaran-age leucosomes. **50**

Fig. 2.3 - Photomicrographs of L-tectonites from the centre of the Ida Dome. **51**

Fig. 2.4 – Photomicrographs of Abbabis Complex rocks from the study area. **53**

Fig. 2.5 – Geochemical plots for Abbabis Complex gneisses and L-tectonites from the study area. **55**

Fig. 2.6 – Mapped distributions of the Abbabis Complex in the Ida Dome. **56**

Fig. 2.7 – Comparison of mapping of the Abbabis Complex in the Palmenhorst Dome. **57**

Fig. 2.8 – A: Map of the northern margin of the Palmenhorst Dome after Poli (1997). B: Map of the northern margin of the Palmenhorst Dome from this study. **59**

Fig. 2.9 – Stratigraphic column for the study area in the Central Zone. **61**

Fig. 2.10 – Etusis Formation rocks from the study area. **63**

Fig. 2.11 – Photomicrographs of Etusis Formation rocks from the study area. **65**

Fig. 2.12 – Satellite image of the Arcadia Syncline. **66**

Fig. 2.13 – Mapped distributions of the Khan Formation in the Ida Dome. **68**

Fig. 2.14 – Comparison of mapping of the Abbabis Complex in the Palmenhorst Dome. **68**

Fig. 2.15 – Khan Formation rocks from the study area. **70**

Fig. 2.16 – Photomicrographs of calc-silicate rocks and amphibole-biotite schists from the Khan Formation. **72**

Fig. 2.17 – Photomicrographs of pelitic (cordierite-bearing) schists from the Khan Formation. **73**

Fig. 2.18 – Photomicrographs of semi-pelitic to psammitic schists from the Khan Formation. **74**

Fig. 2.19 – Rössing Formation rocks. **77**

Fig. 2.20 – Mapped distributions of the Rössing Formation in the Ida Dome. **79**

Fig. 2.21 – Photomicrographs of Rössing Formation rocks. **82**

Fig. 2.22 – Comparison of mapping of the Chuos Formation in the Palmenhorst Dome. **84**

Fig. 2.23 – Field photographs of Chuos Formation lithologies. **85**

Fig. 2.24 – Photomicrographs of Chuos Formation rocks. **88**

Fig. 2.25 – Reinterpretation of the mapped distributions of the Karibib and Kuiseb formations in the Ida Dome according to this study compared to Barnes (1981) and Jacob (1974). **90**

Fig. 2.26 – Lower Damara Supergroup stratigraphic packages found in the Palmenhorst Dome. **93**

Fig. 2.27 – The trace of the Hook Fold. **94**

Fig. 2.28 – Geological map of the study area produced from this study, showing the distribution of the Abbabis Complex and Damara Supergroup rocks, with structural interpretations shown. **98**

Fig. 3.1 – Possible mechanisms suggested for the formation of gneiss domes in orogens, and examples where these mechanisms have been applied to the domes of the Central Zone. **104**

Fig. 3.2 – Geological map of the study area showing major D2 and D3 structural features in the Ida and Palmenhorst domes, and the names of specific areas referred to in this study. **110**

Fig. 3.3 – Fold interference patterns from lithological mapping. **112**

Fig. 3.4 – Remote sensed images showing upright, NE-trending D3 folding. **113**

Fig. 3.5 – A: Highly deformed Abbabis Complex L-tectonites from the centre of the Ida Dome refolded in a complex pattern formed by upright, non-cylindrical folds. B: Abbabis Complex L-tectonites from the Ida Dome. C: Outcrop of m-scale folds in amphibolite dykes, which cut the pre-Damaran fabric. D – Close-up an outcrop where a pre-Damaran fabric is truncated by an amphibolite dyke. E: Abbabis Complex gneisses cut by extensional shear bands. F: Steeply dipping Abbabis Complex gneisses from the Arcadia Inlier. G: Photomicrograph of an Abbabis Complex L-tectonite. H: Photomicrograph of Abbabis Complex gneiss. **117**

Fig. 3.6 – Field evidence for D1 deformation. **120**

Fig. 3.7 – Recumbent folding in the centre of the Ida Dome. **123**

Fig. 3.8 – Non-coaxial folding in the Palmenhorst Dome. **126**

Fig. 3.9 – Shear zones associated with south-verging km-scale folds near the northern margin of the Palmenhorst Dome. **130**

Fig. 3.10 – Shear zones at the basement-cover interface in the Arcadia Syncline, and on the western margin of the Arcadia Inlier. **133**

Fig. 3.11 – Structures developed in a major high-strain zone on the western margin of the Ida Dome. **136**

Fig. 3.12 – Field photographs and photomicrographs from a ductile shear zone along the western margin of the Ida Dome. **138**

Fig. 3.13 – Evidence for NE-SW extension in the southwestern Central Zone. **141**

Fig. 3.14 – A: Schematic diagram illustrating the orientations of the conjugate set of ESBs relative to the principal stress directions. B: NE-SW pure shear extension coeval with SE-vergent simple shear in a constrictional field. **144**

Fig. 3.15 – Mesoscale upright folding across the study area. **147**

Fig. 3.16 – Deformation in the km-scale Arcadia Syncline. **150**

Fig. 3.17 – E-dipping structures on the eastern margin of the Ida Dome. **152**

Fig. 3.18 – Equal area lower hemispheric stereographic projections of all structural data from the Ida Dome. **155**

Fig. 3.19 – Cross-sections through the Ida Dome and Arcadia Inlier. **157**

Fig. 3.20 – Geological map of the southern margin of the Palmenhorst Dome. **158**

Fig 3.21 – D2 deformation along the southern margin of the Palmenhorst Dome. **160**

Fig. 3.22 – Equal area lower hemispheric stereographic projections of structural features along the southern margin of the Palmenhorst Dome. **161**

Fig. 3.23 – Equal area lower hemispheric stereographic projections of structural data from the southern margin of the Palmenhorst Dome, classified according to geographic location. **163**

Fig. 3.24 – Cross section A-B (Fig. 3.19) through the southern margin of the Palmenhorst Dome, and possible explanations for the subvertical to southerly dip of D2 structures in this area. **164**

Fig. 3.25 – Map of the study area showing the fold interference pattern for the Palmenhorst Dome, with the section line A-B shown. **167**

Fig. 3.26 – Brittle structures developed in the study area. **169**

Fig. 3.27 – Structures formed in the southwestern Central Zone in relation to principal stress directions. **176**

Fig. 3.28. – Problems with southwest directed tectonic extrusion in the Central Zone. **179**

Fig. 3.29 – Possible transtensional models for the southwestern Central Zone. **182**

Fig. 3.30 – A possible model of gravitational collapse of uplifted, thickened crust to explain extension and SE-verging structures in the southwestern Central Zone, and the relationship to south-eastwards nappe emplacement in the Southern Margin Zone. **184**

Fig. 4.1 – Field photographs of amphibolites from the study area. **189**

Fig. 4.2 – Photomicrographs of amphibolites from the study area. **190**

Fig. 4.3 –– Geochemical diagrams for the amphibolites from the study area, basalts from the Abbabis Complex (Marlow, 1981) and meta-mafic rocks from the Goas Intrusive Suite (De Kock, 1989). **193**

Fig. 4.4 – Field photographs of red granites from the northern margin of the Palmenhorst Dome. **195**

Fig 4.5 – Photomicrographs of red granites. **197**

Fig. 4.6 – Geochemistry of the red granites from the study area, compared with the red gneissic granite of Smith (1965), the red granite of Marlow (1981), and both the basement-hosted granites and red and grey granites of Nex (1997). **200**

Fig. 4.7 – Field photographs of grey granites from the study area. **203**

Fig. 4.8 – Photomicrographs of dark grey granites from the study area. **206**

Fig. 4.9 – Photomicrographs of leucocratic grey granites from the study area. **207**

Fig. 4.10 – Field relationships of grey granites with the pink-red varieties and pegmatitic granites. **209**

Fig. 4.11 – Geochemistry of the grey granites. **211**

Fig. 4.12 – Geochemistry of the grey granites. **213**

Fig. 4.13 – Characteristics of quartz-feldspar-magnetite pegmatitic granites. **218**

Fig. 4.14 – A: Boudinaged sheet of garnetiferous leucogranite in metapelite from the Rössing Formation. B: Folded white garnetiferous leucogranite from the outcrop shown in A. C: Photomicrograph of the garnetiferous leucogranite. D: Photomicrograph of the garnetiferous leucogranite. **220**

Fig. 4.15 – Google Earth™ image of a D3 anticline east of the Ida Dome, and a schematic cross section across the anticline. **221**

Fig. 4.16 – Photomicrographs of uraniferous leucogranites. **223**

Fig. 4.17 – Pink pegmatitic leucogranites. **225**

Fig. 4.18 – Geochemistry of the sheeted granites. **227**

Fig. 4.19 – Geochemistry of the granites from this study in comparison with the classifications of McDermott (1986). **230**

Fig. 5.1 – Geological map of the Central Zone, showing the locations of samples collected for geochronology. **243**

Fig. 5.2 – Photomicrographs and CL images of zircons from Abbabis Complex gneisses. **247**

Fig. 5.3 – Tera-Wasserburg Concordia plots for samples of Abbabis Complex gneisses. **249**

Fig. 5.4 – A: CL images of zircons analysed from LKR021. B: Photomicrographic images of titanites analysed from LKR021. **253**

Fig. 5.5 – Concordia plots for amphibolite samples. **254**

Fig. 5.6 – A: Photomicrograph of clear, subhedral to euhedral zircons from LKR016 with corroded tips. B: CL images of zircons analysed from LKR016. C: Photomicrograph of pale yellow monazites from LKR016. D: BSE image of monazites analysed from LKR016. **257**

Fig. 5.7 – A: Concordia plot for zircons from LKR016. B: Concordia plot of monazite analyses from LKR016. **258**

Fig. 5.8 – Photomicrographs and CL images of zircons from grey granites. **261**

Fig. 5.9 – Concordia plot of zircons from grey granites. **262**

Fig. 5.10 – Concordia diagrams for quartz-feldspar-magnetite pegmatitic granite (LCZ7-2). **265**

Fig. 5.11 – Images of zircons and monazites from garnetiferous leucogranites. **267**

Fig. 5.12 – A: Concordia plot for zircons from LID038. B: Concordia plot of Monazites from LID038. **268**

Fig. 5.13 – A: Photomicrographs and BSE images of zircons from LRV001. **271**

Fig. 5.14 – Concordia plots for uraniferous leucogranites. **273**

Fig. 5.15 – Concordia diagram for zircons from CZF-2. **276**

Fig. 5.16: Concordia plots of analyses from anatectic leucosomes. **279**

Fig. 5.17 – A: Plot of ε_{Hf} vs. age for sample LID045. B: Relative probability plot of model ages calculated for sample LID045. C: Age (Ma) vs. ε_{Hf} for sample LHA010. D: Relative probability plot of model ages calculated from sample LHA010. **285**

Fig. 5.18 – Binary plots of O-isotopic data for LID045 and LHA010. **287**

Fig. 5.19 – Summary of the temporal relationships between Damaran and pre-Damaran intrusions, deformation and metamorphism. **296**

Figure 6.1 – Map of the study area showing localities where samples were collected for metamorphic study. **308**

Fig. 6.2 – Field relationships between deformation and anatexis in the study area. **311**

Fig. 6.3 – Petrography of garnet-biotite schists. **314**

Fig. 6.4 – Petrography of garnet-biotite schists. **316**

Fig. 6.5 – Photomicrographs of cordierite-biotite schists. **319**

Fig. 6.6 – Photomicrographs of cordierite-biotite schists. **322**

Fig. 6.7 – Photomicrographs of garnet-sillimanite-cordierite schists. **327**

Fig. 6.8 – Chemical profiles across garnet grains. **335**

Fig. 6.9 – Fe, Mg and Ti chemical data of biotites analysed. **342**

Fig. 6.10 – Fe/(Fe + Mg) values of cordierites analysed. **344**

Fig. 6.11 – Chemical data of spinels analysed. **345**

Fig. 6.12 – Chemical data of feldspars analysed. **346**

Fig. 6.13 – Chemical data of orthopyroxene and gedrite amphiboles analysed. **348**

Fig. 6.14 – Phase diagrams for garnet-cordierite-biotite schists. **349**

Fig. 6.15 – Phase diagrams for cordierite-biotite schists. **352**

Fig. 6.16 – Phase diagrams for garnet-sillimanite-cordierite schists. **354**

Fig. 6.17 – Harker plots for pelitic samples. **356**

Fig. 6.18– Petrogenetic grids and possible P-T paths. **361**

Figure 6.19 – Histogram showing the frequency of temperatures calculated using the calibrations of Ferry & Spear (1978), Perchuk & Lavrent'eva (1983), Dasgupta *et al*. (1991) and Bhattacharya *et al*. (1992) at 4 kbar. **365**

Fig. 6.20 – Histograms showing the differences in temperatures (at 4 kbar) calculated using biotite inclusions in garnet compared to matrix biotites, for four calibrations. **367**

Fig. 6.21 – Results of average P-T calculations using THERMOCALC, plotted on a petrogenetic grid, modified after Spear *et al*. (1999) and Jung *et al*. (1998). **372**

Fig. 6.22 – Results of average P-T calculations using THERMOCALC, plotted on a petrogenetic grid, modified after Spear *et al*. (1999) and Jung *et al*. (1998). **374**

Fig. 6.23 – P-T pseudosection for sample CZRL19 in the system NCKFMASH. **378**

Fig. 6.24 – P-T pseudosection for sample LID039 in the system NCKFMASH. **380**

Fig. 6.25 – P-T pseudosection for sample LID039 in the system NCKFMASH. **382**

Fig. 6.26 – P-T pseudosection for sample LKR013 in the system NCKFMASH. **384**

Fig. 6.27 – P-T pseudosection for sample LHA006 in the system NCKFMASH. **386**

Fig. 6.28 – Schematic diagrams illustrating the effects of the inclusion of sillimanite within spinel-cordierite porphyroblasts. **388**

Fig. 6.29 – T-X (Al_2SiO_5) pseudosection for sample LHA006 in the system NCKFMASH at 4 kbar. **390**

Fig. 6.30 – P-T pseudosection for sample CZRL19 in the system NCKFMASHTO. **393**

Fig. 6.31 – P-T pseudosection for sample CZRL19 in the system NCKFMASHTO, with a melt-reintegrated composition. **396**

Fig. 6.32 – Detail of area in melt-reintegrated pseudosection for sample CZRL19 in the system NCKFMASHTO. **398**

Fig. 6.33 – P-T pseudosection for sample LID039 in the system NCKFMASHTO. **400**

Fig. 6.34 – Melt-reintegrated P-T pseudosection for sample LID039 in the system NCKFMASHTO. **402**

Fig. 6.35 – Detail of the peak conditions for the melt-reintegrated P-T pseudosection of sample LID039 in the system NCKFMASHTO. **404**

Fig. 6.36 – P-T pseudosection for sample LKR013 in the system NCKFMASHTO. **406**

Fig. 6.37 – Melt-reintegrated P-T pseudosection for sample LKR013 in the system NCKFMASHTO. **408**

Fig. 6.38 – Peak conditions and P-T paths estimated from phase equilibria modelling, compared to previous P-T estimates for the Central Zone. **410**

Fig. 6.39 – Summary of the P-T-path for the Central Zone. **414**

Fig. 6.40 - Simplified map of peak metamorphic assemblages in the Damara Orogen. **416**

Fig. 7.1 – Schematic illustration of the early tectonic history of the Central Zone. **425**

Fig. 7.2 – Schematic illustration of the collision between the Congo and Kalahari Cratons. **427**

Fig. 7.3 – Schematic illustration of the mid-crust in the Central Zone. **429**

Fig. 7.4 – Following 10 km of exhumation in the Central Zone, a shift in stress directions to subvertical σ3 and subhorizontal σ1 would result in orogen-parallel upright D3 folding. **430**

Fig. 7.5 – Schematic diagram illustrating the relationship between σ_1, dextral movement along the Omaruru & Okahandja Lineaments, and sinistral movement along the NNE-trending Welwitschia Lineament. **432**

Fig. 7.6 – A proposed P-T-t path for the Central Zone. **434**

Fig. 7.7 – Depth vs. temperature diagram illustrating the suggested P-T path for the Central Zone in comparison with the model of England & Thompson (1984), and the average granulite field of Bohlen (1987). **436**

Fig. 7.8 – Map of zones of the Damara Orogen, with major thrusts and lineaments shown. **442**

Fig. 7.9 – Location of the Nama Foreland basin, the Zaris, Witvlei and

Witpütz subbasins, and their relationships to the Damara Orogen in the north and Gariep Orogen in the west. **445**

Fig. 7.10 – Schematic diagram illustrating the evolution of the Damara Orogen, with major events in each of the zones of the orogen. **448**

Fig. 7.11 – Map of Pan-African mobile belts relative to cratonic blocks involved in the assembly of Gondwana. **450**

Fig. 7.12 – Geological map of the Kaoko Belt and northwestern Damara Belt. **452**

Fig. 7.13 – Cratonic blocks and collisional belts of southwestern Gondwana. **457**

Fig. 7.14 – Superfamilies of collisional orogenic belts. **460**

Fig. 7.15 – General tectonic features of the Himalaya. **465**

Fig. 7.16 – Schematic representation of the southern Central Zone as a Himalayan-style ductile channel. **467**

Fig. 7.17 – Simplified map of the Variscan Orogen in southwestern Europe, showing the various zones of the orogen. **471**

Fig. 7.18 – Schematic diagram after Harris et al. (2002) illustrating the relationships between gravitational collapse of thickened crust in the Damara Belt and recumbent folding in the southwestern Central Zone. **477**

Fig. 7.19 – Summary of the timing of events across the Kaoko, Gariep and Damara belts. **480**

LIST OF TABLES

Table 1.1: Comparison of traditionally assigned lithologies in the units of the Damara Supergroup based on Smith, 1964, Jacob, 1974; Nash, 1971 and those assigned by Barnes (1981). **25**

Table 1.2: A summary of previous work on deformation in the Central and Southern Zones. **30**

Table 1.3: Granite classification schemes by various workers on the Central Zone. **32**

Table 1.4: Summary of published U-Pb ages for rocks from the Central Zone. **38**

Table 2.1 – The stratigraphy of the Abbabis Complex (from Brandt, 1987). **49**

Table 2.2 – Stratigraphic sections through the Khan Formation according to Barnes (1981), Berning (1976), Nash (1971) and from this study. **67**

Table 2.3 – The stratigraphy of the Rössing Formation on the eastern margin of the Ida Dome. **80**

Table 4.1 – Classification of granitoids from the Central Zone. **186**

Table 4.2 – Summary of the various intrusions found in the study area. **231**

Table 5.1 – Samples selected for geochronological analysis. **242**

Table 6.1 - Summary of metamorphic conditions estimated for the Central Zone by previous workers. **300**

Table 6.2 – Samples selected for detailed metamorphic study. **308**

Table 6.3: Summary assemblages of samples collected, with comments on the textural features. **332**

Table 6.4 – Summary of geochemical characteristics of pelitic samples. **357**

Table 6.5 – Comparison of temperatures obtained through various calibrations for included biotite and matrix biotite. **366**

Table 6.6 – Average temperatures for each sample for various calibrations, at a range of pressures from 2 to 6 kbar. **369**

Table 6.7 – Results of average P-T calculations using THERMOCALC. **370**

Table 6.8 – Results of average P-T calculations using THERMOCALC for cordierite-biotite schists, comparing calculations run with sillimanite or without sillimanite. **373**

Table 6.9 – Mineral abbreviations used for pseudosection modelling. **377**

Table 7.1 – Heat production values for rocks from this study. **439**

Table 7.2 – Comparison of the major features of Alpine-type and Himalayan-type orogens with the Damara Orogen. **463**

LIST OF ABBREVIATIONS

The following abbreviations (excluding mineral abbreviations) are used in this thesis:

CHUR – Chondritic Uniform Reservoir

DM – Depleted Mantle

Dm – Decametre (10 metres)

dm – decimeter (0.1 metres)

ESB – Extensional Shear Band

HREE: Heavy Rare Earth Elements

L-tectonite – A deformed rock with a dominantly linear penetrative fabric

LA-ICP-MS – Laser Ablation Inductively Coupled Plasma Mass Spectrometry

LREE – Light Rare Earth Elements

Ma – Millions of years ago/before present

MORB – Mid-Ocean Ridge Basalt

MSWD – Meas Square Weighed Deviation

My – Million Years

P-T: Pressure-Temperature

P-T-d-t: Pressure-Temperature-deformation-time

P-T-t: Pressure-Temperature-time

PPL: Plane Polarised Light

S-tectonite – A deformed rock with a dominantly planar penetrative fabric

SHRIMP: Sensitive High Resolution Ion MicroProbe

REE: Rare Earth Elements

XPL: Cross Polarised Light

XRF: X-ray fluorescence

BSE: Backscattered electron

CL: Cathodoluminescence

Examining folded amphibolite dykes in Abbabis Complex gneisses along the Khan River, April 2008.

CHAPTER 1 – INTRODUCTION

The Pan-African Damara Orogen in Namibia comprises two main belts of rocks, the Damara (or Inland) belt, and the Kaoko (or Coastal) belt. These orogenic belts represent the sutures between the Congo, Kalahari and Rio de la Plata Cratons during the assembly of Gondwana (Fig. 1.1). The Kaoko Belt has been the focus of a number of recent studies aimed at understanding its tectonics and metamorphism (e.g. Goscombe *et al.*, 2003a, b; 2004; 2005a,b; Konopásek *et al.*, 2005; 2008), and much of this recent work has included high-precision geochronological results that give the timing of tectonic, metamorphic and magmatic events in this orogen. The timing of the tectonothermal evolution of orogenic belts is crucial to understanding the rates at which orogenic processes occur, and whether there may be a change in the nature of these processes through the lifetime of the orogen. However, in the Damara Belt, there is a paucity of modern high-precision geochronological data that can be used to constrain the timing of metamorphism, magmatism and deformation. This study aims to characterise deformation, metamorphism and magmatism in the high-grade core of the Damara Belt, the Central Zone, and to use high-precision geochronology to constrain the timing of tectonometamorphic events in the Damara Belt.

The Central Zone of the Damara Orogen is a high-temperature, low-pressure tectonometamorphic belt (e.g. Buhn *et al.*, 1995; Nex *et al.*, 2001a) with widespread granitoid magmatism (e.g. Marlow, 1981; McDermott, 1986), and is characterised by polyphase deformation (e.g. Smith, 1965; Sawyer, 1981; Kisters *et al.*, 2004; 2009). This area provides an opportunity to study the high-grade core of an orogenic belt, and to place the results in the context of the Pan-African episode as a whole. Whilst the primary aim of this study is to better constrain the timing of tectonic events in the Central Zone of the Damara Orogen, a secondary aim is to compare the Central Zone (and the Damara Belt as a whole) to other analogous orogens. The study of modern compressional orogens such as the Himalaya (e.g. Godin *et al.*, 2006) or the North American Cordillera (e.g. Coney & Harms, 1984; Hodges & Applegate, 1993) and the

characteristics of other well-studied older orogens such as the Caledonian (e.g. Oliver, 2001) or Grenville (e.g. Davidson, 1998; Gervais *et al.*, 2004), provide useful analogues for the tectonics of ancient orogens such as the Damara. In addition to gathering data on the timing of tectonic events in the Damara Orogen, the orogen should be reviewed in the light of recent thinking on tectonic processes in modern collisional orogens. Current ideas such as ductile channel flow (as has been proposed for the Himalaya – e.g. Beaumont *et al.*, 2001; Grujic *et al.*, 2002) or backarc extension (such as in the North American Cordillera – e.g. Hodges & Applegate, 1993) should be evaluated for applicability to the Central Zone of the Damara Orogen, to test models for the evolution of collisional orogen in general.

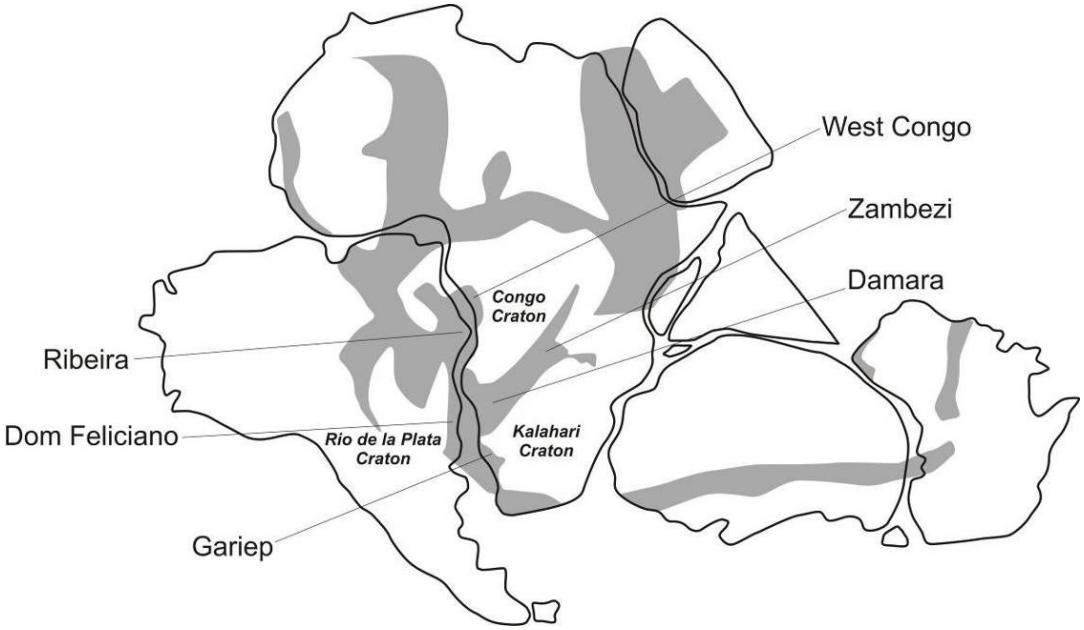

Fig. 1.1 – Distribution of Neoproterozoic (Pan-African) mobile belts (grey) on the world's continents, as they were configured prior to the breakup of the Gondwana Supercontinent. Mobile belts and cratons referred to in the text are labeled. After Unrug (1992).

1.1 An Introduction to the Damara Orogen

The Pan-African orogenic episode (Kennedy, 1964) is a major orogenic event in Earth history, during which the convergence and accretion of a number of cratons and terranes formed numerous orogenic belts which cross-cut the Southern Hemisphere continents (Gray *et al.,* 2008; Fig. 1.1). This orogenic episode occurred between *ca*. 820 and 500 Ma (Unrug, 1992), and the number of tectonometamorphic belts formed across the African continent during this time record a range of metamorphic environments from ultra-high temperature and high pressure (Dasgupta *et al.,* 1994; Sajeev & Osanai, 2004; Sajeev *et al.*, 2007), to high temperature, low pressure (Nex *et al.,* 2001a; Goscombe *et al.,* 2004), and low temperature, high pressure (Kasch, 1983a; John *et al.*, 2003; Goscombe et al., 2004). In Namibia, the Pan-African event gave rise to the Damara Orogen, and a range of Pan-African tectonometamorphic environments are well exposed, making it an ideal area to study the relationship between magmatism, metamorphism, and deformation in orogenesis.

The two branches of the Damara Orogen of Namibia are the Kaoko Belt (or Coastal Branch) and the Damara Belt (or Inland Branch) (Fig. 1.2). The Kaoko Belt trends north-northwest along the Atlantic coastline of Namibia into Angola and the Democratic Republic of the Congo, where it is known as the West Congo Orogen (Alkmim *et al.*, 2006). It is correlated with the Gariep Orogen found in southern Namibia and the Northern Cape Province of South Africa, and some workers consider the Gariep Belt together with the Kaoko Belt to form the Coastal Branch (e.g. Hartnady *et al*., 1985; Stanistreet *et al*., 1991). The Coastal Branch is also correlated with the Ribeira and Dom Feliciano Belts of South America (Fig. 1.2; Alkmim *et al.*, 2006; Gray *et al.*, 2008), and represents the suture between the Congo and Rio de la Plata Cratons (Porada, 1979; Porada *et al.*, 1983; Goscombe *et al.,* 2003a; Gray *et al.,* 2008; Fig. 1.1). The Kaoko Belt has been interpreted as a sinistral transpressional orogen (Goscombe *et al.*, 2003a, b; Goscombe & Gray, 2009), resulting from the collision of the Congo and Rio de la Plata cratons (Prave, 1996), and is made up of a 20-40 km wide orogen core, separated from a magmatic arc to the west by crustal-scale shear zones, and from external domains to the east, where structures verge

away from the orogen core (Goscombe *et al.*, 2005a). Transpressional movement along the shear zones bounding the orogen core has exposed high-grade rocks and granitoids in a half-flower structure (Goscombe *et al.,* 2003a). The timing of collision and of metamorphism in the Kaoko Belt predates events in the Inland Branch (Damara Belt), with most events taking place at 580-550 Ma (Goscombe *et al.*, 2003b), although the Coastal Terrane preserves a record of even earlier metamorphism at 650 Ma (Goscombe *et al.*, 2003b).

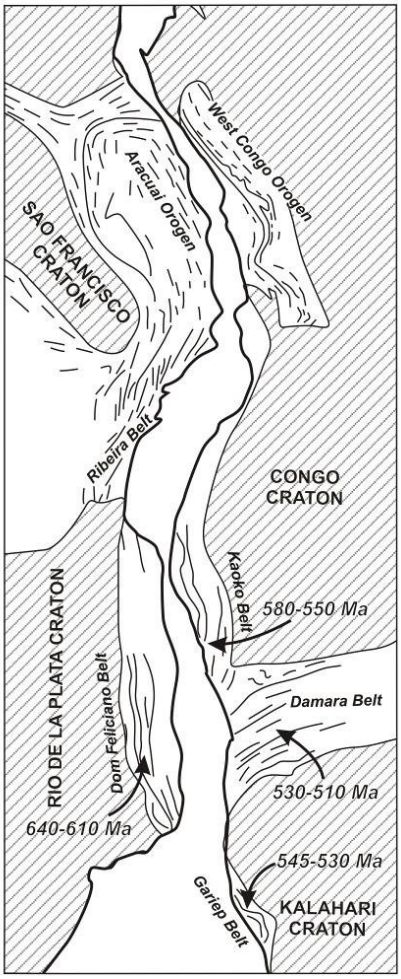

Fig. 1.2 – Cratons involved in Pan-African collision, and the resultant orogenic belts formed during the Pan-African. The approximate ages of orogenic suturing for the various belts are shown. Modified after Gray et al*. (2008).*

The Damara Belt (or Inland Branch) is a NE-trending orogenic belt that formed during the collision of the Kalahari Craton with the Congo Craton. It continues along strike into

Zambia and the Democratic Republic of the Congo, where it is known as the Zambezi Belt (Fig. 1.1). This collision occurred after the suturing of the Congo and Rio de la Plata cratons to form the Kaoko Belt (Prave, 1996; Gray *et al.*, 2008). Prior to the advent of collision in the inland branch, a brief period of subduction below the Congo Craton occurred (Barnes & Sawyer, 1980).

Both the Kaoko Belt (Coastal Branch) and Damara Belt (Inland Branch) are part of the Damara Orogen as a whole. However, the term 'Kaoko Belt' refers specifically to the NNW-trending branch in northwestern Namibia, and the term 'Damara Belt' refers to the NE-trending belt crossing central and northeastern Namibia (e.g. Miller, 2008), and henceforth these terms are used as such.

There has been subdivision of the Damara Belt into a number of zones (Fig. 1.3), based on lithological and structural variation, metamorphic grade, and large-scale geophysical lineaments (Miller, 1983). As with the Kaoko Belt, the Damara Belt has an orogenic core, with high-grade rocks and voluminous granitoids (Miller, 1983; 2008). To the north of this high-grade core, syn-tectonic molasse deposits of the Mulden Group (Figs. 1.3, 1.4; Miller, 2008) have been overthrust by older sediments along northwards-verging thrusts (e.g. the Khorixas-Gaseneirob Thrust – Fig. 1.3; Miller, 2008) that moved material away from the orogen core. To the south, a higher-pressure, lower-temperature accretionary wedge has strongly S- or SE-verging structures (Sawyer, 1981). Even further south from this, sediments sourced from the elevated orogen were deposited in a foreland basin, forming the Nama Group (Figs. 1.3, 1.4; Grotzinger & Miller, 2008). These various tectonic environments of the Damara Belt (Inland Branch) form the basis for the various zones into which it has been divided.

The Damara Belt comprises (from south to north – Miller, 1983): the Southern Foreland and Platform, the Southern Margin Zone, the Southern Zone, the Okahandja Lineament Zone, the Central Zone, the Northern Zone, and the Northern Foreland and Platform (Fig. 1.3). It is the Central Zone of the Damara Belt that forms the focus of this study. The term "Damara Supergroup" (Miller, 2008) is used to describe all lithologies that were deposited

on either the Congo or Kalahari cratonic basement, and which are principally the rock types observed throughout the Damara Orogen. A brief outline of the lithological, structural and metamorphic characteristics of each of these zones is presented below, to set the Central Zone within the context of the entire Damara Orogen.

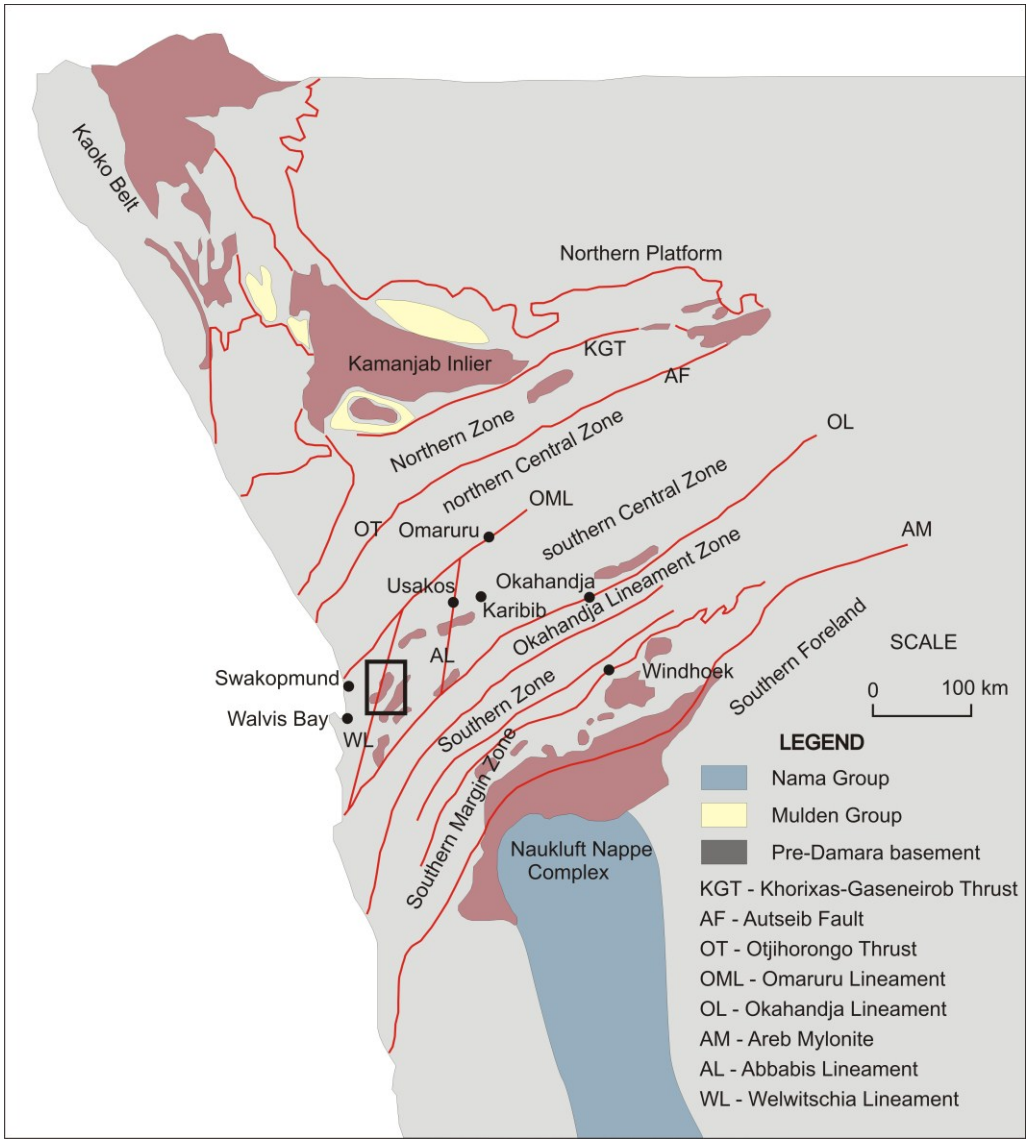

Fig. 1.3 – Map of the Damara Orogen, showing the subdivision of the Damara Belt (Inland Branch) into a number of tectonometamorphic zones, major lineaments, and the location of the study area (indicated by the black rectangle). Note that large areas of pre-Damaran basement are found to the north and south of the orogen (the Kamanjab and Rehoboth Inliers, respectively), and that the Central Zone contains numerous smaller areas of pre-Damaran basement. Also note the position of the Mulden Group molasse and the Nama Group foreland basin. Modified after Miller (1983), Goscombe et al*. (2003a, 2005a) and Grotzinger & Miller (2008).*

1.2 Zones of the Damara Orogen

Each zone in the Damara Orogen is characterised by its own tectonometamorphic and lithological characteristics and is defined by geophysical lineaments (Corner, 2008). These zones represent different metamorphic, magmatic and structural environments within the orogen, and each evolved through a combination of the various processes that were taking place during the collision of the Congo and Kalahari cratons. Hence, these zones differ in their degree and style of deformation, metamorphism and magmatism depending on their context within the orogen. Prior to Pan-African collision, the Khomas Sea existed between the Congo and Kalahari cratons (Stanistreet *et al*., 1991; Prave, 1996). This ocean was formed between these two cratons during the breakup of the Rodinia Supercontinent, with sediment deposition starting at *ca*. 750 Ma (Hoffman *et al.*, 1996; Hoffmann *et al.*, 2004). A number of the major structures separating the zones are thought to have controlled deposition of sediments (De Kock, 2001) during the rifting event which preceded closure and collision. During the opening and growth of this ocean, sediments were deposited in a variety of environments, and it is these sediments that make up the stratigraphy of the Damara Supergroup. This variety of sedimentary environments has resulted in each zone having characteristic lithological and sedimentary characteristics, in addition to their unique structural, metamorphic and magmatic character.

The thick Hakos Group (Fig. 1.4) sedimentary package of the Southern Margin Zone is a passive margin sequence made up of graphitic and quartz-mica schists, marbles, quartzites, conglomerates and amphibolites of the Valgras and Kudis Subgroups (Fig. 1.4; Hoffmann, 1983), that was deposited on the edge of the stable Kalahari Craton, whilst the schists and amphibolites of the Southern Zone are part of a deeper-water sequence, deposited in the rifting Khomas Sea prior to convergence. The Southern Zone, also referred to as the Khomas Zone or Khomas Trough (Sawyer, 1981), contains the Matchless amphibolite member, a narrow, 350 km long belt of MORB-like metabasic rocks, interpreted as representing mid-ocean ridge magmatism (Barnes & Sawyer, 1980; Breitkopf & Maiden, 1986). Lithologically, the Southern Zone is composed almost entirely

of ‘spreading-phase’ metapelitic schists (with minor quartzite, marble and amphibole schist) of the Kuiseb Formation (Fig. 1.4; Miller, 1983), and the overlying active continental margin turbidites of the Hureb Formation (Fig. 1.4). These turbidite sequences, deposited in a deep-water ocean during spreading of the Khomas Sea, were thrust onto the Kalahari Craton during the closure of the Khomas Sea and the collision between the Congo and Kalahari Cratons (Kukla & Stanistreet, 1991).

In the Central Zone, the Kuiseb Formation schists form only the upper part of the Damara Supergroup, and a sequence of rift sediments is preserved at the base of the sequence. These sediments were deposited during the initial rifting which began with the breakup of the Rodinia Supercontinent (Miller, 2008), and precede the deposition of the deep-water sediments that make up the stratigraphy of the Southern Margin Zone and Southern Zone (Miller, 2008). These less mature rift sediments (quartzofeldspathic rocks and calcareous rocks of the Nosib Group; Fig. 1.4) make up the lower portion of the Damara Supergroup in the Central Zone, whilst carbonates, diamictites and pelites of the Swakop Group (Fig. 1.4) form the higher levels of stratigraphy in the Central Zone (e.g. Smith, 1965; Jacob, 1974; Nash, 1971). Contemporaneous with the Swakop Group, a sequence of platform carbonates was deposited on the Congo Craton to the north, forming the Otavi Group (Fig. 1.4) of the Northern Platform (Miller, 2008). Like the Swakop Group, the Otavi Group carbonates are overlain by Kuiseb Formation clastic sediments, and the distinctive Chuos Formation and Ghaub Formation diamictites are found in both the Swakop Group in the Central Zone and the Otavi Group on the Northern Platform (Miller, 2008).

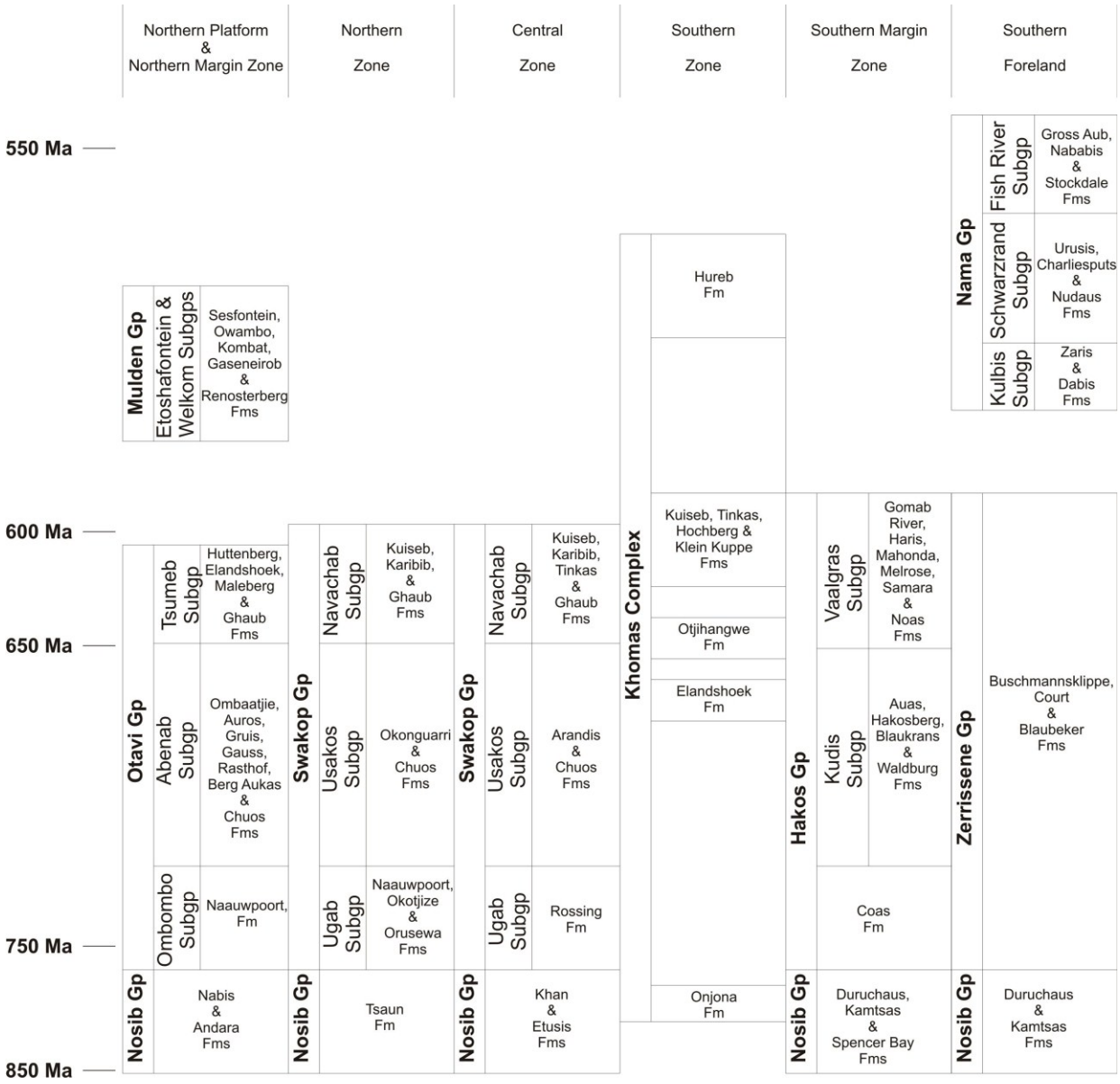

Fig. 1.4 – Lithostratigraphic correlations across the Damara Orogen, with approximate ages of deposition for the Damaran Stratigraphy. Thicknesses are not to scale. Note that the deposition of the Mulden and Nama groups takes place after 600 Ma, and is synchronous with the onset of collision. After Miller (2008).

Rocks of the Southern Margin Zone and Southern Zone were thrust onto the Kalahari Craton during NW-directed subduction below the Congo Craton, and the passive margin and ocean-floor sediments were intensely deformed (Sawyer, 1981; Miller, 2008). Both

the Southern Margin Zone and the Southern Zone contain SSE-verging structures, which are most intense in the Southern Zone, and increase in intensity towards the southern edge of the Southern Zone (Miller, 2008), and along the margin between the two zones, where complex thrust packages of both cover and basement rocks are observed (Hill, 1975; Kasch, 1981). In the Southern Margin Zone less deformed thrust sheets of mainly pre-Damaran basement rocks are observed (Miller, 1983). During this accretion, the ocean-floor rocks of the Southern Zone were subducted below the Central Zone to the north preceding the collision of the Congo and Kalahari Cratons (Miller, 2008), and were subjected to low-temperature, high-pressure metamorphism, with metamorphic assemblages of kyanite-staurolite-garnet-biotite-muscovite-quartz, indicating lower blueschist-facies conditions of *ca*. 9 kbar and *ca*. 550 ˚C (Kasch, 1981; 1983a). Metamorphic conditions in the Southern Margin Zone are lower grade, with greenschist- to amphibolite-facies conditions being reached (Miller, 2008).

In the core of the orogen, the sediments of the Damara Supergroup were subjected to high-temperature, low-pressure metamorphism (e.g. Masberg *et al.*, 1992; Nex *et al.*, 2001a) and intense polyphase deformation (Blaine, 1977; Barnes, 1981; Sawyer, 1981), and were intruded by voluminous granitoids (Marlow, 1981; McDermott, 1986; Nex, 1997). Metamorphic conditions reached upper amphibolite- to lower granulite-facies conditions (Masberg *et al.*, 1992; Nex *et al.*, 2001a; Ward *et al.*, 2008). Numerous domal structures, commonly cored by pre-Damaran basement (Smith, 1965; Jacob *et al.*, 1983; Poli, 1997; Miller, 2008), are found. The Central Zone has been subdivided into a northern Central Zone and a southern Central Zone (Miller, 1983), the latter of which forms the area of focus for this study. This subdivision is based on the generally higher stratigraphic levels exposed in the northern Central Zone (Kuiseb, Karibib and Chuos Formations dominate), with lower stratigraphic levels (including pre-Damaran basement – Figs. 1.3 and 1.5) typically found in the southern Central Zone. Details of the stratigraphy, metamorphism, polyphase deformation and the various granites, all of which characterise the Central Zone, are provided below. An important characteristic of the Central Zone is the existence of numerous exposures of pre-Damaran rocks, typically in the cores of domal structures. Although a number of these domal structures do expose cores of lower

Damara Supergroup metasediments (e.g. Oliver & Kinnaird, 1996) rather than pre-Damaran gneisses, the occurrence of gneiss-cored domes is nonetheless an important characteristic of the Central Zone. Whilst pre-Damaran rocks are also found in the Kamanjab and Rehoboth Inliers (Fig 1.3), the numerous exposures of pre-Damaran rocks and lower Damara Supergroup metasediments indicates that maximum exhumation occurred in the southern Central Zone, as no such rocks are found in the Southern Zone or the northern Central Zone, which expose only rocks of the upper Damara Supergroup.

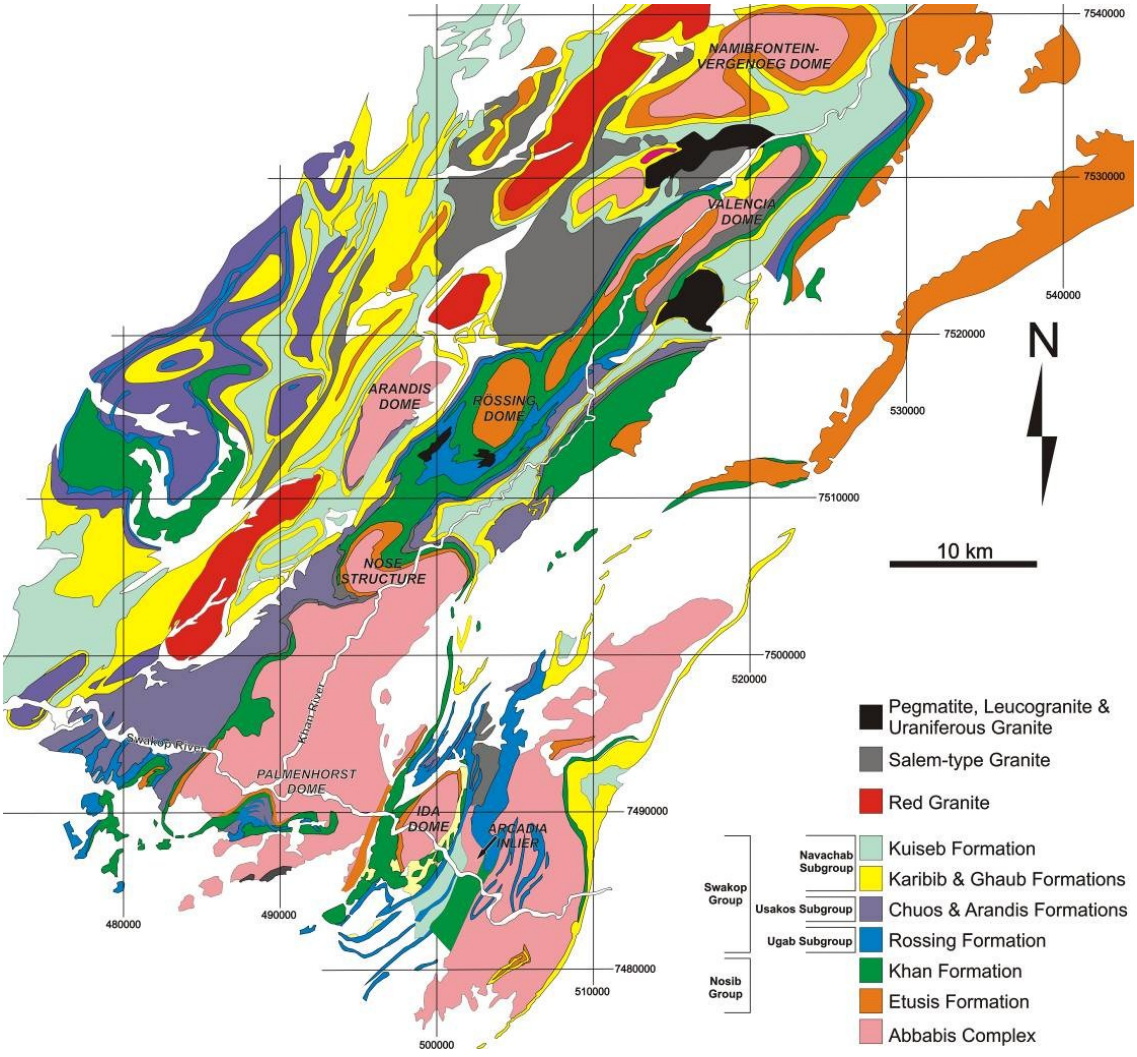

Fig. 1.5 – Detailed geological map of the Central Zone south of the Namibfontein-Vergenoeg Dome. Note the numerous exposures of Abbabis Complex basement, including the Palmenhorst and Ida Domes, and the Arcadia Inlier, around which this study is focused. Coordinates are UTM (WGS84, Zone 33S). After Lehtonen et al. *(1995).*

The boundary between the high-temperature, low-pressure Central Zone and the low-temperature, high-pressure Southern Zone is defined by the Okahandja Lineament or Okahandja Lineament Zone (Figs 1.3, 1.6), which has a similar stratigraphy and structural style to the Southern Zone (Miller, 1983), and is defined by a 0.5-2 km wide belt of isoclinal folding, with almost completely transposed bedding and an axial planar cleavage, subparallel to the main NE-SW foliation trend observed in the Central Zone (S_3; Miller, 1983). The Okahandja Lineament Zone and the Southern Zone grade into one another, with a linear trace of the structural fabric between both zones, but more upright structures, and a single upright schistosity in the Okahandja Lineament Zone (Blaine, 1977; Sawyer, 1981; Downing, 1982). The Okahandja Lineament is a major crustal lineament, and is thought to represent the southern margin of the Congo Craton (Miller, 1979). Both vertical and strike-slip movement occurred along this structure during Pan-African collision – the higher-temperature rocks of the Central Zone were moved vertically upwards relative to the lower-temperature rocks of the Southern Zone (Blaine, 1977), in addition to late-stage sinistral movement along the lineament (Blaine, 1977; Downing & Coward, 1981). It is the boundary between zones of different stratigraphy and tectonic style that is thought to have originally been the locus for block faulting during the rifting that preceded collision, and is the margin of the deep water Karibib to Kuiseb sedimentary depository (see stratigraphy of the Central Zone – Fig. 1.4). The Okahandja Lineament marks the zone where up to 25 km (Corner, 1983) of uplift of the Central Zone relative to the Okahandja Lineament Zone and Southern Zone took place (Miller, 1979). Additionally, the Okahandja Lineament Zone has been intruded by the voluminous granites that make up the large batholith of the Donkerhuk Granite (Sawyer, 1981).

During the climax of collision, uplift in the core of the orogen led to the formation of a foreland basin to the south, where the sediments of the Southern Foreland and Platform were deposited on the stable Kalahari Craton. This southernmost zone of the Damara Orogen is covered largely by the Nama Group (Fig. 1.4; Germs, 1972; Germs & Gresse, 1991), comprising a lower portion of quartzites, shales, conglomerates and minor limestone (the Kuibis and Schwarzrand Subgroups – Fig. 1.4), and an upper portion comprising sandstones, mudstones and conglomerates (the Fish River Subgroup)

deposited in a fluvial or deltaic environment, with sediment sourced from the rising Damara Orogen to the north (Gresse & Germs, 1993; DiBenedetto & Grotzinger, 2005). The Southern Foreland and Platform is relatively unmetamorphosed, and syn-sedimentary deformation along its northern edge resulted in small-scale thrusts (Korn & Martin, 1959) and open to tight, NE-trending, commonly SE-verging folds (Miller, 2008), with a slaty axial-planar cleavage that dies out to the southeast (Ahrendt *et al.*, 1977). The Naukluft Nappe Complex (Figs. 1.3, 1.6) was tectonically emplaced over the Southern Foreland, locally overturning the upper Nama Group (Hartnady, 1978).

To the north of the uplifted orogen, the syn-tectonic molasse sediments (shales, greywackes, sandstones and carbonates) of the Mulden Group were deposited over the platform carbonates of the Otavi Group, to form the Northern Zone (Miller, 2008). Structures in the Northern Zone are controlled by basement inliers, forming an E-W trending northern edge, an E-W structural tend with upright to N-verging folds dominating, and several dome-like interference folds (Miller, 1980; Clifford, 2008). The Northern Zone also includes rocks of the Nosib and Swakop Groups, which have been thrust northwards over the Otavi and Mulden Groups (Miller, 2008).

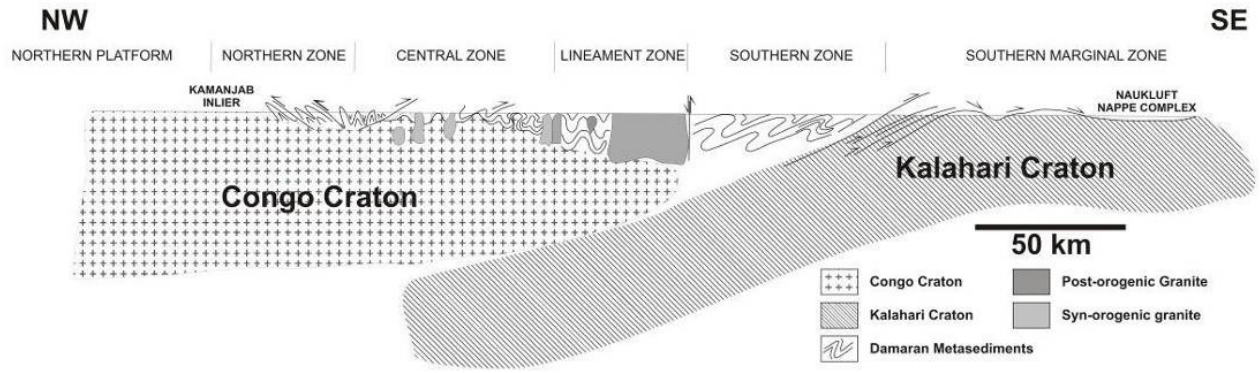

Fig. 1.6 – Cross section through the Damara Orogen, showing the location of various zones of the orogen. Modified after Barnes & Sawyer (1980).

Thus, each of these zones represents the result of an evolving set of processes in an orogenic system, and must be regarded as parts of the system, rather than individually. Although the general relationships between these zones are established, many of the details regarding the timing of events, and the temporal relationships between zones, are unclear. Among other things, questions remain about the relative ages of the high-temperature metamorphism in the Central Zone and the higher-pressure (lower temperature) metamorphism in the Southern Zone, and the source of the large volume of granitoid magma that has intruded the Okahandja Lineament Zone to form the Donkerhuk Granite. A review of previous work and a discussion of the outstanding issues on the Central Zone are presented below.

1.3 A Review of Previous Work on the Central Zone

Within the Central Zone of the Damara Orogen, numerous workers have established the detailed stratigraphy, which is spatially highly variable, as well as characterising the deformation, metamorphism, and magmatism both in terms of peak P-T conditions as well as the P-T-t path for the Central Zone:

1.3.1 The Stratigraphy of the Central Zone

In the Central Zone, the Damara Supergroup is subdivided into two groups, the lower Nosib Group and the upper Swakop Group (Figs. 1.4, 1.7), which unconformably overlie the pre-Damaran basement of the Abbabis Complex (Smith, 1965; Nash, 1973; Jacob, 1974; Brandt, 1985). Within these groups, a diverse range of lithologies is found (Fig. 1.7), including quartzites, marbles, metapelites, diamictites and diopside-plagioclase gneisses. Such a range of lithologies is useful in mapping out large-scale structures in the polydeformed terrane of the Central Zone.

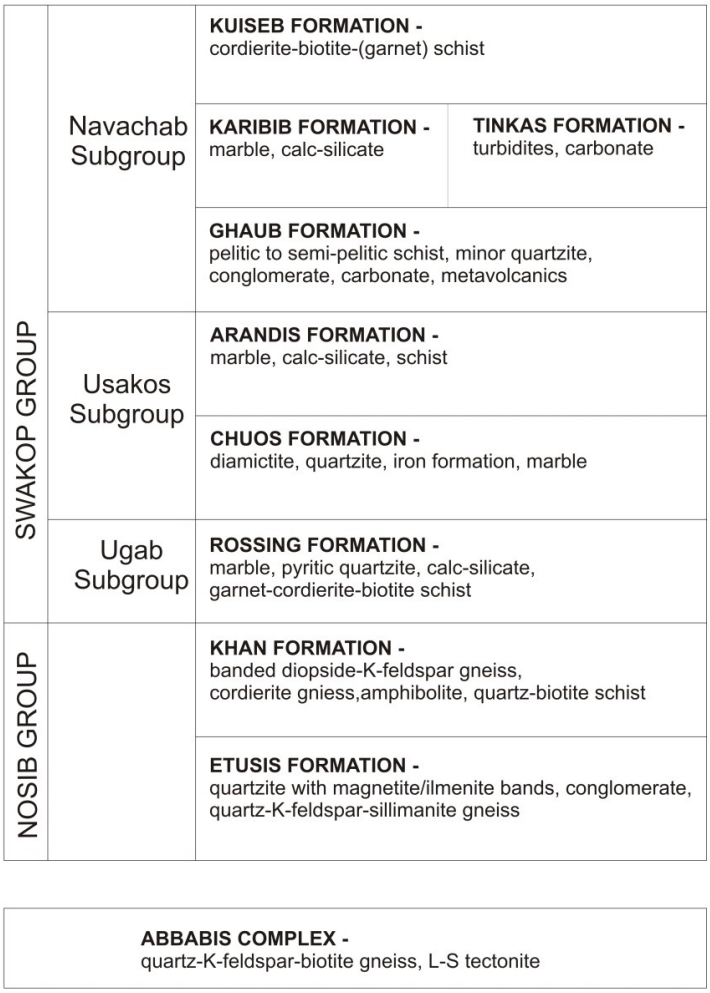

Fig. 1.7 – Stratigraphic column for the study area in the Central Zone. Detailed descriptions of lithologies found in the study area are provided in Chapter 3. Modified after Badenhorst (1992), Lehtonen et al*. (1996), and Miller (2008).*

1.3.1.1 Abbabis Complex

The Abbabis Complex, (or Abbabis Metamorphic Complex – Brandt, 1987) was initially recognised simply as a meta-igneous suite with subordinate metasedimentary and metavolcanic rocks (Smith, 1965). Subsequently it has been subdivided it into the lower Tsawisis Formation, the Noab Formation, and the upper Narubis Granitoid Complex (Brandt, 1987). Although a stratigraphic sequence has been recognised for the Abbabis Complex, detailed mapping of the lithological distribution of these rocks in the vicinity of

the type locality (on Farm Abbabis 70, approximately 100 km northeast of the study area) and field relationships between the various rock types are not well described (the most detailed description is that provided by Brandt, 1987). The Tsawisis Formation is made up of feldspathic quartzite, biotite schist and biotite-sillimanite schist (locally with garnet, muscovite and tourmaline – Brandt, 1987). There are minor amphibole schist, marble and calc-silicate units. The Noab Formation comprises a lower biotite schist (with subordinate calc-silicate) member, a middle quartzite, marble and calc-silicate member, and an upper metavolcanic member. The Narubis Granitoid Complex contains numerous phases of granitic intrusions, which have been deformed to form augen gneisses. These augen gneisses are characteristic of the Abbabis Complex elsewhere in the orogen, where the Tsawisis and Noab Formations are generally not described. Throughout the Abbabis Complex in the Central Zone, amphibolite dykes cut these augen gneisses, and are considered to be the youngest event in the Abbabis Complex, as they are not generally described intruding the Damara Supergroup (Steven, 1994; Barnes, 1981). The occurrence of amphibolites has been used to distinguish the basement from the cover Damara Supergroup (Barnes, 1981), although they have been noted intruding Damaran metasediments at Rössing Mine (P. Nex, Pers. Comm. 2009).

The exact age of the Abbabis Complex is unclear. Although Kröner *et al.* (1991) suggested ages of 1100 to 1040 Ma, older ages of *ca.* 2 Ga have commonly been obtained for Abbabis Complex gneisses and inherited cores in Damaran magmatic zircons (Jacob *et al.*, 1978; Jacob *et al.*, 2000; De Kock *et al.*, 2000; Tack *et al.*, 2002). The younger ages of Kröner *et al.* (1991) may represent a *ca*. 1 Ga Kibaran (Rumvegeri, 1991) overprint on older, *ca*. 2 Ga Eburnian basement from the Congo Craton (Rainaud *et al.*, 2005a), or may represent a northwest extension of the younger Rehoboth terrane of the Kalahari Craton (Kröner *et al.*, 1991). No ages have been published for amphibolites from the Abbabis Complex. Pre-Damaran deformation and metamorphism in the Abbabis Complex is poorly described. Although Smith (1965) and Blaine (1977) noted an obliquity between pre-Damaran fabrics in the Abbabis Complex and fabrics developed in the overlying Damaran metasediments, and Poli (1997) described pre-Damaran structures in the Abbabis Complex at the Nose Structure and Namibfontein-Vergenoeg Dome (Fig. 1.4), little is

known about the nature of this pre-Damaran deformation, as it has largely been overprinted by Damaran fabrics (Smith, 1965; Blaine, 1977). A single sample described by Poli (1997) suggests a higher metamorphic grade in the Abbabis Complex than in the Damara Supergroup cover, but this has not been confirmed by other workers. Additionally, little is known of the nature of the Narubis Granitoid Complex, which makes up most of the volume of Abbabis Complex rocks found in the Central Zone.

1.3.1.2 Nosib Group

This group, at the base of the Damara Supergroup, comprises the Etusis Formation and overlying Khan Formation (Smith, 1965; Nash, 1971; Lehtonen *et al.*, 1995; 1996). The Etusis Formation consists of quartzites, conglomerates and quartzofeldspathic gneisses (arkoses). Cross-bedded quartzites, with foresets marked by layers of heavy minerals (ilmenite and magnetite) are distinctive of the Etusis Formation (Sawyer, 1981). Conglomerates are more common in the lower parts of the Etusis succession (Miller, 2008), and much of the rest of the sequence contains alkali-feldspar rich arkoses, suggesting that much of the Etusis Formation is recrystallised felsic volcanics (Miller, 2008), with wedge-shaped outcrops suggestive of deposition in half-grabens (Miller, 2008). Some cyclicity is observed (Henry, 1992), and there is a lateral heterogeneity in the Etusis Formation; in some areas the entire sequence is apparently missing, whilst elsewhere it reaches over 3000 m in thickness (Henry, 1992). This suggests that there was differential subsidence during deposition of the Etusis Formation, consistent with an extensional tectonic setting. Although conglomerate is present, there is a paucity relative to what might be expected in alluvial fan deposits, which was the depositional environment suggested by De Kock & Botha (1988), and the Etusis Formation most likely represents an extensive, sandy, braided fluvial system (Henry, 1992). Locally it is difficult to distinguish tectonised Etusis Formation from the gneisses of the Abbabis Complex (Narubis Granitoid Complex), as both comprise predominantly quartzofeldspathic lithologies (Sawyer, 1976). Thus, it is possible that in places the Etusis Formation has not been recognised.

In contrast to the coarser underlying Etusis Formation, the Khan Formation comprises a finer-grained facies, with ferromagnesian and calcareous minerals (amphibole and diopside) being common (Sawyer, 1981). Interfingering of the Etusis and Khan Formations has been noted (Jacob, 1974), and there is a stacking of sequences, suggesting cyclical deposition (Henry, 1992). Sedimentary structures produced by current action are present, and it has been suggested that these rocks were deposited in a distal fluvial system characterised by floodplains with ephemeral lakes (Henry, 1992). The presence of significant carbonate (calc-arenites and calc-pelites are common) has been attributed to the introduction of carbonate during diagenesis (Henry, 1992). Volcanic units preserved in the Nosib Group in the Summas Mountains (north of the study area) have been dated at *ca*. 750 Ma (Hoffman *et al.*, 1996) and 752 ± 7 Ma by De Kock *et al.* (2000), suggesting that deposition of Nosib Group rocks began at this time. A date of 765 ± 16 Ma for xenotime overgrowths on zircon (Wall *et al.,* 2008) is also consistent with this age.

1.3.1.3 Swakop Group

The Rössing Formation (Ugab Subgroup) is the lowermost unit of the Swakop Group, and its base is marked by the appearance of the first carbonate unit in the Damara Supergroup (SACS, 1980). The Rössing Formation comprises the largest variety of rock types in the Damara Supergroup of the Central Zone, and is also the thinnest stratigraphic unit. It is made up of quartz-biotite gneiss, quartz-feldspar gneiss, quartzite, quartz-feldspar-biotite-calc-silicate rock, quartz-biotite schist, marble and pelitic schist. It is likely to have been deposited in a shallow marine environment, such as an epicontinental marine platform (Henry, 1992). There are large lateral variations within the Rössing Formation, and it is bounded on its upper limit by an unconformity (Henry, 1992; Nex, 1997). During the deposition of the Swakop Group, tectonic subsidence led to the widening of the fluvial and lacustrine system in which the Nosib Group was deposited, allowing a marine transgression (Stanistreet *et al.*, 1991), and leading to the deposition of the carbonates and siliciclastics of the Rössing Formation.

Unconformably overlying the Rössing Formation is the Chuos Formation (Usakos Subgroup), a distinctive unit within the study area consisting primarily of glacial diamictite (Henry *et al.*, 1986), which renders it easily recognisable even when highly deformed. In addition to the diamictite, the Chuos Formation also contains subsidiary banded ironstone, quartzite and minor marble and pelitic units. It has been correlated with a world-wide Sturtian glacial event at *ca*. 710 Ma by Hoffman (2005). The Arandis Formation (Usakos Subgroup) forms the cap-carbonate to the diamictite of the Chuos Formation, and also includes overlying calc-silicate, metagreywacke and schist.

The Ghaub, Karibib and Kuiseb Formations (Navachab Subgroup) represent a change in sedimentary environment to a passive continental margin (Miller, 1983). The Ghaub Formation represents the world-wide Marinoan glacial event, dated at 635 Ma (Hoffmann *et al.*, 2004), and contains another diamictite unit, although this is poorly developed in the Central Zone, and the Ghaub Formation is usually recognised by isolated dropstones in siliciclastic rocks (Hoffmann *et al.*, 2004) and mafic volcanics. The Karibib Formation consists almost entirely of carbonate (marble and dolomite), and usually forms a thick marble in the study area. The turbidites of the Tinkas Formation (Jacob, 1974) are the lateral equivalents of the Karibib Formation carbonates toward the southeastern edge of the Central Zone. The Kuiseb Formation is a very thick pelitic unit, which also makes up the bulk of the Okahandja Lineament Zone and the Southern Zone, and has been suggested to reach a maximum thickness of 10 000 m in the Khomas Trough (Miller, 1983), although it is likely that it has been tectonically thickened (Kukla, 1990).

1.3.1.4 Stratigraphy used in this study

The Damaran stratigraphic sequence was well established by early workers (Smith, 1965, Jacob, 1974; Nash, 1971), and the depositional environments characterised largely by the seminal work of Henry (1992), as well as by that of De Kock & Botha (1988; 1989) and De Kock (2001). The typical stratigraphy of the Damara Supergroup

(Figs. 1.4, 1.7) has been established by these workers and is used by most subsequent workers (e.g. Brandt, 1986; Marlow, 1981; Smith, 1965; Nash, 1971; Nex, 1997; Blaine, 1977, Mouillac *et al.*, 1985; Lehtonen *et al.*, 1996). An exception, however, occurs in the work of Barnes (1981). Although he adopted a traditional Damaran nomenclature for his sequence (i.e. Etusis, Khan, Rössing, Chuos, Karibib and Kuiseb formations) he differed significantly over the lithologies that make up the stratigraphic units described. As a result, much of the work of Barnes (1981) has been disregarded, and is scarcely mentioned in the literature. However, although his stratigraphy may differ from that of other workers, Barnes (1981) did propose that Damara Supergroup rocks occur either as infolds or as tectonic slivers in the Abbabis Complex, an observation that has potentially important tectonic significance. For this study the traditional stratigraphy of the Damara Supergroup (Figs. 1.4, 1.7) is used. The stratigraphy of the Central Zone comprises a number of distinctive units and packages. Although some of these may be sufficiently distinctive to be recognised as individual units (e.g. the diamictite of the Chuos Formation), care has been taken during this study to identify complete stratigraphic packages, rather than individual units, before conclusively labelling them as Damara Supergroup rocks.

1.3.2 Metamorphism in the Central Zone

Several studies have evaluated the metamorphism and P-T evolution of portions of the Central Zone (Buhn *et al.*, 1995; Masberg *et al.*, 1992; Poli., 1997; Jung *et al.*, 1998; Nex *et al.*, 2001a), and ages for the peak of metamorphism have been suggested (Jung, 2000; Jung & Mezger, 2003a, b), together with several P-T-t paths (Jung, 2000; Nex *et al.*, 2001a; Jung & Mezger 2003a). The majority of workers agree on the peak metamorphic conditions in the Central Zone, which reached the upper amphibolite-facies, although Masberg *et al.* (1992) suggested that granulite-facies grades were reached. One of the characteristic features of the Central Zone is that metamorphic grade increases towards the southwest, along the strike of the orogen (Puhan, 1983), and highest grades are reached in the region around the coastal town of Swakopmund (Fig. 1.8). However, whilst there is general agreement on the peak

metamorphic conditions, there is debate about whether metamorphism was single-phase or polyphase.

There has been argument for both a single metamorphic episode (Jacob, 1974; Masberg *et al.*, 1992; Hoffer, 1977; Blaine, 1977; Puhan, 1979; Haack *et al.*, 1980; Hartmann *et al.*, 1983) and for two metamorphic pulses (Nash, 1971; Barnes, 1981; Horstmann *et al.*, 1990; Nex *et al.*, 2001a). However, all authors agree on peak temperatures of *ca*. 650-750 ˚C, with pressures of *ca*. 4 kbar. Additionally, most workers agree that the peak thermal evolution of the Central Zone proceeded via an isothermal decompression P-T path, with peak pressures having been reached syn-tectonically, followed by a post-tectonic thermal peak (Miller, 1983). Nash (1971) suggested that peak pressures reached 7-8 kbar at *ca*. 700˚C, and Nex *et al.* (2001a) proposed that, following a syn-tectonic drop in pressure from these peak M1 conditions, the Central Zone went through a period of post-tectonic isobaric heating as a result of voluminous granitoid intrusion (M2). The decompression of the Central Zone is recorded as spinel symplectites in the cores of cordierite porphyroblasts (Nex *et al.*, 2001a), whilst the post-tectonic M2 thermal peak resulted in the annealing and recrystallisation of deformed minerals. These conditions are not dissimilar to those calculated by Buhn *et al.* (1995), who suggested a post-tectonic thermal peak, with conditions of 660-700 ˚C at 3.5-4.5 kbar, following a pressure drop from a syn-tectonic peak of 5-6 kbar. An interesting point to note is that the peak P-T conditions suggested by Buhn *et al.* (1995) were obtained for rocks in the Otjosondu area, *ca*. 100 km northeast of Windhoek, and these conditions are within error of the peak conditions estimated by Nex *et al.* (2001a) from the Goanikontes area, which is *ca.* 350 km southwest, along strike, from Otjosondu. These observations appear to contradict the widely held view that metamorphic grade in the Central Zone increases to the southwest (Fig. 1. 8), as proposed by Puhan (1983), and which persists in recent literature (e.g. Goscombe, 2004). It is perhaps not surprising that the Central Zone is not a simple area of gradually increasing metamorphic grade, given that regional geophysical interpretations (Corner, 1983; 2008) show that a number of major crustal-scale lineaments transect the Central Zone (e.g. the Abbabis Lineament Zone

and Welwischia Lineament Zone; Fig. 1.3), along which there may have been vertical movement.

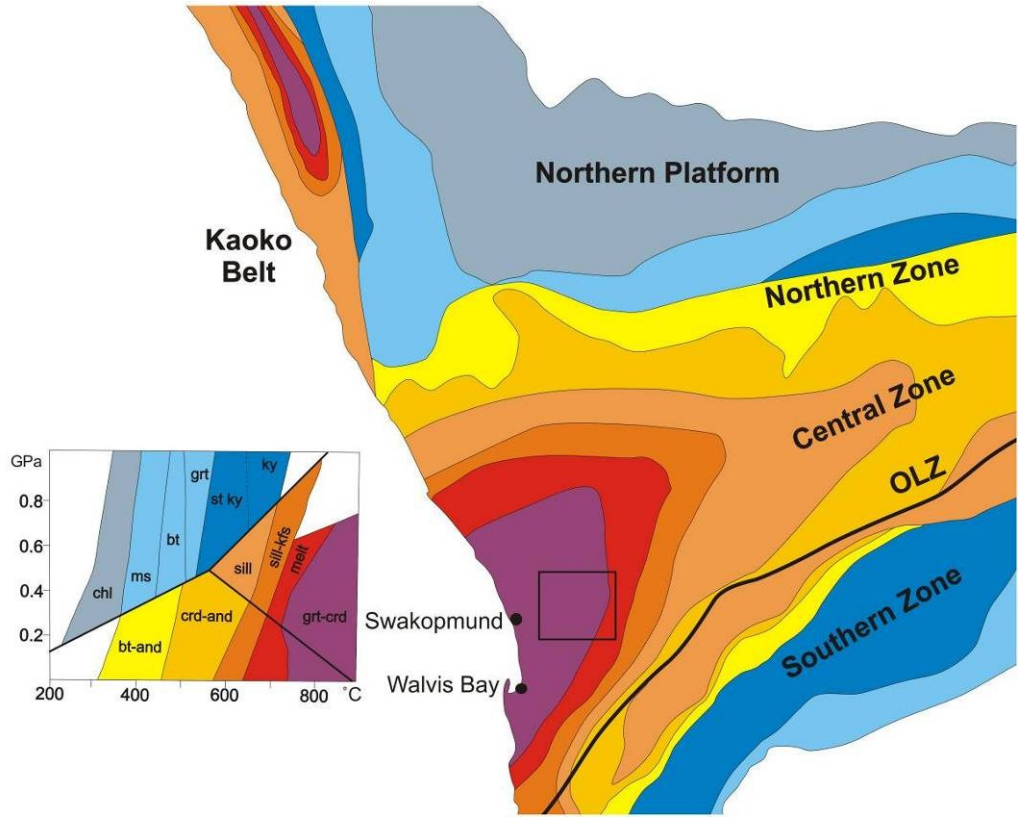

Fig. 1.8 - Simplified map of peak metamorphic assemblages in the Damara Orogen (Modified after Puhan, 1983 and Goscombe, 2004). Note the increase in peak conditions towards the southwest in the Central Zone. The area chosen for this study (shown east of Swakopmund) lies in the highest temperature zones (above the melt-in isograds).

There has only been a single attempt to obtain metamorphic conditions for the Abbabis Complex (Poli, 1997), where garnet-biotite thermometry on a sample of basement gneiss from the Namibfontein-Vergenoeg Dome (Fig. 1.5) gave temperatures and pressures higher than those from samples in the Damara Supergroup. This was interpreted as evidence for a metamorphic gap between the basement and the cover, as a result of orogen-parallel extensional unroofing of the Central Zone along a low-angle detachment during orogen-normal constriction (Poli, 1997; Poli & Oliver, 2001).

1.3.3 Lithological Mapping in the Central Zone

The seminal work of Smith (1965) resulted in 1:100 000 scale mapping of a large portion of the Central Zone (Fig. 1.4), and this work of Smith (1965) remains the basis for the Geological Survey of Namibia Map (Lehtonen *et al.*, 1995), although subsequent studies have brought more detail to this regional mapping. Other larger scale studies were done by Jacob (1974), Sawyer (1981), and Barnes (1981). Barnes (1981) covered an area similar to that mapped by Smith (1965), but on a scale of 1:40 000 and with more detail than the previous work. More detailed mapping on the Nose Structure and Namibfontein-Vergenoeg twin dome was completed by Poli (1997), whose lithological mapping confirms the distribution of lithologies previously published (Lehtonen *et al.*, 1995) and served as the base for his detailed structural study of these two basement domes. The Rössing Dome was mapped in detail by Oliver & Kinnaird (1996), who argued that, rather than having a core of Abbabis Complex gneisses, the Rössing Dome contains a core of Etusis Formation. Despite the detailed mapping of Barnes (1981), who disputed much of the lithological distributions mapped by previous workers, and who identified a deeper level of complexity in his study area, this work has not been included on the most recent Geological Map of the Central Zone. This is most likely because his stratigraphic column was in disagreement with those previously published and his reasons for adopting a different stratigraphy are not supported by other workers. Together with lithological mapping, most of these workers carried out structural studies of the Central Zone. These structural studies rely in part on the mapped distribution of Damara Supergroup lithologies and, thus, it is imperative to the understanding of the structural evolution of the Central Zone that detailed accurate lithological mapping is undertaken. Consequently, it is important to review the mapping of Barnes (1981) and the earlier work of Smith (1965) in the study area.

The area where the mapping of Smith (1965) overlaps with that of Barnes (1981) is the area referred to in this study as the Palmenhorst Dome (Fig. 1.5), along the Khan River, north of its confluence with the Swakop River (Fig. 1.9). The published

geological map from the Geological Survey of Namibia (Lehtonen *et al.*, 1995) is very similar to that of Smith (1965; Fig. 1.9), and shows that the entire Palmenhorst Dome comprises rocks of the Abbabis Complex. The same area, as mapped by Barnes (1981) shows a great deal more complexity, with a much smaller area of Abbabis Complex mapped, and a number of folds and slivers of Nosib Group rocks (Fig. 1.9).

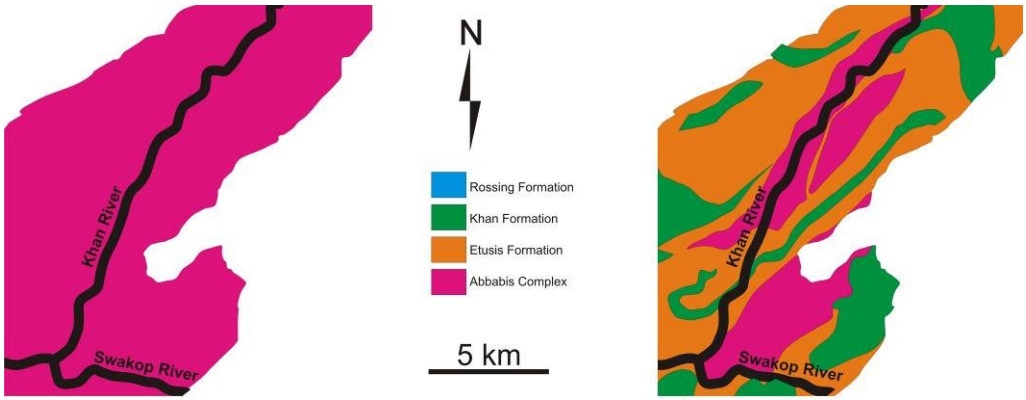

Fig. 1.9 – Distributions of Abbabis Complex and Damaran Sequence rocks in the Palmenhorst Dome along the Khan River. On the left is the lithological distribution as mapped by Smith (1965), whilst on the right the lithological distribution of Barnes (1981) is shown.

Barnes (1981) not only differed from previous work in his lithological distribution and stratigraphic subdivision of the Damara Supergroup (Table 1.1), but also noted a marble unit below the level of the Etusis Formation, in contrast to previous and subsequent work, which recognises no such unit (e.g. Smith, 1965; Brandt, 1987; Lehtonen *et al.*, 1996). Apart from this marble unit, Barnes (1981) identified amphibolite dykes, augen gneisses and metasediments in the basement, lithologies similar to the traditional classification of the Abbabis Complex (Smith, 1965; Brandt, 1987). However, in the Etusis Formation, Barnes (1981) identified amphibolites, Fe-rich gneiss, and augen gneiss, which had not been noted by earlier workers. In addition, marbles and calc-silicates were noted by Barnes (1981) in the Khan Formation, whilst traditional Damaran stratigraphic nomenclature places the lower boundary of the Rössing Formation at the first appearance of marble in the Damara

Supergroup (SACS, 1980). However, despite these differences, the stratigraphic column proposed by Barnes (1981) is on the whole not entirely dissimilar to the stratigraphy previously established, with augen gneisses in the basement, quartzite and conglomerate in the Etusis Formation, green diopside-bearing gneisses in the Khan Formation, marbles and red/pyritic/ferruginous quartzite in the Rössing Formation, diamictite/conglomerate in the Chuos Formation, and a thick marble making up the Karibib Formation. Thus, although his stratigraphy may be more complex than that previously published, there appears to be no obvious reason to conclusively discount his work, and it should be given consideration.

Table 1.1 – Comparison of traditionally assigned lithologies in the units of the Damara Supergroup based on Smith, 1965, Jacob, 1974; Nash, 1971 and those assigned by Barnes (1981).Note that Arandis and Ghaub Formations (Figs 1.4, 1.7) do not occur in the southwestern Central Zone.

Unit	Traditional Lithologies (e.g. Nash, 1971)	Lithologies according to Barnes (1981)
Karibib Formation	Marble	Marble with calc-silicate bands
Chuos Formation	Diamictite, quartzite, iron formation, marble	Conglomerate, migmatised biotite schist
Rossing Formation	Marble, pyritic quartzite, calc-silicate, garnet-cordierite-biotite schist	Quartzites, sillimanite-bearing red quartzites, biotite schist, thin calc-silicate bands, cordierite gneiss, marble
Khan Formation	Banded diopside-K-feldspar gneiss, cordierite gneiss, amphibolite, quartz-biotite schist	Quartz-feldspar-diopside-hornblende gneiss, garnet-bearing gneiss, quartzite, ferruginous sandstone, ferruginous schist, calc-silicate, marble
Etusis Formation	Quartzite with magnetite/ilmenite bands, conglomerate, quartz-K-feldspar-sillimanite gneiss	Biotite gneiss and schist, quartzite, augen gneiss, amphibolite, Fe-rich gneiss, conglomerate, migmatite, sillimanite gneiss, banded gneiss
Pre-Damaran Rocks	Narubis Granitoid Complex, Noab Formation, Tsawisis Formation	Amphibolite dyke suite, augen gneiss, metasedimentary suite

1.3.4 Deformation in the Central Zone

The Central Zone of the Damara Orogen is a polydeformed metamorphic belt with a complex structural history. In addition to deformation of the Damara Supergroup during the Pan-African, a pre-Damaran history has also been recognised in the rocks of the Abbabis Complex (Smith, 1965; Jacob *et al.*, 1983; Poli, 1997), although it has

been noted that the intensity of Damaran deformation makes it difficult to distinguish pre-Damaran from Damaran structures, and fabrics in the Abbabis Complex are generally subconformable to those in the Damara Supergroup (Smith, 1965).

The deformation resulting from Pan-African collision has been the focus of most structural studies in the area and, in particular, the relationship between deformation and the formation of basement-cored domes, characteristic of the Central Zone, has received attention (Smith, 1965; Barnes, 1981; Barnes & Downing, 1979; Jacob *et al.*, 1983; Oliver, 1994, 1995; Nex, 1997; Poli, 1997; Poli & Oliver, 2001). Although a number of detailed structural studies exist on these domes (e.g. Poli, 1997; Jacob *et al.*, 1983), a number of more speculative models for dome formation have also been published (e.g. Kröner, 1984; Barnes & Downing, 1979) that are based on field evidence, but which make use of little or no detailed structural data.

1.3.4.1 Formation of Domes in the southern Central Zone of the Damara Orogen

There have been a number of ideas published regarding the origins of domes of the Central Zone, although not all work published has been based on detailed structural studies. Models published include:

- Interference folding by two sequential events (Smith, 1965; Jacob *et al.*, 1983)
- A single phase of constrictional deformation (Poli, 1997; Poli & Oliver, 2001)
- Metamorphic/extensional core complex development (Oliver, 1994, 1995)
- Diapiric remobilisation of basement into Damara Supergroup cover rocks (Barnes, 1981; Barnes & Downing 1979)
- Magmatic deformation by ballooning granites (Kröner, 1984)
- Mega-scale sheath folding (Coward, 1981)
- Tip-line folds located above blind thrusts (Kisters *et al.*, 2004)

Thus, several different mechanisms have been proposed for the domes of the Central Zone. Barnes (1981) suggested that these mechanisms are not necessarily mutually

exclusive, and that more than one mechanism may have acted to varying degrees on the same domes – for example, diapiric granite intrusion acted together with the superposition of multiple phases of folding. The mechanisms by which domal structures in orogens may be produced are diverse, and each mechanism contains its own characteristic features that may distinguish it from other mechanisms. A more detailed review of dome formation in orogens is provided in Chapter 3. In order to understand the mechanisms for the formation of the domes of the Central Zone, the structural context in which they formed must first be understood, through detailed field-based structural studies, before applying theoretical models to these domes. A number of studies have characterised the deformation history of the Central Zone, the results of which are reviewed below.

1.3.4.2 The Structural History of the Central Zone

A number of workers have studied the deformation in the Central Zone (Table 1.2). Some authors have suggested that fabrics in the Abbabis Complex predate deformation in the Damara Supergroup cover rocks, although details as to the nature of the deformation which formed these fabrics is less clear, because of the intense Damaran deformation overprint that has formed intense fabrics in both the Abbabis Complex and the Damara Supergroup.

It has been suggested that during the Pan-African event between two (Jacob *et al.*, 1983) and five (Blaine, 1977) deformation events affected the Central Zone. Sawyer (1981), who worked in both the Central Zone and the Southern Zone, noted six events. The later events described by most authors are considered to occur only locally, and associated structures are weakly developed (Smith, 1965; Nash, 1971; Barnes, 1981; Coward, 1983). Some workers describe an early regional fabric-forming event, preserved as rootless isoclinal intrafolial folds within the regional fabric, which has been reworked by later events (Barnes, 1981; Coward, 1983; Blaine, 1977). Despite differences in the nature and extent of early and late events described by various workers, two main events are commonly noted. Although the finer details of these two events may not be identical, and

the studies are often in different areas, these two main events can nonetheless be correlated between different authors. They are termed D2 and D3 (in acknowledgement of the early D1 regional fabric-forming event described by some workers), and are summarised as follows:

D2 – this is a strongly non-coaxial, broadly S-verging event that resulted in the formation of tight to isoclinal, gently N-dipping to recumbent folds, with associated S-verging thrusts and shear zones (Smith, 1965; Nash, 1971; Coward, 1983; Blaine, 1977). Boudinage of layers (Smith, 1965), and the formation of a penetrative fabric (Nash, 1971) is associated with this event. During D2, folding of the basement-cover interface occurred, resulting in infolding of the Damara Supergroup into the Abbabis Complex (Barnes, 1981; Jacob *et al.*, 1983).

D3 – this event is more coaxial than D2, forming upright folds with NE-trending axes and moderate plunges (Smith, 1965; Nash, 1971; Blaine, 1977; Barnes, 1981; Coward, 1983; Jacob *et al.*, 1983), although strain intensity is highly variable (Barnes, 1981). This event is responsible for the regional NE-SW fabric observed on aerial photographs and satellite images (Nash, 1971), and it is the fold interference caused by the superposition of this D3 event on the D2 structures that is considered by some workers to have led to the formation of the NE-trending domal structures in the southern Central Zone (Smith, 1965; Jacob *et al.*, 1983).

An exception to the generally held consensus that deformation in the Central Zone consisted of a number of discrete events which overprint one another is the work of Poli (1997). Rather than interpreting structures as belonging to discrete ‘D1’, ‘D2’ or ‘D3’ pulses, he considered deformation as penecontemporaneous across the southern Central Zone and divided the structural history of the Central Zone into two stages (which form part of a progression, rather than being distinct from one another). During the initial stage, unequal constriction led to the formation of gentle domes and the development of a regional fabric by mimetic growth, subparallel to sedimentary bedding. This was followed by domes reaching their maximum amplitude, folding of the regional fabric, the

tightening of earlier developed structures, and the development of heterogeneous strain during the second stage.

The validity of Poli's (1997) model of deformation and associated dome formation in the Central Zone by constriction with perpendicular extension in a transpressional zone relies on whether it is possible to establish if earlier formed structures are re-oriented by later deformation, or if deformation events can be shown to be punctuated by discrete intrusive events. If this is consistently the case, then deformation may be regarded as discrete events rather than a continuum, and a model for dome formation by fold interference would be more appropriate. However, progressive deformation in a uniform stress field may result in the overprinting of earlier structures by later structures (Lister & Williams, 1983), and the three-dimensional nature of strain in transpressional environments can form a spectrum of complex deformation histories (Fossen & Tikoff, 1998). Thus, it would need to be shown (via dating of deformation) that events are temporally discrete, in order to conclusively discount a progressive deformation history for the Central Zone.

Table 1.2 - A summary of previous work on deformation in the Central and Southern Zones.

	Smith (1965)	Nash (1971)	Barnes (1981)	Jacob et al. (1983)	Poli (1997)	Coward (1983)	Blaine (1977)	Sawyer (1981)
								D_{C6} - Small-scale open concentric folds, plunging N to ENE
							D5 - Dextral movement along the northern margin of the Okahandja Lineament	D_{C5} - Close to tight small to medium-scale folds, plunging NNE.
			F4 - Weak deformation producing upright N- or NW-trending, gentle folds. Postdates metamorphism and igneous activity.			F4 - Local N-verging folds.	D4 - zone of metamorphic banding cleavage along the Okahandja Lineament	D_{C4} - Close to tight folds, plunging moderately N or NNE.
D3	Slightly bent D2 folds indicate a possible weak D3	F3 - E-W trending minor mesoscopic folds	F3 - Upright folds, plunging NE. Upright faults in high strain areas, highly variable strain intensity.		Stage 3 - strain is partitioned into mylonites at the basement-cover interface.	F3 - Upright to SE-verging, large folds. Locally sheath folds.	D3 - large, open, upright concentric folds.	D_{C3} - Tight to isoclinal upright folds, plunging gently to N. Subvertical axial planar cleavage or crenulation cleavage.
D2	D2 - refolding of NW-trending folds by NE-SW trending folds & associated dome formation with domes elongate NE-SW.	F2 - NE-SW trending upright folds, formation of the main Damaran structural trend.	F2 - Intense fabric, infolding of the pre-Damaran & Damaran rocks. Development of the regional fabric. Development of recumbent folds and thrusts.	D_{BD2} - upright folds with N-trending axes, formation of some ductile shear zones.	Stage 2 - main dome formation, & formation of L-& S-tectonites. Local progressive tightening of structure.	F2 - Recumbent, SW-verging sheath folds. Syn-tectonic high-grade metamorphism. Early granites and migmatites	D2 - Recumbent folding, low angle thrusting, transposition of earlier fabrics, and development of a macroscopically penetrative cleavage.	D_{C2} - Gently inclined folds with W-dipping axial planes, N-S-trending hinges. Thrusting with N-S strike.
D1	Folds with NW-SE trending axes. Boudinage associated with this event.	F1 - NE-SW trending, tight recumbent folds. Development of a penetrative cleavage.	F1 - Very rare, minor, tight (often rootless & isoclinal) folds. Largely obliterated by F2. Preserved as inclusion trails in M1 porphyroblasts.	D_{BD1} - tight, recumbent, south-verging folds. Folding of the basement-cover interface. Formation of 'ductile shear zones' (extensional shear bands)	Stage 1 - unequal constrictional shortening begins gentle dome formation. Formation of S1 by mimetic growth.	F1 - Early thrusts and folds, probably SW-verging	D1 - Intrafolial, isoclinal folds with angular hinges. Biotite or biotite-fibrolite foliation	D_{C1} - Moderately inclined folds with W-dipping axial planes and NW-trending hinges. Axial planar schistosity
Pre-Damaran	Pre-Damaran deformation noted, but not characterised			D_B - foliation developed (augen gneisses), ductile shears with steeply dipping shear planes.				

1.3.5 Granites of the Central Zone

In addition to mantled gneiss domes, the Central Zone is characterised by large volumes of syn- and post-orogenic granitoids that have been studied and classified by a number of authors (Smith, 1965; Barnes, 1981; Marlow, 1981; Brandt, 1985; McDermott, 1986; McDermott *et al.*, 1996, 2000; Nex & Kinnaird, 1995; Nex, 1997; Nex *et al.*, 2001b). The granitoids are divided into a number of groups, based on their mineralogy and context within the tectonic history of the Central Zone. A review of the granite types in the Central Zone is provided by Miller (2008), who notes that there is a strong stratigraphic control on the location of specific granites, a definite sequence of intrusion of the granites, and that granite intrusions have distinctive forms, depending on granite type. The oldest granitoids noted in the Central Zone are the diorites (with minor associated metagabbros and hornblendites) of the Goas Intrusive Suite (Lehtonen *et al.*, 1995; Miller, 2008), the emplacement of which was followed by the Salem-type granites (Smith, 1965; Jacob, 1974; Sawyer, 1981; Marlow, 1981), red granites (Smith, 1965; Jacob, 1974; Sawyer, 1981; Marlow, 1981), post-tectonic leucogranites (Jacob, 1974; Marlow, 1981; Brandt, 1985), and the post-tectonic alaskites, leucogranites and pegmatites (Marlow, 1981; Brandt, 1985; Nex, 1997). A comparison of the common intrusive rock types in the Central Zone is presented in Table 1.3.

Table 1.3: Granite classification schemes by various workers on the Central Zone.

Smith (1965)	Jacob (1974)	Marlow (1981)	Brandt (1985)	McDermott (1986)
		youngest		
Pegmatite and aplite of various ages with regard to strutural and metamorphic events.		Alaskites - fine-grained to pegmatitic, highly leucogratic, anastomosing or vein-style of intrusion, and may host uranium mineralisation.	Alaskites and leucogranites, which occur as sheets at various stratigraphic levels, and are syn- to post tectonic	Within-plate granitoids - peraluminous to metaluminous, extremely low Ca, variable initial $^{87}Sr/^{86}Sr$, ~1.2 Ga model ages, low $\delta^{18}O$, high Nb, Y, Zr, Hf, REE
Intrusive granite and pegmatitic granite, homogeneous unfoliated leucogratic granite, or very coarse-grained pegmatitic granite.	Post-tectonic granites (Gawib, Achas, Bloedkoppie, Horebis, and Donkerhuk granites. Alaskitic pegmatites are also included.	Leucogranites, which are late- to post-tectonic, typified by the Bloedkoppie and Donkerhuk granites.	Post-tectonic granites, which occur as stocks or plutons (the Gawib, Achas, Bloedkoppie and Kubas intrusives). The large Donkerhuk Granite is the most important of these.	
			Red and grey homogenous syntectonic granites.	Crustal-melt granitoids - peraluminous, high initial $^{87}Sr/^{86}Sr$ (>0.710), ~2.0 Ga model ages, high $\delta^{18}O$, high Rb, low Nb, Y, Zr (high Th, U in some)
Red gneissic granite - red, inhomogeneous banded gneisses with metasedimentary xenoliths, occur in domes and anticlines.	Red granite-gneiss, an inhomogeneous, foliated red granite with metasedimentary xenoliths, occurs in anticlinal structures below the level of the Karibib Formation	Red granites, characterised by large amounts of K-feldspar and small amounts of ferromagnesian minerals. Occur as dykes, domes or lit-par-lit intrusions	Red inhomogeneous syntectonic granites, occurring at the stratigraphic level of Nosib Group or Abbabis Complex rocks.	
Salem gneiss and granite - porphyritic biotite granite, may be leucocratic in places, and confined to synclines.	Salem Granite Suite, comprising non-porphyritic gneissic granite, porphyritic biotite granite and leucogranite, with the non-porphyritic granite the youngest and the leucogranite the youngest.	Salem-type granites, a suite of different generations of granites, granodiorites and adamellites which may be porphyritic.	The Salem granites. These grey, porphyritic granites may be pre-, syn- or post-tectonic.	
Quartz diorite and diorite-gneiss, found locally in synclinal structures occupied by Kuiseb Formation schists (Goas Intrusive Suite)		Gabbros within foliated diorites and granodiorites (Goas Intrusive Suite)		Calc-alkaline diorites - metaluminous, low initial $^{87}Sr/^{86}Sr$ (<0.710), ~1.0-1.4 Ga model ages, variable $\delta^{18}O$, low Rb/Sr, low HFSE
		oldest		

1.3.5.1 The Goas Intrusive Suite

Found in an area south of Karibib (Fig. 1.3), this suite of metagabbroic to dioritic rocks contains a D2 foliation, with xenoliths of Kuiseb Formation schists and metamafics containing a fabric interpreted as D1 (McDermott, 1986; De Kock, 1989, 1991). The Suite occurs as a number of individual diorite plutons (the Okatuwo, Mon Repos, Oamikaub, Gamikaub, Okongava and Palmental diorites – Miller, 2008). The diorites are generally light to dark grey, fine- to medium-grained, foliated and equigranular, and consist of plagioclase + hornblende + biotite + quartz + K-feldspar (Miller, 2008). The intrusions are dated at 564 ± 5 Ma, 546 ± 6 Ma (Jacob *et al.*, 2000), 558 ± 5 Ma (De Kock *et al.*, 2000), and 552 ± 1 Ma (Jung *et al.*, 2002).

1.3.5.2 Salem-type granites

The term “Salem Granite” or “Salem-type Granite” incorporates a suite of granodiorites, granites and adamellites (Blaxland *et al.*, 1979). They are the most abundant of the Damaran intrusive rocks, and commonly form large plutons up to 3400 km^2 in area (Miller, 2008), and are largely monzogranitic in composition (Jacob, 1974; Miller, 2008). They are thought to generally be pre- or syn-D2 in age, but some may be post-D3 (Miller, 2008). Field relationships indicate that earlier intrusions appear more dioritic, and later intrusions more leucocratic, with a sequence from non-porphyritic through porphyritic to leucocratic (Kröner, 1982), and the suite has been subdivided into a non-porphyritic gneissic granite, a porphyritic biotite granite, and a leucogranite (Jacob, 1974). The most abundant rock types in the Salem suite of granites are coarse-grained, porphyritic biotite granites, which commonly occur as large bodies or plutons in synforms between domes (Miller, 2008); these may have a high biotite content and large phenocrysts of perthitic K-feldspar. Although the Salem-type granites are thought to be both pre- or syn-D2 to syn- and post-D3 in age (Miller, 2008), the earlier syn-tectonic variety is more abundant, and contains a clear tectonic fabric. The Salem-type granites have been considered by some authors (Smith, 1965; Miller, 1973; Jacob, 1974; Hoffmann, 1976) to be a product of melting of the Kuiseb Formation schists (xenoliths of Kuiseb schist are commonly found in

various stages of digestion along the margins of Salem-type plutons). However, the Salem Suite occurs locally well below the level of the Karibib Formation, which, together with sharp contacts with the Kuiseb Schist (rather than a diatexite), suggests that another source is likely. Based on Rb-Sr geochronology, Allsopp *et al.* (1983) proposed a "juvenile" source and an anatectic source, which could be reinterpreted as a single juvenile source contaminated by assimilation of Kuiseb Formation material. Johnson *et al.* (2006) published a U-Pb zircon LA-ICP-MS age of 549 ± 11 Ma for a syn-tectonic Salem-type granite that they interpret as dating the main collisional event between the Congo and Kalahari cratons, whilst other published ages are Rb-Sr isochron ages (548 ± 31 Ma and 563 ± 63 Ma – Hawkesworth *et al.*, 1983; 533 ± 22 Ma – Haack *et al.*, 1980; 554 ± 17 Ma – Kröner, 1982; 554 ± 33 Ma – Downing, 1982), which may be considered less reliable, but which nonetheless indicate ages of *ca*. 540-560 Ma, similar to the ages for the Goas Suite. A number of authors have described gradational contacts between Goas Suite diorites and Salem-type granites (Sawyer, 1976; Jacob *et al.*, 2000), suggesting that the Goas Suite and Salem-type granites may be related.

1.3.5.3 Red granites

The term 'red granites' includes a variety of granite types, including red gneissic granites, red homogeneous granites and buff leucocratic granites, which were thought to be contemporaneous and have interrelated origins (Sawyer, 1976; 1981). Although some authors considered the red gneissic granites to be distinct from red homogeneous granites (e.g. Brandt, 1985, 1987), the most recent classification of Miller (2008) follows the proposal of Sawyer (1976; 1981), and groups these granite types together. The red gneissic granites occur predominantly in the southwestern parts of the orogen (Smith, 1965; Brandt, 1985, 1987), suggesting that they occur at lower structural levels, whilst the red homogeneous granites are found more extensively throughout the Central Zone (Brandt, 1985, 1987). Red gneissic granites are restricted to anticlinal structures below the level of the Swakop Group (Smith, 1965; Jacob, 1974; Sawyer, 1976), and are thought to be the product of almost complete in-situ melting of the Etusis Formation arkose or pre-Damaran gneiss (Smith, 1965; Jacob, 1974; Hoffmann, 1976; Miller, 2008). Elsewhere,

more homogeneous red granites also intrude as major dykes and occur as lit-par-lit intrusions (Marlow, 1983), intrude the Salem-type granites (Sawyer, 1981), and are emplaced into Rössing and Chuos Formation lithologies in the Goanikontes area (Nex, 1997). The red granites contain a large percentage of K-feldspar, few ferromagnesian minerals, and generally contain aluminium-rich minerals (sillimanite, garnet, muscovite). Although suggested to be the oldest of the Damaran granitoids (Figs. 13.264, 13.266 in Miller, 2008), the observation of Sawyer (1976; 1981) that they intrude (and thus post-date) the Salem-type Granites, together with the age of 534 ± 7 Ma (Briqueu *et al.*, 1980) for red anatectic granites, suggests that they may be younger than the Goas Intrusive Suite and Salem-type granites.

1.3.5.4 Homogeneous syn-tectonic granites

The red and grey homogeneous syn-tectonic granites (Brandt, 1985), which have a well-developed tectonic foliation, are common throughout the Central Zone. Similar granites have been noted by Nex (1997) and Nex *et al.* (2001b), who observed that homogeneous red granites are syenogranites, similar to equigranular basement-hosted granites, with a suggested age of 534 Ma (Briqueu *et al.*, 1980; Nex *et al.*, 2001b). Homogeneous grey granites, however, are monzogranites, and are considered to be younger than the red granites, at 517 Ma (Briqueu *et al.*, 1980; Nex *et al.*, 2001b). It is thus possible that the homogeneous syn-tectonic red granites are part of the red granites, as suggested by Sawyer (1976, 1981), and are distinct from the homogeneous grey granites. The 517 Ma homogeneous grey granites of Nex *et al.* (2001b) are similar in age to a group of non-porphyritic granites and leucogranites dated at 514 ± 22 Ma (Haack *et al.*, 1980). Although these non-porphyritic granites and leucogranites are a voluminously minor granite type in the southern Central Zone, in the northern Central Zone they are more important, and are seen to be syn-D2 (Klein, 1980; Haack *et al.*, 1980), with both D2 and D3 fabrics developed (Miller, 2008). Their age of 514 Ma suggests a younger age for D2 in the northern Central Zone than the 555 Ma age (Miller, 2008) suggested for D2 the southern Central Zone. However, a grey granite from the Ida Dome has been dated at 542 Ma (Tack *et al.*, 2002), leading to some ambiguity regarding the ages of these grey granites.

1.3.5.5 Post-tectonic leucogranites

Post-tectonic leucogranites form a number of small dykes and plugs throughout the Central Zone (Otjua, Kubas, Stinkbank and Elba Granites (De Kock, 1989; Brandt, 1985; Marlow, 1983), as well as two major batholiths, the Donkerhuk and Bloedkoppie Granites. These leucogranites are commonly garnetiferous and muscovite-bearing, and are likely to be the result of anatexis of sedimentary material, although some bodies are suggested to be residual melts of the Salem-type granites (Marlow, 1983).

1.3.5.6 Post-tectonic alaskites, leucogranites and pegmatites

In addition to the larger granite bodies, there are a number of locally pegmatitic granite sheets present throughout the study area and elsewhere in the Central Zone. In the area around Goanikontes Farm, these granite sheets have been classified into six groups (Nex & Kinnaird, 1995; Nex, 1997). Two of these groups (locally termed alaskites) contain significant U-mineralisation, and similar granite (alaskite) sheets are mined for uranium at Rössing Mine. The classification into groups is based on field characteristics and structural setting, colour, grain size and texture, and geochemistry from a study in the area surrounding the Goanikontes Farm along the lower Swakop River. The six types defined in the Goanikontes area by Nex & Kinnaird (1995) and Nex (1997) were labeled A-F, in a chronological sequence:

A-type: These are narrow, fine-grained leucogranites with a weak foliation. They are boudinaged and folded, occur infrequently, and are restricted to a high-strain zone near the basement-cover interface along the Swakop River near Goanikontes.

B-type: These are white, fine-grained to pegmatitic, weakly foliated, boudinaged and folded, and may contain garnet and/or tourmaline. They are more common outside the high strain zone.

C-type: These are leucogranites with variable grain size, composed of two feldspars with interstitial quartz and accessory magnetite, ilmenite and tourmaline. They are locally boudinaged and are preferentially emplaced into the flexures of D2 age (The deformation scheme of Nex, 1997 is similar to that of previous workers described above). They are the dominant leucogranite in the area, occurring throughout the Damara Supergroup and the high-strain zone.

D- and E- types: These are grouped together as they both host uranium mineralisation, and comprise white feldspar with smoky quartz. Type E leucogranites are distinguished by their characteristic reddened oxidation haloes (Corner & Henthorn, 1978). It is possible that type D and E leucogranites are the same granite type, with type E sheet bodies having been extensively oxidised by late fluids, which remobilised the uranium within the granites (P. Nex, Pers. Comm., 2008).

F-type: These are the youngest of the leucogranites, and are notably red in colour. They are coarse grained, and occur as tabular, parallel-sided bodies comprising coarse pink feldspar, milky quartz and accessory biotite, magnetite and/or ilmenite.

1.3.6 Geochronology and the timing of events in the Central Zone

Geochronological results from the Central Zone are largely restricted to ages obtained using the Rb-Sr method (Marlow, 1983; Allsopp *et al.*, 1983, McDermott, 1986; Haack *et al.*, 1982; 1988), and there are few reliable U-Pb zircon or monazite ages available. A summary of ages for the Central Zone can be found in Miller (2008), and a list of granite emplacement ages and metamorphic ages is presented in Table 1. 4.

Table 1.4 - Summary of published U-Pb ages for rocks from the Central Zone.

Rock	Age (Ma)	Method	Reference
Goas Intrusive Suite diorites and related rocks			
Goas granite	580 ± 30	U-Pb discordia	Allsop *et al*. (1983)
Mon Repos quartz diorite	564 ± 5	U-Pb single zircon	Jacob *et al*. (2000)
Palmental diorite	564 ± 55	Rb-Sr whole rock	McDermott (1986)
Okangava diorite	558 ± 8	U-Pb single zircon	De Kock *et al*. (2000)
Mon Repos quartz diorite	546 ± 6	U-Pb single zircon	Jacob *et al*. (2000)
Rotekuppe granite	543 ± 5	U-Pb single zircon	Jacob *et al*. (2000)
Rotekuppe granite	539 ± 6	U-Pb single zircon	Jacob *et al*. (2000)
Okangava diorite	539 ± 10	U-Pb titanite	Jung *et al*. (2002)
Goas granite	535 ± 2	U-Pb discordia	Allsop *et al*. (1983)
Salem-type granites			
Salem-type granite	601± 79	Rb-Sr whole rock	Marlow (1983)
Salem-type granite	563 ± 63	Rb-Sr whole rock	Hawkesworth *et al*. (1983)
Salem-type granite	554 ± 17	Rb-Sr whole rock	Kroner (1982)
Salem-type granite	554 ± 33	Rb-Sr whole rock	Downing (1982)
Red granites			
Goanikontes red granite	534 ± 7	U-Pb zircon/monazite discordia	Briquet *et al*. (1980)
Leucogranites and grey granites			
Stinkbank leucogranite	549 ± 11	U-Pb zircon	Johnson *et al*. (2006)
Ida Dome grey granite	542 ± 6	U-Pb single zircon	Tack *et al*. (2002)
Ida Dome granite	526 ± 17	U-Pb single zircon	Tack *et al*. (2002)
Baukwab leucogranite	525.5 ± 1	Pb-Pb zircon evaporation	Jung *et al*. (1998)
Oetmoed granite	526-516	U-Pb monazite, titanite	Jung *et al*. (2000)
Alaskites and mineralised veins			
Goanikontes uraniferous alaskite	508 ± 2	Concordant monazite	Briquet *et al*. (1980)
Goanikontes uraniferous alaskite	509 ± 1	Concordant uraninite	Briquet *et al*. (1980)
Navachab lamprophyre	496 ± 6	U-Pb single titanites	Jacob *et al*. (2000)
Navachab Au veins	500 ± 10	U-Pb single titanites	Jacob *et al*. (2000)
Navachab Au veins	494 ± 8	U-Pb single titanites	Jacob *et al*. (2000)
Metamorphic ages			
Migmatites and granites	540-530	Sm-Nd garnet-whole rock	Jung & Mezger (2003a)
Unmigmatised metapelite	525-504	U-Pb monazite, Sm-Nd garnet	Jung & Mezger (2003a)
Migmatite	518 ± 3	Sm-Nd garnet	Jung & Mezger (2003a)
Anatectic granites	509-515	U-Pb monazite, Sm-Nd garnet	Jung & Mezger (2003a)

The oldest reliable ages for granitoids in the Central Zone are those from the Goas Intrusive Suite, a group of diorites (with minor metagabbros) found south of Karibib, which have been dated at between *ca*. 550 and 560 Ma (Jacob *et al*., 2000; De Kock *et al.*, 2000). Although these are the oldest ages obtained for granitoids, the red gneissic granites are considered by Miller (2008 – Figs. 13.264, 13.266) to predate the Goas Suite. These diorites have also been dated at similar ages of 540-560 Ma using the Rb-Sr method (Allsopp *et al.*, 1983; McDermott, 1986; Miller & Burger, 1983; Hawkesworth *et al.*, 1983;

Haack *et al.*, 1980), although these dates have larger errors, and some ages appear unreliable (e.g. 720 ± 77 Ma for the Goas Granite; Allsopp *et al.*, 1983). Similar, 540-560 Ma, ages have been obtained using Rb-Sr for the Salem-type granites (Marlow, 1983; Hawkesworth *et al.*, 1983; Kröner, 1982; Downing, 1982), and Johnson *et al*. (2006) obtained a U-Pb zircon age of 549 ± 11 Ma for the Salem-type Stinkbank leucogranite. Grey granite and 'alaskite' from the Ida Dome have been dated at 542 ± 6 Ma (U-Pb zircon; Tack *et al.*, 2002) and 542 ± 33 Ma (Rb-Sr; Marlow, 1983), although grey granites from Goanikontes give a 517 ± 7 Ma (Briqueu *et al.*, 1980; Nex *et al.*, 2001b). The only age for a red granite is an anatectic red granite from Goanikontes, which has a U-Pb age of 534 ± 7 Ma (Briqueu *et al.*, 1980). A pegmatite from the Khan Mine has been dated at 518 ± 2 Ma (Kinny *et al*., 1994), and uraniferous alaskites from Goanikontes have been dated at 508 ± 2 Ma (Briqueu *et al.*, 1980). Pegmatites, Au-bearing veins and a lamprophyre have been dated at 494-500 Ma (Haack *et al*., 1980; Jacob *et al.*, 2000). Thus, it appears that magmatism in the Central Zone began at *ca.* 560 Ma with the intrusion of diorites and metagabbros, and a range of intrusions were emplaced until *ca.* 500 Ma, with uraniferous alaskites, pegmatites and Au-bearing veins forming the last stages of magmatism in the Central Zone.

The basement of the Abbabis Complex has been dated at between *ca*. 1 and 2 Ga. Jacob *et al.* (1978) obtained a U-Pb age of 1925 +330/-280 Ma. This ca. 2 Ga age was refined by Kröner *et al.* (1991) (2014 ± 39 Ma and 2093 ± 51 Ma using U-Pb) and by Tack *et al.* (2002) (2038 ± 5 Ma), although Kröner *et al.* (1991) also obtained ages of 1040-1100 Ma for Abbabis Complex gneisses, suggesting that two pre-Damaran events may be preserved in the Abbabis Complex. Many Damaran granitoids contain inherited zircons with similar 2 Ga ages (e.g. Jacob *et al.*, 2000). Model ages for a range of Damaran granitoids have been obtained using Nd isotopes by McDermott (1986) and give a range between 1.13 Ga and 2.57 Ga, and Damaran metasediments give similar Nd model ages of 1.19 Ga to 2.39 Ga (McDermott *et al.*, 1989). There is a paucity of model ages for Abbabis Complex gneisses, which are higher, at up to 2.88 Ga (McDermott, 1986; McDermott *et al.*, 1989). The age of peak M2 metamorphism in the Central Zone has been suggested by Miller (2008) as being constrained by the 534 ± 7 Ma anatectic red granite from Goanikontes (Briqueu *et al.*,

1980), with M1 suggested to have been earlier than 565 Ma (Miller, 2008). However, U-Pb monazite and Sm-Nd garnet ages of metamorphic rocks obtained by Jung (2000) and Jung & Mezger (2003a, b) indicate peak conditions were reached later, at between 525 and 504 Ma, with anatectic granites generated during this event dated at between 515 and 509 Ma (Jung & Mezger 2003a). Older ages of 540-530 Ma (Jung, 2000; Jung & Mezger, 2003a, b) suggest that the 534 Ma age suggested for M2 by Miller (2008) may represent an earlier, rather than a later, phase of metamorphism. Nex *et al.* (2001a) constrained peak temperatures (of the regional heating event, namely M2) at between 534 and 508 Ma, based on the ages of Briqueu *et al.* (1980), with a possible earlier, higher pressure, M1 event at 571 ± 64 Ma (Kröner *et al.*, 1991).

The timing of D2 deformation is suggested by Miller (2008) to be about 555 Ma in age. The post-D3 Rotekuppe Granite near Karibib gives a 539 ± 6 Ma age (Jacob *et al.*, 2000) and ages of between 542 and 526 Ma for 'post-tectonic' granites from the Ida Dome (Tack *et al.*, 2002), led Miller (2008) to suggest that D3 is about 542 Ma in age. However, these granites, although unsheared, do contain a weak fabric (Tack & Bowden, 1999), and the 534 Ma red granite from Goanikontes is also noted to be foliated (Briqueu *et al.,*1980), raising doubt as to whether these granites are truly post-tectonic. Post-tectonic uraniferous alaskites dated at 508 Ma (Briqueu *et al.*, 1980) may be a better constraint on the end of D3 deformation.

1.4 Aims of the Project

This project was initiated in order to gain an understanding of the processes occurring in the core of the Damara Orogen and, more generally, to contribute to an understanding of continent-continent collision. This project aims to integrate mapping, metamorphic and granite petrological studies, and geochronology over a portion of the southern Central Zone, in order to gain an holistic understanding of the tectonics of the Central Zone of the Damara Orogen.

The aim is to address the following questions specific to the Damara Orogen:

- What is the origin of the basement-cored domes in the Central Zone? By what mechanism did they form?
- What is the sequence of deformation in the Central Zone and is there a sequence of overprinting deformation events, or was deformation continuous?
- What is the metamorphic P-T-t evolution of the Central Zone, and the relationship to deformation and dome formation? Did the rocks of the Central Zone experience multiple metamorphic events or a continuous metamorphic evolution?
- What is the absolute timing of deformation, metamorphism and granite emplacement in the Central Zone?
- What are the sources of the granites in the Central Zone?
- What is the relationship between deformation and granite emplacement in the Central Zone?

In addition to the above questions, which are specific to the Damara Orogen, this study aims to contribute to the resolution of a number of issues pertaining to collisional orogens in general. Such questions include:

- In the core zone of a collisional orogen, how are rocks heated? What is the heat source, and what is the metamorphic evolution of the rocks?
- How are high-grade rocks exhumed in the cores of orogen? Is the exhumation of these high-grade rocks linked to the formation of gneiss domes?
- Does deformation in the core of high grade orogens take place as a series of sequential overprinting events, or is it a progressive evolution.
- What is the source of granitoids in high-grade orogenic belts? Are they locally derived or do they come from a deeper source?
- Over what timescale does a collisional orogen develop?

These primary questions are not only specific to the Damara Orogen, but are some of the important questions which need to be answered when studying collisional orogens in general (Brown, 1994; McQuarrie *et al.*, 2008). By answering them for the Damara Orogen, a well-exposed collisional orogen with a high-grade core, analogies may be made to similar collisional orogens elsewhere.

In the succeeding chapters, the results of an integrated structural, metamorphic and geochronological study of a specific area of the southern Central Zone are presented. By using these results together with the results of other studies of the Central Zone, the questions outlined above will be answered. A variety of techniques have been used, including structural and lithological mapping, field, petrographic and geochronological studies of intrusive rock types, SHRIMP U-Pb geochronology, petrographic studies of metamorphic rocks and phase equilibria modeling. Each chapter addresses a specific aspect of the study.

1.5 Location of the Study Area

The study area is located along the Khan and Swakop Rivers, in the National West Coast Recreation Area and the Namib-Naukluft National Park, Namibia. The area is approximately 200 km^2 in size, extending from the confluence of the Khan and Swakop Rivers northeast along the Khan River to the Blauer Heinrich mountain (reaching the southern border of the area mapped by Poli (1997), and extending east from the confluence along the Khan River to *ca*. 5 km east of the Ida Dome (Figs. 1.3, 1.5). The area was chosen because of the excellent exposure in the gorges formed by the Khan and Swakop rivers, because it lies adjacent to areas studied by Nex (1997) and Poli (1997), and because it includes two areas of Abbabis Complex rocks as shown on the 1:250 000 Geological Survey of Namibia map (Lehtonen *et al*., 1995), namely the Palmenhorst Dome and the Ida Dome, which appear distinctly different both in size and in outcrop pattern. The Palmenhorst Dome is an area where complex folding of the basement-cover interface has previously been suggested (Barnes, 1981), whilst the Ida Dome appears to be a far more typical “domal structure” with an ovoid, NE-SW trending outcrop pattern.

1.6 Approach and Thesis Outline

This study aims to understand the tectonometamorphic evolution of the Central Zone of the Damara Orogen through the integration of structural, metamorphic and geochronological studies. The results of lithological mapping are presented in Chapter 2, which also outlines in detail the stratigraphy found in the study area. This lithological mapping forms the basis for the detailed structural study that follows in Chapter 3, and Chapter 2 addresses the lithological distribution of the various Damaran metasediments and pre-Damaran gneisses and whether this differs from mapping by previous workers. Chapter 3 describes the results of a detailed structural study of the Ida and Palmenhorst domes, in order to evaluate various histories proposed for the deformation history of the Central Zone (see section 1.3.4.2) – i.e., was deformation progressive and penecontemporaneous across the study area (the models of Poli, 1997 and Poli & Oliver, 2001), or can temporally discrete deformation events be identified (e.g. Smith; 1965; Jacob *et al.*, 1983)? This structural study incorporates the results of lithological mapping together with detailed structural measurements of large and small-scale features resulting from Damaran deformation. In addition to establishing the deformation history, Chapter 3 also evaluates the various models for dome formation proposed for the Central Zone (see section 1.3.4.1) in light of the detailed structural work presented. However, the identification of temporally discrete deformation events relies not only on whether deformation events appear to overprint one another, but also on whether they can be shown to be truly temporally discrete. In order to do this, the relationships between deformation and intrusions in the study area have been investigated, and the variety of intrusions described in detail. The field relationships, petrography and geochemistry of the intrusions are presented in Chapter 4, and these various intrusions are evaluated in the light of the various classification schemes presented for the Central Zone (e.g. Brandt, 1985; McDermott, 1986; Nex, 1997). The identification of intrusive rock types with specific recogniseable characteristics and distinct relationships with deformation structures has enabled these intrusions and, hence, the deformation events with which they are associated, to be dated using U-Pb SHRIMP dating of zircon, monazite and titanite from these intrusions. The results of this dating are presented in Chapter 5, in

addition to the results of Lu-Hf and O-isotopic studies of selected granitoids and pre-Damaran gneisses. The geochronological results for the various granitoids have enabled the timing of deformation to be constrained, and this is discussed in the light of the established views regarding the ages of deformation for the Central Zone (e.g. Kisters *et al.*, 2004; Miller, 2008). In addition to dating intrusions, an attempt has also been made in Chapter 5 to constrain the ages of high-grade metamorphism in the Central Zone – anatectic granites and leucosomes generated through partial melting as the result of this metamorphism have also been dated using U-Pb SHRIMP dating on zircon and monazite, and these results are compared with the established views regarding the timing of metamorphism in the Central Zone (Miller, 2008), as well as with other recent dating of high-grade metamorphism in the Central Zone (e.g. Jung, 2000; Jung & Mezger, 2003a). Chapter 6 further expands on the high-grade metamorphism in the Central Zone, where the results of a detailed study of this metamorphism are presented, and compared with other metamorphic studies (e.g. Masberg *et al.*, 1992; Nex *et al.*, 2001a; Ward *et al.*, 2008), and previous ideas regarding the P-T-t evolution of the Central Zone (e.g. Jung, 2000; Nex *et al.*, 2001a). The metamorphic conditions for the study area are evaluated initially using traditional thermobarometric methods, as have been previously applied to the Central Zone (e.g. Nash, 1971; Poli, 1997), as well as using mineral equilibria modeling with the programme THERMOCALC (Powell & Holland, 1988). Discrepancies between the two approaches, and implications for the thermal history of the Central Zone, are also discussed in Chapter 6. Finally, Chapter 7 evaluates the results of the lithological mapping, structural mapping, granite petrology, geochronology and metamorphic petrology, and discusses these new results in the light of previous work on the Central Zone, as well in the context of the other zones of the orogen, in order to place the processes taking place in the Central Zone during collision within the overall evolution of the Damara Orogen. Ideas regarding the tectonometamorphic evolution of the Central Zone and Damara Orogen are also evaluated in the light of current thinking on the evolution of collisional orogens in general, and the processes operating during continent-continent collision.

CHAPTER 2 - STRATIGRAPHY

In an investigation into the structural history and overall architecture of the Central Zone, much of the interpretation of the large-scale structural features is dependent on accurate mapping of the distribution of Damara Supergroup and Abbabis Complex lithologies. The stratigraphy of the Damara Supergroup includes a number of distinctive lithological units and sequences, which can be unequivocally identified and correlated across the study area, forming the basic framework for more detailed structural work. This chapter aims to characterise the lithologies of the study area, and describe their distribution in the Ida and Palmenhorst domes (Fig. 1.5). Details of the field characteristics, mineralogy, and regional distribution of lithologies found in the Ida and Palmenhorst Domes during the course of this study are presented here. This includes the results of lithological mapping of the Ida and Palmenhorst Domes, and the large-scale structure of these domes, which is elucidated by this lithological mapping, and which is examined in more detail in Chapter 3. The results of mapping of the study area are shown in Fig. 2.1. This chapter does not aim to reproduce the detailed lithological and sedimentological studies that have been carried out in the Central Zone (e.g. Martin, 1965; De Kock, 1989; Henry, 1992), although any significant differences in the lithostratigraphy have been noted, as are any differences in the mapped distribution of Abbabis Complex and Damara Supergroup rocks.

Mapping of the study area was conducted during two field seasons in 2007 and 2008, over an area of *ca*. 200 km^2 in size. This mapping focused on two principal aims: the distribution of lithologies in the study area, and structural configuration of lithologies, with an aim of establishing the overall architecture of the area around the confluence of the Khan and Swakop rivers. The geology of the Ida and Palmenhorst Domes is dominated by rocks of the Abbabis Complex and the lower Damara Supergroup (Smith, 1965; Barnes, 1981), in particular the Nosib Group and lower Swakop Group (see section 1.3.1), as well as the various granitoid rocks found in the southwestern portion of the Central Zone.

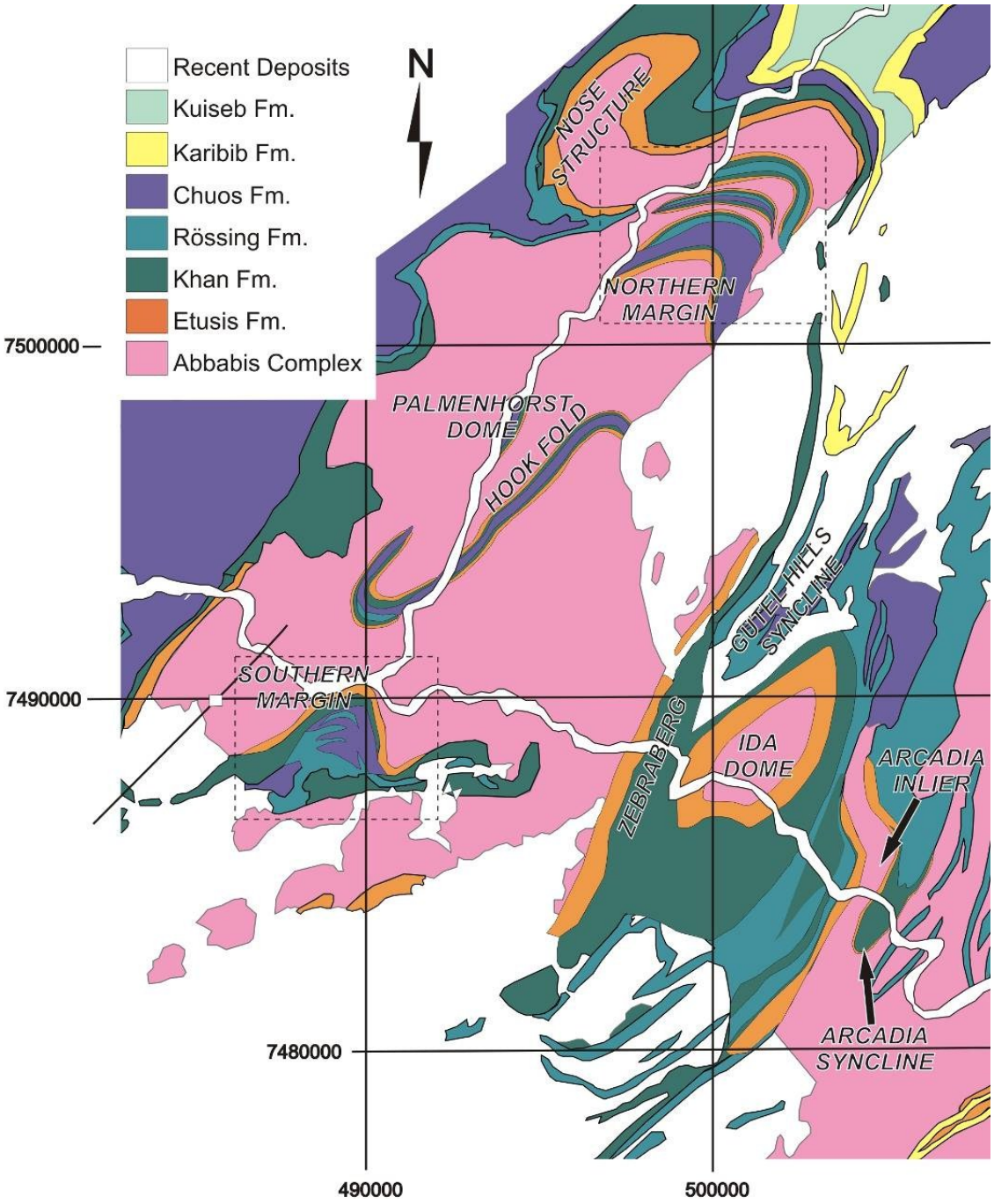

Fig. 2.1 – Geological map of the study area produced from this study, showing the distribution of the Abbabis Complex and Damara Supergroup rocks. Structural interpretations are not shown. Notice the difference between this map and that in Fig. 1.5 (which is after Lehtonen et al.*, 1995). This map shows Damara Supergroup rocks within the Palmenhorst Dome, an area previously mapped as comprising entirely Abbabis Complex gneisses. Also note that the eastern margin of the Ida Dome is mapped as Rössing Formation, whereas previous mapping (Barnes, 1981; Lehtonen* et al.*, 1995) has mapped this marble as Karibib Formation. See text for discussion.*

The rocks of the Damara Supergroup and Abbabis Complex have been subjected to upper-amphibolite to granulite facies metamorphism (Masberg *et al.*, 1992) and intense deformation (Barnes, 1981; Poli, 1997) and, in many cases, the nature of the precursor lithologies is obscured by these events. This uncertainty with regard to the identification of lithologies is enhanced by the variable nature of some units in the Damara Supergroup, and the similarity between the quartzofeldspathic Etusis Formation and the Abbabis Complex gneisses. This requires the identification of key marker horizons and lithological features in order to establish the stratigraphy in some areas. Some of these features include:

- Cross-bedded quartzites are characteristic of the Etusis Formation (Smith, 1965; Sawyer, 1981; De Kock, 2001). Since both the Abbabis Complex and the Etusis Formation are quartzofeldspathic, it is commonly difficult to distinguish these units. Cross-bedding is used to define the Etusis but in some areas where no cross bedding is observed, the presence of Etusis Formation is suggested by the presence of sillimanite-rich layers in a quartzofeldspathic rock, indicating an aluminous component and a likely sedimentary origin, rather than a granitic composition typical of the Abbabis Complex. However, some granites are seen to be aluminous (see Chapter 4) and the presence of sillimanite is not a characteristic feature of the Etusis Formation.
- Layers enriched in clinopyroxene are characteristic of the upper Khan Formation (Smith, 1965; Nash, 1971; SACS, 1980; Miller, 2008), and these are not reported elsewhere in the Damaran stratigraphy (Miller, 2008).
- The association of marble with calc-silicates, quartzites and pelitic units is characteristic of the Rössing Formation (Nash, 1971; SACS, 1980). These lithologies are commonly repeated in a sequence of Rössing rocks. Although the Karibib Formation consists of a number of thick carbonate units, it does not contain the variety of lithologies seen in the Rössing Formation.
- The presence of clasts of a variety of lithologies in quartz-biotite schist is characteristic of the Chuos Formation (Martin, 1965; SACS, 1980). Many lithologies may contain pseudo-pebbles, formed by boudinage or transposition of quartz and/or granite veins, but conclusive evidence for the diamictite which

characterises the Chuos Formation is found where clasts of different lithologies are present. Iron formations, although generally thin and not widespread, are also indicative of Chuos Formation (Jacob, 1974; SACS, 1980; Henry; 1992).

The intense deformation in the area, together with high-grade metamorphism and abundant partial melting requires the description of structural and metamorphic characteristics of the lithologies prior to an identification and correlation of lithologies, and interpretations of their protoliths. Generally, it is not a single key feature that has been used, but rather the association of many of these characteristics (e.g. pyroxene-feldspar gneiss or massive pyroxene-feldspar material adjacent to a marble indicates a Khan-Rössing contact), but in some cases only one of these features is noted. The association of a number of features characteristic of a Damaran succession is particularly important in the Palmenhorst Dome, where a number of areas of Damara Supergroup rocks have been identified in an area previously mapped as Abbabis Complex basement (Fig. 2.1).

2.1 The Abbabis Complex

A variety of lithologies have been identified previously in the Abbabis Complex by Smith (1965), Marlow (1981), Sawyer (1981) and Brandt (1987), particularly in the type locality in the Abbabis Inlier near the town of Usakos. The subdivision of the Abbabis Complex (Table 2.1), as proposed by Brandt (1987), includes the lower metasedimentary Tsawisis Formation, the metasedimentary and metavolcanic Noab Formation, and the Narubis Granitoid Complex, which is intrusive into the Tsawisis and Noab formations (Sawyer, 1981; Brandt, 1987). The basement rocks in the study area are, however, made up entirely of quartzofeldspathic gneisses, and no calc-silicates, marbles, or metavolcanics (Noab or Tsawisis formations – Brandt, 1987) have been identified within the basement rocks in either the Ida Dome or the Palmenhorst Dome, although some of the quartzofeldspathic gneisses may be paragneisses, and are not unequivocally of igneous origin.

Table 2.1 – The stratigraphy of the Abbabis Complex (from Brandt, 1987).

Sawyer (1981) **Area south-east of Walvis Bay**	**Smith (1965)** **Abbabis Inlier**	**Marlow (1981)** **Abbabis Inlier**	**Brandt (1987)** **Abbabis Inlier**	
	Ortho-amphibolite	Amphibolite dykes	Amphibolite dykes	
(Augen) gneiss		Gneisses (several of granitic composition)	Ortho (augen) gneisses	Narubis Granitoid Complex
			Metavolcanic rocks	
Gneiss, schist, glassy quartzite	Biotite schist-gneiss & para-amphibolite	Metasediments (quartzite, schist, conglomerate, marble, calc-silicate) + interbedded metabasaltic and pyroclastic rock	Alternating (feldspathic) quartzite, marble, calc-silicate	Noab Formation
Calc-silicate, marble	Dolomitic marble, calc-silicate		Schist (dark) and meta-basite	
Quartz-feldspar gneiss, quartzite, micaceous quartzite, schist	Abbabis gneiss, phyllitic quartzite, conglomerate		Schist, (para-) gneiss, meta-arkose, subordinate marble, calc-silicate, conglomerate	Tsawisis Formation

Note: horizontal lines do not always imply correlation

Throughout the study area, the Abbabis Complex consists of quartzofeldspathic gneisses and augen gneisses, which have been tectonised to S-tectonites, and L-tectonites in areas of intense deformation (Fig 2.2). Augen gneiss (Fig. 2.2A) is the most commonly observed basement lithology in the Ida Dome, whilst areas of L-tectonite are also locally seen (Fig. 2.2B). The majority of basement rocks are orthogneisses of granitic origin, representing the Narubis Granitoid Complex (Brandt, 1987) However, in the Palmenhorst Dome, in addition to the more common augen gneisses (Fig. 2.2C), some areas of pre-Damaran basement appear to be paragneisses (Fig. 2.2D).

In the centre of the Ida Dome (0500773/7487516 – Coordinates are UTM zone 33S, WGS84, see Chapter 1), the quartzofeldspathic lithologies of the Abbabis Complex have been intensely deformed, and contain a linear fabric (see section 3.2), forming pale olive green to cream-coloured quartz-plagioclase-chlorite (after biotite) L-tectonites. These rocks contain a strong linear fabric, defined by stretching of all minerals (Fig. 2.2B). The strong linear fabric is pre-Damaran and has been refolded in a complex pattern involving overprinting generations of folds (see section 3.2).

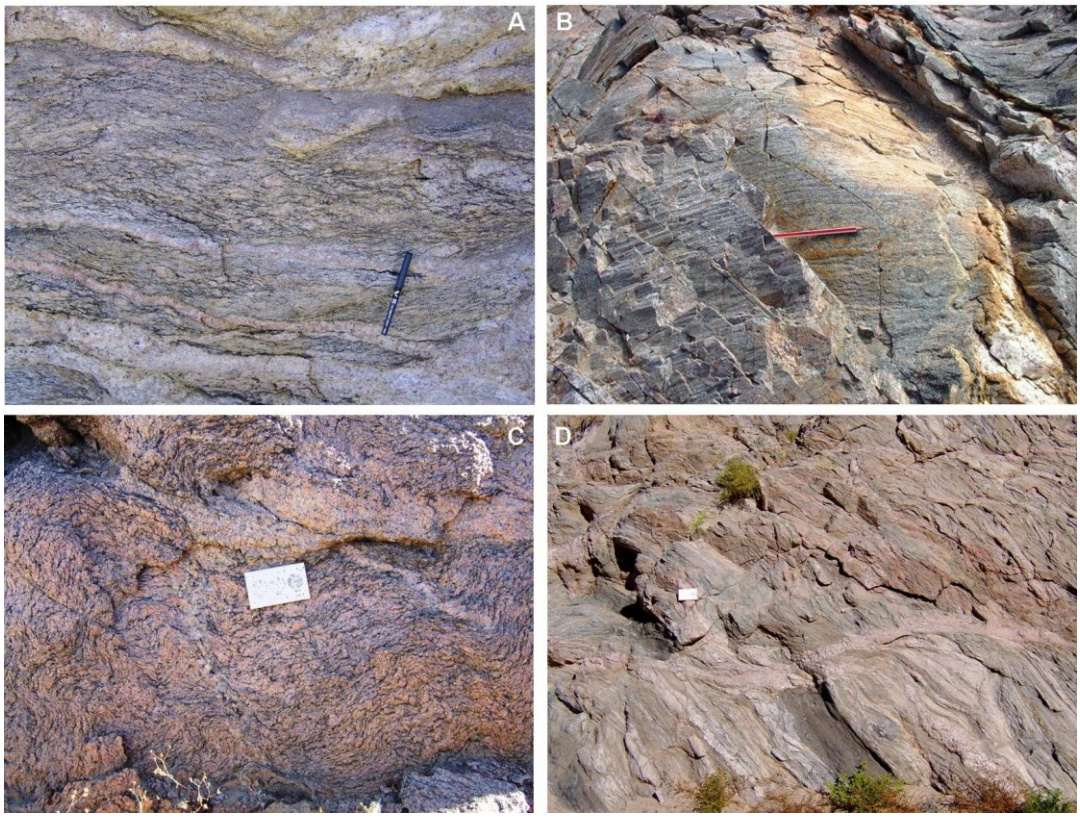

Fig. 2.2 – A: Quartzofeldspathic augen gneiss from the study area – these gneisses are typical of the Abbabis Complex in the study area (locality 0501295/7487247). B: Complex refolding of a pale green L-tectonite in the Abbabis Complex, near the centre of the Ida Dome. Although it is unclear whether the deformation responsible for the folding is pre-Damaran or Damaran in age, the linear fabric is pre-Damaran in age. Pen is aligned with the lineation direction (locality 0500773/7487516).C: Crenulated quartzofeldspathic augen gneisses from the Palmenhorst Dome (locality 0489275/7493444). D: Banded (para) gneisses from the Palmenhorst Dome, cut by Damaran-age leucosomes (locality 0494568/7499464).

This L-tectonite is composed of 0.5 mm – 1 mm plagioclase feldspar and quartz, with chlorite (after biotite) and magnetite. The strong fabric is defined by the alignment of subhedral laths of biotite (now altered to chlorite – Fig. 2.3A). Alteration postdates the formation of the linear fabric. Quartz and plagioclase show irregular grain boundaries, which may be cuspate, and commonly rounded inclusions of quartz are found within plagioclase (Fig. 2.3B), suggesting the former presence of melt (Sawyer, 2008). Quartz has very weak undulose extinction, and no elongate quartz ribbons are noted – it appears to have been polygonised during annealing under the high-grade conditions in the Central

Zone, although the cuspate nature of some quartz grains indicates that melting of these gneisses post-dates annealing.

In addition to the large amount of chlorite (after biotite), which gives the rock a pale green colour in hand sample, plagioclase is extensively sericitised (Fig. 2.3C, D). This alteration is particularly strong around phyllosilicate-rich areas (Fig. 2.3A), which may be due to the fluids responsible for this alteration moving preferentially along the fabric, (defined by phyllosilicates), rather than along bands where there are no phyllosilicates.

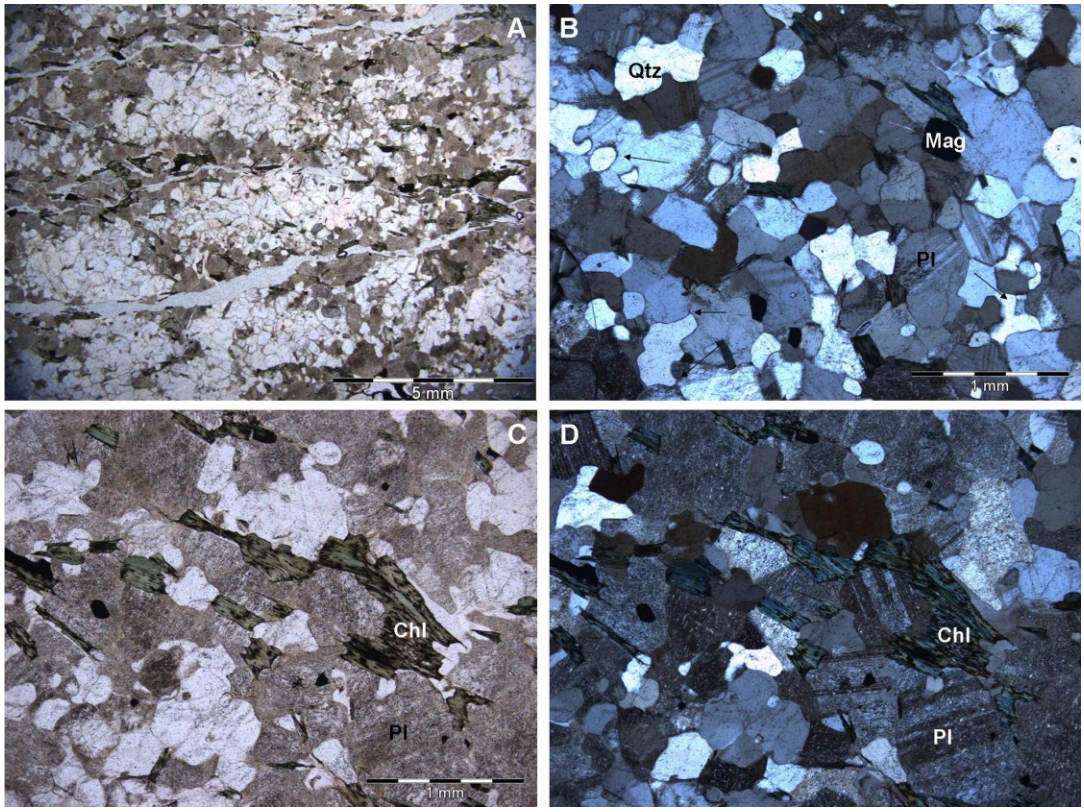

Fig. 2.3 - Photomicrographs of L-tectonites from the centre of the Ida Dome. A: Strong fabric defined by aligned chlorite, with extensive alteration of feldspar around fractures and chlorite-rich zones. Fractures are due to thin-section preparation, as the linear fabric renders the rock quite fissile (PPL). B: Unaltered zone of the rock, showing rounded quartz in feldspar, and sutured, cuspate-lobate quartz grain boundaries (indicated by arrows), possibly indicating the former presence of melt (XPL). C: Altered zone of the rock, with sericitised plagioclase and green chlorite, which has replaced laths of biotite (PPL). D: The same altered zone as C, in XPL. Note the preservation of the twinning in plagioclase despite alteration. Mineral abbreviations are after Kretz (1983). All images are from sample LID013, locality 0500774/7487518.

Other L-tectonites in the Abbabis Complex found in the core of the Ida Dome (0501220/7487524) are cream and grey in colour, comprising quartz, plagioclase feldspar, biotite and magnetite – the biotite is unaltered. These L-tectonites have been refolded into open to tight, gently E- or W-plunging, N- to NW-dipping folds by D2 Damaran deformation (see section 3.2). All the augen gneisses, L- and S-tectonites from the Ida Dome appear to be orthogneisses, and no compositional (i.e. sedimentary) banding is noted; feldspar augen in the gneisses may represent phenocrysts of the igneous protolith. The apparent differences between the augen gneisses and L- and S-tectonites may be solely due to variability in strain type or degree of strain.

The majority of Abbabis Complex gneisses and L-S tectonites in the study area comprise quartz, plagioclase feldspar and biotite, with minor K-feldspar and accessory magnetite. Allanite is found in one sample. Plagioclase is the more common feldspar, with K-feldspar abundant in only one sample, where it is considered to be crystallised anatectic melt. These rocks have a strong fabric, defined by euhedral to subhedral laths of biotite (Fig. 2.4A), as well as by elongate quartz grains. In places, this fabric wraps around augens of quartz, plagioclase and K-feldspar (Fig. 2.4A), and the biotite may be slightly altered to chlorite. Many of the basement samples show a slightly annealed texture, although much of the quartz is strained, showing undulose extinction (Fig. 2.4B, C). Large microcline grains containing rounded inclusions of quartz (Fig. 2.4D, E), and partially resorbed plagioclase, as well as large grains of unstrained quartz containing rounded inclusions of plagioclase feldspar and strained quartz provide evidence for migmatisation. Such textures are considered evidence for crystallisation of melt in a migmatite (Sawyer, 2008), although large quartz grains with inclusions of rounded strained quartz may also be evidence for dynamic recrystallisation (Vernon, 2004). In the single sample that contains abundant K-feldspar, the K-feldspar and quartz are graphically intergrown (Fig. 2.4F), and are likely to be crystallised anatectic melt. The grain size in these gneisses is generally 1 mm, although it ranges between 0.5 mm and 2 mm, and aggregates of these grains make up 0.5-2 cm augen in the gneisses.

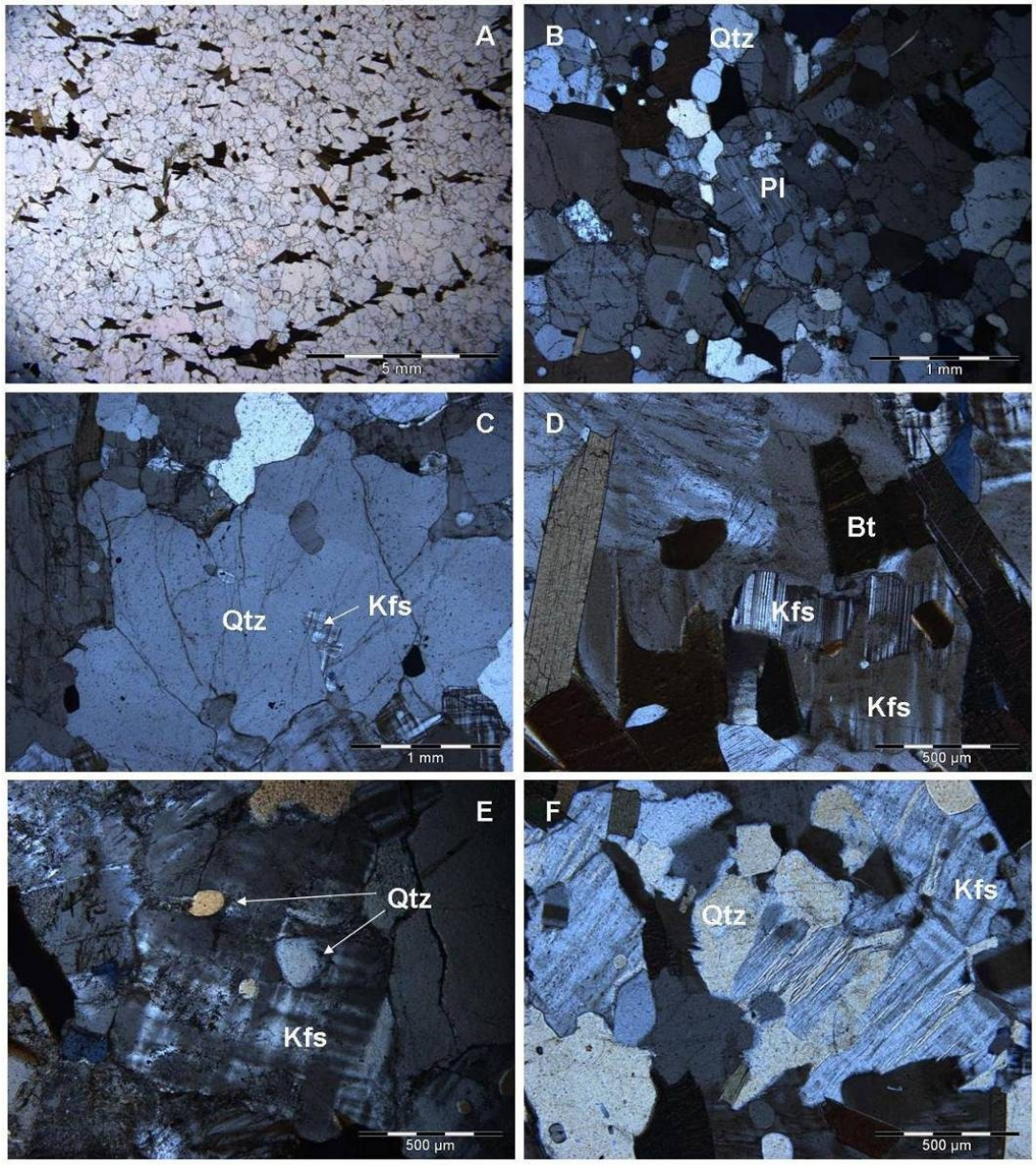

Fig. 2.4 – Photomicrographs of Abbabis Complex rocks from the study area. A: Moderate fabric defined by laths of biotite, wrapping around augen of quartz and plagioclase feldspar (PPL, sample LID036, locality 0500422/7487668). B: Plagioclase feldspar with numerous small, rounded inclusions of quartz (XPL, sample LID036, locality 0500422/7487668). C: Slightly undulose extinction in a quartz crystal with irregular, cuspate-lobate edges, and inclusions of rounded quartz and K-feldspar (XPL, sample LID016, locality 0500364/7487670). D: K-feldspar crystal with corroded inclusions of K-feldspar and biotite (XPL, sample LID012, locality 0501018/7487505). E: K-feldspar with rounded inclusions of quartz (XPL, sample LID012, locality 0501018/7487505). F: Graphic intergrowth of K-feldspar and quartz (XPL, sample LID012, locality 0501018/7487505). Mineral abbreviations are after Kretz (1983).

The metasedimentary units of the Noab and Tsawisis Formations of the Abbabis Complex (Brandt, 1987) contain carbonate or calc-silicate rocks, metavolcanics, meta-arkose, and quartzites in their type locality in the Abbabis Inlier (Table 2.1), but no such metasedimentary units have been noted in the Abbabis Complex of the Ida Dome and, thus, the gneisses of the Abbabis Complex in the Ida Dome appear to comprise entirely Narubis Granitoid Complex (Brandt, 1987). Although augen gneisses and L- and S-tectonites are all found in the core of the Ida Dome, only white-grey augen gneisses are found in the Arcadia Inlier. In the Palmenhorst Dome, augen gneisses are the dominant lithology, although some banded quartzofeldspathic gneisses are noted, which may be interpreted as paragneisses. The major element geochemistry (Figs. 2.5A, B) of these rocks is inconclusive with regard to whether the rocks of the Abbabis Complex are paragneisses of the lower Tsawisis or Noab Formation or orthogneisses of the Narubis Granitoid Complex (Brandt, 1987). Normative calculations show that samples of the Abbabis Complex (augen gneisses, banded gneisses and L-tectonites) plot as granites, granodiorites and quartz diorites on a Streckeisen diagram (Fig. 2.5A) and as granites, granodiorites, tonalites and trondhjemites on a An-Or-Ab diagram (Fig. 2.5B), but that based on major element normative calculations they are indistinguishable from typical greywackes (Figs. 2.5A, B). However, REE patterns of all samples are similar, and are comparable to the patterns expected for granitoid igneous rocks, with smooth patterns showing LREE enrichment and moderate negative Eu anomalies (Fig. 2.5C) as opposed to REE patterns for sedimentary rocks, which would show more erratic patterns (Rollinson, 1993). Thus, it appears that the Abbabis Complex in the study area is made up of orthogneisses of the Narubis Granitoid Complex, and that there is little evidence for metasedimentary material in the Abbabis Complex.

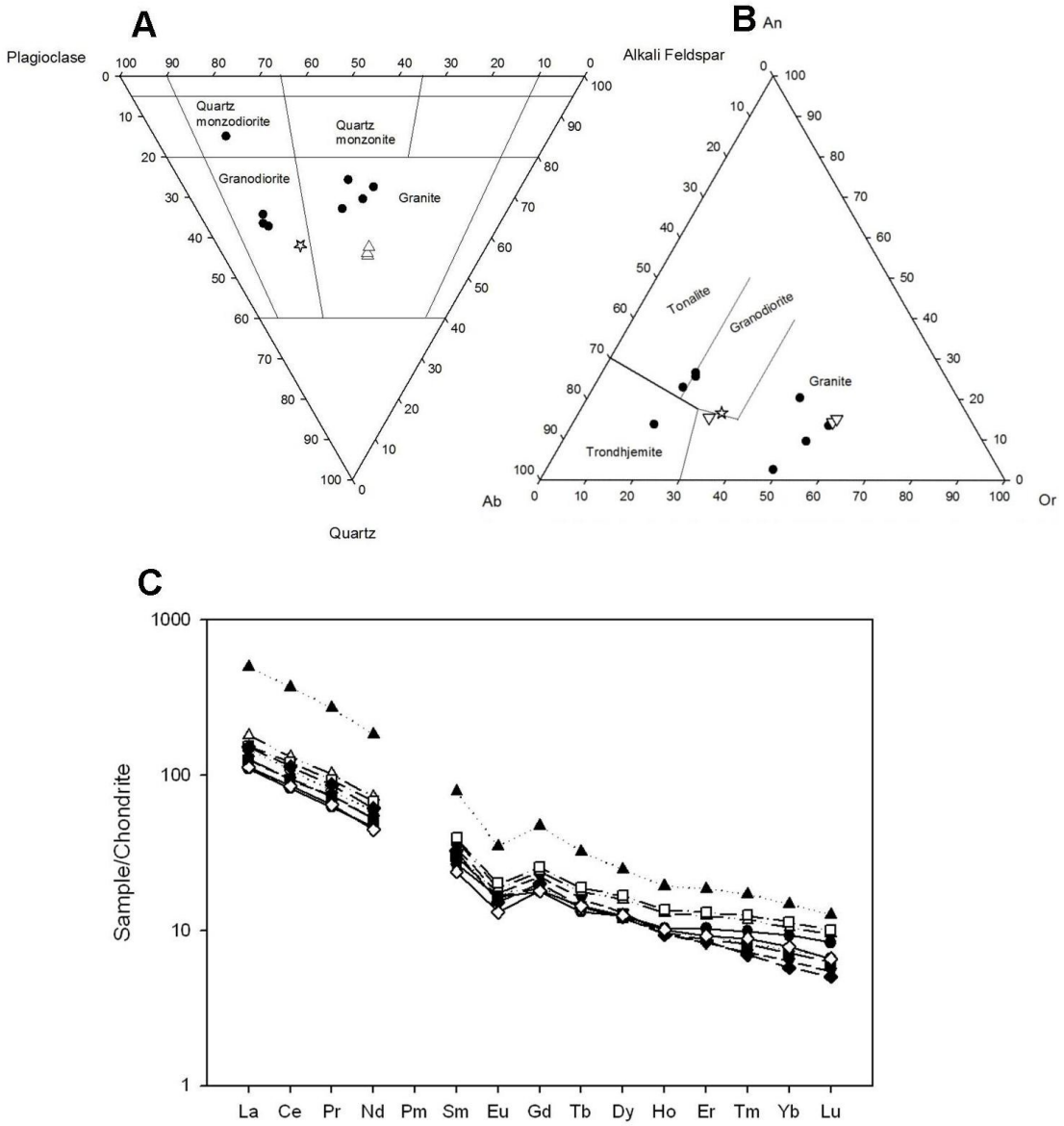

Fig. 2.5 – Geochemical plots for Abbabis Complex gneisses and L-tectonites from the study area. A: Streckeisen diagram for Abbabis Complex rocks (filled circles) compared to typical greywacke compositions (open triangles – data from Stevens et al.*, 1997 and star – data from Vielzuef & Montel, 1994)). B: Anorthite-orthoclase-albite diagram for Abbabis Complex rocks (filled circles) compared to typical greywacke compositions (open triangles – data from Stevens* et al.*, 1997 and star – data from Vielzuef & Montel, 1994). C: Chondrite-normalised REE plot showing LREE enrichment and moderate negative Eu anomalies. Geochemical data are contained in Appendix 1.*

In the Ida Dome, the Abbabis Complex forms the roughly crescent-shaped core of the dome, and also crops out in a large sliver to the east of the dome (termed the Arcadia Zone, Figs. 2.1, 2.6A). The distribution of Abbabis Complex gneisses mapped in this study (Fig. 2.6A) shows some similarities to the mapping of both Barnes (1981) and Jacob (1974), who noted Abbabis Complex gneisses in the Arcadia Inlier, and to the west-northwest of the Ida Dome (Figs. 2.6 B, C). However, there are significant differences in the mapped distribution of the Abbabis Complex in the core of the Ida Dome.

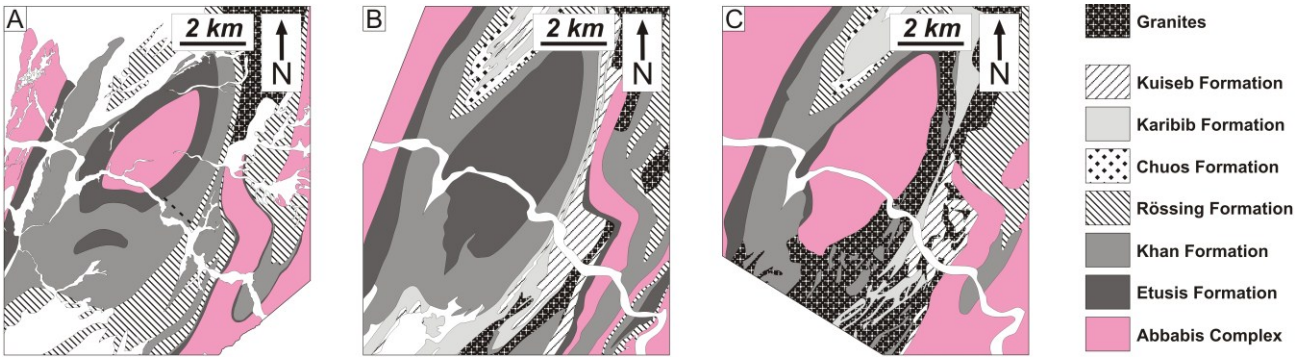

Fig. 2.6 – Mapped distributions of the Abbabis Complex in the Ida Dome according to A: This study. B: Barnes (1981). C: Jacob (1974).

Barnes (1981) considered the entire core of the Ida Dome as comprising Etusis Formation (Fig. 2.6B), and included quartzo-feldspathic paragneisses (in places augen gneisses) as part of the Etusis Formation (in addition to quartzites, meta-arkoses, pelitic schists and biotite schists). The presence or absence of amphibolite dykes was used by Barnes (1981) as the distinguishing feature between the Etusis Formation and the Abbabis Complex (the Abbabis Complex contains amphibolite dykes, supposedly absent in the Etusis Formation). In contrast, Jacob (1974) considered the core of the Ida Dome to be made up of Abbabis Complex gneisses, overlain by Etusis Formation quartzites and meta-arkoses. The mapped distribution of the Abbabis Complex from this study has similarities to the map of Jacob (1974), and the core of the Ida Dome is indeed cored by Abbabis Complex gneisses (Fig. 2.6C). U-Pb SHRIMP dating of gneisses from the core of the Ida Dome confirms that they are pre-Damaran (see section 5.1.1), and U-Pb SHRIMP dating of amphibolite dykes indicates thatsome amphibolite dykes were emplaced during Damaran collision (see

section 5.1.2), invalidating the theory of Barnes (1981) that amphibolites are restricted to the Abbabis Complex basement. Although the Ida Dome is cored by Abbabis Complex gneisses, these rocks cover a smaller area than that suggested by Jacob (1974), and south of the Swakop River much of the area mapped by Jacob (1974) as Abbabis Complex is underlain by lower Damara Supergroup lithologies.

The Palmenhorst Dome has previously been shown to be a very large area of pre-Damaran basement (Smith, 1965; Lehtonen *et al*., 1995), whereas mapping undertaken for this study has revealed that Damara Supergroup rocks are infolded with rocks of the Abbabis Complex (Figs. 2.1, 2.7). The infolding of the Damara Supergroup into the Abbabis Complex in the Palmenhorst Dome is a feature originally recognised by Barnes (1981). However, Barnes (1981) considered the Abbabis Complex to be constrained in a number of smaller slivers, with much of the Palmenhorst Dome underlain by the Etusis Formation (Fig. 2.7A). This study has shown that the bulk of the Palmenhorst Dome is underlain by gneisses of the Abbabis Complex (Fig. 2.7B), with smaller slivers of Damara Supergroup rocks infolded into km-scale synclines within the Abbabis Complex basement.

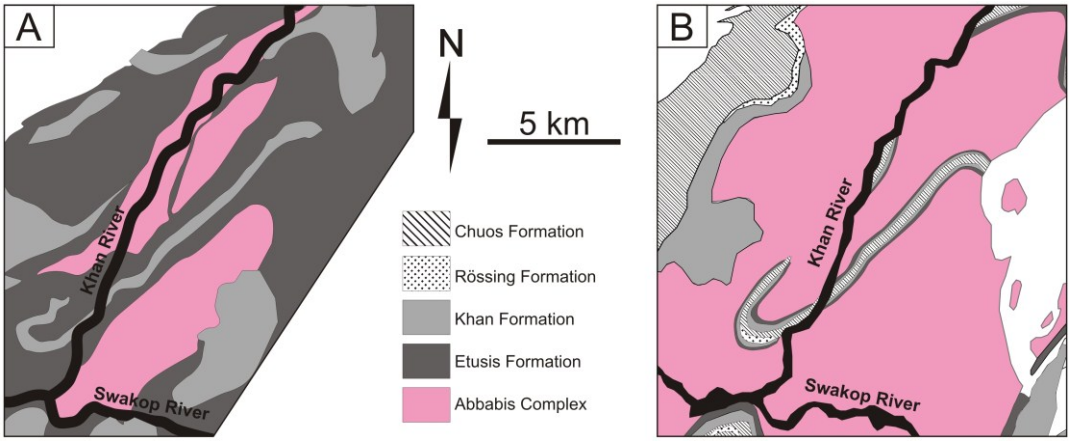

Fig. 2.7 – Comparison of mapping of the Abbabis Complex in the Palmenhorst Dome. A: Distribution of lithologies according to Barnes (1981). B: Distribution of lithologies according to this study.

Along the northern margin of the Palmenhorst Dome, near the so-called Nose Structure (Figs. 2.1, 2.8), Poli (1997) mapped a number of outcrops of amphibolite and

metasediments as part of the Tsawisis Formation (Brandt, 1987). These isolated slivers of metasediments and amphibolites are found as rafts within masses of granite (Fig. 2.8A). However, mapping of the northern margin of the Palmenhorst Dome from this study shows that these isolated rafts of metasediments and amphibolite can be traced along strike towards the east (Fig. 2.8B), where a full lower Damara Supergroup succession is found (see section 2.2). Although the voluminous nature of the granitoids that have intruded these metasediments makes conclusive identification of these lithologies as Damara Supergroup in the area mapped by Poli (1997) difficult, the occurrence of a more complete lower Damara Supergroup succession along strike to the east (outside of the area mapped by Poli, 1997) indicates that these do not represent the Tsawisis Formation, but are rafts of Damara Supergroup lithologies within voluminous granitoids (also see section 2.3).

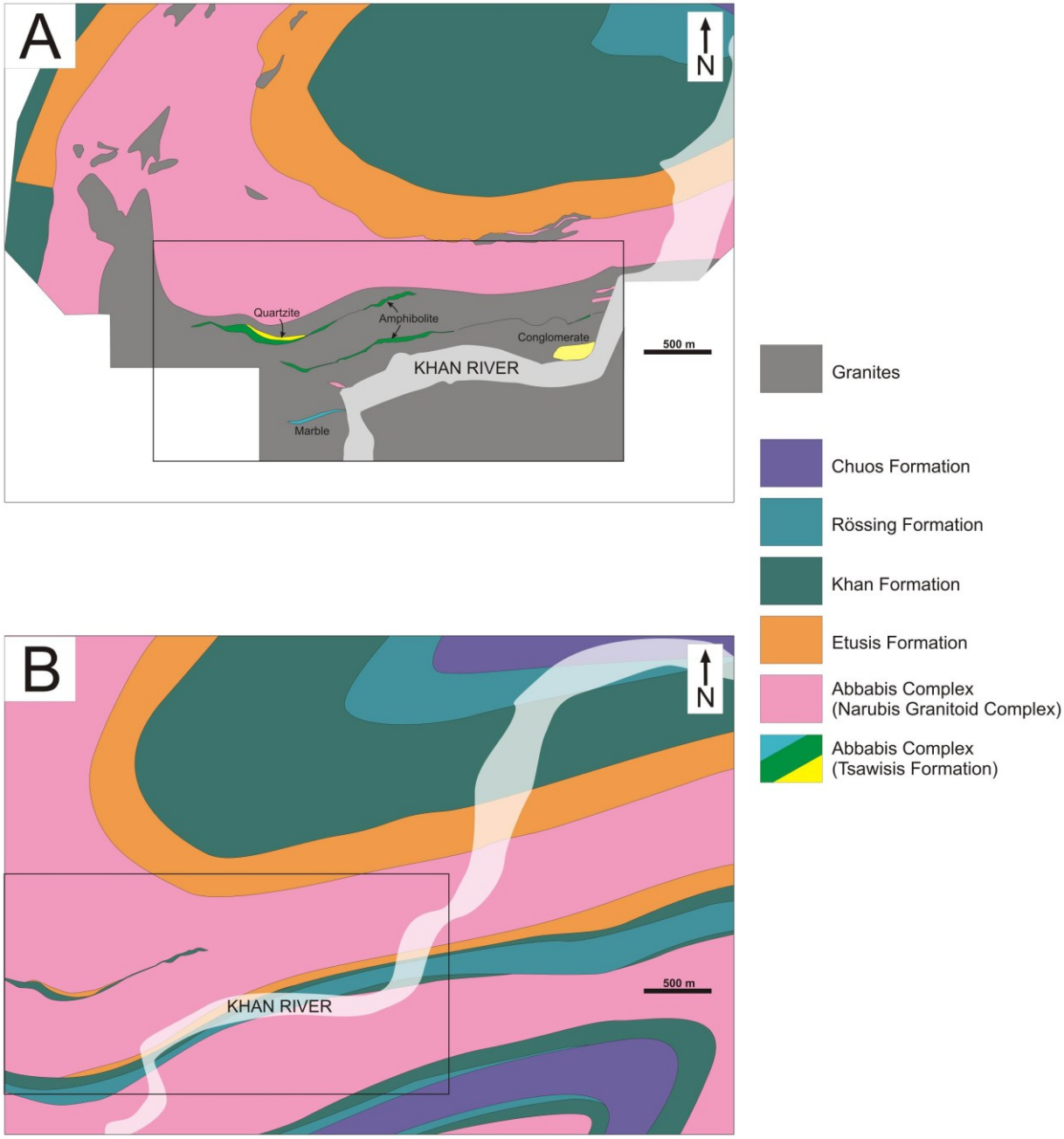

Fig. 2.8 – A: Map of the northern margin of the Palmenhorst Dome after Poli (1997). Note the quartzite, amphibolite, conglomerate, and marble rafts within granite. B: Map of the northern margin of the Palmenhorst Dome from this study. Note that the rafts of quartzite, amphibolite, conglomerate and marble are correlated with a more complete package of lower Damara Supergroup rocks found to the east of the Khan River, outside of the area mapped by Poli (1997). Note that granitoids are not mapped.

2.2 The Damara Supergroup

The Damara Supergroup makes up the bulk of the rocks exposed in the Central Zone, and rocks of the Abbabis Complex are generally only exposed in the domal structures characteristic of this portion of the orogen. In these domes, the basement core is typically surrounded by a mantle of Damara Supergroup lithologies, hence they are mantled gneiss domes (Eskola, 1949). However, as already mentioned above, in the Palmenhorst Dome, Damara Supergroup metasediments are infolded into the gneisses of the Abbabis Complex (Figs. 2.1, 2.7). The units mapped within the study area are mostly those of the Nosib Group (Etusis and Khan Formations), which are overlain by the Swakop Group (Rössing, Chuos, Arandis, Ghaub, Karibib and Kuiseb Formations (Fig. 2.9). Rocks of the Arandis, Ghaub, Karibib and Kuiseb Formations do not make up a significant proportion of the study area; in both the Ida Dome and the Palmenhorst Dome the highest stratigraphic level for which lithologies are noted is the Chuos Formation. Any tillite found in the study area has been classified as Chuos Formation, as whilst the Chuos and Ghaub formations may be difficult to distinguish (Miller, 2008), no cap carbonate of the Arandis Formation has been noted overlying the Chuos Formation. Rocks of the Karibib and Kuiseb Formations crop out immediately north of the study area, and along the northern and eastern margins of the Palmenhorst Dome (Lehtonen *et al*., 1995). The distribution of these rocks is shown in Fig. 2.1.

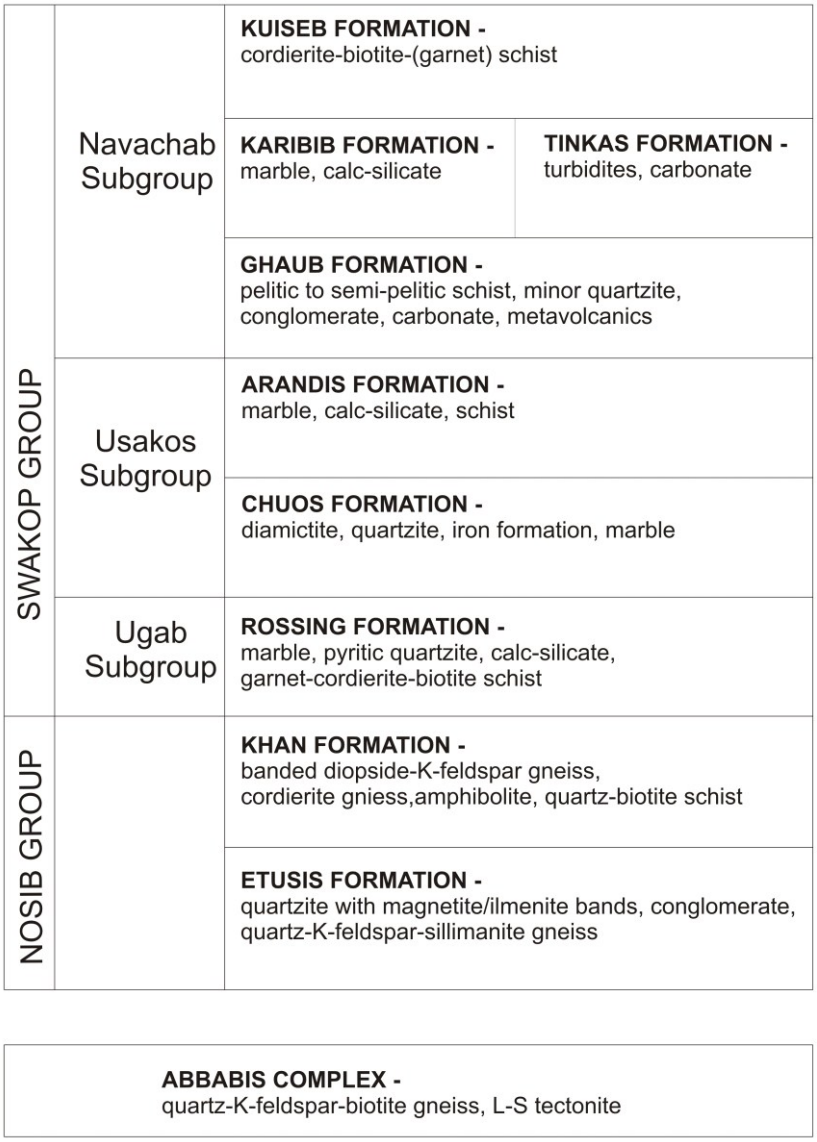

Fig. 2.9 – Stratigraphic column for the study area in the Central Zone. Modified after Badenhorst (1992), Lehtonen et al*. (1996), Hoffmann* et al*. (2004), and Miller (2008).*

2.2.1 The Nosib Group

The Nosib Group incorporates the quartzofeldspathic Etusis Formation, which unconformably overlies the gneisses of the Abbabis Complex basement, and is succeeded by the Khan Formation, a distinctive package of calc-silicate rocks and schists. In some areas, the contact between these two formations is indistinct, and the quartzites and

meta-arkoses of the Etusis Formation are interbedded with biotite-hornblende schist and clinopyroxene-hornblende paragneisses of the Khan Formation (Smith, 1965; Jacob, 1974; Sawyer, 1981).

2.2.1.1 The Etusis Formation

The Etusis Formation in the study area is made up of quartzite, meta-arkose, pelitic schist, sillimanite schist and minor biotite schist. In the Ida Dome, pale orange-red quartzites and meta-arkoses comprising quartz with minor amounts of feldspar make up the Etusis Formation. In places, ilmenite and magnetite form thin bands of heavy minerals (Fig. 2.10A, B). These quartzites and meta-arkoses grade upwards into biotite schists, which grade into the cordierite-biotite schists of the lower Khan Formation. Despite the intense deformation in the study area, the heavy mineral bands generally preserve primary sedimentary trough cross-bedding (Fig. 2.10B), which may be slightly distorted by deformation but which is nonetheless recognisable. Cross-bedding, in addition to planar and graded bedding, has been commonly noted by various workers throughout the Central Zone, in spite of intense deformation (Sawyer, 1981; Barnes, 1981; Henry, 1992; Lehtonen *et al*., 1995). In the Arcadia Syncline (Fig. 2.1), the Etusis Formation is highly sheared, and is made up of sillimanite schist and pelitic schist. In the Palmenhorst Dome, the Etusis Formation is much more arkosic than in the Ida Dome, and quartzites with recogniseable cross-bedding are rare, and planar- and cross-bedding structures are only locally observed (Fig. 2.10C). The bulk of the Etusis Formation in the Palmenhorst Dome comprises quartz-biotite schists or quartzofeldspathic, sillimanite-bearing arkoses (Fig. 2.10D), which are red in colour and locally develop a gneissic fabric. Barnes (1981) observed that the Etusis Formation near the northern margin of the Palmenhorst Dome contained far more sillimanite gneiss and sillimanite biotite gneiss units than in the vicinity of the Ida Dome. Although conglomerates are commonly observed at the base of the Etusis Formation (Smith, 1965; Barnes, 1981; Poli, 1997), or as intraformational units up to 15 m thick (Barnes, 1981; Brandt, 1985; Lehtonen *et al*., 1995), no conglomerate units were recognised in the study area. In the Ida Dome, the generally quartzitic nature of the Etusis Formation, with recognisable cross-beds (Figs. 2.10A, B), means that it is

relatively easily distinguished from the underlying Abbabis Complex, although both the Etusis Formation and Abbabis Complex are intruded by voluminous granitoids and, thus, the contact between these two units is commonly indistinct. In the Palmenhorst Dome, the quartzofeldspathic nature of the Etusis Formation, with a paucity of recognisable bedding, has resulted in difficulty in distinguishing the Etusis Formation from the quartzofeldspathic paragneisses of the Abbabis Complex, and the contacts between these units are somewhat obscure in places. The difficulty in distinguishing the Etusis Formation from the Abbabis Complex, owing to their compositional similarity, together with the high-grade metamorphism and intense deformation in the southwestern Central Zone, is a common problem noted by a variety of workers (Barnes, 1981; Lehtonen *et al*., 1995).

Fig. 2.10 – Etusis Formation rocks from the study area. A: Planar cross-bedding, defined by heavy minerals, near the centre of the Ida Dome (locality 0500606/7487048). B: Trough cross-bedding defined by heavy minerals, which has been over steepened as a result of Damaran Deformation, south of the centre of the Ida Dome (locality 0499707/7485645). C: Red-coloured, steeply dipping, bedded quartzites from the north of the Palmenhorst Dome (locality 0494530/7495765). D: Sillimanite knots in pink meta-arkose near the northern edge of the Palmenhorst Dome (locality 0500363/7504555).

The quartzofeldspathic rocks of the Etusis Formation typically contain abundant quartz, lesser K-feldspar, minor amounts of plagioclase feldspar, magnetite and ilmenite, and trace amounts of biotite (Fig. 2.11A). Grain size is 1-3 mm. Quartz is slightly strained and, although an annealed texture is locally developed, typically quartz has highly irregular grain boundaries indicative of dynamic recrystallisation (Vernon, 2004). K-feldspar commonly has irregular, cuspate-lobate edges (Fig. 2.11B), and locally shows perthitic exsolution (Fig. 2.11C). Quartz may contain inclusions of K-feldspar, with rounded, thermally corroded shapes, or subhedral inclusions of biotite (Fig. 2.11D). Minor amounts of plagioclase feldspar are locally found, and the rock has a fabric, defined by aligned laths of subhedral biotite, with quartz and feldspar grains elongate along the fabric direction.

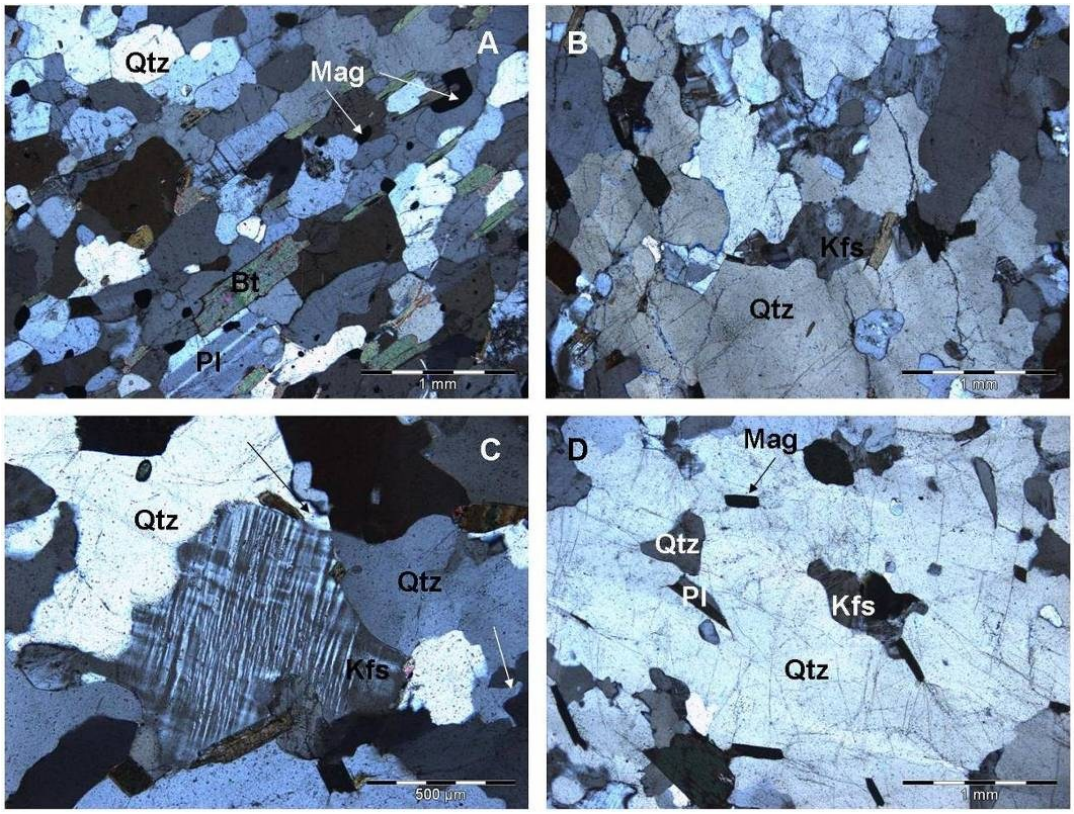

Fig. 2.11 – Photomicrographs of Etusis Formation rocks from the study area. A: Moderate fabric defined by aligned subhedral to euhedral laths of biotite, and elongate plagioclase and quartz grains. Note the finer grained magnetite (XPL, sample LID001, locality 0501769/7486593). B: Quartz with irregular grain boundaries and slightly undulose extinction, and an irregular-shaped grain of K-feldspar, suggesting the former presence of melt (XPL, sample CZRL24, locality 0500606/7487048). C: Perthitic exsolution in K-feldspar. Note the extremely cuspate quartz grain boundaries (shown by arrows), indicating that this quartz was part of a melt pool (XPL, sample CZRL24, locality 0500606/7487048). D: Large quartz grain containing inclusions of quartz, magnetite and biotite and K-feldspar (XPL, sample CZRL24, locality 0500606/7487048). Mineral abbreviations are after Kretz (1983).

2.2.1.2 The Khan Formation

The Khan Formation forms one of the most distinctive units in the stratigraphy of the Damara Supergroup in the Ida and Palmenhorst Domes, and is useful as a marker horizon, especially as the quartzofeldspathic nature of the Etusis Formation may make the contact between the Etusis Formation and the Abbabis Complex difficult to distinguish. The Khan

Formation contains a number of amphibole-, pyroxene- and biotite-rich units and is thus dark green. It is distinctive both on remotely-sensed imagery (Fig. 2.12) and in the field (Table 2.2).

Fig. 2.12 – Satellite image of the Arcadia Syncline (axial trace shown – see section 3.5.2), showing the distinctive dark green Khan Formation (circled), which is easily recognisable on remote sensing images (from Google Earth™).

In the Ida Dome, the Khan Formation forms a distinctive mantle of calc-silicate rocks around the quartzofeldspathic core of the Abbabis Complex and the Etusis Formation. A section through the eastern margin of the dome (Table 2.2) is the most complete section through the Khan Formation in the study area, although the rocks are nonetheless folded by Damaran deformation, and intruded by voluminous granitoids. This section shows that the upper and lower portions of the Khan Formation contain clinopyroxene-feldspar (± amphibole) gneisses, similar to the Khan Formation in the Rössing Mine area (Nash, 1971;

Berning *et al*, 1976), which contains a lower and an upper gneiss unit (Table 2.2). The para-amphibolite (Nash, 1971) or biotite-amphibole schist (Berning *et al*., 1976) noted at the top of the Khan Formation is not found in this section, or elsewhere in the study area.

Table 2.2 – Stratigraphic sections through the Khan Formation according to Barnes (1981), Berning et al.*(1976), Nash (1971) and from this study. Although the section through the eastern Ida Dome constitutes the most complete Khan Formation section in the study area, deformation means that estimated thicknesses for individual units, as shown, may not be accurate. Dashed lines indicate possible correlations between units from this study and other studies. The section line shown is indicated in Fig. 2.13A.*

Barnes (1981)	Berning (1976) Rössing Mine	Nash (1971) Rössing Mine	This study (eastern Ida Dome)	
Hornblende-pyroxene banded gneiss/calc-silicate gneiss	Biotite-amphibole schist	Para-amphibolite	Diopside-feldspar (± amphibole) gneiss	250 m
	Upper pyroxene-hornblende gneiss	Upper basic gneiss	Quartz-biotite schist	350 m
			Quartz-biotite-magnetite schist	30 m
Hornblende/biotite schist/gneiss	Pyroxene-garnet gneiss	Orthoamphibolite/ pyroxene-garnet gneiss	Biotite (± amphibole) schist	50 m
	Lower basic gneiss	Lower basic gneiss	Cordierite gneiss	50 m
			Pyroxene-amphibole-feldspar banded gneiss	100 m

The distribution of the Khan Formation (Fig. 2.13) as mapped in this study for the Ida Dome is similar to the distribution shown by Barnes (1981) and Jacob (1974), with the exception that much of the area south of the Swakop River in the core of the Ida Dome is mapped as Khan Formation (Fig. 2.13A) rather than Abbabis Complex gneisses (Figs. 2.13B, C), and that an area east of the Ida Dome, to the west of the Arcadia Inlier, is mapped as Khan Formation, rather than Kuiseb Formation (see also section 2.2.2.3).

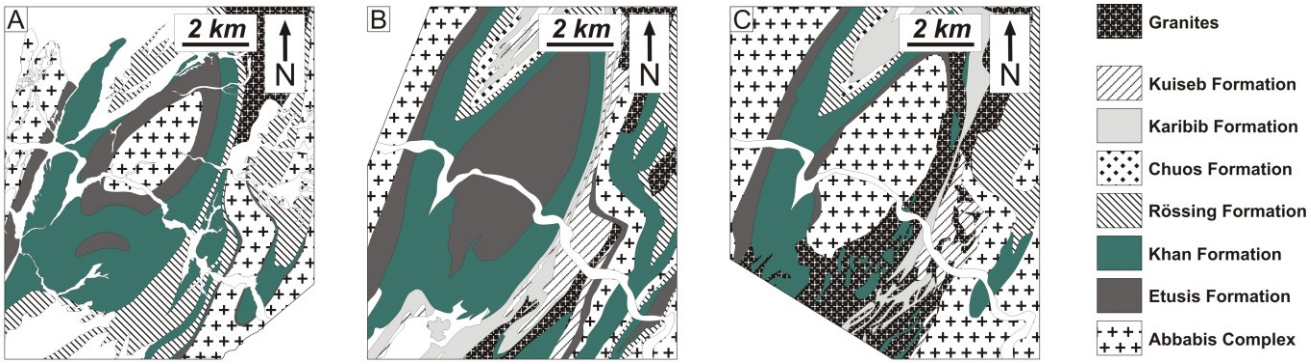

Fig. 2.13 – Mapped distributions of the Khan Formation in the Ida Dome according to A: This study. B: Barnes (1981). C: Jacob (1974). The section shown in Table 2.2 is indicated by the dashed line in A.

In the Palmenhorst Dome, Barnes (1981) noted numerous infolds of Damara Supergroup rocks in an area previously mapped by Smith (1965) as Abbabis Complex (Fig. 2.14A). However, Barnes (1981) considered these infolds to be entirely Khan Formation. This study shows that these infolds are made up of lower Damara Supergroup rocks, particularly the km-scale fold termed the Hook Fold (Figs. 2.1, 2.14B), which shows a complete lower Damaran succession (see section 2.3). Additionally, some of the other areas mapped by Barnes (1981) as Khan Formation are considered here to be underlain by gneisses of the Abbabis Complex.

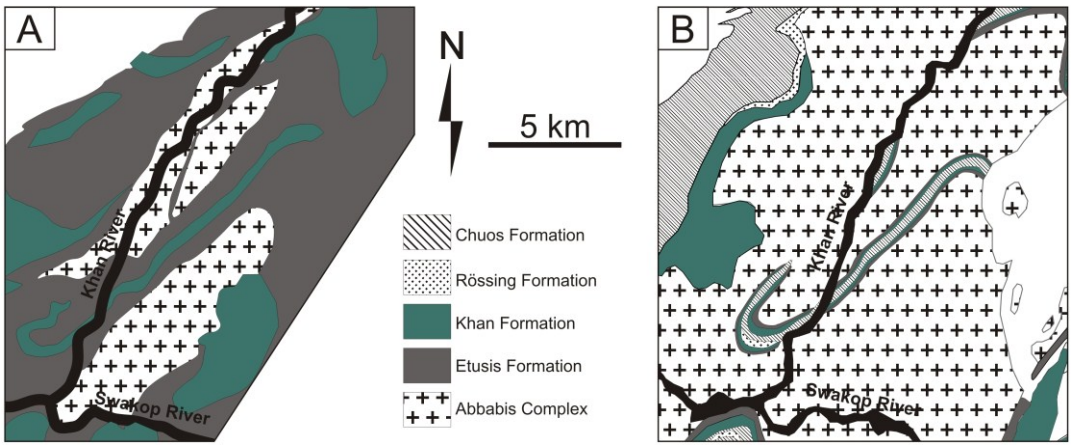

Fig. 2.14 – Comparison of mapping of the Abbabis Complex in the Palmenhorst Dome. A: Distribution of lithologies according to Barnes (1981). B: Distribution of lithologies according to this study.

The majority of the lithologies found in the Khan Formation throughout the study area are the dark green and cream coloured diopside-feldspar (± amphibole) gneisses (e.g. Fig. 2.15A), although pale grey quartz-biotite schist or dark green-black biotite-amphibole schist (Fig. 2.15B) are also noted in places, particularly in the lower portions of the formation (Table 2.2). The Khan Formation forms a thick package on both the eastern margin of the Ida Dome, as well as to the west of the dome, where it forms the distinctive ridge of dark green hills known as the Zebraberg (Fig. 2.1), named for the contrasting banding of the dark green Khan Formation and the numerous lighter coloured leucogranite sheets that intrude in this area. To the east of the Ida Dome, in the Arcadia Zone, a km-scale syncline contains a thick package of Khan Formation metasediments, known as the Arcadia Syncline (Fig. 2.1). Here, the Khan Formation is also dominated by green diopside-feldspar gneisses. Distinctive green gneisses are very coarsely recrystallised, with grain sizes of 5-10 mm (Fig. 2.15C, D). Cordierite schist (locality 0501940/7486662) and quartz-biotite-magnetite schist (locality 0501933/7486360) also occur within the lower Khan Formation (Table 2.2).

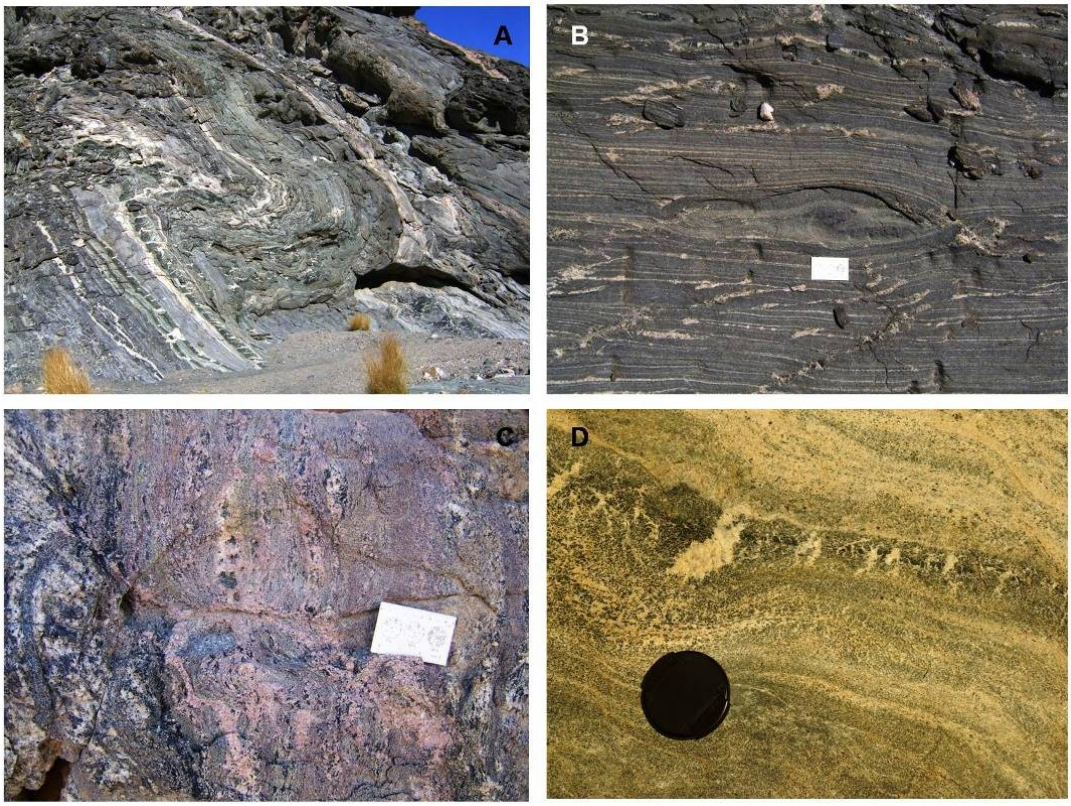

Fig. 2.15 – Khan Formation rocks from the study area. A: Folded diopside (green-bands) and feldspar (white bands) gneisses in the Arcadia Syncline, east of the Ida Dome (locality 0504973/7484338). B: Amphibole-biotite schist from the Khan Formation in the Arcadia Syncline. Note the migmatitic nature of the outcrop, with bands of leucosome, parallel and slightly oblique to the banding (locality 0504759/7483900). C: Coarse grained diopside-feldspar gneisses typical of the Khan Formation in the Ida Dome (locality 0502508/7486113). D: Boudinaged diopside-feldspar gneisses. Note the brittle nature of fractures forming in diopside-rich layers. This brittle deformation is a feature typical of the Khan Formation in the study area, and in this case is due to extension on the limbs of a m-scale D2 fold (locality 0504258/7483388).

Generally, the Khan Formation is made up of diopside-plagioclase gneisses (Fig. 2.16A), with minor quartz and opaque minerals (magnetite and ilmenite). There is generally a gneissic fabric, defined by diopside-rich layers, which generally contain more opaque minerals than diopside-poorer, more felsic, layers. Locally, layers with the assemblage sphene-diopside-plagioclase are found. These may comprise almost entirely sphene, with minor blebs of diopside, and define a gneissic fabric with bands enriched in plagioclase.

Grain size is highly variable, and a banding defined by grain size exists, with fine- (0.2-0.5 mm) and coarse- (2-3 mm) grained layers. Elsewhere, similar lithologies are found with no diopside. Rather, there are amphibole-biotite schists (Figs. 2.16B, C, D), comprising hornblende, biotite, plagioclase feldspar, opaque minerals (ilmenite/magnetite) and minor amounts of quartz. Biotite generally occurs as small euhedral to subhedral laths, and hornblende as stubby to slightly elongate crystals (Fig. 2.16D), both of which are aligned to form the schistose fabric in these rocks. In one sample, biotite occurs as large (ca. 5 mm) porphyroblasts (Fig. 2.16C), with a fabric of hornblende, which does not wrap around these porphyroblasts, and a depletion halo surrounding this biotite. Stubby and subhedral to euhedral inclusions of hornblende are found in quartz. These schistose rocks typically have an annealed texture, with numerous 120˚ triple junctions (Fig. 2.16D).

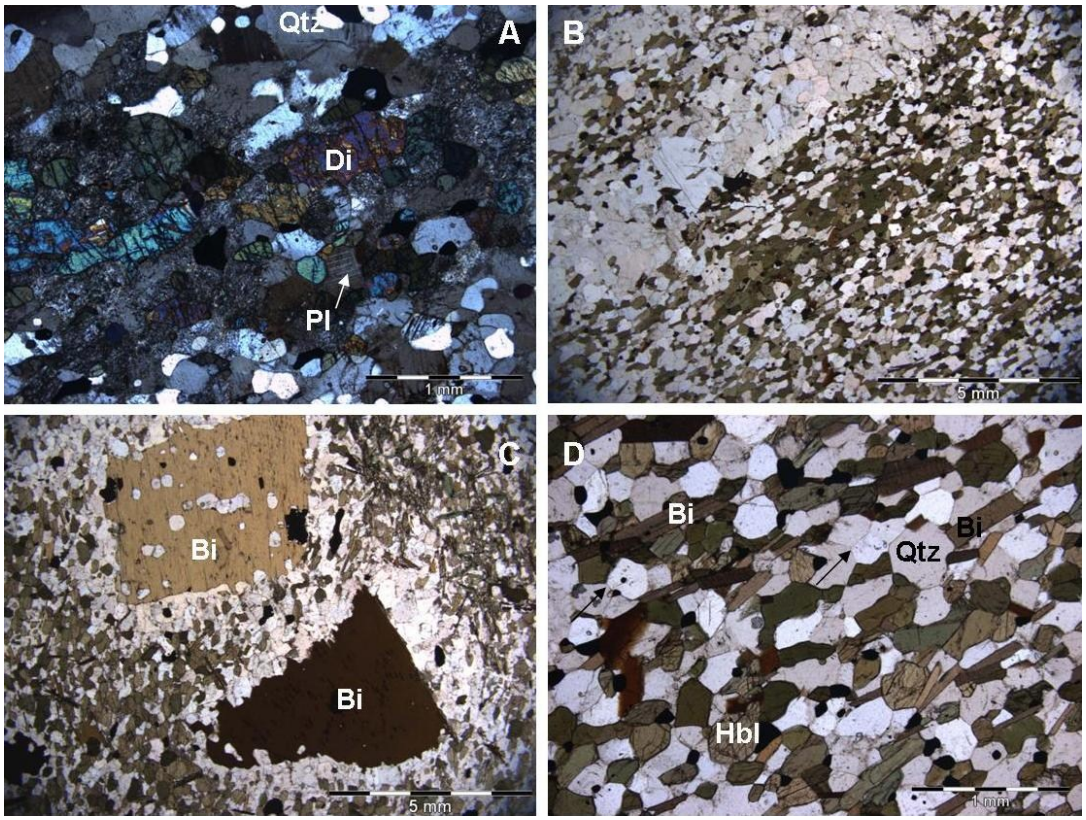

Fig. 2.16 – Photomicrographs of calc-silicate rocks and amphibole-biotite schists from the Khan Formation. A: Diopside-quartz-plagioclase gneiss, with diopside aligned with the gneissic fabric (XPL, sample LID027, locality 0499057/7488915). B: Compositional banding in an amphibole-biotite schist, with aligned biotite and hornblende crystals parallel to the compositional layering (PPL, sample LID034, locality 0504756/7483916). C: Large porphyroblasts of biotite, surrounded by a felsic halo, in an amphibole-biotite schist (PPL, sample CZRL17, locality 0504226/7483646). D: Aligned subhedral to euhedral biotite and stubby hornblende in an amphibole-biotite schist. Note the annealed texture of the quartz and feldspar, with straight grain boundaries and 120˚ triple junctions (indicated by arrows) (PPL, sample LID034, locality 0504756/7483916). Mineral abbreviations are after Kretz (1983).

In addition to these diopside- and amphibole-bearing samples, there are also pelitic and psammitic rocks within the Khan Formation. Cordierite-bearing schists (Fig. 2.17) are common in the lower parts of the formation, typically with 0.2-0.5 mm quartz, biotite, K-feldspar and plagioclase in addition to the 1-2 mm cordierite porphyroblasts, which contain numerous inclusions of *ca*. 0.1 mm rounded quartz and subhedral to slightly rounded biotite, and which may define a fabric (Fig. 2.17A).

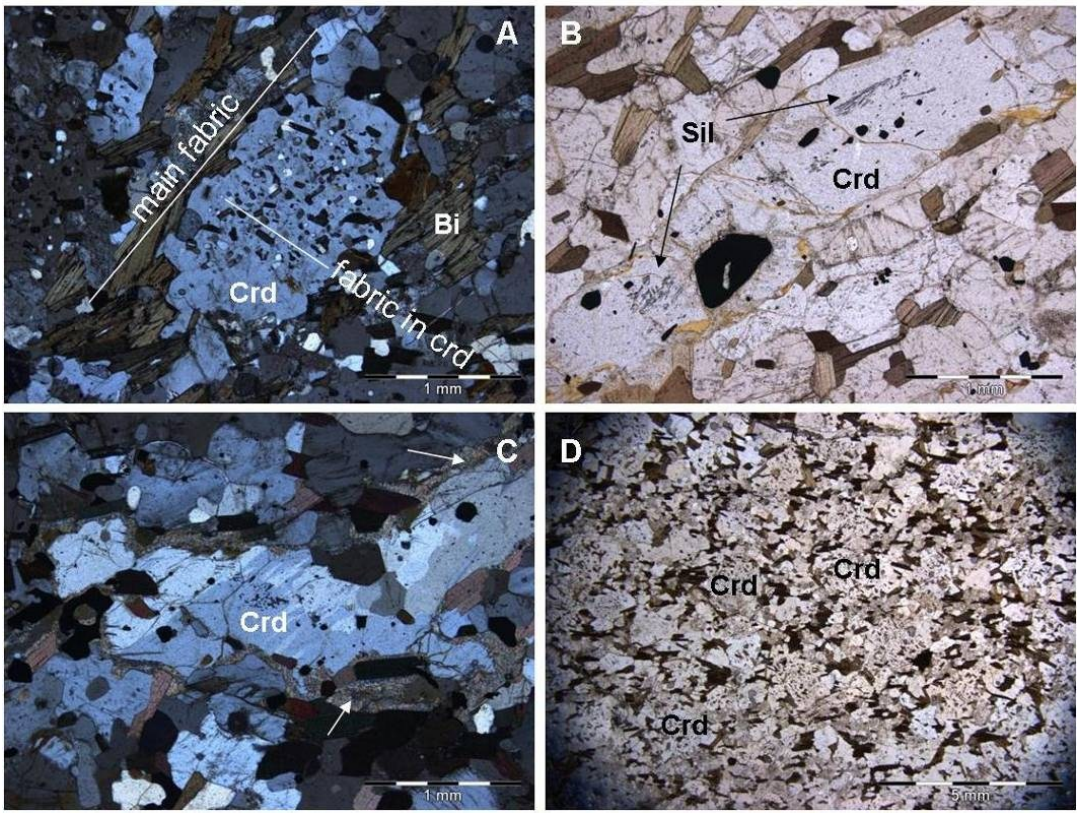

Fig. 2.17 – Photomicrographs of pelitic (cordierite-bearing) schists from the Khan Formation. A: Cordierite porphyroblast containing tiny inclusions of quartz and biotite. Note the weak fabric defined by these inclusions is approximately perpendicular to the main fabric in the schist (XPL, sample LKR024, locality 0494293/7498246). B: Elongate cordierite porphyroblast containing inclusions of opaque minerals and fibrolitic sillimanite (PPL, sample LID008, locality 0501940/7486662). C: A relatively inclusion-free, twinned porphyroblast of cordierite, with slight pinitisation along the margins, shown by arrows (XPL, sample LID008, locality 0501940/7486662). D: Very cordierite-rich (possibly restitic) sample with numerous cordierite porphyroblasts containing fine inclusions of quartz and biotite. Note the biotite surrounding cordierite is much coarser than the biotite inclusions in cordierite (PPL, sample LKR024, locality 0494293/7498246). Mineral abbreviations are after Kretz (1983).

The biotite in these schists defines a weak fabric, which does not wrap around cordierite (Fig. 2.17A). Quartz in the groundmass is slightly strained, and strain shadows are observed adjacent to inclusions in cordierite. Cordierite, locally with inclusions of sillimanite, may be slightly pinitised around the margins (Fig. 2.17B), and may show

twinning (Fig.2.17C). Some samples are extremely cordierite-rich, and contain >50 % cordierite (Fig.2.17D).

Lithologies that are less pelitic (semi-pelitic to psammitic) also have a schistose fabric defined by aligned biotite laths (Fig. 2.18A), and comprise quartz, K-feldspar, biotite, opaques (magnetite), and minor plagioclase (Fig. 2.18B).

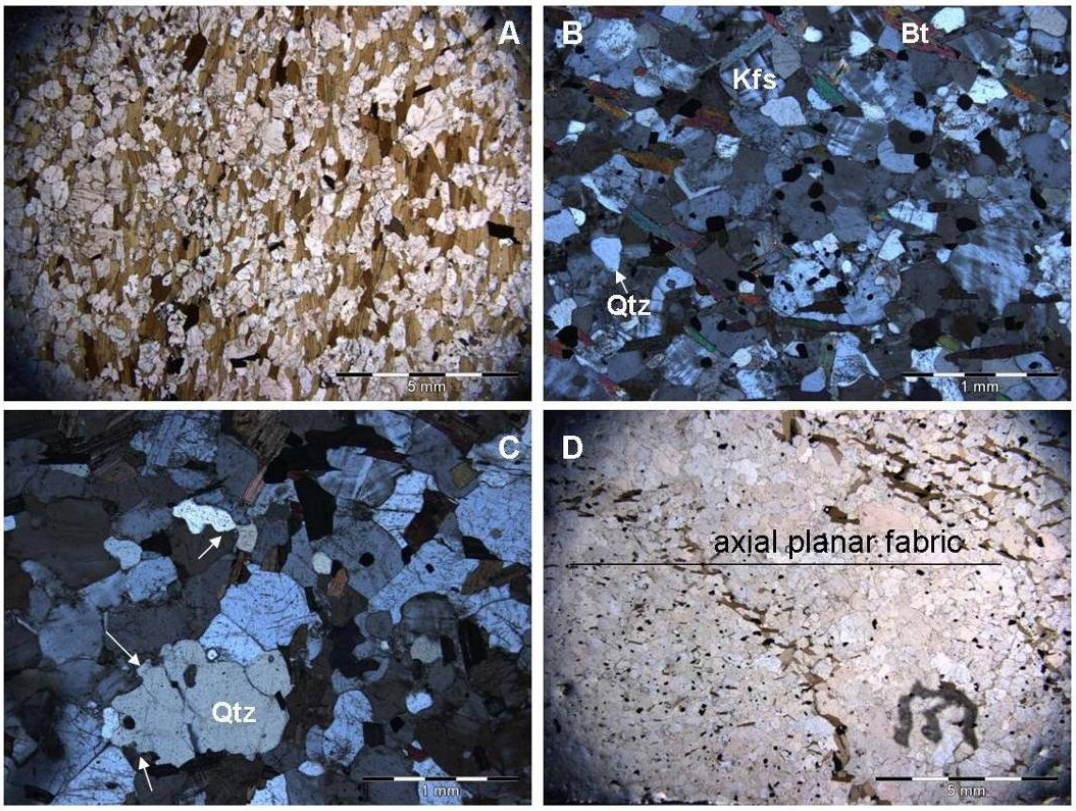

Fig. 2.18 – Photomicrographs of semi-pelitic to psammitic schists from the Khan Formation. A: Aligned anhedral to subhedral biotite laths in a semi-pelitic schist form a strong schistose fabric (PPL, sample LKR025, locality 0502209/7484972). B: Psammitic units containing K-feldspar, biotite, quartz and opaques also have a weak fabric (XPL, sample LID026, locality 0498220/7488760). C: Quartz grains with irregular, cuspate grain boundaries (shown by arrows) indicating dynamic recrystallisation (XPL, sample LID006, locality 0501940/7486662). D: Folded compositional layering, with biotite aligned with both the layering, and parallel to the axial plane of the fold (PPL, sample LID006, locality 0501928/7486355).

Quartz has irregular grain boundaries (Fig. 2.18C), suggesting dynamic recrystallisation. In these schists, the fabric is commonly parallel to compositional layering (quartz-rich or biotite-rich layering), and may be mimetically controlled. Where these schists are folded, an axial-planar fabric of aligned biotite is also commonly visible in the hinges of these folds, where it is at high angles to the layer-parallel (mimetic) fabric (Fig. 2.18D).

The Khan Formation in the Palmenhorst Dome is far thinner than observed in the Ida Dome area, although its distinctive nature is a useful stratigraphic marker. In the centre of the Palmenhorst Dome, in an area previously mapped as Abbabis Complex rocks (Lehtonen *et al*., 1995), there is an isoclinal infold of Damara Supergroup rocks that was originally identified by Barnes (1981), and is termed the ”Hook Fold” (Figs. 2.1, 2.14). The Damara Supergroup in this area is thinned by the intense deformation, and the Etusis Formation is generally indistinguishable from the Abbabis Complex, making the distinctive Khan Formation a useful indicator as to the presence of Damaran stratigraphy. Here, the Khan Formation occurs as green diopside-feldspar gneisses and cordierite-biotite schist, although in places the gneissic nature of the rocks has been lost and instead these rocks occur as blocky masses of diopside and feldspar. Like the rest of the Damara Supergroup, the Khan Formation is also thinned here, and is locally only a few metres thick.

Along the northern margin of the Palmenhorst Dome, another series of infolds of Damaran lithologies occurs (Fig. 2.1). Again, the distinctive nature of the green diopsidic Khan Formation is indicative of the presence of Damara Supergroup rocks. As with the Hook Fold, intense deformation has resulted in the Khan Formation being significantly thinner than in the Ida Dome (1 m – 10 m thickness, as opposed to 10 m – 100 m thickness in the Ida Dome), and the gneissic nature has been lost in places, with the Khan Formation occurring as 30 cm to 1 m blocks of diopside and feldspar.

Along the southern margin of the Palmenhorst Dome, the Khan Formation shows more similarity with the Ida Dome, occurring as diopside-feldspar gneisses. Although diopside gneisses are more widespread here than through the rest of the Palmenhorst Dome, the Khan Formation occupies the cores of tight E-W trending anticlines, and is less

widespread than in the Ida Dome. In addition to the diopside-feldspar gneisses, cordierite-bearing schists and gneisses are common as a part of the Khan Formation along the southern margin of the Palmenhorst Dome.

2.2.2 The Swakop Group

In contrast to the Nosib Group, the Swakop Group contains a more diverse range of lithologies, including a number of carbonate units (Fig. 2.9). The Rössing Formation (Ugab Subgroup) is separated from the Khan Formation by an unconformity (Smith, 1965; Nash, 1971; Jacob, 1974), although an alternative viewpoint that the contact is gradiational was provided by Nex (1997). The Rössing Formation is highly variable, including marble, calc-silicate and siliciclastic units (Smith, 1965; Nash, 1971; Jacob, 1974, Henry, 1992). To the southeast, the Rössing Formation pinches out, and upper Damaran lithologies rest directly on the Nosib Group as the Okahandja Lineament is approached (Miller, 2008), and the Rössing Formation is not found southeast of the Husabberg (Miller, 2008), to the east of the study area. Overlying the Rössing Formation are the tillites, iron-formations, marbles and quartzites of the Chuos Formation (Usakos Subgroup). Although not represented in the study area, the Arandis Formation (Usakos Subgroup), and the Ghaub, Karibib, Tinkas and Kuiseb formations (Navachab Subgroup) form a succession of carbonates, tillites and pelitic schists, respectively, above the Chuos Formation along the Khan River north of the Palmenhorst Dome.

2.2.2.1 The Rössing Formation

The Rössing Formation marks the first appearance of pure carbonate lithologies in the Damaran succession (SACS, 1980) and, hence, is typically characterised by a marble unit (Table 2.3; Fig. 2.19A, B). However, the Rössing Formation is also the most lithologically varied formation in the Damara Supergroup, and can include calc-silicates, metapelites (Figs. 2.19C, D), and quartzites (Fig. 2.19E). Since it is the first marble in the sequence, the Rössing Formation is a crucial marker horizon, especially where this marble is found adjacent to diopsidic material of the Khan Formation, or diamictite of the Chuos Formation.

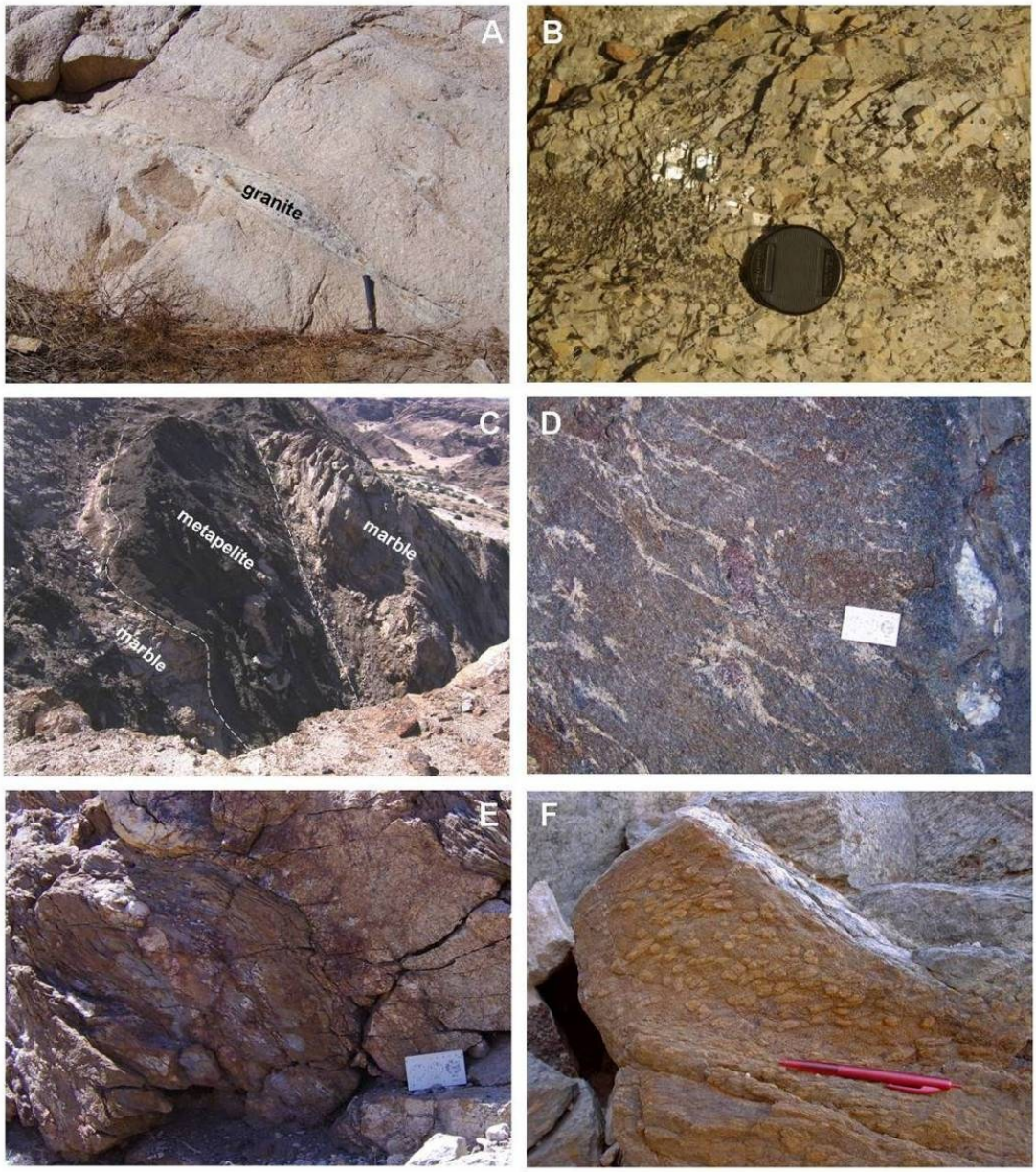

Fig. 2.20 – Rössing Formation rocks. A: Pure marble intruded by a boudinaged granite vein (locality 0502674/7485947). B: Very coarse-grained, impure marble showing recrystallised calcite and forsterite (locality 0499706/7503852). C: View (looking N) of the Rössing Formation along the eastern margin of the Ida Dome. Width of metapelite is 30-50 m (locality 0502209/7484972). D: Leucosomes and restitic garnet from partially melted metapelite (locality 0502725/7485877). E: Characteristic red-orange weathering of quartzite from the Rössing Formation (locality 0502667/7485996). F: Calc-silicate layer from the Ida Dome with elongate scapolite nodules (locality 0502712/7485921).

The Rössing Formation is well developed in the Ida Dome, forming a *ca*.150 m wide section along the eastern margin of the dome, which can be seen along the Swakop River (Figs. 2.1, 2.20). Here the sequence comprises a lower and an upper marble, with calc-silicate and metapelite units sandwiched between them (Fig. 2.19C; Table 2.3). This is similar to the Rössing Formation at Rössing Mine (Nash, 1971), where a lower and an upper marble are separated by pelites and quartzites (Table 2.3). Towards the south and east of the Ida Dome, deformation has folded the Khan and Rössing Formations into numerous tight to isoclinal folds, and the marbles of the Rössing Formation have been duplicated, forming marble packages up to *ca*. 1 km thick (Fig. 2.1). Previous workers (Jacob, 1974; Barnes, 1981) have suggested that these marbles are, in fact, Karibib Formation (Figs. 2.20B, C), but a number of factors suggest otherwise. First, these marbles lie adjacent to the diopside-feldspar gneisses of the Khan Formation. If these rocks actually do represent the Karibib Formation, then an explanation is required for the missing Rössing and Chuos Formations. The Chuos Formation, in particular, is a thick, distinctive package, present throughout the study area, and is commonly the best-developed unit in the Damara Supergroup, even where other Damaran units are missing. The thinning or removal of this formation in an area where the Khan Formation is very well developed seems implausible, although Sawyer (1981) noted a major unconformity at the base of the Karibib Formation in the southern Central Zone, south of the study area, which was clearly marked by up to 60˚ of discordance between the Chuos Formation and the Karibib Formation. To the northwest, Nex (1997) noted no removal of the Chuos and Rössing Formations.

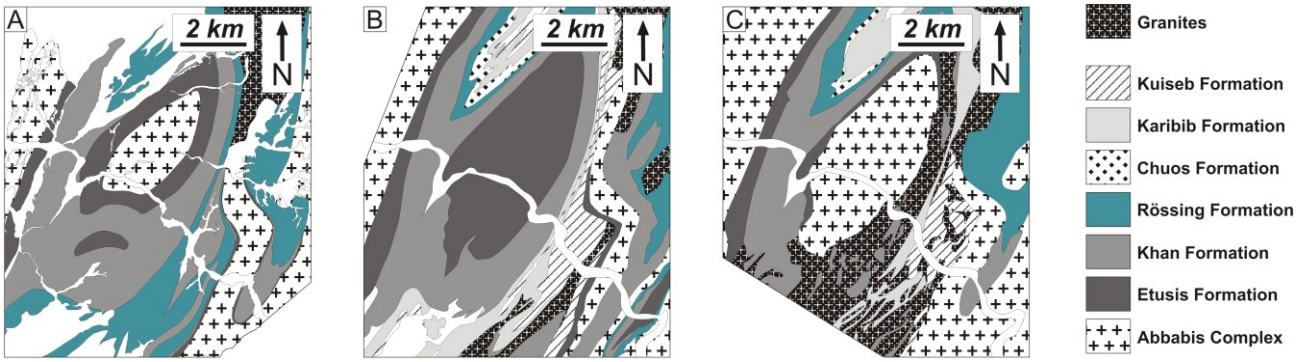

Fig. 2.20 – Mapped distributions of the Rössing Formation in the Ida Dome according to A: This study. B: Barnes (1981). C: Jacob (1974). Note that areas previously mapped as Karibib Formation are now interpreted as Rössing Formation.

Second, although it appears that the package of marbles found along the southeastern margin of the Ida Dome is up to 1 km thick (Fig. 2.1), this apparent thickness is caused by tectonic thickening of the marbles owing to upright, NE-trending folding (see section 3.5). In the Swakop River along the eastern margin of the Ida Dome, a cross-section through these marbles does not show such a thick package, as is evident from the mapped distribution of lithologies. Here, the package is less than 150 m thick, in contrast to the thicknesses of up to 1000 m commonly reached for the Karibib Formation (Sawyer, 1981; Miller, 2008), and does not show the massive marble units characteristic of the Karibib Formation elsewhere in the Central Zone (Miller, 2008), but rather a sequence similar to other Rössing Formation sequences (Table 2.3).

Table 2.3 – The stratigraphy of the Rössing Formation on the eastern margin of the Ida Dome, and comparisons with the stratigraphy described by Nash (1971) for a Rössing succession in the SJ area near the Rössing Dome, and with the stratigraphy described by Jacob (1974) for a Rössing succession in the Gurtel Hills Syncline (Fig.2.1). Thickness (in m) is given to the left of the lithology. Note that each succession contains two marble units (correlated in grey).

East Ida Dome		Nash (1971)		Jacob (1974)	
				37	Cordierite Gneiss
		100	Quartzite	33	Quartz-biotite Schist
		4-50	Upper Pelitic Gneiss	80	Quartzite
50	Upper Marble	50-70	Upper Marble	4	Marble
30	Metapelite	30-40	Lower Pelitic Gneiss	3	Quartzite
10	Calc-silicate				
40	Lower Marble	20-50	Lower Marble	5	Marble
10	Quartzite			40	Quartzite

This package of marble and metapelite continues to the northwestern margin of the Ida Dome in the Gurtel Hills Synform (Figs. 2.1, 2.20), where it was described by Jacob (1974). To the east of the Ida Dome, marbles of the Rössing Formation are recognised in the Arcadia Syncline (Fig. 2.1), where they are well developed, reaching up to 100 m in thickness.

In addition to marbles (Figs. 2.19A, B), the Rössing Formation contains a number of other lithologies, including metapelites (Figs. 2.19C, D), metapsammites (Fig. 2.19E), calc-silicates (Fig. 2.19F) and quartzites, which are locally found without any associated marble. Calc-silicate rocks comprise massive wollastonite-bearing outcrops, with variable amounts of scapolite or diopside. Along the eastern margin of the Ida Dome, a well-defined calc-silicate layer contains “nodules” of scapolite, which are elongate and form a NE-plunging mineral stretching lineation (Fig. 2.19F). In thin section, the scapolite occurs both as these large (mm-size) grains, and as small (*ca*. 0.2 mm) ‘dusty’ grains (Fig. 2.21A). Quartz is strongly annealed, with numerous 120° triple junctions. Minerals are aligned

along the lineation direction, and a banded appearance is noted in thin section. Minor magnetite and ilmenite also occur with the quartz and scapolite.

Apart from the distinctive marbles within the Rössing Formation that are forsterite- or graphite-bearing, the most common lithologies in the Rössing Formation are metapelite and quartzite with minor semipelites. Metapelites typically contain the assemblage biotite-cordierite-garnet-quartz-plagioclase-K-feldspar-ilmenite-magnetite (Fig. 2.21B). Less commonly sphene, sillimanite and muscovite may be present, although muscovite appears to be a retrograde mineral. The metapelites typically have a strong fabric, defined by aligned subhedral to euhedral biotite laths (Fig. 2.21B, C), and are commonly fairly coarse-grained, with garnet up to 20 mm in size, 5 mm cordierite, and biotite laths up to 1-2 mm in size. Garnet may be poikiloblastic, with many inclusions of rounded quartz, or the garnet may form as smaller (1-2 mm), inclusion-free subhedral porphyroblasts. The strong schistose fabric 'wraps' around cordierite, which generally has a clear, biotite-free rim. Cordierite typically contains a core of aligned needles of fibrolitic sillimanite (Fig. 2.21D); cordierite with rounded inclusions of biotite and quartz is less common. K-feldspar is observed commonly adjacent to, or surrounding cordierite, indicating a possible reaction texture (see Chapter 6). Although neither spinel nor sillimanite are present in the groundmass of any samples, locally these minerals may be found as inclusions in cordierite. Quartz in the metapelites is typically unstrained. Minor semipelites occur (Fig. 2.21E), containing biotite-quartz-plagioclase-ilmenite-magnetite, with anhedral plagioclase and quartz showing irregular grain boundaries, a strong biotite fabric, large opaques, and both strained and unstrained quartz. Quartzites from the Rössing Formation are pyrite-bearing, and weather to a deep orange-red colour (Fig. 2.19E).

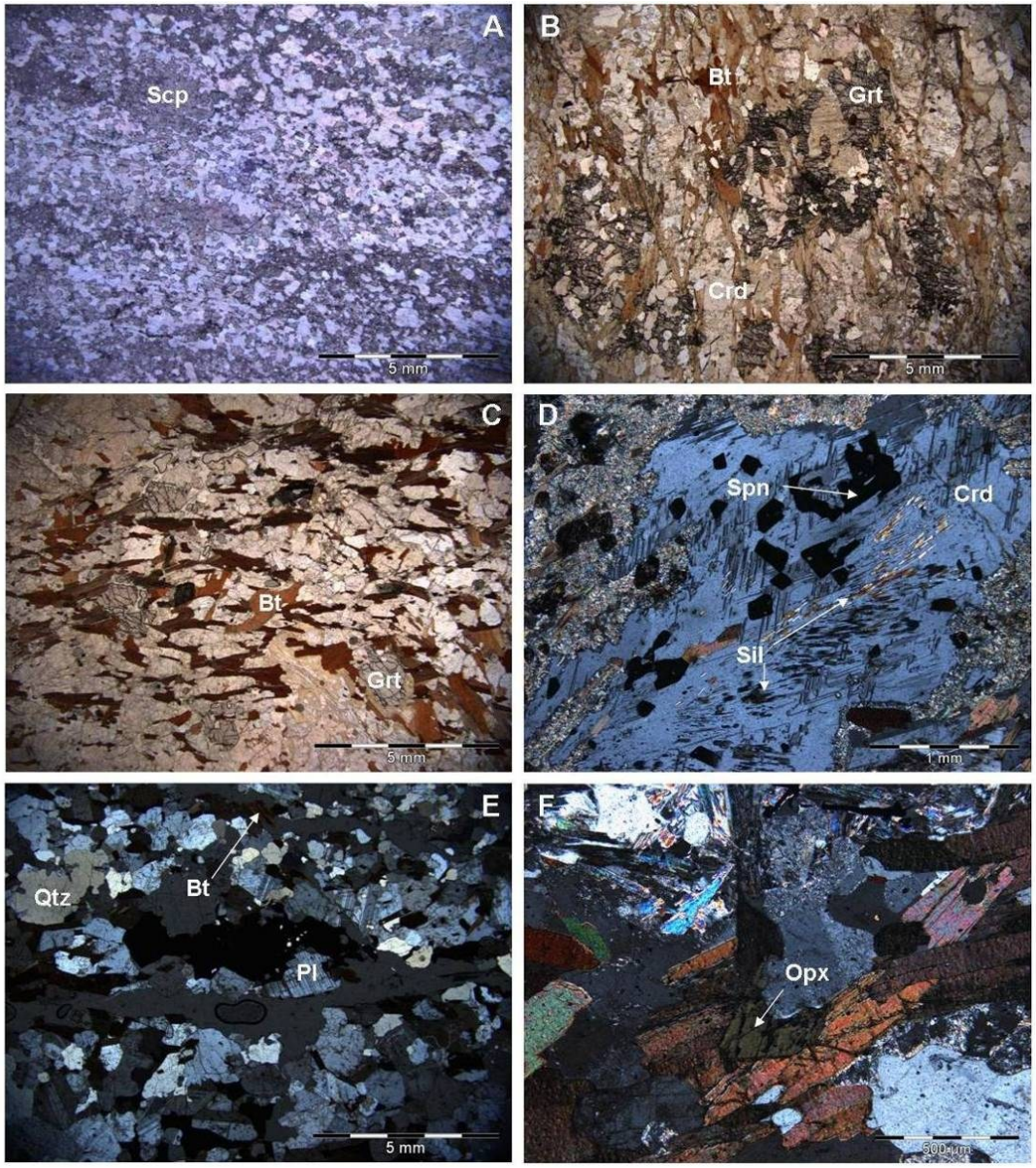

Fig. 2.21 – Photomicrographs of Rössing Formation rocks. A: Scapolite-wollastonite calc-silicate (PPL, sample LID037, locality 0502712/7485921). B: Metapelite with anhedral, poikiloblastic garnet and a strong schistose biotite fabric which wraps around porphyroblasts of cordierite (PPL, sample LID039, locality 0502737/7485903). C: Metapelite with small garnet porphyroblast and a folded biotite fabric (PPL, sample LID002, locality 0502764/7485934). D: Large, twinned porphyroblast of cordierite with inclusions of spinel and fibrolitic sillimanite, and extensive pinitisation around the margins (XPL, sample LID040, locality 0502749/7485934). E: Metapsammite containing quartz, plagioclase feldspar and biotite. Note the highly irregular shape of the quartz grain near the top left of the image (XPL, LID023, locality 0502207/7485024) F: Orthopyroxene-bearing metapelite. This orthopyroxene grain is the only one noted in this study (XPL, sample LID039, locality 0502737/7485903).

Along the southern margin of the Palmenhorst Dome, the Rössing Formation is well developed to the west of the farm Hildenhof (locality 0489303/7489440). Here, the Rössing Formation comprises a lower marble unit, overlain by wollastonite- and scapolite-bearing calc-silicates, which have a deep reddish-brown weathered surface and contain cm-scale layering. These calc-silicates are overlain by a light grey quartzite. This sequence of rocks is developed in the cores of km-scale tight, shallowly E-plunging, upright anticlines and is highly folded on a Dm- to m-scale. To the north (locality 0489330/7489990), another outcrop of Rössing Formation is found, as a small ridge of marble, running approximately E-W.

Elsewhere in the Palmenhorst Dome, Rössing Formation lithologies are found both along the northern margin of the Dome, and in the centre, where they are found together with other Damaran units in the Hook Fold (Fig. 2.1). In the Hook Fold, the Rössing Formation is found near the hinge of the synform that forms the 'hook' after which the fold is named. The Rössing Formation here comprises a marble and a gritty quartzite, however, these units thin towards the limbs of this fold, and eventually pinch out; no marble is found along the eastern limb of the Hook Fold. Along the northern margin of the Palmenhorst Dome, various marble units occur in association with calc-silicates, ferruginous quartzites, and metapelites, and which form part of a number of infolds of Damara Supergroup metasediments into the Abbabis Complex.

2.2.2.2 The Chuos Formation

The Chuos Formation is a distinctive package of diamictite with a subordinate iron formation, quartzite, and marble (Fig. 2.9). The Formation is thick and well developed in the study area, near the confluence between the Khan and Swakop rivers and north to the areas of Trekkopje and Rössing Mountain (Miller, 2008) and typically has thicknesses of a few hundred metres (Henry, 1992; Miller, 2008). In the vicinity of the Ida Dome, however, the Chuos Formation is not exposed, owing to the lower level of erosion, which results in the thickened and duplicated Khan and Rössing Formations constituting the bulk of the outcrop in the area. In contrast, the Chuos Formation makes up a significant

proportion of the Damara Supergroup rocks exposed in the Palmenhorst Dome (Figs 2.1, 2.22), and the distinctive diamictite unit, with layers of iron formation, makes this formation fairly easily recognisable. Along the northern margin of the Palmenhorst Dome, a number of thick (10s to 100s of metres) Chuos Formation packages crop out (Fig. 2.1), and the Chuos Formation also makes up the bulk of the rocks exposed in the so-called Hook Fold (Figs 2.1, 2.22). Barnes (1981) considered the entire Hook Fold to be made up of Khan Formation rocks but, in this study, a complete package of lower Damara Supergroup lithologies is recognised, including diamictite, quartz-biotite schist and banded iron formation. Thus, much of the area previously mapped in the Palmenhorst Dome by Barnes (1981) as Khan Formation is now interpreted as being underlain by Chuos Formation (Fig. 2.22).

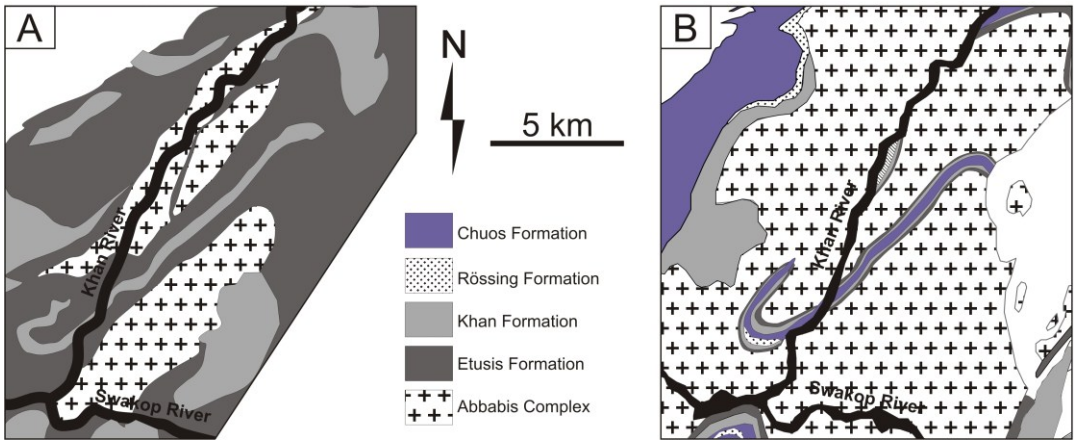

Fig. 2.22 – Comparison of mapping of the Chuos Formation in the Palmenhorst Dome. A: Distribution of lithologies according to Barnes (1981). B: Distribution of lithologies according to this study.

The packages of Chuos Formation rocks in the Palmenhorst Dome generally comprise quartz-biotite schist and diamictite (Fig. 2.23A) (with pebbles of various compositions) and a number of subordinate lithologies. The most common of these minor lithologies is an iron formation (Fig. 2.23C), forming 10 cm to 1 m thick magnetite-rich bands. Quartzites and metapsammites are also common (Fig. 2.23D), and are interbedded on a cm- to dm-scale with quartz-biotite schist. It is within these layers that the intense

deformation preserved in these rocks is best displayed. Minor pelitic lithologies are found, with cordierite-biotite-quartz (± garnet) assemblages, which display evidence for anatexis and contain cm-scale leucosomes.

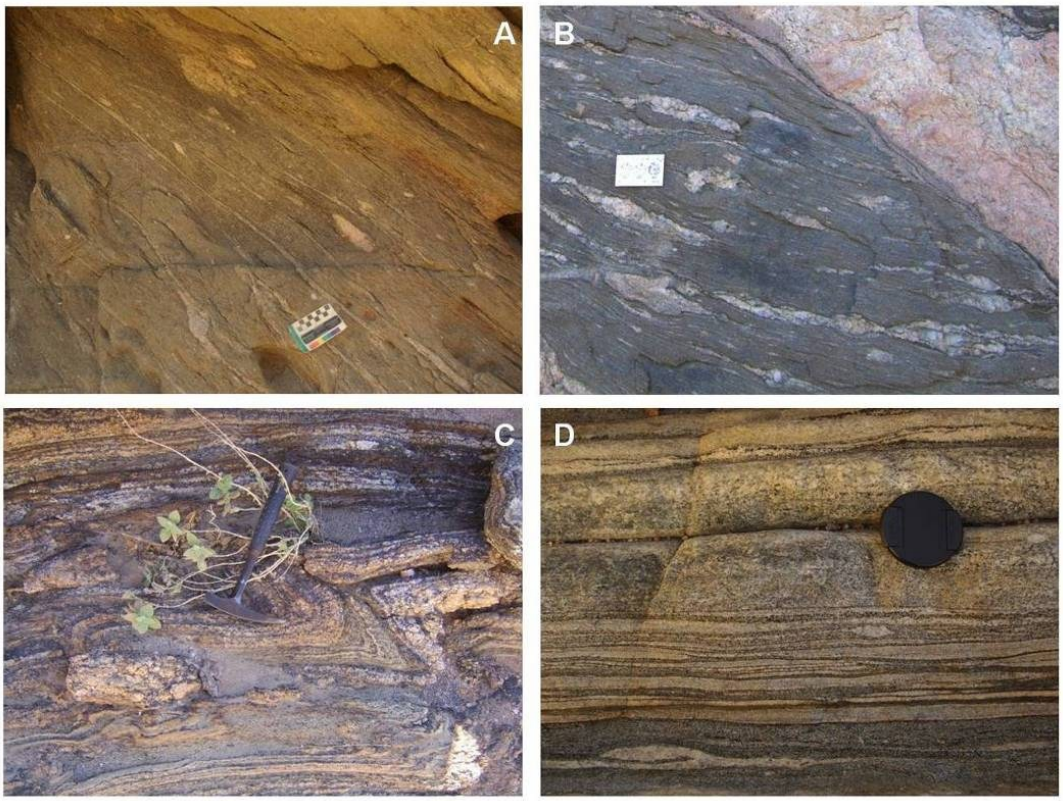

Fig. 2.23 – Field photographs of Chuos Formation lithologies. A: Typical Chuos diamictite containing a variety of clast types, as well as deformed quartzofeldspathic veins (locality 0500177/7502330). B: Quartz-biotite schist with numerous dismembered, sheared quartz veins, which may be mistaken for diamictite clasts (locality 0489439/7489720). C: Folded iron formation, containing coarse (1-3 mm) magnetite and quartz (locality 0497680/7502139). D: Quartzite with a highly transposed fabric and intrafolial folds (locality 0497638/7502030).

In the "Hook Fold" (Fig. 2.1), the Chuos Formation is the best preserved, and thickest, of the Damara Supergroup units. Here, the Chuos Formation comprises quartz-biotite schist, diamictite and minor iron formation. The diamictite contains quartzofeldspathic pebbles/clasts. Quartz-rich layers are interbedded with quartz-biotite schists, and spectacularly display the deformation. As with the Khan and Rössing Formations, the

Chuos Formation is thickest near the western hinge of the Hook Fold, and thins towards the east. However, unlike the units of the Khan and Rössing Formations, the Chuos Formation is recognisable for over 10 km towards the northeast. Although thinned to ca. 100 m, the Chuos Formation is generally the only recognisable remnant of the Damara Supergroup along the southeastern limb of the Hook Fold. It is preserved as quartz-biotite schist, with rare quartzofeldspathic clasts, which are generally 1-3 cm in size.

In addition to the Hook Fold, another sliver of Chuos Formation crops out in the core of the Palmenhorst Dome, to the north of the Hook Fold, along the Khan River (locality 0494169/7498126). Here, the Chuos Formation comprises metapsammites and quartzites interbedded with quartz-biotite schist on a cm- to dm-scale, in addition to quartz-biotite schist/diamictite with quartzofeldspathic clasts. The layers are moderately N- to NW-dipping. Along strike to the southwest, minor pelitic cordierite-biotite schists crop out.

Along the southern margin of the Palmenhorst Dome, west of the farm Hildenhof (locality 0489488/7489626), a thick Chuos Formation package is preserved. Here, the Chuos Formation is made up almost entirely of quartz-biotite schist/diamictite with cm-scale quartzofeldspathic clasts. No iron formation was found, and only minor, cm- to dm-thick psammitic layers are preserved. The rocks are highly deformed, and the apparent thickness of the Chuos Formation is due to duplication by a number of large (100's of m) upright to S-dipping, shallowly E-plunging, anticlines and synclines (see Chapter 3). Numerous m-scale folds occur, and the variable vergences of these smaller scale folds define the larger folds.

The matrix of the diamictite that makes up the bulk of the Chuos Formation exposed in the study area is biotite-quartz schist, and contains an assemblage of biotite, quartz, plagioclase feldspar, and minor amounts of K-feldspar. These rocks contain a strong schistose fabric defined by aligned subhedral to euhedral laths of ca. 1 mm biotite (Fig. 2.24A). Quartz, and rarely plagioclase, may also be elongate in the direction of the fabric, and the rocks display a partially annealed texture, with local 120˚ triple junctions (Fig. 2.24B). Plagioclase and quartz are 0.5-1 mm in size, and plagioclase may contain rounded

inclusions of quartz. Clasts are typically quartzofeldspathic (quartzite, gneiss), although schist and diopside gneiss are also locally noted as clasts. Elsewhere, cordierite schists are locally found in the Chuos Formation (Figs. 2.24C, D). These cordierite-bearing samples typically contain a biotite-quartz-cordierite-K-feldspar-plagioclase assemblage, with minor opaque minerals. A strong schistose fabric is common, defined by alignment of biotite, which is generally anhedral to subhedral, and appears interstitial to the other minerals. Cordierite is locally present as small (ca. 1 mm) porphyroblasts, with inclusions of biotite, but it is far more common as larger (ca. 3 mm) porphyroblasts of inclusion-free cordierite, aligned along the fabric, which contain a core of fibrolitic sillimanite, and are surrounded by a biotite-free halo enriched in K-feldspar and plagioclase (Fig. 2.24D). Magnetite may also be associated with this cordierite, which may be a solid restite product of the reaction sillimanite + biotite = cordierite + magnetite + melt (see Chapter 6). The bulk of these cordierite-bearing lithologies are made up of 1-2 mm sized biotite, quartz and plagioclase feldspar grains, with bands of finer quartz and biotite (0.2-0.5 mm) in more felsic layers. K-feldspar may appear as anhedral “pools”, with cuspate amoeboid boundaries (Fig. 2.24E), containing inclusions of quartz, indicating that this may be crystallised residual melt in the rock (Sawyer, 2008). Quartz shows evidence for strain (undulose extinction) in some places, elsewhere it appears entirely unstrained.

Mylonitic quartzites, which in the field show evidence for transposition and extreme flattening of layering (Fig. 2.23D), contain a quartz-biotite-K feldspar assemblage. These rocks contain a strong fabric (Fig. 2.24F), owing to aligned 0.2-1 mm biotite, and small quartz grains (0.2-0.4 mm), which appear unstrained and well annealed, with numerous 120˚ triple junctions. K-feldspar does not appear annealed, and has cuspate grain boundaries, and occurs in bands with euhedral K-feldspar grains, suggesting that the K-feldspar may be crystallised melt.

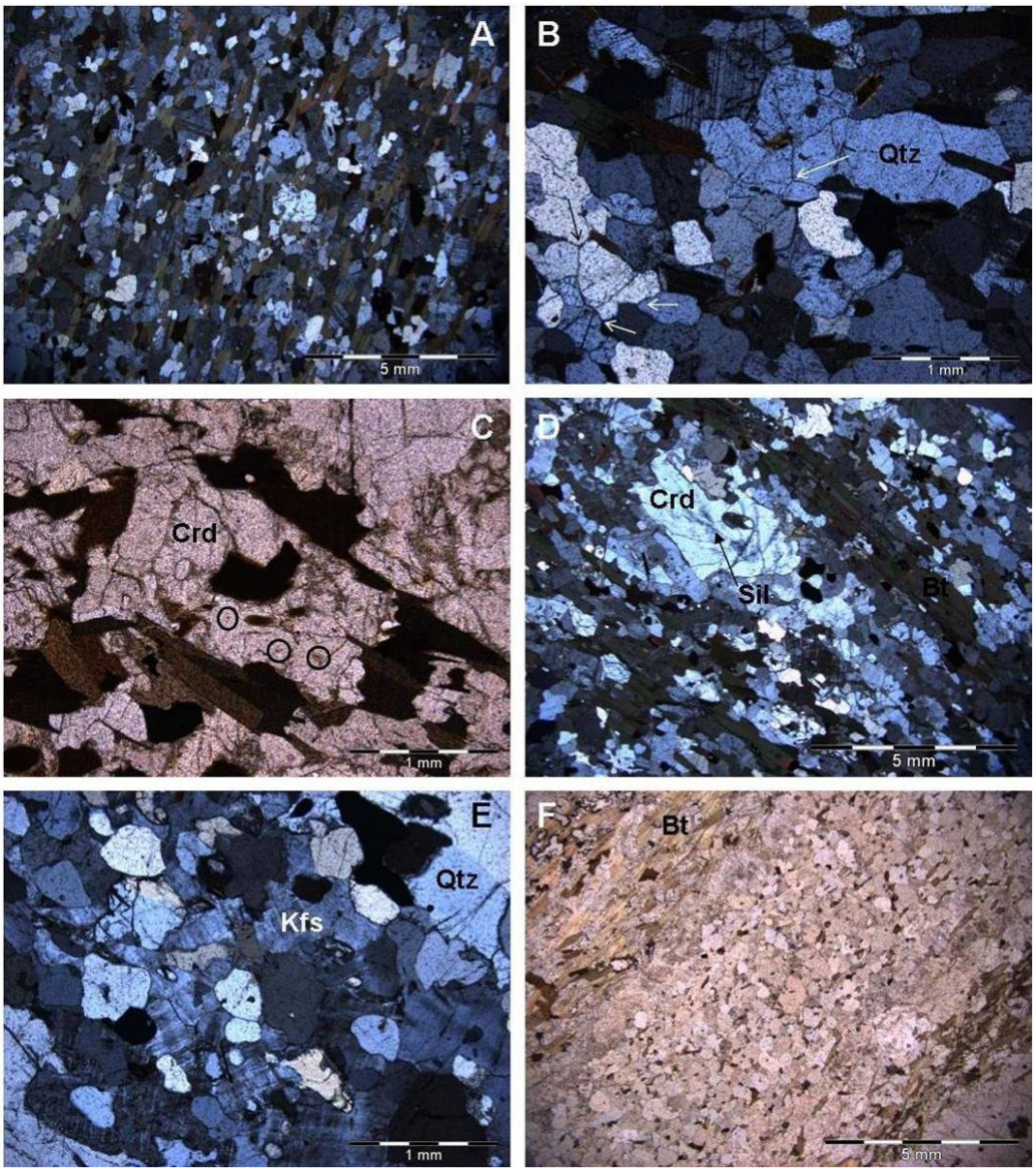

Fig. 2.24 – Photomicrographs of Chuos Formation rocks. A: Fabric in quartz-biotite schist, defined by aligned laths of subhedral to euhedral biotite (XPL, sample CZRL9, locality 0499432/7503611). B: Annealed quartz-biotite schist, showing 120˚ triple junctions in quartz, indicated by arrows (XPL, sample CZRL9, locality 0499432/7503611). C: Elongate cordierite porphyroblast, with inclusions of biotite, and radioactive accessory minerals producing yellow pleochroic haloes, which are circled (PPL, sample CZRL8, locality 0499432/7503611). D: Cordierite-biotite schist, with a strong biotite fabric, and inclusions of fibrolitic sillimanite in cordierite (XPL, sample CZRL13, 0499695/7503871). E: Large irregular K-feldspar, with irregular boundaries and rounded inclusions of quartz, indicating that this was likely to have been a pool of melt (XPL, sample CZRL13, 0499695/7503871). F: Strong biotite fabric and compositional banding in a mylonitic quartzite (PPL, sample CZRL6, locality 0499675/7504400).

2.2.2.3 The Arandis, Ghaub, Karibib and Kuiseb Formations

The Arandis Formation (Usakos Subgroup) is thought to form the cap carbonate to the glacial Chuos Formation (Miller, 2008). It is thin to poorly developed on the northern margin of the southern Central Zone but thickens to the north, reaching almost 4000 m in the northern Central Zone (Miller, 2008). It has not been recognised in the study area, and may have been removed by the major unconformity below the Karibib Formation (Sawyer, 1981). The Ghaub Formation (Navachab Subgroup), a second diamictite unit in the Swakop Group representing the 635 Ma Marinoan glaciation (Hoffmann *et al*., 2004), is also not recognised in the study area, and neither are the thick marbles (with minor calc-silicate and schist – Miller, 2008) of the Karibib Formation and the extensive, thick pelitic schists of the Kuiseb Formation. However, the Karibib and Kuiseb Formations are regionally significant, and further east and north of the study area, where higher stratigraphic levels are exposed, these formations crop out along the Khan River (e.g. Ward *et al*., 2008; Kisters *et al*., 2009). Within the study area, lower levels of erosion have resulted in only the lower Damara Supergroup being exposed. It should be noted, however, that marble along the eastern margin of the Ida Dome has been previously recorded as Karibib Formation (Figs. 2.25 A-C; Jacob, 1974; Barnes, 1981; Lehtonen *et al*., 1995), but is reinterpreted as Rössing Formation in this study (see section 2.2.2.1). Additionally, in the area between the Ida Dome and Arcadia Inlier, rocks previously mapped as Kuiseb Formation are reinterpreted as Khan Formation (Figs 2.25 D-F; Jacob, 1974; Barnes, 1981; Lehtonen *et al*., 1995). Biotite (± amphibole) schists exposed in this area do not show the pelitic affinity of the cordierite- (± garnet) biotite-schists which characterise the Kuiseb Formation northeast of the study area, but rather resemble the lower Khan Formation, and diopside-amphibole gneisses are also found in this area. Thus, rather than invoking a major unconformity between the Khan Formation and the Karibib Formation, for which there is no field evidence. The Khan Formation and overlying marbles (interpreted here as Rössing Formation) appear concordant along the eastern margin for the Ida Dome, and the area between the Ida Dome and Arcadia Inlier contains a number of upright, NE-trending km-scale folds, with Khan Formation forming the cores of anticlines and Rössing Formation exposed in synclines (also see section 3.5). Thus, only

rocks of the Abbabis Complex and lower Damara Supergroup (up to the level of the Chuos Formation) are found around the Palmenhorst and Ida domes, and the Arandis, Ghaub, Karibib and Kuiseb Formations are either not developed or have been eroded.

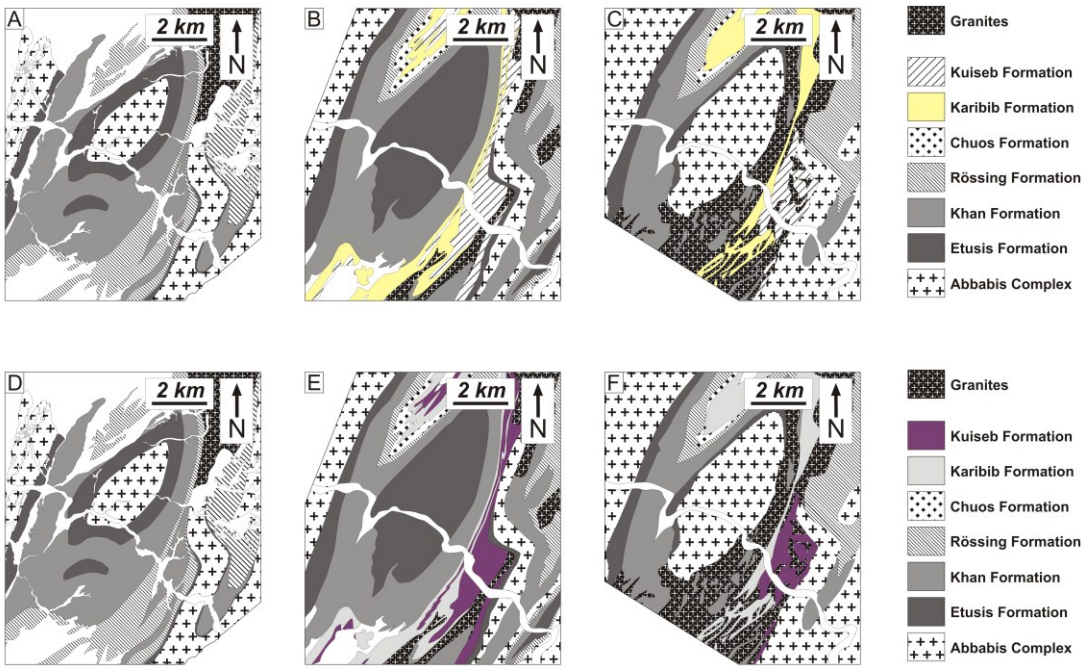

Fig. 2.25 – Reinterpretation of the mapped distributions of the Karibib and Kuiseb formations in the Ida Dome according to this study compared to Barnes (1981) and Jacob (1974). A, D: Lithological distribution according to this study. B, E: Lithological distributions according to Barnes (1981), with Karibib (B) and Kuiseb (E) formations highlighted. C, F: Lithological distributions according to Jacob (1974), with Karibib (C) and Kuiseb (F) formations highlighted. Note that areas previously mapped as Karibib Formation and Kuiseb Formation are now interpreted as Rössing Formation and Khan Formation, respectively.

2.3 Implications of Lithological Mapping

The new results regarding the mapped distribution of Damara Supergroup and Abbabis Complex lithologies in the study area have a number of implications for the structural interpretations for the Palmenhorst and Ida Domes. The Palmenhorst Dome has previously been suggested to comprise solely Abbabis Complex basement. However, a number of characteristic sequences of Khan, Rössing and Chuos Formations can be

recognised, providing conclusive evidence that Damara Supergroup rocks are present in this area. In the hinge of the Hook Fold (Fig. 2.1), where attenuation of Damaran strata is less intense than along the limbs of this fold, a full lower Damara Supergroup stratigraphy can be recognised (Fig. 2.26A). Although the Etusis Formation is missing here (owing to either non-deposition or removal during deformation) or is indistinguishable from the quartzofeldspathic gniesses of the Abbabis Complex, the diopside-feldspar gneisses of the Khan Formation, the marble and quartzite of the Rössing Formation, and the diamictite and banded iron formation of the Chuos Formation are clearly recognisable.

Similarly, along the northern margin of the Palmenhorst Dome, a distinct Damaran succession is identifiable (Fig. 2.26B), with quartzites of the Etusis Formation adjacent to biotite-amphibole schist of the Khan Formation, followed by a thick, distinctive marble (with ferruginous quartzite and metapelite) of the Rössing Formation, and diamictite and schist of the Chuos Formation. Other similar packages of Damara Supergroup strata are found along the northern margin of the Palmenhorst Dome (Figs. 2.1; 2.26). Although the map of Lehtonen *et al*. (1995) does not show any Damaran units in this area, Rössing Formation rocks were originally identified in this area by Smith (1965), and Barnes (1981) also identified Damaran units in this area. The results of this study show that there is more than a single infolded package of Damara Supergroup lithologies in this area - in fact, three infolds can be identified (Figs. 2.1; 2.28). The northernmost of these is most easily identified, where a well developed Rössing Formation comprises distinct marble units and associated ferruginous quartzite and metapelite (Fig. 2.26B). These rocks dip steeply to the north, and thin units of Khan Formation biotite-amphibole schist, Etusis Formation quartzite and Abbabis Complex augen gneiss are found sequentially northwards of the Rössing Formation exposures. The sequence appears to be overturned and may represent the inverted limb of a km-scale fold (see Chapter 3, sections 3.4.1 and 3.4.2). This sequence of Damaran lithologies thins to the west, where it is cut by the Swakop River, which trends slightly oblique to the strike of these rocks. Along this section adjacent to the Swakop River, the Rössing Formation is significantly thinned, and is recognised as masses of wollastonite calc-silicate, metapelite, and rare thin marble units as rafts in voluminous granitoids.

This sequence (the northernmost of three infolds near the northern margin of the Palmenhorst Dome) is along strike from metasediments identified by Poli (1997), but interpreted as part of the Tsawisis Formation of the Abbabis Complex (Poli, 1997). These metasediments are reinterpreted as Damaran metasediments rather than being pre-Damaran (also see section 2.1.2). The complete lower Damaran succession identified in this study was outside of the area mapped by Poli (1997), who focused on the "Nose Structure" (Fig. 2.1). To the south of this Damara Supergroup succession, a number of other sequences of overturned Damaran rocks are found, representing other infolds of Damara Supergroup rocks into the Abbabis Complex. The second infold south of the Nose Structure is recognised as a 5-10 m thick marble (Rössing Formation) between diopsidic material of the Khan Formation and diamictite of the Chuos Formation. The Chuos Formation in this area is well developed. Even further south from this, a third succession of N-dipping Damaran stratigraphy in identified, which includes (from north to south) quartzites of the Etusis Formation, a massive diopside-amphibole-phlogopite unit of the Khan Formation, a marble of the Rössing Formation, and iron formation, metapsammite and diamictite of the Chuos Formation. To the south of this Damaran succession, gneisses of the Abbabis Complex occur (Fig. 2.1). A number of shear zones separate these Damaran successions, and record high strains during Damaran deformation. The limbs of these infolds have been thinned in places during this deformation (also see section 3.4.2).

The areas where these sequences are identified represent areas where Damaran metasediments have been infolded together with the gneisses of the Abbabis Complex, and rather than comprising Abbabis Complex gneiss in its entirety, the Palmenhorst Dome contains a number of tightly folded lower Damara Supergroup sequences in the Hook Fold near the centre of the dome, and along the northern margin of the dome (Figs. 2.1, 2.28). The pattern of the lithological distribution in both the Ida and Palmenhorst domes shows similarity to a type-2 (Ramsay, 1967) fold interference pattern, and the implications of the infolding of the Damara Supergroup with Abbabis Complex for the structural history of the study area is addressed in Chapter 3).

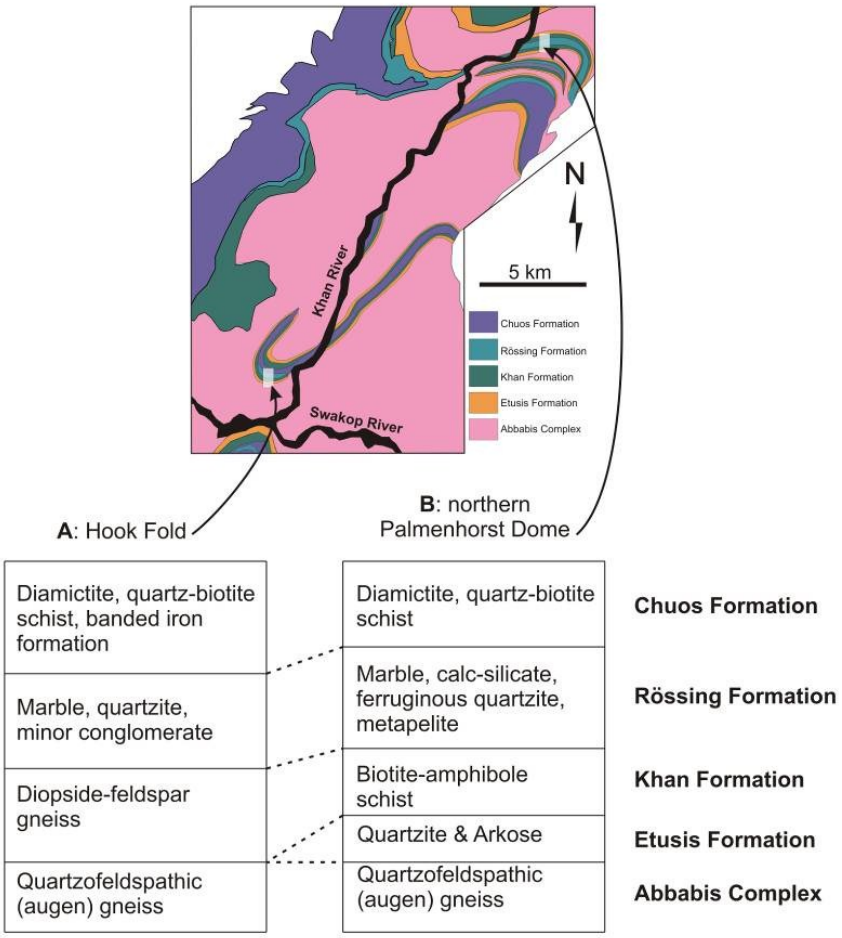

Fig. 2.26 – Lower Damara Supergroup stratigraphic packages found in the Palmenhorst Dome. A: The hinge of the Hook Fold. B: The northern margin of the Palmenhorst Dome.

The presence of a package of Damaran lithologies in the Hook Fold was first recognised by Barnes (1981). In this area, a distinctive Damaran succession is developed only at the southwestern extremity of the fold. A 10-20 m thick marble, and an overlying 5 m thick gritty quartzite (Rössing Formation), lie above a thin, poorly developed Khan Formation (which comprises massive blocks of diopside-amphibole rock, with associated phlogopite), and below thick, well developed diamictites and associated iron formation of the Chuos Formation. The marble, quartzite and diopsidic material of the Khan and Rössing Formations thin towards the east, as does the iron formation of the Chuos Formation. Along the eastern limb of the Hook Fold, the Rössing Formation is entirely missing, and

the Khan Formation is preserved as diopsidic masses that continue irregularly along strike. However, even where the entire Damaran succession has been thinned to a few hundred metres, distinctive quartz-biotite schist with quartzofeldspathic clasts (the diamictite of the Chuos Formation) is preserved along strike. Although a distinctive Damaran stratigraphy can only be identified in the hinge zone of the Hook Fold, this package is continuous along strike, and is visible on remote-sensed imagery and aerial photographs (Fig. 2.27).

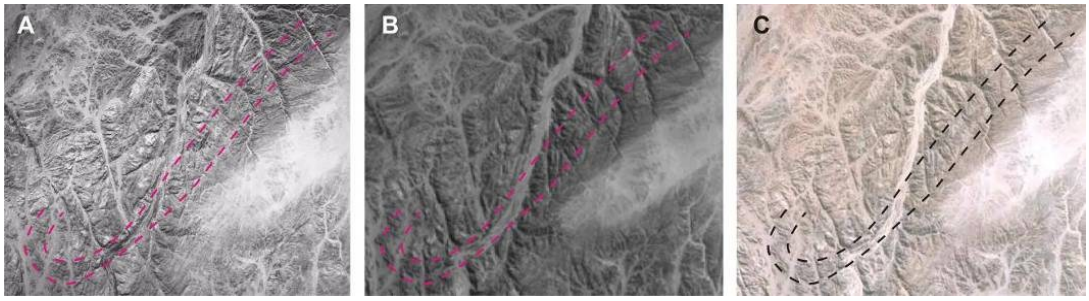

Fig. 2.27 – The trace of the Hook Fold (dashed line), on A: An aerial photograph of the Palmenhorst Dome. B: A Landsat image of the Palmenhorst Dome. C: A Google Earth™ image of the Palmenhorst Dome. Note that on all images, the strike of the Damaran units which make up this structure (generally Chuos Formation) is subtly visible, and can be traced northeast from the hinge of the fold across the Khan River.

In addition to the finding that the Palmenhorst Dome contains a number of infolds of Damaran Sequence units, two other interpretations are important. The first is the reclassification of the carbonate, calc-silicate and metapelite unit from the eastern margin of the Ida Dome as Rössing Formation, rather than Karibib Formation, and the biotite schist as Khan Formation, rather than Kuiseb Formation, as previously mapped (e.g. Lehtonen *et al*., 1995). The reasons for this reclassification have been discussed above but it is emphasised here, as this interpretation has implications for the deformation history of the study area. The second observation is that the Abbabis Complex in the Ida Dome comprises only orthogneisses, whilst a paragneissic affinity is locally noted within the Palmenhorst Dome. This observation may be reflected in the various ages obtained from basement rocks in the Ida and Palmenhorst Domes, with augen orthogneisses (granitoids) from the Ida Dome yielding *ca*. 2 Ga ages (Tack *et al*., 2002 and Chapter 5, this study),

similar to ages from the Abbabis Inlier (Jacob *et al*., 1978), whilst younger ages (1100-1040 Ma) were found for rocks in the Palmenhorst Dome (Kröner *et al*., 1991), where paragneisses have been noted in this study. These ages may imply that the granitic Narubis Complex (orthogneisses) are older (*ca*. 2 Ga) and the metasedimentary (i.e. paragneissic) Noab and Tsawisis Formations (*ca*. 1 Ga), and that the stratigraphic column proposed for the Abbabis Complex (Brandt, 1987 – see table 2.1) is, in fact, inverted. Alternatively, these different ages could represent a 2 Ga event overprinted by a 1 Ga event on the Congo Craton (Rainaud *et al*., 2005a).

2.4 Summary

The stratigraphy of the Abbabis Complex in the study area appears far simpler than that suggested for the type locality (Brandt, 1987). No obvious metasedimentary or metavolcanic successions are noted, and the Ida Dome and Arcadia Inlier appear to comprise entirely orthogneisses of the Narubis Granitoid Complex (Table 2.1). Although paragneisses are evident in places within the Palmenhorst Dome, they are quartzofeldspathic, and no marbles, calc-silicates, metavolcanics, quartzites or meta-arkoses (Noab or Tsawisis formations – Brandt, 1987) have been noted. The metasedimentary rafts within voluminous granitoids near the Nose Structure (northern margin of the Palmenhorst Dome), have been interpreted here as Damara Supergroup strata, rather than as the Tsawisis Formation, as suggested by Poli (1997).

The Damara Supergroup stratigraphy in the study area appears similar to that mapped elsewhere in the southern Central Zone by various workers, and only the lower parts of the Damaran succession (Etusis to Chuos formations) are found in the Ida and Palmenhorst domes. The Etusis Formation comprises quartzite, meta-arkose, pelitic schist, sillimanite schist and minor biotite schist and pelitic schist, with cross-bedding commonly defined by heavy minerals (magnetite and ilmenite), and easily recognisable. This is similar to the Etusis Formation near Goanikontes (Nex, 1997), as well as elsewhere in the Central Zone (Smith, 1965; Sawyer, 1981; De Kock & Botha, 1989; Henry, 1992).

Commonly, the Etusis Formation is thin, or not present, owing either to tectonic removal or non-deposition. The deposition of the Etusis Formation in half-grabens, separated by basement highs (Miller, 2008), may explain the erratic distribution and variability in thickness of the Etusis Formation in the study area. Although augen gneisses were considered by Barnes (1981) to be part of the Etusis Formation, they are included in the Abbabis Complex in this study, and U-Pb dating shows them to be clearly pre-Damaran in age (see Chapter 5). No conglomerates have been noted in the Etusis Formation in the study area, although they are locally noted elsewhere in the Central Zone (Marlow, 1981; Henry, 1992; Miller, 2008). The Khan Formation in the Ida Dome is similar to that noted elsewhere in the Central Zone, with a lower pyroxene-amphibole-feldspar gneiss, a number of schist and semi-pelite units, and an upper pyroxene-feldspar (± amphibole) gneiss (Table 2.2). Sections through the Khan Formation elsewhere in the Central Zone show a similar sequence of lithologies (Nash, 1971; Barnes, 1981; Berning, 1986; Nex, 1997) found in this study, although many workers note para-amphibolite or biotite-amphibole schist at the top of the formation (e.g. Nash, 1971; Nex, 1997), lithologies that are not noted in this study. In the Palmenhorst Dome, the Khan Formation is thin, and a full stratigraphy is unrecognisable. Here, it is identified as pyroxene-feldspar (± amphibole) gneisses, or locally as masses of diopside-amphibole-feldspar skarn. The Rössing Formation is well developed throughout the study area, and an excellent section through it can be seen on the eastern margin of the Ida Dome (Table 2.3), where similarities to Rössing Formation sections elsewhere are apparent. Throughout the study area, it is commonly seen as a single marble unit, with associated calc-silicate, metapelite, and ferruginous quartzite/arkose, and a second upper marble unit may be seen, as well as local conglomerate horizons. On the eastern margin of the Ida Dome, it was previously mapped as Karibib Formation, but this interpretation is challenged here (see section 2.2.2.3). The Chuos Formation is not present in the Ida Dome, but is well developed in the Palmenhorst Dome, where a thick diamictite package is found, with subordinate metapsammite and banded iron formation. Much of the biotite schists of the Chuos Formation were mapped by Barnes (1981) as Khan Formation, but clearly recognisable diamictite has led to their being recognised as definitively Chuos Formation. No units above the Chuos Formation are found in the study area, and the marble and schist east of

the Ida Dome interpreted previously as Karibib and Kuiseb formations, respectively (Jacob, 1974; Barnes, 1981; Lehtonen *et al*., 1995) have been reclassified as Rössing (marble) and Khan (schist) formations. Thus, the lower Damara Supergroup stratigraphic package recognised in the study area is similar to the Damaran stratigraphy found throughout the Central Zone (Smith, 1965; Nash, 1971; Jacob, 1974; Sawyer, 1981; Barnes, 1981; Nex, 1997; Poli, 1997; Miller, 2008).

The mapped distributions of the Abbabis Complex and Damara Supergroup lithologies shown in this chapter (Fig. 2.28), however, do differ somewhat from previous work. Damara Supergroup rocks have been recognised within the Palmenhorst Dome, both in the Hook Fold and along the northern margin, in contrast to the maps of Jacob (1974) and Lehtonen *et al*. (1994), which show this area as being entirely underlain by Abbabis Complex gneisses. Barnes (1981) recognised Damara Supergroup rocks in the Palmenhorst Dome, but the exact distribution of these rocks, and the stratigraphic classification of the lithologies, differs from that presented in this study. In the Ida Dome, the lithological distribution mapped in this study is more similar to that in previous studies (e.g. Jacob, 1974), although the area underlain by Abbabis Complex gneiss (Figs. 2.1, 2.3) is thought to be smaller than that shown by some workers (Jacob, 1974; Lehtonen *et al*., 1995). Barnes (1981) considered there to be no Abbabis Complex gneisses exposed in the core of the Ida Dome, a view challenged by the results of this study.

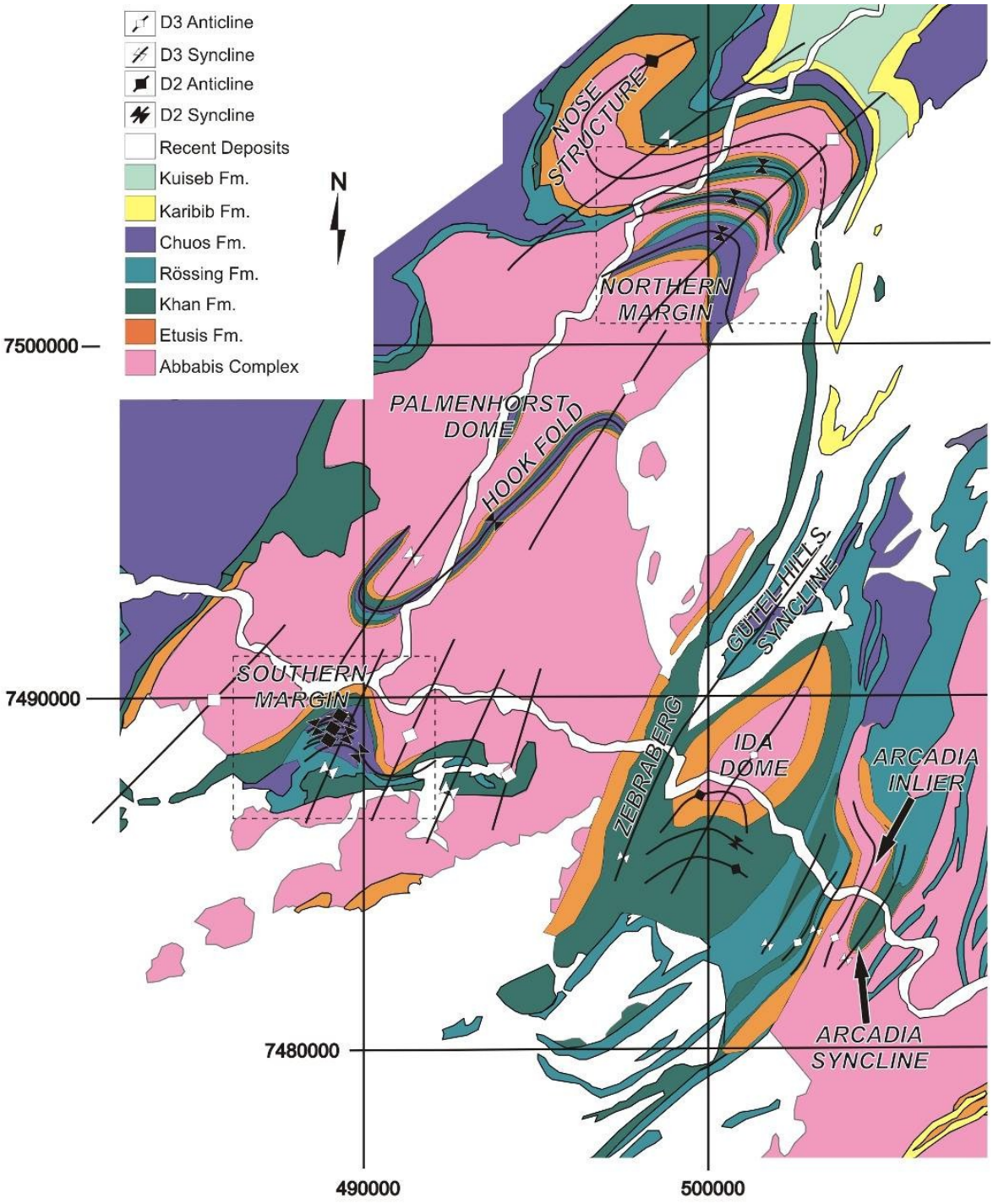

Fig. 2.28 – Geological map of the study area produced from this study, showing the distribution of the Abbabis Complex and Damara Supergroup rocks, with structural interpretations shown. Notice the apparent type-2 (Ramsay, 1967) fold interference pattern for the Ida and Palmenhorst domes. The main deformation events apparent from lithological mapping are termed D2 and D3 (see Chapter 3 for details of the structure and deformation in the study area).

The mapped distributions of Damara Supergroup and Abbabis Complex rocks have implications for the deformation history of the study area. Damaran rocks in the Palmenhorst Dome appear to be infolded synclines within gneisses of the Abbabis Complex, and the overall pattern of both the Ida and Palmenhorst domes is suggestive of a type-2 (Ramsay, 1967) fold interference pattern (Fig. 2.28). Sequential overprinting folding has been suggested for the Central Zone previously (Smith, 1965; Jacob *et al*., 1983; Miller, 2008), although this has been challenged by Poli (1997) and Poli & Oliver (2001) who considered deformation in the Central Zone (and the apparent fold interference pattern) to be the result of a single phase of progressive deformation. The large-scale structures identified by lithological mapping form the basis for more detailed investigation into the structural history of the Ida and Palmenhorst Domes, and the results of a structural investigation in the study area is presented in Chapter 3.

CHAPTER 3 – STRUCTURE

Domes (commonly cored by Abbabis Complex gneisses) are a characteristic feature of the Central Zone (Smith, 1965; Barnes, 1981; Sawyer, 1981; Jacob *et al*., 1983; Poli, 1997; Miller, 2008), and the formation of these is related to the intense deformation that has been recorded in the Central Zone by various workers (Smith, 1965; Barnes, 1981; Sawyer, 1981; Jacob *et al*., 1983; Buhn *et al*., 1994; Poli, 1997; Kisters *et al*., 2004). Whilst there have been a number of ideas published regarding the origins of domes of the Central Zone, not all work published has been based on detailed structural studies. A detailed review of dome formation models is provided here, followed by a review of previous studies of the deformation in the Central Zone. Models published for the domes of the Central Zone include:

- Interference folding by two sequential events (Smith, 1965; Jacob *et al*., 1983)
- A single phase of constrictional deformation (Poli, 1997; Poli & Oliver, 2001)
- Metamorphic/extensional core complex development (Oliver, 1994, 1995)
- Diapiric remobilisation of basement into Damara Supergroup cover rocks (Barnes & Downing 1979; Barnes, 1981; Sawyer, 1981)
- Magmatic deformation by ballooning granites (Kröner, 1984)
- Mega-scale sheath folding (Coward, 1981)
- Tip-line folds located above blind thrusts (Kisters *et al*., 2004)

Each of these models contains its own characteristic features that may distinguish it from other mechanisms. However, these are not the only models that have been proposed regarding formation of mantled gneiss domes (i.e. a dome of crystalline gneiss mantled by younger metasedimentary rocks – Eskola, 1949), which are a common feature in many high-grade orogenic belts. In addition to the mechanisms proposed for the domes of the Central Zone, a number of general mechanisms have been invoked to explain the formation of gneiss-cored domes in other areas. These include:

1. Diapiric flow by density inversion (e.g. the Scandinavian Caledonides – Ramberg, 1980).
2. Coeval horizontal constriction and extension (with extension perpendicular to compression) (e.g. the North American Cordillera – Yin & Dunn, 1992; Fletcher *et al*., 1995)
3. Orthogonal contraction or superposition of multiple phases of folding (e.g. the Pan-African, Egypt – Fowler & Osman, 2001).
4. Instability induced by vertical variation in viscosity (e.g. Fletcher, 1991; 1995).
5. Arching of corrugated detachment faults by extension-induced isostatic rebound (i.e. metamorphic core-complex development) (e.g. the North American Cordillera – John, 1987).
6. Formation of doubly-plunging antiforms induced by thrust-duplex development (e.g. the North American Cordillera – Yin & Kelty, 1991).

Some of these general mechanisms are similar to those proposed for the Central Zone. Diapiric flow by density inversion may explain the rapid decompression and partial melting commonly observed in orogenic middle crust (e.g. Teyssier & Whitney, 2002), and should show distinctive structural features such as radial stretching lineations or tangential flattening foliations around the dome, and top-outwards shearing in gneiss domes (e.g. Gapais *et al*., 1992; Fig. 3.1 A). The evidence for whether or not the hypothesis is valid that the gneiss domes of the Central Zone are the result of diapirism of remobilised basement into Damara Supergroup cover rocks (Fig. 3.1B; Barnes & Downing, 1979; Barnes, 1981; Sawyer, 1981) should be whether such distinctive structural features are found in these domes. Similarly, the formation of the domes of the Central Zone by magmatic deformation by ballooning granites (Fig. 3.1B; Kröner, 1984) should have resulted in tangential or radial fabrics around these domes. There is not a great amount of difference between these two mechanisms – both involve the diapiric rise of lower density material (remobilised basement or granite) into higher density material (the metasediments of the Damara Supergroup. Barnes & Downing (1979) suggested that the cores of some domes in the Central Zone comprise 50-70 % granite, and that flattening strains and folded veins around the margins of the dome indicate a “ballooning-type”

expansion of the granites, and Kröner (1984) speculated that the Namibfontein-Vergenoeg twin domes are largely occupied by Damaran-age granitoids, and were formed by magmatic deformation by ballooning granites. In support of this, he noted that granitoid veins intruded subparallel to the regional fabric along the margins of the domes were boudinaged, whilst those cutting the fabric were folded, suggesting flattening parallel to the dome margins. A slight variation on the diapiric mechanism is that domes are the result of crustal instability induced by vertical viscosity variation under contraction (Fletcher, 1991). This theoretical model has not been suggested for the Central Zone, and it does not require a density inversion in the crust. Fold patterns simulated via this approach can reproduce the patterns of domal structures in orogenic belts (Fletcher, 1995), and it should be considered as a possible mechanism for the Central Zone. Transverse compression perpendicular to regional extension under horizontal constriction has been suggested as a mechanism for many gneiss domes in orogens (Yin, 2004). Supporting evidence for this coeval development of contraction perpendicular to extension is the formation of folds with axes parallel to the regional extensional direction, with folding of syn-detachment-faulting strata concordant with faulting (Fig. 3.1C). This mechanism may result in evenly spaced domes (Yin, 1991).

The mechanism proposed by Poli (1997) and Poli & Oliver (2001) for the formation of domes in the Central Zone, whereby they are the result of a single phase of constrictional deformation, is similar to the general case mechanism of contraction perpendicular to extension. They propose a progressive evolution of deformation in the Central Zone, with initial constriction of a subhorizontal fabric to form gentle domes, proceeding to SW-vergent, subvertical flow of thickened crust resulting in peak amplitudes for the domes (Fig. 3.1 D). As these domes form, higher strains develop at or near the basement-cover contact, forming areas of extension, and linear fabrics. This mechanism is in contrast to the general case of orthogonal constriction or superposition of two phases of folding (Ramsay, 1967; Fig. 3.1E), where extension perpendicular to the contraction direction is not noted. Interference folding by two sequential events has been proposed for the domes of the Central Zone (Smith, 1965; Jacob *et al*., 1983; Fig. 3.1F), based on detailed structural studies of domes in the Central Zone. Arching of extensional detachment faults

owing to isostatic rebound (i.e. metamorphic core-complex development – Fig. 3.1G) has been proposed both for a number of domes in various orogens (e.g. Lister & Davis, 1989) and for the domes of the Central Zone (Fig. 3.1H) (Oliver, 1994; 1995), and this model has distinctive characteristics, making it a testable hypothesis for the domes of the Central Zone. The most important of these is that brittle upper crust is separated from deep exhumed crust by a zone of high-temperature mylonites, with a metamorphic gap developed between the high-temperature lower crust and the cooler upper crust. Coward (1981) proposed that the domes of the Central Zone were formed by mega-scale sheath folding in a major, gently-dipping shear zone, and that these folds were modified by diapirism owing to the intrusion of late granites. The formation of domes as doubly-plunging antiforms has been documented in thin-skinned fold and thrust belts, such as those in the Cordilleran foreland (e.g. Fermor & Price, 1987; Yin & Kelty, 1991). Such a mechanism is generally applicable to lower-grade rocks (Fig. 3.1I), and has been suggested for domes in lower-grade portions of the Central Zone by Kisters *et al*. (2004), who documented thin-skinned fold-and-thrust style tectonics in the areas around Usakos and Karibib, and who proposed that the Usakos and Karibib domes are tip-line folds located above blind thrusts (Fig. 3.1J).

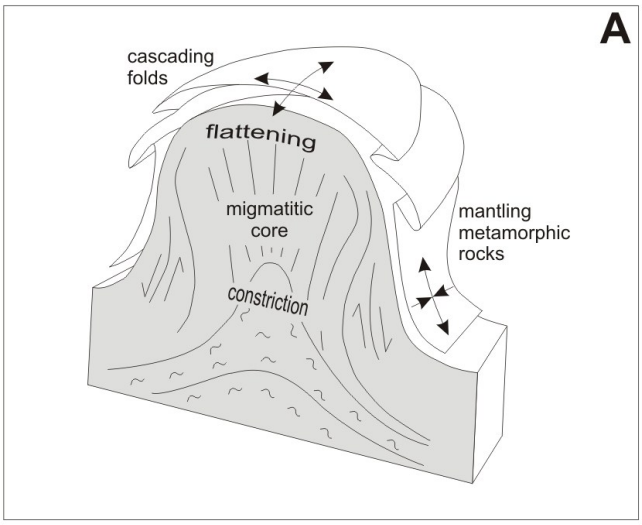
A
cascading folds
flattening
migmatitic core
constriction
mantling metamorphic rocks

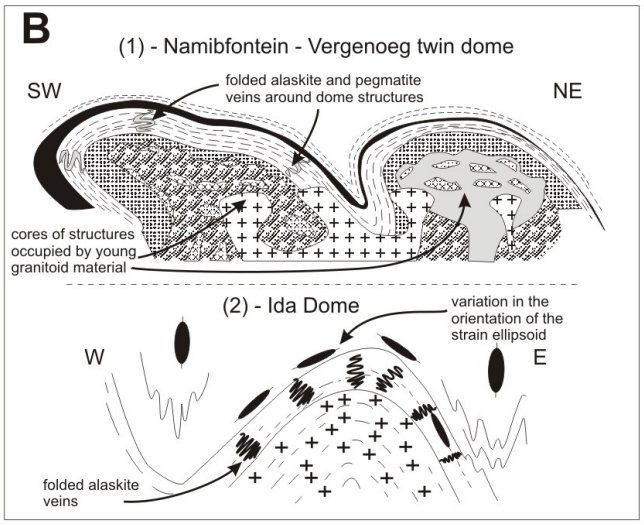
B
(1) - Namibfontein - Vergenoeg twin dome
SW
NE
folded alaskite and pegmatite veins around dome structures
cores of structures occupied by young granitoid material
(2) - Ida Dome
variation in the orientation of the strain ellipsoid
W
E
folded alaskite veins

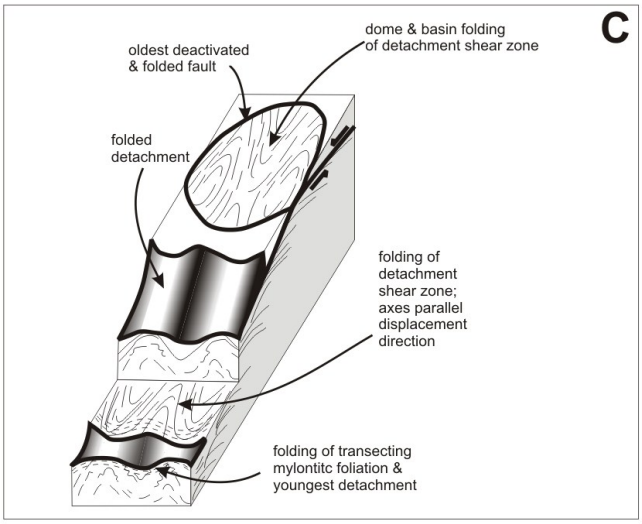
C
oldest deactivated & folded fault
dome & basin folding of detachment shear zone
folded detachment
folding of detachment shear zone; axes parallel displacement direction
folding of transecting mylontitc foliation & youngest detachment

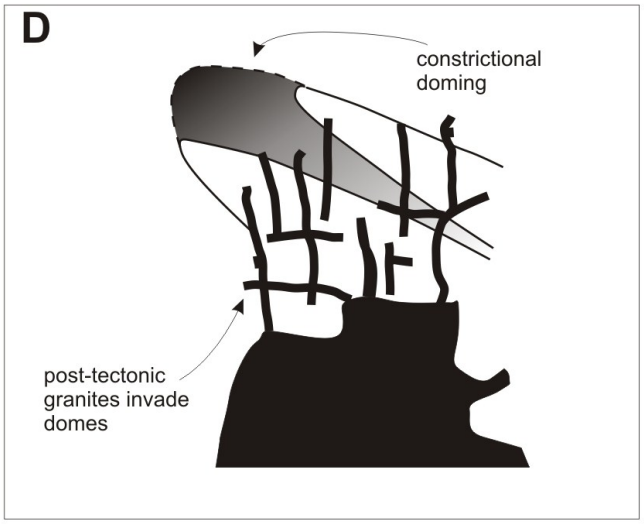
D
constrictional doming
post-tectonic granites invade domes

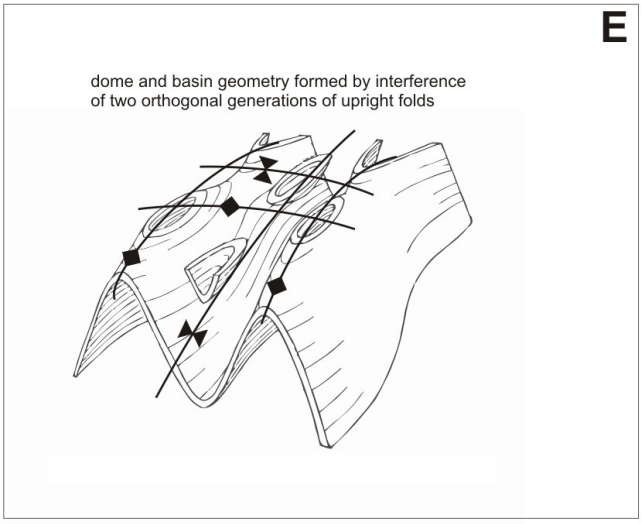
E
dome and basin geometry formed by interference of two orthogonal generations of upright folds

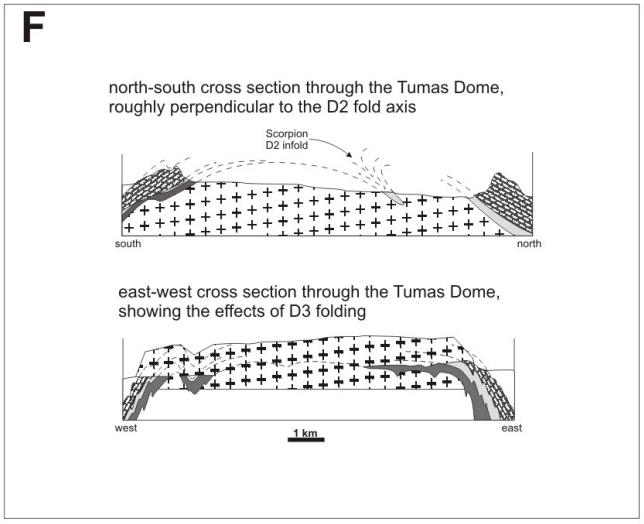
F
north-south cross section through the Tumas Dome, roughly perpendicular to the D2 fold axis
Scorpion D2 infold
south
north
east-west cross section through the Tumas Dome, showing the effects of D3 folding
west
east
1 km

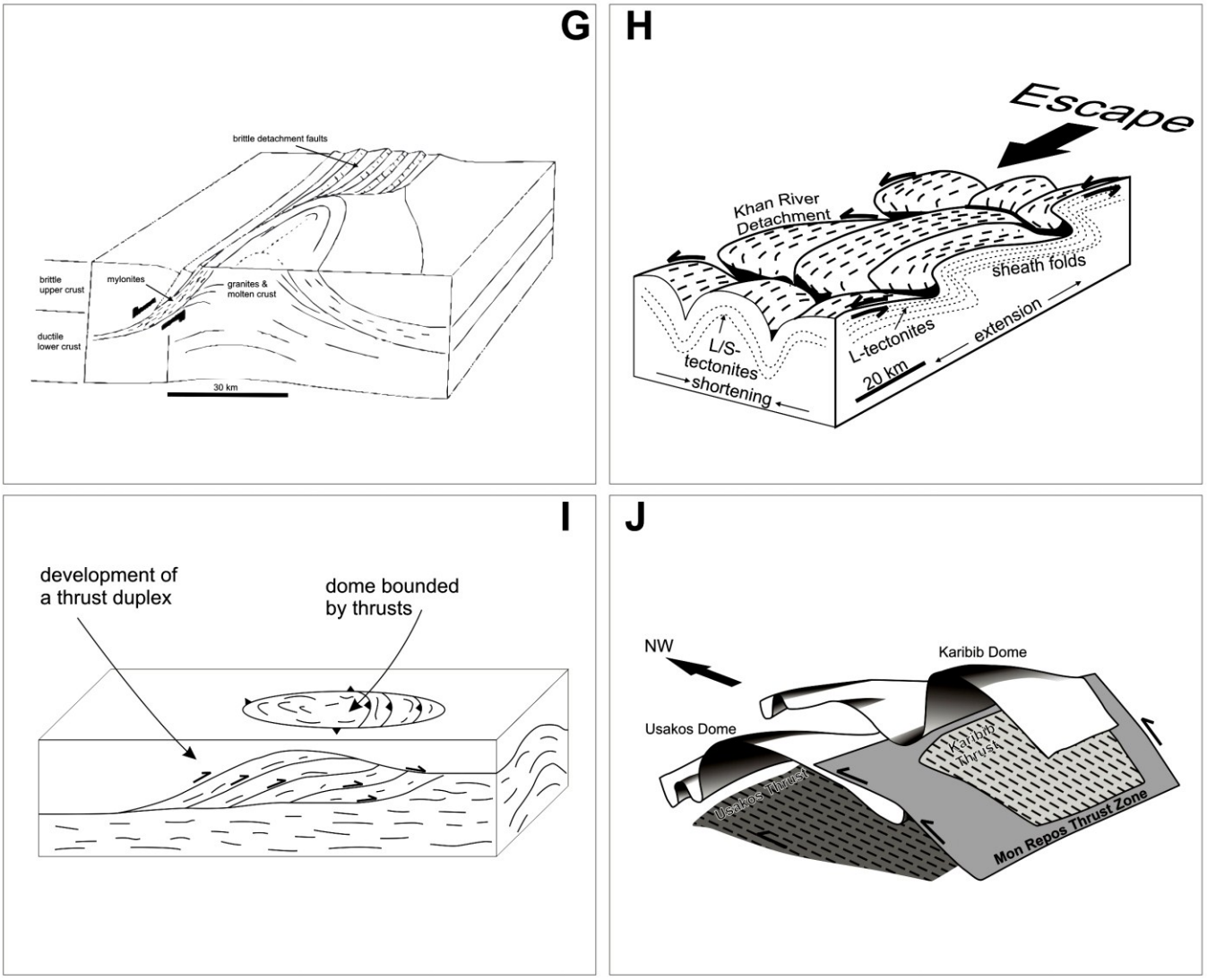
G
brittle detachment faults
brittle upper crust
mylonites
granites & molten crust
ductile lower crust
30 km
H
Escape
Khan River Detachment
sheath folds
L-tectonites
extension
L/S-tectonites
shortening
20 km
I
development of a thrust duplex
dome bounded by thrusts
J
NW
Karibib Dome
Usakos Dome
Karibib Thrust
Usakos Thrust
Mon Repos Thrust Zone

Fig. 3.1 (previous pages) – Possible mechanisms suggested for the formation of gneiss domes in orogens, and examples where these mechanisms have been applied to the domes of the Central Zone. A: Schematic cross-section of a gneiss dome formed by diapiric ascent, showing constriction in the core of the dome, flattening at the dome margins, and mantling metamorphic rocks forming cascading folds off the rising diapir (After Whitney et al*., 2004). B: Examples of domes from the Central Zone where diapirism/deformation by ballooning granites has been suggested as a possible mechanism of formation. 1 – The Namibfontein-Vergenoeg twin domes (after Kröner, 1984). 2 – The Ida Dome (after Barnes & Downing, 1979). C: Schematic diagram of the structural features developed during folding of an extensional detachment, where constriction is perpendicular to the extensional movement direction (after Harris* et al*., 2002). D: Schematic diagram of the model proposed by Poli (1997), where constrictional deformation led to dome formation, and post-tectonic granites cut these domes. E: Schematic diagram of a dome-and basin geometry formed by overprinting of two orthogonal generations of upright folds (after Ramsay & Huber, 1987). F: North-south and east-west cross sections through the Tumas Dome (after Jacob* et al*., 1983). The north-south section shows S-verging D2 structures, and the infolding of the Damara Supergroup into the basement, whilst the east-west cross section shows upright D3 structures. G: Schematic cross-section of a typical Cordilleran metamorphic core complex (after Brun & Van den Driessche, 1994). H: Diagram of the Central Zone as a deep metamorphic core complex (after Oliver, 1994) showing ductile failure along the basement-cover interface, dragging the domes into sheath folds. I: Schematic diagram of dome formation due to the development of a thrust-duplex (after Yin, 2004). J: Simplified schematic diagram of the development of the Usakos and Karibib domes and their relationships with inferred blind thrusts and with the Mon Repos Thrust Zone (after Kisters* et al*., 2004).*

The mechanisms by which domal structures in orogens may be produced are therefore diverse, and several of these different mechanisms have been proposed for the domes of the Central Zone. Barnes (1981) even suggested that several different dome-forming mechanisms may have operated in the Central Zone, with both diapiric granite intrusion and superposition of multiple phases of folding. Barnes (1981) also suggested that these mechanisms are not mutually exclusive, and that both may have acted to varying degrees on the same domes. In order to understand the mechanisms for the formation of the domes of the Central Zone, the structural context in which they formed must be understood, through detailed field-based structural studies, before applying theoretical models to these domes. A number of studies have characterised the deformation history of the Central Zone, the results of which are reviewed below.

Intense deformation has been recorded in the Central Zone by various workers (Smith, 1965; Barnes, 1981; Sawyer, 1981; Jacob *et al*., 1983; Buhn *et al*., 1994; Poli, 1997; Kisters *et al*., 2004), and early workers recognised an overprinting fold interference pattern of two major deformation events (D2 and D3 – see section 1.3.4.2) (Smith, 1965; Barnes, 1981; Sawyer, 1981; Jacob *et al*., 1983). The interference between structures related to these two events was considered to be the mechanism for forming the basement-cored domes characteristic of the Central Zone (Smith, 1965; Barnes, 1981; Jacob *et al*., 1983). However, a number of other models have subsequently been suggested for the formation of these domes – the occurrence of extensional shear bands and stretching lineations led to suggestions that domes are the result of metamorphic/extensional core complex development (Oliver, 1994, 1995; Oliver & Kinnaird, 1996), but diapirism of remobilised basement into Damara Supergroup cover rocks (Barnes & Downing 1979; Barnes, 1981; Sawyer, 1981), magmatic deformation by ballooning granites (Kröner, 1984), mega-scale sheath folding (Coward, 1981), and the formation of domes owing to tip-line folds located above blind thrusts (Kisters *et al*., 2004) have all been suggested as possible mechanisms. Some more recent work considers the D2 and D3 deformation events of earlier workers in the Central Zone not as polyphase overprinting events, but as a single, progressive, constrictional event in the southern Central Zone (Poli, 1997; Poli & Oliver, 2001). Poli (1997) and Poli & Oliver (2001), divided the structural history of the Central Zone into two progressive stages, which formed part of a continuum of deformation: initially unequal constriction led to the formation of gentle domes and the development of a regional fabric by mimetic growth of metamorphic minerals subparallel to sedimentary bedding; thereafter, continued constriction led to the folding of the regional fabric, the tightening of earlier developed structures, and of domes reaching their maximum amplitudes (Fig. 3.1D). Heterogeneous strains developed during the later stages of deformation, forming high-strain zones near the basement-cover interface. The apparently widespread occurrence of prolate strain markers and the moderately plunging extensional lineation in the Central Zone led Poli (1997) to argue against the core complex model of Oliver (1994, 1995) (Fig. 3.1H) on the basis that, although stretching lineations are common in extensional core complexes (e.g. Fletcher & Bartley, 1994), they are generally near-horizontal (not plunging) and, thus, exhumation and dome formation in the Central Zone

was through sub-vertical elevation of the mid-crust rather than being controlled by a shallowly plunging footwall exposure of a regional detachment.

In contrast to this idea of progressive deformation, the structural history of the Central Zone described by earlier workers includes two intense, Damaran events. These two events are comparable between different authors, and are termed D2 and D3 (where D1 is the earlier regional fabric-forming event described by some workers – see section 1.3.4). Strongly non-coaxial D2 deformation formed tight to isoclinal recumbent folds and associated shear zones (Smith, 1965; Nash, 1971; Sawyer, 1981; Coward, 1983; Blaine, 1977), as well as a penetrative fabric (Nash, 1971). Infolding of Damara Supergroup rocks into the Abbabis Complex has also been ascribed to D2 folding (Barnes, 1981; Jacob *et al*., 1983). D3 was more coaxial, and upright folds with NE-trending axes and moderate plunges were formed during this event (Smith, 1965; Nash, 1971; Blaine, 1977; Barnes, 1981; Sawyer, 1981; Coward, 1983; Jacob *et al*., 1983). A Pre-Damaran fabric-forming event has also been widely recognised in the gneissic basement of the Abbabis Complex (Smith, 1965; Jacob *et al.*, 1983; Poli, 1997), and an early Damaran event (termed D1) may have formed the regional bedding-parallel transposition fabric observed in the Damaran Supergroup (Blaine, 1977; Barnes, 1981; Sawyer, 1981; Coward, 1983). No macroscale D1 structures appear to be preserved, however, and evidence for this event is found locally as rootless isoclinal intrafolial folds (Barnes, 1981; Blaine, 1977) or Type-1 (Ramsay, 1967) fold interference patterns (Sawyer, 1981). Although D2 is widely recognised as an intense non-coaxial event, the vergence of deformation is less certain. A SE-vergence for F2 folds was recognised by De Kock (1989), and Sawyer (1981) noted west-dipping axial planes and N-S trending hinge lines for F2 folds in the Central Zone, implying an easterly vergence for these structures. Downing & Coward (1981) recognised large scale SE-facing non-cylindrical folds, but a NE-SW extension lineation subparallel to the fold hinges led to them interpreting a southwesterly vergence for deformation in the Central Zone. Coward (1983) and Downing & Coward (1981) interpreted the NE-SW extension lineation as subparallel to the hinge-lines of SW-verging km-scale sheath folds, where SE-closing southern limbs of km-scale SW-verging sheath folds would explain the impression of a SE vergence for folds in the Central Zone (Miller, 2008). A similar southwesterly vergence for

the southwestern Central Zone was also suggested by Oliver (1994, 1995), based on NE-SW lineations and SW-verging shear bands. The occurrence of NW-verging deformation in the Karibib area (Kisters *et al.*, 2004), orthogonal to the SW-vergence generally recognised for the southwestern Central Zone (Downing & Coward, 1981; Coward, 1983; Oliver, 1994; Poli & Oliver, 2001) was considered the result of SW-verging orogen-parallel tectonic escape at mid-crustal levels, coeval with NW-verging folding and thrusting at shallow crustal levels (Kisters *et al.*, 2004).

Key to understanding the intense deformation in the Central Zone is which, if any, of the contrasting viewpoints regarding the structural history is more accurate – for instance:

- Did deformation occur in discrete 'pulses', or was it continuous, with no distinguishable 'D2' and 'D3' events? Conclusive evidence that earlier formed structures have been reoriented by later formed structures, and whether this re-orientation is consistent over the study area, may resolve this, although it is possible for structures to be reoriented during continuous progressive strain.
- What are the relationships between SE-verging folds, supposed SW-verging km-scale sheath folds, NE-plunging stretching lineations and other extensional features, and high-strain zones at the basement-cover contact?
- Is there any mesoscopic evidence for sheath folding?
- What mechanism is responsible for the characteristic domes of the Central Zone?

A detailed study of the structural history and nature of deformation in the study area is essential for answering these questions, and this chapter aims to characterise deformation in the southwestern Central Zone in an area around the Palmenhorst and Ida Domes (Fig. 3.2), and thereby to evaluate the various structural and geodynamic models for the Central Zone. This forms the basis for an understanding of the relationships of deformation to metamorphism and magmatism, and the geochronology thereof, which are discussed in later chapters.

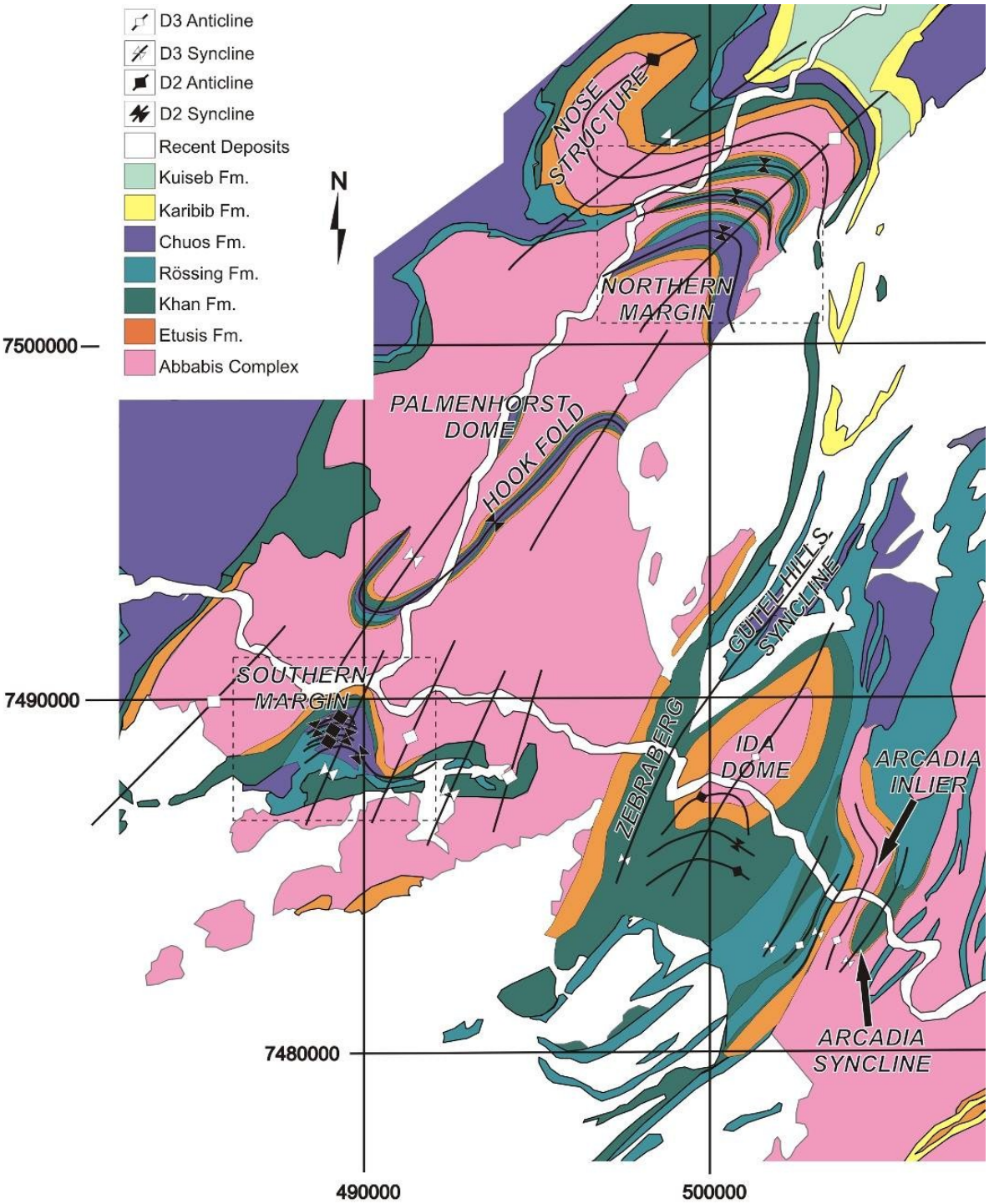

Fig. 3.2 – Geological map of the study area (combined from this study and Lehtonen et al.*, 1995), showing major D2 and D3 structural features in the Ida and Palmenhorst domes, and the names of specific areas referred to in this chapter (Nose Structure, Hook Fold, Zebraberg, Gurtel Hills Syncline, Arcadia Inlier, Arcadia Syncline). The domains studied along the northern and southern margins of the Palmenhorst Dome are indicated by the dashed rectangles. Note that the lithological mapping of large-scale structures suggests interference of two generations of folds.*

3.1 Results from Lithological Mapping

The pattern of lithologies produced from mapping of the distribution of the Abbabis Complex and Damara Supergroup strata (Chapter 2) appears to resemble a fold interference pattern (Fig. 3.3A) for the Palmenhorst and Ida domes. NE-trending, upright folds appear to have refolded more recumbent, south- to SE-verging folds. This gives a Type-2 (Ramsay, 1967) fold interference pattern for the study area, which is particularly evident for the Ida Dome (Fig. 3.3B). The Ida Dome seems to be a fairly simple structure, based on the overall distribution of lithologies, relative to the larger, apparently more complicated pattern found in the Palmenhorst Dome (Figs. 3.2, 3.3). The core of the Ida Dome comprises a core of Abbabis Complex gneisses, and is surrounded by metasediments of the lower Damara Supergroup. Strata dip towards the northwest, northeast, east and east-southeast across the domes but, near the centre of the dome, the general dip is towards the north. The overall pattern is suggestive of interference folding produced when the angle between the two interfering fold generations is slightly less than 90˚ (Fig. 3.3B). It appears as though a series of tight, N-dipping D2 anticlines and synclines, with fold hinges that have E-W or ENE-WSW trends (indicating a S- or SSE-verging D2 event) have been refolded by a more open, upright, NE-trending D3 anticline (Fig. 3.3B). In addition to revealing an apparent fold interference pattern for the Ida Dome, mapping has resulted in recognition of a number of km-scale Damaran structures within and around the Palmenhorst Domes (Fig. 3.2), some of which were indentified by Barnes (1981), but many of which have not been identified by previous workers. Near the centre of the Palmenhorst Dome, an isoclinal, N-dipping km-scale syncline (the Hook Fold – Chapter 2) is the dominant structure recognised. Along the northern margin of the Palmenhorst Dome, Damara Supergroup rocks have been isoclinally infolded with Abbabis Complex gneisses. These km-scale folds generally have N- or NW-dipping axial planes, and the Damaran successions found here are highly attenuated; locally entire limbs of these folds have been removed during Damaran deformation. Along the southern margin of the Palmenhorst Dome, a series of S-dipping km-scale tight to isoclinal anticlines and synclines are found, folding Damara Supergroup lithologies.

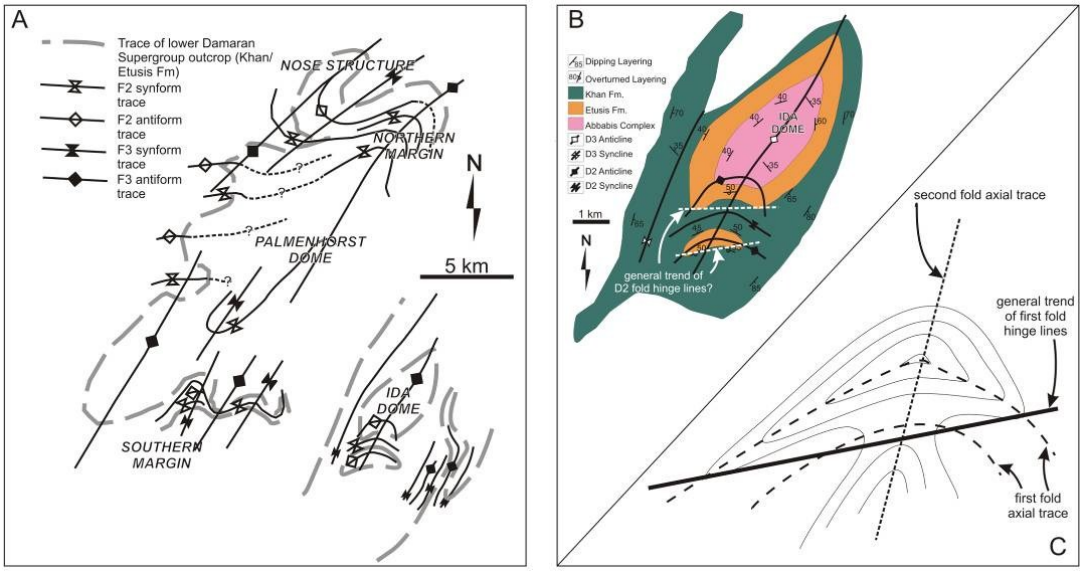

Fig. 3.3 – Fold interference patterns from lithological mapping. A: Fold interference patterns for the Ida and Palmenhorst dome, showing apparent interference between NE-trending D3 structures and E- to NE- trending D2 structures. B: Simplified geological map of the Ida Dome, showing the apparent Type-2 fold interference pattern caused by refolding of tight to isoclinal, shallow N- or NW-dipping to recumbent D2 folds by an upright, NE-trending D3 anticline. The N- or NW-dip of D2 axial planes and the E-W or ENE-WSW trend of D2 fold hinges suggest a S- or SSE-verging D2 event. C: A Type-2 fold interference pattern developed where the angle between the hinge lines of the two fold generations is slightly less than 90° (after Ramsay & Huber, 1987), for comparison with the interference pattern in B.

All of these intense structures appear to have been refolded by km-scale, NE-trending synforms and antiforms. In the centre of the Palmenhorst Dome, this apparent refolding forms the 'hook-shaped' outcrop pattern after which the Hook Fold is named (Fig. 3.2). The upright, NE-trending folding apparent along the northern and southern margins of the Palmenhorst Dome is clearly visible on remote sensing images (Fig. 3.4). Repetition of Damaran stratigraphy by a number of steeply WNW-dipping to upright, shallowly NNE-plunging km-scale anticlines and synclines (Fig. 3.2) is also seen to the east of the Ida Dome (the Arcadia Inlier and Arcadia Syncline – Fig. 3.2). This upright, NE-trending orientation for these km-scale folds is similar to the upright, NE-trending D3 folds widely described in the Central Zone (Smith, 1965; Nash, 1971; Blaine, 1977; Barnes, 1981;

Sawyer, 1981; Coward, 1983). Intense, recumbent, tight to isoclinal folds that appear throughout the study area and which have axial planes dipping to the north or northeast are similar to the intense, recumbent D2 structures also widely described in the Central Zone (Smith, 1965; Nash, 1971; Blaine, 1977; Barnes, 1981; Sawyer, 1981; Coward, 1983).

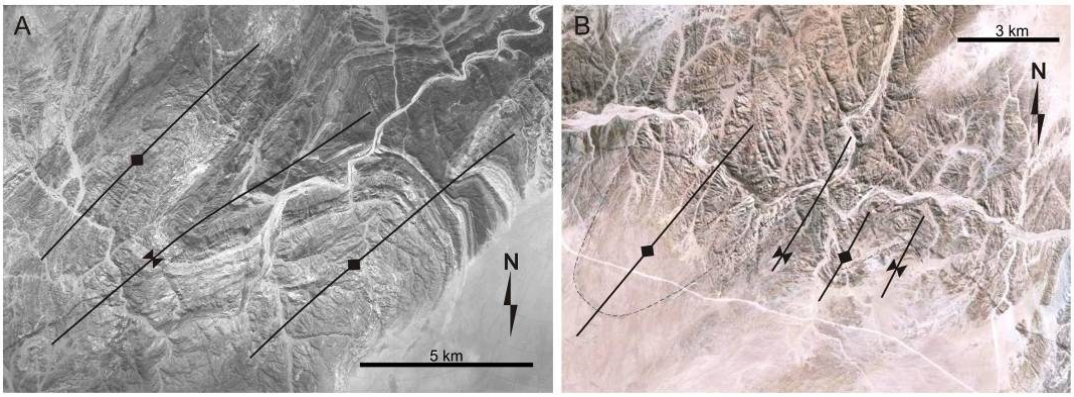

Fig. 3.4 – Remote sensed images showing upright, NE-trending D3 folding. A: Aerial photograph of the northern margin of the Palmenhorst Dome, showing km-scale anticlines and synclines forming the so-called Nose Structure. B: Google Earth™ image of the southern margin of the Palmenhorst Dome showing similar NE-trending anticlines and synclines.

Although a fold-interference pattern is apparent from lithological mapping, Poli (1997) and Poli & Oliver (2001) suggested that deformation in the Central Zone did not occur as sequential overprinting events, but rather formed a continuum, where the curvature of anticlinal and synclinal hinges (such as around the Nose Structure – Fig. 3.2) is ascribed to continued constriction of structures, rather than being due to the overprinting of an early structure by a subsequent deformation event. Oliver (1994, 1995) also did not regard dome formation in the Central Zone as the result of interfering folds, and noted an apparent lack of re-folded folds at the outcrop scale. He regarded domal structures as the effect of NW-SE compression and SW-NE extension, with tectonic escape to the southwest. Thus, whilst the outcrop pattern and orientations of strata noted from lithological mapping suggests type-2 (Ramsay, 1967) fold interference between upright, NE-trending D3 structures and recumbent, S- to SE-verging D2 structures (as noted by a variety of earlier workers), one would need to demonstrate that earlier-formed structures

are consistently reoriented by younger deformation across the study area as conclusive evidence for fold interference, and preferably show mesoscale fold interference patterns.

In this chapter, mesoscale structural features (folds, shear zones, shear bands, etc.) recorded and measured during mapping are shown to be related to either the D2 or D3 events of previous workers (Smith, 1965; Nash, 1971; Blaine, 1977; Barnes, 1981; Sawyer, 1981; Coward, 1983), and it is demonstrated that earlier formed (D2) structures are reoriented by later, NE-trending (D3) structures, although mesoscale fold interference is rare. In addition, the widespread occurrence of extensional structures noted by Oliver (1994), but not widely recognised in the Central Zone, is related to the D2 and D3 events of previous workers. This is then discussed with regard to previously-proposed models which regard deformation and dome formation in the southwestern Central Zone as, *inter alia*, the result of a continuum of constrictional deformation (Poli, 1997; Poli & Oliver, 2001), due to NW-SE compression coeval with NE-SW extension (Oliver, 1994, 1995), or due to SW-verging sheath folding (Coward, 1983). In addition to these two main deformation events, pre-Damaran structures in Abbabis Complex gneisses and early Damaran D1 structures are also discussed.

3.2 Pre-Damaran Deformation in the Abbabis Complex

The cores of the Ida Dome, Palmenhorst Dome and the Arcadia Inlier expose large areas of Abbabis Complex gneisses, S/L (planar fabrics more dominant than linear fabrics) and L/S (linear fabrics more dominant than planar fabrics) tectonites (Fig. 3.2) that predate the Damara Supergroup (Jacob *et al.*, 1978; Kröner *et al.*, 1991), and where any evidence for deformation predating the Pan-African event may be found. In the core of the Ida Dome well-developed linear fabrics in pre-Damaran gneisses are seen to be refolded by Damaran structures. In an outcrop near the core of the Ida Dome (locality 0500773/7487516), L-S tectonites are refolded by non-cylindrical open folds, creating a dome-and-basin type interference pattern on a dm-scale (Fig. 3.5A). The general trend of the linear fabric in these tectonites is E-W and differs from the NE-plunging lineation widely recognised in Damaran metasediments and basement gneisses (Downing &

Coward, 1981; Oliver, 1994; Poli & Oliver, 1997; Kisters *et al.*, 2009), suggesting that it is unrelated to Damaran deformation. Further to the east (locality 0501220/7487524), a strong linear fabric in Abbabis Complex gneisses has been refolded by S-verging, N-dipping tight m-scale folds (Fig. 3.5B) that have the same orientation as the intense D2-Damaran folding in the study area (see section 3.4 below), and which are interpreted as Damaran-age folds. Within the Palmenhorst Dome, most of the Abbabis Complex rocks exposed do not show any decisive evidence for pre-Damaran deformation and have a strong gneissic fabric subparallel to the regional S2 fabric in Damaran metasediments, with boudinaged and folded granite veins and amphibolites. However, localised areas of lower Damaran strain (localities 0496481/7501723 and 0495396/7500431) preserve evidence of pre-Damaran deformation, manifest as L- and S-tectonites in the para- and ortho-gneisses of the Abbabis Complex in the study area (see section 3.4 below). Recognition of these locally developed pre-Damaran fabrics is aided by the fact that they are truncated by amphibolite dykes in the study area. Although generally folded and boudinaged into lenses within Abbabis Complex quartzofeldspathic gneisses (likely during Damaran deformation), amphibolites remain intact in lower strain areas where they are folded into m- to Dm-scale folds by S-verging Damaran deformation (Fig. 3.5C). Here, the fabric in the Abbabis Complex gneisses is truncated by these amphibolites, and is also folded by Damaran deformation (Fig. 3.5D). These amphibolites represent the earliest phase of magmatism associated with the Damara event, and are dated at 557 Ma (see Chapter 5). Elsewhere, the strong gneissic, S/L or L/S fabrics characteristic of the Abbabis Complex basement gneisses are in places complexly folded, and are cut by extensional shear band structures (Fig. 3.5E) interpreted as Damaran in age (see section 3.4.3). Intense fabrics are locally found in Damaran lithologies even where sedimentary structures in nearby Etusis Formation quartzites are visible (such as the centre of the Ida Dome – locality 0501426/7487100). This, together with the fact that intense fabrics in the Abbabis Complex are deformed by Damaran deformation, truncated by the earliest Damaran intrusions, and differ in orientation from fabrics in Damaran metasediments, suggests the local preservation of a pre-Damaran deformation event. Poli (1997) observed mesoscale folds in basement gneisses from the Namibfontein area and Nose Structure that he considered to be pre-Damaran. Pre-Damaran fabrics have been noted elsewhere

in the Abbabis Complex (Miller, 2008), and are locally deformed by folds that do not continue into the overlying cover rocks (Smith, 1965; Bunting, 1977). However, fabrics in the Abbabis Complex are commonly subparallel to strong planar and linear fabrics in adjacent Damaran metasediments, and are not necessarily pre-Damaran. In the Arcadia Inlier, no definitive evidence of pre-Damaran deformation has been found, and these rocks have a strong gneissic fabric subparallel to the subvertical orientation of the S2 foliation in adjacent Damaran metasediments. Numerous folded and boudinaged granite veins and amphibolites are aligned with this gneissic fabric (Fig. 3.5F). The fabrics thought to be the result of pre-Damaran deformation, and observed in gneisses, S/L- and L/S-tectonites of the Abbabis Complex, are defined by oriented subhedral laths of biotite (Fig. 3.5 G, H). Neither quartz nor feldspar grains are elongate along the fabric, and quartz grains have irregular grain boundaries, or may occur as small, rounded grains on the margins of other grains (Fig. 3.5G). Such textures are typical of grain boundary migration recrystallisation at high temperatures (Passchier & Trouw, 2005), and indicate that recrystallisation of pre-Damaran fabrics may have occurred during Damaran tectonometamorphism.

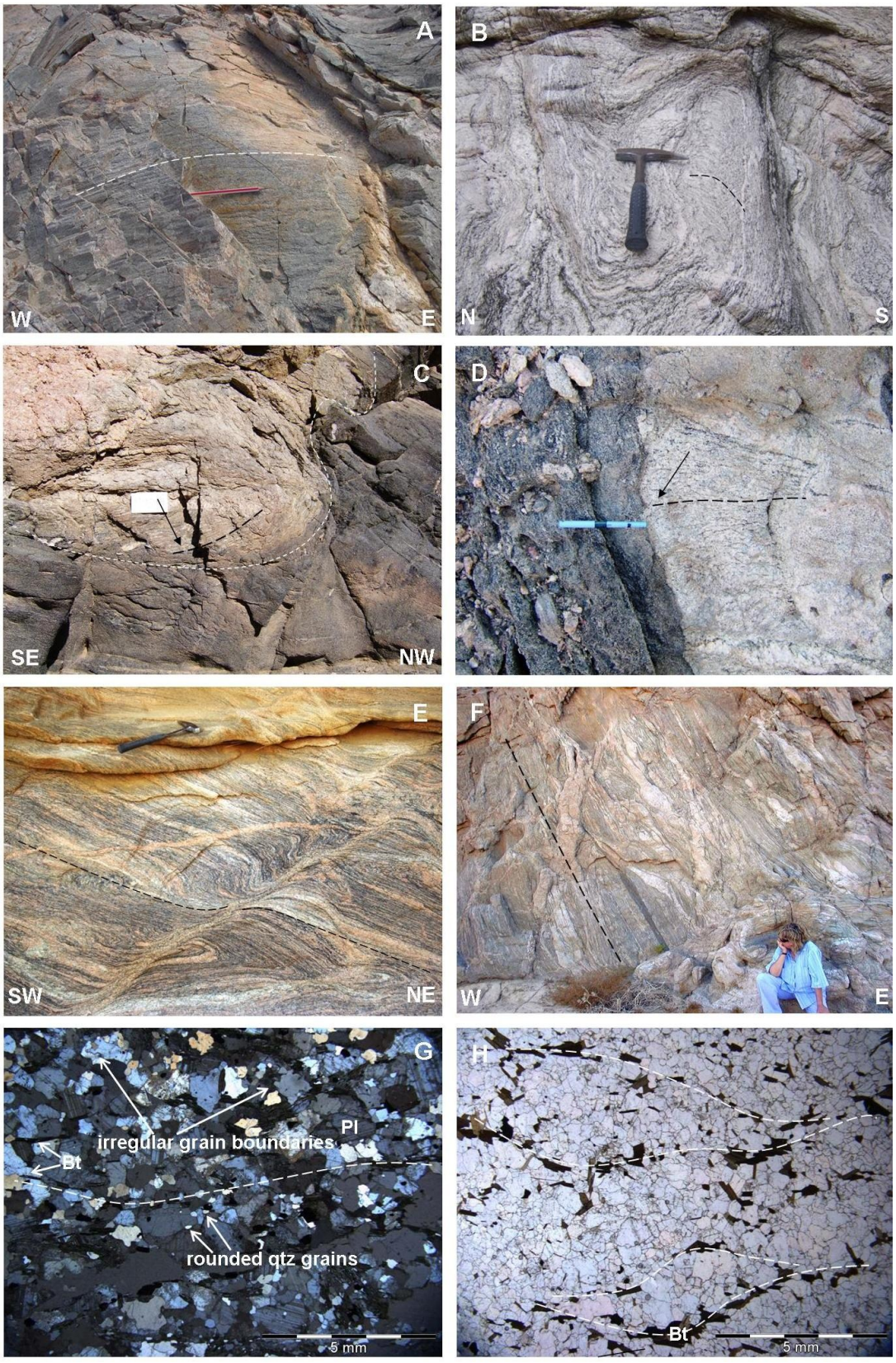
A
W
E
B
N
S
C
SE
NW
D
E
SW
NE
F
W
E
G
irregular grain boundaries
Pl
Bt
rounded qtz grains
5 mm
H
Bt
5 mm

Fig. 3.5 (previous page) – A: Highly deformed Abbabis Complex L-tectonites from the centre of the Ida Dome (locality 0500773/7487516), refolded in a complex pattern formed by upright, non-cylindrical folds. The east-west linear fabric (dashed line) is interpreted to predate Damaran deformation. B: Abbabis Complex L-tectonites from the Ida Dome (locality 0501220/7487524). The pre-Damaran linear fabric (dashed line) is folded by south-verging, open to tight m-scale folds, interpreted to be Damaran in age. C: Outcrop of m-scale folds in amphibolite dykes, which cut the pre-Damaran fabric. Arrow indicates where the pre-Damaran fabric (dashed line) is truncated by an amphibolite dyke. (locality 0495396/7500431). D – Close-up an outcrop where a pre-Damaran fabric (dashed line) is truncated by an amphibolite dyke (indicated by arrow) (locality 0494493/7499069). E: Abbabis Complex gneisses (with a pre-Damaran gneissic fabric – dashed line) cut by extensional shear bands formed in a Damaran shear zone near the basement-cover interface along the western margin of the Ida Dome (locality 0500485/7488813). F: Steeply dipping Abbabis Complex gneisses (dashed line) from the Arcadia Inlier with folded granitic veins and amphibolite lenses subparallel to the east-dipping fabric (locality 0504090/7484518). G: Photomicrograph of an Abbabis Complex L-tectonite, showing unaligned quartz and feldspar grains, and a fabric of aligned biotite laths (indicated by dashed line). Note the irregular grain boundaries and rounded quartz grains along grain margins, indicating high-temperature grain boundary migration recrystallisation (Passchier & Trouw, 2005). (XPL, sample LCZ2-1, locality 0502331/7488512). H: Photomicrograph of Abbabis Complex gneiss, showing the fabric defined by aligned biotite laths, which wrap around augen of quartz and K-feldspar (PPL, sample LID036, locality 0500422/7487668). Mineral abbreviations are after Kretz (1983).Thin sections are cut perpendicular to the gneissic fabric.

3.3 D1 Deformation

There is evidence for the early regional D1 event, thought to be a regional transposition foliation in the Damara Supergroup, predating the main D2 and D3 events widely described in the Central Zone (Blaine, 1977; Barnes, 1981; Nex, 1997). Possible evidence for this event in the study area is found in the form of rootless isoclinal intrafolial folds within pelites and calc-silicates of the Rössing Formation (Fig. 3.6A) along the eastern margin of the Ida Dome and the southern margin of the Palmenhorst Dome, in semi-pelitic biotite-quartz schists of the Chuos Formation along the southern margin of the Palmenhorst Dome (Fig. 3.6B), and in diopsidic gneisses of the Khan Formation in the Arcadia Syncline (Fig. 3.6C). These intrafolial folds lie within the $S_{0/1}$ lithological layering, which is subsequently folded by later recumbent, south-to SE-verging folds, suggesting that these may be the result of an early Damaran deformation event, predating the

intense non-coaxial deformation ascribed to D2 (Blaine, 1977; Barnes, 1981; Sawyer, 1981; Coward, 1983). It is possible that in areas of intense deformation (such as the Central Zone), a regional transposition of bedding can occur, and subsequently this transposition fabric may be itself refolded during progressive deformation. Although overprinting fabrics are not generally preserved, intrafolial folds are locally refolded by recumbent structures (Fig. 3.6D). Such fold interference structures, although rare, suggest that this early fabric-forming event may be regarded as a separate event to that which formed the recumbent structures that are characteristic of Damaran deformation in the study area. These intrafolial folds, which lie within the main lithological layering, are termed D1 structures, and are considered separate from other rootless, isoclinal, intrafolial folds are also found in major shear zones in the Ida Dome, and along the northern margin of the Palmenhorst Dome. These N- to NW-dipping shear zones were formed during the S- to SE-verging main phase of non-coaxial deformation (see section 3.4.2). The regional bedding-parallel fabric within which these intrafolial folds lie is termed $S_{0/1}$, and there is little petrographic evidence for overprinting fabric relationships between this and S_2, likely due to dynamic regrowth of minerals owing to high-grade metamorphism during D2.

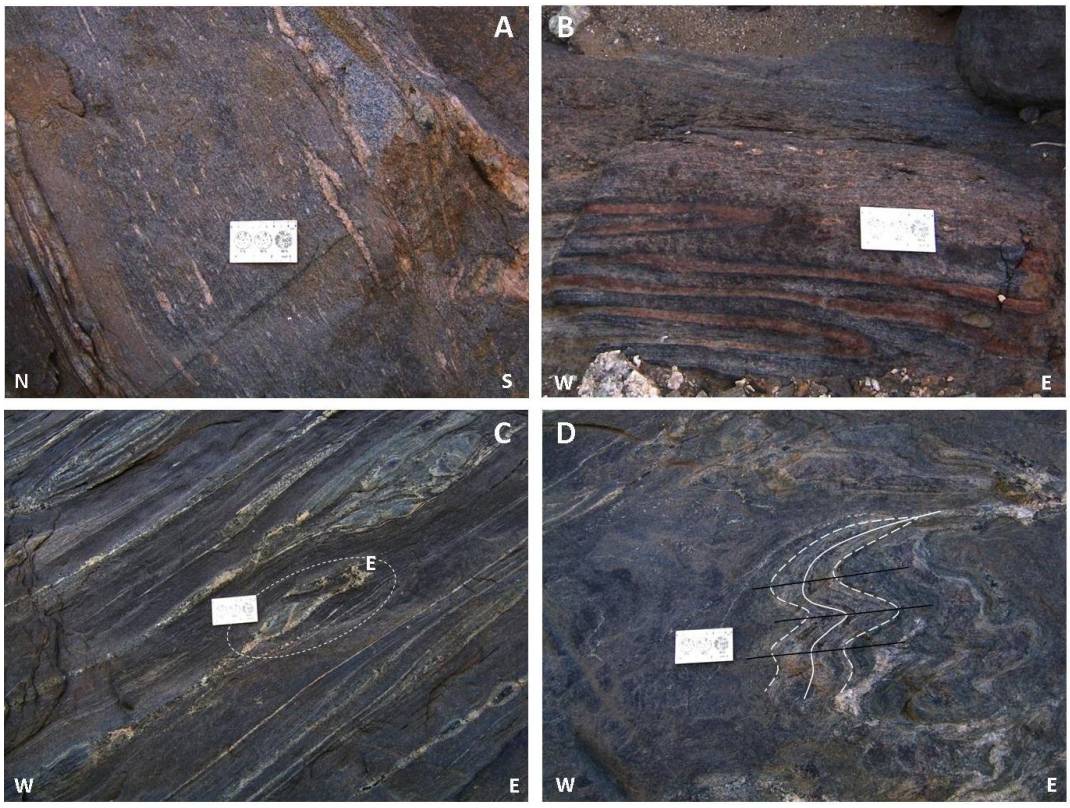

Fig. 3.6 – Field evidence for D1 deformation. A: Rootless isoclinal fold in a quartz vein within biotite-quartz schist of the Chuos Formation, on the limb of a m-scale Damaran-age fold (locality 0489390/7489693). B: Isoclinal folds in Rössing Formation calc-silicates (locality 0489303/7489440). C: Isoclinal intrafolial fold (circled) in amphibole-biotite schist. Although it appears as though the exposed surface is subparallel to fold hinge lines, this is due to extreme asymmetric attenuation of fold limbs, with thickening of the fold hinge (locality 0504759/7483900). D: Type-1 fold interference structure, with an earlier D1 fold (white) refolded by shallow NW-dipping later folds (axial planes shown by black lines) (locality 0504796/7483830).

3.4 Non-Coaxial, S- to SE-Verging Deformation and NE-SW Extension

The major deformation observed in the southwestern Central Zone is an intense, strongly vergent event, forming km-scale folds, which are recumbent or have gently N- to NW-dipping axial planes. Smaller-scale parasitic folds are also developed, in addition to a number of high-strain shear zones. A conjugate set of shear bands and a shallow NE-plunging mineral stretching lineation are also apparently associated with NE-SW

extension during this event. S- to SE- verging folding, high-strain zones and extensional deformation are each discussed separately below.

3.4.1 S- to SE- verging folding in the southwestern Central Zone

S- to SE-verging folds are developed in both Abbabis Complex gneisses and Damaran metasediments, and show a similar vergence throughout the study area. The fold interference pattern apparent from the lithological mapping and on remote sensed images of the study area means that these structures may have been reoriented by later upright folding. Hence, orientations of these structures are best investigated near the hinges of km-scale upright structures, where any re-orientation of recumbent structures would be less pronounced.

Based on lithological mapping, the Ida Dome appears to consist of km-scale south to SE-verging folds refolded by an upright, NE-trending anticline. Along the hinge of this anticline (Fig. 3.7) any rotation due to upright folding is likely to be minimal. Indeed, there are no upright structures found in the centre of the Ida Dome, and the structures preserved are recumbent or shallowly dipping. A number of m-scale folds in rocks of the Abbabis Complex and the Nosib Group are found. These folds are open to tight, have sub-horizontal to shallow north-dipping axial planes and subhorizontal, ENE-WSW hinge lines (Figs. 3.7A-C), and display a south or south-southeasterly vergence. Narrow zones of higher strain are also found, with strong planar fabrics (Fig. 3.7B) and cm- to dm-scale folding indicating a similar vergence to the larger scale folds. These folds appear to be located on the overturned limb of a larger, km-scale, S-verging anticline; on average, lithological layering dips northwards more steeply than the axial planes of folds (Fig. 3.7D). A spaced cleavage is strongly developed axial planar to folds, particularly those developed in the more brittle (see Fig. 2.15D) calc-silicate rocks of the Khan Formation. Locally, these recumbent folds are symmetric M-folds that do not display any vergence (Fig. 3.7C), and may represent the hinge zones of larger scale structures. Elsewhere in the centre of the Ida Dome, pre-Damaran linear fabrics in Abbabis Complex tectonites have been refolded by early Damaran structures (Fig. 3.5B, locality 0501220/7487524). These

folds are the result of S-verging Damaran deformation, and their orientations are consistent with other Damaran structures found in the centre of the Ida Dome (Fig. 3.7E).

Along the northern margin of the Palmenhorst Dome, a series of isoclinal, N-dipping km-scale synclines of Damara Supergroup rocks are found, some of which have been previously noted by Barnes (1981) and Smith (1965). This area is immediately south of the so-called 'Nose Structure' (Figs. 3.2, 3.8), a feature mapped by Poli (1997), who considered slivers of marble, quartzite and pelite near the southern limit of his mapping to be part of the Tsawisis Formation of the Abbabis Complex. However, since distinctive Damaran stratigraphic sequences can be identified, these rocks are more likely Damaran rocks (see Chapter 2), and are interpreted as such here. These synclines appear to be refolded by a km-scale upright, NE-trending anticline, and mesoscale structures (parasitic to km-scale isoclinal folds) measured along this hinge zone are likely to be relatively unaffected by any rotation owing to upright folding. This area is marked by extremely intense strain, with shearing and thinning of the inverted limbs of km-scale synclines, transposition of layering (Fig. 3.8A) and possible local sheath folds (Fig. 3.8B) that are rarely noted elsewhere in the study area. Small-scale folds are commonly tight to isoclinal and have moderately to steeply N-dipping axial planes (Fig. 3.8C). Measurements of structures (Fig. 3.8D) show that NNW-dipping lithological layering (S_L avg – 256/54N – notation is strike/dip plus dip direction), is subparallel to axial planes of mesoscale folds (AP_2 avg – 278/56N) but mesoscale fold hinge lines show a range of orientations, suggesting possible sheath folding. Possible sheath folds are locally found (Fig. 3.8B), but may be related to intense shearing in discrete shear zones – generally tight to isoclinal, N-dipping mesoscale folds have subhorizontal hinge lines (Fig. 3.8C) consistent with a southward vergence.

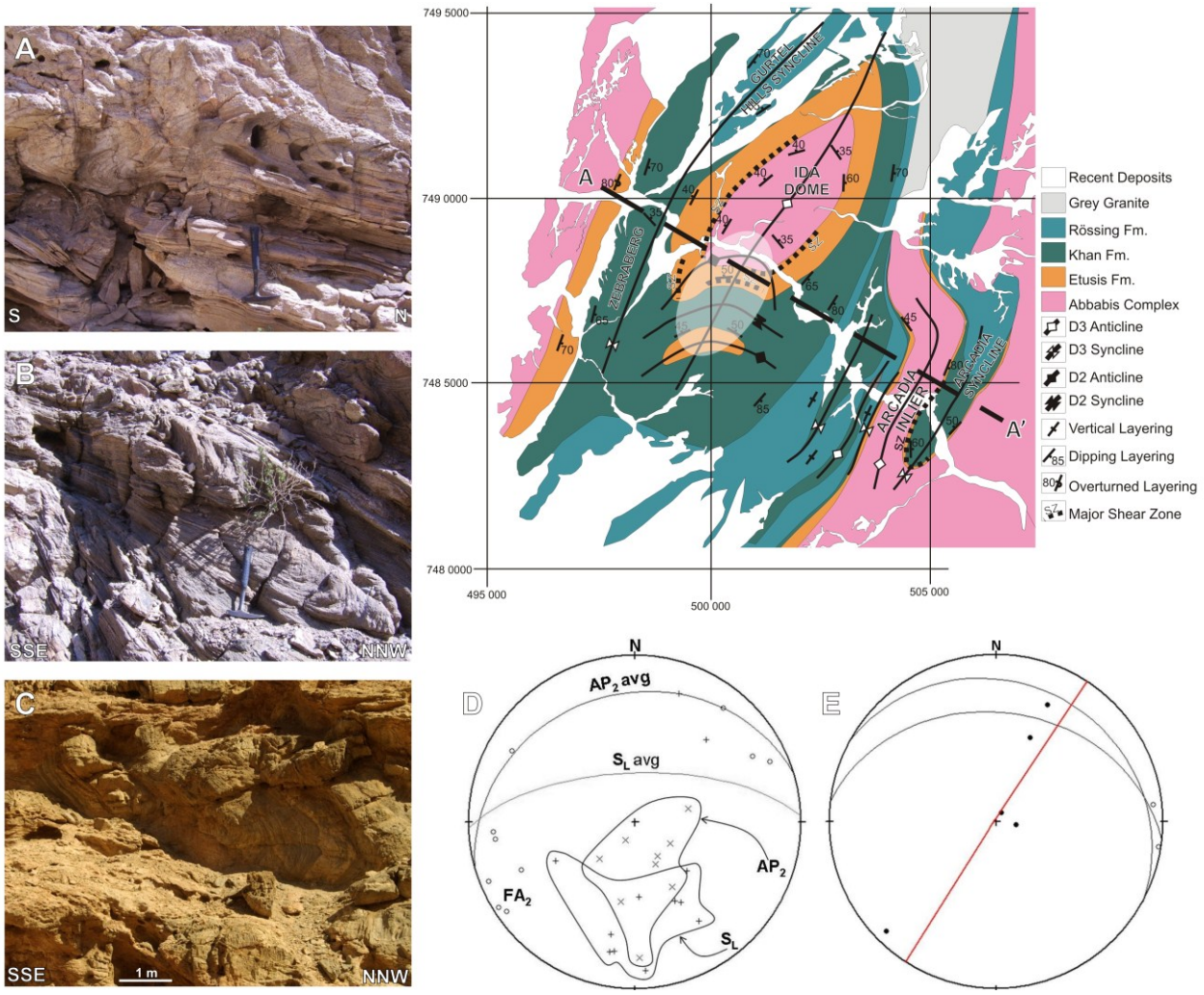

Fig. 3.7 – Recumbent folding in the centre of the Ida Dome, along the hinge of an apparent upright anticlinal hinge (shaded area on the map of the Ida Dome). A: Tight, recumbent folds in quartzites of the Etusis Formation (locality 0500914/7486738). B: Tight, SSE-verging folds in quartzofeldspathic gneisses (Etusis Formation or Abbabis Complex), bounded by zones of high strain, with planar fabrics (locality 0500659/7486884). C: Open M-folds, with subhorizontal axial planes and hinge lines, in diopside-plagioclase calc-silicates of the Khan Formation (locality 0500862/7486784). D: Equal area lower hemispheric stereographic projection of data from structures in the centre of the Ida Dome (near locality 500862/7486784). Open circles are fold hinge lines of recumbent folds (FA_2, n = 10). X symbols are poles to axial planes of folds (AP_2, n = 9). + symbols are poles to lithological layering (S_L, n=10). Average orientations of fold axial planes (AP_2 avg – 254/24 N) and lithological layering (S_L avg – 268/56 N) are shown. Note that lithological layering dips more steeply north than axial planes of folds, indicating that overall, this outcrop lies on the overturned limb of a larger scale fold. E: Equal area lower hemispheric stereographic projection of structural data of an outcrop of folded Abbabis Complex gneisses in the Ida Dome, shown in Fig. 3.5B (locality 0501220/7487524). Open circles are fold hinge lines (n = 2), closed circles are lineations (n = 5), black great circles represent the orientations of the axial planes of folds (n = 2). Red great circle represents a best fit pi-pole girdle through the lineation data, indicating that the lineation in the basement gneisses has been refolded by subhorizontal, N- to NE-dipping folds.

The bulk of the rocks that crop out in the core of the Palmenhorst Dome are pre-Damaran rocks of the Abbabis Complex. Along the Khan River, a number of dykes of amphibolite were emplaced into these gneisses, and both Abbabis Complex gneisses and amphibolites are locally folded by SE-verging m-scale folds (Figs. 3.8E, F). These folds have subhorizontal to moderate NE- or SW-plunging fold hinge lines, and moderate NW-dipping axial planes subparallel to the lithological layering in the area, which is WNW-dipping (average dip of 214/48W – 3.8D). However, folds are not widely observed in Abbabis Complex gneisses in the core of the Palmenhorst Dome, and the most common deformation feature obserevd is shear bands (see section 3.4.3).

Within the quartzofeldspathic gneisses that make up the bulk of the core of the Palmenhorst Dome, a large syncline of Damara Supergroup rocks is evident from lithological mapping (Figs. 3.2, 3.8). This syncline shows as the symmetrical repetition of Damaran stratigraphy (Chapter 2), and is an infold of Damaran lithologies within the Abbabis Complex, previously identified by Barnes (1981), and Jacob (1974), although it was considered by Jacob (1974) to be possibly part of the Abbabis Complex. Owing to its shape on the lithological map (Figs. 3.2, 3.8) it has been termed the Hook Fold. In addition to this, another sliver of Damara Supergroup rocks has been found along the Khan River near the centre of the Palmenhorst Dome, and has not been previously identified (Figs. 3.2, 3.8). The deformation in this area is intense; the Hook Fold is an isoclinal fold, with highly attenuated limbs, and much of the Damaran stratigraphy is thinned or missing. However, along the hinge of the Hook Fold, the sequence is somewhat thicker, and a full lower Damara Supergroup succession is preserved.

In the area around the Hook Fold hinge, m-scale folding is rare, but dm-scale parasitic folds are locally developed (Fig. 3.8G). At one locality (0490015/7492296), chaotic m-scale folding is found (Fig. 3.8H), associated with migmatisation of schists in the Chuos Formation, which are interbedded with quartzofeldspathic layers. Locally features resembling sheath folds are found (Fig. 3.8I), further evidence for intense non-coaxial strain, and limited data for mesoscale folds show a range of fold hinge line and axial plane orientations (Fig. 3.8J), which may reflect this sheath folding. However, the isoclinal Hook

Fold does appear to have been rotated by upright folding (Figs. 3.2, 3.3), and such a range of axial planar orientations may reflect the reorientation of structures by later upright folding. Although there is a large amount of scatter in the data for lithological layering around the Hook Fold, lithological layering is steep to moderately NW-, N- or NE-dipping, with an average orientation of 272/42N (Fig. 3.8J). The variability in lithological layering may reflect the sheath folding and chaotic deformation observed, but most likely reflects re-orientation of structures by NE-trending, upright folding.

Fig. 3.8 (following page) – Non-coaxial folding in the Palmenhorst Dome. A: Isoclinal intrafolial folds of psammitic rocks in biotite schist, indicating transposition of lithological layering (locality 0499996/7503858). B: Possible sheath folds near the northern margin of the Palmenhorst Dome (locality 0497680/7502139). C: N-dipping isoclinal fold in Damaran metasediments near the northern margin of the Palmenhorst Dome (locality 0500320/7503859). D: Equal area lower hemispheric stereographic projections of structural data from the northern margin of the Palmenhorst Dome. Open circles are D2 fold hinge lines (n=24). X symbols are poles to axial planes of D2 folds (AP_2; n=27). + symbols are poles to lithological layering (S_L; n=81). Average orientations of axial planes (AP_2 avg) and lithological layering (S_L avg) are shown by the great circles. Average fold hinge line orientation (not shown) is 10˚ on 094. E: Equal area lower hemispheric stereographic projections of structural data from the centre of the Palmenhorst Dome. Open circles are fold hinge lines (FA_2; n=8). + symbols are poles to lithological layering (S_L; n=17). Great circles are axial planes of folds (AP_2; n=6). Average orientation lithological layering (S_L avg) is shown by the bold great circle. F: Tight, NE-dipping F2 folds of amphibolite dykes and Abbabis Complex gneisses in the centre of the Palmenhorst Dome (locality 0495396/7500431). G: Rare parasitic dm-scale z-fold, on the inverted limb of a larger scale D2 fold (locality 0490058/7492264). H: Chaotic folding and boudinage of quartzofeldspathic layers within migmatitic biotite-quartz schists, near the hinge of the D2 fold (locality 0490015/7492296). Due to the chaotic nature of the deformation, no consistent orientation can be found for folds. I: Possible sheath fold in Damaran metasediments near the southern end of the Hook Fold (locality 0490587/7493407). J: Equal area lower hemispheric stereographic projections of structural data from the centre of the Palmenhorst Dome. Open circles are D2 fold hinge lines (FA_2; n=8). + symbols are poles to lithological layering (S_L; n=37). Great circles are axial planes of D2 folds (AP_2; n=3). Average orientation lithological layering (S_L avg) is shown by the bold great circle.

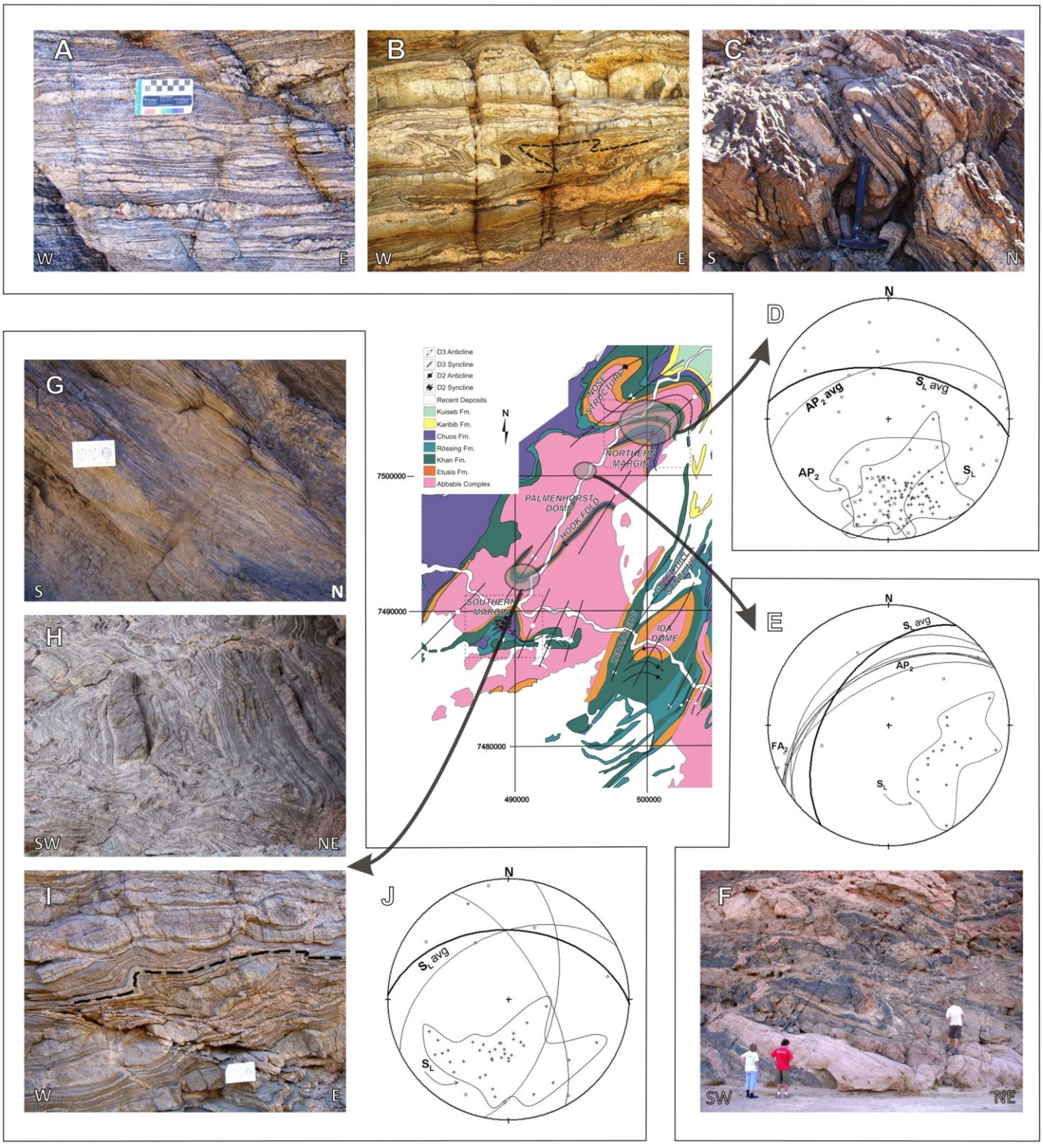
A
W
E
B
W
E
C
S
N
D
N
S_L avg
AP_2 avg
AP_2
S_L
E
N
S_L avg
AP_2
FA_2
S_L
F
SW
NE
G
S
N
H
SW
NE
I
W
E
J
N
S_L avg
S_L
D3 Anticline
D3 Syncline
D2 Anticline
D2 Syncline
Recent Deposits
Kuiseb Fm.
Karibib Fm.
Chuos Fm.
Rössing Fm.
Khan Fm.
Etusis Fm.
Abbabis Complex
N
NOSE STRUCTURE
NORTHERN MARGIN
PALMENHORST DOME
HOOK FOLD
SOUTHERN MARGIN
ZEBRA RIVER
IDA DOME
7500000
7490000
7480000
490000
500000

The intense, non-coaxial deformation observed throughout the study area, in both Abbabis Complex gneisses and in Damaran metasediments, shows a consistent vergence towards the south or southeast. The general parallelism between N- to NW-dipping fold axial planes and lithological layering indicates that the km-scale folds are tight to isoclinal, reflected by the tight to isoclinal nature of mesoscale folds.

The occurrence of recumbent structures related to an intense, non-coaxial deformation event has been widely described in the southwestern Central Zone. Tight, recumbent, S-verging folds and folding of the basement-cover interface was described by Jacob *et al*. (1983), and Blaine (1977) described similar recumbent folds, low-angle thrusts and fabric transposition formed during intense non-coaxial deformation. Although Smith (1965), Nash (1971), Blaine (1977), Barnes (1981), Jacob *et al*. (1983) and Coward (1983) all describe intense recumbent folding and shearing; the suggested vergence of this deformation varies from the southwest to southeast. The vergence of non-coaxial folds in this study, based on measurements of fold hinge-lines and fold axial planes (Figs. 3.7, 3.8), is toward the south or southeast. Mesoscale folds throughout the study area have fold hinge lines that plunge shallowly to the west or southwest, and intersection lineations have similar plunges to these hinge lines. Folds have shallow to moderate N- to NW-dipping axial planes, subparallel to the north or northwest dip of lithological layering. These mesoscale folds are parasitic to km-scale S- to SE- verging, tight to isoclinal, shallow dipping to recumbent folds.

This vergence for non-coaxial deformation is at odds with the notion that non-coaxial deformation in the southwestern Central Zone is SW-vergent (Coward 1983; Oliver 1994, 1995; Poli & Oliver 2001; Miller, 2008). All interpretations of a southwesterly vergence for deformation in the southwestern Central Zone are based upon a pronounced NE-plunging extension lineation (see section 3.4.3). Although Downing & Coward (1981) noted km-scale SE-facing fold nappes, and large SE-facing non-cylindrical folds, consistent with the SE-vergence of folds from this study, the presence of a NE-SW extension lineation in zones of intense deformation led them to invoke sheath folding, implying a rotation of fold hinges towards the NE-SW extension direction (Downing & Coward 1981), and

explaining SE-verging folds formed during SW-verging deformation. A range of fold closures from northwest to southeast and folds with curvilinear hinges are suggestive of sheath folding. This study has also shown large variations in hinge-line orientations in some areas (Figs. 3.8D, J). Coward (1983) notes a mineral lineation on the axial planar fabric of tight to isoclinal folds with hinges which plunge to the northeast, and that mineral lineations are parallel to fold hinges. Such parallelism between hinge lines and lineations suggests SE-verging folding, with a NE-plunging intersection, rather than a stretching, lineation. This geometry of structures is explained by Coward (1983) to be due to rotation of fold hinges into the southwest transport direction during continued shearing – i.e. owing to sheath folding, similar to the explanation given by Downing & Coward (1981). It is possible, however, that intersection lineations parallel to the hinges of SE-verging folds have been mistaken for NE-plunging stretching lineations. The structural data of Poli (1997), also presented by Poli & Oliver (2001) for the Namibfontein-Vergenog Dome and for the Nose Structure show that lineations have similar orientations to fold hinge lines, suggesting that these lineations are intersection lineations between the axial-planar cleavage and hinges of the folds. Although hinge-lines of folds may have been rotated into parallelism with the movement direction, neither Coward (1983) nor Poli & Oliver (2001) observed mesoscale SW-verging sheath folds, and Poli (1997) only noted local sheath folding near the basement-cover contact in a high-strain zone. Any possible sheath folds noted in this study are rare, and are confined to high-strain zones (see section 3.4.2 below). S_1/S_0 data from the Namibfontein-Vergenoeg Dome (Poli, 1997 – Fig. 3.1 or Poli & Oliver, 2001 – Fig. 4) show that this fabric has been refolded about gently ENE- to E-plunging axes, suggesting that folding was largely cylindrical, and S-to SSE-verging, rather than SW-verging. Similarly, the structural data presented for the Nose Structure by Poli (1997) and Poli & Oliver (2001) show that the general regional fabric in both the basement and cover has been folded about gently ENE-plunging fold axes, and that lineations (largely in the basement) are approximately parallel to these fold axes, again suggesting that these are intersection lineations, rather than stretching lineations. Furthermore, Poli (1997) noted that strain related to NE-SW extension in the southwestern Central Zone was largely irrotational, with little evidence for the simple shear required to generate sheath folds. Thus, although the locally large variability of

hinge-line orientations does suggest possible sheath folding, it is appears that, in general, folding is S- to SE- vergent. In addition to km-scale S- to SE-verging folds, a number of zones of intense deformation and high degrees of strain have been found throughout the study area. A high-strain zone is typically found at or near the contact between the Abbabis Complex and Damara Supergroup, but other high-strain zones with intense deformation are found within rocks of the Damara Supergroup.

3.4.2 High-strain zones in the study area

The northern margin of the Palmenhorst Dome contains a number of zones of high strain (Fig. 3.9), which appear to be related to the intense deformation found in this area. Along the northern margin of the Palmenhorst Dome, a number of isoclinal, N-dipping km-scale synclines of Damaran metasediments are found, and the limbs of these synclines appear to be sheared out by intense deformation. The sheath folding noted in this area (Fig. 3.8B) is probably related to these zones of intense shearing, but widespread transposition of bedding is also found, with intrafolial isoclinal folds (Fig. 3.8A), and the inverted limbs of dm-scale folds are extended and thinned, similar to the large-scale thinning of the stratigraphy in the inverted limbs in this domain. Shear zones near the northern margin of the Palmenhorst Dome appear to be localised on the upright lower limbs of synclines (i.e. the upper limbs of anticlines of Abbabis Complex gneisses – Fig. 3.9), and hence seem to be related to intense deformation associated with extension of these limbs.

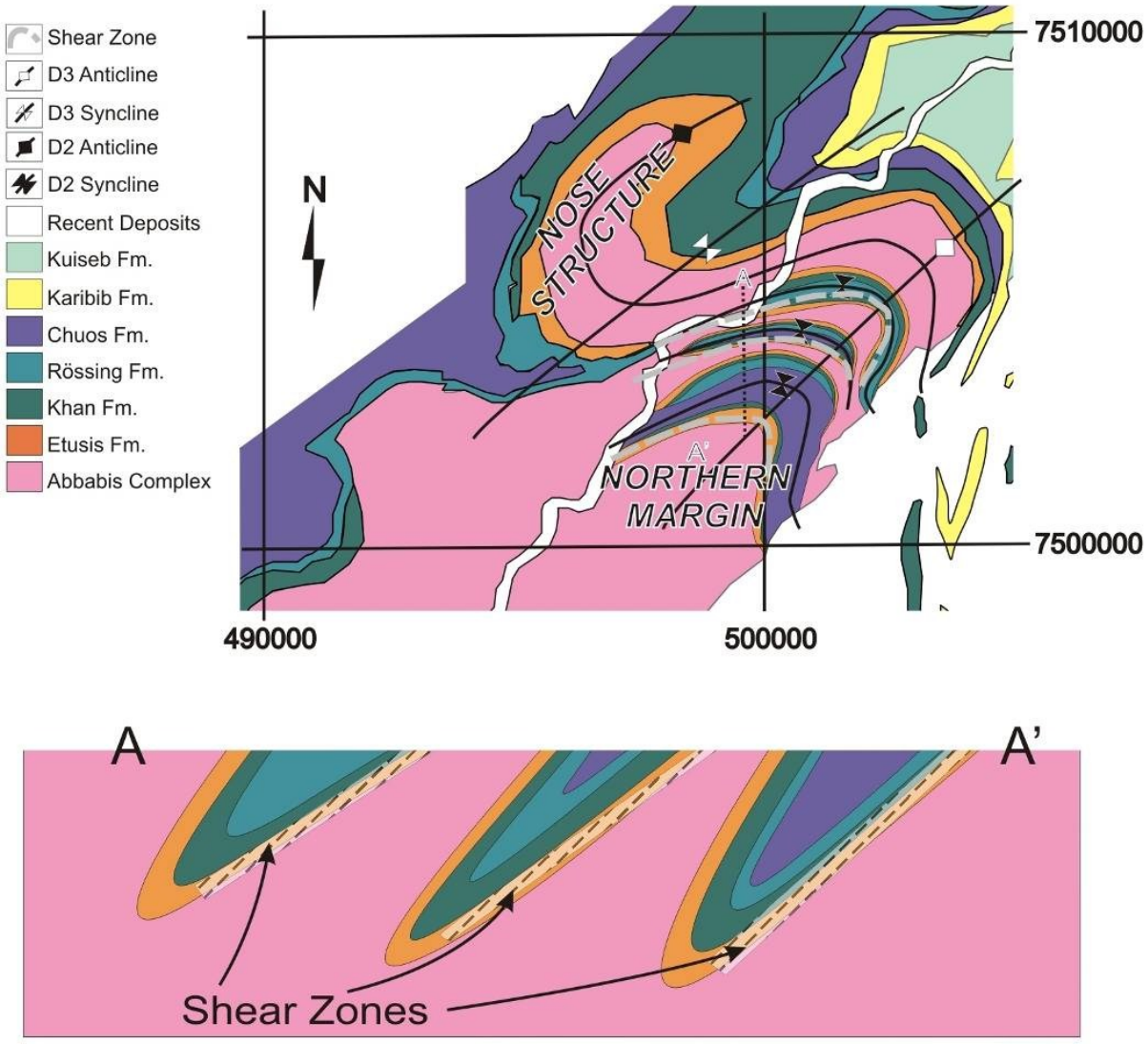

Fig. 3.9 – Shear zones associated with S-verging km-scale folds near the northern margin of the Palmenhorst Dome. Note that on the cross-section A-A', shear zones are found on the upright limbs of folds, and may be related to extension and shearing on the limbs of these folds.

In contrast to the shear zones along the northern margin of the Palmenhorst Dome, other high-strain zones in the study area do not appear to be obviously related to SE-verging non-coaxial deformation and km-scale folds. Such shear zones are localised at or near the interface between the Abbabis Complex basement and the Damara Supergroup cover. One such shear zone is a high-grade shear zone developed along the contact between the Abbabis Complex and the Damara Supergroup rocks, around the Arcadia Syncline. The

Arcadia Syncline is a km-scale NE-trending structure, and the shear zone is developed on both limbs of the syncline, and around the hinge of the syncline (Fig. 3.10A). Although exposed on both limbs of the syncline, exposures are poor along the eastern limb owing to the voluminous granitoids that have intruded in this area. On the western limb of the Arcadia Syncline, the shear zone is subvertical and trends N-S across the Swakop River. This shear zone contains very tight to isoclinal folds in pelitic or quartzofeldspathic rocks (Fig. 3.10B, C, D), which are interpreted to represent the remains of an intensely sheared Etusis Formation. The pelitic rocks found in this shear zone have undergone extensive migmatisation, forming garnetiferous leucogranites which cut the shear zone and are deformed within the shear zone. Outside of the shear zone, leucogranites occur as regular sheets, and appear undeformed (Fig. 3.10E), indicating that high-grade metamorphism and anatexis leading to formation of leucogranites was synchronous with deformation. A similar ductile shear zone is developed in psammitic and pelitic rocks of the Etusis Formation, along the western margin of the Arcadia Inlier, and granite sheets within this zone are deformed, whilst those intruding the adjacent Abbabis Complex are undeformed sheets (Fig. 3.10F). Owing to the fact that this shear zone is found around the hinge of the NE-trending Arcadia Syncline (and, thus, may have been folded by the syncline), extends over a wide area, and contains a number of complex structural features, it has been examined on an outcrop-by-outcrop basis, rather than as a whole, in order to understand its geometry and importance.

Four outcrops from this shear zone (Fig. 3.10) show intense deformation – cm-scale folds have steep SE- or E-dipping axial planes (outcrops A and D – Figs. 3.10G, J), and fold axial planes are subparallel to the general orientation of the shear zone. S-C fabrics are locally observed (outcrops B and C – Figs. 3.10 H, I), illustrating the non-coaxial nature of deformation in the shear zone. Both S- and C-surfaces dip towards the east or northeast, and C-surfaces dip more shallowly than S-surfaces, indicating a vergence to the west or southwest (Fig. 3.10 H, I). Principal stress orientations determined from extensional shear bands indicate a shallow to moderate NW- or SW-plunging σ_1. Depending on the location of the outcrop around the Arcadia Syncline, the orientation of structures is variable, but σ_1 is consistently perpendicular or at a high angle to lithological layering, fold axial planes

and S-C fabrics, whilst σ_3 lies within the plane of the shear zone. This indicates that intense layer-perpendicular flattening (perpendicular to the contact between the Abbabis Complex and Damara Supergroup) occurred during shear zone formation (Fig. 3.10K). The westerly or southwesterly vergence indicated by S-C fabrics differs from the shear zones along the northern margin of the Palmenhorst Dome and folding elsewhere in the study area, which have a southerly to southeastery vergence. However, such a vergence is consistent with the shear zone being related to formation of the NE-trending Arcadia Syncline owing to flexural-slip folding, with slip concentrated at the basement-cover interface (Fig. 3.10K). Although the test (four outcrops) is quite small, the consistency of features between each outcrop confirms its validity.

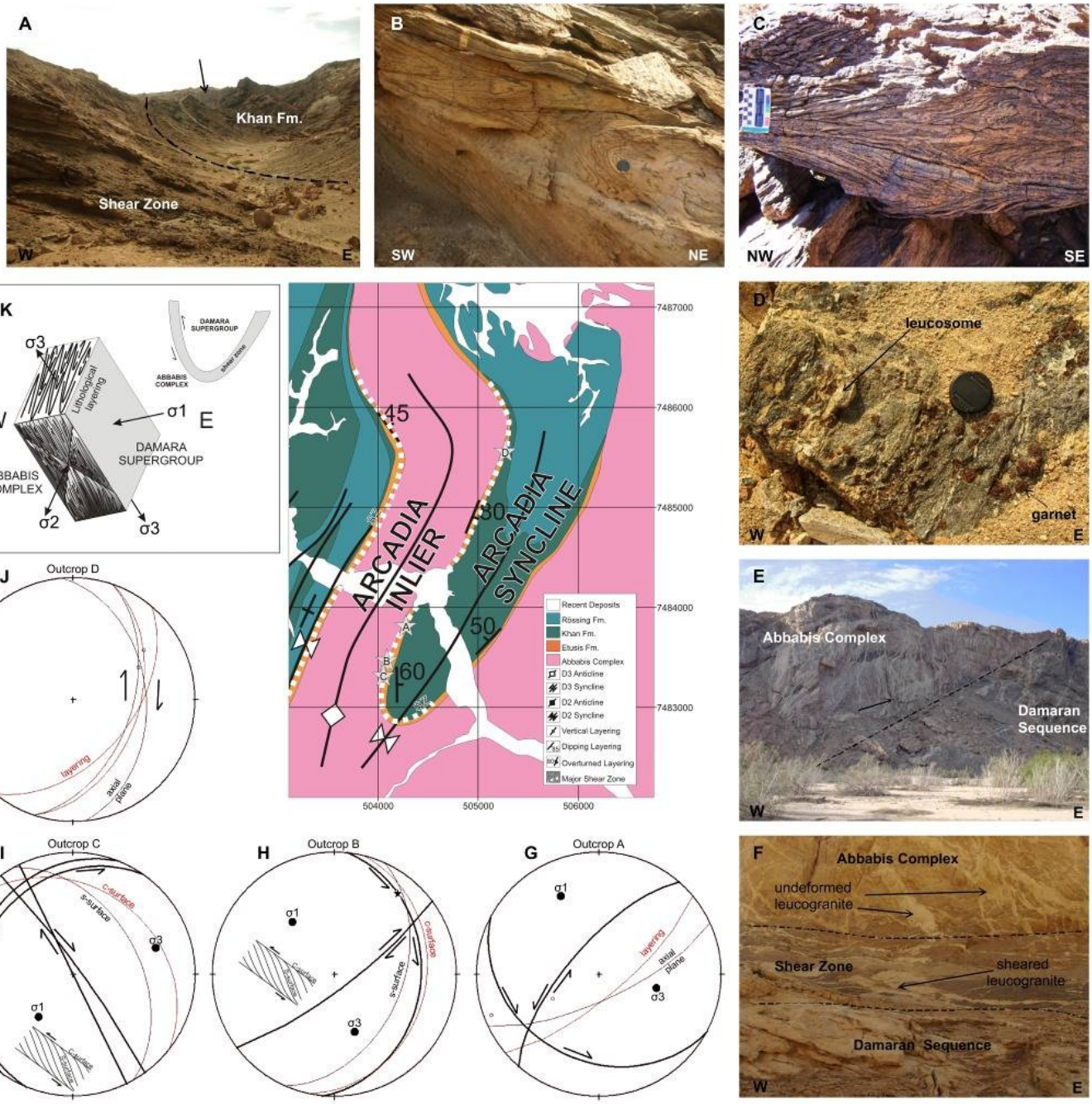
A
Khan Fm.
Shear Zone
W
E
B
SW
NE
C
NW
SE
K
DAMARA SUPERGROUP
ABBABIS COMPLEX
shear zone
σ3
Lithological layering
W
σ1
E
DAMARA SUPERGROUP
ABBABIS COMPLEX
σ2
σ3
ARCADIA INLIER
ARCADIA SYNCLINE
45
60
50
60
Recent Deposits
Rössing Fm.
Khan Fm.
Etusis Fm.
Abbabis Complex
D3 Anticline
D3 Syncline
D2 Anticline
D2 Syncline
Vertical Layering
Dipping Layering
Overturned Layering
Major Shear Zone
7487000
7486000
7485000
7484000
7483000
504000
505000
506000
D
leucosome
garnet
W
E
J
Outcrop D
layering
axial plane
E
Abbabis Complex
Damaran Sequence
W
E
I
Outcrop C
c-surface
s-surface
σ3
σ1
Caudate foliation
H
Outcrop B
σ1
Caudate foliation
c-surface
s-surface
σ3
G
Outcrop A
σ1
layering
axial plane
σ3
F
Abbabis Complex
undeformed leucogranite
Shear Zone
sheared leucogranite
Damaran Sequence
W
E

Fig. 3.10 (previous page) – Shear zones at the basement-cover interface in the Arcadia Syncline, and on the western margin of the Arcadia Inlier. A: View north from the southwestern margin of the Arcadia Synform (locality 0504151/7482975). The hinge of the synform is to the right of the photograph. The shear zone and the contact with the Khan Formation (dashed black line) are curved, giving the appearance of having been folded by the Arcadia Synform, but this is likely related to the development of the shear zone during folding. The arrow shows the location of the Swakop River in the distance, and the continuation of the shear zone, shown in E. B: Tight to isoclinal fold in an outcrop of psammitic, sillimanite-bearing schists and gneisses of the Etusis Formation, south of the Swakop River (locality 0504058/7483234). C: Tight to isoclinal folding in a pelitic boulder north of the Swakop River (locality 0505233/7485548). D: Garnet-sillimanite-biotite schist near the basement-cover contact on the northern bank of the Swakop River (locality 0504581/7484479), showing large (up to 3 cm) garnets and small patches of leucosome. E: Contact between the Abbabis Complex and Damara Supergroup on the northern bank of the Swakop River (in foreground). The contact, with a shear zone in pelitic and psammitic gneisses, is shown by the dashed black line. The arrow points to undeformed sheets of garnetiferous leucogranite, intruded in the Abbabis Complex. Granites in Damaran rocks appear more deformed. Height of cliff face is approximately 50 m. F: Deformed and undeformed leucogranites near the basement-cover contact on the western margin of the Arcadia Inlier. As in E, leucogranites intruded into the Abbabis Complex are undeformed, whilst those near the contact have been deformed in a shear zone developed in pelitic and psammitic rocks of the Etusis Formation. Width of shear zone is approximately 10 m. G-J: Equal area lower hemispheric stereographic projections of structural data from the Arcadia shear zone. Outcrops A-C (G-I) are south of the Swakop River and show slight variation in the orientation of structures due to the position of outcrops around the NE-trending Arcadia Syncline, outcrop D (J) is north of the Swakop River. Bold great circles represent shear bands, with vergence and approximate principal stress direction indicated. Open circles represent fold hinge lines, star (Outcrop B) represents intersection lineation. G: Outcrop A (locality 0504272/7483866) shows a gentle NNW-plunging σ_1, perpendicular to fold axial plane and lithological layering, and shallow WSW-plunging folds. H: Outcrop B (locality 0504055/7483435) indicates a similar moderate northwesterly plunge for σ_1. An S-C fabric in this outcrop, with a shallow NE-plunging intersection lineation, indicates top-to-the-NW shear sense, consistent with the principal stress directions from shear bands. I: Outcrop C (locality 0504015/7483307), shows an S-C fabric, with NE- to ENE-dipping orientations, perpendicular to a SW-plunging σ_1 direction. The S-C fabric indicates a top-to-the-SW shear sense, consistent with the σ_1 orientation. J: Outcrop D (locality 0505233/7485548) shows moderately NE- to ENE-plunging folds, with E-dipping axial planes. Z-folds indicate a dextral shear sense. K: Schematic diagram illustrating the general structural relationships in the shear zone. Layer-parallel extension and flattening perpendicular to the contact between the Abbabis Complex and Damara Supergroup has resulted in shear band formation, and intense strain has formed isoclinal folds with axial planes subparallel to lithological layering. Vergence of the shear zone from S-C fabrics is consistent with formation due to flexural slip during formation of the Arcadia Syncline.

Although high-strain zones show evidence for strain localisation, not all show bedding transposition, sheath folding and S-C fabrics, suggesting that, whilst strains may have been high, non-coaxial simple shear may have been subordinate to more coaxial pure shear in some high-strain zones. The well-exposed western margin of the Ida Dome shows concentrated ductile deformation in a 0.5-1 km thick high-strain zone, developed in both the Etusis Formation and the Abbabis Complex. The style of deformation varies according to lithology; in the Etusis Formation, dm-scale layering of quartzite and semi-pelite has resulted in a competence contrast, producing tight to isoclinal m-scale folding of more competent quartzite and less competent semi-pelite layers (Fig. 3.11A, B). The folding developed in the Etusis Formation gives a consistent southeasterly vergence; folds have shallow SW-plunging hinge lines, and shallow NW-dipping axial planes, which are subparallel to the lithological layering in the area (Fig. 3.11C). Locally, intersection lineations are noted subparallel to the hinges of folds. However, folds are not common in the Abbabis Complex and the quartzofeldspathic gneisses form only minor, cm-scale folds. Most of the deformation seen in the Abbabis Complex in the high-strain zone on the western margin of the Ida Dome takes the form of shear bands (Fig. 3.11D, E). These cm- to m-scale shear bands are similar to the 'extensional shear zones' noted by Oliver (1994), and are developed in conjugate sets; a steeply N-dipping set with a normal sense of displacement, and a W-dipping, SW-verging set (Fig.3.11F). Using these two conjugate sets of shear bands, it is possible to calculate principal stress orientations (Fig. 3.11C) – σ_1 is moderately SE-plunging, σ_2 is more steeply NW-plunging, and σ_3 is subhorizontal, and NE-SW trending.

A
NW
SE

B
S
N

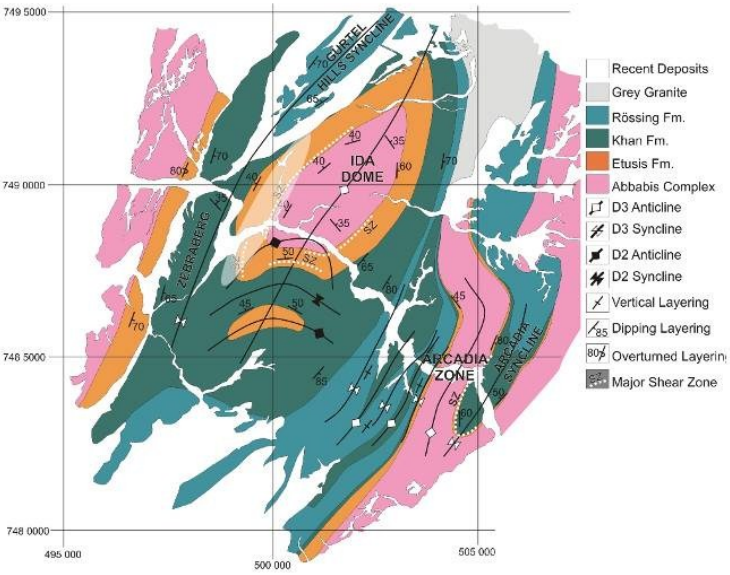
749 5000
749 0000
748 5000
748 0000
495 000
500 000
505 000
CURTEL HILLS SYNCLINE
IDA DOME
ZEBRABERG
ARCADIA ZONE
ARCADIA SYNCLINE
Recent Deposits
Grey Granite
Rössing Fm.
Khan Fm.
Etusis Fm.
Abbabis Complex
D3 Anticline
D3 Syncline
D2 Anticline
D2 Syncline
Vertical Layering
Dipping Layering
Overturned Layering
Major Shear Zone

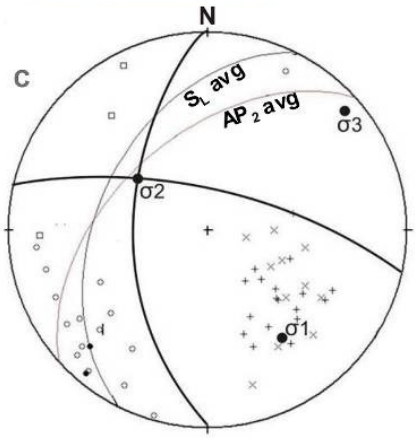
C
N
S_L avg
AP_2 avg
σ3
σ2
σ1

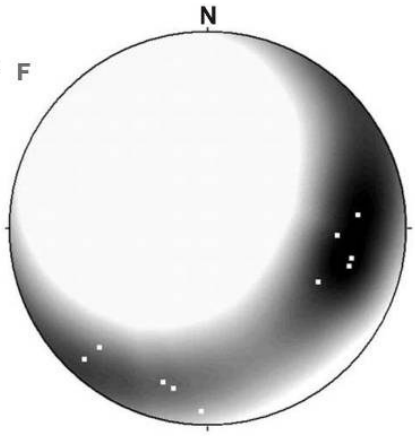
F
N

D
SW
NE

E
SW
NE

Fig. 3.11 (previous page) – Structures developed in a major high-strain zone on the western margin of the Ida Dome. A: NW-dipping isoclinal fold in Damaran metasediments near the contact with the Abbabis Complex. B: Tight, recumbent folding of 10-20 cm wide layers of quartzite interbedded with biotite schist C: Equal area lower hemispheric stereographic projections of structural data. Open circles are fold hinge lines (n=15). Closed circles are intersection lineations (n=2). Open squares are boudin axes (n=3). X symbols are poles to axial planes of D2 folds (n=11). + symbols are poles to lithological layering (n=17). Average orientations of axial planes (AP_2 avg) and lithological layering (S_L avg) are shown by great circles. Bold great circles are averages for the conjugate set of shear bands shown in F, and the approximate stress orientations deduced from these shear bands. D: SW-verging cm-scale shear band in Abbabis Complex gneisses. E: SW-verging m-scale shear band in Abbabis Complex gneisses. The shear plane contains leucosome. (F): Equal area lower hemispheric stereographic projections of contoured poles to planes for shear bands (white squares), indicating a conjugate set of steep N-dipping and moderate W-dipping shear bands.

Anatectic leucosomes are found intruding into shear bands in Abbabis Complex gneisses (Fig. 3.12A), and form lensoid bodies subparallel to the lithological layering in the Etusis Formation. Numerous cm- to dm-thick sheets of coarse to pegmatitic leucogranite are intruded subparallel to the axial planes of folds, and show pinch-and-swell structures, indicating continuing flattening perpendicular to these sheets following their intrusion (Fig.3.12B). The migmatitic nature of this shear zone indicates that its development was contemporaneous with high-grade metamorphism leading to anatexis. Microtextures indicate that rocks from the shear zone have undergone dynamic recrystallisation. Quartz grains have highly irregular grain boundaries, and quartz may be strained or elongate subparallel to the shear foliation that is defined by aligned laths of biotite (Fig. 3.12C). Other samples display extensive static recrystallisation; quartz grain boundaries may be only slightly irregular, and 120° triple junctions are found. Very small magnetite and quartz grains (<0.1 mm) indicate that grain size reduction during deformation may have taken place, with subsequent recrystallisation in order to reduce internal free energy associated with large grain boundary surface areas (grain boundary area reduction; Passchier & Trouw, 2005) to create the overall coarser grain size observed; these rocks are consequently described as blastomylonites (Fig. 3.12D).

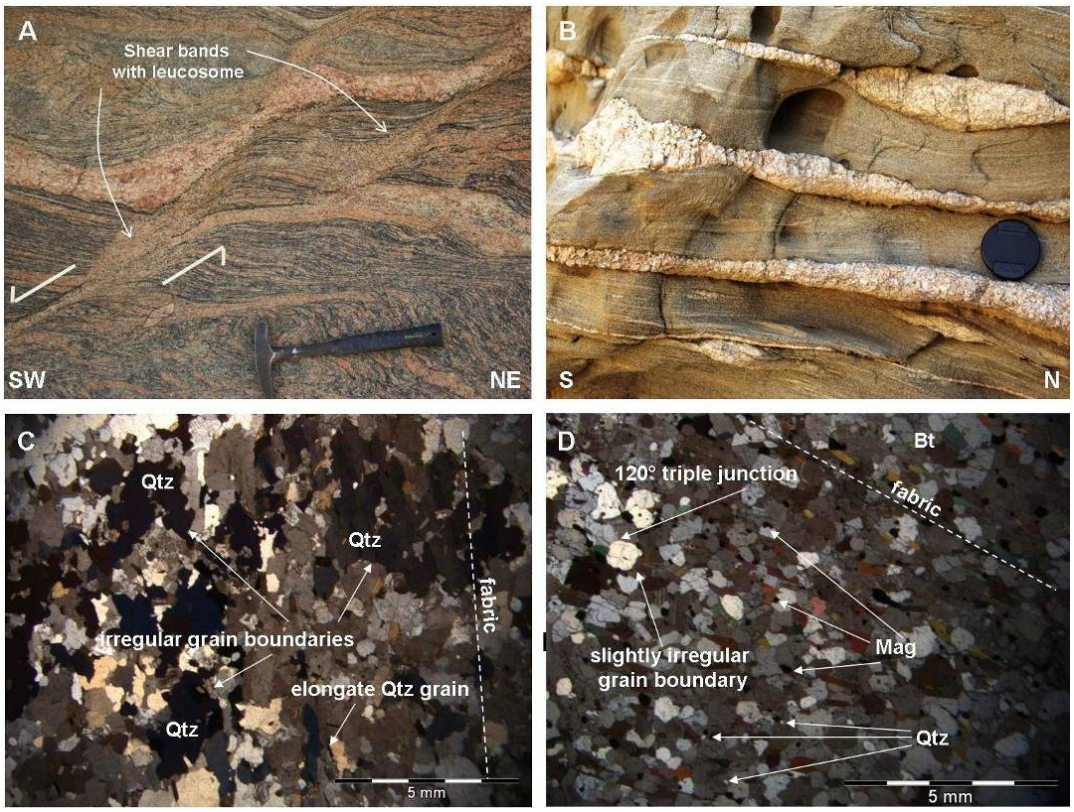

Fig. 3.12 – Field photographs and photomicrographs from a ductile shear zone along the western margin of the Ida Dome. A: Leucosomes emplaced into shear bands in Abbabis Complex gneisses on the western margin of the Ida Dome (locality 0500289/7488670). B: Numerous cm-scale rootless isoclinal folds in quartz-biotite schist of the Etusis Formation (left of lens cap), with boudinaged leucogranite sheets intruded subparallel to the axial planes of isoclinal folds and lithological layering (locality 0498888/7486840). C: Photomicrograph of an Etusis Formation quartzite from the shear zone. Note strained quartz (upper right corner), with highly irregular grain boundaries, and quartz grains elongate with the fabric direction (XPL, sample CZRL24, locality 0500606/7487048). D: Photomicrograph of Abbabis Complex gneiss from the shear zone, showing a recrystallised texture, with 120° triple junctions, and only slightly irregular grain boundaries. Note the numerous tiny rounded quartz grains indicating recrystallisation may be incomplete (XPL, sample CZRL22, locality 0500485/7488813). Mineral abbreviations are after Kretz (1983).

This high-strain zone may be part of a regional-scale detachment at the basement-cover contact, as described by Oliver (1994, 1995), Oliver & Kinnaird (1996), and Poli (1997). Although not identified in previous structural studies of the Ida Dome (e.g. Barnes, 1981), this high-strain zone was noted by Tack *et al.* (1995). The NE-SW extension indicated by shear bands from the high-strain zone on the western margin of the Ida Dome is found

throughout the study area. However, extensional deformation is not always restricted to high-strain zones near the contact between the Abbabis Complex and Damara Supergroup, and shear bands are common in both Abbabis Complex and Damaran Supergroup lithologies throughout the study area. Shear bands are also not the only expression of NE-SW extension – a shallow NE-plunging extension lineation is also common throughout the study area. This lineation is defined by elongate metamorphic minerals. Although the orientation is similar to that the intersection lineation also common in the study area, elongate minerals growth is not associated with the intersection lineation, which creates pencil structures due to the fissile nature of the rock.

3.4.3 NE-SW extension in the study area

Shear bands are found in both the Abbabis Complex and Damara Supergroup, and are not restricted to high-strain zones. Conjugate sets of shear bands are better developed in the basement gneisses of the Abbabis Complex, and are generally smaller (<1 m) in length than those in Damaran metasediments, where conjugate sets are less common (Fig. 3.13C). This may be due to the more homogeneous nature of the Abbabis Complex gneisses relative to the highly layered Damara Supergroup lithologies. In the Damaran metasediments where schists and psammites are banded on a cm- to dm-scale, a S- to SW-verging set is better developed (Fig. 3.13D). These shear bands are commonly developed on a m-scale and, in places, are clearly visible from a distance, imparting a sigmoidal appearance to the dip of lithological layering in outcrops. Throughout the study area, similar orientations for shear bands are found. Along the northern margin of the Palmenhorst Dome, two sets are recorded (Fig. 3.13A): a steep NNE-dipping, N-verging set (Fig. 3.13B), and a shallower W-dipping, SW-verging set. These two sets are found in an area with a number of high-strain shear zones, but extension is not necessarily concentrated in these zones. Further south, near the centre of the Palmenhorst Dome (Figs. 3.13C-E), and near the southern end of the Hook Fold (Figs. 3.13F-H), two similar sets of shear bands are again developed: a shallow WSW-dipping, SW-verging set (Set 1 – average orientation of 148/24SW), and a subvertical to steeply N-dipping, N-verging set (Set 2 – average orientation of 276/72N). The orientation of the principle stress directions

(calculated from the average orientations for the conjugate set of shear bands) shows that σ_1 plunges 57˚ on 158˚, whilst σ_3 plunges of 26˚ on 021˚, with σ_2 plunging shallowly west.

Also noted locally in the study area are shallow NE- to SW- plunging mineral stretching lineations (Figs. 3.13 I, J, K). These mineral stretching lineations are usually aligned, elongate porphyroblasts of high-grade metamorphic minerals (Fig. 3.13I), but may be pressure shadows adjacent to metamorphic minerals (Fig. 3.13J). The average orientation of lineations measured is 8˚ on 028˚.

Fig. 3.13 (following page) – Evidence for NE-SW extension in the southwestern Central Zone. A: Equal area lower hemispheric stereographic projections of poles to shear bands from the northern margin of the Palmenhorst Dome. Averages for the two sets are shown by great circles, and the orientations of the associated stress directions are indicated. B: Steeply north-dipping, north-verging shear bands near the northern margin of the Palmenhorst Dome. C: Conjugate set of shear bands in Abbabis Complex gneisses from the centre of the Palmenhorst Dome. D: Shallow, SW-verging shear band in psammitic beds in Damaran Metasediments from the centre of the Palmenhorst Dome. E: Equal area lower hemispheric stereographic projections of poles to shear bands from the centre of the Palmenhorst Dome. Averages for the two sets are shown by great circles, and the orientations of the associated stress directions are indicated. F: Steep north-dipping shear bands in Damaran metasediments from the Hook Fold in the Palmenhorst Dome. G): Equal area lower hemispheric stereographic projections of poles to shear bands from the hinge of the Hook Fold in the Palmenhorst Dome. Averages for the two sets are shown by great circles, and the orientations of the associated stress directions are indicated. H: Shallow, S-verging shear bands from the hinge of the Hook Fold in the Palmenhorst Dome. I: NE-plunging stretching lineation defined by elongate porphyroblasts of scapolite in calc-silicate. J: NE-plunging extension lineation defined by elongate leucosomes in pressure shadows between garnet porphyroblasts in pelitic schist. K: Equal area lower hemispheric stereographic projections of stretching lineations across the study area. Average of lineations (shown by red dot) is 8˚ on 028˚.

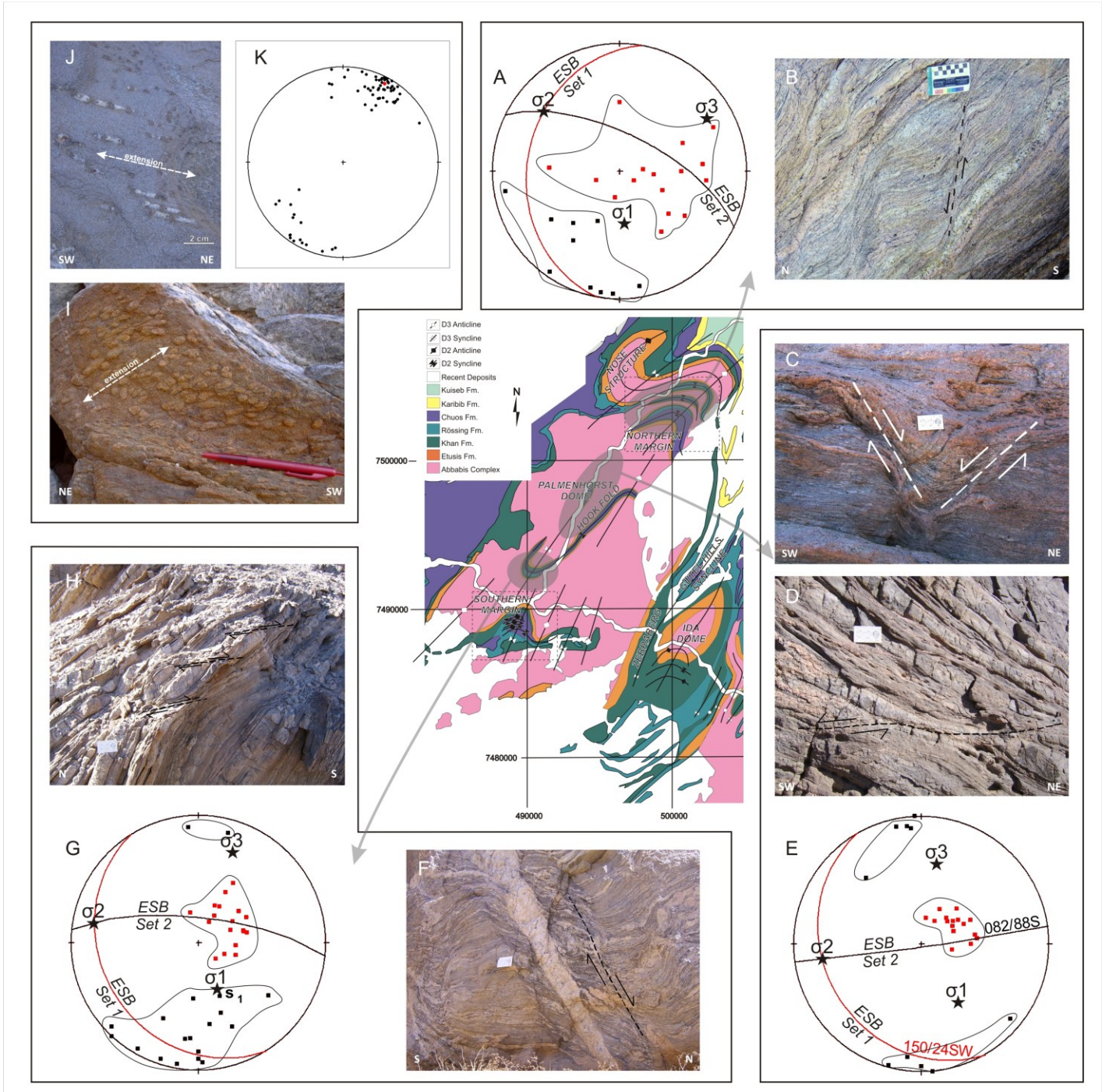
J
extension
2 cm
SW
NE
K
A
ESB Set 1
σ2
σ3
σ1
ESB Set 2
B
N
S
I
extension
NE
SW
D3 Anticline
D3 Syncline
D2 Anticline
D2 Syncline
Recent Deposits
Kuiseb Fm.
Karibib Fm.
Chuos Fm.
Rössing Fm.
Khan Fm.
Etusis Fm.
Abbabis Complex
N
NOSE STRUCTURE
NORTHERN MARGIN
PALMENHORST DOME
HOOK FOLD
SOUTHERN MARGIN
IDA DOME
7500000
7490000
7480000
490000
500000
C
SW
NE
H
N
S
D
SW
NE
G
σ3
σ2
ESB Set 2
σ1
ESB Set 1
F
S
N
E
σ3
σ2
ESB Set 2
082/88S
σ1
ESB Set 1
150/24SW

Similar stretching lineations have been noted elsewhere in the southwestern Central Zone by a number of workers (Coward, 1983; Oliver, 1994; Poli & Oliver, 2001; Kisters *et al.*, 2009) and suggest a close relationship between high-grade metamorphism and NE-SW extension. Whilst extensional deformation commonly appears to be concentrated in major extensional detachments near the basement-cover contact, NE-SW extension lineations and conjugate shear bands are found in both Abbabis Complex gneisses and Damaran metasediments. Whilst it is possible that many of the so-called stretching lineations measured previously may in fact be intersection lineations, subparallel to the hinge lines of S- to SE-verging folds, definite NE-SW trending stretching lineations are found. From the orientations of conjugate shear bands, the corresponding stress orientations which relate to shear band formation can be calculated. Calculations of principal stress direction from conjugate steep N-dipping, N-verging shear bands and shallow W-dipping, SW-verging shear bands indicates that, throughout the study area, a steep SE-plunging σ_1, shallow W-plunging σ_2 and shallow NE-plunging σ_3 are consistently calculated. These stress directions are consistent with the NE- to SW-plunging mineral stretching lineations, and indicate that SW-NE directed extension took place in the southwestern Central Zone (Fig. 3.14A). NE-SW extension in the southwestern Central Zone has previously been associated with supposed SW-verging deformation. Downing & Coward (1981) and Coward (1983) suggested SW-verging sheath folding, where hinge lines of folds were rotated into parallelism with the stretching lineation, in order to explain the occurrence of SE-closing folds. Folds in the study area are shown to have a southerly to southeasterly vergence, but no evidence for SW-verging sheath folding has been found. The similar field relationships between high-grade metamorphism, NE-SW extension, and S- to SE-verging folding suggest that folding and extension were near synchronous. It is likely that isoclinal, recumbent S- to SE-verging folding and NE-SW extension were part of a progressive sequence of deformation. Since there is no evidence for SW-verging sheath folding, the formation of folds with hinge lines subparallel to the NE-SW extension direction cannot be accounted for by sheath folding, where fold axes are reoriented towards the displacement direction with progressive deformation (Downing & Coward 1981; Coward 1983). Shear bands in the southwestern Central Zone occur as a conjugate set, and NE-SW extension does not have a vergence to the

southwest, as suggested by Oliver (1994). The lack of kinematic indicators parallel to the stretching lineations suggests that orogen-parallel extensional deformation occurred as a result of pure shear, rather than simple shear. The vergence of folds to the south or southeast, however, indicates that a component of simple shear was involved in producing orogen-oblique to orogen-perpendicular deformation. The σ_1 direction calculated from conjugate shear bands is consistently moderately to steeply S- to SE-plunging, with σ_2 shallow W- or NW-plunging, and σ_3 shallowly NE-plunging. Poli (1997) showed using the widespread occurrence of prolate porphyroblasts and deformed pebbles that strain in the southwestern Central Zone was constrictional – i.e. σ_1 and σ_2 were almost equivalent. If one considers that NE-SW extension occurred as a result of pure shear in a constrictional field, with SE-verging folds the result of orogen-perpendicular simple shear, then the occurrence of SE-verging folds coeval with NE-SW extension is possible (Fig. 3.14B). This model explains the S- to SE-vergence for folding in the southwestern Central Zone, as recorded by the SE-facing folds of Downing & Coward (1981), and the NE-trending hinge lines of Poli (1997), rather than being formed by SW-verging sheath folds (Downing & Coward 1981; Coward 1983). There is a lack of mesoscale sheath folds, as well as any NW-verging folds (which would be converse to SE-verging folds suggested to form on the limbs of supposed SW-verging sheath folds. A model of SE-verging simple shear deformation coeval with NE-SW extension in a constrictional field does not require sheath folding as a mechanism, and also explains the lack of SW-verging asymmetrical porphyroblasts or shear sense markers (Oliver 1994), and the irrotational strains in the southwestern Central Zone (Poli, 1997). Folds in ductile shear zones generally initiate with hinges normal, or at a high angle, to the displacement direction (Harris *et al.*, 2002), and in this case the displacement direction is suggested to be perpendicular to the extension direction.

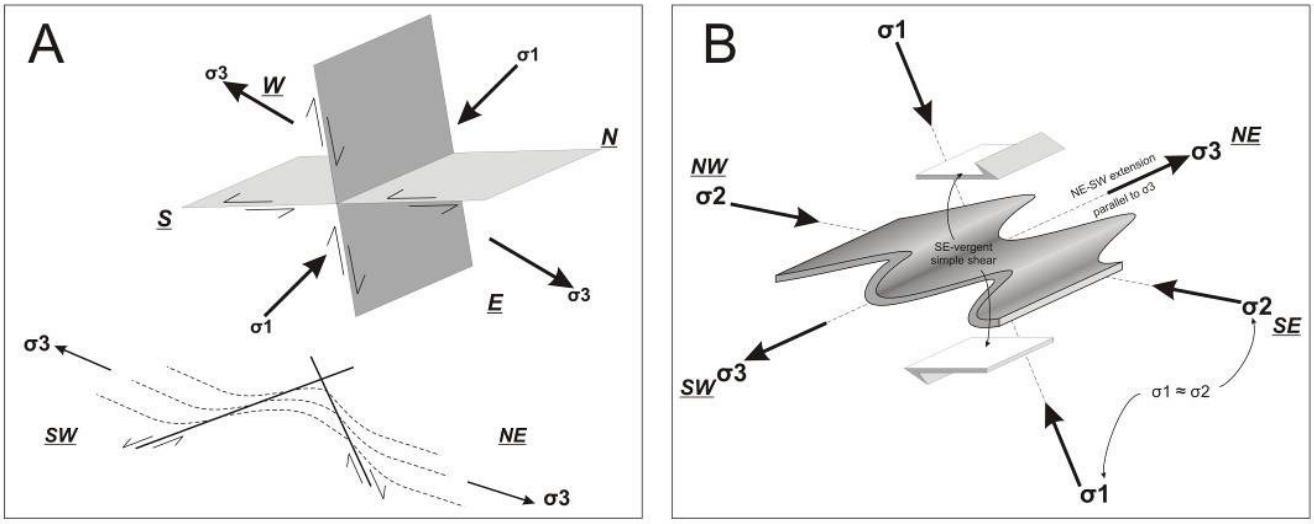

Fig. 3.14 – A: Schematic diagram illustrating the orientations of the conjugate set of ESBs relative to the principal stress directions, and showing how the shear bands develop during shallow NE-plunging extension, with steep SE-plunging compression. B: NE-SW pure shear extension coeval with SE-vergent simple shear in a constrictional field. The resultant structures are tight to isoclinal, recumbent to NW-dipping, SE-verging folds with hinge lines subparallel to NE-SW extensional lineations.

Thus progression of deformation in the southwestern Central Zone is suggested to have resulted in orogen-perpendicular, tight to isoclinal, SE-verging recumbent folding, with localisation of intense deformation into SE-verging shear zones, and high-strain zones near the basement-cover contact. This SE-verging deformation occurred in a constrictional stress field, and was accompanied by NE-SW directed orogen-parallel extension, which led to the formation of a strong mineral stretching lineation, a conjugate set of shear bands, and the development of a regional-scale extensional detachment at or near the contact between the Abbabis Complex and the Damara Supergroup during the later stages of deformation. All the deformation documented thus far is in the form of recumbent to shallow-dipping folds, and subhorizontal NE-SE extension. The extension of the upper limbs of large-scale S- to SE-verging folds and the consistent vergence of folds and later shear zones suggests that this non-coaxial deformation was progressive, with deformation shifting from largely S- to SE-verging folding to the formation of shear zones and NE-SW extension. Furthermore, similar field relationships of both folds and extensional structures to high-grade metamorphism and granitoid magmatism indicate

that folding and extension are part of a single deformation event. The generally recumbent or shallow dipping nature of structures formed during this major non-coaxial deformation event means they are not generally obvious from satellite imagery and aerial photos, but in the field they are by far the most obvious structures observed. Lithological mapping indicates that recumbent, S- to SE-verging fold structures (such as have been documented) were affected by km-scale, upright NE-trending structures. Should these upright structures postdate recumbent structures, there should be evidence for overprinting relationships between these two generations of folds.

3.5 Upright Folding in the Study Area

The large-scale structure of the Ida Dome is dominated by a km-scale upright anticline, and the fold interference pattern apparent from lithological mapping suggests similar km-scale upright folds throughout the study area, which are visible on aerial photographs and remote sensed images (Fig. 3.4). Mesoscale evidence for upright folding, however, is rare. Despite the fact that the main N-dipping fabric in rocks of the northern edge of the Palmenhorst Dome can be seen on aerial photographs and remote sensed images to be refolded about a NE-trending axis (Fig. 3.4A), few outcrop-scale upright structures have been observed in the field in this area. Elsewhere in the study area, (in the centre of the Palmenhorst Dome and along its southern margin) mesoscale upright folds are locally observed. The paucity of mesoscale upright folding may be the result of a lower intensity of strain during upright folding, or large wavelengths for upright folds due to a thicker competent layer.

3.5.1 Mesoscale upright folding

Small-scale upright folds are locally seen on the southern margin of the Palmenhorst Dome (Fig. 3.15A), and in the Ida Dome (Fig. 3.15B). These folds are generally gentle to open, and rarely tight, in contrast to the tight to isoclinal recumbent to shallow-dipping folds that have a S- to SE-vergence in the study area. Despite the apparent fold interference in the study area, mesoscale fold interference structures are extremely rare

– only one case (locality 0489350/7487244), was found where a complex fold interference pattern is apparent (Fig. 3.15C), and any possible fold interference seems to only be evident on a large scale. Although the axial planes of these folds are generally upright (average of 038/86E), fold hinge lines for these folds have a range of plunges, but give an average orientation of 10˚ on 042 (Fig. 3.15D). From the limited upright mesoscale folds found in the study area, little or no vergence is noted for these folds, and the deformation that led to the formation of these folds appears to have been generally coaxial. Although only one case has been documented in this study, Sawyer (1981) did note a number of mesoscale Type-2 (Ramsay, 1967) fold interference structures formed from the interaction between F2 and F3 folds in the Central Zone.

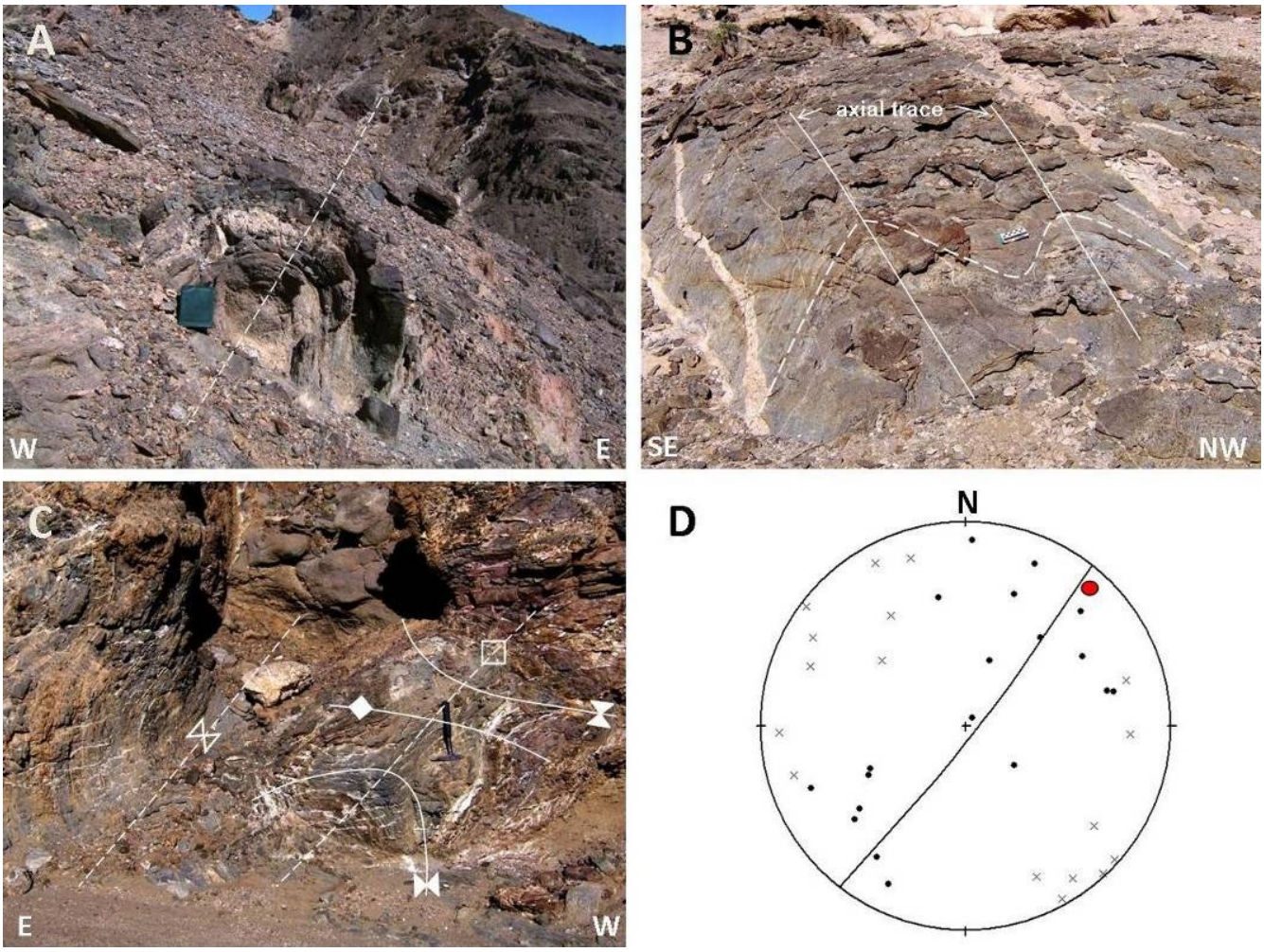

Fig. 3.15 – Mesoscale upright folding across the study area. A: Steeply W-dipping, open, m-scale anticline in calc-silicates of the Rössing Formation, southern margin of the Palmenhorst Dome (locality 0489997/7489927). B: Southwest plunging, upright, m-scale folds, developed in diopside-amphibole-plagioclase gneisses of the Khan formation, southeast Ida Dome (0499871/7483354). C: Rare example of D2/D3 fold interference – NE-trending upright folds (axial traces shown by dashed lines) refold earlier E-W trending folds (axial traces shown by solid lines), southern margin of the Palmenhorst Dome (locality 0489350/7489244). D: Equal area lower hemispheric stereographic projection of structural data for upright folds in the study area. Closed circles represent fold hinge lines (n=18), X symbols represent poles to axial planes (n=17). The great circle represents the average orientation for the axial planes to upright folds (038/86E). Red circle represents the average orientation of fold hinge lines (10˚ on 042) Note the large amount of scatter for fold hinge lines, which may be due to variable orientations of lithological layering due to earlier deformation.

3.5.2 The Arcadia Syncline

The effects of NE-trending, km-scale upright folding, whilst poorly developed at the outcrop scale, are apparent on a larger scale. East of the Ida Dome, between the Ida Dome and the Arcadia Inlier, a number of NE-trending, km-scale, upright to steeply NW-dipping isoclinal folds are developed in Khan and Rössing formation rocks (Fig. 3.16). These folds consist of anticlinal cores of Khan Formation diopsidic gneisses, between which Rössing Formation marbles and calc-silicate units form tight synclines. These anticlinal structures appear to have localised the intrusion of large masses of uraniferous leucogranite, the intrusion of which has resulted in extensive skarns developed in Rössing Formation carbonates (Freemantle, Pers. Comm.). These skarns form ridges of massive garnet-diopside material, which can be traced onto the desert plain southeast of the Ida Dome. Further to the east, the km-scale Arcadia Syncline trends northeast (Fig. 3.16). Along the Swakop River, where the best exposures are found, Khan Formation diopsidic gneisses and amphibole-biotite schist dominate, but to the north of the river, marbles of the Rössing Formation are found, indicating that this km-scale fold plunges to the northeast. Dm-scale parasitic folds on the km-scale Arcadia Syncline (Fig. 3.16A), and m-scale folds parasitic to these Dm-scale folds (Fig. 3.16B) have moderate to steep W- to NW-dipping axial planes, and plunge to the north or northeast (Fig. 3.16C). The westerly or northwesterly dips of axial planes are suggestive of a SE-vergence for these folds, and local Z-folds confirm this vergence (Fig. 3.16B). Lithological layering shows a range of orientations, consistent with folding about a NE-trending axis (Fig. 3.16C). The Arcadia Syncline is a NE-trending, steeply WNW-dipping km-scale fold, as indicated by its NE-trending axial trace, W- to NW-dipping parasitic folds, and the rotation of lithological layering about a NE-trending axis. To the east of the syncline, slivers of Damara Supergroup rocks are infolded into and sheared over the gneisses of the Abbabis Complex (Barnes, 1981; Jacob, 1974) and, to the west of the syncline, gneisses of the Abbabis Complex in the Arcadia Inlier lie above the Damaran Supergroup, consistent with a south-easterly vergence for these structures. The series of anticlines and synclines between the Ida Dome and Arcadia Inlier, which have similar axial traces (Fig. 3.16), appear to share a similar NE-trending geometry to the Arcadia Syncline, but are more upright. This more

upright geometry is distinct from the recumbent or shallow dipping, S- to SE-verging folds noted elsewhere in the study area (see section 3.4.1), and is consistent with the upright m-scale folds found locally (Fig. 3.15). The upright geometry of these folds suggests that they are related to a separate deformation event to that which formed S- to SE-verging folds and shear zones. Some of these more upright structures display a southeasterly vergence, but many of them appear to have no vergence, in contrast to the intense non-coaxial nature of the folds and shear zones noted elsewhere.

Additionally, some folds are found in the Arcadia Syncline with geometries that differ from the steeply NW-dipping geometry of the syncline. These m-scale folds (Fig. 3.16D) also plunge towards the north or northeast, but have NE-dipping axial planes (Fig. 3.16C), in contrast to the steep WNW-dipping axial planes of folds parasitic to the Arcadia Syncline. The orientations of the axial planes of these folds indicate that they cannot be parasitic to the km-scale Arcadia Syncline, but are likely to have been formed through earlier deformation. This indication of earlier formed folds, which may have been reoriented by the later upright deformation, is consistent with the observations from mapping that an earlier generation of recumbent or shallow N- to NW-dipping folds has been affected by later, upright NE-trending folding. The NE-dipping folds in the Arcadia Syncline are likely related to this earlier event, and steep WNW-dipping folds were produced by the younger event (Fig. 3.16E).

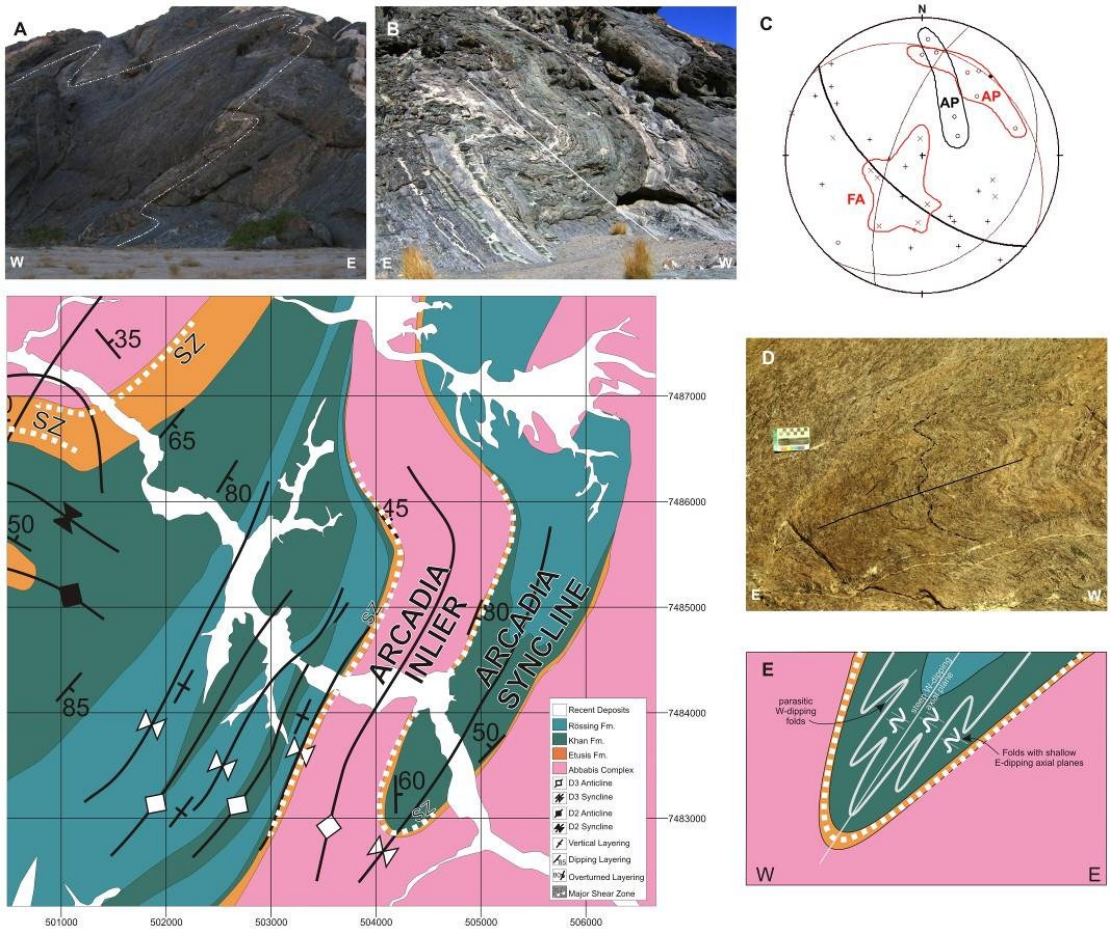

Fig. 3.16 – Deformation in the km-scale Arcadia Syncline. A: Large (Dm-scale), W-dipping anticline, with m-scale parasitic folds (locality 0504759/7483900). B: M-scale W-dipping fold in diopsidic gneisses, with boudinage on the limbs of the fold (locality 0504973/7484338). C: Equal area lower hemispheric stereographic projection of structural data from the Arcadia Syncline. Black X symbols are poles to axial planes of upright folds, with the fine black great circle representing the average orientation (200/72W). Red X symbols are poles to axial planes of NE-dipping folds (FA, outlined), with the red great circle showing the average orientation (306/26N) Red open circles are fold hinge lines of NE-dipping folds (AP, outlined). Black open circles are fold hinge lines for upright folds (AP, outlined). + symbols are poles to lithological layering around the Arcadia Syncline, and the bold great circle is the best-fit pi-pole girdle through these data, showing that the bedding has been folded around an axis plunging 25° on 041° (black filled circle). Note that both upright and NE-trending folds have similar plunges, with a large amount of scatter for both, and these folds are best distinguished by the orientations of their axial planes. D: Folded and crenulated gneissic fabric in the hinge of a shallowly E-dipping fold developed in diopside-feldspar gneisses (locality 0504258/7483388). E: Schematic W-E cross-section across the Arcadia Syncline, illustrating the relationship between steeply NW-dipping folds parasitic to the km-scale syncline and shallow NE-dipping folds, likely related to an earlier deformation event. Note the shear zone at the level of the Etusis Formation, which may be related to flexural slip during the formation of the Arcadia Syncline (see section 3.4.2 and Fig. 3.13).

3.5.3 Eastern margin of the Ida Dome

Similarly to the Arcadia Syncline, the eastern margin of the Ida Dome contains a number of recumbent or shallow-dipping mesoscale folds. Lithological layering on the western margin of the Ida Dome is moderately W- to NW-dipping, and is steeply SE-dipping to subvertical on the eastern margin (Fig. 3.17). A number of open to isoclinal folds are developed in pelitic schist, diopside-plagioclase gneiss, quartz-biotite schist and quartzite of the Rössing, Khan and Etusis formations on the eastern margin of the dome. Leucosomes are commonly developed along the axial planes of these folds (Fig. 3.17B) and tabular sheets of coarse to pegmatitic leucogranite have been emplaced axial planar to the folds (Fig. 3.17C). These folds plunge towards the northeast or north-northeast, and have shallowly E-dipping axial planes (average 009/38E), with similar orientations for granite sheets (350/32E) (Fig. 3.17D). Lithological layering on the eastern margin of the Ida Dome is steeply ESE-dipping, with an average orientation of 020/79E (Fig. 3.17C). Although they plunge to the northeast or north-northeast, the moderately E-dipping axial planes of these folds are incompatible with them being parasitic to a NE-trending, upright to steeply NW-dipping fold. Indeed, the vergence of these folds is opposite to the sense of vergence expected for parasitic folds developed on the eastern limb of such an anticline through flexural flow folding (Fig. 3.17 E). Thus, like the NE-dipping folds in the Arcadia Syncline, mesoscale E-dipping folds on the eastern margin of the Ida Dome cannot be related to the formation of the upright to steeply NW-dipping, NE-trending anticline that forms the Ida Dome and these folds must be related to an earlier folding event. These mesoscale folds have field relationships indicating that high-grade metamorphism and the emplacement of granites was coeval with this folding – folds have leucosomes developed along their axial planes, and tabular granite sheets are emplaced along the axial planes of some folds.

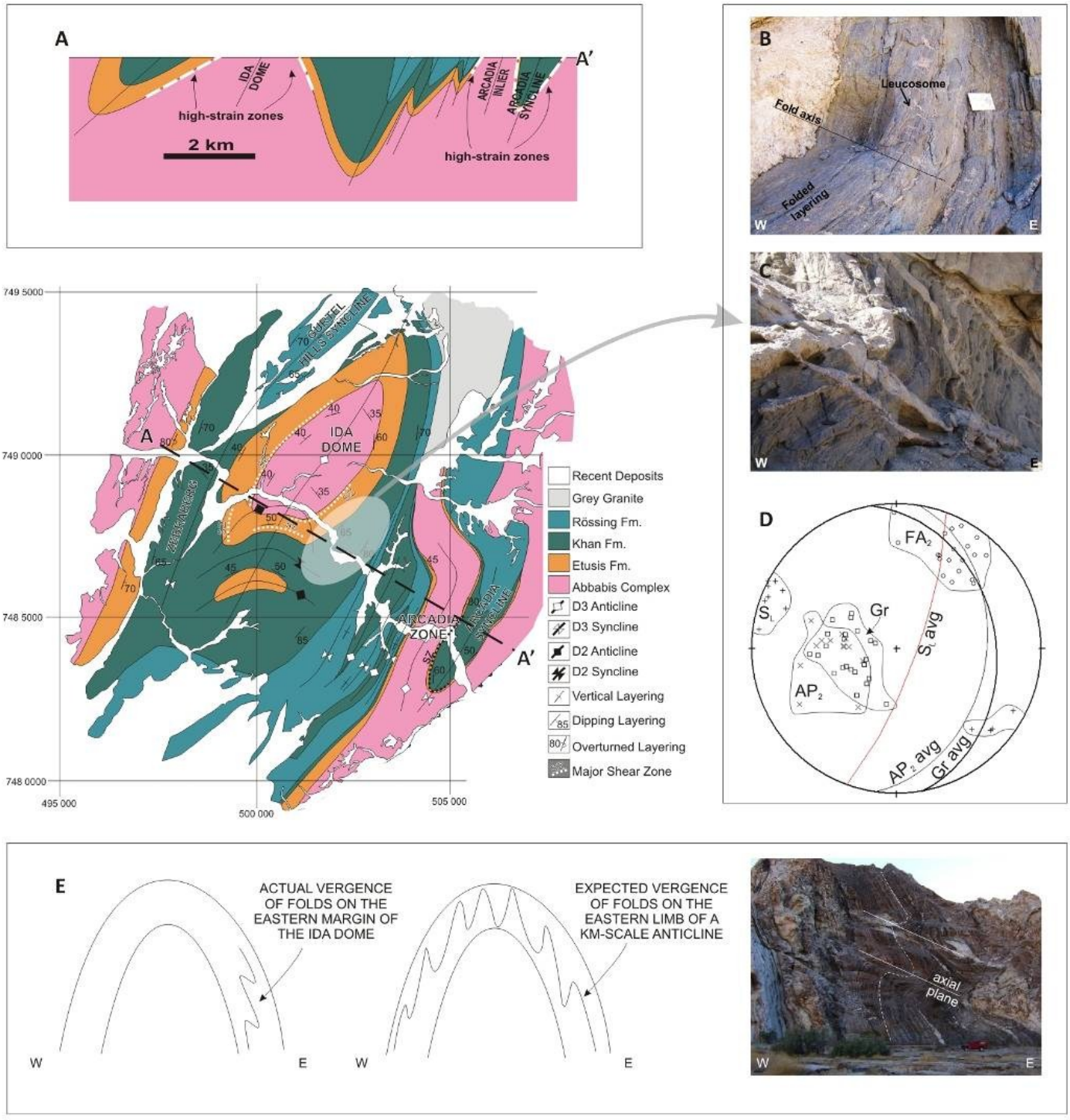
A
A'
IDA DOME
high-strain zones
2 km
ARCADIA INLIER
ARCADIA SYNCLINE
high-strain zones
B
Leucosome
Fold axis
Folded layering
W
E
C
W
E
D
FA2
SL
Gr
SL avg
AP2
AP2 avg
Gr avg
749 5000
749 0000
748 5000
748 0000
495 000
500 000
505 000
GUNFLINT HILLS SYNCLINE
IDA DOME
ARCADIA ZONE
ARCADIA SYNCLINE
Recent Deposits
Grey Granite
Rössing Fm.
Khan Fm.
Etusis Fm.
Abbabis Complex
D3 Anticline
D3 Syncline
D2 Anticline
D2 Syncline
Vertical Layering
Dipping Layering
Overturned Layering
Major Shear Zone
E
ACTUAL VERGENCE OF FOLDS ON THE EASTERN MARGIN OF THE IDA DOME
EXPECTED VERGENCE OF FOLDS ON THE EASTERN LIMB OF A KM-SCALE ANTICLINE
W
E
W
E
axial plane
W
E

Fig. 3.17 (previous page) – E-dipping structures on the eastern margin of the Ida Dome. A: Cross-section A-A' along the Swakop River, through the Ida Dome – section line shown on the map. This NW-SE section shows that Damaran metasediments and Abbabis Complex gneisses have been folded by steeply NW-dipping km-scale folds. B: Shallow E-dipping fold, showing cm-scale anatectic leucosome veins developing subparallel to the axial plane. Also note the leucogranite mass (top left, with a mafic selvedge along the contact with the schist. C: Open, m-scale fold in quartz-biotite schist, showing leucogranite sheets intruding along the axial plane of the fold, which dips gently to the east. D: Equal area lower hemispheric stereographic projection from the eastern portion of the Ida Dome, showing gently E-dipping axial planes of folds and tabular granite sheets, and steeply ESE-dipping lithological layering. Shallow E-dipping folds must be reoriented owing to their position on the subvertical eastern limb of a km-scale NE-trending anticline. Open circles are fold hinge lines of east-dipping folds (FA_2; n=19), X symbols are poles to axial planes of east-dipping folds (AP_2; n=13), + symbols are poles to lithological layering (S_L; n=12), open squares are poles to orientations of tabular granite sheets (Gr; n=23). The average orientations of fold axial planes (AP_2 avg; 009/38E), lithological layering (S_L avg; 020/79E) and tabular granite sheets (Gr avg; 350/32E) are shown by the great circles. E: E-dipping folds on the eastern limb of the Ida Dome, with a sketch to illustrate that these cannot be parasitic fold on the eastern limb of an upright km-scale anticline.

3.6 Fold Interference in the Study Area

Although mesoscale fold interference is very rarely noted in the field, a number of features of deformation in the study area point to fold interference. The obvious large-scale Type-2 (Ramsay, 1967) fold interference pattern seen in the pattern of lithological distribution (Fig. 3.3) and evident on aerial photographs and remote-sensed images (Fig. 3.4) points to fold interference. Although Poli (1997) and Poli & Oliver (2001) suggested that such a fold interference pattern could be formed from a single phase of constrictional deformation, and separate overprinting events need not be invoked, it is apparent from the structural data for the Ida Dome and the Arcadia Syncline that mesoscale folds have been reoriented about a NE-trending axis, and cannot be formed as the result of parasitic folding to larger-scale upright to steeply NW-dipping, NE-trending folds. This is only evident when measuring the axial planes of mesoscale folds, and noting the vergence of these folds – mesoscale folds have hinge lines that plunge shallowly to the northeast and, thus, are indistinguishable from more upright, NE-trending folds on

the basis of hinge lines alone. The earlier intense, non-coaxial deformation event, leading to the formation of recumbent to shallow dipping folds has been widely recognised in the Central Zone (Smith, 1965; Nash, 1971; Blaine, 1977; Barnes, 1981; Sawyer, 1981; Coward, 1983; Jacob *et al.*, 1983) despite the range of vergences suggested for this event, and the NE-trending extension lineation is also noted to be associated with this event (Kisters *et al.*, 2009). Since early isoclinal intrafolial folds have been termed D1 for this study, here it is suggested that the recumbent, non-coaxial deformation event that formed S- to SE-verging folds coeval with NE-SW extension be termed D2, and that the event leading to more upright or steeply NW-dipping, shallow NE-plunging folding be termed D3. In this regard, the general sequence of deformation suggested by previous workers for the Central Zone is retained; i.e., isoclinal intrafolial folds and the regional bedding-parallel foliation are assigned to D1 (Blaine, 1977; Barnes, 1981; Coward, 1983). The overall structural pattern of the study area is dominated by this fold interference pattern. Both the Ida Dome and the Palmenhorst Dome show evidence for this fold interference, although along the southern margin of the Palmenhorst Dome, D2 structures have orientations which differ somewhat from those elsewhere in the study area (see section 3.6.3 below).

3.6.1 The Ida Dome

The distribution of lithologies across the Ida Dome is suggestive of Type-2 fold interference (Ramsay, 1967), where km-scale folds with recumbent to shallow NNW-dipping axial planes have been refolded about a NE-trending upright anticline. Lithologies vary from NW-dipping to ESE-dipping on the western and eastern margins of the dome, respectively. Plotting all structural data from the Ida Dome reveals that, on a broad scale, fabrics appear to have been folded about a shallow NE- to NNE-plunging axis. Poles to lithological layering (Fig. 3.18A) fit a pi-pole girdle to give a plunge of 7° on 035°, similar to the average plunge of 10° on 042° from mesoscale upright folds across the study area (Fig. 3.15D). Thus, although these upright mesoscale folds are rare, the large-scale structure of the Ida Dome appears to be controlled by a steeply WNW-dipping to upright, shallow NE-plunging, km-scale anticline. However, measurements of the axial planes of

most mesoscale folds across the Ida Dome, and of the tabular granite sheets emplaced axial planar to these mesoscale folds, show that poles to axial planes of folds (Fig. 3.18B) and granite sheets (Fig. 3.18C) give almost identical pi-pole girdles to poles to lithological layering (13° on 033° and 13° on 032°, respectively). The fact that axial planes of folds are refolded about a NE-trending axis confirms field observations that mesoscale folds on the eastern margin of the Ida Dome cannot be formed as parasitic folds to a km-scale upright, NE-trending fold, and must be the result of an earlier deformation event. In fact, all recumbent or shallow-dipping mesoscale folds are likely related to the non-coaxial, S- to SE-verging event described earlier, and have been subsequently reoriented by an upright event. Granite sheets intruded along the axial planes of these earlier folds have also been reoriented by upright folds. Mesoscale upright structures are found only locally, and these structures are most evident on satellite images, where km-scale upright folds can be seen folding earlier structures, resulting in the formation of the domes characteristic of the Central Zone, and forming a Type-2 (Ramsay, 1967) fold interference pattern with earlier-formed S- to SE-verging folds.

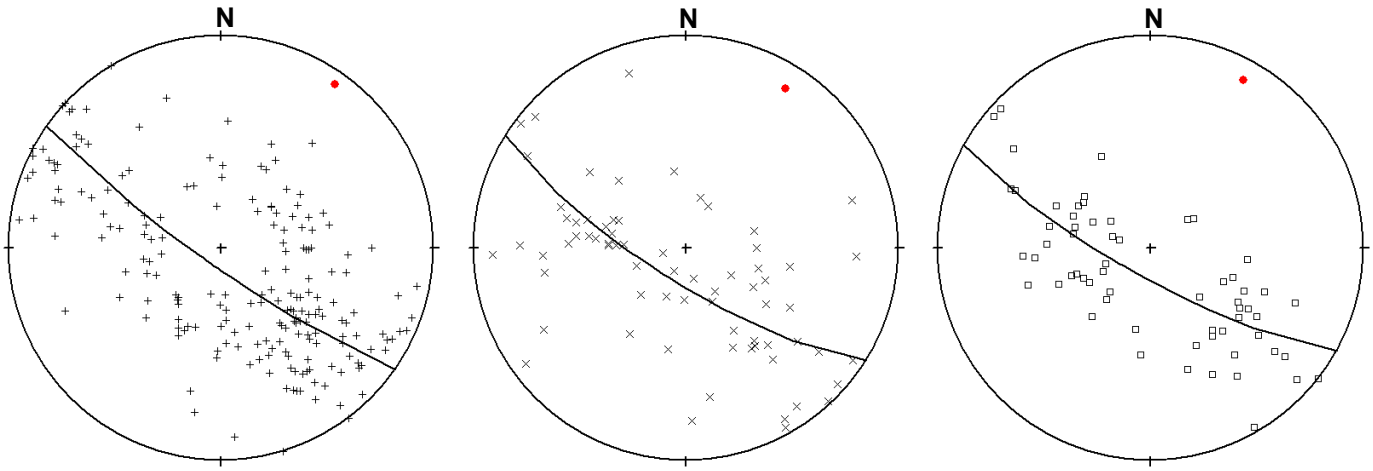

Fig. 3.18 – Equal area lower hemispheric stereographic projections of all structural data from the Ida Dome. A: Poles to lithological layering (+ symbols, n = 205) give a best-fit pi-pole girdle (great circle) indicating folding about an axis plunging 7° on 035° (red dot). B: Poles to axial planes of folds (X symbols, n = 70) give a best-fit pi-pole girdle (great circle) indicating folding about an axis plunging 13° on 033° (red dot). C: Poles to tabular granite sheets (open squares, n = 62) give a best-fit pi-pole girdle (great circle) indicating folding about an axis plunging 13° on 032° (red dot).

3.6.2 Structural synthesis of the Ida Dome

The overall geometry of the Ida Dome is the result of the interference between two generations of folding. The initial generation of folding occurred as a consequence of intense non-coaxial deformation, during which a series of tight S- to SE-verging, N- to NW-dipping km-scale folds developed (Fig. 3.19A); these are termed D2 folds. In the hinges of these km-scale D2 folds, symmetric M-folds are developed (Figs. 3.7C, 3.19A), whilst elsewhere in the Ida Dome m-scale D2 folds consistently show a S- or SE-vergence (Figs. 3.7A, B). Granite sheets have intruded along the axial planes of these D2 folds (Fig. 3.17C). High-strain zones concentrated deformation near the contact between the Abbabis Complex and the Damara Supergroup (Fig. 3.19A), where NE-SW subhorizontal extension formed shear bands (Figs. 3.11D, E), from which a moderate SSE-plunging σ_1 and shallow NE-plunging σ_2 are calculated (Fig. 3.11C), and elsewhere a NE-SW mineral stretching lineation is noted (Fig. 3.13I). Following this, a series of upright to steeply WNW-dipping km-scale folds was formed during D3 deformation, and it is one of these km-scale anticlines that has refolded a km-scale D2 anticline to form the Ida Dome (Fig. 3.19B). An increase in the intensity of D3 is apparent to the east of the Ida Dome, where a number of km-scale, upright to steeply WNW-dipping, isoclinal folds are developed in Khan and Rössing formation rocks (Fig. 3.19B). This variation in structural style is likely the result of the more stratified nature of the less competent, layered Khan and Rössing formations, whereas the more massive, competent basement in the Ida Dome resulted in larger wavelength D3 folding.

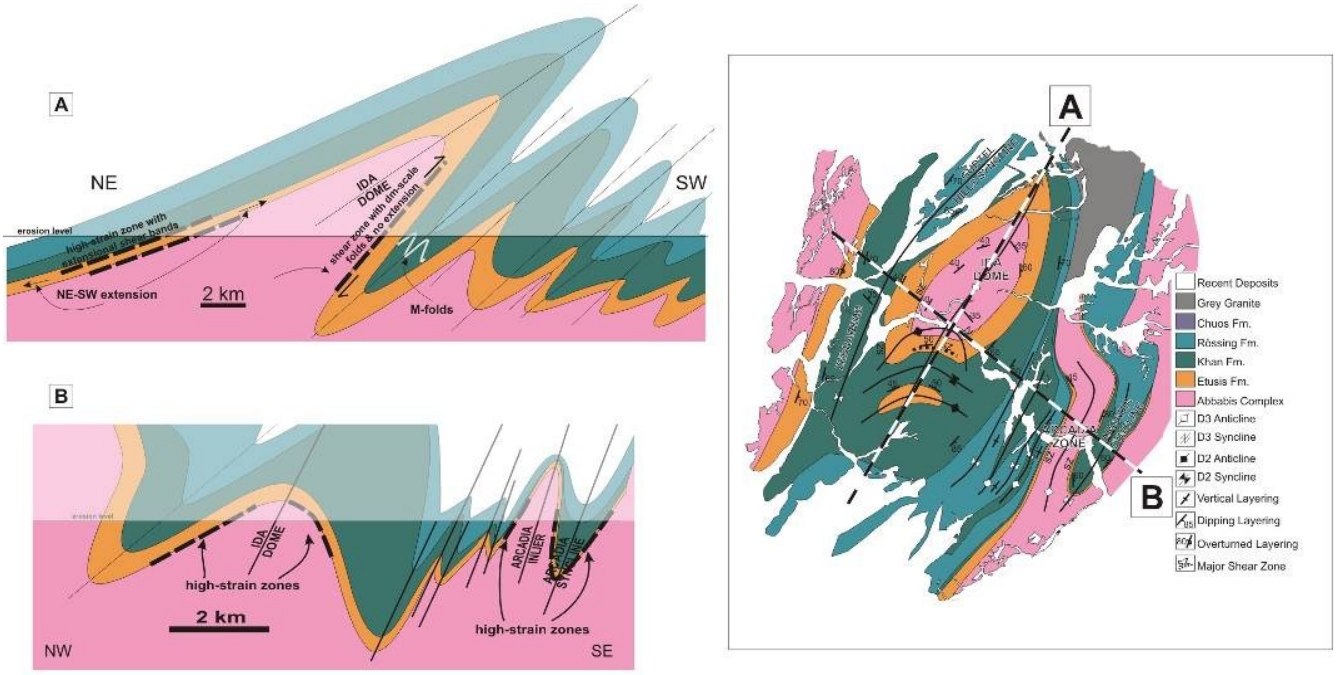

Fig. 3.19 – Cross-sections through the Ida Dome and Arcadia Inlier. A: NE-SW cross-section (along the axial trace of the D3 antiform), showing S-verging D2 structures. Note the position of a high-stain zone D2 on the long limb of the basement-cored anticline, where extensional structures are developed, whilst on the short limb a shear zone shows no extension, and is possibly a D2 thrust. B: NW-SE cross section, perpendicular to the axial trace of the D3 antiform, showing D3 structures. Note the folding of D2 high-strain zones by D3 structures. Map inset shows the section lines for A and B. Vertical exaggeration of sections 4x.

3.6.3 Southern margin of the Palmenhorst Dome

Upright, NE-trending km-scale folds are also apparent along the southern margin of the Palmenhorst Dome (Fig. 3.4B), where fold interference is also apparent from lithological mapping (Fig. 3.20). No major shear zones are found in this area, and folds do not have a strong vergence. Upright, mesoscale D3 folds are noted (Fig. 3.15A). The only mesoscale fold interference structures (Fig. 3.15C) are found in Damara Supergroup rocks that crop out south of the Swakop River Gorge, near the confluence with the Khan River Gorge (Fig. 3.2). The overall geometry of structures in this area comprises a series of tight to isoclinal, upright to S-dipping, E- or W-plunging folds, which are refolded by NE-trending upright folds (Fig. 3.20). The cores of S-dipping anticlines are made up of marbles, quartzites and

calc-silicates of the Rössing Formation or diopsidic gneisses of the Khan Formation, whilst S-dipping synclines preserve masses of quartz-biotite schist of the Chuos Formation. To the north and east of this area, quartzofeldspathic gneisses of the Abbabis Complex are found.

D2 folds are the most well developed structures in this area. These are particularly obvious in a number of N-S trending gorges that form tributaries to the Swakop River Gorge to the north (Fig. 3.20).

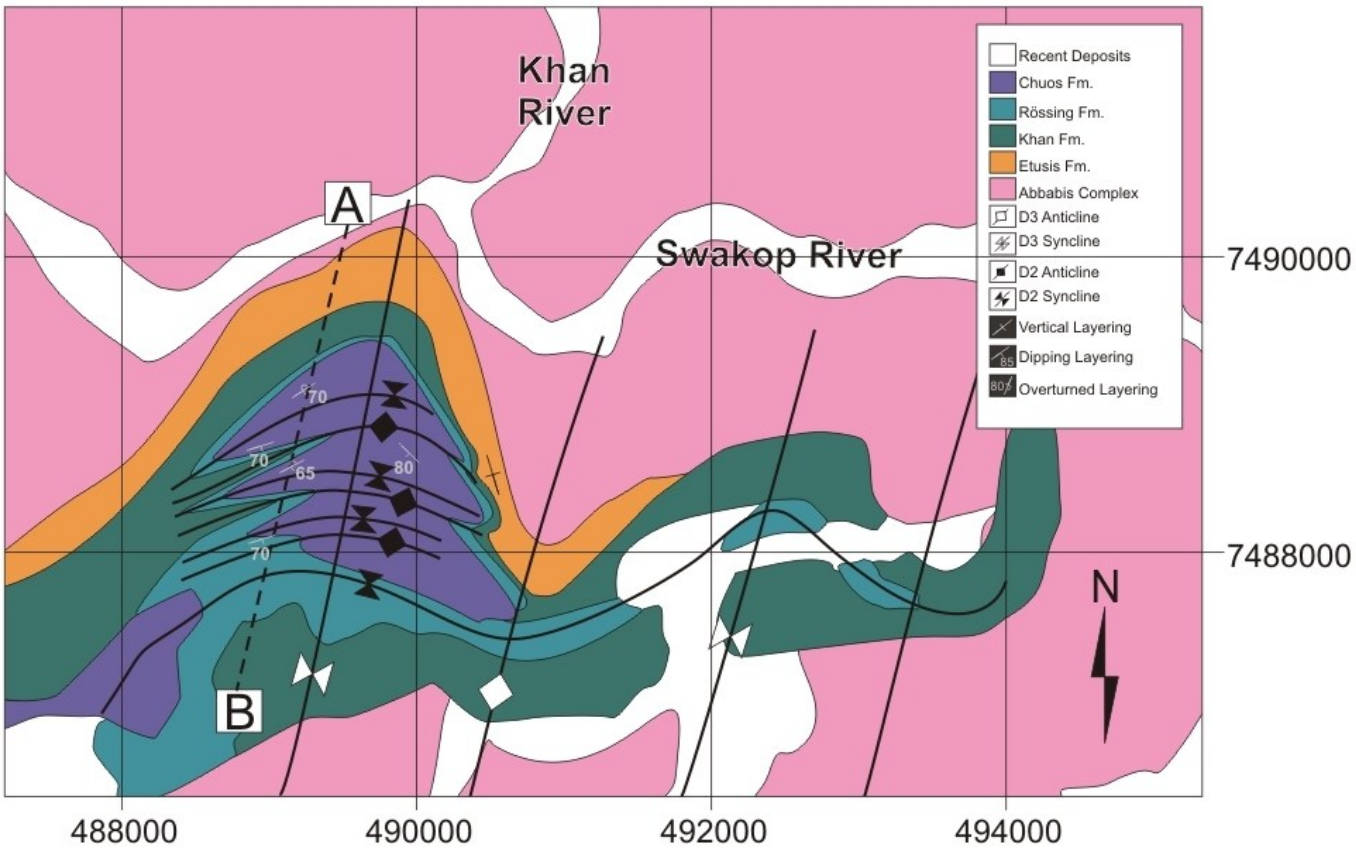

Fig. 3.20 – Geological map of the southern margin of the Palmenhorst Dome, showing a number of steeply S-dipping D2 folds, refolded by upright, NE-trending D3 folds. Note that the regional trend of D3 folding is visible on an aerial photograph (Fig. 3.4B). A-B is the section line shown in Fig. 3.24.

To the south, towards the desert plain, deformation features are less obvious as rock is highly weathered. The most obvious features developed in this area are found in rocks of the Rössing and Chuos formations, and consist of moderate to steeply S-dipping m-scale folds (Figs. 3.21A, B). To the west, the variety of lithologies found in the Rössing Formation makes identification of larger (tens to hundreds of m-scale) folds possible. The more monotonous nature of the Chuos Formation means that larger-scale folds must be inferred from the variation of m-scale fold vergences within larger-scale folds. D2 folds are open to tight, and are especially well developed in the quartzites of the Rössing Formation (Fig. 3.21A).

As with the Ida Dome, numerous granite sheets intrude along the axial planes of these folds (Fig. 3.21B, C); these are generally fine- to medium-grained grey granites, which may be pegmatitic along the margins.

Locally, the axial planar granite sheets are entirely pegmatitic. In contrast to the Ida Dome, shear bands are rare, occurring locally in Chuos Formation biotite-quartz schist (Fig. 3.21D), on the long limbs of D2 folds. In addition to intruding along the axial planes of D2 folds, grey granites typically contain a foliation, with a similar orientation to the axial planar foliation of folds in the vicinity. This foliation is strongly developed in the more biotite-rich grey granites, and weak in the leucogranite varieties.

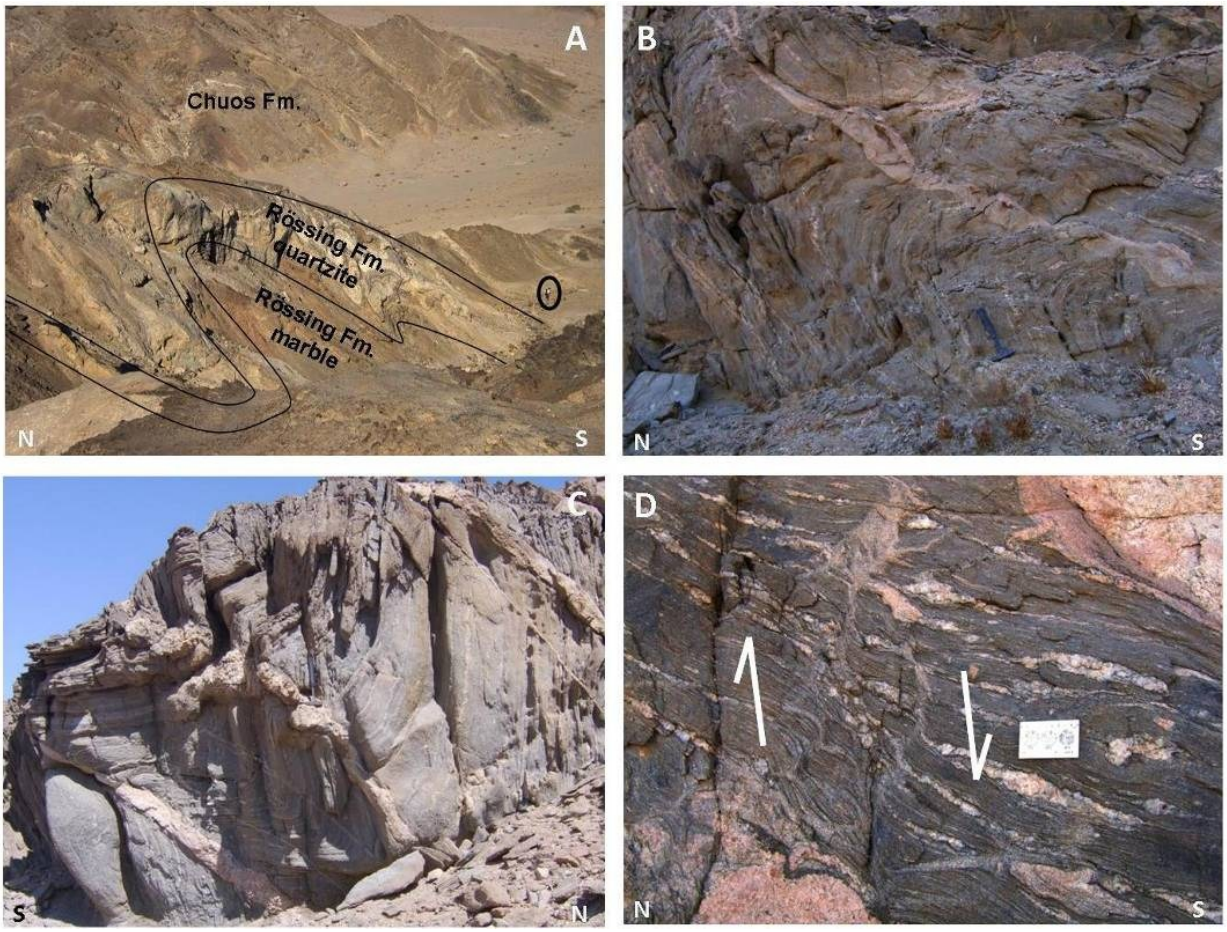

Fig 3.21 – D2 deformation along the southern margin of the Palmenhorst Dome. A: Dm- to m-scale, tight D2 folds in quartzite and marble of the Rössing Formation on the limb of a 100 m-scale fold (locality 0489332/7489428). Person for scale (circled). B, C: Open to tight folds in biotite-quartz schist (B – locality 0489731/7489401)) and metapsammite (C – locality 0490055/7488617) of the Chuos Formation, with granite/pegmatite intruding along the axial planes of the D2 folds. Note the slight boudinage of the granite sheet in B, indicating that deformation continued after intrusion. D: Rare S-verging extensional shear bands in quartz-biotite schist of the Chuos Formation (shear sense is indicated). Note the numerous coarse-grained quartzofeldspathic veins, which have been boudinaged, and are aligned with the lithological layering in the rock, which may be mistaken for diamictite pebbles (locality 0489454/7489694).

Satellite imagery (Fig. 3.4B) and the pattern of lithologies on the southern margin of the Palmenhorst Dome (Fig. 3.20) suggests that these D2 folds have been refolded by NNE-trending, upright D3 folds. Along the hinge of one of these km-scale D3 folds, where the rotation of D2 structures is expected to be minimal (assuming no rotation by smaller-scale

D3 structures, which are rare), the D2 folds plunge moderately towards the east (Fig. 3.21A).

Axial planes of D2 folds in this region display a wide range of orientations from subvertical to subhorizontal, but most are either S- or W-dipping (Fig. 3.22A). Although rather scattered, plotting a pi-pole girdle through these data reveals that the axial planes may have been folded by a larger D3 fold, with a plunge of 26° on 232° (Fig. 3.22A).

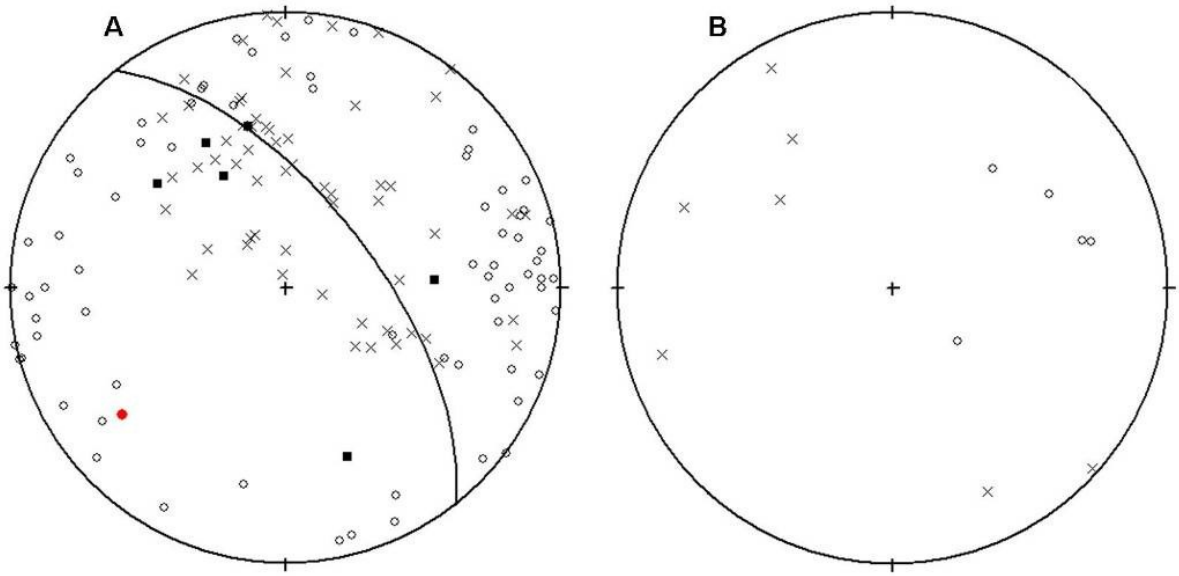

Fig. 3.22 – Equal area lower hemispheric stereographic projections of structural features along the southern margin of the Palmenhorst Dome. X symbols are poles to axial planes of folds, open circles are fold hinge lines; black squares are poles to granite sheets. A: D2 features. Note the wide spread in fold hinge line orientations, which are shallow plunging. Axial planes also show a range of orientations; however a statistically determined best-fit pi-pole girdle (black great circle) through the poles to axial planes indicates that they may have been refolded by a fold with a hinge plunging 26° on 232° (red dot). Axial planes n = 59. Fold hinge lines n = 72. Granite sheets n = 6. B: Fold hinge lines (n = 5), and poles to axial planes (n = 7) for rare D3 folds. D3 fold axial planes are generally steeply NW- or SE-dipping, reflecting the subvertical, NE trend for D3, and D3 folds plunge more steeply than D2 folds, probably reflecting steeper dips of layering as a result of D2 deformation.

Granite sheets show similar orientations to the axial planes of D2 folds, and are seen in the field to intrude along fold axial planes of these folds (Figs. 3.21B, C). Fold hinge lines along the southern margin of the Palmenhorst Dome have a range of orientations – although the majority of folds plunge shallowly to the west or east, shallow northerly and southerly plunges are also found, which may suggest sheath folding. However, no mesoscale sheath folds are found and most folds found do not show a strong vergence, suggesting that non-coaxial strain in this area was not very intense, at variance with any suggestion of sheath folding. The range in orientations is more likely to be a consequence of reorientation by later D3 folding. A large-scale NE-trending D3 fold is the major structure visible on aerial photographs and remote sensing imagery of the Hildenhof Area (Fig. 3.19), although the shallow southwest plunge for this structure obtained from the pi-pole girdle through D2 axial planes differs from the moderate to steep east to northeast plunge of smaller-scale D3 folds (Fig. 3.22B).

The rotation of D2 structures by upright structures is best illustrated by examining the orientations of D2 structures on the western and eastern limbs of the large-scale D3 fold visible from lithological mapping on aerial photographs. This reveals statistical differences in the orientations of these structures; D2 axial planes along the western limb of the large D3 fold have an average orientation of 068/48S, whilst the average on the east limb is 150/26W (Fig. 3.23A). Lithological layering displays far more scatter than D2 axial planes (Fig. 3.23B); likely due to the initial D2 folding event, but data from the western limb gives an average of 054/66S, different from the average for the eastern limb (252/30N). Similarly, the shallowly-plunging hinge lines of D2 folds show significant scatter, but data from the western limb of the D3 fold gives an average of 12° on 086°, compared to 14° on 308° for the eastern limb (Fig. 3.23C).

The statistical differences in the orientations of structures from the eastern and western limbs of an apparent D3 structure on the southern margin of the Palmenhorst Dome suggest that structures have been rotated about a NE-SW trending axis. Although structural data from the southern margin of the Palmenhorst Dome show far more scatter

than the data from the Ida Dome, the variability in the axial planar orientations for D2 folds suggests rotation about a NE-SW-trending axis (Fig. 3.22A).

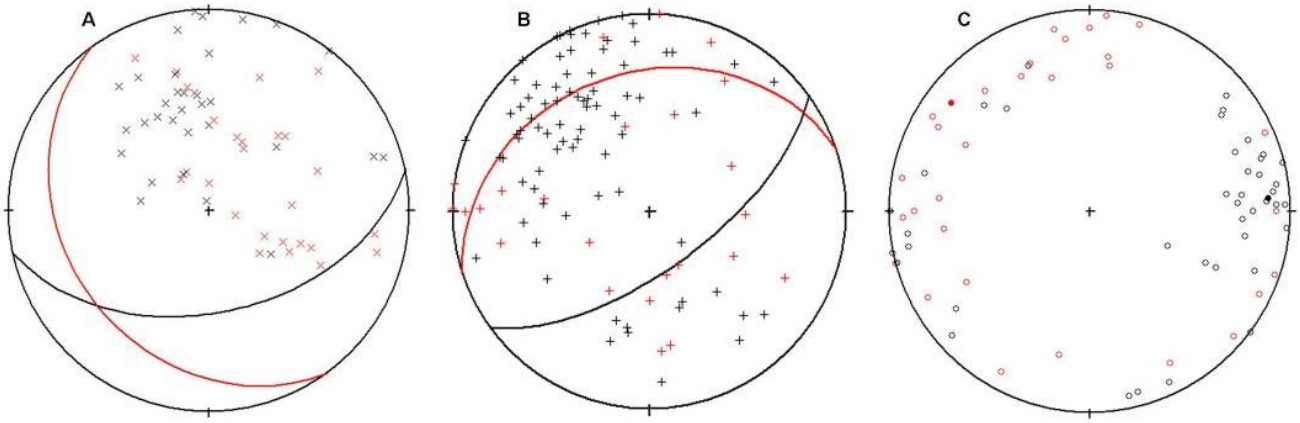

Fig. 3.23 – Equal area lower hemispheric stereographic projections of structural data from the southern margin of the Palmenhorst Dome, classified according to geographic location. Data shown in black represent the western limb of the large-scale D3 fold (west of the approximate hinge line of the D3 fold, taken as 0489800 east), whereas red data represents measurements from the eastern limb of the fold. A: Poles to axial planes of D2 folds (X symbols, n = 59), and average orientations for each limb (great circles). B: Poles to lithological layering (+ symbols, n = 106), and average orientations for each limb (great circles). C: Fold hinge lines (open circles, n = 72) and averages for each limb (closed circles).

It is also apparent from the lithological mapping that a series of tight, upright to steeply S-dipping E-trending D2 folds have been refolded by a large, upright NE-trending D3 synform (Fig. 3.20). However, a peculiar feature of the structures along the southern margin of the Palmenhorst Dome is that, in contrast to the strongly SSE-verging, NNW-dipping D2 structures observed in the Ida Dome, D2 structures along the southern margin of the Palmenhorst Dome are steeply SSE-dipping (Fig. 3.24), and do not generally show a strong vergence. Possible explanations are that this area may represent the nose of a km-scale, SSE-verging D2 nappe structure (Fig. 3.24A), that the structures are parasitic to a more open, upright E-W trending D2 fold (Fig. 3.24B), or that the current orientation of D2 structures reflects refolding of recumbent D2 structures by upright D3 structures (Fig. 3.24C). D2 structures with shallow north or northeasterly dips prior to D3 folding, may have been reoriented to dip steeply to the south on the northwestern limb of a km-scale

D3 syncline (Fig. 3.24C). The lack of vergence of D2 structures suggests that non-coaxial strain during D2 deformation along the southern margin of the Palmenhorst Dome was less intense than elsewhere in the study area, and no other km-scale nappe structures have been found in the study area.

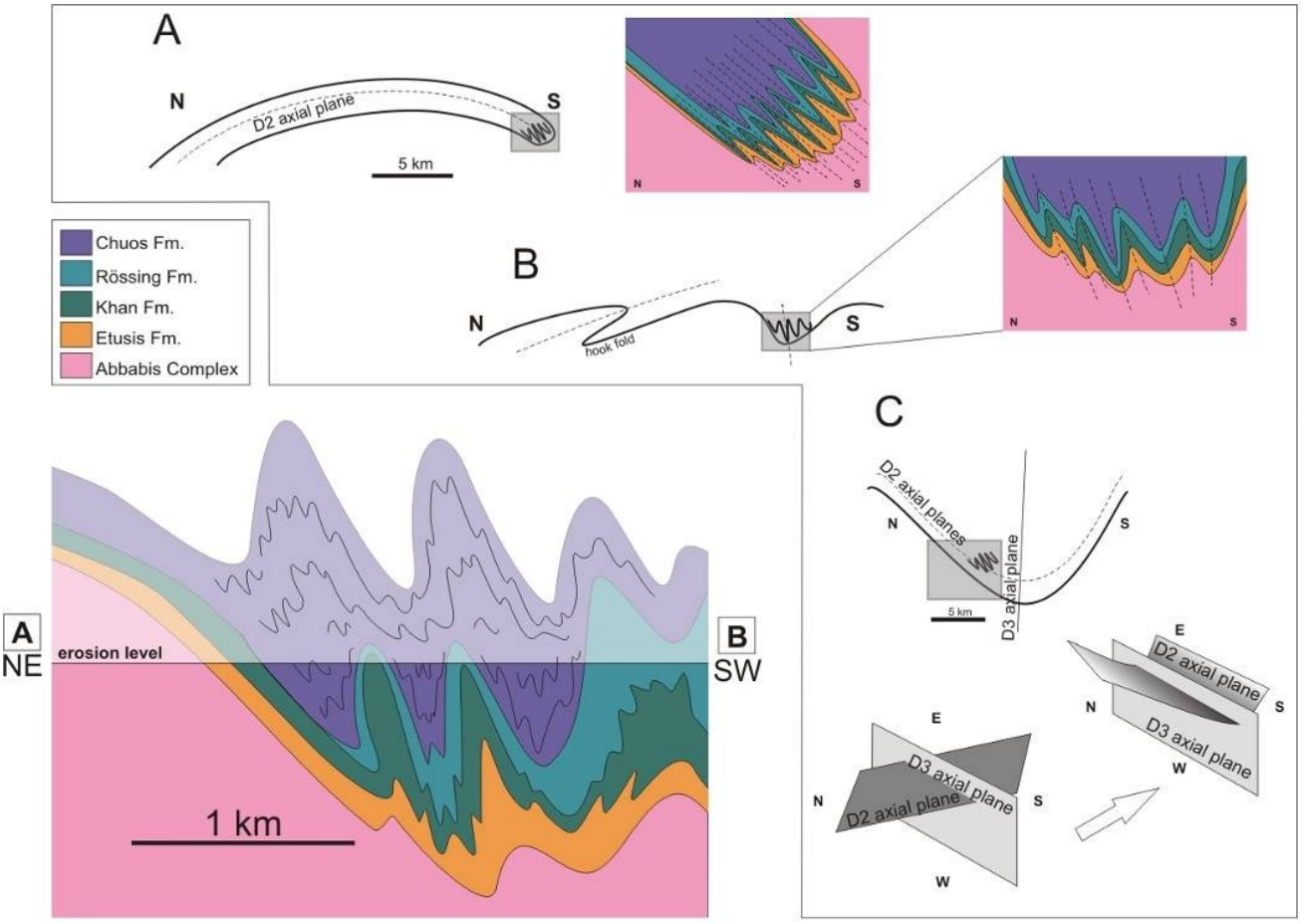

Fig. 3.24 – Cross section A-B (Fig. 3.19) through the southern margin of the Palmenhorst Dome, and possible explanations for the subvertical to southerly dip of D2 structures in this area. Section is along the axial trace of a km-scale D3 syncline, and shows tight, km-scale, upright to steeply N-dipping, D2 folds. Note the vergence of smaller-scale folds, which indicate the larger-scale structures. Vertical exaggeration 4x. A: The southern margin of the Palmenhorst Dome on the nose of a hypothetical km-scale D2 nappe, explaining the SSE-dipping D2 structures in this area. B: The southern margin of the Palmenhorst Dome as a km-scale open, not strongly vergent E-W trending D2 fold. C: Southerly dips for D2 axial planes owing to refolding of shallow N-dipping D2 folds by an upright D3 Syncline.

Fold structures formed at the overturned nose of a km-scale south-verging D2 nappe structure would be expected to be M-folds without a strong vergence, and could have a southerly dip (Fig. 3.24A). A southerly dip for parasitic D2 structures would only be possible should the nappe nose be overturned, as a S-verging nappe would be expected to produce N-dipping structures, as observed elsewhere in the study area. The lower intensity of D2 deformation and lack of vergence for D2 structures suggests that these folds are most likely related to a more open, less strongly vergent km-scale D2 fold (Fig. 3.24B). Such a situation would also explain the lack of shear zones and high-strain zones along the southern margin of the Palmenhorst Dome, whilst these features occur elsewhere in the study area, commonly due to a concentration of strain at the basement-cover contact, or on the extending limbs of km-scale D2 folds (Fig. 3.19A).

3.6.4 Structural synthesis of the Palmenhorst Dome

Lithological mapping has revealed a number of km-scale folds of Damaran Supergroup rocks within the Palmenhorst Dome, in areas previously interpreted as comprising exclusively Abbabis Complex lithologies, (see also Barnes, 1981). Small-scale structures indicate that these are tight to isoclinal infolds that have a southerly to southeasterly vergence and formed during intense non-coaxial D2 Damaran deformation. They have been refolded by upright, NE-trending D3 structures. This picture of fold interference is consistent with the large-scale structural pattern observed for the Ida Dome (section 3.6.2). A NE-SW cross-section across the Palmenhorst Dome (Fig. 3.25) shows the S-verging nature of D2 deformation across the Palmenhorst Dome, and shows the shallow-dipping to recumbent structures associated with D2. Maps of the study area and the southwestern Central Zone, however, are dominated by the Type-2 fold interference pattern formed from the interference between these shallow-dipping to recumbent structures and NE-trending upright D3 structures.

It is this fold interference structural pattern that has been previously identified throughout the southwestern Central Zone (Smith, 1965; Nash, 1971; Blaine, 1977; Barnes, 1981; Sawyer, 1981; Jacob *et al.*, 1983; Nex, 1997). However, although this fold

interference pattern has been widely recognised, it is not necessarily suggested by previous workers as the sole mechanism for dome formation in the Central Zone. Additionally, the fold interference pattern is only recognised in large-scale features, and mesoscale fold interference structures are exceedingly rare. In addition to fold interference (for which there is little mesoscale evidence), there have been a variety of other suggestions for alternative mechanisms for dome formation in the Central Zone, including sheath folding (Coward, 1983), extensional core-complex development (Oliver, 1994; 1995), and progressive deformation in a constrictional stress field (Poli, 1997; Poli & Oliver, 2001). Although mesoscale fold interference is rarely seen, there is nonetheless evidence that D2 structures formed earlier than D3 structures, and have been subsequently reoriented by km-scale upright to steeply NW-dipping D3 folds. Alternative models for deformation and dome formation in the southwestern Central Zone were suggested not only to explain the paucity of mesoscale fold interference structures, but also the NE-SW stretching lineation and the numerous shear bands associated with intense deformation in the southwestern Central Zone. Models for dome formation and the structural evolution of the southwestern Central Zone must take into account the evidence for large-scale fold interference, the lack of mesoscale fold interference structures, and the evidence for NE-SW extension.

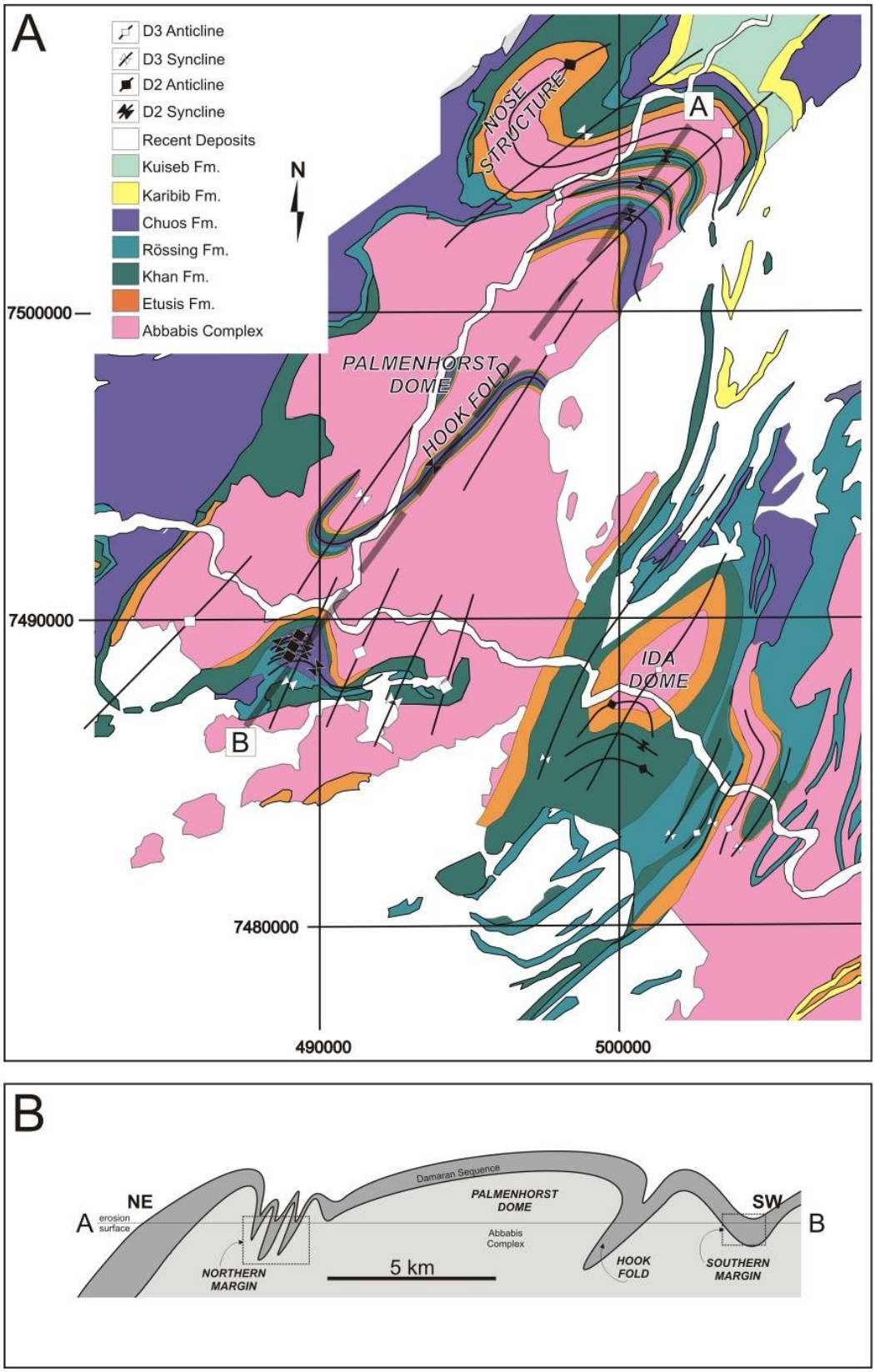
A
D3 Anticline
D3 Syncline
D2 Anticline
D2 Syncline
Recent Deposits
Kuiseb Fm.
Karibib Fm.
Chuos Fm.
Rössing Fm.
Khan Fm.
Etusis Fm.
Abbabis Complex
N
NOSE STRUCTURE
A
PALMENHORST DOME
HOOK FOLD
IDA DOME
B
7500000
7490000
7480000
490000
500000
B
NE
A
erosion surface
Damaran Sequence
PALMENHORST DOME
Abbabis Complex
SW
B
NORTHERN MARGIN
5 km
HOOK FOLD
SOUTHERN MARGIN

Fig. 3.25 (previous page) – Map of the study area showing the fold interference pattern for the Palmenhorst Dome, with the section line A-B shown. B: NE-SW cross section through the Palmenhorst Dome, showing the major structures mapped during this study. Note that the southern margin is shown as an area of less intense deformation near the hinge of a more open km-scale D2 syncline, explaining the subvertical to S-dipping structures along this margin.

3.7 Post-D3 Deformation in the Study Area

A number of previous workers have recognised structures indicating post-D3 deformation (Jacob, 1974; Blaine, 1977; Barnes, 1981; Basson & Greenway, 2004). These late structures are generally of lower intensity and are only locally noted (Barnes, 1981) and include folds (Jacob, 1974), spaced cleavage (Jacob, 1974; Barnes, 1981), kink bands (Barnes, 1981), and faults (Jacob, 1974; Blaine, 1977; Barnes, 1981; Basson & Greenway, 2004). No evidence for post-D3 folds or crenulations has been noted. Brittle structures are only locally noted in the study area. Where present, brittle structures cross-cut D2 fabrics and upright D3 folding. These include brittle faults (Figs. 3.26A, B), fractures (Fig. 3.26C) and tension gashes (Fig. 3.26D). Pegmatitic granites and leucocratic veins are locally emplaced into these brittle structures (Figs. 3.26C, D), and the brittle nature of deformation suggests that it took place following exhumation and cooling of the Central Zone. Late-tectonic strike-slip movement along major structures has been noted in the Central Zone (D5 – Blaine, 1977 and D4 – Basson & Greenway, 2004), and it has been suggested that brittle fractures developed during this movement controlled the emplacement of uraniferous leucogranites (Basson & Greenway, 2004). Brittle structures in the study area may be a response to sinistral movement along the Welwitschia Lineament (Basson & Greenway, 2004), but the emplacement of uraniferous leucogranites appears to have been controlled by upright D3 folding.

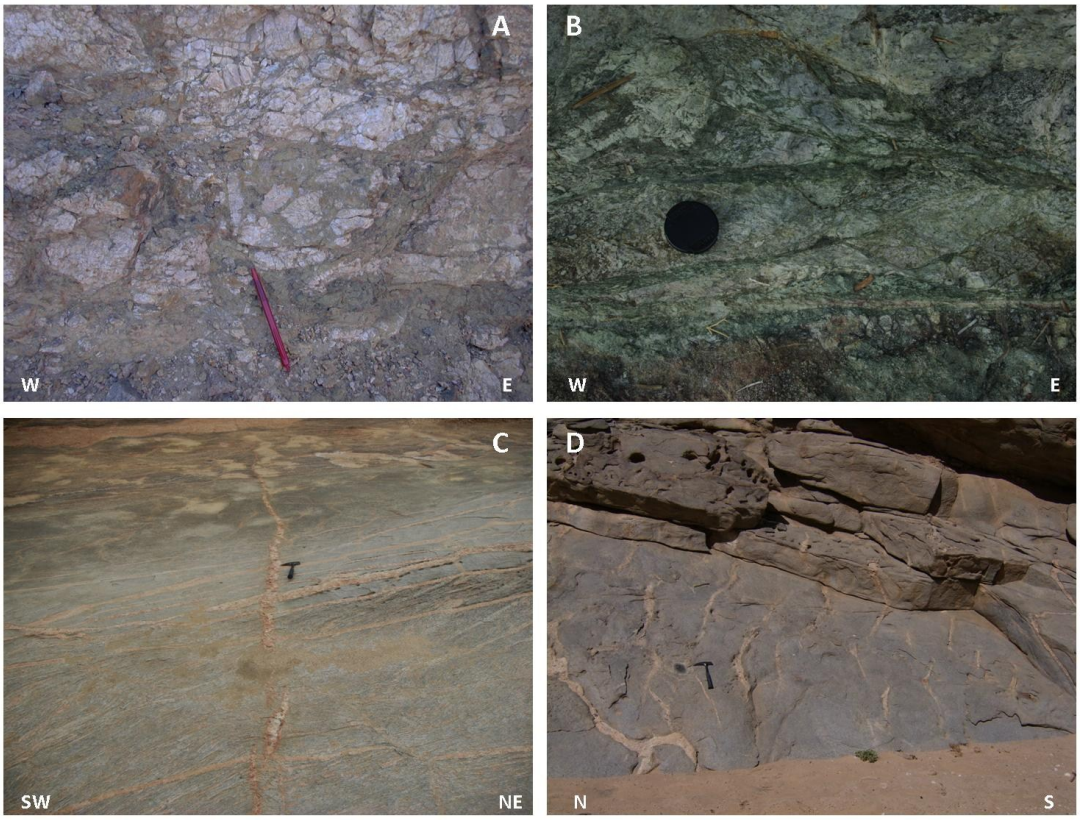

Fig. 3.26 – Brittle structures developed in the study area. A: Breccia along a fault plane near the northern margin of the Palmenhorst Dome (locality 499280/7504659). B: Small brittle fault near the northern margin of the Palmenhorst Dome (locality 499700/7503843). C: Brittle fracture intruded by pegmatitic granite, western margin of the Ida Dome (locality 050499/7488950). D: Tension gases in grey granite from the centre of the Ida Dome (locality 0500183/7488313).

3.8 Dome Formation and the Structural Evolution of the Southwestern Central Zone

The km-scale outcrop pattern in the study area is controlled by the interference between km-scale recumbent to shallow N- or NW-dipping folds (D2, although locally mesoscale F2 folds may be upright to S-dipping – section 3.6.3) and upright to steeply W to NW- dipping folds (D3). Although a bedding-parallel fabric and rootless isoclinal intrafolial folds may be preserved remnants of an earlier fabric-forming event (D1), and in some cases pre-Damaran fabrics are found (Section 3.2), it is the interference between these two folding events that has formed the basement-cored domes characteristic of the southwestern

Central Zone. D2 is the most intense deformation event affecting the lithologies in the study area, and most mesoscale structures in the study area were formed by this deformation event. D2 structures are the result of intense, SSE-verging, non-coaxial shearing, and in addition to km-scale tight to isoclinal folds (with associated m-scale parasitic folds), ductile shear zones, shear bands and a NE-SW mineral stretching lineation were formed during D2. In the Palmenhorst Dome, this deformation has resulted in isoclinal synclines of Damara Supergroup rocks within the Abbabis Complex. Orientations of principle stress directions during D2 can be calculated from the orientations of conjugate shear bands, and indicate a moderate to steep SE-plunging σ_1, a shallow to moderate W- to NW-plunging σ_2, and a shallow NE-plunging σ_3. The SE-plunging σ_1 is consistent with orientations of D2 folds, which are S- to SE-verging, and do not verge to the SW as previously suggested (Downing & Coward, 1981; Coward, 1983; Miller, 2008). In fact, it appears that mineral stretching lineations and extensional shear bands formed during essentially non-coaxial NE-SW extension, and that high-strain zones and extension may have occurred slightly later than D2 folding, as extension and shearing was concentrated on the extending long limbs of km-scale D2 folds. Intense D2 folding, shearing and extension was followed by a less intense D3 event that formed km-scale, gentle to tight upright, NE-plunging folds, which may locally verge towards the southeast or east-southeast in the east of the study area (the Ida Dome and Arcadia Zone). On the outcrop scale, D3 folds are very rare, and are m-scale and open to tight. Granite sheets have intruded along the axial planes of D2 folds and anatectic leucosomes are developed axial planar to D2 folds. D2 shear bands and high-strain zones also contain leucosomes and granite sheets, indicating that high-grade metamorphism and granitoid magmatism were coeval with D2. Along the eastern margin of the Ida Dome, D3 folds appear to have localised the emplacement of uraniferous granitoids in the cores of anticlinal structures.

The domal structures characteristic of the Central Zone appear to have been formed by the interference between km-scale D2 and D3 anticlines, and interference folding by two sequential events was the original mechanism proposed for the formation of these domes (Smith, 1965; Jacob *et al.*, 1983). However, a variety of other models have been suggested for the formation of these structures, including interference folding by a single phase of constrictional deformation (Poli, 1997; Poli & Oliver, 2001), metamorphic/extensional

core complex development (Oliver, 1994, 1995; Oliver & Kinnaird, 1996), diapirism of remobilised basement into Damara Supergroup cover rocks (Barnes, 1981; Barnes & Downing 1979), magmatic deformation by ballooning granites (Kröner, 1984), mega-scale sheath folding (Coward, 1981), and tip-line folds located above blind thrusts (Kisters *et al.*, 2004). Domes formed by tip-line folds above blind thrusts (Kisters *et al.*, 2004) are found further to the northeast, near Karibib, at shallower crustal levels than the study area, and are considered to be the effects of a different crustal response to Damaran collision at shallower levels than the high-grade mid-crustal rocks under consideration here. Models involving diapirism of remobilised basement into Damara Supergroup cover rocks (Barnes, 1981; Barnes & Downing 1979), or magmatic deformation by ballooning granites (Kröner, 1984) are inconsistent with observations of structures and field relationships both in the study area and elsewhere in the southwestern Central Zone. Diapiric rise of the Abbabis Complex into the Damaran metasedimentary succession would require a density contrast, and Damaran metasediments (quartzites, quartz-biotite schists, marbles, calc-silicates, metapelites) are not particularly more dense than the quartzofeldspathic Abbabis Complex basement. Additionally, the diapiric rise of this basement or of granitoids would be expected to produce radial flattening fabrics and tangential lineations around domal structures formed by this mechanism, and no such fabrics are found in the domes studied – rather, lineations are consistently NE- to ENE-trending intersection or mineral stretching lineations. Neither the Palmenhost nor Ida Domes have cores of granitoids – although granitoids are widespread, they occur as sheeted dykes, subparallel to the axial planes of folds, or as small (m- to Dm-scale) bodies and, thus, deformation by ballooning granites cannot be a mechanism for dome formation. Indeed, this would not explain the complex fold interference pattern apparent across the study area. The sheath-folding model for dome formation (Downing & Coward, 1981; Coward, 1983) was originally proposed to explain the NE-trending mineral stretching lineation and SE-verging folds and is, thus, consistent with the NE-SW extension lineation noted in the southwestern Central Zone (this study; Poli, 1997; Poli & Oliver, 2001; Kisters *et al.*, 2009). However, this model assumes that the extension lineation is related to intense SW-vergent non-coaxial deformation, and that the SE-verging folds noted by both Downing & Coward (1981) and Coward (1983) are parasitic to km-scale SW-verging sheath folds, and the parallelism

between hinge lines of D2 folds and the L2 stretching lineation is due to rotation of fold hinge lines into a south-westerly transport direction during simple shear (Coward, 1983). However, only SE-verging mesoscale folds were noted – no converse NW-verging folds are described by Downing & Coward (1981) or Coward (1983), and non-cylindrical sheath folds were noted to be SE-verging (Downing & Coward, 1981). This study has shown that any mesoscale sheath folds are related to intense S- to SE-verging non-coaxial folding and shearing in the southwestern Central Zone, and are localised in high-strain zones. The NE-SW extension that was coeval with this folding is largely coaxial. Thus, rather than explaining the parallelism of hinge lines and stretching lineations as due to sheath folding, this geometry is due to orogen-parallel stretching and extension coeval with orogen-perpendicular top-to-the-SE simple shear (Fig. 3.14B). A SW-verging sheath-folding model for the southwestern Central Zone does not account for the consistently south to southeasterly vergence of folds, or for the fold-interference pattern observed for the Central Zone and, hence, cannot be a viable model for dome formation. Oliver (1994; 1995) recognised that the subhorizontal to shallow-dipping NE-SW lineation in the Central Zone is consistent with an extensional tectonic setting, but also proposed a south-westerly vergence for deformation in the southwestern Central Zone, whereby domes were formed as part of a mid-crustal extensional core-complex during SW-vergent tectonic escape. The SW-vergence for shearing was based on the observation of W-dipping, SW-verging shear bands (Oliver, 1994), but it has been shown that these shear bands are part of a conjugate set, with steeply N-dipping, N-verging shear bands being the other set. The conjugate nature of the shear bands indicates that extensional deformation does not have an overall SW-vergence. Oliver (1995) explained the fold interference pattern of the southwestern Central Zone as due to the effect of simultaneous shortening in two directions, followed by the development of a major high-strain zone at the basement-cover contact during extension. This model of shortening in two directions followed by the development of a major detachment surface was further developed by Poli (1997) and Poli & Oliver (2001), who envisaged that shortening formed gentle domes that were then amplified by sub-vertical flow of thickened crust towards the southwest (Poli & Oliver, 2001). These models suggest that the fold interference patterns in the southwestern Central Zone are the result of simultaneous subhorizontal compression in

two directions, rather than sequential overprinting folding events, as had been previously suggested (Smith, 1965; Nash, 1971; Blaine, 1977; Barnes, 1981; Sawyer, 1981; Jacob *et al.*, 1983). However, it has been shown that earlier formed recumbent folds have been reoriented by later-formed upright folds (see sections 3.5 and 3.6), indicating that at least locally, D2 and D3 were sequential, and not simultaneous. Barnes (1981) noted large variability in the trend of D3 fold axial traces, and variations in D3 strains, and Poli (1997) noted that many of the domes in the southwestern Central Zone and their adjacent synclinal domains have 'convergence points' where fold hinges meet. These features are not common to typical fold interference models, where regular interference patterns are produced (Ramsay & Huber, 1987), but curvilinear fold hinge lines and convergence points are formed under general layer-parallel constriction (Ghosh *et al.*, 1995). Dating of the deformation events (D2 and D3) could resolve this issue – should these two events be separated by a geologically meaningful period of time, they would be distinct overprinting events, whereas if they are contemporaneous, the apparent fold interference pattern of the southwestern Central Zone would be the result of a single phase of constrictional deformation. The relationships between deformation, magmatism and metamorphism (see Figs. 3.8H, 3.10E, F, 3.12A, 3.17B, C, and 3.21 B, C) means that the timing of deformation may be constrained by dating of syn-deformational granitoids and leucosomes, and this is investigated in Chapter 5. The results of this dating indicate that S- to SE-verging folding occurred at *ca*. 520-515 Ma, and formed a progression with extensional deformation, which is slightly younger at *ca*. 510 Ma, Upright folding immediately postdates extension at *ca*. 508 Ma. These age constraints confirm that upright folding does postdate S- to SE-verging folding, and that these two events are not the result of a single phase of constriction.

The strain markers noted by Poli (1997) in the southwestern Central Zone record uniaxial prolate to general prolate strains, consistent with constriction, (which was the basis for his suggestion that the fold interference pattern apparent for the southwestern Central Zone may be the result of a single phase of constriction, rather than sequential events, separated by geologically meaningful periods of time) but one of the key findings was that NE-SW extension in the southwestern Central Zone was generally non-vergent (Poli,

1997). Poli (1997) found that strain markers indicated prolate irrotational strains throughout the southwestern Central Zone. This observation is key to the model for the geodynamics of the southwestern Central Zone (whereby domes were formed from a single phase of constrictional deformation) presented by Poli (1997) and Poli & Oliver (2001), which differs from the extensional core complex model of Oliver (1994, 1995) and the sheath folding model of Downing & Coward (1981) and Coward (1983) in that it does not assume a south-westerly vergence for deformation, but rather proposes that domes were formed during a single phase of deformation in a constrictional stress field with a moderately NE-plunging σ_3 stretching direction. In Poli's (1997) model, the development of extensional structures is due to the development of higher strains at or near the basement-cover contact during doming. In the present study it has been shown that extensional structures are not developed solely at or near the basement-cover contact, but that both shear bands and mineral stretching lineations are found throughout the Damaran metasedimentary succession and the Abbabis Complex. The reorientation of D2 structures by upright D3 structures is also inconsistent with a single phase of constrictional deformation, although the local reorientation of younger structures by later structures was considered by Poli (1997) to be the possible effect of local variations in the relative magnitude of strain and the relative importance of shortening directions. The model for dome formation as the product of a single phase of coaxial constrictional deformation (Poli, 1997; Poli & Oliver, 2001) also does not account for the strong southerly to south-easterly vergence of shallow-dipping folds and shear zones in the study area. Thus, an alternative model for the deformation and the formation of domes in the southwestern Central Zone must take into account the coaxial NE-SW D2 extension, the non-coaxial S- to SE-verging D2 folding, and the upright NE-trending D3 folding, which reorients D2 structures. The stress field orientation calculated from conjugate shear bands is consistent with the NE-trending mineral stretching lineation formed during NE-SW extension, and a component of SE-verging simple shear can explain SE-verging folding and shearing (Fig. 3.27A). During D2 deformation, the strain ellipse lies within the uniaxial prolate to general prolate field, where σ_1 and σ_2 are nearly equal, and σ_3 is subhorizontal to shallow NE-plunging (Fig. 3.27A). However, a small component of SE-verging non-coaxial strain results in the south- to southeastwards vergence of D2 folds. However, the

more upright D3 folding (which also appears to be more coaxial) suggests that, during D3 deformation, σ_1 was subhorizontal, whilst σ_3 was steeply dipping to subvertical (Fig. 3.27B). Such as switch in the orientations of the principal stress directions must be related to tectonic processes during collision. A steeply dipping σ_1 is likely related to a thickened crust – fold and thrust tectonics have been noted at shallower crustal levels in the Central Zone (Kisters *et al.*, 2004), and may record such crustal thickening. However, the timing of this crustal thickening relative to extension in the study area has not yet been evaluated. The switch from a steep σ_1 and largely recumbent folding during D2 to a shallow σ_1, a steep σ_3 and more upright folding during D3 is potentially related to the exhumation of the southwestern Central Zone during the latter stages of D2 deformation. However, the timing of D2 relative to D3 is crucial to an understanding of the change in deformation styles between these two events, and is crucial to understanding whether these two apparently structurally distinct events are temporally distinguishable. A record of crustal thickening, extension and uplift is likely to be preserved not only in the deformation history and changing stress orientations during collision, but the thermal effects of such a process may be recorded in the metamorphic history of the southwestern Central Zone. Indeed, a clockwise P-T-t path (i.e. crustal thickening, followed by heating and extension) has been suggested for the Central Zone (Nex *et al.*, 2001a). Evidence for the metamorphic effects of this P-T-t path is examined further in Chapter 6.

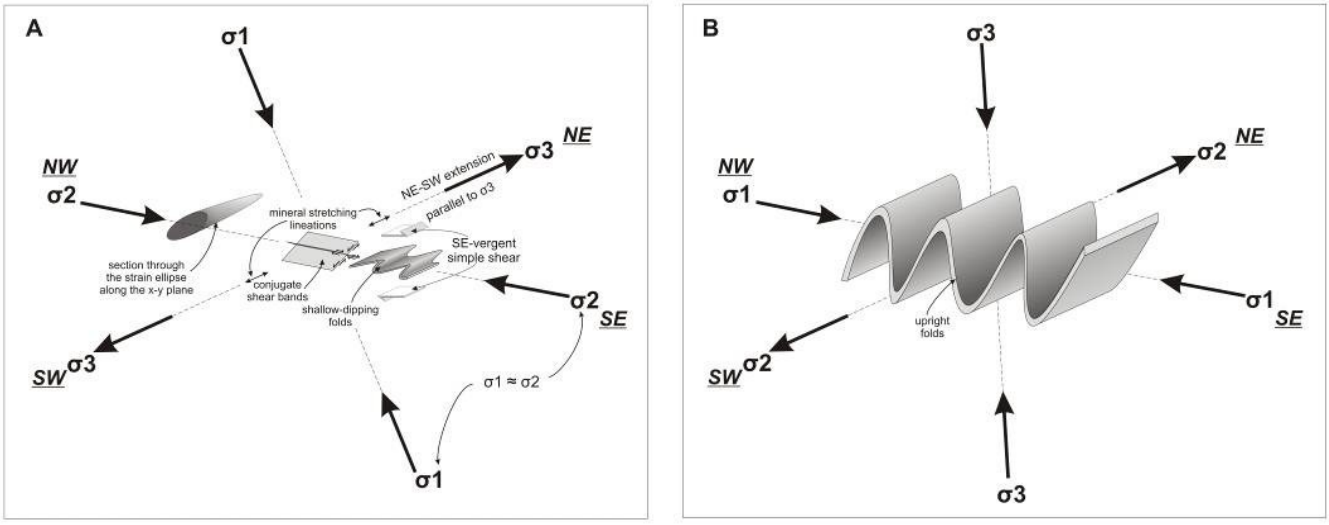

Fig. 3.27 – Structures formed in the southwestern Central Zone in relation to principal stress directions. A: Steeply-dipping σ_1 and subhorizontal σ_3 associated with recumbent to shallow-dipping folding and NE-SW extension during D2. B: Upright folding associated with a steep σ_3 and subhorizontal σ_1 during D3.

The question of the overall tectonic setting of the Central Zone is another issue that needs to be addressed, and must account for the largely coaxial nature of D2 extension, the vergence for D2 folding, and the switch in stress orientations during continued deformation. Whilst the Damara Belt is suggested to be a sinistral transpressional belt (Downing & Coward, 1981; Coward, 1983; Miller, 2008), transpressional orogens generally form flattening strains, whereas the stretching lineations measured for his study and by other workers (Poli, 1997; Kisters *et al.*, 2009) record generally prolate, constrictional strains, which are only developed in special cases in transpressive orogens (Dewey *et al.*, 1998). Constrictional strains are generally associated with transtensional tectonic environments, and the subhorizontal extension direction (subhorizontal σ_3) deduced from conjugate shear bands (see section 3.4.3) is consistent with subhorizontal extension. The widespread evidence for extension led Oliver (1994, 1995) to suggest an extensional core-complex model for the Central Zone. The fact that extension in the Central zone is orogen-parallel led Oliver (1994, 1995) and Kisters *et al.* (2004) to propose that the mid-crust underwent SW-vergent lateral extrusion and tectonic escape (coeval

with thrusting and crustal thickening at shallow-crustal levels – Kisters *et al.*, 2004). However, it has been shown from the conjugate sets of shear bands that extension in the southwestern Central Zone was not strongly vergent, but largely coaxial, consistent with the observations of Poli (1997) that prolate strain was largely irrotational. Additionally, lateral extrusion requires that the deformation zone stretch in the horizontal direction, lengthening relative to the relatively undeformed zone boundaries (Jones *et al.*, 1997). This creates a space problem for material being laterally extruded, and situations where lateral extrusion and escape are extremely rare and generally unlikely at the plate-boundary scale (Dewey *et al.*, 1998). In particular, tectonic escape to the southwest of material from the Central Zone would have been inhibited by the Rio de la Plata Craton to the west. It has been shown by Prave (1996), based on sedimentological and stratigraphic data from the Otavi and Mulden Groups, and on the timing of the onset of deposition the Otavi and Nama foreland basins, that the suturing of the Congo and Rio de la Plata cratons predated the suturing of the Congo and Kalahari cratons. Ages for subduction, collision and high-grade metamorphism in the Kaoko, Gariep and Damara belts show that peak metamorphism in the Kaoko Belt took place at 580-570 Ma, with transpressional reworking at 570-550 Ma (Goscombe *et al.*, 2005; Gray *et al.*, 2008). Closure of the southern Adamastor Ocean took place between 550 Ma and 540 Ma (Frimmel & Frank, 1998; Gray *et al.*, 2008) resulting in transpression in the Gariep Belt), whilst closure of the Khomas Sea and collision in the Damara Belt occurred at 530-520 Ma (Gray *et al.*, 2008). The closure of the Adamastor Ocean is considered to have taken place as a 'zipper effect', with the ocean closing progressively from north to south (Germs & Gresse, 1991). Thus, the Adamastor Ocean (between the Congo Craton and South America) was closed prior to closure of the Khomas Sea (between the Congo and Kalahari Cratons), and that the Congo and South American Cratons were unified prior to Damaran collision. This would mean that tectonic escape of material from the Central Zone to the southwest would be blocked by the Rio de la Plata Craton (Fig. 3.28).

Thus, material is unlikely to have escaped to the southwest during Damaran collision, and NE-SW extension appears to have been largely coaxial. Non-coaxial deformation in the form of folding and shearing was not orogen-parallel, like extension, but rather oblique to

perpendicular to the margins of the southern Central Zone (defined by the Omaruru and Okahandja lineaments), which run NE-SW. The vergence of folds in the study area is south to southeast, and similar SE-verging folds have been noted elsewhere (Downing & Coward, 1981; Sawyer, 1981), indicating roughly orogen-perpendicular top-to-the-SE non-coaxial deformation, although deformation may be S-verging and more oblique. Thus, a model for the southwestern Central Zone must explain orogen-parallel pure shear extension coeval with orogen-perpendicular recumbent folding and shearing. The subhorizontal to moderately NE-plunging extension direction and the constrictional strains recorded in the southwestern Central Zone suggest an overall transtensional setting, in contrast to the transpressional tectonic environment expected from oblique collision between the Congo and Kalahari cratons. It is thus possible that the D2 deformation in the study area is a feature of the post-collisional extensional collapse of the Damara Belt.

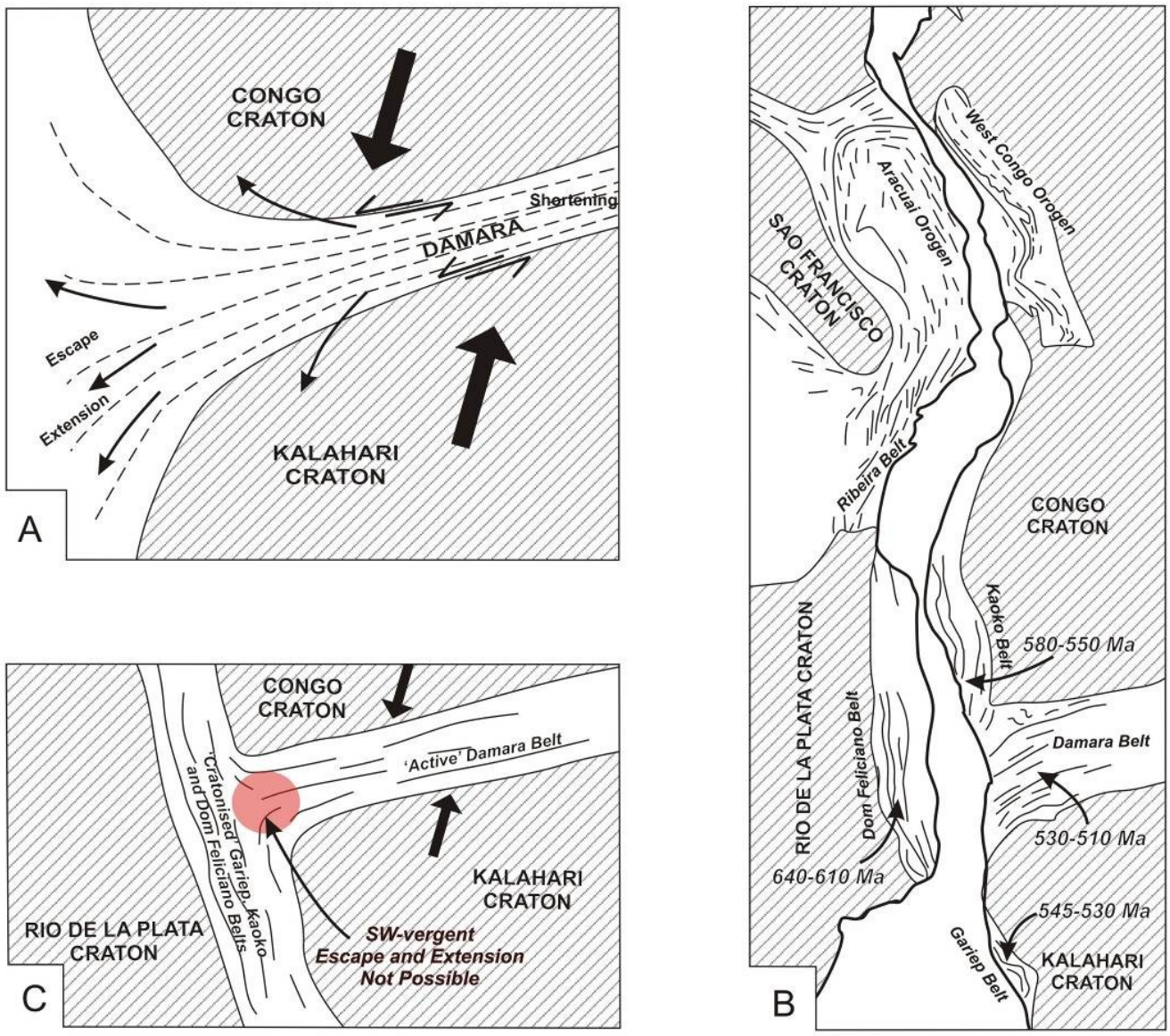

Fig. 3.28. – Problems with southwest directed tectonic extrusion in the Central Zone. A: Proposed escape an extrusion to the southwest, between the colliding Congo and Kalahari Cratons, with sinistral movement along the Central Zone (after Oliver, 1994). B: Timing of peak metamorphism and deformation (i.e. collision) in Pan-African orogens involving the Congo, Kalahari and Rio de la Plata Cratons. Note that closure of the Adamastor Ocean and collision in the Gariep, Kaoko and Dom Feliciano belts preceded closure of the Khomas Sea and Damaran collision (after Gray et al*., 2008). C: Schematic diagram showing that southwest directed escape from the Damara Belt would be impeded by the Rio de la Plata Craton, and by the cratonised Gariep, Kaoko and Dom Feliciano Belts.*

Constrictional strains may be developed in transpressional orogens where there is lateral stretch and vertical shortening (Dewey *et al.*, 1998), and Poli (1997) suggested that general constriction in a moderately plunging stress field could be accounted for by a Type-A (Fossen & Tikoff, 1998) transpressional scenario, where domes in the Central Zone were formed from extrusion of material to the southwest (Fig. 3.29A). However, such a scenario involves vertical extension, and Poli (1997) recognised that stretching directions were not subvertical, but plunged shallowly to moderately northeast, hence envisaged a modified Type-A (Fossen & Tikoff, 1998) scenario where the principal stress axes are slightly shifted, leading to the plunging domes in the Central Zone (Fig. 3.29B). Poli (1997) noted lineations that were somewhat moderately NE- to ENE-plunging (mean vectors of plunges up to 55˚), and whilst some of these may be intersection lineations (see section 3.4.3), similar steep (average 60˚) NE-plunging mineral stretching lineations were noted by Kisters *et al.* (2009). In contrast, the σ_3 direction obtained from conjugate shear bands (this study) plunges very shallowly to the northeast, and extension may well be near-horizontal and orogen-parallel, rather than in the steeply dipping or subvertical, as implied in the Type-A model for transpression. Furthermore, Poli (1997) did not take into account any non-coaxial strain in his model for dome formation. He recognised the irrotational strains associated with NE-SW extension (and confirmed by the conjugate set of shear bands develeloped during this extension), but did not note any strike-slip shear zones to account for non-coaxial strike-slip movement. No such strike-slip zones are found in this study, and major crustal lineaments in the Central Zone may have taken up this strain. However, the southerly or southeasterly vergence of folds and some shear zones noted in this study are not accounted for in the model of Poli (1997), and in this regard, his model of purely constrictional deformation is insufficient to account for the deformation in the southwestern Central Zone. Thus, an alternative to the Type-A model of Fossen & Tikoff (1998) is required. If we assume for the time being that the σ_3 orientation is subhorizontal (as suggested by the conjugate shear bands) rather than steeply dipping, and that σ_1 and σ_2 are near equivalent (as suggested by the prolate strain markers of Poli, 1997), then such a situation can only occur in a transpressional zone where significant vertical shortening (i.e. crustal thickening) has taken place. Such a scenario is similar to a Type-E (Fossen & Tikoff, 1998) model where the coaxial

component causes a vertical shortening of equal magnitude to the shear-zone normal shortening, compensated by stretching in the x direction (Fossen & Tikoff, 1998). However, a critical difference is that in the Type-E model of Fossen & Tikoff (1998), non-coaxial deformation is accommodated by strike-slip movement with a subvertical shear plane, whereas recumbent to shallow-dipping D2 folds and shear zones indicate that the plane of non-coaxial deformation is subhorizontal (Fig. 3.29C). This is more analogous to a Type-A scenario where the *z* direction is horizontal and the x direction is vertical. Even with a moderately-plunging σ_3 (Fig. 3.29D), as envisaged by Poli (1997), and closer to a Type-A (Fossen & Tikoff, 1998) scenario, non-coaxial deformation remains largely shallow-dipping. The basic definitions of transpression or transtension do not take into account such a scenario, as they are defined as 'strike-slip deformations that deviate from simple shear because of a component of shortening (transpression) or extension (transtension) orthogonal to the deformation zone' (Dewey *et al.*, 1998). The strike-slip nature of deformation is implicit in the definition, and whilst strike-slip deformation has been documented in major shear zones within and adjacent to the Central Zone (Blaine, 1977; Kasch, 1978; Downing & Coward, 1981; Kukla, 1992) all strike-slip movement appears to have been taken up in these zones, and is not partitioned into the high-grade rocks of the Central Zone. The vergence of recumbent structures indicates that neither regular transpression nor transtension can account for the deformation in the southwestern Central Zone.

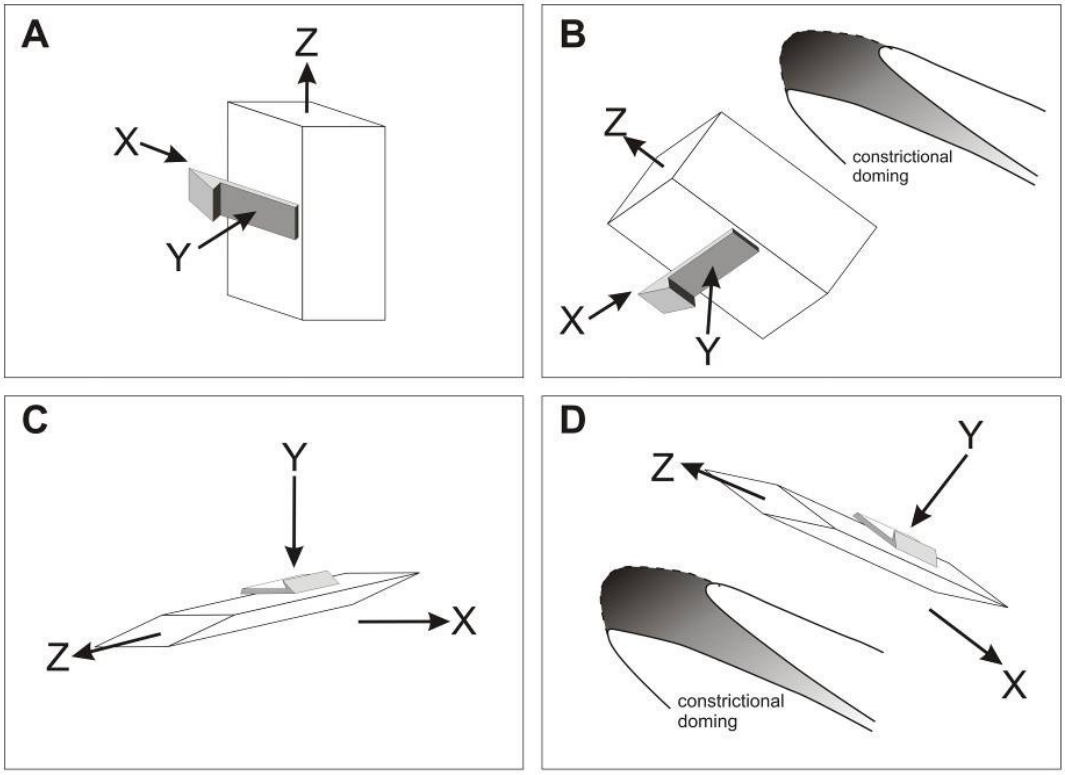

Fig. 3.29 – Possible transtensional models for the southwestern Central Zone. A: Type-A transpressional model with subvertical extension (after Fossen & Tikoff, 1998). B: Type-A model modified by Poli (1997) to explain plunging stretching lineations. C: The suggested model for deformation in the southwestern Central Zone – note the similarity between this and a Type-A scenario, with the orientations of the axes shifted. D: Variation of the model shown in C, with the axes shifted to account for plunging lineations.

A possible explanation for the geometry of structures in the southwestern Central Zone may be that this area records extensional collapse of the orogen. Rather than SW-verging tectonic escape (which is unlikely, as discussed above), the southwestern Central Zone may have experienced orogen-parallel stretching coeval with orogen-perpendicular folding. The generally recumbent nature of D2 deformation is consistent with an extensional tectonic setting, and the steeply-dipping σ_1 stress direction suggests that the crust must have been significantly thickened prior to D2 extension. Orogenic belts with thickened crusts may have high regional elevations, weaker lithospheres and lower vertically integrated shear strengths than adjacent continental shields, and are preferential sites for extension (Dewey, 1988). Apart from suggestions of SW-vergent

tectonic escape (Oliver, 1994, 1995; Kisters *et al.*, 2005), no mention has previously been made of any evidence for orogenic collapse in the Central Zone (Miller, 2008), despite metamorphic evidence for clockwise P-T-t paths (Buhn *et al.*, 1995; Jung, 2000; Nex *et al.*, 2001), implying crustal thickening, high-grade metamorphism and exhumation of the mid-crust during the life of the orogen. Whilst Barnes & Sawyer (1980) suggested up to 10 km of uplift of the Southern Zone relative to the Central Zone following collision, Miller (1979) argued that juxtaposed stratigraphic levels between the Central and Southern Zones indicate approximately 24 km of uplift of the Central Zone during D3. The hot, uplifted crust of the Central Zone was likely to be gravitationally unstable, resulting in outward collapse of the orogen. The gravitational emplacement of nappes in the Southern Margin Zone (Korn & Martin, 1959; Pfurr *et al.*, 1987) possibly represents a record of the gravitational collapse of the uplifted orogen (Fig. 3.30). The Naukluft Nappe Complex was emplaced towards the SE over a distance of at least 78km (Hartnady, 1978), and such a direction for vergence is similar to recumbent, SE-verging folding and shearing at mid-crustal levels in the southwestern Central Zone. The isostatic rebound of the southern Central Zone, Southern Zone and Southern Margin Zone is suggested to have occurred at 515-510 Ma (Miller, 2008) and the gravitational emplacement of the Naukluft Nappe Complex is suggested to have occurred at 495 Ma (Miller, 2008). However, Kisters *et al.* (2004) considered thrusting at shallow crustal levels in the Central Zone to be coeval with mid-crustal NE-SW extension in the southwestern Central Zone, at 560-540 Ma (the ages for syntectonic mafic to granitic magmatism), significantly older than the suggested ages for the south-eastwards emplacement of nappes in the Southern Margin Zone.

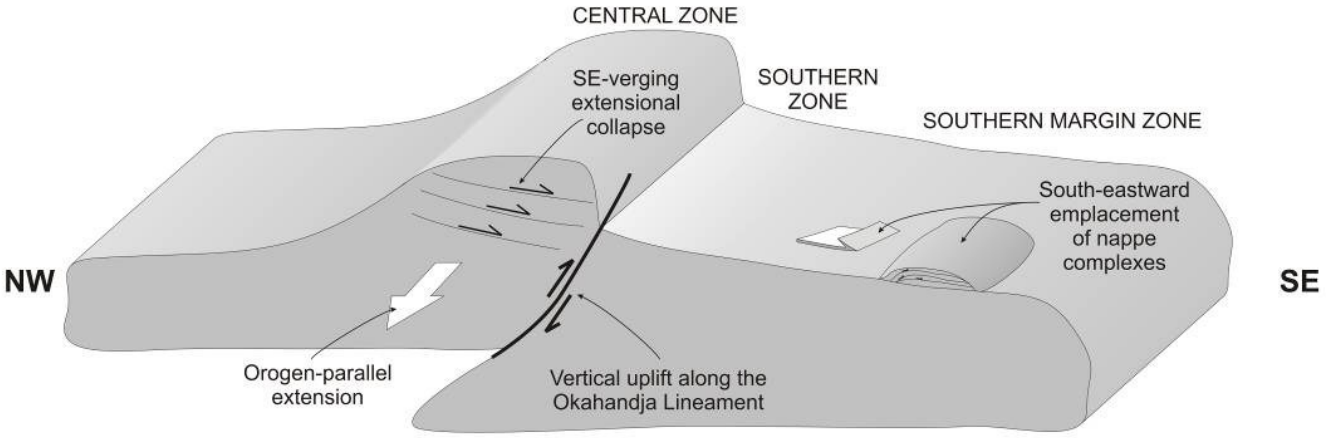

Fig. 3.30 – A possible model of gravitational collapse of uplifted, thickened crust to explain extension and SE-verging structures in the southwestern Central Zone, and the relationship to south-eastwards nappe emplacement in the Southern Margin Zone.

A viable model to explain the evolution of the southwestern Central Zone should take into account the evolution of the orogen as a whole, and processes in the other zones of the Damara Orogen. In order to do this, detailed knowledge of the temporal evolution of the Central Zone is required in order to constrain both the timing of deformation events (and whether they are discrete deformation pulses, or part of a continuum of constrictional deformation), as well as the timing of events in the Central Zone relative to processes in other zones. Whilst orogenic collapse as a possible model for the development of the southwestern Central Zone implies crustal thickening prior to extensional collapse, evidence for crustal thickening from the metamorphic history is also required. In the following chapters, the granitoids present in the study area are described, with an emphasis on their relationships to deformation, and the results of dating of these structurally constrained granitoids (in order to constrain the timing of deformation) are presented in Chapter 5. The metamorphic evolution of the study area is investigated in Chapter 6, and related to deformation. A detailed understanding of the structural and metamorphic evolution of the southwestern Central Zone and constraints on the ages for deformation and metamorphism are required before a geodynamic model can be constructed.

CHAPTER 4 – INTRUSIVE ROCKS

The Central Zone contains a high proportion of intrusive rocks of various ages, including a variety of mafic to leucogranitic intrusions that were emplaced during the Pan-African collisional event, and large areas of felsic gneisses and amphibolites which make up the pre-Damaran basement. The large volume of granitoids is a characteristic feature of this tectonometamorphic belt, as are km-scale domes cored by Mesoproterozoic (Kröner *et al*., 1991) to Neoproterozoic (Jacob *et al*., 1978) gneisses. Amphibolite dykes are found emplaced into the Damara Supergroup, and are not exclusively found within these basement gneisses, as previously suggested (Barnes, 1981), and it is unclear whether the amphibolites in the basement differ in age from those in the Damaran cover. The pre-, syn- or post-tectonic nature of intrusions and any relationships with metamorphism in the Central Zone are crucial in constraining the timing of deformation and metamorphism through dating of these intrusions. The relationships between intrusive rocks and pre-Damaran gneisses are also crucial in understanding the sources of the various intrusions, as are any possible relationships between Damaran-age intrusions. The geochemical and petrogenetic relationships of the various intrusions, and their structural relationships, are important for the understanding of the overall tectonic context and evolution of the orogen. Miller (2008) includes 17 intrusive rock types in his classification of the intrusive rocks of the Central Zone (Table 4.1). Many of the intrusions classified by Miller (2008) are late, post-tectonic granitoids, and are restricted to the northern Central Zone (Table 4.1), but there is a temporal evolution of intrusive rocks in the southern Central Zone, ranging in age from early (*ca*. 560 Ma) mafic to dioritic magmas through to late (*ca*. 508 Ma) post-tectonic alaskites and leucogranites. In addition to the classification of Miller (2008), granitoid intrusions in the Central Zone have been geochemically classified (McDermott, 1986), and smaller subdivisions exist within these major granite types (e.g. Nex & Kinnaird, 1995). The granitoid types defined by Miller (2008) that fall in the southern Central Zone (and, hence, which might be found in the study area) include red gneissic granite, metagabbro, diorite, Salem-type granite, uraniferous alaskite, post-tectonic red homogenous granite, post-

tectonic red, pink to grey leucogranite, and Donkerhuk granite. Additionally, amphibolite dykes found in the Abbabis Complex, which may be pre-Damaran (Steven, 1994), are discussed in this chapter.

Table 4.1 – Classification of granitoids from the Central Zone (after Miller, 2008).

Age (Ma)	Granite
	Pegmatite, syn- to post-tectonic
	Biotite granite, fine-grained, post-tectonic, nCZ
460-480	Leucogranite, syn- to post-D3, nCZ
460-480	Salem-type granite, syn-D3, nCZ
480?	Diorite, syn-D3, nCZ
514?	Leucogranite, syn-D2, nCZ
514?	Migmatised leucogranite, syn-D2, nCZ
527	Donkerhuk Granite, southern edge of the sCZ
	Post-tectonic I-type, mainly at the southern edge of the sCZ
534-539	Red, pink to grey leucogranite, post-tectonic
516?-543	Red homogeneous granite, post-tectonic
542-508	Uraniferous alaskite, sCZ only
550	Salem-type granite in antiforms
550	Salem-type granite in synforms, pre-to syn-D2
565-540	Diorite, mainly in synforms, pre- to syn-D2, sCZ
	Differentiated metagabbro, hornblendite
	Red gneissic granite, only in anticlines

nCZ = northern Central Zone; sCZ = southern Central Zone

The classification of granite types shown in Table 4.1 is based on studies by a number of workers (Smith 1965; Jacob; 1974; Marlow; 1981; Brandt, 1985; Nex, 1997). There are some small differences in the various classification criteria used by these workers, but overall the major granite types described by these various workers are similar. In contrast, McDermott (1986) proposed a three-fold classification for Damaran intrusions based on chemical characteristics, and used these characteristics to identify specific petrogenetic processes for each granite type. Although he proposed abandoning terms such as ‘red granites’ and ‘Salem-type granites’, these terms are still widely used for granites of the Central Zone. In this chapter, granites are described based on mineralogy, macrotextural characteristics, cross-cutting field relationships and structural context, and their classification is discussed with regard

to previous classification schemes. The chemistry of the granites is also examined, and compared to the classification scheme of McDermott (1986). However, the purpose of this chapter is not simply to characterise granitoids in a portion of the Central Zone, but to understand the relationship of the intrusions to the overall tectonometamorphic evolution of the Central Zone, with the aim of using the intrusions as a means to constrain the timing of deformation and metamorphism through precise dating of these intrusive rocks (presented in Chapter 5). In this regard the field relationships of the granites relative to deformation and metamorphism are crucial. Intrusive rock types found in the study area are: amphibolites, red granites, grey granites, quartz-feldspar-magnetite pegmatitic granites, garnet (±cordierite)-bearing leucogranites, uraniferous leucogranites and pink pegmatitic leucogranites. Important questions relating to these intrusions are:

- What is the timing of the intrusions relative to one another?
- What is the timing of the intrusions relative to the structural evolution described in Chapter 3?
- Is the emplacement of the intrusions controlled by any structures?
- Are any of the intrusive rocks stratigraphically localised?
- What is the timing of the intrusions relative to metamorphism?
- What is the source of the intrusions?

In order to answer questions regarding the sources of intrusions, and in order to facilitate characterisation of the various intrusive rock types found in the study area, petrographic and geochemical studies have been carried out on these various rock types. This also enables comparison of the various intrusive rocks characterised in the study with intrusions elsewhere in the Central Zone that have been studied by previous workers. Whole-rock X-ray fluorescence (XRF) analyses have been carried out in order to determine major and trace element concentrations, and inductively coupled plasma mass

spectrometry (ICP-MS) has been used for the determination of selected trace elements. XRF data are contained in Appendix 1A, ICP-MS data are contained in Appendix 1B, and details of analytical techniques and procedures are contained in Appendix 1C.

4.1 Amphibolites

In both the Ida and Palmenhorst Domes, there are numerous ortho-amphibolite dykes cross-cutting the rocks of the Abbabis Complex (Fig. 4.1A), and similar amphibolites have also been found in the Abbabis Inlier (Steven, 1994). Amphibolites are less well documented than the various granitoids in the Central Zone. They have been considered by many workers as part of the pre-Damaran geology in the Central Zone (Smith, 1965; Marlow, 1981; Brandt, 1987), and have even been used as a defining characteristic of the Abbabis Complex (Barnes, 1981). However, Jacob (1974) noted amphibolites intruding Damaran lithologies, and there have been ortho-amphibolite dykes noted from the Rössing Mine, intruding Damaran metasediments (P. Nex, Pers. Comm., 2009). Metagabbro and hornblendite are also commonly found associated with the diorites of the Goas Intrusive Suite, and it is possible that amphibolites are related to these basic rocks, which have been interpreted as the earliest phase of a Damaran, calc-alkaline active margin plutonic suite (Miller, 2008).

Amphibolites are dark green-black, and intrude as dykes that vary in width from decimetres up to a few metres. They usually cross-cut the pre-Damaran fabric preserved in these basement rocks (Fig. 4.1A) although they are commonly deformed into parallelism with the regional fabric during Damaran deformation, and for some intensely deformed amphibolites (Fig. 4.1B) their original intrusion geometry is unclear. Where Damaran deformation is less intense, they are typically folded into open to tight m- to Dm-scale folds, attributed to D2 deformation (Fig. 3.8F).

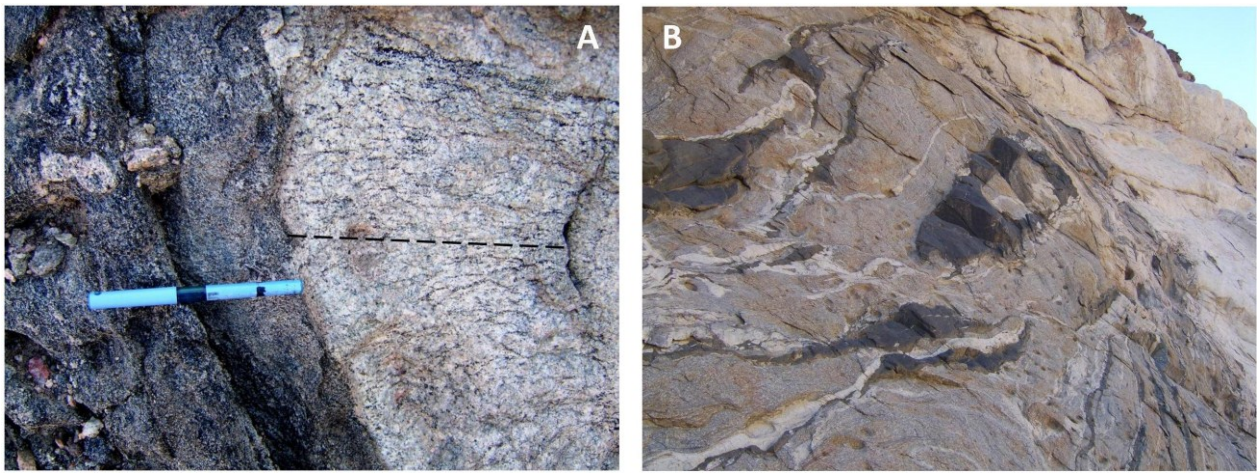

Fig. 4.1 – Field photographs of amphibolites from the study area. A: Amphibolite dyke in quartzofeldspathic basement gneisses along the Khan River (locality 0496468/7501731). Note that the contact of the amphibolites is oblique to the fabric in the gneiss (indicated by dashed line). Since the amphibolite truncates the gneissic fabric, it must postdate fabric development. B: Highly deformed amphibolite dykes in basement gneisses east of the Ida Dome and Arcadia Zone (locality 0503994/7482006). Amphibolites are subparallel to the S2 fabric in the gneisses, and are cut by leucogranites, seen at the top right of the photograph. Note geological hammer for scale near the amphibolite in the centre of the image.

The amphibolites comprise predominantly dark green to tan hornblende and white plagioclase feldspar, with minor ilmenite and accessory quartz, titanite, apatite, and K-feldspar, and variable amounts of biotite (Fig. 4.2). The hornblende and plagioclase are generally 0.5 mm to 1 mm in size, as is the biotite where it is present in significant amounts (*ca.* 10%), and the ilmenite is typically finer grained (*ca*. 0.25 mm) (Fig. 4.2A). The hornblende is generally stubby to elongate (Fig. 4.2B), subhedral to anhedral, and apatite occurs as fine needles in quartz or plagioclase (Fig. 4.2C). The amphibolites contain a moderate fabric, defined by alignment of hornblende, or elongate laths of subhedral to euhedral biotite (Fig. 4.2D). This fabric is commonly defined by banding of hornblende-rich layers on a sub-mm scale. The amphibolites are slightly altered; biotite (and locally hornblende) may be altered to chlorite; feldspars may be sericitised (Fig. 4.2B).

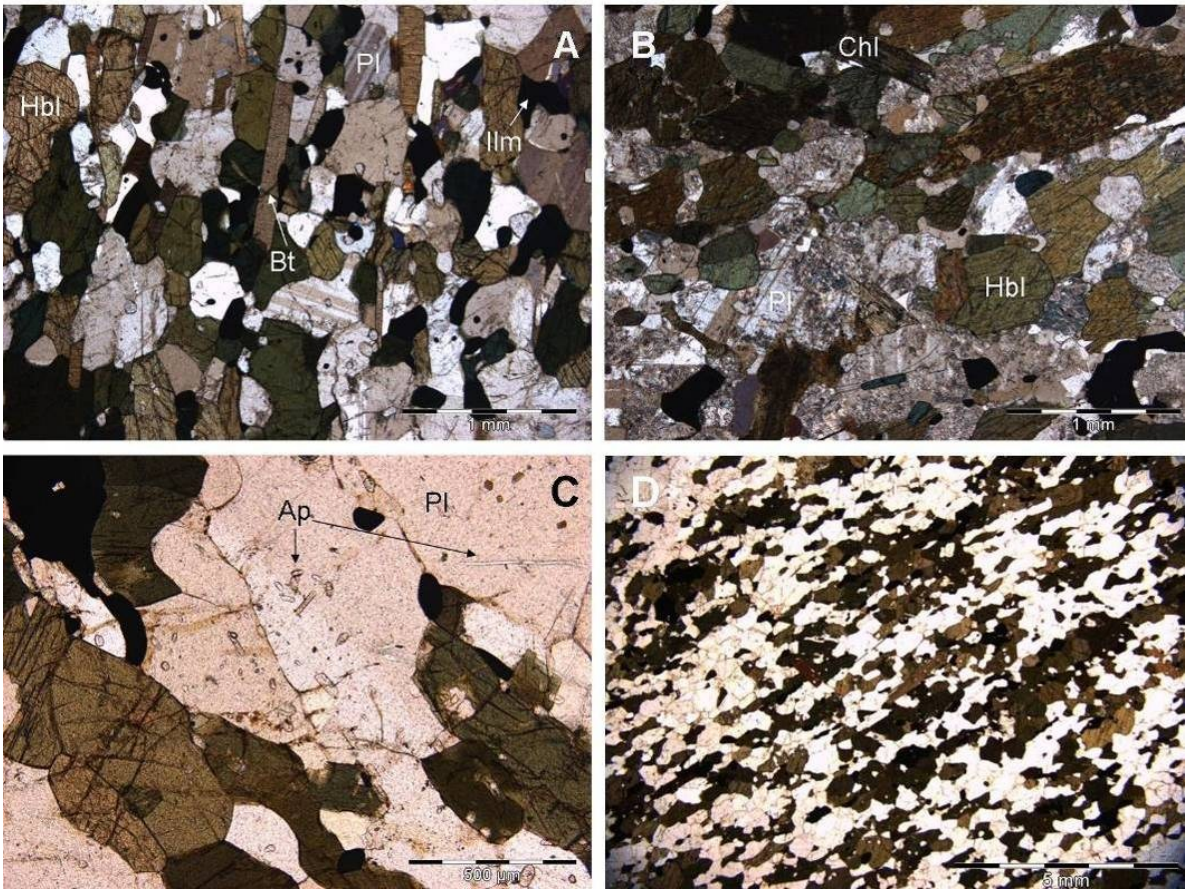

Fig. 4.2 – Photomicrographs of amphibolites from the study area. A: Typical unaltered amphibolite containing stubby, anhedral hornblende, anhedral plagioclase, euhedral to subhedral biotite laths, opaque minerals (ilmenite) and tiny apatite crystals (sample CZAM2, locality 0496481/7501723, XPL). B: Alteration of amphibolite, with saussuritised plagioclase, and chloritised biotite (sample CZAM1, locality 0494493/7499069, XPL). C: Small (<100 µm) apatite crystals within a larger plagioclase crystal (PPL). D: Fabric in an amphibolite, defined by elongate grains of hornblende and biotite, and hornblende-rich bands (sample CZAM3, locality 0503961/7484481, PPL). Mineral abbreviations are after Kretz (1983).

Geochemically, the amphibolites are classified as basalts on a total-alkali-silica (TAS) diagram, with a single lower-SiO_2 sample falling into the tephrite field (Fig. 4.3A). No previous chemical data for amphibolite dykes in the Central Zone have been published, but data exists for basalts found in the Abbabis Complex (Marlow, 1981), as well as for mafic xenoliths in the Okongava Diorite (De Kock, 1991). These form part of the 560-540 Ma Goas Intrusive Suite (Miller, 2008), found *ca*. 100 km

northeast of the study area. Hence, data from amphibolites are compared to these groups of rocks. Samples fall in both the alkaline and tholeiitic fields of the TAS diagram defined by MacDonald (1968) (Fig. 4.3A), and are similar to the Goas Suite metagabbros and hornblendites, whilst the basalts from the Abbabis Complex are more tholeiitic. On an AFM diagram, the amphibolites are generally tholeiitic, rather than calc-alkaline (Fig. 4.3B), and less magnesian than many of the basalts (Marlow, 1981) or Goas Suite metamafics (De Kock, 1991). However, there is little distinction between Abbabis Complex basalts, Goas Suite metamafics and amphibolite dykes from this study on an AFM diagram. On a K_2O vs. SiO_2 diagram, basalts from the Abbabis Complex are low-K tholeiites (Marlow, 1981), whereas the amphibolites have much higher K_2O, falling into the medium-K or high-K calc-alkaline series (Fig. 4.3C). They appear similar to the metagabbros and hornblendites analysed by De Kock (1991), and both the rocks analysed in this study and those from De Kock (1991) are distinct from the basalts analysed by Marlow (1981). This suggests a possible relationship between mafic dykes in the Abbabis Complex and mafic rocks of the Goas Intrusive Suite, and such a relationship would be consistent with the fact that amphibolite dykes commonly show cross-cutting relationships to the gneissic fabric in the Abbabis Complex (Fig. 4.1). When plotted on a Zr/Y-Zr diagram (Pearce & Norry, 1979), both Abbabis Complex basalts (Marlow, 1981) and amphibolites plot in a number of fields, although most samples plot as “within-plate basalts” (Fig. 4.3D), and are distinct from the Goas Suite metamafics (De Kock, 1991), which plot as island arc basalts. Additionally, both basalts and amphibolites generally plot as continental arc basalts rather than oceanic arc basalts (i.e. above the line of Zr/Y = 3; Pearce, 1983), and are thus discriminated from the Goas Suite metamafics. Zr is more incompatible than Y and will thus fractionate more into continental crust, thus basaltic magmas generated at continental margins may be contaminated, and have higher Zr/Y. When attempting to discriminate the amphibolites, basalts and metamafics as island-arc tholeiites, calc-alkaline basalts or within-plate basalts on a Ti-Zr-Y discrimination diagram (Fig. 4.3E), basalts from the Abbabis Complex are calc-alkaline, metagabbros and hornblendites of the Goas Intrusive Suite are island-arc tholeiites, whilst amphibolites from this study are within-plate basalts. Similar results are apparent

from a Zr-Ti discrimination diagram (Fig. 4.3F) - metagabbros and hornblendites are island-arc tholeiites and basalts from the Abbabis Complex are calc-alkaline, but amphibolites from this study fall closest to the mid-ocean ridge basalt (MORB) field. REE patterns show moderate LREE enrichment, with La/Lu between 1.95 and 8.50. No Eu anomalies are seen (Fig. 4.3G). A spidergram shows that amphibolites have a closer affinity with oceanic island basalts (OIBs) than with MORBs (Fig. 4.3H).

Thus, whilst major element data do suggest a possible relationship between the amphibolites from this study and the mafic rocks of the Goas Intrusive Suite, trace element data show no clear relationship between the amphibolites in the Abbabis Complex and either the Goas Suite mafic rocks (which may be related to arc-magmatism overlying a subduction zone – De Kock, 1991), or the Abbabis Complex basalts (which are calc-alkaline – Marlow, 1981), and discrimination diagrams are inconclusive in determining the tectonic setting of the amphibolites.

Fig. 4.3 (following page) – Geochemical diagrams for the amphibolites from the study area, basalts from the Abbabis Complex (Marlow, 1981) and meta-mafic rocks from the Goas Intrusive Suite (De Kock, 1989). A: TAS diagram, showing that amphibolites plot as basalts, bordering the alkaline/tholeiitic fields defined by MacDonald (1968). B: AFM diagram, showing that most samples fall into the tholeiitic field defined by Kuno (1968), and all samples are tholeiitic according to the classification of Irvine & Baragar (1971). C: K_2O vs. SiO_2 plot, showing that amphibolites are medium- to high-K. D: Zr/Y vs. Zr plot (after Pearce & Norry, 1979; Pearce, 1983), showing that most samples plot in the continental arc field of Pearce (1983) (Zr/Y > 3), and in the "within-plate basalt" field of Pierce & Norry (1979). Fields labeled are island-arc tholeiites (A), MORB basalts, island-arc tholeiites and calc-alkali basalts (B), calc-alkali basalts (C) and within-plate basalts (D). E: Ti-Zr-Y discrimination diagram (after Pearce & Cann, 1973), showing that most amphibolites plot in the within-plate basalt field. F: Ti-Zr variation diagram (after Pierce & Cann, 1973), showing that most amphibolites plot outside any of the fields, or within the MORB field. Fields labeled are for island-arc tholeiites (A), MORB, calc-alkali basalts and island-arc basalts (B), calc-alkali-basalt (C) and MORB (D). G: Chondrite-normalised REE plot, showing slight LREE enrichment and no Eu anomaly. H: Chondrite-normalised spidergram, showing amphibolites, and averages for OIBs and MORBs (from Saunders & Tarney, 1984; Sun, 1980). Chondrite normalisation factors are from Anders & Grevesse (1989). Geochemical data and analytical methods are presented in Appendix 1. Diagrams A through F compare with data from basalts in the Abbabis Complex, analysed by Marlow (1981), and with metagabbros and hornblendites analysed by De Kock (1991).

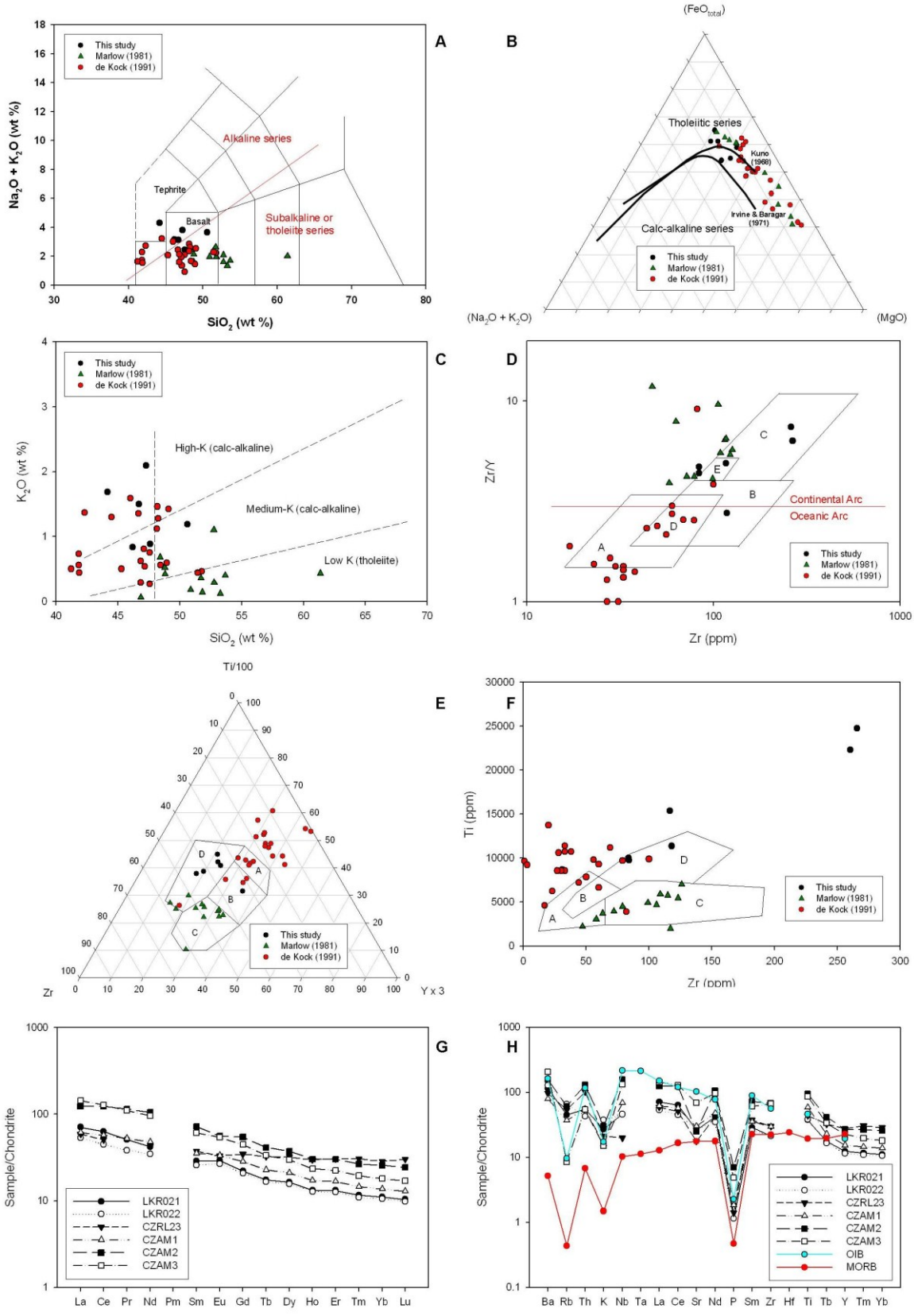
A
This study
Marlow (1981)
de Kock (1991)
Alkaline series
Tephrite
Basalt
Subalkaline or tholeiite series
Na2O + K2O (wt %)
SiO2 (wt %)
B
(FeOtotal)
Tholeiitic series
Kuno (1968)
Irvine & Baragar (1971)
Calc-alkaline series
(Na2O + K2O)
(MgO)
C
High-K (calc-alkaline)
Medium-K (calc-alkaline)
Low K (tholeiite)
K2O (wt %)
SiO2 (wt %)
D
Zr/Y
Continental Arc
Oceanic Arc
Zr (ppm)
E
Ti/100
Zr
Y x 3
F
Ti (ppm)
Zr (ppm)
G
Sample/Chondrite
LKR021
LKR022
CZRL23
CZAM1
CZAM2
CZAM3
La Ce Pr Nd Pm Sm Eu Gd Tb Dy Ho Er Tm Yb Lu
H
Sample/Chondrite
OIB
MORB
Ba Rb Th K Nb Ta La Ce Sr Nd P Sm Zr Hf Ti Tb Y Tm Yb

The amphibolites may represent an early phase of mafic magmatism prior to the onset of collision in the Damara belt. The fact that amphibolites post-date the fabric in the Abbabis Complex gneisses also suggests that they may be Damaran in age, but such a link is tenuous, and U-Pb dating of these amphibolites is needed to give a more conclusive result (see Chapter 5). Additionally, since these amphibolites contain a fabric of aligned biotite and hornblende, which is subparallel to the D2 fabric in the study area, metamorphism of the precursor mafic dykes to form these amphibolites may have taken place during D2 deformation, and U-Pb dating of zircon overgrowths may constrain the timing of metamorphism (see Chapter 5).

4.2 Red Granites

In the study area, the oldest recognised granitoids (based on field relationships) are the red granites. These red granites are found within the study area only near the northern margin of the Palmenhorst Dome, but also occur to the west of the Palmenhorst Dome where they form a large body. Along the northern margin of the Palmenhorst Dome, they occur in an E-W striking belt near to the contact between the Etusis Formation and the Abbabis Complex, in the vicinity of a number of tight km-scale folds of Damara Supergroup rocks (see Fig. 3.9). They are deep red in colour (Fig. 4.4), and contain a gneissic fabric, which is moderately N-dipping (Fig. 4.4A), and approximately parallel to the regional strike and D2 fabric in the adjacent Damaran metasediments (Fig.4.4A). The gneissic fabric in the red granites is cut by late-D2 shear bands, indicating that these granites predate D2. No cross-cutting relationships with any other granite types are observed, but the strong gneissic fabric, not developed in any of the other granitoids, suggests that the red granites are the oldest Damaran granitoid in the study area. In places, quartzofeldspathic xenoliths are found (likely derived from the Abbabis Complex or Etusis Formation) that contain aligned sillimanite knots (Fig. 4.4B) and define a fabric oblique, or even perpendicular, to the gneissic fabric in the granite, suggesting that the gneissic fabric is not inherited from the host rock, but that it is, rather, a syn-D2 tectonic fabric. Elsewhere, sillimanite knots and seams are found within the granites. These range in size from 5 mm to 5 cm, do not display any obvious relation to visible xenoliths (Fig. 4.4C), and contain

fine, fibrolitic sillimanite. Locally, 1-3 cm blue cordierite grains are also found in the red granites, indicating an aluminous composition, and suggesting derivation from or assimilation of metasedimentary material (Fig.4.4D).

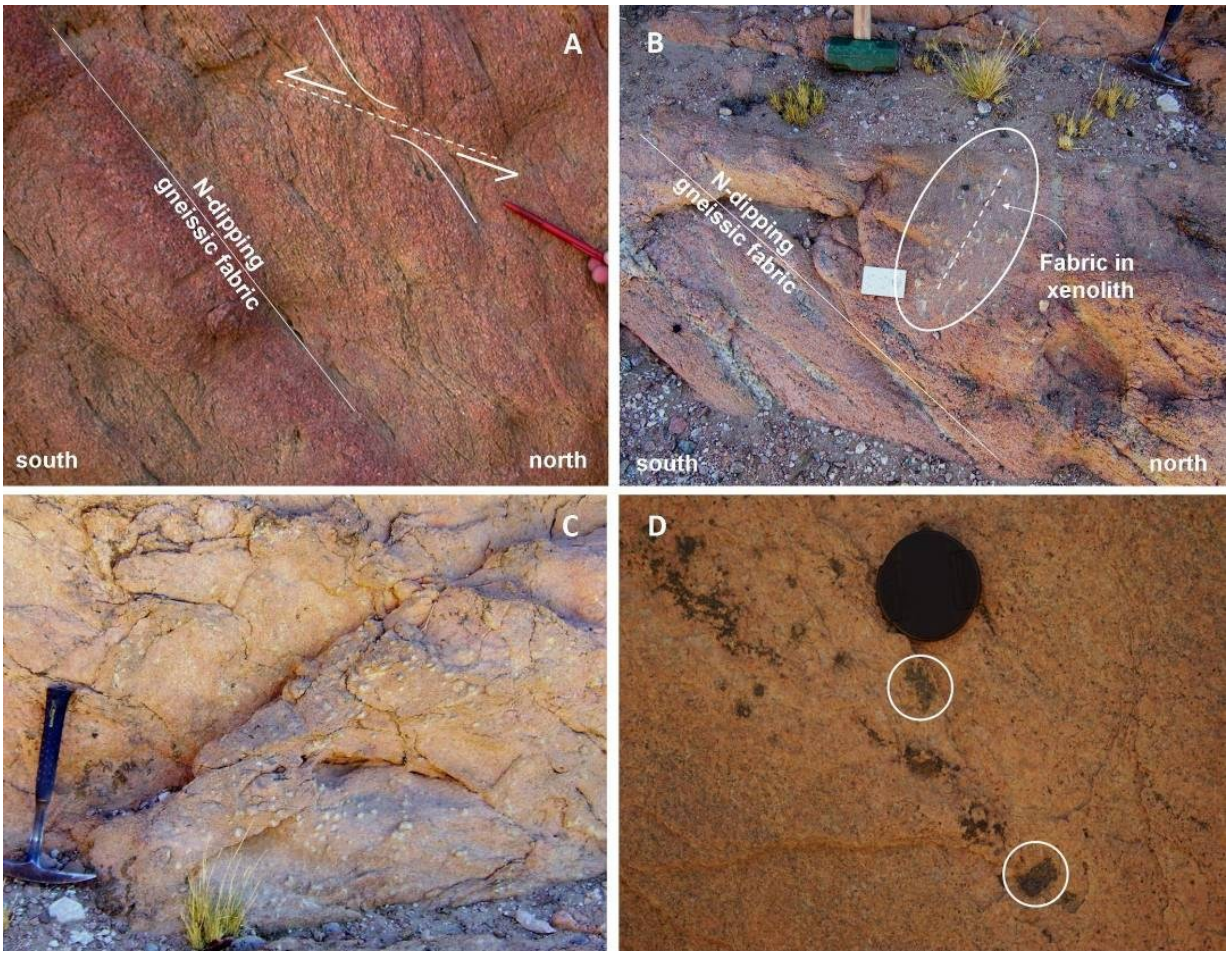

Fig. 4.4 – Field photographs of red granites from the northern margin of the Palmenhorst Dome. A: Undulating, N-dipping gneissic fabric in the red granite, defined by biotite, the orientation of which is shown with the white line. Note how the fabric is cut by Damaran D2 extensional shear bands (shown by dashed line). Locality 0500360/7504659. B: A xenolith of sillimanite-bearing, quartzofeldspathic material (circled). Note that the fabric in the xenolith is perpendicular to the N-dipping gneissic fabric in the host red granite. Locality 0500363/7504555. C: Sillimanite knots, with no obvious xenolith margins. Locality 0500363/7504555. D: Large (1-2 cm) blue cordierite crystals (circled) in red granite. Locality 0499675/7504400.

The granites have very small amounts of mafic minerals, and comprise mostly microcline (*ca*. 60%), with lesser quartz (*ca.* 25 %), plagioclase feldspar (*ca.* 10 %) and biotite (*ca.* 5 %), as well as accessory sillimanite, cordierite, muscovite, and magnetite (Fig. 4.5A, B). Biotite and magnetite, which are present in minor proportions, generally appear to be interstitial to the microcline and quartz grains (Fig. 4.5A). However, biotite also occurs locally as subhedral to euhedral laths, included in plagioclase or microcline (Fig. 4.5C, D). Cordierite is found with inclusions of fibrolitic sillimanite and, rarely, magnetite (Fig. 4.5D). Coarser muscovite (up to 1 mm) is found adjacent to seams of fibrolitic sillimanite. Microcline is commonly subhedral to euhedral, and may contain inclusions of thermally rounded quartz. Alteration has partially sericitised the microcline in places, and the biotite is locally altered to chlorite.

Local graphic intergrowths of quartz and microcline are noted. The moderate to strong foliation is defined by biotite and sillimanite, as well as by differential proportions of the component minerals (biotite, quartz, K-feldspar), but may not be visible in thin section owing to the coarse-grained nature of the granite. Although the cordierite and sillimanite may be up to a few cm in size (Fig. 4.4C, D), the bulk of the granite has a fairly homogenous coarse grain size of 1-3 mm, with smaller grains of biotite and magnetite (typically *ca*. 0.1 mm to 1 mm in size).

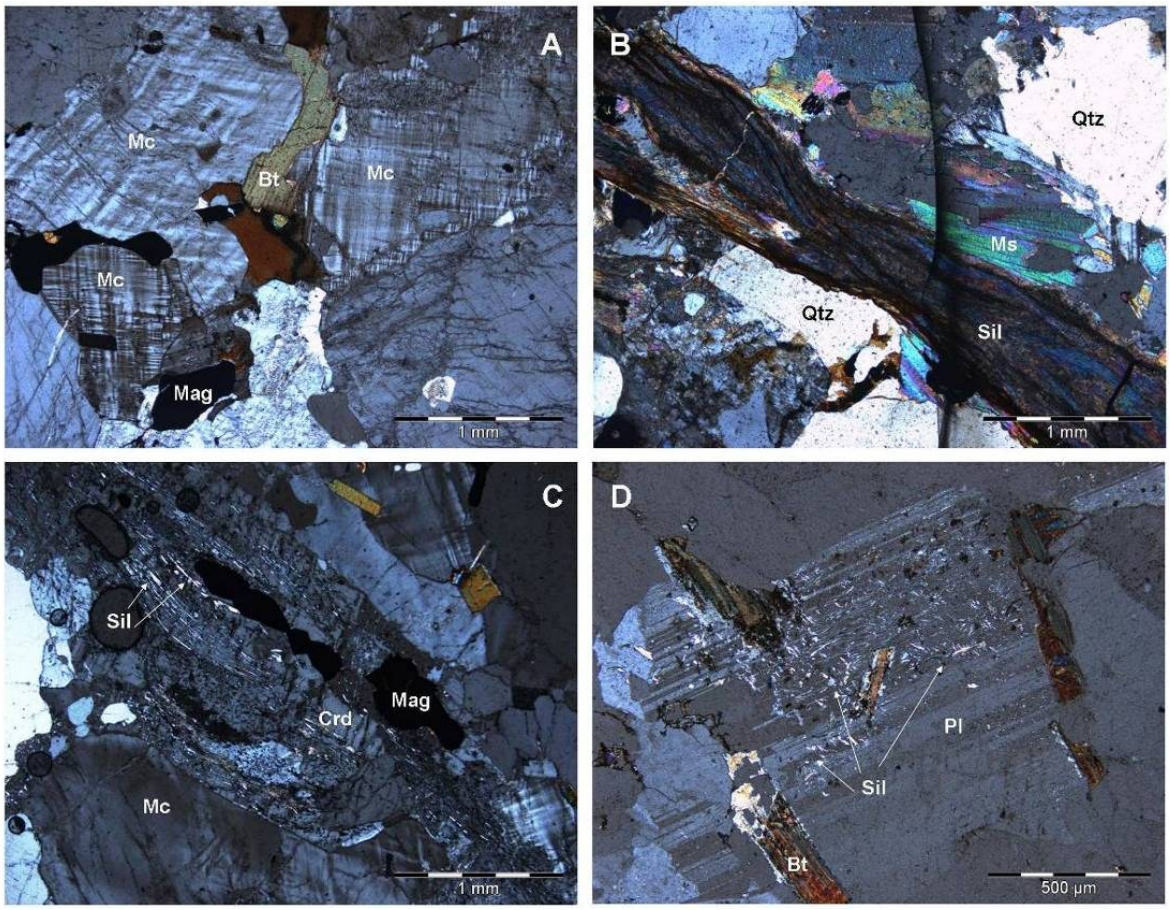

Fig 4.5 – Photomicrographs of red granites. A: Typical red granite, containing a large proportion of microcline, with quartz and interstitial biotite and magnetite (sample CZRL14, locality 0499675/7504400, XPL). B: A seam of fine, fibrolitic sillimanite, associated with coarse muscovite (sample LKR003, locality 0499669/7504383, XPL). C: Large cordierite crystal with inclusions of sillimanite and magnetite (sample LCZ11-2, locality 0497765/7501846, XPL). D: Fine (<100 µm) needles of fibrolitic sillimanite within a plagioclase crystal (sample CZRL14, locality 0499675/7504400, XPL).

The red granites described above show similar field and petrographic characteristics to the red gneissic granite of Smith (1965), the red granite gneiss of Jacob (1974), the red inhomogeneous syn-tectonic granite of Brandt (1985) and the basement-hosted granite of Nex (1997). All of these granite types are recognised as being K-feldspar-rich, with small amounts of ferromagnesian minerals, and may contain sillimanite. These granites are confined to the lower levels of Damaran stratigraphy, and are typically found near the level of the Abbabis Complex or Etusis Formation, commonly

occupying anticlinal or domal structures (Smith, 1965). They are inhomogeneous, and contain a gneissic fabric. The term 'red gneissic granites' as defined by Miller (2008) is limited to relatively homogeneous, equigranular, anatectic red granite that is markedly foliated. Miller (2008) considers this foliation not to be tectonic, but the result of original sedimentary layering or gneissic fabric, and that these red gneissic granites are the product of almost complete in-situ melting of Etusis Formation arkose or Abbabis Complex gneiss during high-grade metamorphism. However, field relationships show that the fabric in xenoliths within the red granite is oblique or perpendicular to the gneissic fabric in the red granite (Fig. 4.4B) and, thus, the gneissic fabric is not an inherited 'ghost' fabric. Based on outcrop studies, it is suggested here that it is a N-dipping D2 tectonic fabric. Additionally, almost complete in-situ melting, as suggested by Miller (2008) is highly unlikely – temperatures of 1150-1250 ˚C are required for complete fusion (Vielzeuf & Holloway, 1988), and segregation of melt from residuum will begin as soon as permeability is reached in the matrix of a migmatite (Sawyer, 2008), except in special cases under conditions of purely lithostatic stress (which are not likely in an active orogen). The liquid percolation threshold (Vigneresse *et al*., 1996), where melt will begin to move into or through a solid framework, will be reached at less than 2% melt (Sawyer, 2008). Thus, red granites with a gneissic fabric are not the products of near-total in-situ melting, and the fabric is not a ghost fabric, but rather these granites are the mobilised melt products of partial melting elsewhere (likely the Abbabis Complex), which were emplaced at the contact between the Abbabis Complex and Etusis Formation, and which contain xenoliths of Abbabis Complex gneisses. The gneissic fabric is a N-dipping tectonic foliation, subparallel to the regional D2 fabric.

It should be noted that the red granites described above are not identical to the red granites described by Marlow (1981). Although some characteristics are shared, such as small amounts of ferromagnesian minerals, large amounts of K-feldspar, and local development of muscovite and sillimanite, Marlow (1981) also included foliated red granite dykes, which may contain primary hornblende, and which may be fine-grained, equigranular and porphyritic. The characteristics of these dykes show little

similarity to the gneissic red granites of this study or those of Smith (1965) and Jacob (1974), but they do show similarity to the red and grey homogeneous syn-tectonic granites (Brandt, 1985) and the grey granites from this study (see 4.3 below). Hence, it appears that Marlow (1981) may have included two granite types in his red granite classification that have been classified separately by other workers. The red granites described in this study may also be similar to the equigranular red granites of Nex (1997), which are homogeneous, fine- to medium-grained, emplaced in a high strain zone between the Abbabis Complex and Damaran metasediments, and are generally syenogranites (Nex, 1997).

Geochemically, red granites are classified as granites on both Streckeisen (Fig. 4.6A) and An-Ab-Or (Fig. 4.6B) diagrams. They show similar major element characteristics to the red gneissic granite of Smith (1965), the red granite gneiss of Jacob (1974), the red granites of Marlow (1981) and the basement-hosted granite of Nex (1997), and are alkalic to alkali-calcic on a SiO_2 vs. Na_2O+K_2O-CaO plot (Fig. 4.6C). All granites analysed are peraluminous, although some granites analysed by Marlow (1981) may be metaluminous (Fig. 4.6D). Red granites analysed in this study are highly potassic, with elevated K_2O/Na_2O+CaO relative to similar granites analysed by earlier workers (Fig. 4.6E). REE patterns (Fig. 4.6F) show highly enriched LREEs (La_N/Lu_N = 17.10-83.60), with LEE fractionation greater than HREE fractionation (La_N/Sm_N = 5.61-6.53; Gd_N/Lu_N = 2.28-8.09), and moderate Eu anomalies (Eu/Eu* = 0.47-0.77). Geochemically, the red granites in this study are more alkalic than the alkali-calcic to calc-alkalic red and grey granites described by Nex (1997) (Fig. 4.6C).

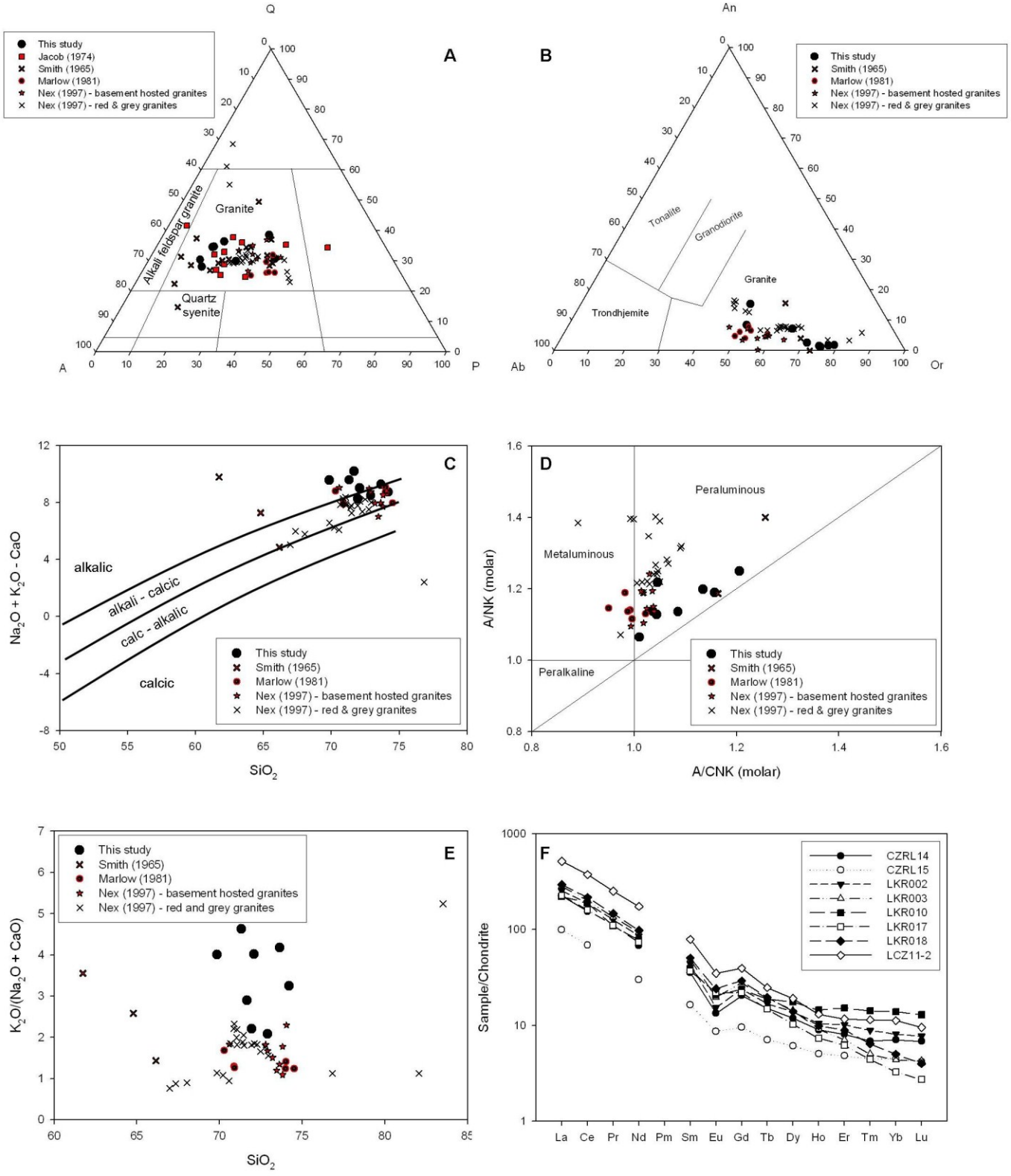
A
Q
P
This study
Jacob (1974)
Smith (1965)
Marlow (1981)
Nex (1997) - basement hosted granites
Nex (1997) - red & grey granites
Granite
Alkali feldspar granite
Quartz syenite
B
An
Ab
Or
Tonalite
Granodiorite
Trondhjemite
C
$Na_2O + K_2O - CaO$
SiO_2
alkalic
alkali - calcic
calc - alkalic
calcic
D
A/NK (molar)
A/CNK (molar)
Peraluminous
Metaluminous
Peralkaline
E
$K_2O/(Na_2O + CaO)$
This study
Smith (1965)
Marlow (1981)
Nex (1997) - basement hosted granites
Nex (1997) - red and grey granites
F
Sample/Chondrite
CZRL14
CZRL15
LKR002
LKR003
LKR010
LKR017
LKR018
LCZ11-2
La Ce Pr Nd Pm Sm Eu Gd Tb Dy Ho Er Tm Yb Lu

Fig. 4.6 (previous page) – Geochemistry of the red granites from the study area, compared with the red gneissic granite of Smith (1965), the red granite of Marlow (1981), and both the basement-hosted granites and red and grey granites of Nex (1997). A: Streckeisen diagram, showing that all samples analysed plot as granites. B: An-Ab-Or diagram, showing that red granites are all granites, and are K-feldspar (orthoclase) rich. C: SiO_2 vs. Na_2O+K_2O-CaO plot, showing the alkalic to alkali-calcic nature of the red granites. D: A/CNK vs. A/NK plot, showing the peraluminous nature of the red granites. E: $K_2O/(Na_2O + CaO)$ vs. SiO_2 plot, showing the highly potassic nature of the red granites. F: Chondrite-normalised REE plot, showing that red granites are enriched in the LREE and show moderate Eu anomalies. Chondrite normalisation factors are from Anders & Grevesse (1989). Geochemical data and analytical procedures are included in Appendix 1.

Thus, the red granites described in this study are similar in terms of both field and geochemical characteristics to the red gneissic granite of Smith (1965), the red granite gneiss of Jacob (1974), the red inhomogeneous syn-tectonic granite of Brandt (1985), the equigranular red and basement-hosted granites of Nex (1997), and the red gneissic granite defined by Miller (2008). The peraluminous character of these granites, their stratigraphic localisation near the contact between the Abbabis Complex basement and Damaran cover, and their quartzofeldspathic xenoliths suggest confirm that it may have been derived from migmatisation of the Etusis Formation or Abbabis Complex (Smith, 1965; Jacob, 1974). However, the granite is not the result of near-total melting of the protolith, as suggested by Miller (2008), nor is the fabric a relict ghost fabric (Miller, 2008), but is a D2 gneissic fabric.

4.3 Grey Granites

The most voluminous granitoid type found in the study area is a suite of dark grey to white or pink, fine- to medium-grained, equigranular, foliated granites. This suite of granites is termed the grey granites, as the different varieties are generally light to dark grey. The grey granites display a range of intrusive geometries, from cross-cutting dykes (from a cm- to m-scale) to large bodies (10s to 100s of m in size). Although present throughout the study area, they are most voluminous in the area around the Ida Dome, and along the southern margin of the Palmenhorst Dome (Figs. 2.1, 3.2, 3.20). The granites range in colour from dark grey, to very light grey (almost

white), owing to variable proportions of biotite and hornblende (Fig. 4.7A). Although there is a range of colour and composition, the granites may be grouped into three general groups; dark (mafic) grey granite, intermediate grey granite, and leucocratic grey granite (Fig. 4.7A). Based on field relationships, the dark grey granite appears to be the earliest, and contains the highest proportion of biotite, in addition to hornblende. This granite is highly foliated, and is cross-cut by the intermediate and leucocratic grey granites (Fig. 4.7A). The intermediate phase contains less biotite than the early grey granite, and no hornblende, whilst the youngest grey granite is essentially a leucogranite with minor amounts of biotite, and cross-cuts both earlier types of grey granite. Although the darker grey granites are coarser grained (grain size *ca*. 2 mm) than the younger phases, which are uniformly fine- to medium-grained (grain size *ca*. 1 mm), the younger phases locally contain large (up to 10 cm) phenocrysts of K-feldspar (Fig. 4.7B). In one case, near the southern margin of the Palmenhorst Dome (locality 0489454/7489694), an outcrop shows the early "mafic" phase of dark grey granite, cross-cut by a pink, K-feldspar-rich pegmatite (Fig. 4.7C). This pegmatite and the "mafic" granite are, in turn, both cross-cut by the intermediate phase of grey granite and the intermediate phase incorporates xenoliths of the K-feldspar pegmatite, which appear as phenocrysts. Although only found in this single outcrop, this could explain the K-feldspar phenocrysts found in the rest of the younger grey granites. In numerous outcrops of the "mafic" phase of the grey granites, both in the Ida Dome and in the Palmenhorst Dome, veins of more leucocratic material are found within the earliest phase.

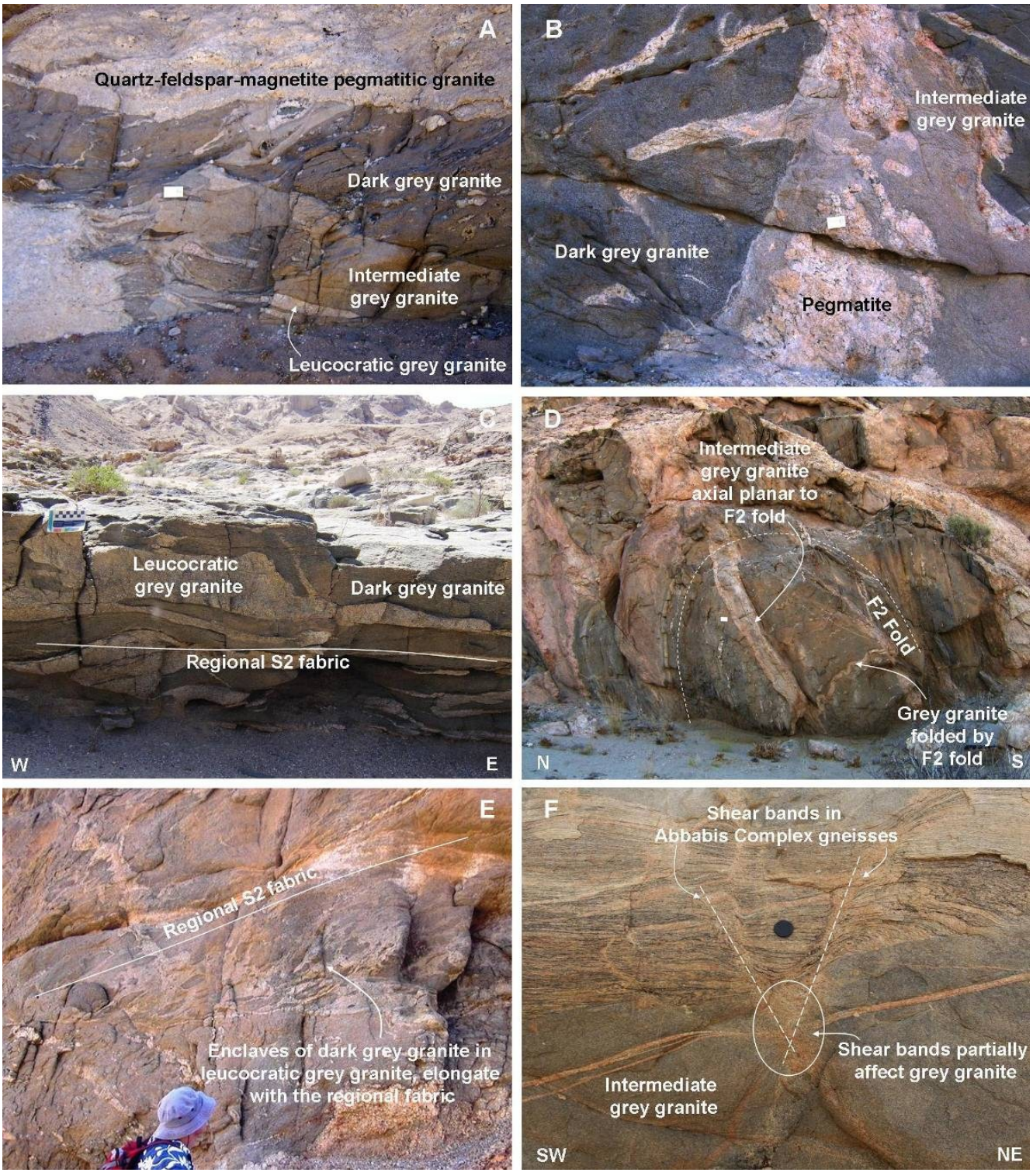
A
Quartz-feldspar-magnetite pegmatitic granite
Dark grey granite
Intermediate grey granite
Leucocratic grey granite
B
Intermediate grey granite
Dark grey granite
Pegmatite
C
Leucocratic grey granite
Dark grey granite
Regional S2 fabric
W
E
D
Intermediate grey granite axial planar to F2 fold
F2 Fold
Grey granite folded by F2 fold
N
S
E
Regional S2 fabric
Enclaves of dark grey granite in leucocratic grey granite, elongate with the regional fabric
F
Shear bands in Abbabis Complex gneisses
Shear bands partially affect grey granite
Intermediate grey granite
SW
NE

Fig. 4.7 (previous page) – Field photographs of grey granites from the study area. A: Multiple phases of grey granite, showing changing maficity and cross-cutting relationships. Locality 0500425/7504675. B: Multiple phases of grey granite and pegmatite – the early dark grey granite is cut by pink pegmatite, following which both phases are cut by intermediate grey granite, forming large phenocrysts of K-feldspar in the intermediate grey granite. Locality 0489454/7489694. C: Leucocratic grey granite intruding into dark grey granite, with both flattened subparallel to the N-dipping regional S2 fabric. Both granites also contain the N-dipping S2 fabric. Locality 0502428/7488534. D: Intermediate grey granite intruding along the axial plane of a D2 fold in Chuos Formation schists, as well as being folded by D2. Locality 0489390/7489693. E: Elongate enclaves of dark grey granite in leucocratic grey granite. Note the alignment of these mafic enclaves along the S2 fabric. Locality 0489766/7489118. F: Late-D2 shear bands in Abbabis Complex gneisses partially affecting intermediate grey granites. Locality 0500289/7488670.

There is a clear temporal relationship between the grey granites and D2 deformation, and a number of features indicate that these grey granites intruded syntectonically during D2 deformation. All three phases of granite contain a D2 fabric (Fig. 4.7D), subparallel to the regional D2 fabric and axial planar to D2 folds. This fabric is most well developed in the dark-grey phase, and less developed in the more leucocratic phase, owing either to the higher proportion of biotite or to a higher degree of strain in the darker phase. Grey granites commonly intrude as dykes axial planar to D2 folds (Fig. 4.7D), and may also be folded by these folds. This axial planar intrusive relationship and axial planar fabric is best seen in the numerous m-scale folds in the Chuos Formation west of the farm Hildenhof, along the southern margin of the Palmenhorst Dome. The intermediate phase of grey granites (and to a lesser extent the leucocratic phase) commonly contains rounded elongate fragments/xenoliths of the earlier, more mafic phase (Fig. 4.7F). These xenoliths are generally highly elongate, with length-to-width ratios of 6:1, and are aligned along the S2 fabric in the grey granites. In the Ida Dome, the S2 fabric in the grey granites has, like the regional fabric in the host rocks, been folded about a km-scale NE-plunging, upright F3 fold. The emplacement of a younger, leucocratic, phase of grey granite into older dark grey granite occurred during D2 deformation – the sheets of leucocratic grey granite are flattened along the S2 fabric direction (Fig. 4.7D). Furthermore, shear bands

developed during NE-SW directed extension at the late stages of D2 deformation partially affect the grey granites (Fig. 4.7F), indicating that these shear bands developed after the grey granites were emplaced, but prior to total crystallisation of the grey granites, confirming the syn-D2 timing of the grey granites. The relationship of sheets of the grey granite to D2 folding and extension, the well developed S2 fabric in the grey granites, and the flattening of sheets of grey granite parallel to this S2 fabric all indicate that these grey granites have intruded syntectonically during D2 deformation.

The variability of the grey granites, which range from dark grey granite to a pale leucogranite, is reflected in their mineralogy. The darker varieties of the grey granites contain a higher proportion of mafic minerals, and comprise plagioclase feldspar (*ca*. 50%), quartz (*ca*. 10%), hornblende (*ca*. 20%), biotite (*ca*. 10%), and accessory opaque minerals (pyrite and magnetite) (Fig. 4.8A, B). These mafic rocks are typically coarse-grained (1-3 mm), with subhedral to euhedral laths of biotite, and stubby anhedral hornblende (which may make up to 30% of the rock volume). Plagioclase is slightly sericitised, and biotite may be altered to chlorite. Quartz grain boundaries are highly irregular, and small aggregates of quartz are present. Quartz and plagioclase locally display rounded inclusions of resorbed hornblende or biotite (Fig. 4.8B), and apatite is an accessory mineral. Locally, cordierite occurs in the darkest of the grey granites (Fig. 4.8C). Quartz is slightly strained, with undulose extinction. Biotite grains (and to a lesser degree stubby hornblende) are aligned to form a planar fabric in these granites (Fig. 4.8D).

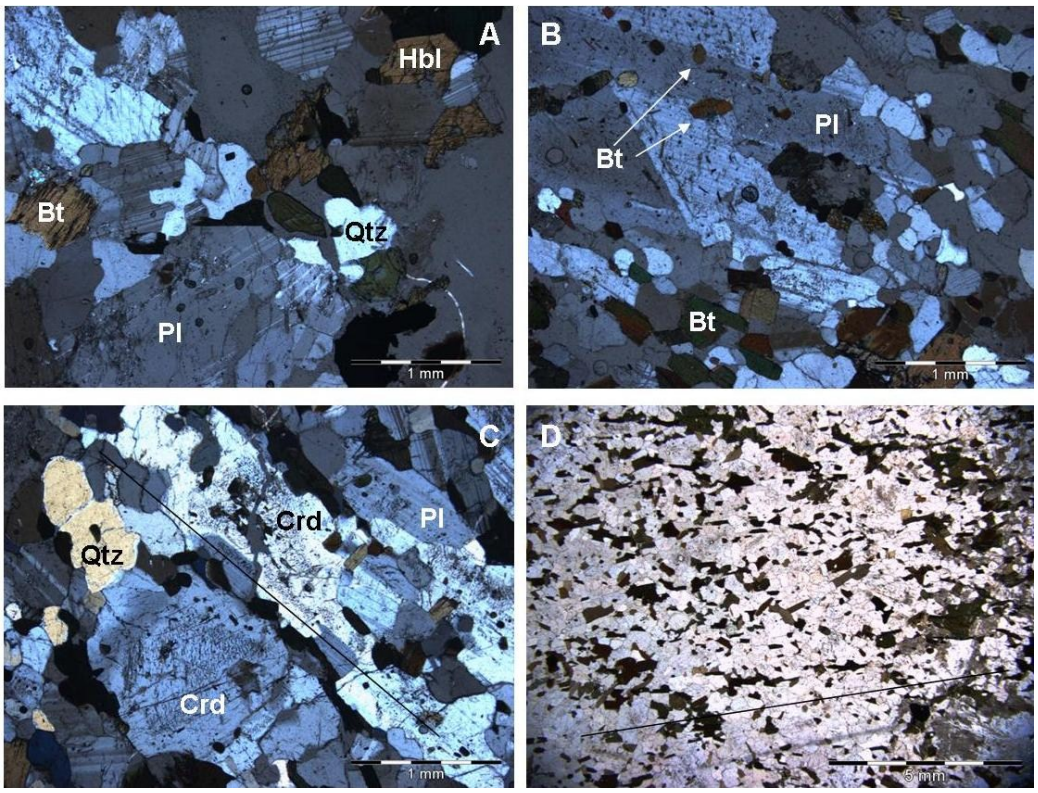

Fig. 4.8 – Photomicrographs of dark grey granites from the study area. A: Typical dark grey granite with an assemblage of plagioclase feldspar, hornblende, biotite and quartz (LHA003, locality 0489450/7489661, XPL). B: Rounded inclusions of biotite in plagioclase crystal (LHA010, locality 0489766/7489118, XPL). C: Cordierite grains with inclusions of biotite. Note the fabric defined by biotite (direction indicated by line), and the alignment of the cordierite along this fabric (LHA010, locality 0489766/7489118, XPL). D: Fabric in dark grey granite defined by aligned biotite and hornblende (direction indicated by line) (LHA010, locality 0489766/7489118, PPL).

In the intermediate variety of the grey granites, hornblende is no longer present, and the granites have an assemblage of quartz (*ca*. 40%), plagioclase feldspar (*ca*. 30%), biotite (*ca*. 20%), and K-feldspar (*ca*. 10%), with accessory magnetite. A moderate fabric is defined by subhedral to anhedral interstitial biotite. Grain size is between 0.5 mm and 2 mm, and is slightly smaller than the dark grey granites. K-feldspar is present, although plagioclase remains the more common feldspar in the intermediate phase. The K-feldspar generally displays perthitic exsolution. Allanite is found rarely in these rocks.

The more leucocratic grey granites contain lesser amounts of biotite and plagioclase and more K-feldspar than the intermediate grey granites, comprising K-feldspar (*ca*. 40%), quartz (*ca*. 30%), biotite (<10%), plagioclase (*ca*. 20%), and accessory opaque minerals (magnetite). The minor amounts of biotite are aligned as euhedral laths to form a weak fabric (Fig. 4.9A), and may be locally altered to chlorite (Fig. 4.9B). Quartz displays undulose extinction, indicating strain (Fig. 4.9C). K-feldspar is present as large (1-2 mm) anhedral to subhedral crystals, with rounded inclusions of quartz (Fig. 4.9D).

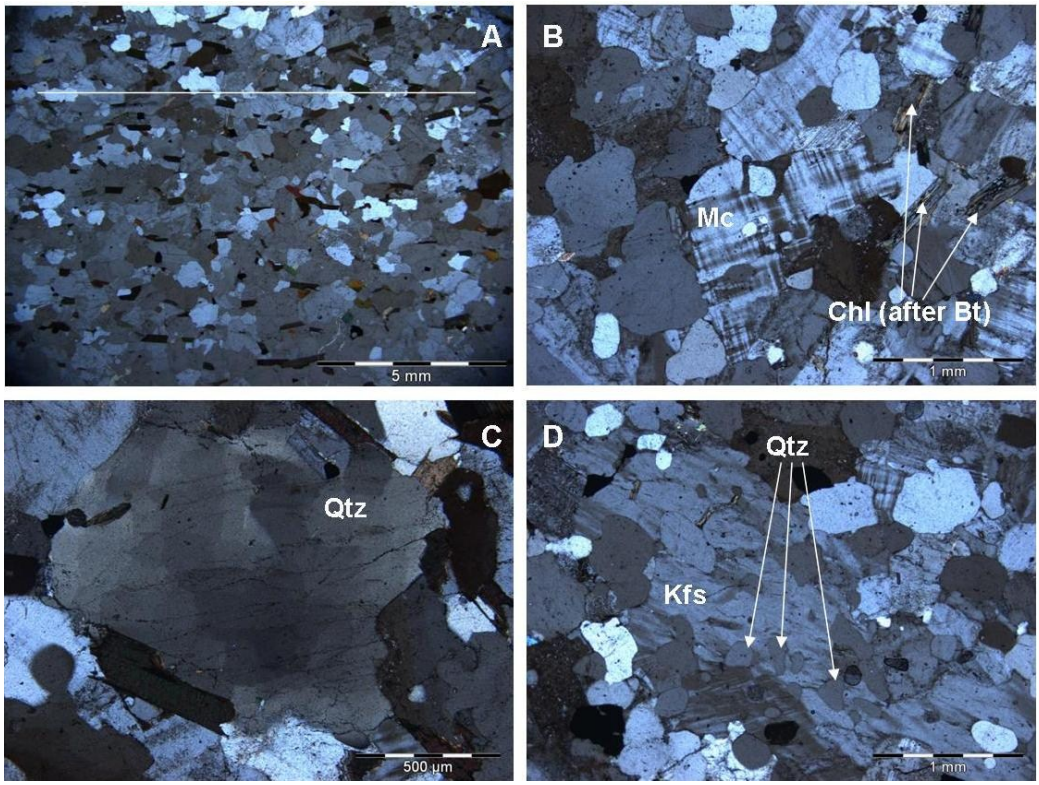

Fig. 4.9 – Photomicrographs of leucocratic grey granites from the study area. A: Moderate fabric defined by aligned laths of biotite and elongate sutured quartz (orientation indicated by line) (LID 019, locality 050075/7487718, XPL). B: Typical leucocratic grey granite, with K-feldspar (microcline), quartz and biotite (altered to chlorite), and no plagioclase feldspar (LID032, locality 0501164/7488206, XPL). C: Strained quartz, showing undulose extinction (LHA011, locality 0489766/7489118, XPL). D: Large K-feldspar grain, with abundant inclusions of rounded quartz (LHA011, locality 0489766/7489118, XPL).

The more leucocratic granites have a uniform medium grain size of *ca.* 1 mm, with slightly smaller (*ca.* 0.5 mm) biotite. Plagioclase feldspar is commonly altered to sericite, forming *ca.* 0.3 mm muscovite in places. Zircon is a common accessory mineral.

Locally, the leucocratic variety of the grey granites (and rarely the intermediate variety) is pink or red in colour (Fig. 4.10A), rather than the more typical white or light grey. These pink or red granites show all of the other features common to the grey granites, namely their fine to medium grain size, equigranular, homogeneous texture, and the planar fabric of aligned biotite laths. They also intrude along the axial planes of D2 folds, and have a fabric that is axial-planar to these folds (Fig. 4.10A). The pink-red colour appears to be the result of local alteration and oxidation of the grey granite – oxidation of the grey granite to a pink-red colour can be seen in zones of alteration (Fig. 4.10B) locally developed around quartz veins, and in thin section pink-red granites appear more altered than the grey varieties. Another feature locally observed is the association between the grey granites and white-pink pegmatitic granites in the study area. Pegmatitic granites (termed quartz-feldspar-magnetite pegmatitic granites, and equated with the C-type Leucogranites of Nex, 1997 and Freemantle, Pers. Comm. – see section 4.4 below) are ubiquitous in the study area, and share similar syn-D2 structural relationships to the grey granites. Similar pegmatitic granites are observed associated with intermediate to leucocratic grey granites (Fig. 4.10C, D) – either along the margins of grey granite sheets (Fig. 4.10C) or closely associated with grey granites (Fig. 4.10D).

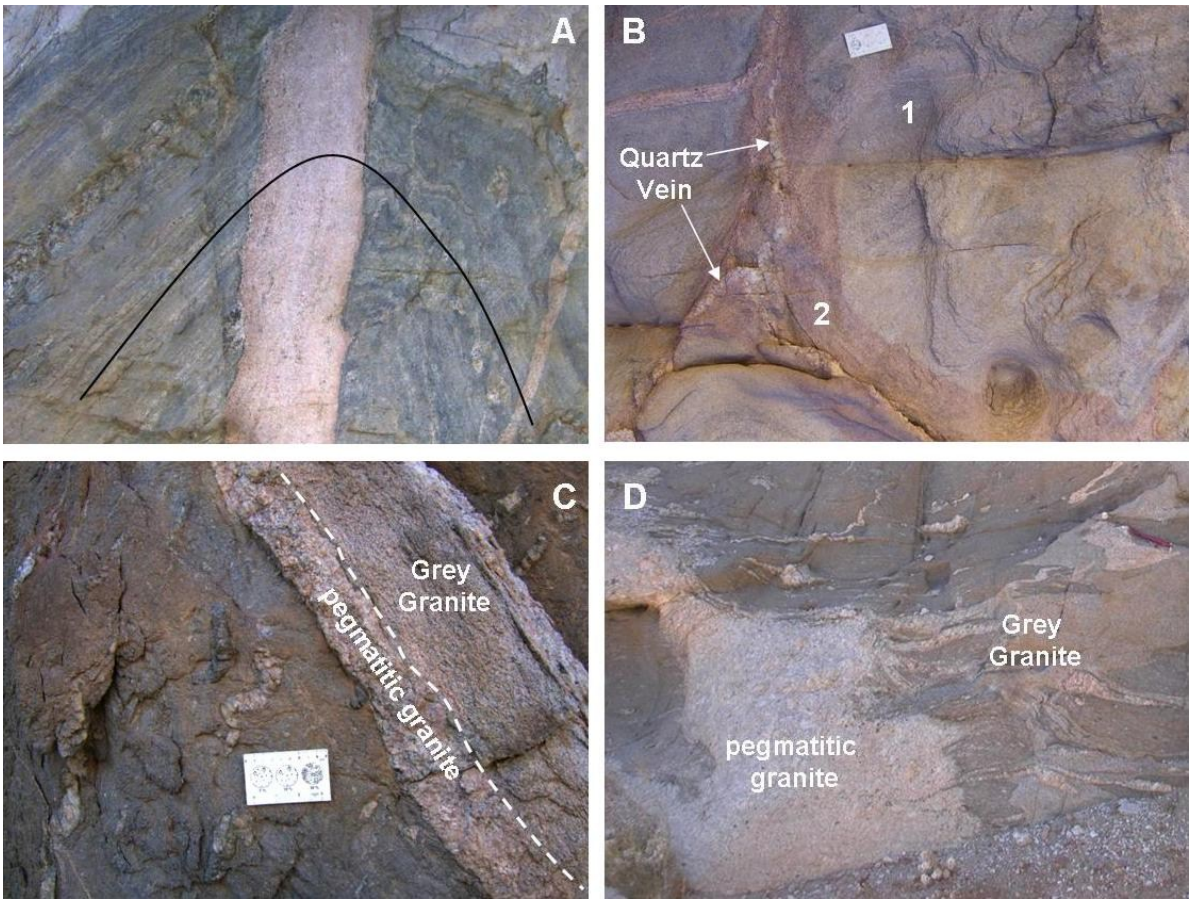

Fig. 4.10 – Field relationships of grey granites with the pink-red varieties and pegmatitic granites. A: A foliated sheet of medium-grained pink granite intruding Khan-Formation calc-silicates along the axial plane of a D2 fold (indicated by black line). Locality 0499068/7488836. B: Relationship between fresh grey granite (1), which has been altered to a red colour (2) adjacent to a vein of quartz (indicated). Locality 0500544/7487613. C: Foliated grey granite sheet intruding quartz-biotite schists of the Chuos Formation, with pegmatitic granite along the margin of the sheet. Locality 0489390/7489693. D: Pegmatitic granite cross cutting dark grey granite, and showing local apophyses into the grey granite, subparallel to the granite foliation. Locality 0500425/7504675.

Grey granites plot as quartz monzodiorites, granodiorites or granites on a Streckeisen diagram (Fig. 4.11A), and as tonalites, granodiorites or granites on an Or-An-Ab diagram (Fig. 4.11B), based on their normative mineral proportions. These trends may reflect fractionation from an original dioritic or granodioritic magma. They show similar compositions to grey granites analysed by Freemantle (Pers. Comm.), red and

grey granites analysed by Nex (1997), and Salem-type granites analysed by Marlow (1981) and McDermott (1986). Since they show similar field relationships to, and are commonly associated with quartz-feldspar-magnetite pegmatitic granites, which have been equated with the C-type leucogranites of Nex (1997), they have also been compared to C-type leucogranites analysed by Freemantle (Pers. Comm.). Na_2O+K_2O-CaO vs. SiO_2 (Fig. 4.11C) and A/NK vs. A/CNK (Fig. 4.11D) diagrams show that grey granites are generally peraluminous, and range from calcic (at low SiO_2) to alkalic with increasing SiO_2, possibly reflecting a fractionation trend, and showing similarity to data gathered by other studies. Tonalitic to granodioritic compositions (Fig. 4.11B), calcic to calc-alkalic compositions (Fig. 4.11C) and metaluminous compositions (Fig. 4.11D) are all for dark grey granite varieties, reflecting elevated CaO relative to K_2O and Na_2O in the early (more mafic) grey granites, and further confirming a fractionation trend from dark to light grey varieties.

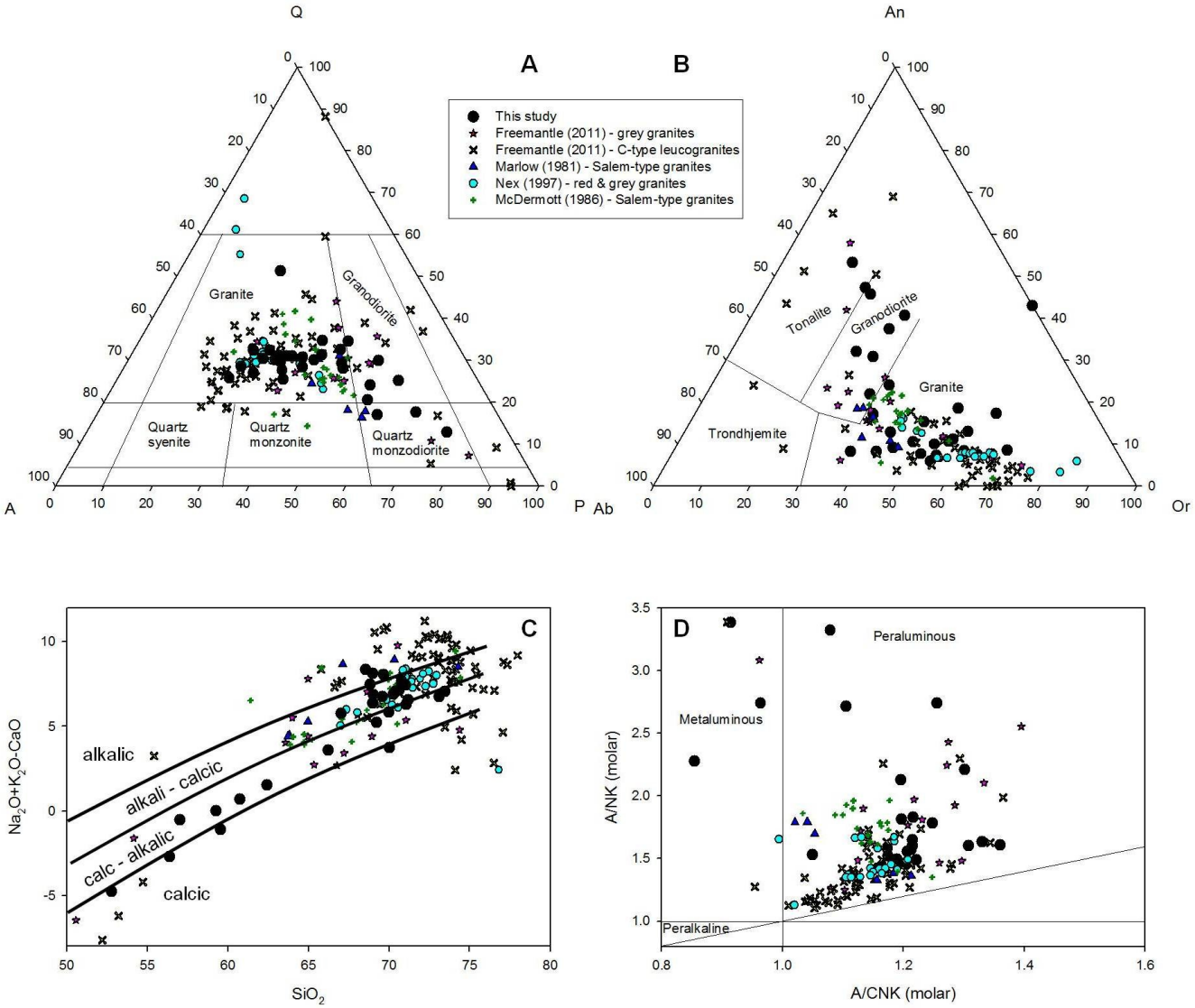

Fig. 4.11 – Geochemistry of the grey granites. A: Streckeisen diagram, showing classification of grey granites as quartz monzodiorites, granodiorites or granites. B: Or-An-Ab diagram, showing classification of grey granites as tonalites, granodiorites or granites. C: Na_2O+K_2O-CaO vs. SiO_2 diagram, showing grey granites as calcic for lower values of SiO_2 to alkalic for higher SiO_2. D: A/NK vs. A/CNK diagram, showing that almost all grey granites are peraluminous, with a few samples (dark grey granites) plotting as metaluminous. Geochemical data is contained in Appendix 1. Data has been compared to that of Freemantle (Pers. Comm.), Marlow (1981), Nex (1997) and McDermott (1986).

Fractionation trends are also supported by plots of Mg # vs. K_2O (Fig. 4.12A) and Mg # vs. Sr (Fig. 4.12B), which show an increase in K_2O with decreasing Mg # (Fig. 4.12A), and a decrease in Sr with decreasing Mg #. Since Sr partitions into plagioclase feldspar, fractionation of plagioclase would lower the amount of Sr in the remaining magma.

A plot of Th vs. U (Fig. 4.12C) shows that the grey granites have Th/U ratios of between 1 and 100, similar to most of the grey granites analysed by Freemantle (Pers. Comm.), the red and grey granites analysed by Nex (1997) and the Salem-type granites analysed by Marlow (1981) and McDermott (1986), although the C-type leucogranites and some of the grey granites analysed by Freemantle (Pers. Comm.) show elevated U:Th ratios. REEs show steep patterns (Fig. 4.12D), with La_N/Lu_N between 5.33 and 147.92. LREE are slightly more enriched than HREE (La_N/Sm_N = 2.45-8.98, Gd_N/Lu_N = 1.00-13.87), and samples show small to large Eu anomalies (Eu/Eu* = 0.15-0.92), with a single sample showing no Eu anomaly (Eu/Eu* = 1.03). Eu/Eu* vs. Mg # (Fig. 4.12E) shows that Eu anomalies correspond to plagioclase fractionation, confirming the fractionation trend seen in the Sr data (Fig. 4.12B), and La_N/Lu_N vs. K_2O (Fig. 4.12F) further supports the steepening of REE patterns owing to fractionation.

Fig. 4.12 (following page) – Geochemistry of the grey granites. A: Mg # vs. K_2O, showing a fractionation trend. B: Mg # vs. Sr (ppm), showing a trend indicating fractionation of plagioclase. C: Th (ppm) vs. U (ppm), showing that all grey granites have Th/U > 1. D: Chondrite-normalised REE plot, showing enrichment in the LREE, and small to large Eu anomalies. Chondrite normalisation factors are from Anders & Grevesse (1989). E: Eu/Eu vs. Mg #, showing that Eu anomalies increase with increasing fractionation (i.e. decreasing Mg #). F: La_N/Lu_N vs. K_2O, showing further evidence for a fractionation trend in the grey granites. Geochemical data is contained in Appendix 1. Data has been compared to that of Freemantle (Pers. Comm.), Marlow (1981), Nex (1997) and McDermott (1986).*

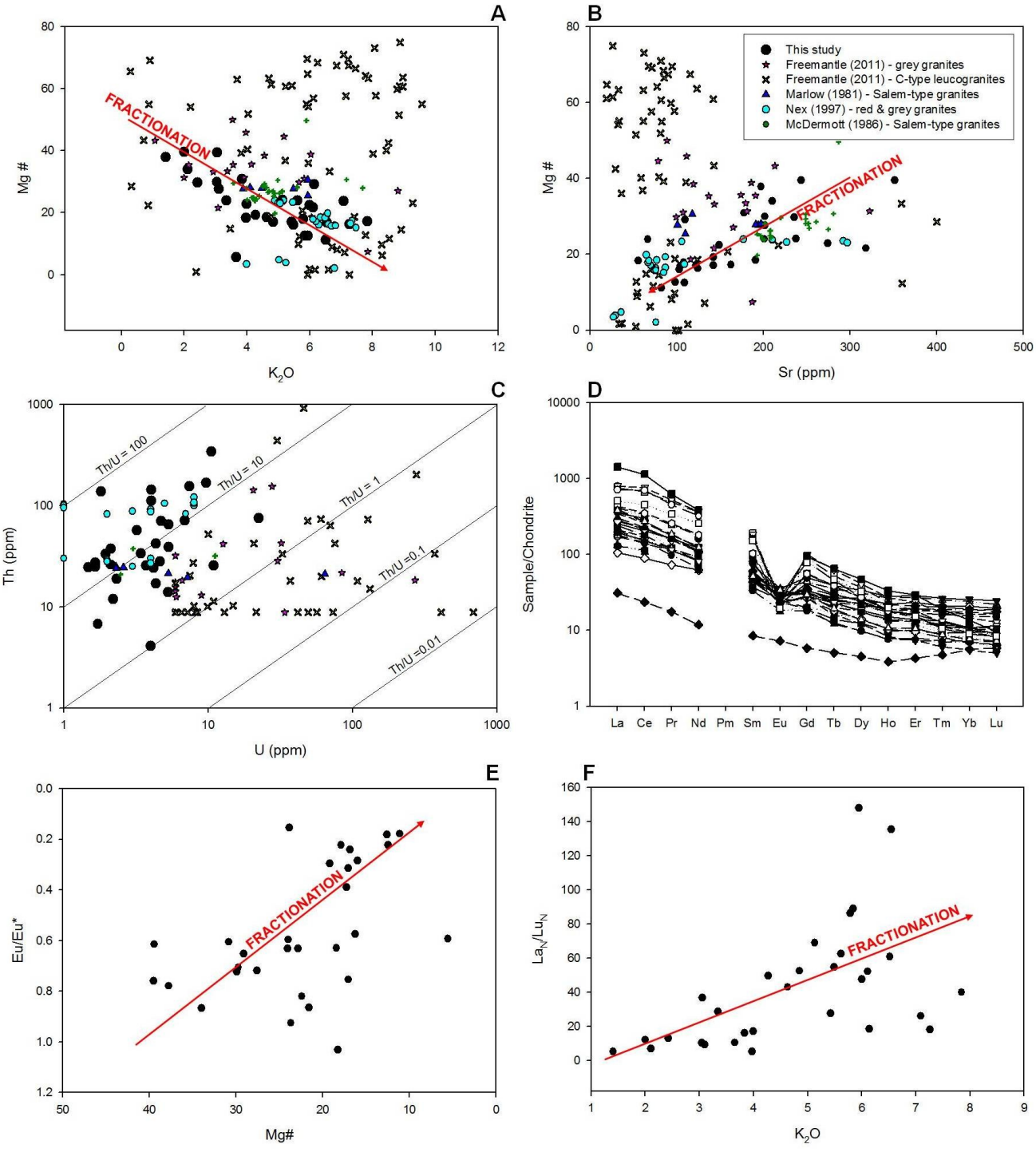
A
Mg #
K2O
FRACTIONATION
B
Mg #
Sr (ppm)
FRACTIONATION
This study
Freemantle (2011) - grey granites
Freemantle (2011) - C-type leucogranites
Marlow (1981) - Salem-type granites
Nex (1997) - red & grey granites
McDermott (1986) - Salem-type granites
C
Th (ppm)
U (ppm)
Th/U = 100
Th/U = 10
Th/U = 1
Th/U =0.1
Th/U =0.01
D
Sample/Chondrite
La Ce Pr Nd Pm Sm Eu Gd Tb Dy Ho Er Tm Yb Lu
E
Eu/Eu*
Mg#
FRACTIONATION
F
LaN/LuN
K2O
FRACTIONATION

The field and petrographic characteristics of the suite of granites described above and termed the grey granites show similarities to the characteristics of the equigranular red or grey granites described by Nex (1997), and the red and grey homogeneous syn-tectonic granites of Brandt (1985). These granite types are fine- to medium-grained homogeneous red or grey granites that intrude as irregular stocks or sheets, and which have a foliation defined by mafic minerals (Nex, 1997). The outcrop appearance of the red and grey granites is essentially the same, apart from the colour (Nex, 1997). The grey granites described above share these characteristics. Their position within the classification of Miller (2008) is somewhat cryptic. They are younger than the red gneissic granites, and their syn-D2 timing suggests that they might be related to the Salem-type granites, also known as the Salem granites (Brandt, 1985), the Salem gneiss and granite (Smith, 1965), and the Salem Granite Suite (Jacob, 1974). The Salem-type granites also show an evolution from early, biotite-rich granites to late, leucocratic varieties (suggested to be a differentiation sequence – Jacob, 1974). However, Salem granites generally occur above the level of the Kuiseb Formation, are emplaced as large batholiths, and have large (up to 5 cm) K-feldspar phenocrysts (Smith, 1965; Jacob, 1974), whilst the grey granites occur at all stratigraphic levels, are emplaced as sheets or irregular bodies, and only locally display a porphyritic texture. The grey granites are more similar to the early non-porphyritic granites and leucogranites, which occur predominantly in the northern Central Zone (Miller, 2008) and which are also syn-D2 (Klein, 1980; Haack *et al*., 1980; Badenhorst, 1988). Although voluminous in the northern Central Zone, a few small bodies of biotitic, pre- to syn-D2 leucogranite do occur in the southwestern Central Zone (Miller, 2008). These granites cross-cut the Salem-type granites, and have a strong S2 penetrative fabric defined by biotite; they are thus suggested to be syn-D2.

4.4 Sheeted Granites

In addition to the larger, more voluminous grey granites and red granites, a number of other less voluminous granite types are found in the study area. Common to all of these granite types is their intrusion geometry – rather than forming stocks or irregular bodies, these granites intrude as sheet-like bodies, and hence are collectively termed the sheeted granites. Very commonly, these granites are coarse-grained to pegmatitic, and may be highly leucocratic. Some have previously been referred to as intrusive granite and pegmatite granite (Smith, 1965), alaskitic pegmatitic granite (Jacob, 1974), alaskites or leucogranites (Brandt, 1985), alaskites (Marlow, 1981) or sheeted leucogranites (Nex, 1997). Although many of these granites are leucogranites, they should not be confused with the leucogranites of Marlow (1981), who referred to a group of leucocratic, post-tectonic dykes, sills or plugs, also known as the post-tectonic granites (Brandt, 1985), which include the Bloedkoppie, Achas, Gawib, Donkerhuk and Kubas Granites (Jacob, 1974; Marlow, 1981; Brandt, 1985), and which are not found in the study area. Although they are grouped together as sheeted granites, a number of distinctive varieties occur, and the different types of sheeted granites have been classified in the Goanikontes area by Nex & Kinnaird (1995) and Nex (1997) into six groups, labeled A-F. The characteristics of these six groups, according to Nex (1997), are as follows:

A – These are relatively narrow, discontinuous, sinuous and irregular in form, and occur infrequently within a high strain zone. They are cross-cut by type D, E and F sheets, and are pink, fine- to medium-grained, homogeneous, and have a saccharoidal texture with a weak foliation, defined by biotite.

B – These are generally white, of variable width (1-4 m) and grain size (fine to coarse), and commonly have a foliation defined by biotite. Accessory minerals include garnet, tourmaline, biotite, allanite and apatite, and macroscopic garnet is only observed where a sheet is emplaced within garnetiferous schists. Tourmaline and biotite are locally abundant.

C – These are the predominant leucogranite found within the undeformed cover sequence, and are regarded as the typical leucogranite of the area. They are of variable width (0.5-10 m) and can be traced along strike in the order of 1000 m. They are pale pink to cream in colour, comprising predominantly K-feldspar and plagioclase, and are commonly coarse to pegmatitic, with interstitial quartz and accessory minerals (tourmaline, magnetite-ilmenite, biotite, muscovite, epidote and dark green amphibole), which are usually clustered together.

D – These are uraniferous, and form irregular, anastomosing sheets 1-7 m in width restricted to host lithologies of the Khan and Rössing Formations. They are fine- to medium-grained, white, and have a homogeneous granular texture. They cross-cut grey granites, type A sheets, and the regional foliation, and comprise white feldspar, characteristic smoky quartz, accessory blue apatite, uraninite and rare pyrochlore group minerals.

E – These uraniferous granites are inhomogeneous and occur as sheets that are infrequently boudinaged and occasionally bifurcated. The sheets are never foliated, vary both in width (cm- to dm-scale) and grain size (fine-grained to pegmatitic), and cross-cut basement gneiss, basement-hosted granite, red granite, and type A, B and D sheeted leucogranites. Type E sheets have a similar mineralogy to type D sheets, but are characterised by irregular ellipsoidal coronas, termed “oxidation haloes” by Corner & Henthorn (1978) and “iron rings” by Barnes (1981). There are two types of corona: one forms ubiquitous grey cores with distinct red rims, the other exhibits amorphous red cores with gradational margins.

F – These are the youngest sheets, and cross-cut basement-gneiss, basement-hosted granite and type B, C, and E sheets. They are 0.5-3 m in width, generally tabular in form, with sharp contacts and parallel sides, and are coarse to pegmatitic in grain size. They are distinctly red, and comprise red, euhedral perthitic feldspar with interstitial milky quartz and accessory biotite and opaque minerals.

Not all of these varieties of sheeted granite have been found in the study area, and hence the different granite types described are not labelled according to the scheme

of Nex & Kinnaird (1995) and Nex (1997), but are rather named according to their mineralogical and textural characteristics. Nonetheless, the granite sheets show similarities to the granite types described above, and may be correlated with one of the six varieties described above.

4.4.1 Quartz-feldspar-magnetite pegmatitic granite

Throughout the study area, but particularly voluminous within the Khan Formation towards the eastern side of the Ida Dome, are leucocratic sheets of quartz-feldspar-magnetite granite. They are generally pegmatitic, but may show local coarse-grained (2-5 mm) areas, where a weak fabric is visible, axial planar to F2 folds. These pegmatites typically occur as dm- to m-scale as planar sheets and intrude along the axial planes of F2 folds (Fig. 4.13A). These axial-planar granite sheets appear to have subsequently been refolded about a km-scale, upright NE-trending anticline in the Ida Dome (Figs. 3.10, 3.15 and 3.16). In the Ida Dome, axial-planar dykes of quartz-feldspar-magnetite granite are found adjacent to a ca. 10 m wide body (Fig. 4.13B), which is vertical (although the current vertical orientation is likely to be the result of D3 rotation), and they may be offshoots from this body, or have coalesced to form it. They contain both K-feldspar (30-40 %) and plagioclase (30-40 %), and are white to pink (Fig. 4.13C) depending on whether plagioclase or K-feldspar is the dominant feldspar. The feldspars form the large crystals that give the rock its pegmatitic character. Feldspars occur together with interstitial clear quartz (*ca*. 20 %), small amounts (*ca*. 5%) of biotite and local patches of mm-size magnetite crystals (Fig. 4.13C). These patches of magnetite crystals are associated with xenoliths of Khan Formation schist that commonly show a mafic selvedge along their margins (Fig. 4.13C). Plagioclase contains inclusions of quartz and microcline, and the microcline appears to be partially resorbed by the plagioclase (Fig. 4.13D).

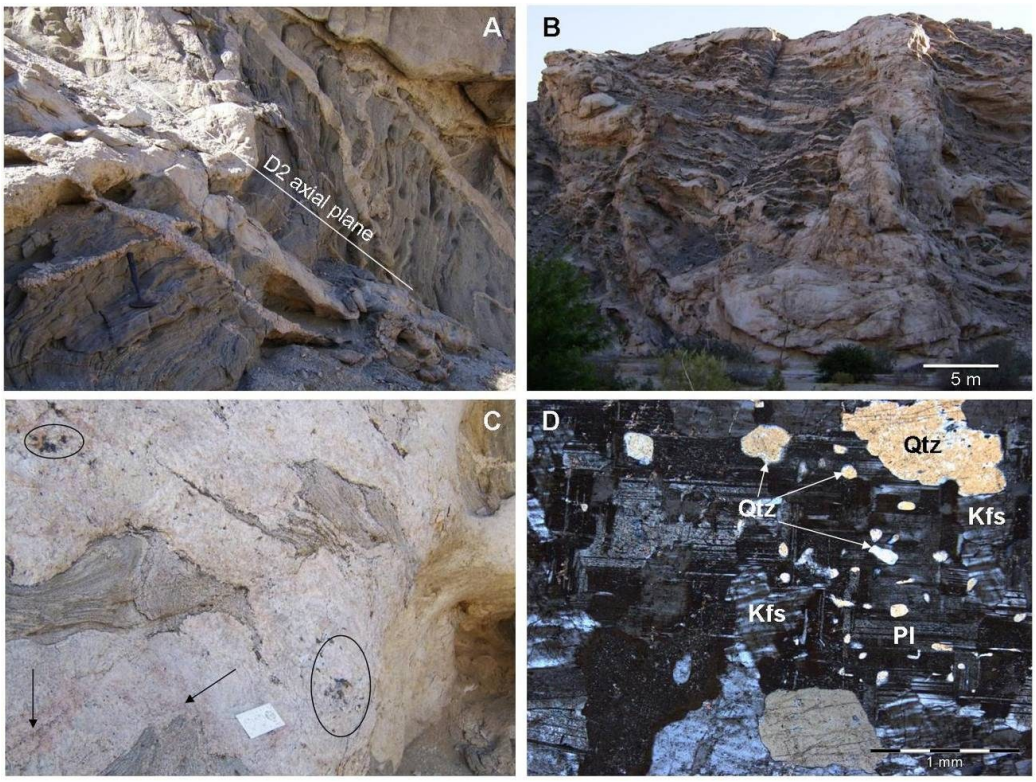

Fig. 4.13 – Characteristics of quartz-feldspar-magnetite pegmatitic granites. A: Intrusion of pegmatites along the axial plane of a D2 fold in Khan Formation metasediments near the eastern margin of the Ida Dome. Geological hammer for scale. Locality 0502135/7486366. B: Multiple subhorizontal pegmatite dykes joining or feeding off a large, subvertical dyke of pegmatite near the eastern margin of the Ida Dome. Locality 0502186/7482690. C: Typical appearance of the pegmatites. Note the patches of magnetite (circled), the pink K-feldspar (indicated by arrows), and the mafic selvedge along the margins of the xenoliths of Khan Formation metasediments. Locality 0502248/7486277. D: Photomicrograph showing a large plagioclase crystal with rounded inclusions of quartz and partially resorbed K-feldspar (sample LCZ7-2, locality 0502300/7486236, XPL). Mineral abbreviations are after Kretz (1983).

4.4.2 Garnet (±cordierite)-bearing Leucogranites

These highly leucocratic granites are white, and comprise 1-3 mm grains of K-feldspar (orthoclase, *ca*. 40 %), plagioclase (*ca*. 30%) and quartz (*ca*. 20%), with accessory biotite and monazite and large (5 mm -3 cm) irregular red patches of garnet (Fig. 4.14A) which make up *ca*. 10% of the rock. They are found as narrow (<1 m) boudinaged, folded dykes, or small bodies (Fig. 4.14A, B). These small bodies are

localised along the axial planes of D2 folds, and the leucogranite sheets have been folded and boudinaged during D2 (Fig. 4.14B). These relationships suggest that, like the grey granites, the garnetiferous leucogranites appear to have intruded synchronous with D2. The large masses of garnet are intergrown with quartz (Fig. 4.14C), although they do not appear to be symplectites, as the quartz is not in optical continuity. Rather, they form as a network of garnet, 0.1-1 mm across, with similar 0.1-1 mm quartz grains filling the network. K-feldspar forms large (2-3 mm) subhedral grains, with rounded inclusions of quartz (Fig. 4.14D) and, locally, quartz-feldspar myrmekites are observed (Fig. 4.14D). The accessory biotite occurs as small subhedral laths, and monazite as small, round euhedral grains. In addition to these garnet-bearing leucogranites, similar leucogranites are locally found comprising plagioclase, K-feldspar, quartz, accessory subhedral flecks of biotite and small (0.2-0.5 mm) needles of green-blue tourmaline: these lack garnet but contain irregular masses of cordierite up to 10 cm across.

Garnet- and cordierite-bearing leucogranite sheets are only found associated with metapelitic rocks, generally within the Rössing Formation in the Ida Dome, or the Chuos Formation in the Palmenhorst Dome, and there is a close association of garnet-bearing leucogranites to partially molten metapelitic rocks. Anatectic leucosomes formed from partial melting of metapelites during high-grade Damaran metamorphism are common in the vicinity of the leucogranite sheets, suggesting that in areas with significant amounts of metapelitic material (i.e. the Rössing or Chuos Formations), metamorphism, anatexis, and resultant migmatite formation, led to the formation of bodies of anatectic leucogranite (i.e. the garnet-bearing leucogranites) through the segregation and migration of melt. Their garnetiferous nature, white colour, syn-D2 timing, association with pelitic schists indicates that they are similar to the Type-B leucogranites of Nex & Kinnaird (1995) and Nex (1997).

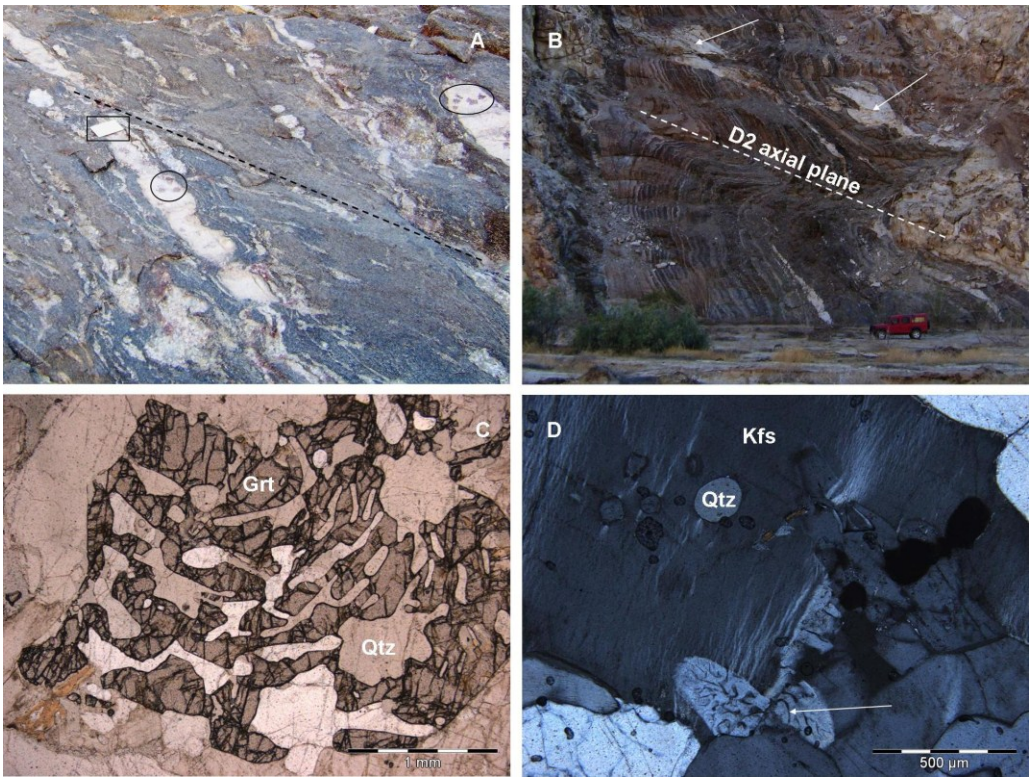

Fig. 4.14 – A: Boudinaged sheet of garnetiferous leucogranite in metapelite from the Rössing Formation. Note the large garnet clusters (circled), and the leucosome aligned with the fabric in the host metapelite (indicated by dashed line). Scale bar (indicated by rectangle) is 10 cm long. Locality 0502755/7485916. B: Folded white garnetiferous leucogranite from the outcrop shown in A. Note the accumulation of large masses of leucogranite near the top of the image (indicated by arrows), subparallel to the axial plane of the D2 folds (axial plane indicated by line). Locality 0502755/7485916. C: Photomicrograph of the garnetiferous leucogranite, showing the intergrowth of quartz and garnet, typical of this granite type (sample LID038, locality 0502755/7485916, PPL). D: Photomicrograph of the garnetiferous leucogranite, showing a large K-feldspar crystal with rounded inclusions of quartz, and a myrmekitic intergrowth of quartz and feldspar (shown by arrow) (sample LID038, locality 0502755/7485916, XPL). Mineral abbreviations are after Kretz (1983).

4.4.3 Uraniferous leucogranites

The presence of U-enriched granites in the Central Zone has been well documented (Jacob *et al*., 1986; Mouillac *et al*., 1986; Bowden *et al*., 1995; Nex *et al*., 2001b; Basson & Greenway, 2004) and these granites are mined for uranium at the Rössing Mine, north of the Palmenhorst Dome. These uraniferous granites occur within both the Ida and Palmenhorst Domes, and are particularly concentrated at or near the contact between the Khan Formation and the Rössing Formation. They are particularly abundant to the east and southeast of the Ida Dome, where they appear to have intruded into numerous tight to isoclinal, km-scale D3 anticlines (Fig. 4.15). These anticlines are cored by Khan Formation, and the rheology contrast between the brittle Khan Formation calc-silicates and the ductile Rössing Formation marbles may have resulted in an accumulation of these granites at this interface (Fig. 4.15).

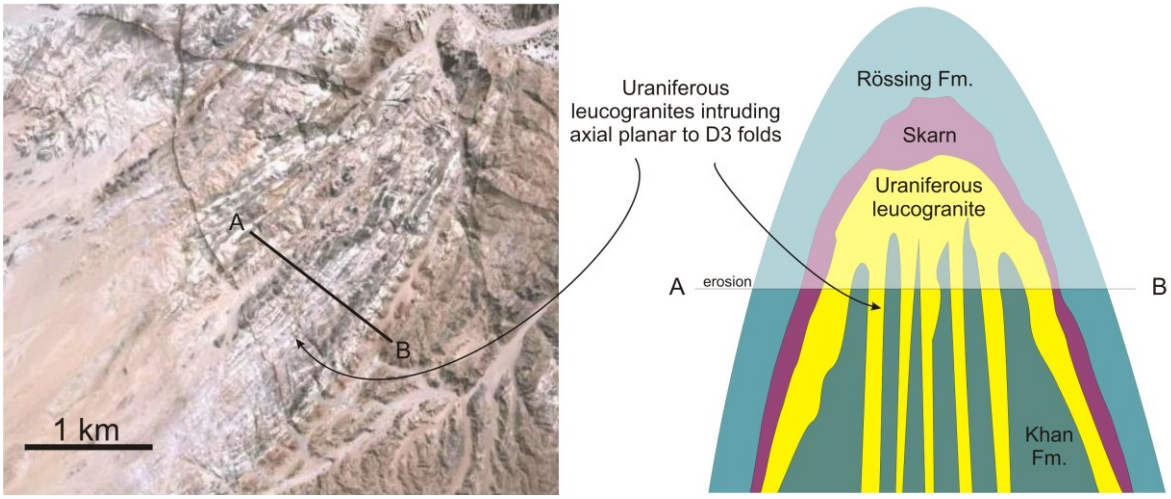

Fig. 4.15 – Google Earth™ image of a D3 anticline east of the Ida Dome, showing axial planar uraniferous leucogranites, and a schematic cross section across the anticline, showing the localisation of these granites at the contact between the Khan and Rössing Formations, and the formation of skarn where granites have reacted with carbonates of the Rössing Formation.

In the field, uraniferous leucogranites appear as massive bodies, continuous along strike of the host metasediments, but on aerial photographs and remote sensed images they are visible as dykes, axial planar to D3 anticlines. A weak fabric is very

rarely observed. The intrusion of these granites along the Khan-Rössing interface, and into the Rössing Formation, has resulted in extensive skarnification caused by reaction of the granites with the Rössing Formation carbonates: this commonly results in ridges of skarn with a garnet-wollastonite-scapolite-diopside assemblage, as remnants of the Rössing Formation. Along the southern margin of the Palmenhorst Dome, uraniferous leucogranites are less voluminous than at the Ida Dome, and intrude as a large body, 10-20 m across, and as 1-5 m wide, subvertical dykes, striking E-W, and cross cutting earlier D2 fabrics. The close association of these uraniferous leucogranites with D3 anticlines suggests that they may be syn-tectonic with the D3 event.

Uraniferous leucogranites are typically very leucocratic, pale pink or cream in colour, with dark (smoky) quartz, although their colour may be variable, as is their grain size – they are generally pegmatitic, but may be medium- to coarse-grained (3-6 mm). They comprise K-feldspar (40-50%), quartz (30-40%) and plagioclase (10-20%), with a variety of accessory minerals, and little to no biotite (Fig. 4.16A). Quartz may show slightly undulose extinction (Fig. 4.16B), and contains rounded K-feldspar inclusions. Quartz grains have irregular grain boundaries. Biotite may have small inclusions of U-bearing minerals, which are surrounded by pleochroic haloes. Many of these inclusions appear to be included along the biotite cleavage (Fig.4.16C). Additionally, some U-bearing minerals are noted, with radiation cracks extending from these minerals into the surrounding minerals due to radiation damage (Fig. 4.16D). The high uranium content of these leucogranites indicates that they may be equivalent with the D- or E-type sheeted granites of Nex & Kinnaird (1995) and Nex (1997). P. Nex (Pers. Comm., 2009) has noted that all uranium-enriched sheeted granites in the Central Zone are likely to be part of a single magmatic event, with locally variable textures resulting in apparent differences between granite types. No uraniferous leucogranites observed in the study area show any of the distinctive oxidation haloes (Corner & Henthorn, 1978) that characterise the E-type granite sheets (Nex & Kinnaird, 1995). Rather, their fairly uniform colour, distinctive smoky quartz and uranium-bearing phases suggests that they are analogous to the D-type sheeted

granites of Nex & Kinnaird (1995), Nex (1997) and Nex *et al*. (2001b), although their variable grain size differs from the homogenous granular texture typically associated with D-type leucogranites (Nex, 1997).

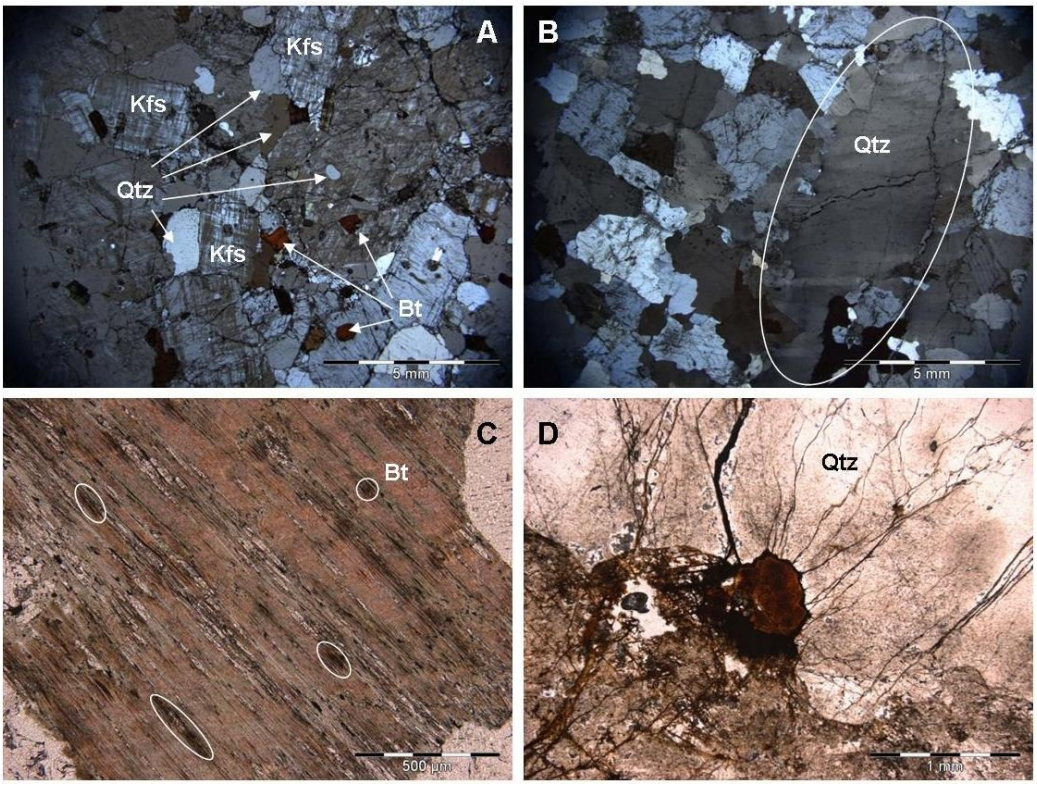

Fig. 4.16 – Photomicrographs of uraniferous leucogranites. A: Typical granite, with large, subhedral K-feldspar crystals, more irregular quartz, and minor amounts of biotite (sample, HILG13, locality 0489174/7489376, XPL). B: Large quartz crystal (circled) with slightly undulose extinction (darker towards the bottom of the image) (sample IDAG5, locality 0503068/7486918, XPL). C: Biotite (partially altered to green chlorite) with numerous uraniferous inclusions (some are circled) resulting in darker pleochroic haloes in the biotite (sample HILG21, locality 0489250/7489485, PPL). D: Dark uranium-rich phase (near centre of image) surrounded by radiating cracks in the adjacent quartz due to radiation damage (sample IDAG46, locality 0503369/7487757, PPL).

Nex *et al*. (2001) noted the emplacement of uraniferous leucogranites in a high-strain zone near the basement-cover contact in the Goanikontes area. They also noted the fact that uraniferous leucogranites are commonly restricted to the boundary between the Khan and Rössing Formations. The emplacement of uraniferous leucogranites is

generally considered to be immediately post-D3 (Nex *et al*. 2001; Kinnaird & Nex, 2007), and appears to be lithologically controlled – uraniferous leucogranites at the Rössing Mine are emplaced at the contact between the Khan and Rössing Formations. The structural control of uraniferous leucogranites from the Ida Dome suggests that they may even be syn-D3, and they are locally emplaced into antiformal structures at the Rössing Mine (Kinnaird & Nex, 2007), indicating a structural as well as lithological control on their emplacement. The emplacement of uraniferous sheeted leucogranites also appears to be related to the transition from ductile to brittle deformation (Kinnaird & Nex, 2007), and has been related to post-D3 brittle deformation (Basson & Greenway, 2004).

4.4.4 Pink pegmatitic leucogranites

These are a voluminously minor phase of granite, and intrude as small (*ca*. 30 cm wide) dykes into brittle fractures, commonly in an en-echelon pattern, or as m-scale bodies, seen to cross-cut grey granites (Fig. 4.17A). They are bright pink and white, comprising large (>3 cm) K-feldspar, milky quartz, and plagioclase feldspar grains, with local 1-3 cm masses of magnetite, and large (2-5 cm) blades of biotite (Fig. 4.17B). Both K-feldspar (orthoclase) and plagioclase may contain rounded inclusions of quartz, and both may also contain irregular contacts with quartz (Fig. 4.17C). Orthoclase is altered to sericite, and locally to muscovite up to 200 µm in size. Quartz appears slightly strained, with rounded, concave grain boundaries. Myrmekitic intergrowths of plagioclase and quartz are also present (Fig. 4.17D).

The pink pegmatitic leucogranites show similarities to the F-type granites, which are red, narrow, tabular and parallel-sided in form, and coarse-grained to pegmatitic (Nex, 1997). The F-type granites also comprise euhedral perthitic feldspar with distinctive interstitial milky quartz and accessory biotite and opaque minerals (Nex, 1997).

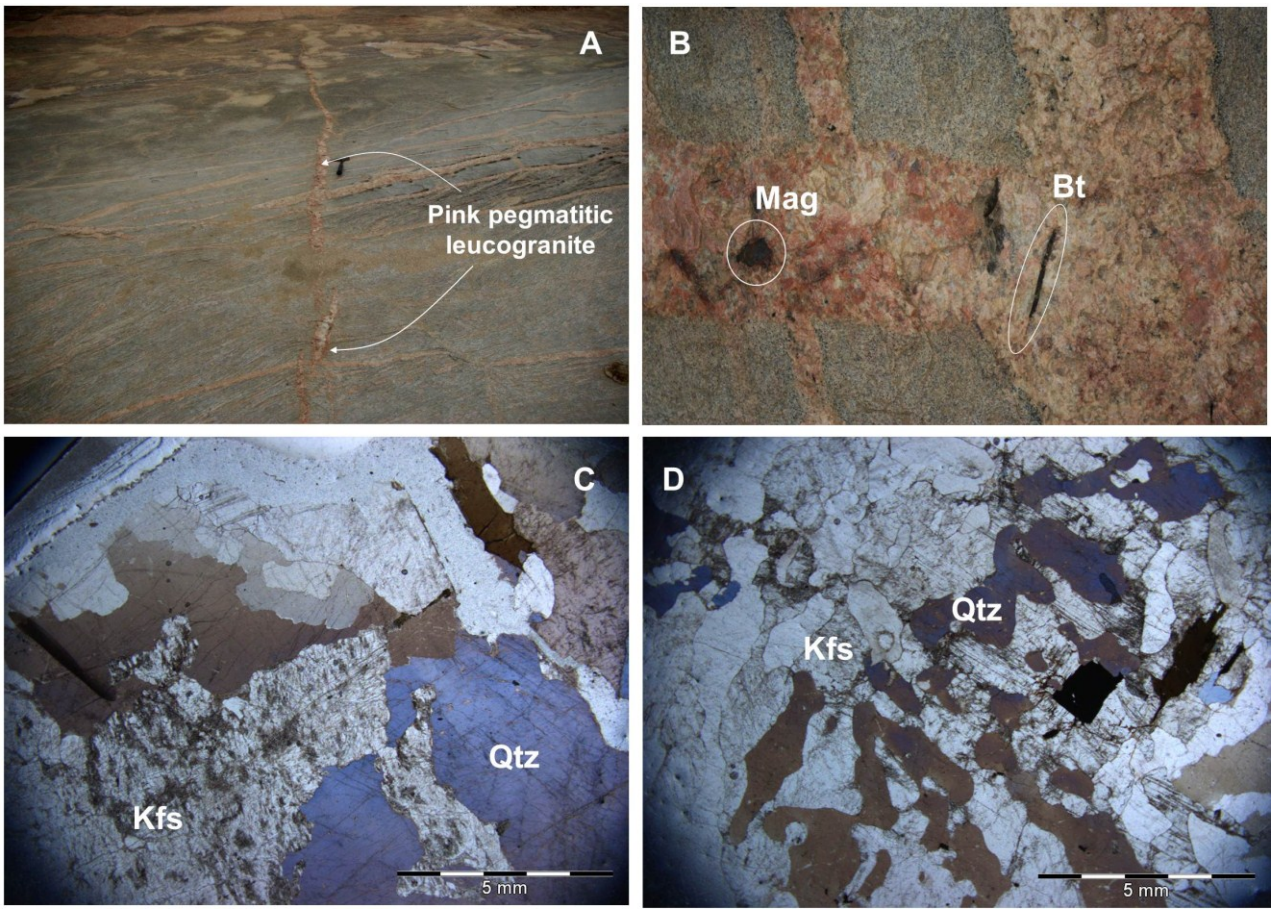

Fig. 4.17 – Pink pegmatitic leucogranites. A: Vein of leucogranite intruding grey granite. Note the en-echelon array pattern of the granite vein. Locality 0500289/7488670. B: Leucogranite vein intruding grey granite, with large biotite and magnetite crystals. Locality 0500289/7488670. C: Photomicrograph of coarse K-feldspar and quartz – note the irregular grain boundaries of the quartz (sample CZF1, locality 0489939/7488741, XPL). D: Photomicrograph of coarse myrmekitic plagioclase and quartz (sample CZF1, locality 0489939/7488741, XPL).

4.4.5 Geochemistry of the sheeted granites

The sheeted granites are voluminously minor in the study area, but are significant to this study owing to their field relationships – detailed studies of their chemistry and mineralogy have previously been conducted by Nex (1997) and Freemantle (Pers. Comm.). Nonetheless, several samples have been analysed, and it is evident that these granites are calcic to alkalic (Fig. 4.18A, B) and, like the majority of granites

analysed in this study, peraluminous (Fig. 4.18C). Some (particularly the uraniferous leucogranites) show elevated U:Th ratios (Fig. 4.18D). REE patterns show more elevated LREE than HREE, and moderate negative or positive Eu anomalies (Fig 4.18E).

Fig. 4.18 (following page) – Geochemistry of the sheeted granites. A: Na_2O+K_2O-CaO vs. SiO_2 diagram, showing that sheeted granites are variably calcic to alkalic, and are highly siliceous. B: Or-An-Ab diagram, showing classification of sheeted granites as granites. C: A/NK vs. A/CNK diagram, showing that sheeted granites are peraluminous. D: Th (ppm) vs. U (ppm), showing that all samples granites have Th/U < 10, with most uraniferous leucogranites having Th/U of < 1. E: Chondrite-normalised REE plot, showing enrichment in the LREE, and small negative or positive Eu anomalies. Chondrite normalisation factors are from Anders & Grevesse (1989). Geochemical data are presented in Appendix 1.

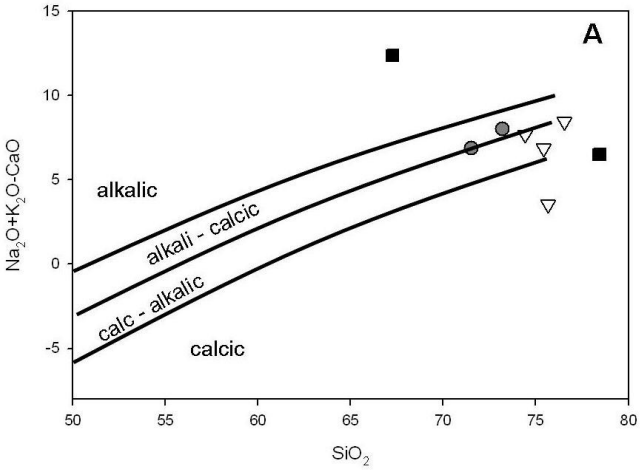
A
alkalic
alkali - calcic
calc - alkalic
calcic
Na_2O+K_2O-CaO
SiO_2

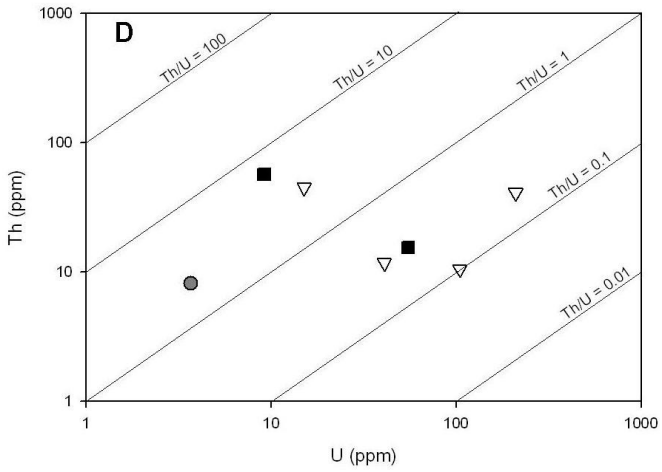
D
Th/U = 100
Th/U = 10
Th/U = 1
Th/U = 0.1
Th/U = 0.01
Th (ppm)
U (ppm)

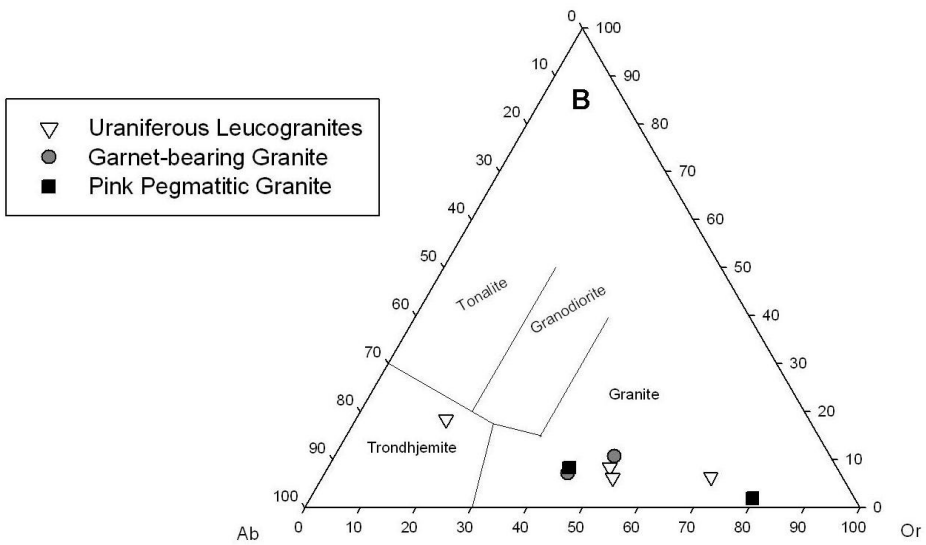
Uraniferous Leucogranites
Garnet-bearing Granite
Pink Pegmatitic Granite
B
Tonalite
Granodiorite
Granite
Trondhjemite
An
Ab
Or

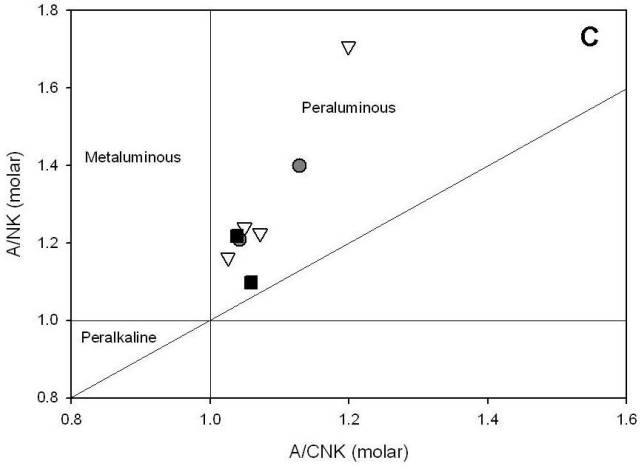
C
Peraluminous
Metaluminous
Peralkaline
A/NK (molar)
A/CNK (molar)

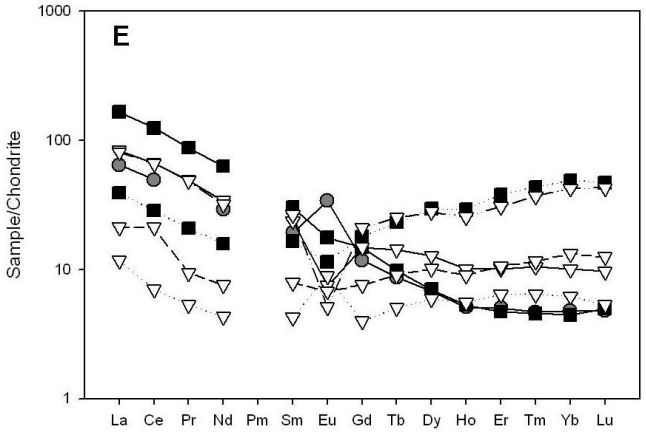
E
Sample/Chondrite
La Ce Pr Nd Pm Sm Eu Gd Tb Dy Ho Er Tm Yb Lu

4.6 Comparison of granite chemistry with the classification of McDermott (1986)

Throughout this chapter, granites have been described based on their field and textural characteristics and their mineralogy, in keeping with the classification schemes of a number of previous workers on the Central Zone (Smith, 1965; Jacob, 1974; Marlow, 1981; Nex, 1997; Miller, 2008). However, McDermott (1986) classified the granitoids of the Central Zone based entirely upon their geochemical and isotopic signatures, rather than their field and petrographic characteristics. According to McDermott (1986), the granitoids of the Central Zone can be subdivided into three categories, namely the crustal-melt granitoids, the calc-alkaline granitoids, and the within-plate granitoids, and these groups are all chemically distinct. The crustal-melt granitoids are characterised by peraluminous compositions, high Rb contents, initial $^{87}Sr/^{86}Sr$ ratios of >0.710, high U and Th contents, low amounts of High Field Strength (HFS) elements (Nb, Y, Zr), old Nd model ages (*ca*. 2.0Ga) and high $\delta^{18}O$. The calc-alkaline granitoids are metaluminous, have both low HFS elements and Rb/Sr ratios, initial $^{87}Sr/^{86}Sr$ ratios of <0.710, model ages of 1-1.4 Ga and variable $\delta^{18}O$. Within-plate granitoids have extremely low CaO, high HFS elements and REE, variable $^{87}Sr/^{86}Sr$ ratios, *ca*. 1.2 Ga Nd model ages, and low $\delta^{18}O$. Although granitoids in this study have not been extensively isotopically characterised, and no Nd model ages or Sr isotopic data have been collected, the granite types defined by McDermott (1986) are recognisable on major and trace element characteristics. Hf model ages and oxygen isotopic data have been collected for the grey granites and these data are discussed in Chapter 5.

An alumina/CaO/alkalis diagram (Fig. 4.19A) shows that most granitoids from the study area are peraluminous, with a few of the grey granites metaluminous. Some of these grey granites fall close to the range for the calc-alkaline diorites (McDermott, 1986). None of the granitoids analysed plot as peralkaline, and none are sufficiently alkali-rich to fall into the field defined by the within-plate granites of McDermott (1986). A plot of 1/Shand index (CNK/A) vs. HFS elements Nb + Y (Fig. 4.19B) shows that almost all samples plot as crustal-melt granites, and none fall into the within-plate granite field (McDermott, 1986). A few of the grey granites have elevated Mol.

% ($Na_2O + K_2O + CaO)/Al_2O_3$ and plot close to the calc-alkaline diorites of McDermott (1986). The grey granites which show high CNK/A (Fig. 4.19A) and have elevated ($Na_2O + K_2O + CaO)/Al_2O_3$ (Fig. 4.19B) are the least leucocratic of the grey granites, and are dioritic in composition. A plot of Rb/Zr vs. HFS elements Nb + Y + Zr (Fig. 4.19C) shows that none of the granites analysed have elevated HFS element contents comparable with the within-plate granites of McDermott (1986), and that most have elevated Rb/Zr, consistent with their being crustal melt granitoids. Whilst most grey granites appear similar to the calc-alkaline diorites of McDermott (1986), some have elevated Nb + Y + Zr and Rb/Zr values – these are the most leucocratic (most fractionated) of the grey granites. Overall, granite samples show affinities to the crustal-melt granitoids of McDermott (1986), with a few dioritic grey granites showing similarities to the calc-alkaline diorites of McDermott (1986). The fairly low levels of HFS elements, and the high Rb contents of the granites are consistent with melting of crustal material to produce these granites.

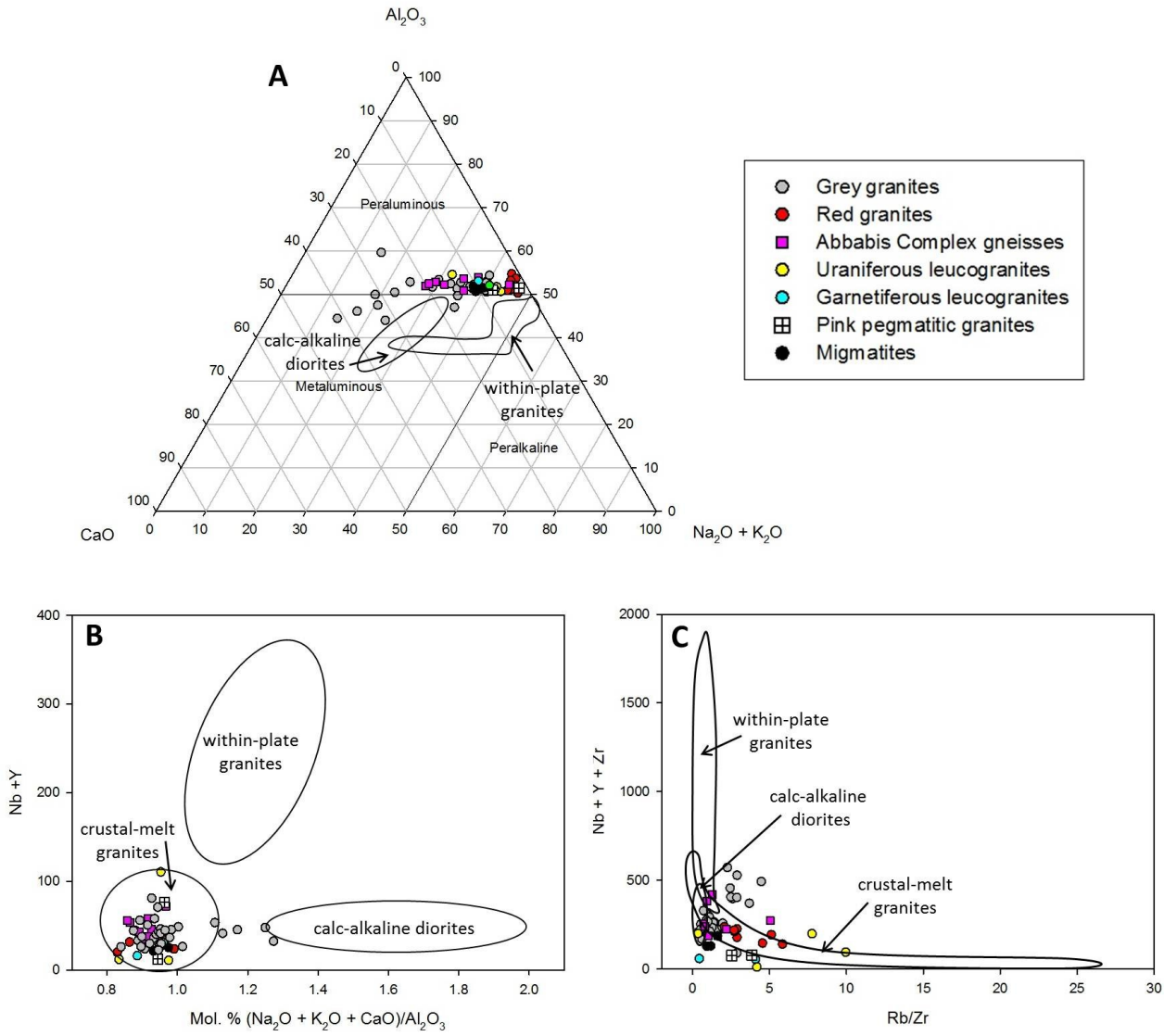

Fig. 4.19 – Geochemistry of the granites from this study in comparison with the classifications of McDermott (1986). A: Alumina/CaO/alkalis diagram, showing that most granites are peraluminous, with some dioritic grey granites metaluminous. B: 1/Shand index vs. Nb + Y diagram, showing that most samples plot as crustal-melt granites, with the exception of a few grey granite samples which plot nearer the calc-alkaline diorites. C: Rb/Zr vs. Nb + Y + Zr diagram, showing that most samples plot as crustal-melt granites, with grey granites showing a possible fractionation trend away from calc-alkaline diorites. Fields for crustal-melt granites, within-plate granites and calc-alkaline diorites are from McDermott (1986).

4.7 Discussion

The variety of intrusions, ranging from amphibolite dykes to leucogranite sheets, have distinctive relationships to deformation and metamorphism in the study area. A summary of the intrusions, their structural and metamorphic contexts, and possible analogous intrusions studied by previous workers are shown in Table 4.2. The classification of Miller (2008) is the most recently published taxonomy for the granitoids of the Central Zone. However, there are some differences between this classification (Table 4.1) and the classifications of the granites of the Central Zone provided other workers. The results of the current study are discussed in the context of all the previous work on the classification of granites in the Central Zone.

Table 4.2 – Summary of the various intrusions found in the study area, their timing relative to deformation and metamorphism, and the various intrusions types with which they are analogous.

Intrusive rock type	**Timing relative to other events**	**Analogous to:**
Uraniferous Leucogranite	Post-D2, syn- to post-D3	Crustal-melt granitoids (McDermott, 1986), D-type sheeted leucogranites (Nex, 1997)
Pink Pegmatitic Granite	Cross-cuts grey granite, but affected by late D2 shear bands	Crustal-melt granitoids (McDermott, 1986), F-type sheeted leucogranites (Nex, 1997)
Garnet (±cordierite)-bearing Leucogranite	Syn-D2. Contemporaneous with peak metamorphic grades, as they are formed from anatexis of Damaran metapelites	Crustal-melt granitoids (McDermott, 1986), B-type sheeted leucogranites (Nex, 1997)
Quartz-Feldspar-Magnetite Pegmatitic Granite	Syn-D2 - intruded along axial planes of D2 folds, rotated by D3	Crustal-melt granitoids (McDermott, 1986), C-type sheeted leucogranites (Nex, 1997)
Grey Granite	Syn-D2 - intruded along axial planes of D2 folds, folded by D2, cut by D2 shear bands	Red and grey homogeneous syntectonic granites (Brandt, 1985), calc-alkaline diorites? (McDermott, 1986), equigranular grey granites (Nex, 1997), non-porphyritic granites and leucogranites (Miller, 2008)
Red Granite	Predate D2 deformation, contemporaneous with a high-T metamorphism as they are anatectic products of melting the Abbabis Complex	Red gneissic granite (Smith, 1965), red granite-gneiss (Jacob, 1974), red inhomogeneous syntectonic granites (Brandt, 1985), crustal-melt granitoids (McDermott, 1986), Basement-hosted Granite or equigranular red granite (Nex, 1997)
Amphibolite	Postdate gneissic fabrics in the Abbabis Complex, predate D2 deformation	Pre-Damaran amphibolites (Barnes, 1981; Steven, 1994), calc-alkaline diorites? (McDermott, 1986), Goas Intrusive Suite (specifically Audawib Suite - De Kock, 1991)

One of the most common, widespread, voluminous granite types in the Central Zone is the Salem-type biotite granite (Miller, 2008), also referred to as “Salem Gneiss and Granite” (Smith, 1965), the “Salem Granite Suite” (Jacob, 1974), the “Salem Granites” (Brandt, 1985) and the “Salem-type granites” (Marlow, 1981). Despite its common occurrence, it was not noted by Nex (1997) in the southwestern Central Zone in the Goanikontes area, and has not been seen in this study. It is, however, the most abundant rock type in the Damaran plutonic suite, and is thought to be pre-or syn-D2 in age. The Salem-type granites are largely monzogranitic to granodioritic in composition (Miller, 2008), and were postulated by Smith (1965) to be related to dioritic rocks in the Central Zone (the Goas Intrusive Suite – Lehtonen *et al*., 1996). However, Salem-type graniotids were classified as crustal melt granitoids by McDermott (1986), and distinguished geochemically from calc-alkaline diorites. The oldest intrusions in the study area are the amphibolites and, although some of these may be pre-Damaran (found exclusively in the Abbabis Complex gneisses), amphibolites also cross-cut the fabric in the Abbabis Complex gneisses, and are thus younger than this gneissic fabric. Amphibolites also cross-cut Damara Supergroup rocks (Jacob, 1974; P. Nex, Pers. Comm., 2009), and thus are Damaran in age. Although geochemical tectonic discrimination diagrams are inconclusive as to the tectonic setting of the amphibolites, they do show some similarities in their major elements to mafic rocks of the Goas Intrusive Suite (Lehtonen *et al*., 1996), analysed by De Kock (1991) (who termed them the Audawib Suite). They may therefore be related to the Goas Intrusive Suite and may be an early phase of Damaran magmatism. Their emplacement does not appear to be controlled by any structures and, although they occur in Abbabis Complex gneisses in the study area, they are not necessarily stratigraphically localised within the Abbabis Complex. They are folded by SE-verging F2 folds, and aligned amphiboles define a fabric subparallel to the S2 fabric in the study area, indicating that they predate D2 deformation. Their alteration from pristine mafic rocks to amphibolites is likely to have occurred during high-grade Damaran metamorphism.

Red gneissic granites are also commonly recognised by earlier workers. Smith (1965), Jacob (1974), Brandt (1985) and Nex (1997) all have a similar granite type described as “red gneissic granite”, “red granite-gneiss”, “red inhomogeneous syn-tectonic granite”, and “red granite”, respectively. These granite types are all red, and share common features, such as their restricted emplacement near the interface between the Nosib Group and Abbabis Complex, their inhomogeneous nature, the fact that they are K-feldspar-rich, and their gneissic fabric, and they are thought to have formed from largely in-situ migmatisation of the Abbabis Complex or lower Damara Supergroup (Smith, 1965; Miller, 2008). Red granites appear to be the oldest granite type in the study area – they are never seen to cross-cut any other granites, and they contain a well-defined D2 gneissic fabric, subparallel to the regional S2 fabric in Damara Supergroup rocks. They are K-feldspar rich, stratigraphically localised near the contact between the Abbabis Complex and the Etusis Formation, and contain xenoliths of Abbabis Complex gneiss, suggesting that they are analogous to the red gneissic granite of Smith (1965), the red granite-gneiss of Jacob (1974), the red inhomogeneous syn-tectonic granites of Brandt (1985) and the basement-hosted granite of Nex (1997). These granites were thought to be derived from anatexis of the Abbabis Complex or Etusis Formation (Smith 1965). However, some confusion exists as to the timing of these granites relative to tectonic events in the Central Zone. Whilst some workers considered the red gneissic granites to have been emplaced early in the history of the Central Zone (Brandt, 1987), and possibly syn- to late tectonic (Jacob, 1974), and the red granites from this study were clearly emplaced pre- or syn-D2, Miller (2008) considers them to be post-tectonic anatectic upper-crustal granites, and applies the term red gneissic granites to relatively homogeneous, equigranular, anatectic red granites that are markedly foliated and confined to anticlinal structures below the level of the Rössing Formation (Miller, 2008). The fabric in these granites is considered by Miller (2008) to be a ghost foliation, remnant after near-total in-situ melting of precursor gneisses. However, as discussed (see section 4.2), near-total in-situ melting is highly improbable, and xenoliths of gneiss in the red granites have fabrics that are oblique to the gneissic fabric in the red granite, indicating that the strong gneissic fabric in these granites is in fact a D2 tectonic fabric

(which is subparallel to the fabric in adjacent Damara Supergroup rocks). Thus, these red granites cannot be considered as post-tectonic in the southwestern Central Zone, when they clearly are pre- or syn-D2 in the study area. The red granites according to Marlow (1981) are not restricted to inhomogeneous gneissic granites found only in the western portion of the Central Zone and emplaced only into the lower Damara Supergroup or the Abbabis Complex, but also include dykes of fine-grained, aplitic red granites further east, which may intrude Salem-type granites. Some of the red granites described by Marlow (1981) are medium-grained and equigranular.

Grey granites are not a widely described granite type in the southwestern Central Zone, but are the most voluminous granites in the study area. The grey granites form a suite of syn-tectonic, foliated, equigranular, fine- to medium-grained, locally porphyritic intrusions of dioritic to granitic composition, which are peraluminous to weakly metaluminous and calcic to alkalic. Although typically light to dark grey, grey granites locally show a red colour where altered. They range in composition from almost dioritic to leucogranitic, have Th:U ratios of >1, and show fractionation trends, which are reflected in both major and trace element compositions. They are not stratigraphically localised, as they occur in both the Abbabis Complex and Damaran metasediments. They were emplaced along the axial planes of F2 folds and folded by F2 folds, and are partially affected by late-D2 shear bands, showing clearly that they were emplaced coeval with D2 in the study area. The grey granites and are correlated on the basis of mineralogy, field characteristics and chemistry with the red and grey homogeneous syn-tectonic granites of Brandt (1985) and the homogeneous, fine- to medium-grained equigranular red or grey granites of Nex (1997), which contain a strong biotite foliation. They are also probably part of a suite of early non-porphyritic granites and leucogranites according to the classification of Miller (2008), which are generally found in the northern Central Zone, and which are syn-D2 (Klein, 1980; Haack *et al*., 1980; Badenhorst, 1986). Although thought to be a minor granite phase in the southern Central Zone (Miller, 2008), they are seen to be voluminously significant in the study area. The fact that they are affected by late-D2 shear bands indicates that they were emplaced in the early stages of D2, preceding the late-D2

NE-SW directed extension. Within the study area, the grey granites appear to be associated with quartz-feldspar-magnetite pegmatitic granites, and show similar structural relationships to quartz-feldspar-magnetite pegmatites. These have also been emplaced axial planar to F2 folds, and have been affected by upright D3 folding, and thus pre-date D3 folding. Pink pegmatitic leucogranites, which cut the grey granites, are also partially affected by late-D2 extension, and thus may only be slightly younger than the grey granites, and not entirely post-tectonic. Questions regarding the timing of emplacement of the grey granites, the timing of D2 deformation, and isotopic studies to constrain the source of the grey granites are further addressed in Chapter 5.

Numerous varieties of sheeted granites have previously been described, and may be syn- or post-tectonic. Within the study area, quartz-feldspar-magnetite pegmatitic granites appear, based on mineralogy and field characteristics, to be analogous to the C-type sheeted leucogranites described from the Goanikontes area by Nex & Kinnaird (1995) and Nex (1997). These C-type leucogranites also occur as veins, sheets or dykes, comprise K-feldspar and plagioclase, are coarse to pegmatitic, have interstitial quartz, and contain clusters of accessory minerals such as magnetite or ilmenite. These are the most voluminous of the sheeted leucogranites described by Nex & Kinnaird (1995), and are emplaced into fold flexures (Nex & Kinnaird, 1995). However, these fold flexures are considered by Nex & Kinnaird (1995) to be F3 folds, rather than F2 folds, which in this study control the emplacement of the quartz-feldspar-magnetite pegmatitic granites. The axial-planar geometry of dykes of this granite type relative to F2 folds, and the rotation of granite sheets by upright D3 folding, constrains them, like the grey granites, to emplacement coeval with D2 deformation. Thus, like the grey granites, an age for the quartz-feldspar-magnetite pegmatitic granites should constrain D2 deformation in the study area. Locally, quartz-feldspar-magnetite pegmatitic granites occur in close proximity to the grey granites (Fig. 4.10C, D), and this, together with the similar style of intrusion and structural context (syn-D2), suggests that they are related. Although no geochemistry on the quartz-feldspar-magnetite pegmatitic granites has been collected during this study, Freemantle (Pers.

Comm.) has analysed a number of samples of this granite type. These data (Figs. 4.11, 4.12) show that quartz-feldspar-magnetite pegmatitic granites have a much more variable geochemistry than the grey granites, and are generally granitic in composition (Fig. 4.11A, B), variably calcic to alkalic (Fig. 4.11C), and consistently peraluminous (Fig. 4.11D). Unlike the grey granites, they do not show evidence for a fractionation trend (Fig. 4.12A, B), and have greater U:Th ratios than the grey granites or Salem-type granites (Fig. 4.12C).

The pink pegmatitic leucogranites also share characteristics with the F-type leucogranites – they are coarse to pegmatitic, and comprise pink perthitic feldspar and milky quartz. However, although in most occurrences the pink pegmatitic leucogranites are tabular and cross-cut structural features (like the post-tectonic F-types of Nex & Kinnaird, 1995), they are locally affected by late-D2 shear bands, indicating that they may not necessarily be post-tectonic. Thus, any correlation between sheeted granites and the variety of sheeted leucogranites described from the Goanikontes area (Nex & Kinnaird, 1995) is made with the caveat that local variability of sheeted leucogranites may occur, and such comparisons are tenuous.

Sheeted granites may also host uranium mineralisation and, on the basis of this particular characteristic, it is possible to correlate these. The terms “alaskitic pegmatitic granite” (Jacob, 1974), “alaskites or leucogranites” (Brandt, 1985), or “alaskites” (Marlow, 1981) have all been applied to these granites, although not all uraniferous granites are strictly alaskites in terms of comprising predominantly quartz and alkali feldspar, and not all so-called alaskites necessarily host uranium mineralisation. Nex & Kinnaird (1995) and Nex (1997) subdivided sheeted leucogranites hosting uranium mineralisation into D- and E-types, which were structurally localised in a high-strain zone, and were distinguished from one another by the characteristic oxidation haloes in E-type leucogranites. This study does not distinguish between D- and E-type leucogranites. Uraniferous leucogranites were considered by Nex & Kinnaird (1995) to be post-D3, and uraniferous alaskites are widely considered to be one of the last phases of magmatism in the Central Zone (Jacob, 1974; Marlow, 1981; Brandt, 1985; Miller, 2008). Basson & Greenway (2004)

considered that emplacement of uraniferous leucogranites was closely linked to late-kinematic evolution of the Rössing Dome, during late-D3 to early-D4 brittle-ductile transition. The emplacement of uraniferous leucogranites from the Ida Dome appears to have been controlled by upright F3 folds, and sheets of leucogranite were emplaced axial planar to these F3 folds, and accumulated at the contact between the Khan and Rössing Formations in anticlinal hinge zones of these folds. The emplacement of uraniferous leucogranites at the contact between these two formations has been noted at Rössing Mine (Kinnaird & Nex, 2007) and at the Goanikontes deposit (Nex *et al*., 2001).

Anatectic (garnet- and cordierite-bearing) leucogranites sheets show a close spatial association with partially melted metapelitic rocks of the Rössing or Chuos Formations, and with anatectic melts of these pelitic rocks. The large poikiloblastic garnet within these granites are likely to be entrained peritectic products of the melting reaction, and they are suggested to be locally derived anatectic melts. Anatectic leucosomes in Kuiseb Formation schists from the Blauer Heinrich syncline (Ward *et al*., 2008; Kisters *et al*., 2009) also contain large (5-12cm) poikiloblastic peritectic garnets, and show clear relationships with D2 deformation – they are seen occupying extensional fractures subparallel to the regional NE-SW D2 extension direction, or in boudin necks, and leucosomes may be folded by D2. They show relationships to leucogranite sills and dykes which are also folded and boudinaged during D2 deformation (Kisters *et al*., 2009). In the area studied by Ward *et al*. (2008), the large amounts of pelitic Kuiseb Formation schist has given rise to significant volumes of anatectic leucosomes and garnet-bearing granite bodies. However, only minor amounts of metapelitic material (in certain pelitic horizons within the Rössing and Chuos Formations) are found in the study area, and this granite type is voluminously minor, reflecting the minor amount of suitable fertile metapelite. The relationships between anatectic leucosomes, garnet-bearing leucogranites and D2 deformation confirms that upper-amphibolite to granulite facies metamorphism was coeval with D2 folding and NE-SW directed extension in the southwestern Central Zone, rather than being post-tectonic, and makes the age of these granites a proxy for

the age of deformation and high-grade metamorphism in the Central Zone (see geochronology, Chapter 5).

These garnet-bearing leucogranites can be correlated with the B-type sheeted leucogranites (Nex & Kinnaird, 1995; Nex, 1997), which are white, fine- to coarse-grained, and commonly contain accessory minerals including garnet and tourmaline, with macroscopic garnet only having been observed where sheets are emplaced into garnetiferous schists. The B-type granites are thought by Nex (1997) to be folded by F3 folds, indicating their pre-D3 timing, and garnet-bearing leucogranites from this study were clearly emplaced syn-D2 – they are folded and boudinaged by D2, and are emplaced along the axial planes of D2 folds. Other late- to post-tectonic leucogranites in the Central Zone form stocks, dykes or sills (the Donkerhuk, Bloedkoppie, Gawib, Achas and Kubas granites; Jacob, 1974; Brandt, 1985; Marlow, 1981), but these distinct bodies and are not found within the study area. The Donkerhuk granite, the largest granite batholith in the Damara Belt, is not strictly a granite of the Central Zone, as it was emplaced on the northern edge of the Southern Zone, approximately along the the Okahandja lineament (the boundary between the Central and Southern Zones). The abundance of biotite and muscovite (each averaging 4%), and the presence of accessory garnet (Miller, 2008) suggests that this peraluminous granite is the product of melting of a heterogeneous upper crust (Miller, 2008), probably of metasedimentary material (McDermott, 1986), and it may be related to high-grade metamorphism in the Damara belt (McDermott, 1986).

4.8 Implications for the tectonometamorphic evolution of the Central Zone

This chapter has described the various intrusive rocks found in the study area, and compared them to the results of previous studies of the intrusive rocks of the Central Zone. These intrusions commonly display distinctive relationships with deformation and metamorphism and, thus, dating of these rocks could help to resolve the ages for deformation and metamorphism in the Central Zone. U-Pb zircon dating of the amphibolites may resolve whether these are pre-Damaran, or are related to the Goas Intrusive Suite, as well as defining an upper limit on the age of D2 deformation (since

they are folded by D2 and have an S2 fabric). Additionally, any metamorphic overgrowths on zircons which occurred during high-grade metamorphism and amphibolitisation of the precursor mafic dykes may give an age for this metamorphic event. Red granites contain a strong D2 gneissic fabric (and are considered here to be pre-D2, although they may be syn-D2), and thus D2 must be younger than the age of the red granites. An accurate age for these red granites would place an upper limit on D2 deformation in the southwestern Central Zone. Furthermore, the red granites are widely considered to be anatectic products of the Abbabis Complex or Etusis Formation (Smith, 1965; Jacob, 1974; Miller, 2008). U-Pb dating may constrain the age of the high-grade event which led to anatexis, and inherited zircons may confirm whether the source of these granites is indeed the Abbabis Complex or Etusis Formation. The grey granites display clear syn-tectonic relationships to D2, as do the quartz-feldspar-magnetite pegmatites, and the garnet-bearing leucogranites. Dating of these three granite types would constrain the timing of D2 deformation, and an age for the garnet-bearing leucogranites (which contain entrained peritectic garnet and are the product of partial malting of metapelitic rocks) would give an age for peak metamorphism in the southwestern Central Zone. Ages for uraniferous leucogranites would also place an upper limit on D3 deformation, and confirm the 508 Ma age (Briqueu *et al*., 1980) for this granite type. These issues are addressed further in the following chapter, which deals with U-Pb zircon, monazite and titanite dating of the granite types in the study area, and also addresses the sources of some of these granites using Lu-Hf and O-isotope studies on zircons from granites and Abbabis Complex gneisses.

CHAPTER 5 – GEOCHRONOLOGY AND ISOTOPE GEOCHEMISTRY

Igneous rocks provide crystallisation ages that can be used to constrain the timing of deformation and metamorphism, where field relationships have been established between intrusions, deformation and metamorphism. These relationships have been established in the preceding chapters for the study area, although it has been pointed out that correlation problems exist across the Central Zone. The problems are not only in terms of petrological differences between various igneous rocks, but also with previously determined ages from other parts of the Central Zone, which are largely less reliable Rb-Sr ages. In addition to dating intrusions, the timing of metamorphism (and any deformation with which it is associated) may also be confirmed by dating anatectic granites generated at the peak of metamorphism in the study area. The ages of the pre-Damaran gneisses of the Abbabis Complex and numerous amphibolites emplaced therein have been raised previously, and this issue is most easily addressed through dating of these lithologies. Further confirmation of metamorphic ages may also be obtained by dating metamorphic overgrowths on zircons in Abbabis Complex gneisses or amphibolites. In this chapter, the results of high-resolution U-Pb zircon, monazite and titanite dating performed on a variety of intrusive rocks from the study area and elsewhere in the Central Zone are presented.

In addition to U-Pb dating of amphibolites, granitoids and Abbabis Complex gneisses, Lu-Hf and O-isotopic analyses have been carried out on selected samples. A final question relating to the source of granites is the focus for the isotope geochemistry at the end of this chapter – what is the source of the granitoids in the Central Zone? McDermott (1986) addressed this question using the Rb-Sr system and Nd-isotopes for samples from Damaran metasediments and granitoids, and here the Lu-Hf isotope and O-isotope characteristics of zircons from one sample of Abbabis Complex orthogneiss and one sample of grey granite have also been analysed, in order to characterise the model ages for the Abbabis Complex and compare these with the results of McDermott (1986). This should indicate whether the grey granites, which

are the most voluminous granite type in the study area and which are present throughout the Central Zone, are sourced from the Abbabis Complex or whether they have a different source.

Samples of Abbabis Complex gneisses, amphibolite dykes, Damaran granitoids and anatectic leucosomes have been selected for U-Pb SHRIMP dating, and two samples have been selected for SHRIMP O-isotopic analysis and LA-ICP-MS Lu-Hf isotopic analysis in order to answer the questions of timing of deformation and metamorphism in the Central Zone, and to investigate relationships to other intrusives previously dated (Table 5.1). Whilst most samples come from within the study area, two come from outside of the study area. A sample of amphibolite was selected from the farm Abbabis 70 near Karibib, *ca*. 100 km northeast of the study area, and one sample of uraniferous leucogranite was selected from the Valencia uranium deposit, *ca.* 40 km northeast of the study area. Table 5.1 shows the samples selected for analysis, their location, and the purpose of analysing each sample.

Table 5.1 – Samples selected for geochronological analysis.

Sample	Locality	Description	Reason for dating
LID036	0500422/ 7487668	Quartzofelspathic gneiss from the Abbabis Complex, centre of the Ida Dome	To date the gneisses of the Abbabis Complex
LID041	0500773/ 7487516	Quartzofeldspathic L-tectonite from the Abbabis Complex, centre of the Ida Dome	To date the gneisses of the Abbabis Complex
LID045	0504090/ 7484518	Quartzofelspathic gneiss from the Abbabis Complex, Arcadia Inlier	To date the Abbabis Complex, and for Lu-Hf and O-isotope analysis to compare with Lu-Hf isotopes of grey granites
ACAM-1	0575111/7 550403	Deformed amphibolite found within Abbabis Complex rocks on the type-locality at the farm Abbabis 70 near Karibib	To date the amphibolites in the Abbabis Complex, and check whether they are pre-Damaran, or related to the Goas Intrusive Suite
LKR021	0495396/ 7500431	Folded amphibolite from an outcrop of Abbabis Complex gneisses along the Khan River in the Palmenhorst Dome	To date the amphibolites in the Abbabis Complex - this sample cuts a fabric in Abbabis Complex gneisses, and thus may be Damaran in age (Related to the Goas Intrusive Suite?)
LHA012	0489766/ 7489118	Early (mafic) grey granite from the southern margin of the Palmenhorst Dome near the farm Hildenhof	To date the grey granites - the emplacement of these granites is controlled by D2 structures, hence this will also date D2 deformation
LHA010	0489766/ 7489118	Late (leucocratic) grey granite from the southern margin of the Palmenhorst Dome near the farm Hildenhof	To date the grey granites - the emplacement of these granitesis controlled by D2 structures, hence this will also date D2 deformation. Also to analyse for Lu-Hf and O-isotopes, to compare with data from the LID045 and McDermott (1986)
LRV001	0484256/ 7491615	Uraniferous leucogranite from "Rabbit Valley" near the farm Goanikontes along the Swakop River	To date uraniferous leucogranites. Since these granites postdate D3 and are emplaced in D3 structures this will constrain the age of D3
LVA001	0523854/ 7528870	Uraniferous leucogranite from farm Valencia near Usakos	To date uraniferous leucogranites - these granites are emplaced into the hinge zone a D3 fold (Freemantle, 2011), and hence this age should date D3
LCZ 7-2	0502300/ 7486236	Quartz-feldspar-magnetite pegmatitic leucogranite from the Ida Dome	To date these voluminous pegmatitic granites, which are emplaced into D2 structures, and hence should date D2. To check whther they are related to grey granites
LID038	0502755/ 7845916	Anatectic garnetiferous leucogranite from partially melted Rossing Formation metapelite, Ida Dome	To date these anatectic leucogranites, the age of metmorphism (since these are anatectic products produced during high-grade metamorphism), and to confirm the age of D2
LKR016	0500360/ 7504659	Red granite from the northern margin of the Palmenhorst Dome	To date the red gneissic granite, place an upper limit on the timing of D2. Inherited zircons should give an indication of the precursor, and should constrain the age of anatexis to produce this granite.
CZF-2	0500574/ 7457122	Pink pegmatitic leucogranite from the Ida Dome	To date this granite type, confirm the timing to late-D2, and possibly to date the 'F-type' pegmatites of Nex (1997).
CZRL-1	0499125/ 7486844	Anatectic melt pool from a SE-verging D2 shear zone along the western margin of the Ida Dome	To date high-grade metamorphism and D2 shearing
CZRL-3	0500289/ 7488670	Anatectic leucosome from a D2 extensional shear band developed in Abbabis Complex gneisses near the western margin of the Ida Dome.	To date high-grade metamorphism and D2 shearing

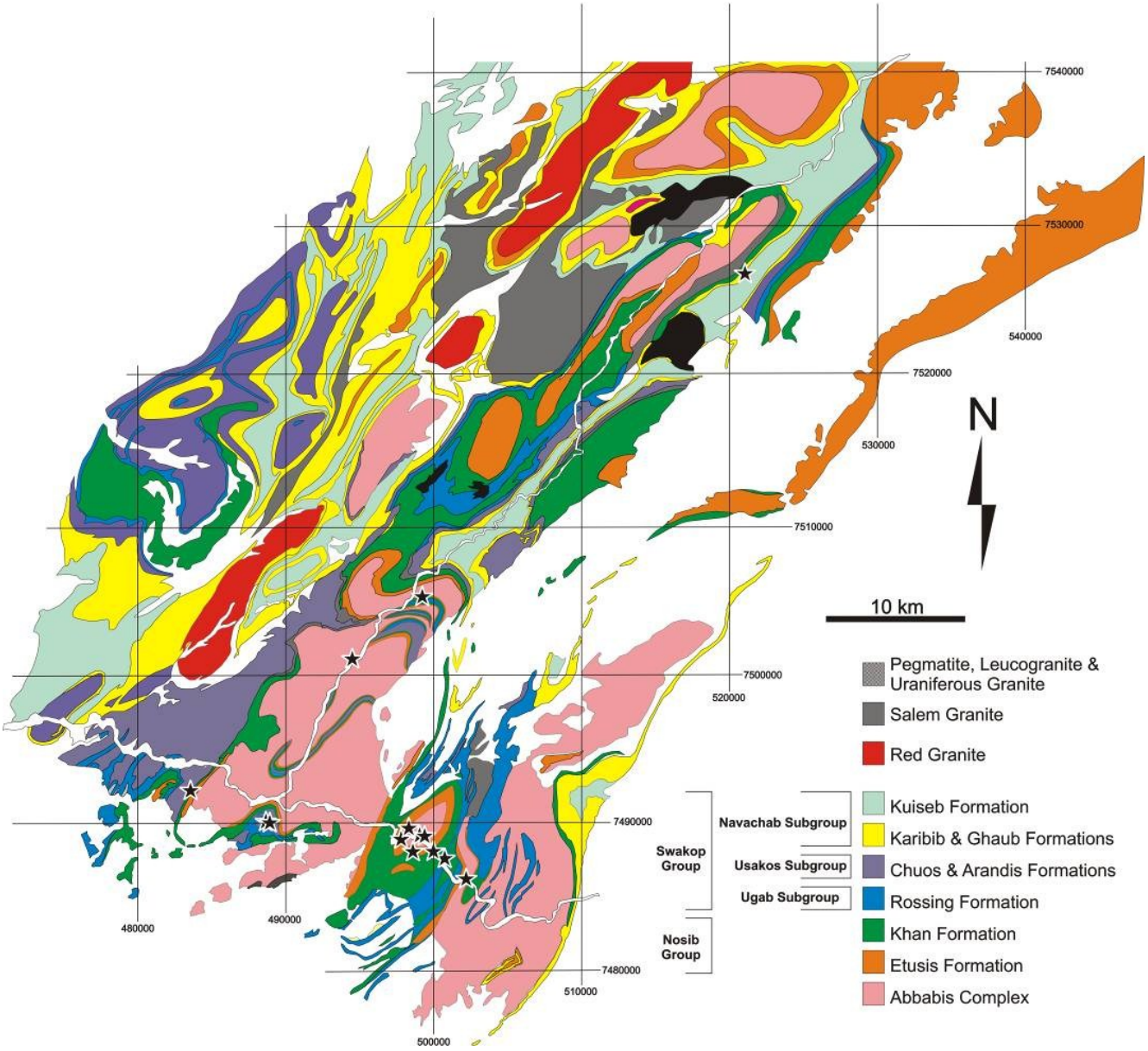

Fig. 5.1 – Geological map of the Central Zone, showing the locations of samples collected for geochronology. Sample localities are given in Table 5.1.

5.1 – SHRIMP U-Pb Geochronology

Each sample collected and analysed has been selected in order to try and answer a question relating to the age of intrusive rocks in the Central Zone, the timing of deformation and metamorphism in the Central Zone, and the source of the granitoids in the Central Zone. Samples have been collected of Abbabis Complex gneisses, amphibolites, red granite, grey granite, quartz-feldspar-magnetite pegmatitic granite, garnet-bearing leucogranite, uraniferous leucogranite, and pink pegmatitic granite. Additionally, two samples of leucosomes from D2 structures have been collected. For each of these samples, the sampling rationale, detailed field description, petrographic description, and description of the zircons (±monazites and/or titanites) is provided below. Geochronological data and analytical procedures can be found in Appendix 2.

5.1.1 Abbabis Complex gneisses

There is a wide range in the ages quoted for for the Abbabis Complex in published age data. The orthogneisses were originally dated at 1925 $^{+330}/_{-280}$ Ma in the Abbabis Inlier near Usakos (Jacob *et al.*, 1978), but later dating gave ages of 1040-1100 Ma for samples along the Khan River (Kröner *et al.*, 1991). Inherited zircons from Damaran granitoids gave an age of 2164 ± 6 Ma (Jacob *et al.*, 2000) and *ca*. 2050 Ma (Tack *et al.*, 2002). An augen gneiss from the Ida Dome has also given an age of 2038 ± 5 Ma (Tack *et al.*, 2002). Three samples of Abbabis Complex gneisses (see section 2.1 for descriptions of the Abbabis Complex) have been collected from the Ida Dome and Arcadia Inlier, namely LID036, LID041 and LID045 (Table 5.1). They have been sampled in order to either corroborate previous *ca*. 2 Ga ages for the Abbabis Complex (Jacob *et al.*, 1978; Jacob *et al.*, 2000; Tack *et al.*, 2002) or to check whether these gneisses are 1040-1100 Ma in age (Kröner *et al.*, 1991).

5.1.1.1 Descriptions of samples and zircons analysed

Sample LID036 is a quartzofeldspathic orthogneiss from near the centre of the Ida Dome (locality 0500422/7487668). The rock is coarse-grained, with a strong N-dipping gneissic fabric consisting of elongate quartz-plagioclase augen wrapped by biotite, and comprises quartz, biotite, plagioclase and magnetite. Quartz is slightly strained, has highly irregular grain boundaries, local cuspate grain edges, and numerous inclusions of unstrained quartz are found as inclusions in feldspar (see Fig. 2.4), suggesting that the rock has partially melted (Sawyer, 2008). Zircons from LID036 are clear to pale brown, and commonly have prismatic, euhedral shapes (Fig. 5.2A), with sizes between 30 µm and 250 µm. A number of these zircons contain inclusions, although many are inclusion free. Zircons may be cracked and broken into anhedral shapes. A number of small, anhedral zircons are found. Cathodoluminescence (CL) imaging shows concentric zonation typical of magmatic zircons (Fig. 5.2B), with rare cores (e.g. spot 14.2).

Sample LID041 is a pale green, highly deformed L-tectonite from the centre of the Ida Dome (locality 0500773/7487516). This is the most deformed basement sample selected, and the linear fabric has been complexly refolded during Damaran deformation (see Fig. 2.2B). The rock comprises plagioclase, quartz, chlorite (after biotite) and magnetite, with extensive sericitisation of the plagioclase (see Fig. 2.3). The green colour is caused by the presence of chlorite in the rock. A strong fabric is defined by alignment of the chlorite (originally aligned biotite laths). The rock has a slightly annealed texture, with some 120° quartz triple junctions, although irregular-shaped quartz grains are common, and the quartz may be slightly strained. Zircons from LID041 are 20 µm to 200 µm in size, highly fractured, clear to light brown in colour, and anhedral to subhedral (Fig. 5.2C). In addition to the fracturing many zircons have been broken into anhedral fragments by the intense deformation that has affected this sample. Nonetheless, concentric, oscillatory magmatic zoning is visible in CL imaging of the zircons (Fig. 5.2D).

Sample LID045 is a quartzofeldspathic gneiss from the Arcadia Inlier, east of the Ida Dome (locality 0504090/7484518). It has a strong, steeply E-dipping gneissic fabric defined by biotite. The gneiss is migmatised, has cm-scale extensional shear bands, and contains lenses of amphibolite. The gneissic fabric is slightly crenulated in places. It contains the assemblage quartz-plagioclase feldspar-biotite-magnetite, with a 0.5 mm to 1 mm grain size. The fabric consists of layering of biotite + magnetite and quartz + feldspar rich zones. Quartz has highly irregular grain boundaries, although rounded inclusions of quartz are found within quartz and feldspar, confirming that the rock was partially molten (Sawyer, 2008).

Fig. 5.2 (following page) – Photomicrographs and CL images of zircons from Abbabis Complex gneisses. A: Photomicrograph of zircons from LID036. B: CL image of zircons analysed from LID036, showing spot locations. Note the concentric zoning and inherited cores (e.g. spot 14.2). C: Photomicrograph of zircons from LID041. Note the dark, highly fractured zircons at the top and lower left of the image. D: CL image of zircons analysed from LID041, showing the location of the SHRIMP spots. Note the magmatic zoning and fracturing of the zircons. E: Photomicrograph of zircons from LID045. Note that the majority of zircons are clear, inclusion free and unfractured, with a few dark zircons. F: CL image of zircons analysed from LID045, showing the location of the SHRIMP spots. Note the magmatic zoning and the inherited core at spot 15.1.

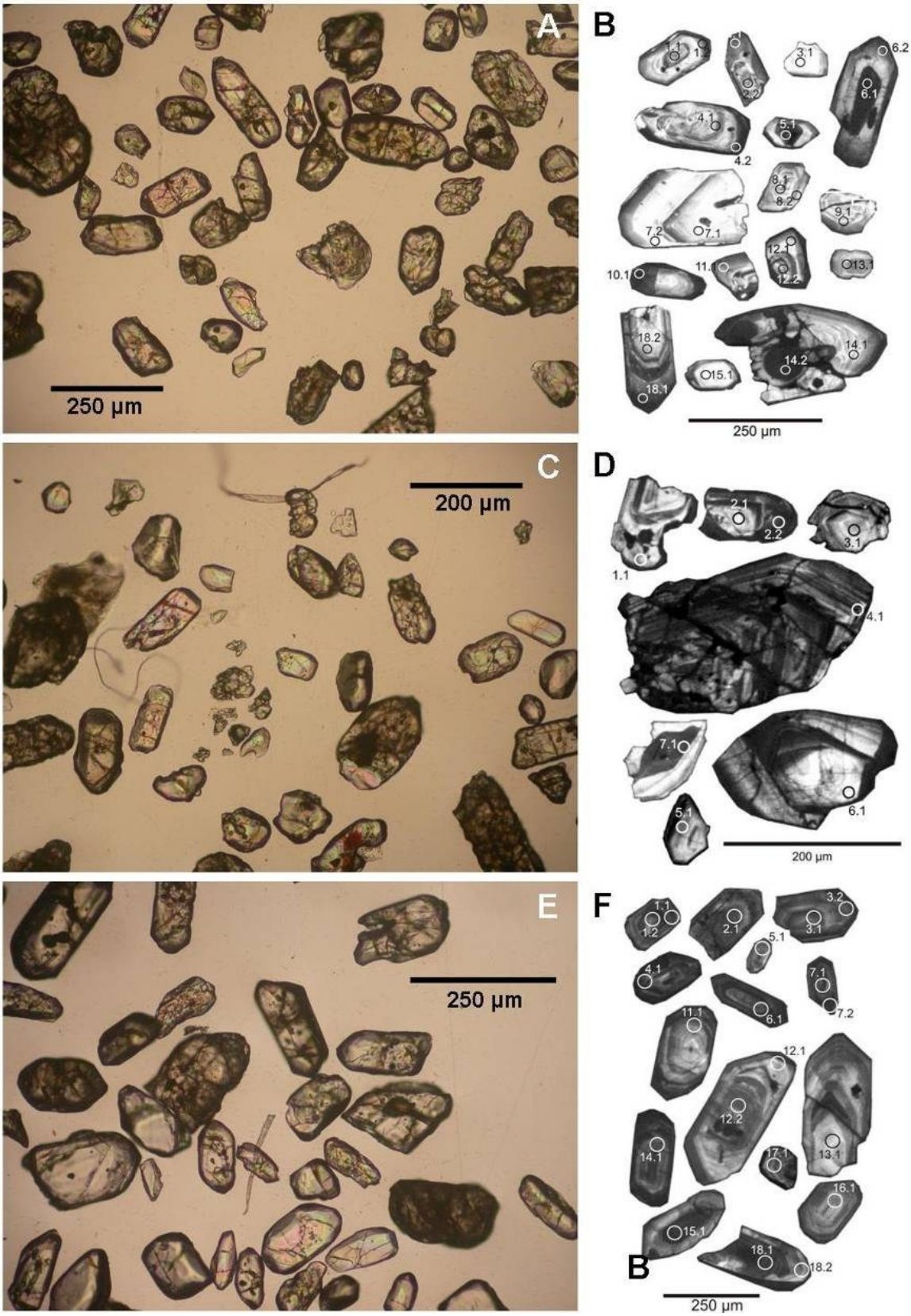
A
250 µm
B
250 µm
C
200 µm
D
200 µm
E
250 µm
F
B
250 µm

Zircon inclusions in quartz and plagioclase are also common. The zircons from LID045 are the least fractured of those from sample of Abbabis Complex gneisses, and are generally clear, with some dark brown zircons (Fig. 5.2E). The zircons are 30 μm to 300 μm in size, and are subhedral to euhedral. Magmatic oscillatory zonation is visible under CL imaging (Fig. 5.2F), and rare inherited cores are evident (e.g. spot 15.1).

5.1.1.2 Results of SHRIMP U-Pb geochronology

Zircons from LID036 are fairly discordant, owing to Pb-loss during Damaran metamorphism, but a Monte Carlo Regression (MSWD = 1.3) through the data gives an upper intercept age of 2056 $^{+11}/_{-10}$ Ma and a lower intercept age of 646 $^{+23}/_{-24}$ Ma (Fig. 5.3A). Two spots analysed (8.1 and 9.1) show 0% discordance and, when plotted, give a concordant age of 2054 ± 7.1 Ma (MSWD = 0.0017) (Fig. 5.3B). The single spot analysed of what appears as a zircon core (spot 14.2) gives a similar *ca*. 2 Ga age to the other spots analysed.

The zircons from LID041 appear to be the most damaged, and show a large degree of discordance owing to Pb-loss during Damaran metamorphism. A Monte Carlo Regression (MSWD = 1.8) through the data gives an upper intercept age of 2044 $^{+32}/_{-27}$ Ma and a lower intercept age of 566 $^{+160}/_{-150}$ Ma (Fig. 5.3C).

Like LID036 and LID041, the zircons in sample LID045 are discordant owing to Damaran Pb-loss. However, the level of discordance appears lower for sample LID045 than for other samples of Abbabis Complex gneisses. A Monte-Carlo Regression (MSWD = 0.67) through the data gives an upper intercept age of 2044 $^{+17}/_{-14}$ Ma (identical to LID041) and a lower intercept age of 464 ± 210 Ma (Fig. 5.3D)

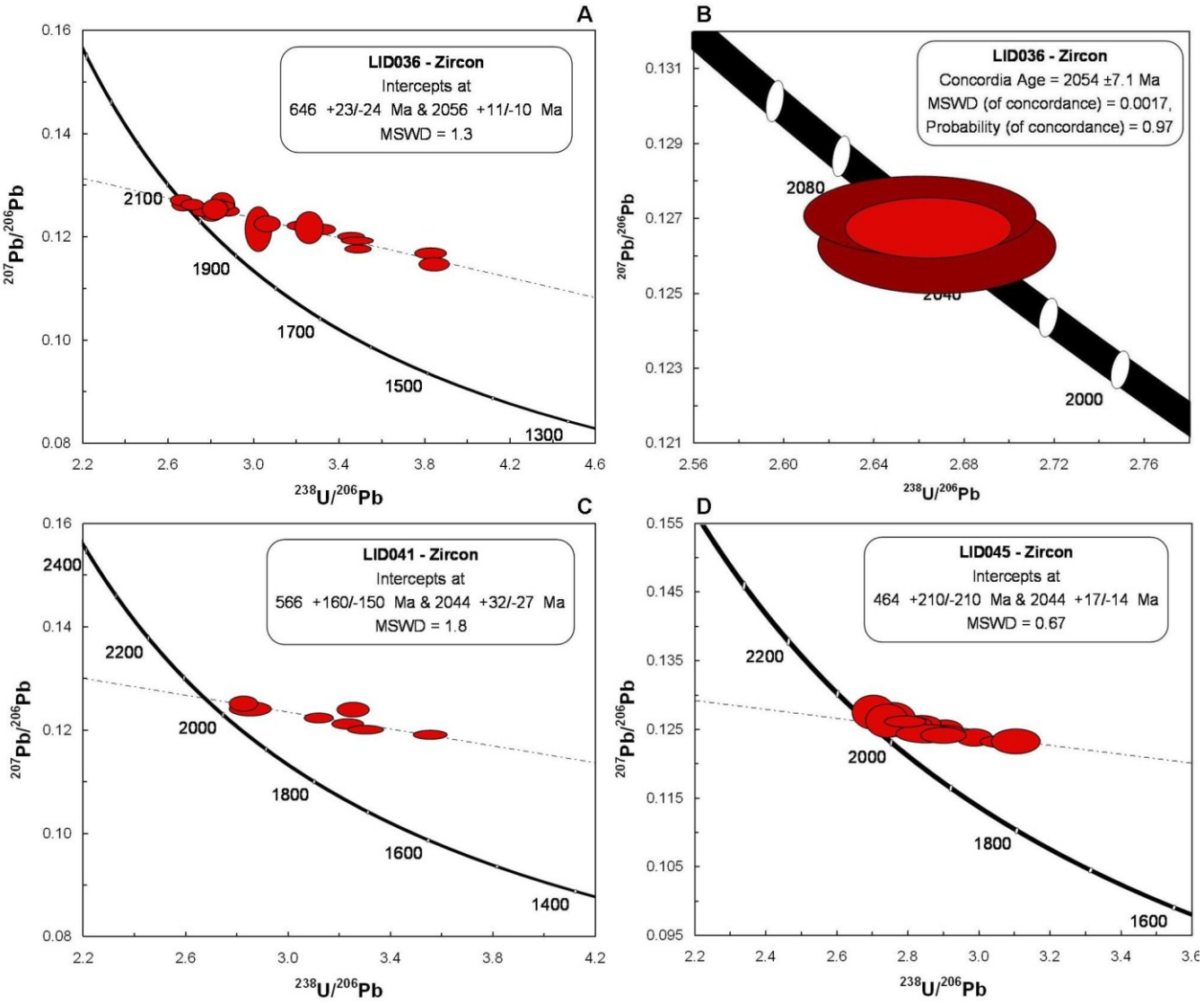

Fig. 5.3 – Tera-Wasserburg Concordia plots for samples of Abbabis Complex gneisses. A: The results of a Monte-Carlo Regression through the data for LID036, giving an upper intercept age of 2056 +11/-10 Ma. B: The results of a weighted mean calculation for two concordant spots from LID036 (8.1 and 9.1), giving a Concordia age of 2054 ± 7.1 Ma. C: The results of a Monte-Carlo Regression through the data for LID041, giving an upper intercept age of 2044 +32/-27 Ma. D: The results of a Monte-Carlo Regression through the data for LID045, giving an upper intercept age of 2044 +17/-14 Ma. Data can be found in Appendix 2.

5.1.1.3 Discussion of results

Monte-Carlo Regression through discordant zircons give upper intercept ages of 2056 $^{+11}/_{-10}$ Ma, 2044 $^{+32}/_{-27}$ Ma, and 2044 $^{+17}/_{-14}$ Ma for samples LID036, LID041, and LID045, respectively, dates that are essentially identical (within error). Two concordant analyses from LID036 give a mean age of 2054 ± 7.1 Ma. These results confirm that Abbabis Complex gneisses from the Ida Dome are *ca*. 2040-2060 Ma in age, similar to *ca*. 2 Ga ages obtained for the Abbabis Complex by Jacob *et al.* (1978), Jacob *et al.* (2000) and Tack *et al.* (2002), and older than the age of 1040-1100 Ma suggested by Kröner *et al.* (1991) for Abbabis Complex gneisses along the Khan River. These ages are similar to ages obtained from rocks in northeastern Namibia (2022 ± 15 Ma – Hoal *et al.*, 2000) and northwestern Botswana (*ca*. 2050 Ma – Singletary *et al.*, 2003). These *ca*. 2 Ga rocks form part of a terrane that stretches from northern Namibia to northern Zambia and the Democratic Republic of the Congo (DRC), and is termed the Kamanjab-Bangweulu arc (Rainaud *et al.*, 2005a), which forms part of the so-called Kambantan Terrane (Rainaud *et al.*, 2005a), a microcontinental entity accreted onto the southern margin of the Congo Craton during the 1.0-1.4 Ga Kibaran Orogeny. The 1040-1100 Ma ages suggested by Kröner *et al.* (1991) may be the parts of the Abbabis Complex generated during the 1.0-1.4 Ga Kibaran Orogeny. Thus, whilst both *ca*. 2 Ga and *ca*. 1 Ga ages may be found for rocks of the Abbabis Complex, both ages confirm that the Central Zone is underlain by rocks of the Congo Craton, which may preserve evidence of multiple Proterozoic orogenic events.

5.1.2 Amphibolites

Amphibolites are commonly found intruding gneisses of the Abbabis Complex throughout the Central Zone (Smith, 1965; Barnes, 1981; Marlow, 1981; Brandt, 1987; Steven, 1994). They are poorly documented compared to other intrusive rocks of the Central Zone, and have generally been considered to be pre-Damaran in age (Smith, 1965; Marlow, 1981; Brandt, 1987). However, ortho-amphibolite dykes cross-cut Damaran metasediments at the Rössing Mine (P. Nex, Pers. Comm., 2009), and

elsewhere in the Central Zone (Jacob, 1974), indicating that they may not necessarily all be pre-Damaran. In both the Ida and Palmenhorst Domes, there are numerous ortho-amphibolite dykes cross-cutting the rocks of the Abbabis Complex. Locally, these amphibolites cross-cut the pre-Damaran fabric preserved in these basement rocks (see Fig. 4.1A), although amphibolites are generally deformed into parallelism with the regional fabric formed during Damaran deformation. Geochemistry of the amphibolites from the study area indicates that they have a high-K, calc-alkaline basaltic composition, and may represent an early phase of arc magmatism preceding Damaran collision, possibly related to the Goas Intrusive Suite (de Kock, 1991), found near Karibib (*ca*. 100 km northeast of the study area). However, no dates exist in the literature for the age of the amphibolites within the Abbabis Complex and, thus, two samples have been selected for U-Pb dating in order to determine whether the amphibolites may be of both Damaran and Abbabis ages. The first (ACAM-1) does not come from within the study area, but is from the Abbabis Complex type locality on the farm Abbabis 70, where amphibolites have been described by Marlow (1981) and Steven (1994). The second (LKR021) is a folded amphibolite dyke intruding Abbabis Complex gneisses along the Khan River, near the centre of the Palmenhorst Dome. This amphibolite cross-cuts the gneissic fabric in the Abbabis Complex, and has been folded by D2 deformation (Figs. 3.8F, 4.1).

5.1.2.1 Descriptions of samples and zircons analysed

Sample ACAM-1 is an amphibolite dyke from within the Abbabis Complex gneisses on the farm Abbabis 70, the type locality for the Abbabis Complex in the Central Zone (locality 0575111/7550403). The amphibolite is highly folded and sheared along with the quartzofeldspathic gneisses into which it is emplaced. Although not from within the main field area for this study, the sample was selected for comparison with sample LKR021, an amphibolite from the study area, as no amphibolites from the Central Zone have previously been dated. Zircons are generally elongate, light brown crystals with corroded edges and rounded tips. Internally they show strong magmatic

oscillatory zoning. A number of crystals are embayed with dark-CL, low Th/U zircon, interpreted here as a metamorphic overgrowth on the magmatic zircons.

Sample LKR021 is an amphibolite dyke found intruding Abbabis Complex gneisses along the Khan River (locality 0495396/7500431). The dyke cross-cuts the pre-Damaran fabric in these gneisses, and has been folded into S-verging, tight N-dipping folds during D2 deformation (Fig. 3.8F). An axial-planar fabric is developed in the hinge zones of these folds. The amphibolite comprises predominantly 0.5 mm to 1 mm dark green to tan hornblende and plagioclase feldspar, with minor ilmenite and accessory quartz, titanite, apatite, and K-feldspar, and variable amounts of biotite (see section 4.1 and Fig. 4.2). A fabric is defined by alignment of the hornblende, and the sample is slightly altered; biotite (and to a lesser extent hornblende) may be altered to chlorite, and feldspar may be sericitised. Both zircon and titanite have been dated. Zircons are found rarely; where they occur, these are small (<100 μm), clear, inclusion-free and unfractured. Concentric growth zonation is rare. In general these zircons contain a bright (under CL) U-poor core, with a narrow dark high-U rim, interpreted as a metamorphic overgrowth (Fig. 5.4A). Titanite is a common accessory phase, and is pale tan to dark brown, transparent, and generally free of cracks and inclusions (Fig. 5.4B). The titanite has been broken into anhedral fragments during sample preparation.

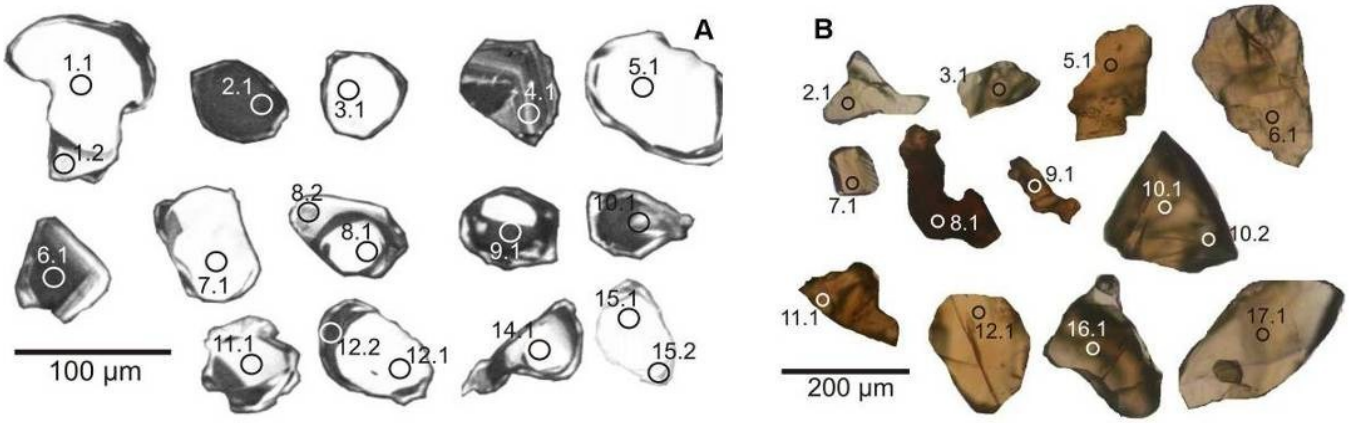

Fig. 5.4 – A: CL images of zircons analysed from LKR021, showing small zircons with bright (low U) cores and dark (high U) metamorphic overgrowths, as well as a uniform high-U metamorphic zircon (spot 2.1). Locations of spots analysed are shown. B: Photomicrographic images of titanites analysed from LKR021, showing the inclusion-free, brown titanite with few fractures. Locations of spots analysed are shown.

5.1.2.2 Results of SHRIMP U-Pb geochronology

Zircons from ACAM-1 are generally concordant, and give a weighted mean $^{207}Pb/^{206}Pb$ age of 2026.9 ± 2.3 Ma (Fig. 5.5A) (N = 17/17; MSWD = 1.18; probability = 0.27). A Model 1 solution through these data gives similar results, with an upper intercept of 2027.2 ± 6.7 Ma. Two embayments analysed (interpreted as metamorphic rims) are highly discordant. They give a Model 1 solution with an upper intercept of 1820 ± 9.8 Ma and a lower intercept of 155 ± 40 Ma (Fig. 5.5B). Magmatic zircon cores from LKR021 (with U < 200 ppm) give a Concordia age of 557.2 ± 7.4 Ma, whilst metamorphic rims (U > 200 ppm, up to 1500 ppm) give a Concordia age of 520 ± 6.9 Ma (Fig. 5.5C). Titanites from LKR 021 contain large amounts of common Pb (^{204}Pb), leading to discordance, but ^{204}Pb-corrected data yield an age of 493.4 ± 6.4 Ma (Fig. 5.5D).

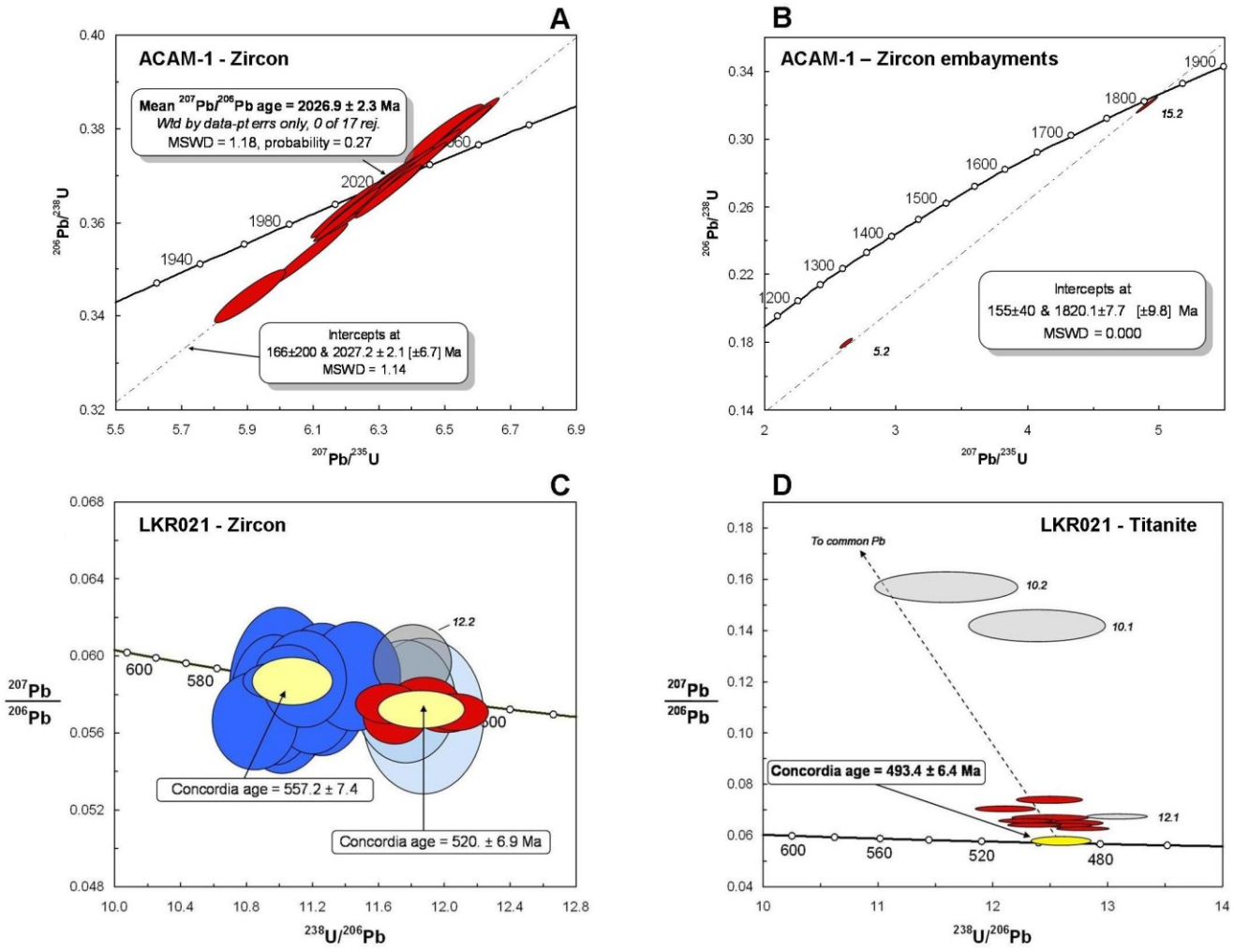

Fig. 5.5 – Concordia plots for amphibolite samples. A: Zircon cores from sample ACAM-1, which give a weighted mean age of 2026.9 ± 2.3 Ma, and a Model 1 solution upper intercept age of 2027.2 ± 6.7 Ma. B: Zircon embayments from sample ACAM-1. A Model 1 solution gives an upper intercept age of 1820 ± 9.8 Ma. C: Zircons from sample LKR021. Magmatic cores give an age of 557.2 ± 7.4 Ma, whilst metamorphic rims give an age of 520 ± 6.9 Ma. D: Titanites from sample LKR021, which contain large amounts of common Pb, give an age of 493.4 ± 6.4 Ma.

5.1.2.3 Discussion of results

Sample ACAM-1 from the Abbabis Inlier gives an age of 2027 Ma, indicating that some of the mafic dykes in the Abbabis Complex are pre-Damaran, and were emplaced within 20 Ma of the granitoid rocks of the Abbabis Complex, which have ages of 2040-2060 Ma (section 5.1.1). The metamorphic embayments in ACAM-1 also give a pre-Damaran age of 1820 Ma, suggesting that a pre-Damaran metamorphic event may have affected the rocks of the basement, although as only two analyses were conducted, and both are highly discordant, this conclusion is speculative. Both the zircon cores and embayments show Pb-loss at 150-170 Ma. This Pb-loss may be related to zircon alteration at the age of Etendeka flood volcanism, associated with the rifting of Africa from South America, which has been dated at 130-135 Ma (Renne *et al.*, 1992; Trumbull *et al.*, 2000; Wigand *et al.*, 2003). Zircons from Abbabis Complex gneisses (section 5.1.1) do not show Mesozoic Pb-loss, but rather show Pb-loss associated with Damaran metamorphism. Magmatic zircons from sample LKR021 give an age of 557 Ma – this demonstrates that some of the amphibolites are Damaran in age. Similar ages of 546-564 Ma have been obtained for zircons from diorites and quartz diorites from the Central Zone (Jacob *et al.*, 2000; De Kock *et al.*, 2000; Jung *et al.*, 2002), and this confirms that the amphibolites are related to early mafic-dioritic magmatism in the Central Zone (the Goas Intrusive Suite; Lehtonen *et al.*, 1995), as suggested by geochemical evidence (section 4.1). This age also indicates that the gneissic fabric in the Abbabis Complex must be older than 557 Ma, and is likely to be pre-Damaran. Metamorphic zircon rims from sample LKR021 give an age of 520 Ma, suggesting that peak metamorphism in the study area occurred at this time. The age of 493 Ma for titanites from LKR021 is similar to ages of 494-500 Ma obtained by Jacob *et al.* (2000) for titanites from lamprophyre dykes and auriferous veins near the Navachab Mine, interpreted as the age for hydrothermal alteration and Au-mineralisation in the Central Zone. Similar young ages of 480-500 Ma have been obtained using Ar-Ar dating of muscovite (Kukla, 1993) and Rb-Sr dating of biotite, muscovite and plagioclase (Blaxland *et al.*, 1979; Hawkesworth *et al.*, 1983) and have been interpreted as cooling ages for the Central Zone (Miller, 2008).

5.1.3 Red granites

Red granites are suggested to predate D2 deformation, with a S2 gneissic fabric subparallel to the regional S2 fabric in the host rocks. They are highly potassic, alkalic and peraluminous (see section 4.2). They contain small amounts of ferromagnesian minerals and are restricted to the stratigraphic level of the Abbabis Complex or Etusis Formation in the highest-grade western portions of the Central Zone. Their stratigraphic localisation indicates that they may be the product of anatexis of the Abbabis Complex or Etusis Formation, and it has been suggested that they are the result of near-total in-situ melting of these lithologies (Miller, 2008). The red granite from this study is clearly younger than D2 (see section 4.2), and may place an upper limit on the age of D2 in the study area. This granite is thought to be the product of anatexis of the Abbabis Complex – inherited zircons should confirm this, and further constrain the age of the Abbabis Complex. Both monazite and zircon from a single sample (LKR016) have been analysed.

5.1.3.1 Descriptions of sample and zircons analysed

LKR016 is a sample of heterogeneous red granite from the northern margin of the Palmenhorst Dome (locality 0500360/7504659). Red granite in this area occurs as large (10's of m-thick), subvertical to N-dipping sheet-like bodies within N-dipping Damaran and Abbabis Complex rocks. The granites have a strong N-dipping fabric subparallel to the regional dip of the Damaran metasediments, and contain large cordierite crystals and sillimanite, which occurs as knots or forms the strong fabric in the granite. Locally, xenoliths of sillimanite-bearing material are found. The granite is made up almost entirely of K-feldspar and quartz, with sillimanite, cordierite and minor amounts of biotite and magnetite. Zircons are clear to pale grey and euhedral to subhedral, with slightly rounded tips (Fig. 5.6A). CL imaging shows that most zircons contain bright, low-U inherited cores, with narrow, dark, high-U (up to 1800 ppm) magmatic overgrowths (Fig. 5.6B). Monazites from LKR016 are anhedral and

pale yellow (Fig. 5.6C). Backscattered electron (BSE) imaging shows that some have internal structure and a weak zoning (Fig. 5.6D).

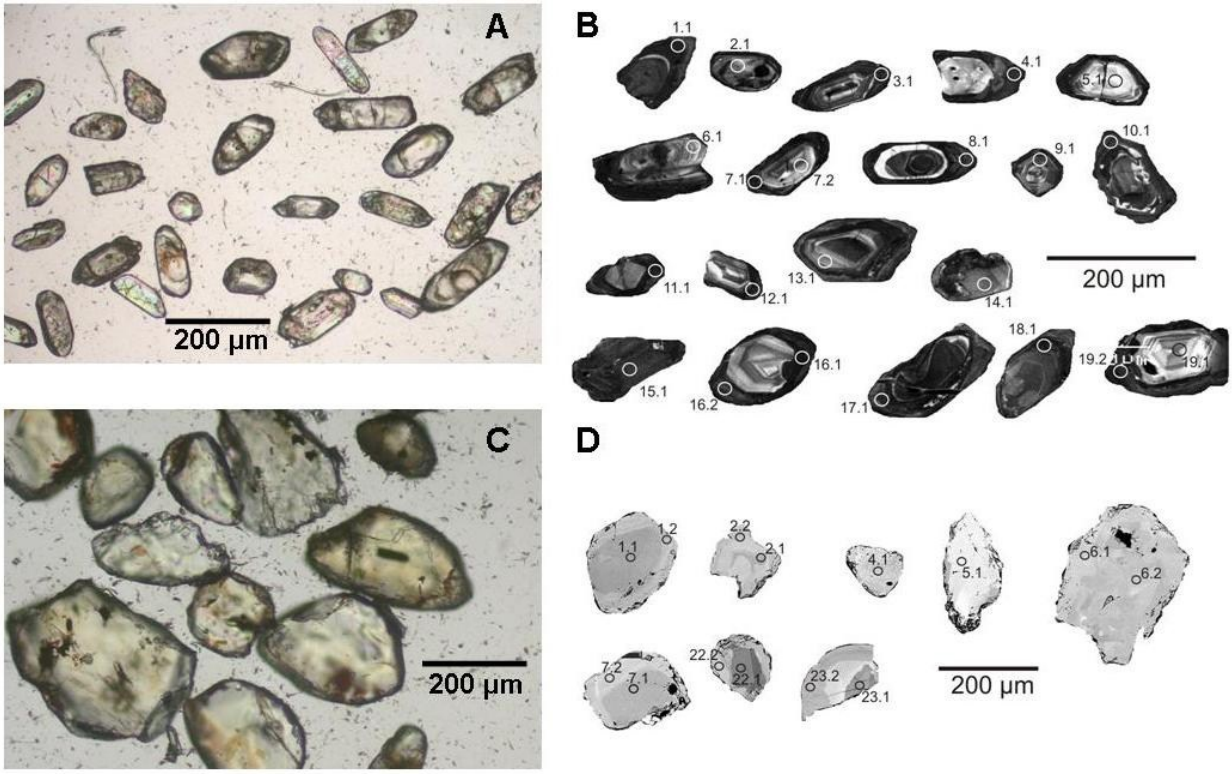

Fig. 5.6 – A: Photomicrograph of clear, subhedral to euhedral zircons from LKR016 with corroded tips. Note that cores are visible in many zircons. B: CL images of zircons analysed from LKR016, showing spot locations. Note that almost all zircons analysed have inherited cores. C: Photomicrograph of pale yellow monazites from LKR016. D: BSE image of monazites analysed from LKR016, showing the location of spots analysed. Note the zoning in some grains (1; 7; 22; 23).

5.1.3.2 Results of SHRIMP U-Pb geochronology

The zircons analysed show a spread of ages. A large number of the analyses are inherited cores. Some of these inherited cores give *ca*. 2 Ga ages, similar to the ages for Abbabis Complex gneisses analysed in this study (spots 5.1, 6.1 and 19.1 – $^{206}Pb/^{207}Pb$ ages of 2037 ± 13 Ma, 1980 ± 8.8 Ma and 2049 ± 10 Ma, respectively). However, some inherited cores give younger ages of *ca*. 1 Ga (spots 7.1, 13.1 and 18.1

- $^{206}Pb/^{207}Pb$ ages of 1043 ± 21 Ma, 1003 ± 17 and 1027 ± 12 Ma, respectively). Inherited cores show Damaran age Pb-loss (Fig. 5.7A). Additionally, some of the rims analysed, although slightly discordant, give Damaran ages (spots 1.1, 8.1 and 17.1 have $^{206}Pb/^{207}Pb$ ages of 514 ± 71 Ma, 528 ± 17 and 520 ± 46 Ma, respectively, and all have discordance <3%). A Model 1 solution through the zircon data gives an upper intercept of 1013 ± 21 Ma and a lower intercept of 539 ± 17 Ma (Fig. 5.7A). Monazites from LKR016, are concordant, and give a weighted mean age of 535.6 ± 7.2 Ma (Fig. 5.7B).

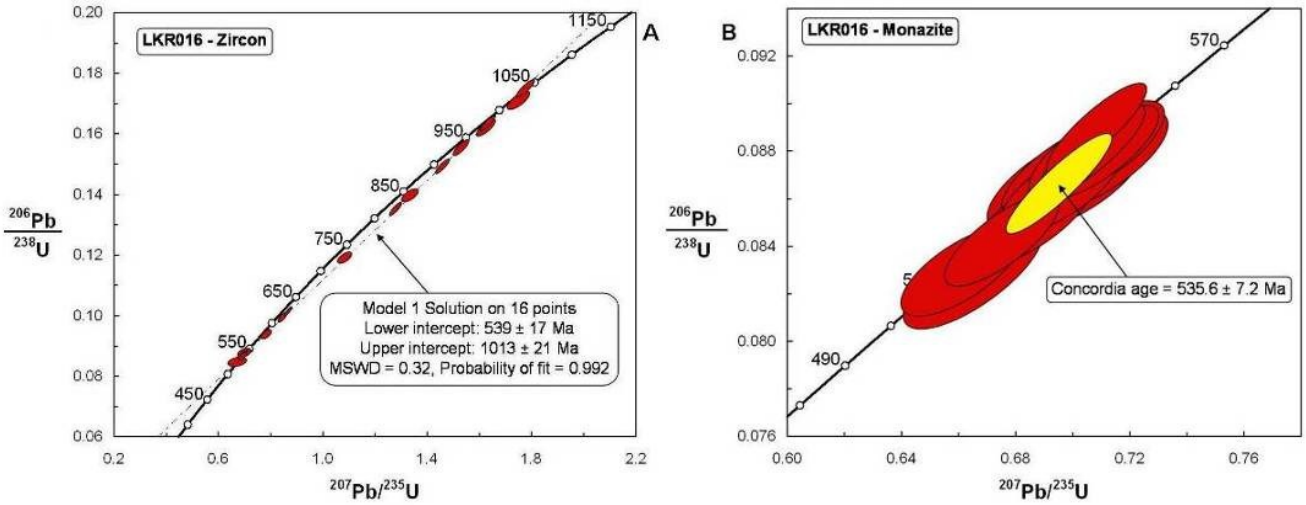

Fig. 5.7 – A: Concordia plot for zircons from LKR016, showing a spread of discordant ages for spots analysed. A Model 1 solution through the data yields an upper intercept 1013 ± 21 Ma and a lower intercept of 539 ± 17 Ma. B: Concordia plot of monazite analyses from LKR016, which gives an age of 535.6 ± 7.2 Ma.

5.1.3.3 Discussion of results

Both the monazite age (536 ± 7.2 Ma) and the lower-intercept zircon age (539 ± 17 Ma) are within error of one another, and indicate granite crystallisation at 536-539 Ma. Both ages are within error of the 534 ± 7 Ma obtained for anatectic red granite from Goanikontes (Briqueu *et al.*, 1980), which was interpreted as a “mobilisate” that formed in situ from the migmatisation of the Etusis Formation, and which contains a

biotite fabric parallel to the fabric in the host rocks (Briqueu *et al.*, 1980). This 534 Ma age is the age suggested for early equigranular red syenogranites also from the Goanikontes area (Nex *et al.*, 2001b). A similar age of 539 ± 6 Ma has been obtained for the Rotekuppe Granite (Jacob *et al.*, 2000), a granite with no fabric, thought to postdate D3 deformation in the Karibib area. This suggests that deformation in the study area may be younger than deformation elsewhere in the Central Zone – 536-539 Ma red granites which clearly predate D2 deformation in the study area are of a similar age to granites which postdate deformation elsewhere in the Central Zone. This idea is discussed further at the end of the chapter. The age of 1013 ± 21 Ma for inherited zircons is similar to the 1040-1100 Ma age for the Abbabis Complex suggested by Kröner *et al.* (1991), and other inherited zircons give *ca*. 2 Ga ages. Since both *ca*. 1 Ga and *ca*. 2 Ga ages are supposedly found in the Abbabis Complex, and the Etusis Formation is likely derived from the Abbabis Complex (Miller, 2008), this result is inconclusive as to whether red granites are derived from the Etusis Formation and Abbabis Complex.

5.1.4 Grey granites

Grey granites are the most voluminous, widespread intrusive rock type in the study area, and show the most obvious relationship to D2 deformation (see Fig. 4.7). They are intruded along the axial planes of D2 folds, and may be folded by D2. They have a fabric of aligned biotite, which is axial-planar to D2 folds, and may be cut by late-D2 extensional shear bands. Similar structural relationships are found with the quartz-feldspar-magnetite pegmatitic granites, and they may be related to the grey granites. By dating the grey granites, the age of D2 deformation can be constrained, confirming whether deformation in the study area is younger than deformation elsewhere in the Central Zone. The grey granites range from dioritic (with 20-40% biotite, and hornblende) to leucogranitic (with <10 % biotite) owing to fractionation (see section 4.3), and less fractionated (i.e. more mafic) varieties show a stronger fabric and more deformation than more fractionated (leucocratic) varieties. More fractionated leucocratic grey granites cross-cut the less fractionated grey granites. For this study,

two samples of grey granite have been selected for geochronology – an early, granodioritic grey granite (LHA012) and a younger, leucocratic grey granite (LHA010).

5.1.4.1 Descriptions of sample and zircons analysed

Sample LHA010 is one of two samples of the grey granites chosen for analysis. It is a sample of the younger, leucocratic phase, and is pale grey. It occurs within a large outcrop of grey granite, where the older phase is also present (locality 0489766/7489118). The granite is uniformly fine- to medium-grained (0.2 mm – 1 mm), and has a moderate fabric. The rock is made up of predominantly K-feldspar and quartz, lesser biotite and magnetite, and minor amounts of plagioclase. The fabric is defined by alignment of biotite laths, and K-feldspar may locally form crystals up to 3 mm in size. Zircons are elongate, prismatic, subhedral to euhedral and clear to pale yellow (Fig. 5.8A). Many zircons contain small inclusions of an opaque phase, in addition to inclusions of an elongate, prismatic euhedral mineral (possibly apatite). CL imaging shows oscillatory magmatic zoning (Fig. 5.8B), and rare inherited cores (spots 9.1 and 14.1).

Sample LHA012 comes from the same outcrop as LHA010 (locality 0489766/7489118), and represents the older, mafic phase of the grey granites in the area. It is dark grey, has a strong fabric, and is coarser grained than the more leucocratic grey granites (1 mm to 2 mm grain size). The sample comprises quartz, plagioclase, biotite, hornblende, magnetite, and minor amounts of K-feldspar and apatite. The strong fabric is defined by aligned hornblende and biotite, and the sample has experienced mild alteration, leading to chloritisation of biotite and sericitisation of plagioclase. Zircons are generally euhedral to subhedral, elongate and prismatic, and clear to pale yellow (Fig. 5.8C). Like those from LHA010, the zircons contain opaque inclusions, and inclusions of an elongate, needle-like euhedral mineral (likely apatite). CL imaging reveals magmatic oscillatory zoning (Fig. 5.8D).

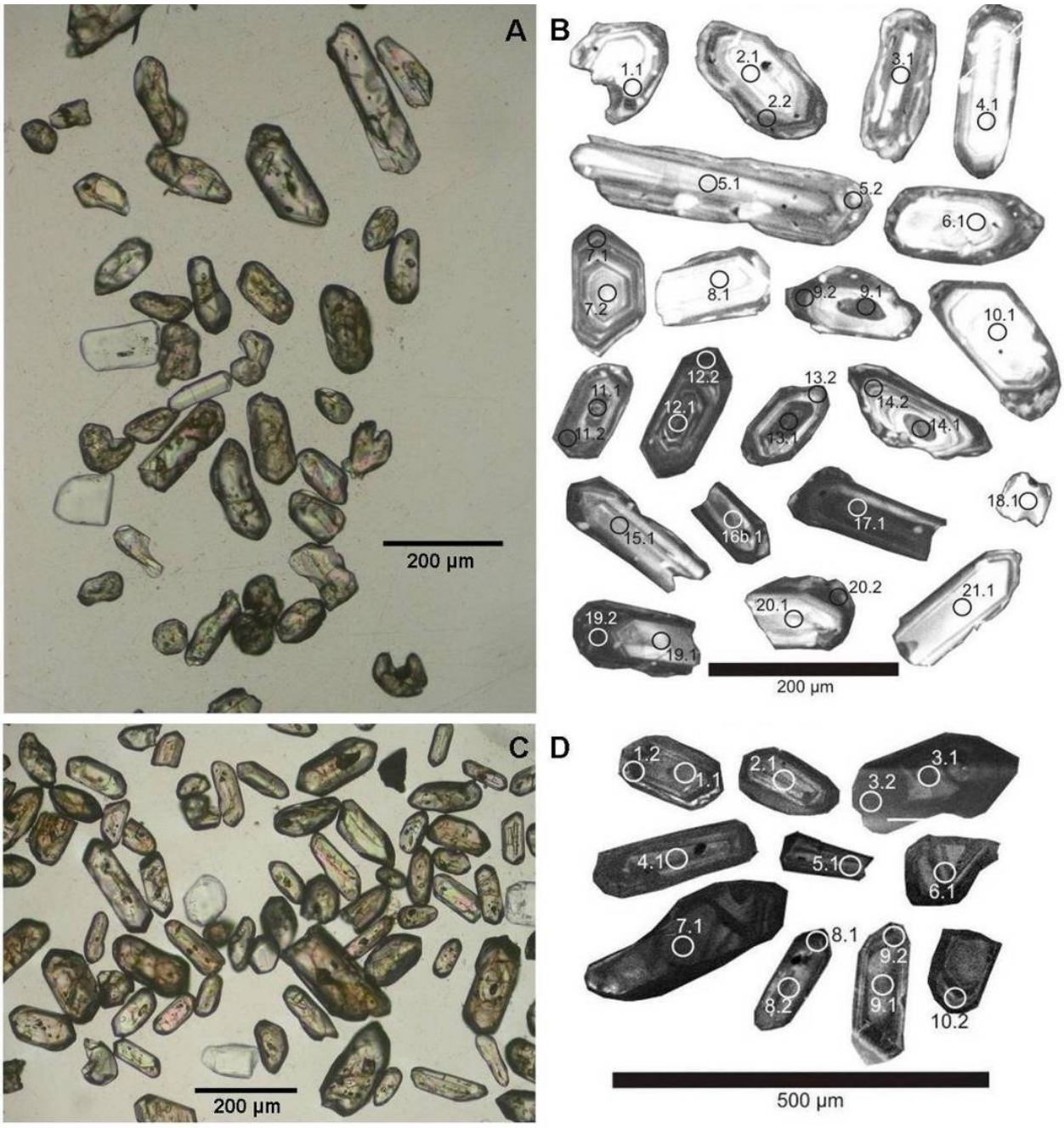

Fig. 5.8 – Photomicrographs and CL images of zircons from grey granites. A: Photomicrograph of clear to pale yellow, elongate zircons from sample LHA010. Note the opaque inclusions in many zircons. B: CL images of zircons analysed from sample LHA010, showing locations of spots analysed. Note the inherited cores at spot 9.1 and spot 14.1, and the oscillatory magmatic zoning in the zircons. C: Photomicrograph of elongate, prismatic zircons from sample LHA012, with numerous opaque inclusions. D: CL images of zircons analysed from sample LHA012, showing locations of spots analysed.

5.1.4.2 Results of SHRIMP U-Pb geochronology

Both samples LHA010 and LHA012 show predominantly concordant zircons, but some of the spots analysed show Pb-loss (Fig. 5.9A), which is possibly the result of zircon alteration owing to tectonometamorphic activity at the time of Etendeka flood volcanism, associated with the rifting of Africa from South America during the Cretaceous (130-135 Ma – Renne *et al.*, 1992; Trumbull *et al.*, 2000; Wigand *et al.*, 2003). However, most analyses are concordant, and sample LHA010 yields a weighted mean Concordia age of 519.1 ± 4.2 Ma when discordant analyses are ignored (Fig. 5.9A). Fewer zircons were analysed from LHA012 than from LHA010, and these give a weighted mean Concordia age of 520.4 ± 4.2 Ma, when discordant zircons are ignored (Fig. 9B). This is within error of, and essentially identical to, the age for LHA010.

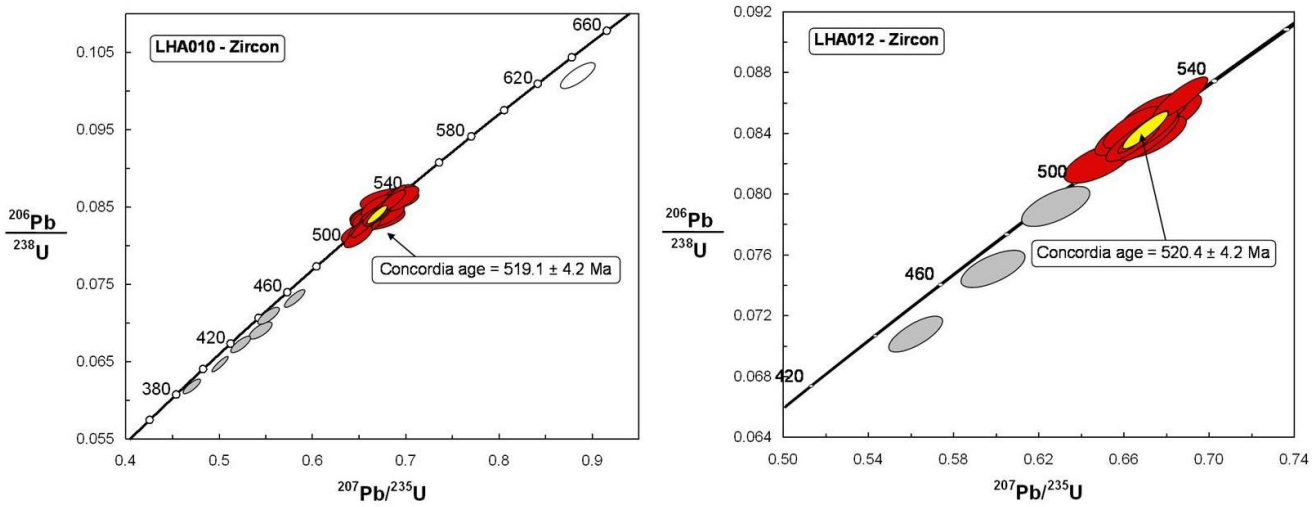

Fig. 5.9 – Concordia plot of zircons from grey granites. A: Sample LHA010 – the data yields a concordant age of 519.1 ± 4.2 Ma when discordant zircons that have experienced recent Pb-loss are ignored. B: Sample LHA012 – the data yields a concordant age of 520.4 ± 4.2 Ma when discordant analyses are ignored. Concordant analyses are shown as red ellipses, discordant analyses are shown as grey ellipses, mean age is shown by yellow ellipse.

5.1.4.3 Discussion of results

Both samples give an age of essentially 520 Ma, confirming that they may be similar to the early non-porphyritic granites and leucogranites found mostly in the northern Central Zone (Haack *et al*., 1980), but are also noted locally in the southern Central Zone (Miller, 2008). These granites and leucogranites are seen to cut the Salem-type granites and are suggested to be syn-D2 in age in the northern Central Zone (Miller, 2008). In the northern Central Zone, one of these, the Okandjou Leucogranite, has been dated using whole rock Rb-Sr at 514 ± 22 Ma (Haack *et al.*, 1980). The grey granites are also probably analogous to the "red and grey homogeneous syntectonic granites" of Brandt (1985) and the "equigranular grey granites" of Nex (1997). Equigranular grey monzogranites (Nex *et al.*, 2001b) from the Goanikontes area have been dated at 517 ± 7 Ma (Briqueu *et al.*, 1980). This constrains the age of D2 folding to *ca*. 520 Ma in the study area (late D2 extension may be slightly younger – D2 shear bands partially cut the grey granites), which is younger than the 536-539 Ma ages for the red granite. This age indicates that red granites are indeed pre-D2 (rather than syn-D2), and that the gneissic fabric is a tectonic fabric that was imposed after crystallisation rather than a ghost gneissosity (as suggested by Miller, 2008). The age for D2 is also identical to the age of high-U metamorphic rims on zircons analysed from a Damaran amphibolite (520 ± 6.9 Ma – sample LKR021 – 5.1.2), confirming field observations that D2 deformation was coeval with high-grade metamorphism in the southwestern Central Zone (this study; Poli, 1997; Ward *et al.*, 2008; Kisters *et al.*, 2009). However, this age is significantly younger than the 550 Ma age suggested for D2 in the Central Zone (Miller, 2008), based on ages for the syn-tectonic Goas Intrusive Suite and Salem-type biotite granites in the Central Zone, which have been dated at between 560 Ma and 540 Ma (Downing, 1982; Kröner, 1982; Hawkesworth *et al.*, 1983; De Kock *et al.*, 2000; Jacob *et al.*, 2000; Johnson *et al.*, 2006). Other syn-tectonic granites (the quartz-feldspar-magnetite pegmatitic granites and the garnet-bearing leucogranites) as well as syn-tectonic leucosomes from D2 extensional features give similar ages and confirm this age for D2 and metamorphism in the study area (see sections 5.1.5 and 5.1.6).

5.1.5 Quartz-feldspar-magnetite pegmatitic granites

Quartz-feldspar-magnetite pegmatitic granites are the most common and most voluminous of the sheeted granites in the study area, and are particularly voluminous on the eastern limb of the Ida Dome, where they intrude the Khan Formation. They have similar structural relationships to the grey granites and can be seen intruding along the axial planes of D2 folds (Fig. 4.13A). Additionally, they show a close association with the grey granites (Fig. 4.10C, D), and it is postulated that they may be part of the same magmatic event as the grey granites. Hence, they should have a similar age to the grey granites. This granite type may be analogous to the "C-type" leucogranite of Nex & Kinnaird (1995). A single sample (LCZ7-2) was collected for geochronological analysis.

5.1.5.1 Descriptions of sample and zircons analysed

Sample LCZ 7-2 is a pale pink, pegmatitic, magnetite-bearing granite from the Ida Dome (0502300/7486236). The sample comprises quartz, K-feldspar and plagioclase, with minor magnetite and chloritised biotite. Zircons from LCZ 7-2 are brown, strongly zoned and altered/metamict. CL imaging reveals dark patches which are testament to the high degree of metamictisation in high-U zones within grains, with local obliteration of zoning in some grains. The zircons have very high U contents and the metamictisation and alteration has resulted in very high common Pb contents.

5.1.5.2 Results of SHRIMP U-Pb geochronology

The high U concentrations and elevated common Pb makes U/Pb calibration very difficult and, hence, the age for this sample is quite imprecise. Analysis #11.1 contains particularly high common Pb (16.84% of Pb is common Pb) and is excluded. A Model 1 regression of all other data gives an upper intercept age of 526 ± 34 Ma (MSWD = 0.049; probability = 1.000) (Fig. 5.10A). Four analyses give similar, near equivalent ages (spots 5.1, 7.1, 14.1, and 16.1) – when only these four analyses are plotted, they

give a weighted mean age of 530.1 ± 5.4 Ma (MSWD (of concordance) = 0.45, Probability (of concordance) = 0.50). However, the small number of analyses and large error of analysis 14.1 implies that this result is not statistically robust.

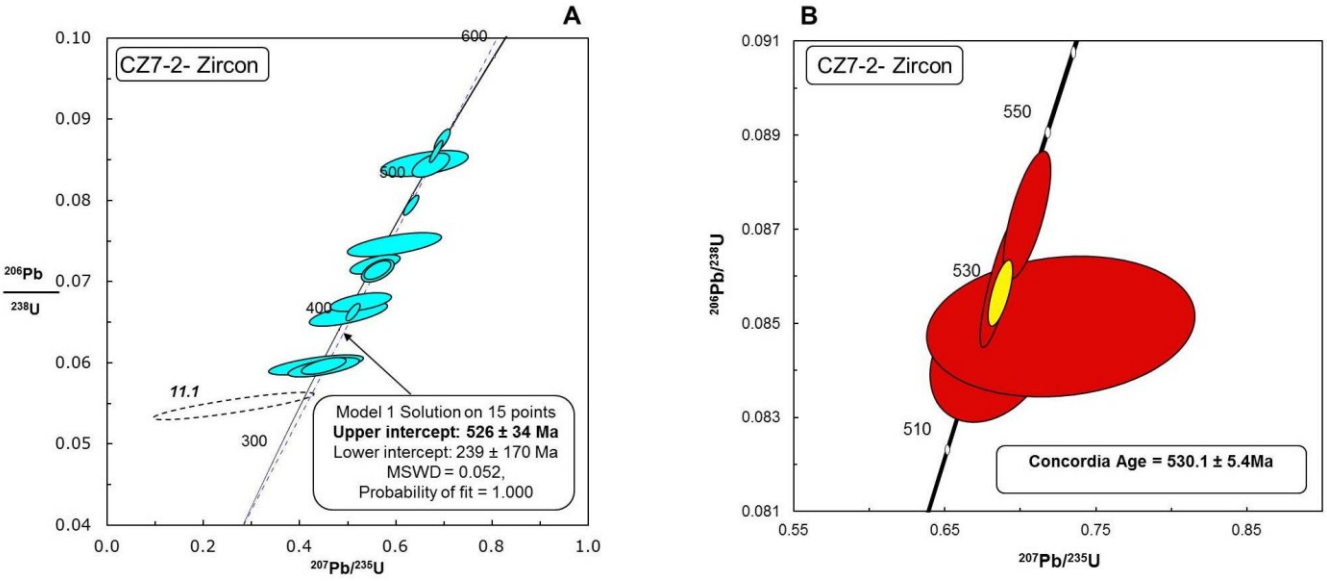

Fig. 5.10 – Concordia diagrams for Quartz-Feldspar-Magnetite Pegmatitic Granite (LCZ7-2) A: Results of a Model 1 solution through all data except #11.1, which gives an upper intercept age of 526 ± 34 Ma. B: Weighted mean of four analyses (spots 5.1, 7.1, 14.1, 16.1), which gives an age of 530.1 ± 5.4 Ma.

5.1.5.3 Discussion of results

The age given by a Model 1 solution of 526 ± 34 Ma has a large error, but is within error of the age of 520 Ma determined for the grey granites. The weighted mean of four analyses (530.1 ± 5.4 Ma) is older than the age for the grey granites, but this age has a low probability of concordance (0.50). The high uranium contents and metamict nature of the zircons from this sample preclude precise geochronology, and the quartz-feldspar-magnetite pegmatitic granites clearly cut grey granites in the field, and therefore cannot be older than the grey granites. Nonetheless, it is clear that the quartz-feldspar-magnetite pegmatitic granites have a similar age to the grey granites,

confirming that these granite types may be related, although the error on the Model 1 solution age is large.

5.1.6 Garnet-bearing leucogranites

Garnet-bearing leucogranites are found closely associated with migmatitic metapelites of the Rössing or Chuos Formations, and although common throughout the Central Zone, they are not voluminous in the study area. They are thought to be the result of migmatisation of the metapelites with which they are associated (Ward, 2008; Chapter 4) and, like the grey granites, they are contemporaneous with D2 – they are folded and boudinaged by D2 deformation, and may be localised along the axial planes of D2 folds (see Fig. 4.14). Although a minor granite phase in the study area, they are more voluminous along the Khan River north of the study area, where they are located in a thick package of cordierite schists of the Kuiseb Formation. Here, they show evidence of having been generated by melting of the Kuiseb Formation, with emplacement of anatectic leucosomes and leucogranites coeval with D2 deformation and NE-SW directed extension in the southwestern Central Zone (Ward *et al.*, 2008; Kisters *et al.*, 2009). Thus, the garnet-bearing leucogranites should give the age for both D2 deformation and for the peak of the metamorphic event during which they were generated. A single sample (LID038) from a garnet-bearing granite found associated with metapelites of the Rössing Formation on the eastern edge of the Ida Dome has been analysed for both zircon and monazite.

5.1.6.1 Descriptions of sample and zircons analysed

Sample LID038 is a garnet-bearing leucogranite from the eastern margin of the Ida Dome (locality 0502755/7485916). Field evidence suggests that the granite is the product of anatexis of metapelite from the Rössing Formation, and it has been boudinaged and folded during D2 deformation. A large mass of garnetiferous granite has accumulated along the axial plane of a m-scale D2 fold at the locality where LID038 was collected (see Fig. 4.14, Chapter 4). The granite is very pale white and

fine-to medium-grained (0.5 mm – 2 mm), with large (5 cm – 10 cm) garnet-quartz intergrowths (see Fig. 4.14C) and rare patches of coarse biotite. With the exception of the garnet and minor biotite, the granite comprises quartz, K-feldspar and plagioclase, with accessory monazite. Zircons from LID038 are subhedral, with rounded tips, and clear to dark brown in colour (Fig. 5.11A). CL imaging shows that zircons have only rare oscillatory zoning, most zircons are dark, lack any internal structure, and may have inherited cores (Fig. 5.11B). Monazite grains are large (>200 µm), clear to pale yellow (Fig. 5.11C), and BSE imaging shows that they lack any internal structure or zoning (Fig. 5.11D).

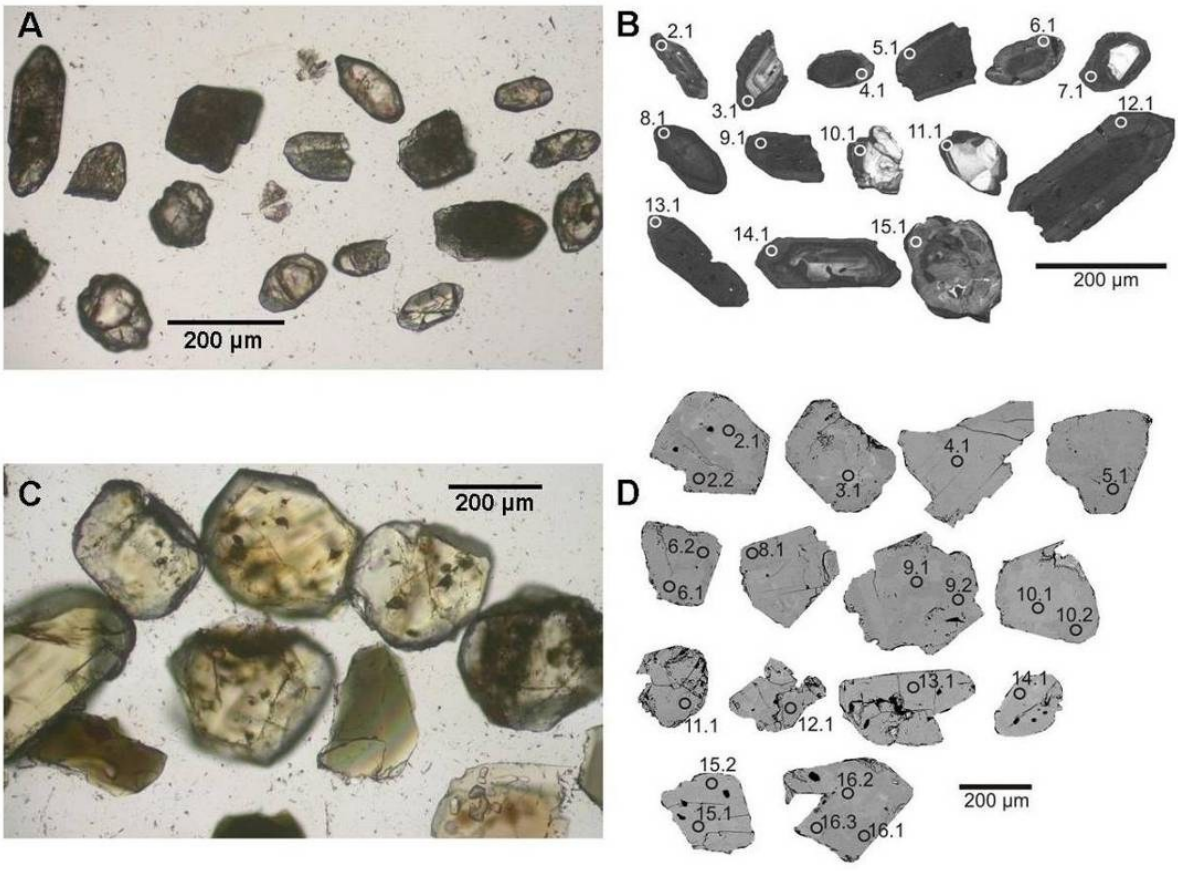

Fig. 5.11 – Images of zircons and monazites from garnetiferous leucogranites. A: Photomicrograph of small, rounded clear to dark brown zircons from sample LID038. B: CL images of zircons analysed from LID038, showing spot locations. Note that some zircons are dark, with no magmatic zoning. C: Photomicrograph of pale yellow monazite from LID038. D: BSE images of monazites analysed from LID038, showing spot locations.

5.1.6.2 Results of SHRIMP U-Pb geochronology

Despite fairly high U contents of up to 2500 ppm, zircons from LID038 are mostly concordant, and yield a weighted mean concordia age of 520.3 ± 4.6 Ma, excluding inherited or discordant analyses (Fig. 5.12A). Monazite analyses are similarly concordant, and yield a weighted mean concordia age of 514.1 ± 3.1 Ma (Fig. 5.12 B), excluding two discordant analyses.

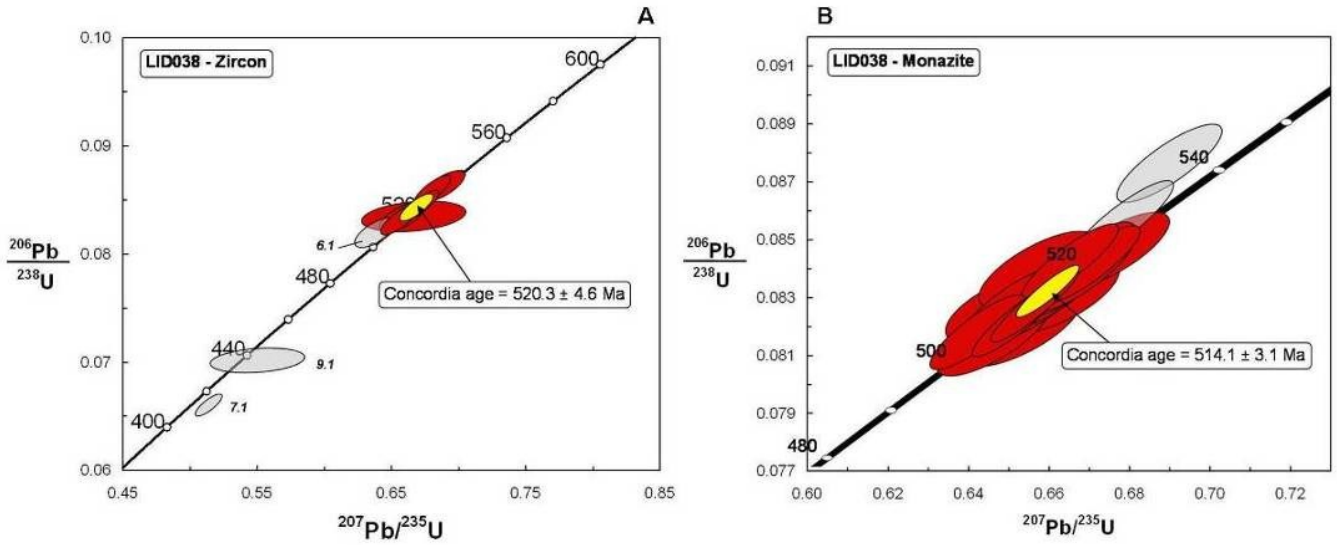

Fig. 5.12 – A: Concordia plot for zircons from LID038, which yield an age of 520.3 ± 4.6 Ma. B: Concordia plot for monazites from LID038, which give an age of 514.1 ± 3.1 Ma.

5.1.6.3 Discussion of results

The age of 520 Ma for zircons from a garnet-bearing leucogranite is identical to the 520 Ma age obtained for metamorphic rims on zircons from amphibolite sample LKR021, and to the age of 520 Ma obtained for the grey granites. Like the grey granites, garnet-bearing leucogranites are emplaced into D2 structures and folded by F2 folds, and this 520 Ma age further confirms that D2 deformation and high-grade metamorphism were coeval at 520 Ma. Monazite analyses give a slightly younger age of 514 Ma, which (although within error of the 520 Ma zircon age) may be due to the

higher diffusivity of Pb in monazite relative to zircon, or the lower closure temperature of monazite (*ca*. 700 °C – Smith & Giletti, 1997) relative to zircon (*ca*. 900 °C – Cherniak & Watson, 2000). Ages of 520-514 Ma fall in the middle of the 525 ± 2 Ma to 504 ± 3 Ma range for peak metamorphic conditions suggested by Jung & Mezger (2003a). These were U-Pb monazite and Sm-Nd garnet ages of unmigmatised metapelites. Restitic garnets also gave Sm-Nd ages of 518 ± 3 Ma, indicating that anatexis took place at this time and confirming the 520-514 Ma age for peak metamorphism. These ages of between 520-514 Ma are, however, younger than the 536-539 Ma age for the anatectic red granites, suggesting that two metamorphic events took place in the southwestern Central Zone – an earlier event at 536-539 Ma (M1), and another high-grade event at 520-514 Ma (M2). This is in conflict with the interpretation of Miller (2008) that the 534 ± 7 Ma age for anatectic red granite from Goanikontes (Briqueu *et al.*, 1980) represents the peak (M2) metamorphic age, and that M1 in the southern Central Zone may be older than 555 Ma. Rather, M1 appears to have occurred at 534-539 Ma (anatectic red granites from this study and Briqueu *et al.*, 1980), with M2 occurring between 525 and 504 Ma (this study; Jung & Mezger, 2003a).

5.1.7 Uraniferous leucogranites

Uraniferous leucogranites are voluminously minor relative to some of the other granitoids of the Central Zone, and in the study area, but they are nonetheless important owing to their apparent relationship with D3 deformation and their economic importance. Within the study area, uraniferous leucogranites occur east of the Ida Dome, where they are localised at the contact between the Khan and Rössing Formations in the cores of D3 anticlines and have formed extensive skarns owing to reaction with the Rössing Formation (Freemantle, Pers. Comm.). They are also found along the southern margin of the Palmenhorst Dome, where sheets of uraniferous leucogranites cross-cut earlier formed D2 structures. West of the study area, around Goanikontes, they have been studied by Nex & Kinnaird (1995) and Nex (1997) and, to the northeast at the Valencia deposit, they are seen to intrude into the hinge of a km-

scale D3 anticline (Freemantle, Pers. Comm.). At the Rössing Mine, their emplacement is suggested to be controlled by late D4 brittle deformation related to movement along the Welwitschia Lineament (Basson & Greenway, 2004). Since their emplacement may be controlled by upright D3 structures, and they cut D2 structures, uraniferous leucogranites may constrain the timing of D3, or at least place a lower limit on the age of D3, and may date the suggested transition from brittle to ductile conditions in the Central Zone (Poli, 1997). Briqueu *et al.* (1980) dated an uraniferous leucogranite from Goanikontes at 508 ± 2 Ma, and mineralisation essentially contemporaneous at 509 ± 1 Ma (using the U-Pb method). Rb-Sr dating of the granites from the Ida Dome (Marlow, 1983) yielded a 542 ± 33 Ma age. Here, two samples have been selected for dating, one from the Goanikontes area (LRV001), and the other from the Valencia deposit (LVA001).

5.1.7.1 Descriptions of samples and zircons analysed

Sample LRV001 is an uraniferous leucogranite from the Goanikontes area, west of the main study area (locality 0484256/7491615). Granites from this area have previously been described in detail (Nex & Kinnaird, 1995; Nex, 1997) and LRV001 is a D-type leucogranite in the classification scheme of Nex & Kinnaird (1995), as it does not show any oxidation haloes. The granite is coarse-grained to pegmatitic, and comprises predominantly quartz and K-feldspar, with minor amounts of biotite. Uraniferous granites from the Goanikontes area have numerous U-bearing accessory phases, including uraninite (Freemantle, Pers. Comm.), and there is a relative paucity of zircon and monazite as accessory phases relative to other granite types in the study area. Zircons are large and euhedral, clear to dark brown, and many are opaque (Fig. 5.13A). CL imaging of zircons from LRV001 was unsuccessful owing to the large amounts of U and Th in the zircons (up to 9000 ppm and 1000 ppm, respectively), and BSE has been used to investigate the zircons (Fig. 5.13B). This reveals that most zircons are metamict, and have suffered radiation damage owing to the high levels of U and Th. The zircons have radial fractures and lack any magmatic zoning. Any primary internal structure has been destroyed, and the zircons have numerous

inclusions and holes, and possibly new U-bearing phases that have exsolved from the zircon. Monazite is very scarce, and only two grains were found.

Sample LVA-1 is an uraniferous granite from the Valencia deposit, *ca.* 40 km northeast of the main study area (locality 0523854/7528870). It is a coarse-grained leucogranite, comprising quartz and K-feldspar, with minor plagioclase and biotite (which has been slightly altered to chlorite). Zircon crystals are dark brown to grey with pearly opaque zones of extreme radiation damage. CL imaging shows relict magmatic oscillatory zoning, but most grains are dominated by blotchy patches of altered, metamict zircon. Bright-CL cores of inherited zircon are present in some grains. Given the poor state of preservation of these grains, it was difficult to find suitable areas to target for dating, and analyses were only done on the least altered areas where original igneous textures were preserved, or where the CL was brightest (with the hope of sampling the areas with the lowest U concentrations).

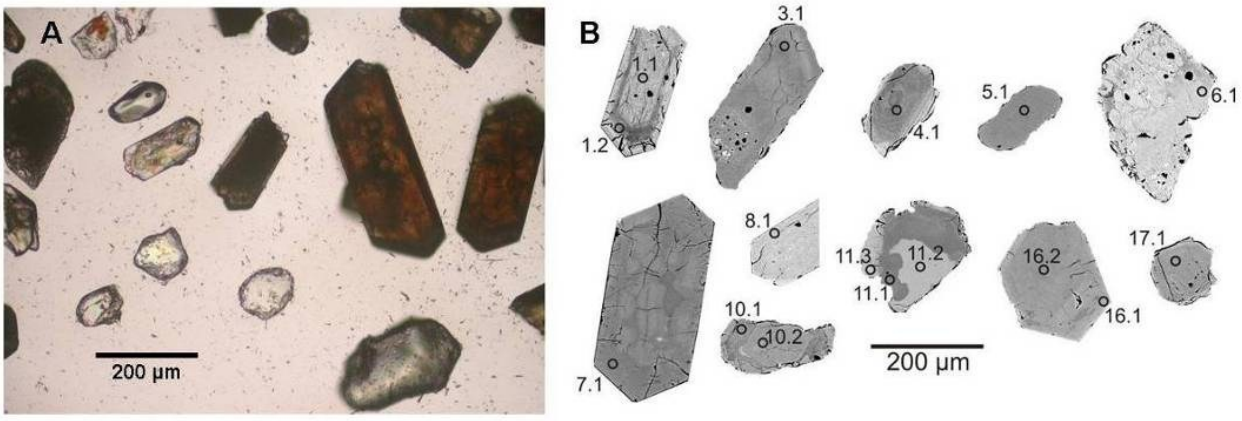

Fig. 5.13 – A: Photomicrograph of zircons from LRV001, showing large, euhedral, dark brown to opaque zircons. B: BSE images of zircons analysed from LRV001, showing spot locations. Note the radial cracks in some zircons, the lack of oscillatory zoning or regular internal structure, and numerous inclusions and holes. Note that spots 2.1 and 18.1 are not shown as the zircons were not imaged.

5.1.7.2 Results of SHRIMP U-Pb geochronology

The metamict nature of the zircons has resulted in Pb-loss and discordance; consequently no coherent age can be determined for zircons from this sample. Zircons commonly plot above Concordia, and show a spread of ages. A Model 2 solution (Ludwig, 2003) through the data yields an upper intercept of 474 ± 63 Ma and a lower intercept of 272 ± 160 Ma (Fig. 5.14A). Three spots analysed show inherited Palaeoproterozoic ages (4.1; 17.1; 18.1), and have lower U contents (300-500 ppm). A Model 1 solution through these data yields an upper intercept age of 1967 ± 11 Ma (Fig. 5.14B). Although an isochron through three data points is unreliable, it nonetheless illustrates that these zircons show an inheritance similar in age to samples from the Abbabis Complex gneisses.

The three spots analysed on the two monazite grains obtained from this sample are not considered sufficient data for a reliable age, and the monazite grains are slightly discordant. A weighted mean Concordia age of 514.8 ± 22 Ma can be obtained (Fig. 5.14C), although this age is statistically unreliable and should be viewed with caution. Similar problems were encountered for zircons from LVA001. Owing to the extreme U contents of the zircons (up to 1% U in selected spots), there is extreme discordance in both directions, including reverse apparent discordance owing to radiation damage, and the U/Pb ages are meaningless. Thus, the $^{207}Pb/^{206}Pb$ data are used to obtain an indication of the age of these zircons. Regression of all data points gives 506 ± 8 Ma (N =16/16; MSWD = 1.19; probability = 0.27). If the two extreme reverse discordant data are left out (spots 2.1 and 3.1) a regression gives an upper intercept age of 508 ± 9 Ma, practically identical to the all-inclusive age. However, when all reverse discordant analyses are ignored, a Model 1 solution through these data gives an age of 515 ± 22 Ma, similar to the monazite age from LRV001. Some cores were also analysed, and give both Palaeoproterozoic ages ($^{207}Pb/^{206}Pb$ ages of 1808.5 ± 5.3 Ma and 1859 ± 13 Ma for spots 4.1 and 5.1, respectively) and a Mezoproterozoic $^{207}Pb/^{206}Pb$ age of 1074 ± 16 Ma for spot 7.1.

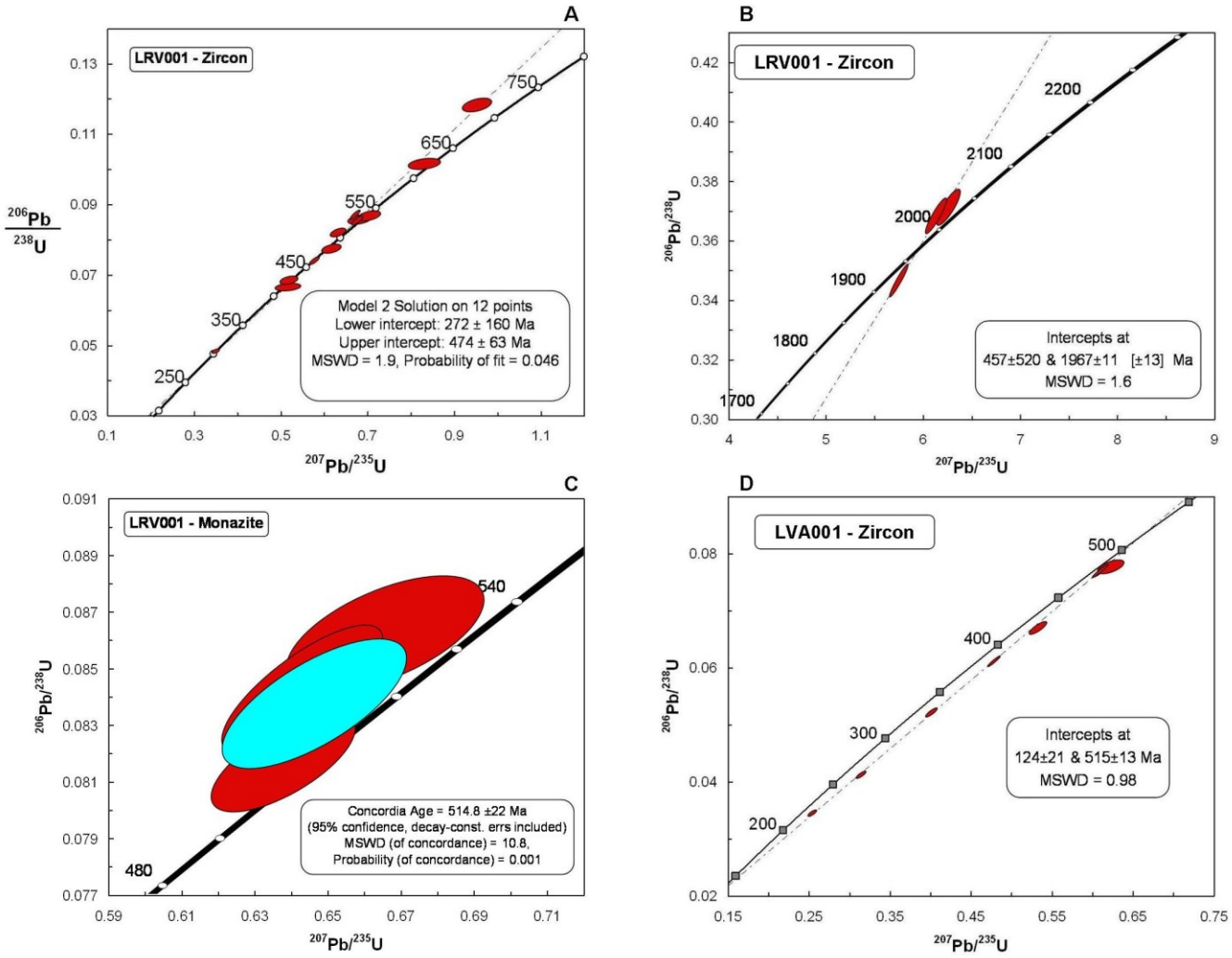

Fig. 5.14 – Concordia plots for uraniferous leucogranites. A: Zircons from LRV001, showing discordance of zircons and an unreliable Model 2 solution through the data. B: Three inherited zircons from LRV001, which give a Model 1 solution with an upper intercept age of 1967 ± 11 Ma. C: Slightly discordant monazite grains from LRV001, which give an age of 514.8 ± 22 Ma. D: Zircons from LVA001, which give a Model 1 solution age of 515 ± 13 Ma if all reverse discordant analyses are discarded.

5.1.7.3 Discussion of results

The high U contents and consequent metamict nature of the zircons from the uraniferous leucogranites has resulted in highly discordant analyses and unreliable dates for these granites. Nonetheless, some conclusions can be drawn from these results. The Palaeoproterozoic to Mesoproterozoic inherited ages of zircons from these granites may indicate a source from the Abbabis Complex, which is also Palaeoproterozoic to Mesoproterozoic in age (see sections 5.1.1 and 5.1.3). The analyses of zircons from LRV001 give an unreliable age, but the monazites appear more concordant and give an age of 515 Ma, similar to the 514 Ma age for monazite from LID038, indicating that they may be metamorphic monazites. Including reverse discordant zircons from LVA001 gives ages of 506-508 Ma, similar to the 508-509 Ma age obtained by Briqueu *et al.* (1980). Thus, in the light of the highly discordant analyses for these two samples, it appears that the ages obtained by Briqueu *et al.* (1980) may be the most reliable ages for the uraniferous leucogranites, and that they intruded at *ca*. 508 Ma – i.e. they postdate the grey granites, garnetiferous leucogranites, D2 deformation and the peak of high grade metamorphism at 520-514 Ma (sections 5.1.4, 5.1.6), but predate the titanite age of 494 Ma obtained for the amphibolite sample LKR021 (section 5.1.2) and, thus, intruded whilst the Central Zone was cooling, but was still at fairly high-grade conditions (upper amphibolite facies). This constrains the timing of D3 to older than 508 Ma, indicating that non-coaxial D2 deformation was followed immediately by upright, coaxial D3 folding. Future attempts to date this granite type should focus on analyzing monazite (which is not damaged by high U contents) rather than zircon (which has been altered in these granites).

5.1.8 Pink pegmatitic leucogranites

This voluminously minor granite type intrudes into brittle structures, and cross-cuts grey granites. It is equated with the F-type leucogranites of Nex & Kinnaird (1995), suggesting that it is the youngest granite type found in the study area. A single sample (CZF-2) has been collected for geochronology, to place a lower limit on the age of Damaran deformation.

5.1.8.1 Descriptions of sample and zircons analysed

CZF-2 is a sample of pink pegmatitic leucogranite which appears to represent the F-type granites recognised by Nex & Kinnaird (1995) in the Goanikontes area, and was collected near the centre of the Ida Dome (locality 0500574/7457122), where it intrudes a body of grey granite. This sample comprises very coarse (3 cm -10 cm) crystals of milky white quartz and euhedral bright pink K-feldspar, with rare coarse flakes of biotite. Zircons from CZF-2 are anhedral, cracked and partially resorbed. They have very high to extreme U concentrations (up to 7000 ppm U), and are metamict. Only rare ghost magmatic zoning is still preserved, and one core was analysed (spot 21.1).

5.1.8.2 Results of SHRIMP U-Pb geochronology

As expected from the extreme U concentrations and metamict nature of the zircons, most data are highly discordant and it is difficult to obtain reliable age data (Fig. 5.15). However, using ^{208}Pb-corrected data, two groups of analyses give concordant ages (Fig. 5.15A). Five analyses with the least discordance (#s 3.1, 6.1, 11.1, 14.1, 17.1) give an age of 523.6 ± 9.2 Ma (Fig. 5.15B), and the same analyses give a weighted ^{207}Pb/^{206}Pb mean age of 515 ± 10 Ma (Fig. 5.15C) (MSWD = 0.47; probability = 0.76). A second group of analyses (#s 5.1, 8.1, 9.1, 15.1, 18.1) give an age of 434.4 ± 2 Ma (Fig. 5.15D). The core analysed gives a Palaeoproterozoic ^{207}Pb/^{206}Pb age of 1784 Ma.

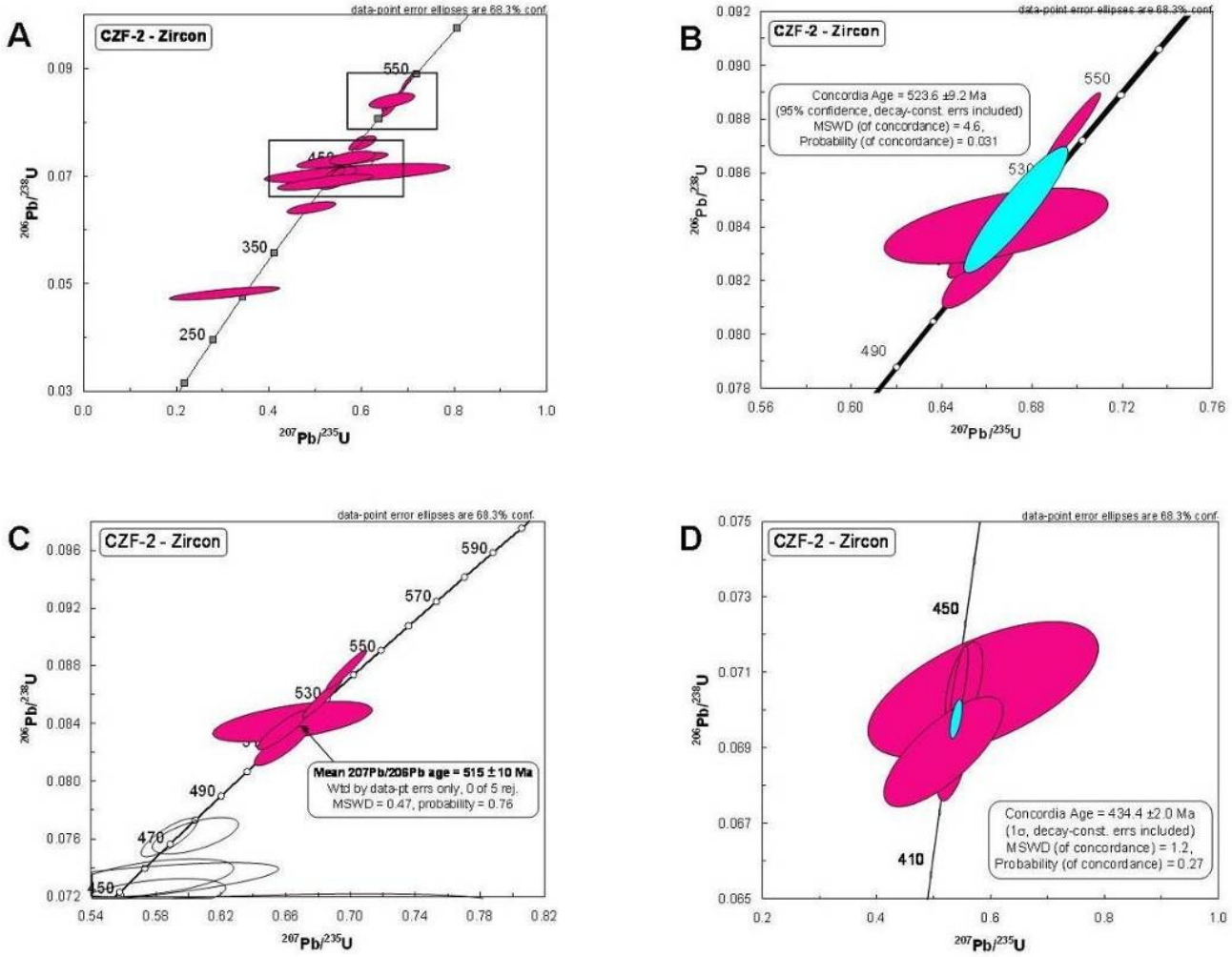

Fig. 5.15 – Concordia diagram for zircons from CZF-2. A: Two groups give concordant ages (indicated). B: Plot of the first group of analyses (#s 3.1, 6.1, 11.1, 14.1, 17.1) gives an age of 523.6 ± 9.2 Ma. C: Plot of the mean $^{207}Pb/^{206}Pb$ age for the first group of analyses, which gives an age of 515 ± 10 Ma. D: Plot of the second group of analyses (#s 5.1, 8.1, 9.1, 15.1, 18.1), which gives an age of 434.4 ± 2 Ma.

5.1.8.3 Discussion of results

The age of the first group of analyses (515-524 Ma) is similar to and within error of the 520 Ma age for the grey granites, into which the pink pegmatitic granite has intruded and, thus, the zircons which give this age are may be xenocrystic zircons,

rather than reflecting the magmatic age of this granite. However, zircons from grey granites analysed (LHA010 and LHA012 – section 5.1.4) do not have high U contents and are not metamict. The younger group of analyses, which give a 434 Ma age, may give the magmatic age of the granite, and is consistent with the transgressive relationship of the pink pegmatitic granite to the grey granite. Thus, it appears that the pink pegmatitic granites (and possibly analogous F-type leucogranites – Nex & Kinnarid, 1995) may be significantly younger than the ages for other granites in the Central Zone, and are similar in age to Rb-Sr biotite and muscovite cooling ages (*ca*. 450 Ma – Hawkesworth *et al.*, 1983) and K-Ar cooling ages (*ca*. 440 Ma – Haack & Hoffer, 1976), indicating that these granites intruded during cooling of the Central Zone through 500 °C to 300 °C (Miller, 2008). Whilst this substantiates field evidence that the pink pegmatitic granites were emplaced into more brittle (and, hence, cooler) country rocks than other granites, the metamict nature of zircons makes the ages suggested tentative.

5.1.9 Anatectic leucosomes

Along the western edge of the Ida Dome, a D2 shear zone contains anatectic leucosomes. Numerous anatectic leucosomes are also found in D2 shear bands within Abbabis Complex gneisses in this area. Both this shear zone and the extensional shear bands demonstrate the relationship between D2 deformation and high-grade metamorphism in the study area, as already highlighted by Poli (1997), Ward *et al.* (2008) and Kisters *et al.* (2009). These shear bands accommodated the NE-SW directed extension that occurred together with non-coaxial strain and associated SE-verging deformation, and shear zones developed on the limbs of km-scale D2 folds near the basement-cover interface (see Chapter 3). Thus, the leucosomes developed in these structures should confirm the age of metamorphism and of D2 shearing and NE-SW directed extension. These anatectic leucosomes would be expected to give ages similar to the ages of 520-514 Ma determined for D2 and peak metamorphism from the grey granites and garnet-bearing leucogranites, but should be older than the

508 Ma (Briqueu *et al.*, 1980) uraniferous leucogranites. Two samples of these anatectic leucosomes were selected for dating.

5.1.9.1 Descriptions of sample and zircons analysed

Sample CZRL-1 is a sample of anatectic melt from a migmatitic, SE-verging shear zone near the western margin of the Ida Dome (locality 0499125/7486844). The sample consists of granitic leucosome, which is coarse-grained and made up of plagioclase and quartz, with lesser biotite and minor amounts of magnetite. Most zircons from CZRL-1 contain cores with various shapes and sizes, overgrown by high-U, poorly zoned rims that have well-developed pyramidal terminations. Sample CZRL-3 is a sample of anatectic melt localised in a SW-verging D2 shear band developed in Abbabis Complex gneisses near the western edge of the Ida Dome (locality 0500289/7488670). Shear bands are widely developed and represent the NE-SW directed extensional component of D2 deformation in the southwestern Central Zone. The sample comprises coarse-grained quartz, K-feldspar and plagioclase, with minor biotite and magnetite. The zircons are anhedral to euhedral with most grains comprising a low-U core and a high-U overgrowth.

5.1.9.2 Results of SHRIMP U-Pb geochronology

The cores of zircons from CZRL-1 give ages that vary from Archaean to Neoproterozoic (reflecting the detrital nature of the zircons in the Damara Supergroup, which forms the host for this migmatitic shear zone and the likely source for the leucosome). The high-U rims, developed during migmatite crystallisation, plot in a spread from *ca*. 500 Ma, showing variable but extensive Pb-loss. A weighted mean $^{207}Pb/^{206}Pb$ age for the four most concordant points (#s 7.1, 8.1, 10.1 and 18.1) is 511 ± 16 Ma. Regression of all data for the overgrowths gives a Model 1 solution with an upper intercept of 511 ± 18 Ma (Fig. 16A). Zircons from CZRL-3 show a cluster of data on concordia for which a weighted mean $^{207}Pb/^{206}Pb$ age of 508.4 ± 8.7 Ma is calculated (Fig. 5.16B). Three analyses are slightly discordant, and plot away from this cluster. These could indicate

an inherited component, or may be the result of subtle mixed core-rim analyses, where the beam was burning through into a small older part of the grain, changing the $^{207}Pb/^{206}Pb$ composition during the run. All cores are Palaeoproterozoic in age, reflecting the age of the Abbabis Complex in which the extensional shear band is developed.

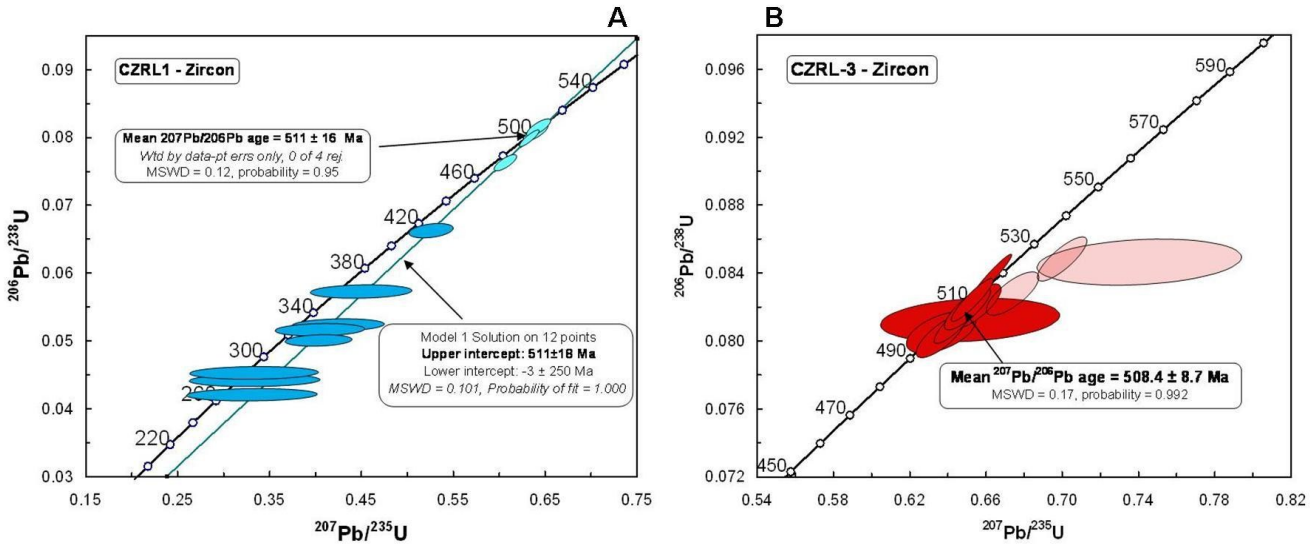

Fig. 5.16: Concordia plots of analyses from anatectic leucosomes. A: CZRL-1, showing the extensive Pb-loss for many of the high-U rims, and the results of both the mean $^{207}Pb/^{206}Pb$ age calculation (511 ± 16 Ma) and a Model 1 solution (upper intercept of 511 ± 18 Ma). B: CZRL-3, showing the mean $^{207}Pb/^{206}Pb$ age of 508.4 ± 8.7 Ma.

5.1.9.3 Discussion of results

The zircons from sample CZRL1 are high-U but, nonetheless, both the weighted mean age and a Model 1 solution give 511 Ma ages. The analyses of zircons from sample CZRL give a 508 Ma age. These ages are *ca*. 10 Myr younger than the 520 Ma age determined for D2 folding from the grey granites and garnet-bearing leucogranites. This age is also similar to the age determined for the uraniferous leucogranites, and for D3 deformation. Thus, D2 deformation may have continued for *ca*. 10 Myr, beginning with folding of Damara Supergroup and Abbabis Complex rocks into km-

scale, recumbent to N-dipping folds at *ca*. 520 Ma, and culminating with extension on the limbs of these folds, and the widespread development of extensional shear bands at *ca*. 510 Ma, and it appears that NE-SW directed extension slightly postdates SE-verging folding. The estimated age for uraniferous leucogranites at 508 Ma (Briqueu *et al.*, 1980) indicates that D3 deformation occurred immediately following and almost contemporaneous to late-D2 extension.

5.2 Hf- and O-isotope Analyses

This section seeks to address the second question posed at the beginning of the chapter, namely, what is the source of the grey granites, which are the most voluminous granitoids in the study area.

The isotopic characteristics of granitoids, metasediments, and basement gneisses in the Central Zone shows that early Damaran diorites and syenites have low initial $^{87}Sr/^{86}Sr$ ratios, less than 0.7059, as do most of the Salem-type granites, with initial $^{87}Sr/^{86}Sr$ ratios of 0.7055-0.7087 for most granites (Haack *et al.*, 1982), although some samples of Salem-type granites do have higher initial $^{87}Sr/^{86}Sr$ ratios of up to 0.7157 (Haack *et al.*, 1982). Initial $^{87}Sr/^{86}Sr$ ratios for Damaran metasediments increase, and initial $^{143}Nd/^{144}Nd$ ratios decrease, with stratigraphic height in the Damaran Supergroup (McDermott *et al.*, 1989), and both the initial $^{87}Sr/^{86}Sr$ and $^{143}Nd/^{144}Nd$ ratios of the Etusis Formation metasediments are similar to those for Abbabis Complex gneisses (McDermott *et al.*, 1989), indicating that the Etusis Formation was derived from the Abbabis Complex (i.e. Congo Craton), whilst sediments higher in the Damara Supergroup stratigraphy were derived from younger sources (McDermott *et al.*, 1989). The non-radiogenic isotopic ratios of early Damaran diorites and granitoids preclude Damaran metasediments, or basement gneisses as source rocks for these intrusions, and suggests that they may be generated from a young volcanogenic source, or may possibly even have a mantle source (Haack *et al.*, 1982). However, younger granitoids have higher initial $^{87}Sr/^{86}Sr$ and negative ε_{Nd}, indicating their

genesis from anatexis of mid-crustal pelitic lithologies or basement gneisses (Haack *et al.*, 1980; Jung *et al.*, 2001). Abbabis Complex gneisses have Nd model ages of up to 2.9 Ga (McDermott *et al.*, 1989), indicating that the *ca.* 2 Ga Abbabis Complex gneisses may have been produced by reworking of older crust. O-isotopes for all Damaran intrusions are fairly heavy, above the $\delta^{18}O$ mantle values of 5.3 ± 0.3‰ (Valley *et al*., 1998), although early diorites, syenites and Salem-type granites may have lower values (8.4‰ – 10.6‰ – Haack *et al.*, 1982) than younger leucogranites, which have values between 10‰ and 15‰ (Haack *et al.*, 1982; Jung *et al.*, 2001). The major and trace element characteristics of Damaran intrusions were used together with O-, Sr- and Nd-isotopic characteristics by McDermott (1986), who defined three main granitoid types: peraluminous crustal melt granitoids, calc-alkaline diorites and within-plate granitoids. Peraluminous crustal melt granitoids have high initial $^{87}Sr/^{86}Sr$ (>0.710), high $\delta^{18}O$, Nd model ages of *ca.* 2 Ga, high Rb, and low Nb, Y and Zr. Calc-alkaline diorites are metaluminous, have low initial $^{87}Sr/^{86}Sr$ (<0.710), variable $\delta^{18}O$, Nd model ages of 1-1.4 Ga, and low Rb/Sr. Within-plate granitoids have low $\delta^{18}O$ (*ca*. 7‰), young model ages of ca. 1.2 Ga, variable initial $^{87}Sr/^{86}Sr$, high Nb, ZR, Hf, Y and REE, and very low CaO. The elevated $\delta^{18}O$ values for most Damaran intrusions (even the 7‰ values for within-plate granitoids) precludes their having a source in the mantle, and indicates intracrustal generation (Haack *et al.*, 1982).

For this study, two samples were selected for both O- and Hf-isotopic analyses of the zircons using SHRIMP and LA-ICP-MS, respectively. First, a sample of Abbabis Complex gneiss was analysed (LID045). The zircons from this sample have been dated (5.1.1), and LID045 was selected over LID036 and LID041 as the zircons from this sample are the least fractured of those from basement samples, and they show the lowest levels of discordance (see Fig. 5.2). A sample of basement gneiss was chosen in order to isotopically characterise the nature of the Abbabis Complex, for comparison with the isotopic characteristics of the grey granites, and with other granites from the Central Zone analysed by McDermott (1986) and Jung *et al.* (2001). Second, a sample of grey granite was analysed (LHA010), in order to establish the source for these granites, which are the most voluminous magmatic rocks present in the study area. Both

samples of grey granite analysed for U-Pb dating (LHA010 and LHA012) have low levels of discordance, and LHA010 was selected as more spots were analysed for U-Pb than for sample LHA012.

5.2.1 Hf-isotopes

Hf-isotopes were analysed using Multi Collector Laser Ablation Inductively Coupled Plasma Mass Spectrometry (MC-LA-ICPMS) at the Australian National University (ANU). Analytical procedures can be found in Appendix 2. The analyses were carried out on the same spots, or as near as possible to, the spots used for U-Pb and O-isotope analyses. Present day (T_0) ε_{Hf} values were calculated using the formula

$$\varepsilon_{Hf} = \left[\left(\frac{\left\{\frac{^{176}Hf}{^{177}Hf}\right\}}{0.282772}\right) - 1\right] * 10\,000$$

ε_{Hf} values at the time of crystallisation, (T_1) were calculated using the formula

$$\varepsilon_{Hf} = \left(\left[\frac{\left(\frac{^{176}Hf}{^{177}Hf}\right)T_1}{\left(0.282772 - 0.0332\left[e^{0.01867*\left\{\frac{Age(Ma)}{1000}\right\}-1}\right]\right)}\right] - 1\right)$$

$^{176}Hf/^{177}Hf$ values at the time of crystallisation, (T_1) were calculated using the formula

$$\left(\frac{^{176}Hf}{^{177}Hf}\right)T_0 - \left(\frac{^{176}Lu}{^{177}Hf}\right)T_0 * \left\{e^{0.01867*\left[\frac{Age(Ma)}{1000}\right]} - 1\right\}$$

Where 0.282772 is the Chondritic Uniform Reservoir (CHUR) $^{176}Hf/^{177}Hf$ value of Blichert-Toft & Albarede (1997), 0.0332 is the CHUR $^{176}Lu/^{177}Hf$ value of Blichert-Toft & Albarede (1997), and 0.01867 is the ^{176}Lu decay constant from Söderlund *et al*.

(2004). Age (Ma) are the U-Pb ages of the spots analysed, and the CHUR values of Blichert-Toft & Albarede (1997).

Model ages at the time of crystallisation (T_1) were calculated using the formula

$$0.283225 - 0.038512\{e^{0.01867*\left[\frac{Age(Ma)}{1000}\right]} - 1\}$$

Model ages at the time of separation from the Depleted Mantle (DM) curve (T_{DM}) were calculated using the formula

$$\left[\frac{\left(\frac{1}{1.867*10^{-11}}\right)*LN\left[\frac{\left\{\left(\frac{^{176}Hf}{^{177}Hf}\right)T_1-\left(\frac{^{176}Hf}{^{177}Hf}\right)T_{DM_1}\right\}}{(0.015-0.038512)}\right]+1}{10^6}\right]+Age(Ma)$$

where $^{176}Hf/^{177}Hf$ (T_{DM1}) values were calculated using the formula

$$0.283225 - 0.038512[e^{0.01867*\left(\frac{Age(Ma)}{1000}\right)} - 1]$$

$1.867*10^{-11}$ is the ^{176}Lu decay constant from Söderlund *et al*. (2004), 0.015 is the $^{176}Lu/^{177}Hf$ value of Goodge & Vervoort, 2006, 0.038512 is the present day DM $^{176}Lu/^{177}Hf$ value of Vervoort & Blichert-Toft (1999), and 0.01867 is the ^{176}Lu decay constant from Söderlund *et al*. (2004).

For LID045, 14 spots on 13 grains were analysed, and ε_{Hf} (T_0) for most grains falls in a narrow range between -47.66 and -52.13, with a single spot (4.1) slightly higher at -42.15. ε_{Hf} at the time of crystallisation (i.e., U-Pb age for the individual spot) is between -3.9 and -8.9, with the exception of spot 4.1 (ε_{Hf} = 1.44). Model ages from LID045 are Mesoarchaean, and fall into a range between 2822 Ma and 3140 Ma, with

spot 4.1 younger, at 2479 Ma (Fig. 5.17A), with a peak in the relative probability at *ca.* 2960 Ma (Fig. 5.17B).

For LHA010, Hf isotope analyses were conducted on 16 spots on 13 grains. With the exception of spot 18.1 (which has an inherited core), the selected spots are on magmatic zircon grains and have $^{176}Hf/^{177}Hf$ of between 0.282097 and 0.282166, yielding ε_{Hf} values of between -23.86 and -21.44. These give ε_{Hf} values at time of crystallisation (T_1 – determined from U-Pb analyses for each individual spot) of between -15.43 and -10.37. Model ages calculated are between 2089 Ma and 2286 Ma, (Fig. 5.17C), with a probability peak at *ca.* 2.2 Ga (Fig. 5.17D). A single inherited zircon (spot 18.1) gives much lower values, with a 2764 Ma model age (2014 Ma crystallisation age). This is similar to crystallisation ages and model ages determined for the gneisses of the Abbabis Complex.

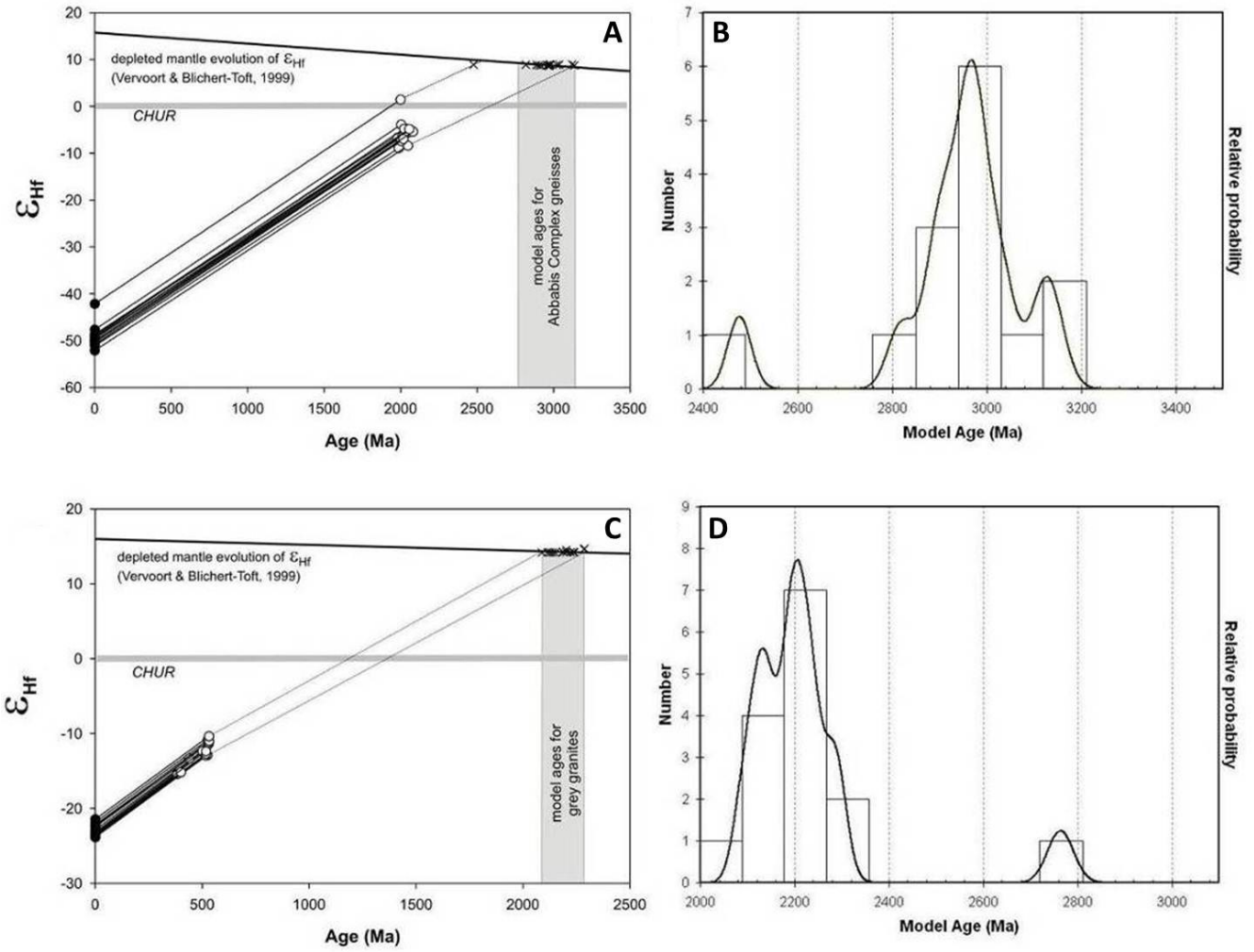

Fig. 5.17 – A: Plot of ε_{Hf} vs. age for sample LID045, showing crystallisation ages of ca. *2 Ga (age from this sample is 2044 Ma), and model calculated ages for this sample. Shaded area indicates the majority of model ages, excluding spot 4.1. B: Relative probability plot of model ages calculated for sample LID045, showing a peak in probability at* ca. *2960 Ma. C: Age (Ma) vs. ε_{Hf} for sample LHA010 (excluding spot 18.1). D: Relative probability plot of model ages calculated from sample LHA010, with most analyses giving DM model ages of* ca. *2200 Ma.*

5.2.2 O-isotopes

O-isotope analyses of zircons were carried out using the SHRIMP at ANU, on the same spot locations as U-Pb analyses were conducted. Analytical procedures can be found in Appendix 2.

LID045 shows a range of $\delta^{18}O$ values for the zircons analysed, from as high as 9.50‰ to 5.03‰, similar to the mantle value of 5.3 ± 0.3‰ (Valley *et al*., 1998). There is no correlation between either the age of the spot analysed (Fig. 5.18A) or the model age of the spot (Fig. 5.18B) as determined from the Hf-isotopic value of the zircon (see 5.2.1 above). Additionally, by checking whether any correlation exists between the $\delta^{18}O$ values and the amount of discordance for each analysis (from U-Pb data) it is possible to see whether the O-isotopic values of the zircons have been affected by the Damaran metamorphism which has resulted in Pb-loss in the zircons. However, zircons from LID045 show a range of $\delta^{18}O$ values even for spots analysed with a very low discordance (Fig. 5.18C), indicating that these zircons do, in fact, reflect variable O-isotopic values for Abbabis Complex gneisses, ranging from approximately mantle values up to 9.5‰. Such a range in values may reflect a mixed source for the protolith to these gneisses.

LHA010 also shows a range in $\delta^{18}O$ values, from 3.37‰ up to 7.47‰, and there does appear to be a correlation between the age of the spot analysed and its O-isotopic value, with most analyses >500 Ma having values between 5.8‰ and 7.47‰, whilst three younger spots have lower values (Fig. 5.18D). This trend is not apparent when comparing the O-isotopic values with model age determinations (Fig. 5.18E). However, what is apparent is that there may be an effect on the O-isotopic value of spots analysed owing to discordance for LHA010. More discordant analyses have lower $\delta^{18}O$ values, whilst concordant analyses have similar $\delta^{18}O$ values of *ca*. 7‰ (Fig. 5.18F). It is apparent that although rare zircons with Palaeoproterozoic ages are found in the grey granites, these are likely to be xenocrystic rather than inherited, as Abbabis Complex gneisses have variable $\delta^{18}O$ values, whilst the grey granites have

values of approximately 7‰, and are thus likely to have originated from a different source to the Abbabis Complex.

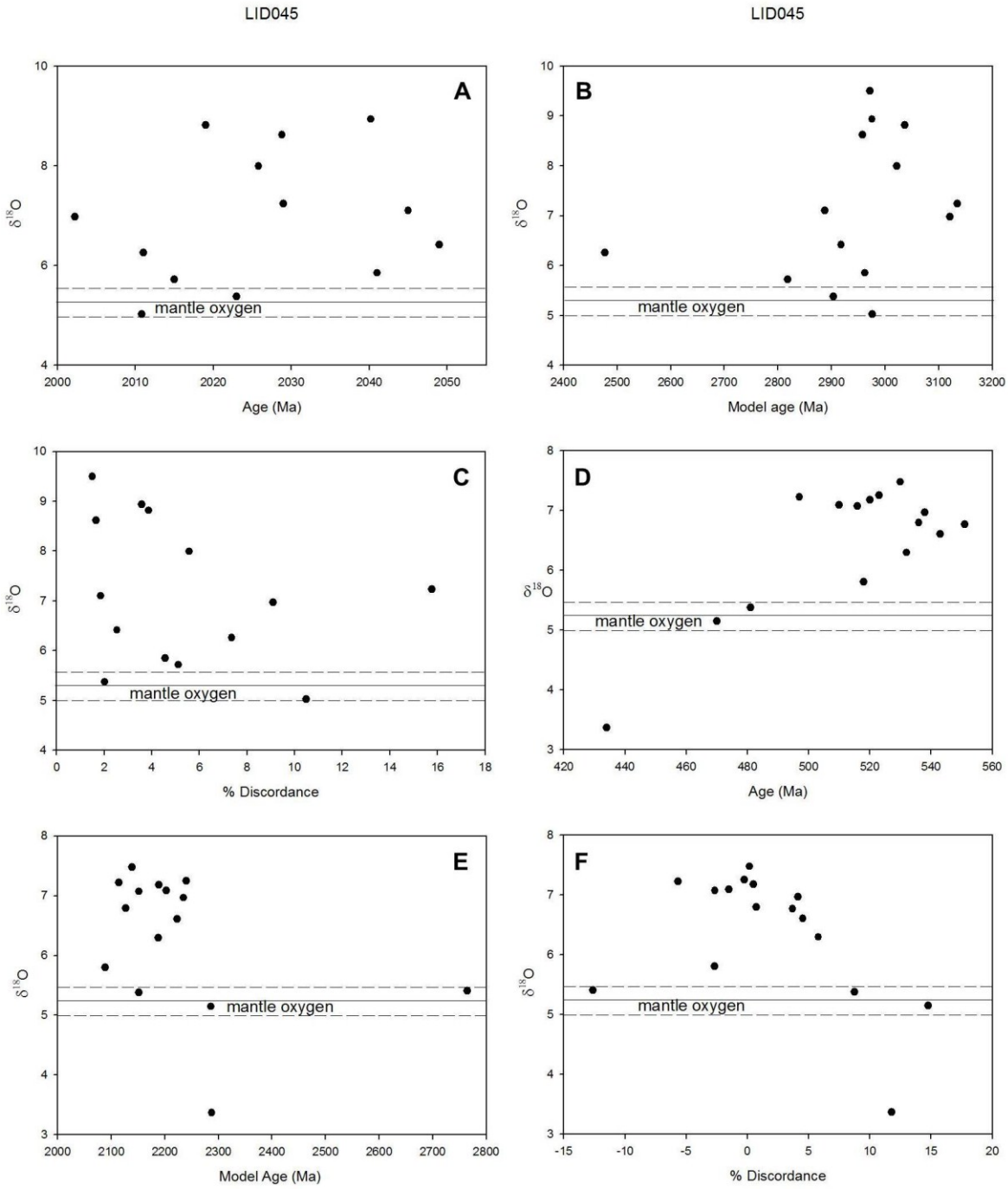

Fig. 5.18 – Binary plots of O-isotopic data for LID045 and LHA010. A: $\delta^{18}O$ vs. Age for LID045. B: $\delta^{18}O$ vs. Model age for LID045. C: $\delta^{18}O$ vs. % Discordance for LID045. D: $\delta^{18}O$ vs. Age for LHA010. E: $\delta^{18}O$ vs. Model age for LHA010. F: $\delta^{18}O$ vs. % Discordance for LHA010.

5.2.3 Discussion of results

The results of the Hf-isotope study of the two samples shows that, although the rocks of the Abbabis Complex have Palaeoproterozoic crystallisation ages (see 5.1.1), they are in fact derived from recycled Mesoarchaean crust. The *ca*. 2 Ga ages for Abbabis Complex gneisses are similar to ages determined for gneisses of the Grootfontein Complex (2022 ± 15 Ma; Hoal *et al.*, 2000), and slightly older than ages of 1985 ± 23 Ma to 1961 ± 4 Ma for gneisses of the Epupa Complex (Seth, 1999), both in northern Namibia. The 2.5-2.8 Ga Sm-Nd model ages and xenocrytic zircons in Epupa Complex gneisses are similar to the Archaean Lu-Hf model ages for Abbabis Complex gneisses from this study, and basement gneisses in the Sesfontein area (northwestern Namibia) have ages of 2584.2 ± 0.6 Ma, 2645 ± 6 Ma 2616 ± 5 Ma (Seth *et al.*, 1998). Archaean Rb-Sr ages of 2850-2650 have been reported for the Congo Craton in Angola (Delhal & Ledent, 1973; Delhal *et al.*, 1976). Thus, the Abbabis Complex gneisses, part of the Congo Craton, were formed from recycling of Archaean crust during the *ca*. 2 Ga Eburnean Orogeny (Cahen *et al.*, 1984). A further crustal recycling event took place in these rocks at *ca*. 1 Ga – inherited zircons from red granites, as well as dates by Kröner *et al.* (1991) indicate *ca*. 1 Ga ages in Abbabis Complex gneisses, representing the Kibaran (Rumvegeri, 1991) event. Similar results have been found in the central African Copperbelt, where Rainaud *et al.* (2005a) obtained largely Eburnian ages (2049 ± 6 Ma to 1976 ± 5 Ma) for zircons from basement rocks to the Katanga Supergroup, with 1059 ± 26 Ma overgrowths and Archaean (2730 ± 7 Ma and 2688 ± 8 Ma) cores.

The fact that Abbabis Complex gneisses are made up of Archaean crustal material that has been repeatedly recycled has implications for the isotopic characteristics of granitoids derived from anatexis of this crust. The 520 Ma grey granites have Lu-Hf model ages of *ca*. 2.2 Ga – should they have been derived from melting of recycled Mesoarchaean crust, they would be expected to have older model ages, and extremely negative ε_{Hf}. Similarly, the fairly narrow range of $\delta^{18}O$ values of *ca*. 7‰ for zircons from grey granites indicates that they are unlikely to be sourced from anatexis

of the Abbabis Complex, where zircons have a wider range of $\delta^{18}O$. The 1.2-2 Ga Nd model ages for granitoids and diorites from the Damara belt (McDermott, 1986) are similarly inconsistent with the Abbabis Complex as a source, although 1.2-2 Ga model ages for Damaran Supergroup rocks (McDermott *et al.*, 1989), and the high $\delta^{18}O$ values of crustal-melt granitoids (McDermott, 1986) are consistent with their generation from anatexis of Damaran metasediments during high-grade Damaran metamorphism. Grey granites have lower $\delta^{18}O$ (*ca*. 7‰) and, thus, must have a different source. Barnes & Sawyer (1980) showed that subduction of oceanic crust below the Congo Craton occurred preceding the Pan-African collision, and this crust may have been generated during rifting at *ca.* 700 Ma (Sm-Nd ages for the Matchless amphibolite; Nagel, 1999). Melting of this material during subduction could not explain the 2.2 Ga model ages for grey granites, or the 1-1.5 Ga model ages for calc-alkaline diorites and within-plate granitoids (McDermott, 1986). The crust of the Kalahari Craton, however, does contain rocks younger than 2 Ga. A number of terranes accreted onto the Kaapvaal Craton are found in southern Namibia, and associated with these terranes are intrusive rocks of the Vioolsdrif Igneous Suite and Fransfontein Granitic Suite, and intrusions associated with the Rehoboth Group. The rocks of these terranes all have ages ranging from 1.7 to 2.0 Ga (Reid, 1997; Ziegler & Stoessel, 1993; Becker *et al.*, 1996; 2004), with model ages indicating fairly juvenile crust with model ages of *ca*. 2.2 Ga (Reid, 1997) for the Vioolsdrif Igneous Suite. Such model ages would fit better with the Lu-Hf model ages of the grey granites from this study, rather than the Mesoarchaean model ages for the Abbabis Complex. Thus, a possible source of the grey granites (and probably many of the other granites in the Central Zone), is juvenile Mesoproterozoic to Palaeoproterozoic crust on the Kalahari Craton, subducted below the Congo Craton, and possibly recycled to form the granitoids of the Damara belt, during the Pan-African Orogeny.

5.3. Summary and Discussion

U-Pb geochronology of a number of samples from the southwestern Central Zone provides new age data for a variety of intrusive rock types that show distinctive relationships to deformation and metamorphism. Both pre-Damaran (2026.9 ± 2.3 Ma – sample ACAM-1) and Damaran (557.2 ± 7.4 Ma – sample LKR021) amphibolite dykes are found in the Central Zone. No previous dates exist for these amphibolites, which have previously been used as a distinguishing characteristic of the Abbabis Complex (Barnes, 1981) and are generally seen emplaced into Abbabis Complex gneisses. Palaeoproterozoic amphibolites from farm Abbabis 70 (sample ACAM-1) are slightly younger than felsic Abbabis Complex gneisses from the Ida Dome (2056 $^{+11}/_{-10}$ Ma – LID036, 2044 $^{+32}/_{-27}$ Ma – LID041, and 2044 $^{+17}/_{-14}$ Ma – LID045), but the 557 Ma amphibolite is the oldest Damaran intrusive rock type from this study, and predates all the granitoid rocks dated, indicating mafic magmatism early in the Damaran history of the Central Zone. Similar ages have been obtained for the Mon Repos diorite (546 Ma – 564 Ma; Jacob *et al.*, 2000) and Okongava diorite (558 Ma; de Kock *et al.*, 2000), part of the Goas Intrusive Suite (Lehtonen *et al.*, 1995) and for the Salem-type biotite granites (563 ± 63 Ma – Hawkesworth *et al.*, 1983; 554 ± 17 Ma – Kröner *et al.*, 1982; 554 ± 33 – Downing, 1982; 549 ± 11 Ma – Johnson *et al.*, 2006). The similar ages, as well as the similarities in major element characteristics with metagabbros and hornblendites of the Goas Intrusive Suite (Fig. 4.3), suggest that these mafic rocks are related. The Goas Suite is thought to have been emplaced following D1 in the Central Zone, and is the earliest member of a Damaran calc-alkaline active margin plutonic suite (Miller, 2008). The mafic to dioritic Goas Suite and the Salem-type granites are thought to be syn-D2 in the southern Central Zone (Miller, 2008), which is suggested to be at 555 Ma (Miller, 2008). This is similar to the 557 Ma amphibolites from this study, which are clearly seen to predate D2 in the study area – they are folded by SE-verging F2 folds, and have an S2 fabric. Furthermore, whilst 555 Ma is the suggested age for D2 deformation in the southern Central Zone (Miller, 2008), U-Pb ages for syn-D2 grey granites (519.1 ± 4.2 Ma – LHA010 and 520.4 ± 4.2 Ma – LHA012), syn-D2 garnet-bearing leucogranites (520.3 ±

4.6 Ma LID038 zircon and 514.1 ± 3.1 Ma monazite), and anatectic leucosomes localised in D2 shear zones (511 ± 18 Ma – CZRL-1) and shear bands (508.4 ± 8.7 Ma – CZRL-3) indicate much younger ages. An age of *ca*. 520-510 Ma for D2 is similar to the 514 ± 22 Ma age (Haack *et al.*, 1980) for syn-D2 early non-porphyritic granites and leucogranites in the northern Central Zone.

Field evidence indicates that intense, non-coaxial D2 deformation and NE-SW extension in the southwestern Central Zone was coeval with high grade metamorphism – syn-D2 garnet- bearing leucogranites are the product of partial melting of pelitic metasediments during the peak of metamorphism, and anatectic leucosomes are localised in D2 shear zones and shear bands. The relationship between D2 and the peak of metamorphism in the southwestern Central Zone has been noted by Poli (1997), Ward *et al.* (2008) and Kisters *et al.* (2009), and U-Pb monazite and Sm-Nd garnet dating of metamorphism in the Central Zone (525-504 Ma – Jung & Mezger, 2003a) gives similar ages to the 520-510 Ma ages suggested here for D2, with a Sm-Nd garnet age of 518 ± 3 Ma (Jung & Mezger 2003a) very similar to the ages of anatectic garnet-bearing leucogranites. High-U metamorphic overgrowths on zircons from 557 Ma amphibolites give an age of 520 ± 6.9 Ma, consistent with other ages for metamorphism. These ages are all younger than the 534 ± 7 Ma suggested by Miller (2008) for the ages of post-tectonic M2 metamorphism in the southern Central Zone. Miller (2008) suggested that M1 was older than 555 Ma. Anatectic red granites (536 ± 7.2 Ma – concordant monazite age and 539 ± 17 Ma – lower-intercept zircon age) are similar in age to the M2 age suggested by Miller (2008), and Jung & Mezger (2003) also obtained some older Sm-Nd garnet-whole rock ages of 530-540 Ma, similar to a 535-540 Ma age for metamorphism. Although 534 Ma is the age suggested by Miller (2008) for M2 metamorphism, in the study area this appears to be M1, with younger 520-510 Ma leucosomes and anatectic granites generated during M2. Furthermore, whilst the 534 Ma 'M2' metamorphism is considered post-tectonic (Miller, 2008), 536-539 Ma anatectic red granites from this study clearly predate D2.

The general inference from these data is that D2 and M2 high-grade metamorphism were coeval at 520-510 Ma in the southwestern Central Zone, with M1 resulting in anatexis of the Abbabis Complex to produce red granites at 535-540 Ma. However, one cannot disregard the 555 Ma age for D2 in the Central Zone – the syn-D2 timing of 560-540 Ma Salem-type granites and diorites of the Goas Intrusive Suite has been widely observed around Karibib (Kisters *et al.*, 2004; Johnson *et al.*, 2006), and the 539 Ma Rotekuppe Granite (possibly related to the 536-539 Ma red granites of this study) clearly post-dates D2 deformation in the Karibib area (Jacob *et al.*, 2000; Kisters *et al.*, 2004). It appears that there are two ages for D2 deformation in the southern Central Zone – 560-550 Ma in the Karibib area and 520-510 in the study area. Such diachronous D2 deformation could explain a number of features:

- 557 Ma amphibolites are pre-D2 in the study area, but related to the 560-550 Ma Goas Intrusive Suite, seen to be syn-D2 near Karibib.
- 536-539 Ma red granites predate D2 in the study area, but are post-tectonic near Karibib.
- 520-510 Ma grey granites, garnet-bearing leucogranites and anatectic leucosomes are all syn-D2 in the study area, but post-tectonic to 555 Ma deformation near Karibib.
- The syn-D2 peak for metamorphism noted in the southwestern Central Zone (Poli, 1997; Ward *et al.*, 2008; Kisters *et al.*, 2009), whilst elsewhere in the Central Zone the peak of metamorphism is suggested to be post-tectonic (Miller, 2008).

In addition to differences in the timing of D2 within the Central Zone, there are also differences in the nature of D2. Intense D2 non-coaxial ductile deformation in the southwestern Central Zone is expressed as km-scale S- to SE- verging folds and shear zones, extensional shear bands and NE-SW stretching lineations, whereas Kisters *et al.* (2004) note that D2 deformation in the Karibib area is characterised by NW-verging folding and thrusting, similar in style to deformation found in foreland fold-and-thrust belts (Kisters *et al.*, 2004). The lower metamorphic grades around Karibib

indicate that NW-verging D2 deformation took place at mid-amphibolite grades and higher crustal levels than the SE-verging folding and NE-SW extension that characterises D2 in the southwestern Central Zone. Deformation in the study area (southwestern Central Zone) took place under higher-grade conditions at mid-crustal levels (Kisters *et al.*, 2004). Although NW-verging folding and thrusting in the shallow crust is suggested to be coeval with NE-SW extension in the mid-crust (Kisters *et al.*, 2004), it is evident that these are two separate tectonic events – NW-verging shallow crustal deformation took place at 560-540 Ma, whilst SE-verging folding and NE-SW directed extension at mid-crustal levels took place at 520-510 Ma. This 560-540 event was associated with lower metamorphic grades, but anatectic red granites emplaced at 540-535 Ma indicate that there was a thermal effect in the crust at this time. Inherited zircons from red granites give ages similar to those for other Abbabis Complex gneisses (Kröner *et al.*, 1991), and red granites are commonly emplaced at the contact between the Abbabis Complex and the Damara Supergoup, indicating they were formed from anatexis of the Abbabis Complex at deeper crustal levels than, and following, the NW-verging folding near Karibib. The event that triggered the intrusion of large volumes of mafic, dioritic and granitic magma at 560-540 Ma (the Goas Intrusive Suite and Salem-type granitoids) is likely to have had a thermal effect in the mid-crust, and may be the cause of melting of the Abbabis Complex at mid-crustal levels to produce the anatectic red granites.

Abbabis Complex gneisses from the Ida Dome and Arcadia Inlier give 2044-2056 Ma ages, consistent with *ca*. 2 Ga ages for the Abbabis Complex (Jacob *et al.*, 1978; De Kock *et al.*, 2000; Jacob *et al.*, 2000; Tack *et al.*, 2002). Inherited zircons in the anatectic red granites (sample LKR016) give an upper-intercept age of 1013 ± 21 Ma, similar to the young (1040-1100 Ma) ages suggested for parts of the Abbabis Complex by Kröner *et al.* (1991). These Palaeoproterozoic (*ca*. 2 Ga) and Mesoproterozoic (ca. 1.0-1.2 Ga) ages for the Abbabis Complex may reflect Eburnean and Kibaran tectonometamorphic events which affected the crust of the Congo Craton. However, it is also possible that red granites are not derived from the Abbabis Complex, but

rather from subducted Kalahari Craton material, and contain inherited zircons which reflect this.

Whilst the timing of SE-verging folding and NE-SW directed extension in the southwestern Central Zone is well constrained at between 520 and 510 Ma by grey granites, anatectic garnet-bearing granites and anatectic leucosomes, the timing of D3 is less clear. Uraniferous leucogranites were emplaced into the hinges of upright D3 folds east of the Ida Dome (see section 4.4.3), suggesting possible syn-tectonic emplacement of these granites during D3. On the southern margin of the Palmenhorst Dome, uraniferous alaskites clearly cut the F2 folds and the S2 fabric, but no clear relationship between D3 structures and these alaskites has been observed. Nex & Kinnaird (1995) and Basson & Greenway (2004) suggested that uraniferous granites at Goanikontes and at the Rössing Mine were emplaced post-D3. Late-kinematic, post-D3 brittle-ductile deformation and rotation of the Rössing Dome is thought to have localised the emplacement of U-enriched granites at the Rössing Mine (Basson & Greenway, 2004). The high-U contents of these late- to post-D3 leucogranites makes U-Pb zircon dating of them difficult, and dating of these granites gives ages between 506 and 515 Ma – and an age of 508 ± 9 Ma (sample LVA001) is identical to the 508 ± 2 Ma age obtained by Briqueu *et al.* (1980) for U-bearing granites from the Goanikontes area. Metamict zircons from sample LRV001 give unreliable age data. Thus, 508 Ma is considered the upper limit for the age of D3 deformation, but is very similar to the age for late D2 leucosomes (508 Ma to 511 Ma), suggesting that D3 occurred immediately following D2, at *ca.* 508 Ma. The similarity in ages for D2 and D3 implies that they may not necessarily be separate events, but part of a single continuum of deformation. Although km-scale upright D3 folding clearly rotates earlier formed D2 folds in the study area (see section 3.6), Poli (1997) and Poli & Oliver (2001) considered deformation in the southwestern Central Zone to be continuous, progressive deformation in a constrictional stress field.

Ages of 511-508 Ma are suggested for late-D2 extension based on the ages of leucosomes in a migmatitic D2 shear zone (511 ± 18 Ma – CZRL-1) and a leucosome-

filled D2 extensional shear band (508.4 ± 8.7 Ma – CZRL-3). Although syn-D2, these ages are younger than the grey granites (520 Ma) and anatectic garnet-bearing leucogranites (520-514 Ma), and suggest that SE-verging F2 folding may have slightly predated D2 shearing and NE-SW D2 extension, i.e., the onset of D2 began at *ca*. 520 Ma with folding of the Damaran Supergroup, and continued to 508 Ma, with later phases of deformation and NE-SW extension accommodated by shear zones and extensional shear bands. This is consistent with the observation that D2 extensional features and shear zones are commonly concentrated on the extending limbs of km-scale F2 folds, indicating that shearing and extension was a late-stage feature of D2 deformation (see section 3.4).

The 493.4 ± 6.4 Ma age for titanite from amphibolite sample LKR012 is likely a cooling age, and similar 480-500 Ma cooling ages (Kukla, 1993; Blaxland *et al.*, 1979; Hawkesworth *et al.*, 1983) are found throughout the Central Zone. Similar ages of 494-500 Ma for titanites from lamprophyre dykes and auriferous veins near the Navachab Mine are interpreted as dating late-stage hydrothermal alteration and Au-mineralisation in the Central Zone (Jacob *et al.*, 2000). The 434.4 ± 2 Ma age for a post-tectonic pink pegmatitic 'F-type' leucogranite from the Ida Dome is much younger than the age of 493 Ma obtained for titanite from LKR021 and other cooling ages in the Central Zone (Kukla, 1993; Blaxland *et al.*, 1979; Hawkesworth *et al.*, 1983; Miller, 2008), and indicates that these granites were emplaced into a significantly cooled Central Zone, and this is reflected by the brittle tension gashes into which this granite intrudes.

A sequence of events for the Central Zone, based on this study and previous geochronology (Fig. 5.19) includes pre-Damaran events in the Abbabis Complex, but the emplacement of amphibolites, the mafic to dioritic Goas Suite, and the Salem-type granites was the first major Damaran event at 560-540 Ma, and was coeval with NW-verging D2 deformation at shallow crustal levels preserved near Karibib. The thermal effects of this event resulted in anatexis of the Abbabis Complex during M1 at 540-535 Ma, forming red granites, which are post-tectonic at shallow crustal levels.

At mid-crustal levels, red granites preceded the SE-verging folding and NE-SW extension of D2 in the southwestern Central Zone. The ductile conditions prevailing during this deformation were coeval with high-grade M2 metamorphism at 520-510 Ma. It is unlikely that the 560-540 Ma crustal thickening recorded by Kisters *et al.* (2004) near Karibib represents a separate terrane to the southwestern Central Zone, where D2 deformation is recorded at 520-510 Ma. Rather, the folding and thrusting recorded by Kisters *et al.* (2004) likely represents an earlier stage in the overall evolution of the Central Zone. It is possible that D1 in the study area is related to this 560-540 Ma crustal thickening event, and that the majority of structures formed at this time have been obliterated by 520-510 Ma D2 deformation. Upright, NE-trending D3 folding followed immediately after D2. Syn- to post-D3 uraniferous leucogranites were emplaced during a change from ductile to brittle conditions at 508 Ma.

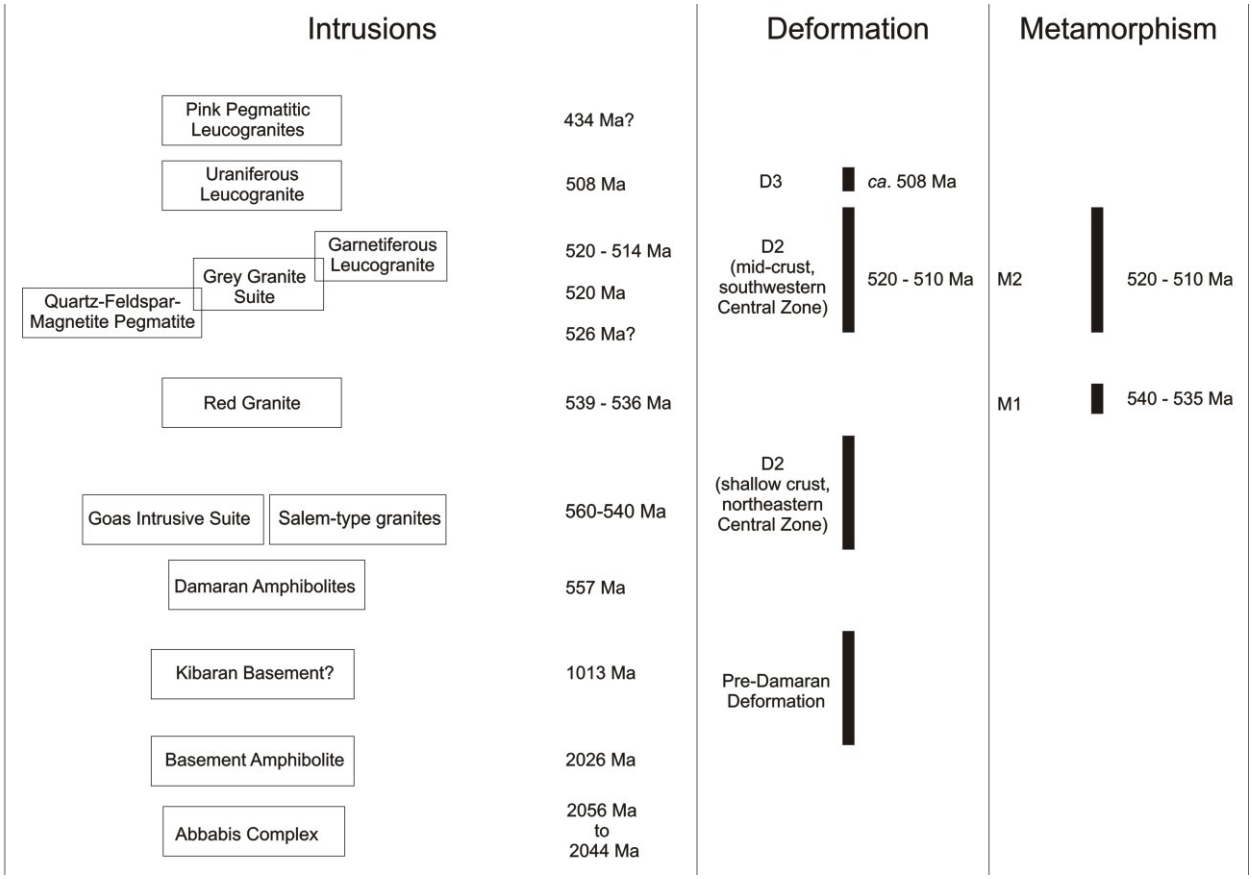

Fig. 5.19 – Summary of the temporal relationships between Damaran and pre-Damaran intrusions, deformation and metamorphism.

The Hf-isotopes show that the *ca.* 2 Ga Abbabis Complex gneisses have Mesoarchaean (2.8-3.2 Ga) model ages. This is consistent with the observation that most crustal growth in southern Africa occurred prior to 2.5 Ga, and that orogenic events since *ca*. 2 Ga have reworked preexisting crustal material (McDermott *et al.*, 1989). Thus, 2 Ga gneisses of the Abbabis Complex were probably formed from the recycling of Mesoarchaean Congo Craton crust during the Eburnean event. The highly variable O-isotope data reflects a mixed source with variable $\delta^{18}O$ values for the Abbabis Complex. Grey granites, however, have *ca*. 2 Ga model ages and are, thus, not likely to have been sourced from the Abbabis Complex, which displays much older model ages. The O-isotope data for grey granites indicate a fairly consistent $\delta^{18}O$ of *ca*. 7‰, which also differs from the wide range of $\delta^{18}O$ values for Abbabis Complex gneisses. Earlier isotopic studies of Damaran diorites (McDermott, 1986) indicate model ages of 1.4 to 1.5 Ga, whilst studies of leucogranites and alaskites (Hawkesworth *et al.*, 1983; McDermott *et al.*, 1991) indicate model ages of 1.5 to 2.4 Ga. Like the Hf model ages of zircons from the grey granites, these are inconsistent with a source from the Abbabis Complex, with its Mesoarchaean model ages (section 5.2.1). Other sources for these Damaran granitoids must be considered. One possibility is that, like the anatectic red granites, other Damaran granites are sourced from recycling of Mesoproterozoic (Kibaran age) rocks in the Abbabis Complex, rather than Palaeoproterozoic Abbabis Complex gneisses, but it seems unlikely that only Mesoproterozoic gneisses would melt, and Palaeoproterozoic gneisses would not. Since it seems unlikely that the various Damaran granitoids are sourced from the Abbabis Complex basement, which is part of the Congo Craton formed during the Eburnian or Kibaran events, a source for the Damaran granitoids is required with 1.5 – 2.5 Ga model ages, and a possible source may be found in rocks on the Kalahari Craton (e.g. the Vioolsdrif Igneous Suite, the Fransfontein Granitic and intrusions associated with the Rehoboth Group) that have ages ranging from 1.7 to 2.0 Ga (Reid, 1997; Ziegler & Stoessel, 1993; Becker *et al.*, 1996; 2004), with model ages indicating fairly juvenile crust (Reid, 1997). This would support the model initially proposed by Barnes & Sawyer (1981) and shown in Fig 1.6 that parts of the Kalahari Craton were subducted below the Congo Craton and partially melted during the Pan-African.

The timing of metamorphism in the southwestern Central Zone has been constrained at syn-D2, between 520 and 510 Ma, but what remains to be examined is the nature of high-grade metamorphism, and how it relates to the diachronous timing of deformation and metamorphism seen in the Central Zone. The NW-verging folding and thrusting seen at shallow crustal levels near Karibib (Kisters *et al.*, 2004) is likely to have caused crustal thickening at 560-540 Ma, and consequent heating of the mid-crust, whilst NE-SW directed extension in the southwestern Central Zone at 520-510 Ma is likely to be associated with crustal thinning and exhumation of the mid-crust. The record of these events should be reflected in the metamorphic history of rocks in the southwestern Central Zone, which is addressed in the following chapter.

CHAPTER 6 – METAMORPHISM

The field relationships described in earlier chapters indicate that a major tectonometamorphic event took place in the Central Zone where S- to SE-verging tight to recumbent folding, thrusting and late extension (D2 deformation in the study area) was coeval with extensive granitoid magmatism and the onset of partial melting of the Damara Supergroup and Abbabis Complex. U-Pb dating of structurally controlled granites and migmatites has constrained the timing of this event to between *ca*. 520 and 510 Ma (see Chapter 5). Additionally, U-Pb dating of anatectic red granites at 536-539 Ma (see section 5.1.3) hints at an earlier high-grade event, where partial melting of the Abbabis Complex (± Nosib Group rocks – Smith, 1965; Jacob, 1974; Miller, 2008) led to the genesis of these red granites. This chapter aims to investigate the metamorphism in the study area in more detail. A detailed review of the metamorphism in the Central Zone is first provided.

6.1 Previous Studies of Metamorphism in the Central Zone

The Central Zone of the Damara Orogen has long been known as a tectonometamorphic terrane characterised by high-temperature, low-pressure metamorphism (Jacob, 1974; Puhan, 1983; Miller, 1983), and has been investigated by numerous previous workers, with metamorphic conditions of *ca*. 650-750 ˚C and 3-5 kbar commonly obtained through conventional thermobarometry (Table 6.1). Metamorphic grade in the Central Zone is thought to increase along strike to the southwest (Hoernes & Hoffer, 1979; Puhan, 1983; Goscombe *et al*., 2004), reaching peak upper-amphibolite to lower-granulite facies conditions along the Atlantic seaboard. However, there is debate on whether the Central Zone evolved via a single phase of metamorphism (Hawkesworth *et al*., 1983; Hartmann *et al*., 1983; Haack, 1983; Puhan, 1983; Haack & Martin, 1983) or whether a multiphase metamorphic evolution is recorded (Nash, 1971; Barnes & Sawyer, 1980; Kröner, 1982; Kasch, 1983a; Ahrendt *et al*., 1983; Oliver, 1995; Nex *et al*., 2001a).

Table 6.1 - Summary of metamorphic conditions estimated for the Central Zone by previous workers.

Author	Method	Peak Conditions	Polyphase?
Nash (1971)	Mineral assemblages	M1 – 700˚ C, 7-8 kbar; M2 – 675-750˚ C, 3-5 kbar	Yes – early higher pressure M1 followed by low pressure M2
Jacob (1974)	Mineral assemblages	650-750˚ C, 4-5 kbar	No
Masberg *et al* . (1992)	Microfabric analysis	Granulite Facies	n/a
Buhn *et al* . (1995)	O-isotope thermometry; petrological constraints and phase relationships	660-700˚ C, 3.5-4.5 kbar, preceded by peak pressures of 5-6 kbar.	Yes – peak pressures precede peak temperatures
Poli (1997)	Grt-bt thermometry	662-700˚ C at 4 kbar	Multiple mineral growth phases are part of a single progressive metamorphic event
Poli (1997)	Pl-hbl thermometry	786-855˚ C at 4 kbar (anomalously high temperatures are due to high Al hornblende)	Multiple mineral growth phases are part of a single progressive metamorphic event
Poli (1997)	Grt-crd thermobarometry using the program NICHOLS	625-660˚ C, 3.5-4.2 kbar	Multiple mineral growth phases are part of a single progressive metamorphic event
Poli (1997)	GTB program	600-670˚ C, 3.8-4 kbar	Multiple mineral growth phases are part of a single progressive metamorphic event
Poli (1997)	THERMOCALC program	604-640˚ C, 3.7-4.4 kbar	Multiple mineral growth phases are part of a single progressive metamorphic event
Nex *et al* . (2001)	Grt-crd thermometry; grt-bt thermometry; grt-crd-sill-qtz barometry	700˚ C, 4 kbar, preceded by decompression from 600˚ C, 6 kbar	Yes – peak pressures precede an episode of decompression and cooling, which is followed by isobaric heating to peak temperatures
Ward *et al* . (2008)	Phase relationships and the program THERMOCALC	750˚ C and 5 kbar	n/a

Buhn *et al*. (1995) investigated the metamorphism of manganiferous formations in the Chuos Formation near Ojosondu, using petrological constraints and phase relationships with O-isotope thermometry on quartz and haematite to show that peak temperatures reached between 660 ˚C and 700 ˚C at pressures of 3.5-4.5 kbar, although Ba-rich pegmatitic horizons were formed owing to partial melting at higher pressures of 5-6 kbar, pre-dating the thermal peak. Nash (1971) also suggested an earlier high-pressure metamorphic event in the Central Zone, with conditions suggested to be *ca*. 700 ˚C and 6-8 kbar, based on the local presence of staurolite in semi-pelitic samples, which is replaced by sillimanite. Nash (1971) suggested that staurolite was largely consumed by the reaction: staurolite + sodic muscovite + quartz = sillimanite + potassic muscovite + biotite + albite + H_2O ± garnet (Guidotti, 1970), and placed M1 at higher pressures, between the beginning of melting and the onset of the staurolite breakdown reaction (Nash, 1971, Fig. 19). Buhn *et al*. (1995) suggested that these high-pressure conditions accompanied the main deformation in the Central Zone, and that the thermal peak was post-tectonic, resulting in recrystallisation of metamorphic textures.

Similar conclusions have been drawn by Nex *et al*. (2001a), who also advocated a two-stage model for the metamorphic evolution of the Central Zone, and an overall clockwise P-T path. Based on garnet-biotite and garnet-cordierite thermometry and garnet-cordierite-sillimanite-quartz barometry, as well as the estimates of Cuney (1980) and Buhn *et al*. (1995) of pressures of 5-8 kbar preceding peak thermal conditions, they suggested peak (M1) conditions with pressures up to 6 kbar and temperatures of *ca*. 600 ˚C, followed by decompression to conditions of 530 ˚C and 4 kbar. Spinel-sillimanite/spinel-biotite symplectites within cordierite porphyroblasts documented by Nex *et al*. (2001a) were attributed to melt-producing reactions that consumed biotite and sillimanite, such as biotite + sillimanite + quartz = spinel + cordierite + melt (Greenfield *et al*., 1998), which may occur during decompression. Nex *et al*. (2001a) suggested that since symplectite growth of two minerals is a textural feature commonly associated with decompression (e.g. Carey *et al*., 1992; Passchier & Trouw, 2005), the spinel-sillimanite and spinel-biotite symplectites were

likely to have formed during decompression, following higher-pressure M1 metamorphism. This decompression event was suggested to precede the higher-temperature (lower-pressure) M2 metamorphism, where conditions of 700 ˚C and 4 kbar were reached (Nex *et al*., 2001a). This regional M2 isobaric heating and anatexis were considered by Nex *et al*. (2001a) to be the result of heating due to the intrusion of the voluminous Salem-type granites.

Poli (1997) proposed a single metamorphic event for the Central Zone, rather than discrete metamorphic events, although his work on rocks from the Nambifontein Dome and the Nose Structure (northern Palmenhorst Dome) indicated that there is some evidence for two phases of mineral growth (especially evident in garnet), with garnet overgrowing a pre-existing fabric (post-tectonic) or enveloped by quartz and biotite (syn-tectonic). He interpreted cordierite growth as generally syn-kinematic, with σ-type relationships and asymmetrical quartz-biotite pressure shadows. K-feldspar was also seen to grow simultaneously with cordierite, as both are partly rotated within matrix biotite folia. No internal compositional mineral zonation was noted by Poli (1997) in cordierite, biotite, plagioclase or amphibole, and although some garnets displayed retrograde rims, no garnet profiles showed prograde zonation, instead giving flat mineral compositional profiles. He suggested that syn-kinematic porphyroblast growth indicates that metamorphism in the Central Zone was largely coeval with progressive deformation, but that post-kinematic porphyroblasts indicate that metamorphism may have outlasted deformation. Poli (1997) used several geothermobarometers (see Table 6.1), which gave peak conditions of 662 ˚C and 3-4 kbar at the Namibfontein Dome, and 690 ˚C and 5 kbar at the Nose Structure.

Earlier, Jacob (1974) also suggested a single metamorphic event in the Central Zone, coeval to slightly postdating both isoclinal ‘F1’ folding and ‘F2’ upright, NE-trending folding (D2 and D3 in this study). However, whilst Jacob (1974) advocated a single metamorphic event for the Central Zone, his suggestion that the red gneissic granites (which were emplaced early in the tectonometamorphic evolution of the Central

Zone) are the product of anatexis of the pre-Damaran basement and the Etusis Formation could be reinterpreted as an indication of polymetamorphism. These anatectic granites, which appear to be similar to 536-539 Ma red granites from this study (Smith, 1965; Jacob, 1974; Miller, 2008) contain xenoliths with aligned sillimanite porphyroblasts (see Chapter 5), indicating that a high-temperature metamorphic event may have been associated with the generation of these granites. Geochronology indicates that this event was older than the 520-510 Ma event which formed leucosomes and anatectic granites in the pelitic units of the Damara Supergroup, in the study area (see Chapter 5).

Another question raised by Poli (1997) is the existence of a metamorphic gap between the Damara Supergroup cover and the basement of the Abbabis Complex. Such a gap would be expected should the Central Zone be a deep metamorphic core complex, with lower-grade Damara Supergroup metasediments separated from higher-grade Abbabis Complex gneisses by a mylonitic shear zone (Oliver, 1994; 1995). Poli (1997) suggested that metamorphic conditions in the basement (800 ˚C and 6-7 kbar) were up to 140 ˚C and 3 kbar greater than in the cover (660-690 ˚C and 3.3-4 kbar), although his model does not show the Central Zone as a metamorphic core complex, but rather as a zone of constrictional deformation. Nonetheless, he suggested that this indicates unroofing during exhumation through sub-vertical elevation of the mid-crust, although he did not provide metamorphic evidence for any decompression associated with such sub-vertical exhumation.

Whilst most workers have calculated upper-amphibolite facies conditions for the Central Zone, Masberg *et al*. (1992) suggested that, despite the absence of metamorphic orthopyroxene, these rocks reached lower-granulite facies conditions. Their study was based on microfabrics and textures (basal <a> and prism <c> glide systems in quartz, oriented exsolution of rutile in quartz, as well as the exsolution of string perthites, mesoperthitic string perthites and antiperthites), and the homogeneous distribution of major elements in garnet. Although not in the granulite facies according to mineral assemblages, they suggested that high-grade

metamorphism took place under generally water-absent conditions. This is in contrast to the recent work of Ward *et al*. (2008) as well as numerous other authors who have suggested that water-present melting occurred in the Central Zone. Ward *et al*. (2008) estimated peak conditions of 750 ˚C and 5 kbar, based on phase relationships and mineral chemistry, using the average P-T function (i.e. conventional thermobarometry rather than the pseudosection approach, which uses quantitative phase diagrams) of the program THERMOCALC (Powell *et al*., 1998). This is 50-100 ˚C lower than the typical onset of fluid-absent biotite melting, which generally takes place at between 800 ˚C and 850 ˚C (Vielzeuf & Montel, 1994; Stevens *et al*., 1997). Ward *et al*. (2008) suggested fluid-present biotite melting in dilational sites, via the reaction biotite + quartz + plagioclase + H_2O = melt + cordierite + garnet. Some temperature estimates from the study by Ward *et al*. (2008) did exceed 750 ˚C, and were recorded in restitic minerals that could not re-equilibrate during cooling as the rock had lost melt following anatexis. There is no published record of orthopyroxene from the Central Zone, although it has been noted by E. Sawyer (Pers. Comm., 2010). Orthopyroxene is commonly formed through melt-producing fluid-absent biotite breakdown reactions (Vielzeuf & Montel, 1994), although at sufficiently low pressures (2 kbar) it is possible to produce melt from fluid-absent biotite breakdown without producing orthopyroxene, through the reaction biotite + plagioclase + quartz = garnet + K-feldspar + melt (Vielzeuf & Montel, 1994).

6.2 Aims of this Study

This chapter aims to address the following question regarding metamorphism in the Central Zone:

- Is there any petrographic evidence for multiple metamorphic events (i.e., for an earlier M1 event)?
- Was metamorphism pre-, syn- or post-tectonic?
- What were the peak metamorphic conditions for M2 in the study area?

- What was the P-T-t path followed by the rocks in the study area?
- What is the heat source for the metamorphism?
- How does the metamorphism in the study area relate to the geodynamics of the Central Zone and the Damara Orogen?

Whilst the aim is not to repeat the work of previous studies, previous estimates of peak metamorphic conditions are based on conventional thermobarometry (Buhn *et al*., 1995; Poli, 1997; Nex *et al*., 2001a; Ward *et al*., 2008), and this approach has a number of drawbacks. Peak metamorphic temperatures calculated for pelitic assemblages using Fe-Mg garnet-biotite exchange thermometry may be significantly lower than the actual peak temperatures attained (Spear, 1991). Since rim compositions of garnet (required to calculate peak temperatures) are most easily modified by diffusion during cooling, it may be very difficult to calculate peak metamorphic temperatures for rocks that have attained temperatures of >550 ˚C (Spear, 1991), and especially problematic for high-grade rocks with high cation diffusion rates (Harley, 1989). A sample may also contain biotite produced by retrograde reactions and earlier formed biotite that may have been affected by Fe-Mg exchange with garnet on cooling, producing a range of calculated temperatures that are geologically meaningless (e.g. Spear & Parrish, 1996). Furthermore, geobarometers and geothermometers may refer to different parts of the P-T path, and peak temperatures may not necessarily correspond with peak pressures (Harley, 1989). Given these problems with conventional geothermobarometry, this study aims to further quantify P-T conditions using the pseudosection approach (Powell & Holland, 1988, 2008; Powell *et al*., 1998), where quantitative phase diagrams (P-T pseudosections) are calculated for a single bulk composition (i.e. a single sample). This approach allows a detailed determination of not only the peak P-T conditions, but also the P-T path of a single rock with a specific bulk composition, when combined with the observed mineral assemblages, compositions and modes of the sample (e.g. Zeh, 2001).

6.3 Approach of this Study

In high-grade rocks that have experienced partial melting and melt-loss, the use of quantitative phase diagrams (pseudosections), together with observed mineral assemblages, modes and compositions, is likely to be more accurate than the use of cation-exchange thermobarometry when calculating the peak conditions of metamorphism. Anhydrous mineral assemblages are unlikely to be retrogressed once H_2O has been removed with the melt (White & Powell, 2002), whereas mineral compositions are affected by cation exchange during retrogression (Spear, 1991; Guiraud *et al*., 2001). Such quantitative phase diagrams can be constructed for specific compositions (i.e. for individual rocks with specific mineral assemblages and compositions). Additionally, the preservation of relict assemblages and textures can be used to infer the P-T path experienced by the sample (e.g. Johnson *et al*., 2004), rather than simply constraining the peak assemblage. Understanding any relict minerals or textures is the key to understanding the early metamorphic evolution of the Central Zone, and whether any prograde path can be accurately determined.

In this chapter, pseudosections are constructed for a number of metasedimentary rocks from the study area, in order to constrain the peak P-T conditions experienced, and to attempt to infer the P-T history of these samples, and hence of the study area. Pseudosections have been constructed using THERMOCALC 3.33 (Powell & Holland, 1988 and subsequent updates). The P-T conditions and histories deduced through the use of pseudosections are also compared to results obtained using conventional cation exchange thermobarometers, as have previously been used for the Central Zone (e.g. Poli, 1997; Nex *et al*., 2001a), as well as to results from the average P-T calculations in the program THERMOCALC, as used by Ward *et al*. (2008) to estimate conditions in the Central Zone. Qualitative phase diagrams and petrogenetic grids have also been used to understand reaction sequences and the preservation of relict assemblages in the specific samples investigated. This approach is used in order to investigate whether P-T estimates of previous workers (using conventional thermobarometry) are replicated using pseudosection modelling, or whether

retrogression and cation diffusion during cooling have resulted in the underestimation of P-T conditions for the Central Zone. The pseudosection approach will hopefully allow better constraints on the peak P-T conditions and on the P-T path. This may allow the issues of fluid-absent vs. fluid-present melting in the production of the large volume of anatectic leucosomes, and of single vs. polyphase metamorphic histories to be more fully addressed. The relationship between metamorphism, deformation, and magmatism is crucial to understanding the overall geodynamics of the Central Zone, and the field and petrographic relationships of metamorphism and mineral growth to deformation and magmatism are addressed before examining compositions and assemblages in more detail.

Detailed petrography combined with mineral chemistry provides the link between the field and geochronological evidence for metamorphism, and the P-T pseudosections, as well as between the metamorphic and structural histories.

Several units in the study area have pelitic compositions, which are ideal for metamorphic petrological studies, and a variety of pelitic and semi-pelitic samples were collected from across the study area for the metamorphic investigation in this chapter. A list of samples, and their basic rock type, is given in Table 6.2, and the locations of the samples are shown in Fig. 6.1. Although a variety of other rock-types exist in the study area (including quartzites, quartzofeldspathic gneisses, quartz-biotite schists, diopside-plagioclase gneisses, and marbles) only rocks of pelitic composition have been chosen for this study, owing to the range of minerals found in such compositions and their suitability for phase equilibrium modelling.

Table 6.2 – Samples selected for detailed metamorphic study.

Sample	GPS Coordinate	Rock Type
CZRL19	0504058/7483234	Garnet-sillimanite-cordierite schist
CZRL20	0504581/7484479	Garnet-sillimanite-cordierite schist
LCZ11-1	0498517/7502723	Garnet-cordierite-biotite schist
LG003	0482019/7493610	Garnet-cordierite-biotite schist
LID004	0502735/7485923	Garnet-cordierite-biotite schist
LID039	0502737/7485903	Garnet-cordierite-biotite schist
LID042	0502855/7456011	Garnet-cordierite-biotite schist
LKR012	0501001/7504885	Garnet-cordierite-biotite schist
LKR013	0501136/7504991	Garnet-cordierite-biotite schist
LHA006	0488817/7489445	Cordierite-biotite schist
LHA008	0489554/7490099	Cordierite-biotite schist
LHA009	0489366/7489937	Cordierite-biotite schist

*GPS coordination zone is UTM WGS84.

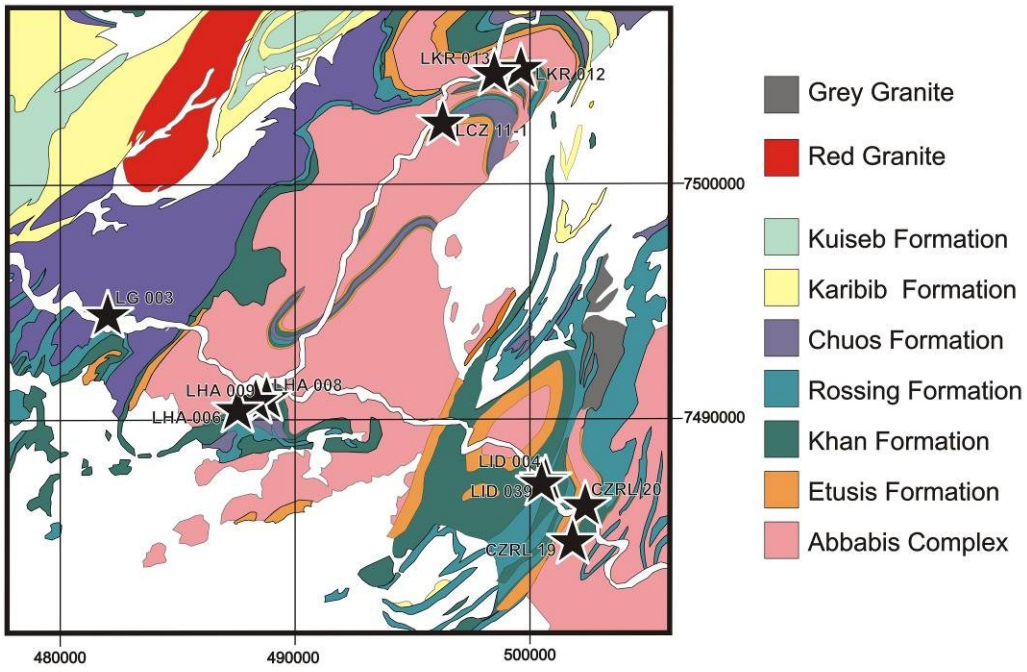

Figure 6.1 – Map of the study area showing localities where samples were collected for metamorphic study. Stars indicate sample localities, sample labels are indicated.

6.4 Field Relationships

In the field, the timing relationships between metamorphism and deformation in the study area are most obvious in the structural controls on the generation and migration of leucocratic melt produced through anatexis during high-grade metamorphism. Although extensive melting of pelitic units in the Damara Supergroup has taken place (e.g. Ward *et al*., 2008; Kisters *et al*., 2009), there is also evidence for melting of more quartzofeldspathic units and of clinopyroxene-amphibole-feldspar gneisses (Miller, 2008). Whilst field evidence indicates that melting was coeval with D2 deformation, and appears to have taken place during what has been referred to here as M2 metamorphism, the red granites provide the only field evidence for an earlier metamorphic event. These anatectic red granites contain xenoliths of quartzofeldspathic metasedimentary material (Fig. 6.2A) that have fabrics of aligned sillimanite porphyroblasts, and which are discordant to the regional D2 fabric in the country rocks (also present as a gneissic fabric in the red granites). Since the sillimanite porphyroblasts and gneissic fabrics present in xenoliths within the granites are discordant to the D2 gneissic fabric within the granites and the country rocks, the fabric in these xenoliths (and hence the porphyroblasts aligned with this fabric) must predate the D2 fabric in the red granites and country rocks. This suggests that a pre-D2 high-grade metamorphic event, which resulted in the growth of sillimanite porphyroblasts in quartzofeldspathic gneisses, took place in the Central Zone, and led to the anatexis of this material to form the red granites.

Throughout the rest of the study area, relationships between anatexis and deformation indicate that M2 metamorphism was largely coeval with S- to SE-verging D2 deformation. Anatectic leucosomes are commonly seen subparallel to the axial planes of D2 folds (Figs. 6.2B, C), or subparallel to the D2 fabric (Figs. 6.2C, D). Locally, leucosomes are emplaced subparallel to the NE-trending extension lineation (Fig. 6.2E), and anatectic leucosomes are common in shear bands formed during NE-SW directed D2 extension (Fig. 6.2F). Although Miller (2008) considered M2 metamorphism and consequent widespread anatexis in the Central Zone to be post-

tectonic, based upon the fact that anatectic leucosomes contain no tectonic fabric (R. Miller, Pers. Comm., 2010), Ward *et al*. (2007; 2008) noted that sites for leucosome generation were structurally controlled, and Kisters *et al*. (2009) considered the structural localisation of anatexis as evidence that melting was syn-D2. Furthermore, Poli (1997) demonstrated that porphyroblast growth was largely syn-tectonic, with only local post-tectonic mineral growth. The lack of a fabric in anatectic leucosomes may be due to their localisation in low-pressure dilational sites (Ward *et al*., 2008; Kisters *et al*., 2009), or their general lack of pyllosilicate minerals, and should not be regarded as evidence for post-tectonic anatexis, when other field evidence points to syn-D2 partial melting in the Central Zone.

Fig. 6.2 (following page) – Field relationships between deformation and anatexis is the study area. A: Xenolith of sillimanite-bearing gneiss in red granite. Note that the fabric in the gneiss (with aligned sillimanite) is discordant to the regional D2 fabric (gneissic fabric in the red granite) indicating that the high-grade event which produced the sillimanite (and possibly the anatectic red granite) must predate D2 deformation (locality 0500363/7504555). B: Leucosomes generated subparallel to the axial plane of a D2 fold in Khan Formation psammites (locality 0502135/7486366). C: D2 intrafolial fold, with anatectic leucosome generated subparallel to the axial plane of the fold, and hence the D2 fabric (locality 0502725/7485877). D: Leucosomes generated parallel to the D2 fabric. Note the large poikiloblastic garnet restite, with minor amounts of leucosome, indicating that melt has been lost (locality 0502725/7485877). E: Anatectic leucosomes (with associated restitic garnet) generated parallel to the NE-trending D2 stretching lineation (locality 0482486/7493497). F: Anatectic leucosomes localised within a D2 extensional shear band in Abbabis Complex gneisses (locality 0497496/7503551).

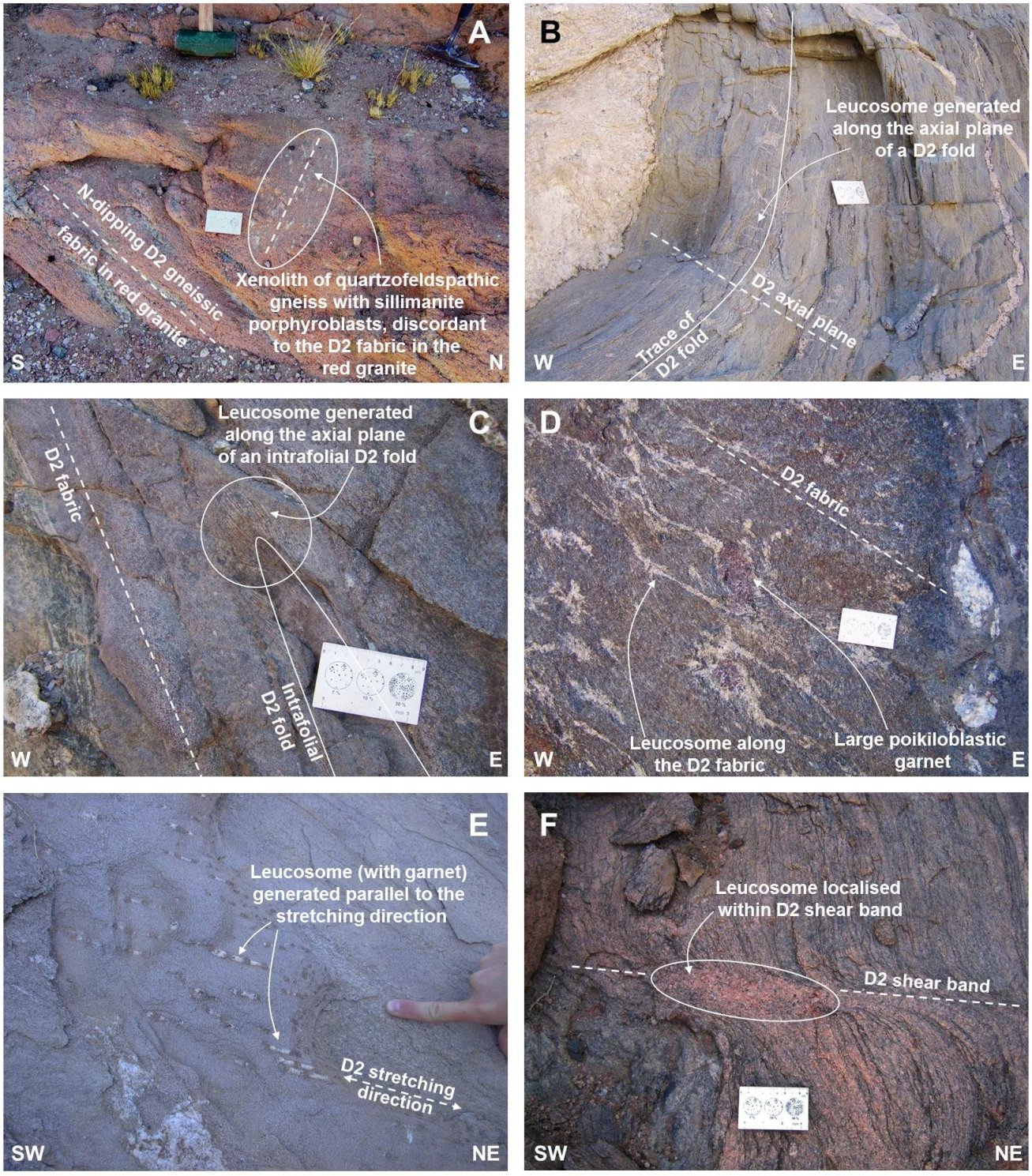
A
N-dipping D2 gneissic fabric in red granite
Xenolith of quartzofeldspathic gneiss with sillimanite porphyroblasts, discordant to the D2 fabric in the red granite
S
N
B
Leucosome generated along the axial plane of a D2 fold
D2 axial plane
Trace of D2 fold
W
E
C
Leucosome generated along the axial plane of an intrafolial D2 fold
D2 fabric
Intrafolial D2 fold
W
E
D
D2 fabric
Leucosome along the D2 fabric
Large poikiloblastic garnet
W
E
E
Leucosome (with garnet) generated parallel to the stretching direction
D2 stretching direction
SW
NE
F
Leucosome localised within D2 shear band
D2 shear band
SW
NE

6.5 Petrography

A number of pelitic samples have been chosen for study. These pelitic samples can be broadly grouped three categories, based on their mineral assemblages. The majority of the samples collected are garnet-cordierite-biotite schists (Samples LCZ11-1, LG003, LID004, LID039, LID042, LKR012 and LKR013), which have a wide geographic spread across the study area (Fig. 6.1). In addition to these there are cordierite-biotite schists (samples LHA006, LHA008 and LHA009), collected near the farm Hildenhof, along the southern margin of the Palmenhorst Dome, and garnet-sillimanite-cordierite schists (samples CZRL19, and CZRL20) from the shear zone at the basement-cover contact adjacent to the Arcadia Synform. A list of samples, and their coordinates, is given in Table 6.2. Locations are shown on the map in Fig. 6.1. The basic petrography of each of these general groups, and the relationships between metamorphism and deformation, are described below.

6.5.1 Garnet-cordierite-biotite schists

These schists contain an assemblage of garnet, cordierite, biotite, quartz, plagioclase, K-feldspar (orthoclase and microcline), ilmenite and magnetite. Orthopyroxene is found in two samples (LID004 and LID039) at a single locality. Fibrolitic sillimanite is commonly found as inclusions in cordierite (Fig. 6.3A), which is commonly partially or totally pinitised (Fig. 6.3A), but sillimanite is never found in the matrix. Although sillimanite is not present in the groundmass, the presence of fibrolite exclusively within cordierite indicates that, in most samples, sillimanite was present as a phase along the prograde path, and cordierite growth post-dated sillimanite growth. It is possible that cordierite grew as a product of a sillimanite-consuming reaction. In samples LID004 and LID039, orthopyroxene is found in the rock matrix and appears, together with cordierite, to be replacing biotite. This orthopyroxene and cordierite is surrounded by pools or films of quartz (Fig. 6.3B). Garnet ranges from small (*ca.* 0.2 mm) subhedral, inclusion-free porphyroblasts (Fig. 6.3A) to large (up to 3-4 mm) poikiloblasts, with inclusions of quartz, biotite (Fig. 6.3C) and, locally, zircon. Rarely,

texturally zoned subhedral garnets are found, which have cores containing quartz and biotite inclusions, and inclusion-free rims (Fig. 6.3D). Inclusions in these garnet cores may show alignment to form fabrics subparallel to the schistose fabric in the rocks (Fig. 6.3D). These texturally zoned porphyroblasts of garnet may be evidence for two generations of growth. Garnet porphyroblasts may have inclusions of pinitised cordierite, indicating that cordierite growth predated garnet growth (Fig. 6.3E). However, some cordierite growth appears to be associated with orthopyroxene, and there appear to be multiple generations of cordierite growth. Biotite may have ilmenite needles along the cleavage (Fig. 6.3F). Rarely, rutile is found associated with biotite, or as inclusions in garnet (Fig. 6.3G). Gedrite amphibole is also locally noted in the matrix of the rock in a single sample (LID004), without any reaction textures apparent (Fig. 6.3H).

Fig. 6.3 (following page) – Petrography of garnet-biotite schists. A: Slightly pinitised cordierite porphyroblast, with inclusions of fibrolitic sillimanite, which is not present in the groundmass of the sample. Note that cordierite is elongate with the S2 fabric in the rock, and that the fabric included in fibrolite (possibly S1) is also aligned with the main schistose fabric (sample LCZ11-1, PPL). B: Orthopyroxene and cordierite replacing biotite, surrounded by quartz (sample LID004, XPL). C: Large poikiloblastic garnet porphyroblasts with inclusions of quartz and biotite. Note that these garnets are not wrapped by the schistose fabric, but rather truncate the fabric (sample LKR012, PPL). D: Texturally zoned garnet porphyroblast with an inclusion-rich core, containing numerous small quartz and biotite inclusions, and a relatively inclusion-free rim, with fewer, larger inclusions of quartz. Note that the fabric (defined by aligned biotite) wraps garnet, and that inclusions in the core of the garnet are weakly aligned with the schistose fabric in the rock (sample LID039, PPL). E: Inclusions of pinitised cordierite in a garnet porphyroblast, indicating that garnet growth postdated cordierite growth (sample LID039, XPL). F: Ilmenite needles adjacent to and intergrown with biotite (sample LG003, PPL). G: Large, texturally zoned garnet porphyroblast with inclusions of rutile (sample LG003, PPL). H: Rare porphyroblast of gedrite amphibole (sample LID004, PPL). Mineral abbreviations are after Kretz (1983).

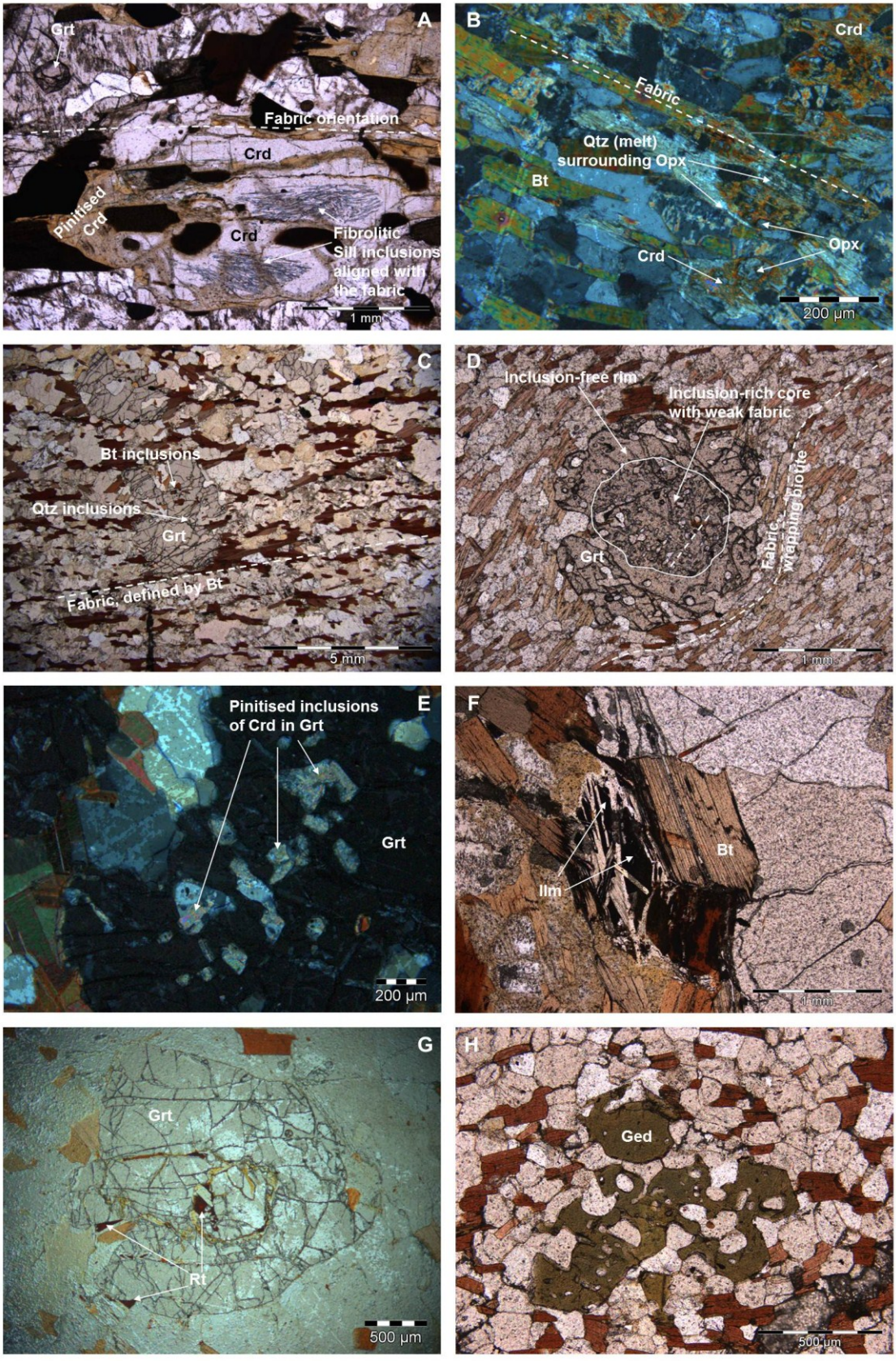
A
Grt
Fabric orientation
Crd
Pinitised Crd
Crd
Fibrolitic Sill inclusions aligned with the fabric
1 mm
B
Crd
Fabric
Qtz (melt) surrounding Opx
Bt
Opx
Crd
200 µm
C
Bt inclusions
Qtz inclusions
Grt
Fabric, defined by Bt
5 mm
D
Inclusion-free rim
Inclusion-rich core with weak fabric
Grt
Fabric wrapping biotite
1 mm
E
Pinitised inclusions of Crd in Grt
Grt
200 µm
F
Bt
Ilm
1 mm
G
Grt
Rt
500 µm
H
Ged
500 µm

The quartz pools and films surrounding orthopyroxene (+ cordierite) are interpreted as relicts of crystallised melt or melt extraction pathways (the original melt would not have been pure quartz), and orthopyroxene growth is also associated with ilmenite. The growth of orthopyroxene, cordierite and ilmenite (together with melt/quartz films) appears to be at the expense of biotite (Fig. 6.4A) indicating that orthopyroxene was the product of a biotite-breakdown melting reaction. In addition to biotite, garnet is also seen to be a reactant, and is locally corroded, with orthopyroxene (+ cordierite and melt) growing in pressure shadows adjacent to garnet (Fig. 6.4B). A possible orthopyroxene-producing melting reaction may be:

biotite + garnet + quartz = orthopyroxene + cordierite + K-feldspar + melt (Spear *et al.*, 1999).

All samples have schistose S2 fabrics defined by aligned laths of subhedral to euhedral red-brown biotite (Figs. 6.3B, C, D), indicating syn-tectonic (syn-D2) biotite growth or mimetic overgrowth. In many samples, cordierite porphyroblasts are elongate, and are aligned with this fabric (Fig. 6.3A), and the fabric may wrap cordierite porphyroblasts (Fig. 6.4A). The elongation of cordierite along the S2 fabric direction (Figs. 6.3A, 6.4C), and the fact that it is wrapped by the biotite fabric (Fig. 6.4C) indicates syn-tectonic (with respect to D2) cordierite growth. Fibrolite inclusions within cordierite are also aligned with the fabric (Fig. 6.3A), suggesting that sillimanite growth (which predates cordierite growth) was also syn-D2. Additionally, fibrolite inclusions within cordierite commonly show intrafolial folds (Fig. 6.4D) that are not observed in the groundmass, suggesting that fibrolite growth was early, and was associated with a deformation event which may not be evident in the field, but found only as crenulations in fibrolite inclusions. This may be petrographic evidence for the D1 event. Orthopyroxene (samples LID004 and LID039) and associated melt also appears to be aligned with the S2 fabric (Fig. 6.4B), further confirming that deformation and fabric development occurred during peak metamorphism. Whilst garnet commonly appears to truncate the S2 fabric, and appears post-tectonic with respect to D2 (Fig. 6.3C), in some cases the biotite fabric wraps garnet porphyroblasts (Fig. 6.3D), indicating that some syn-tectonic (syn-D2) growth of garnet did occur.

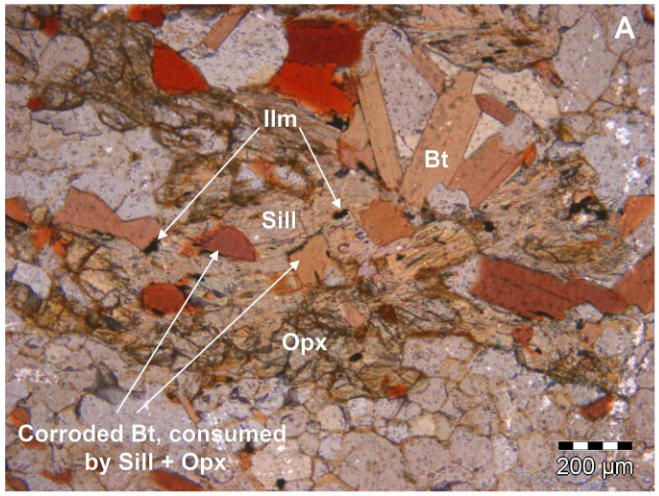
A
Ilm
Bt
Sill
Opx
Corroded Bt, consumed by Sill + Opx
200 µm

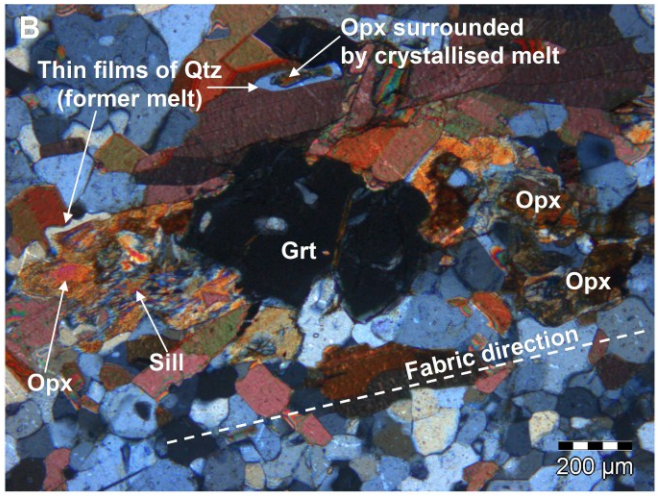
B
Opx surrounded by crystallised melt
Thin films of Qtz (former melt)
Opx
Grt
Opx
Opx
Sill
Fabric direction
200 µm

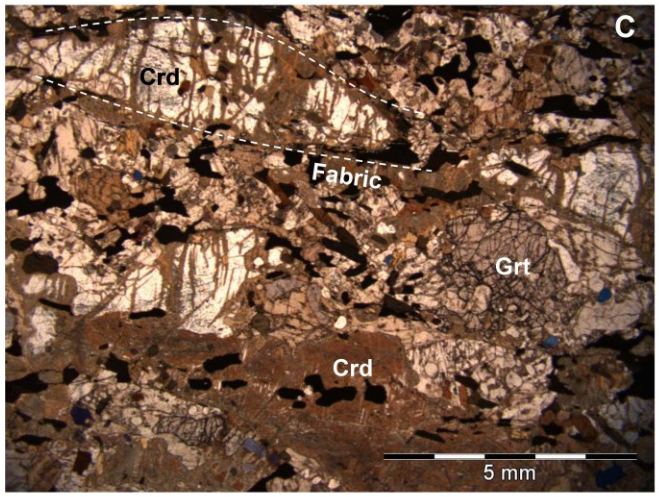
C
Crd
Fabric
Grt
Crd
5 mm

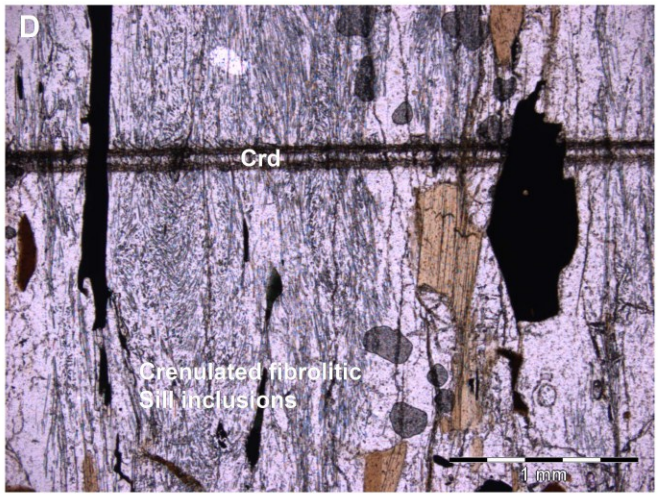
D
Crd
Crenulated fibrolitic Sill inclusions
1 mm

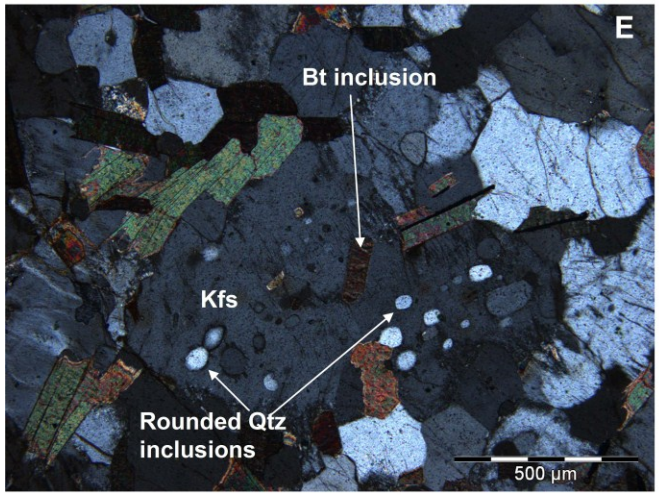
E
Bt inclusion
Kfs
Rounded Qtz inclusions
500 µm

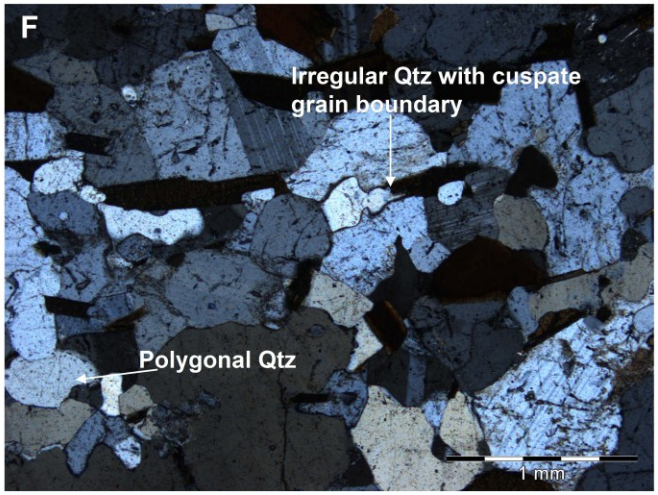
F
Irregular Qtz with cuspate grain boundary
Polygonal Qtz
1 mm

Fig. 6.4 (previous page) – Petrography of garnet-biotite schists. A: Orthopyroxene and cordierite (with associated ilmenite) growing at the expense of biotite (sample LID004, PPL). B: Orthopyroxene, cordierite and quartz (melt) in a pressure shadow adjacent to garnet, growing at the expense of garnet and biotite. Note the thin films of quartz adjacent to orthopyroxene. These melt pools are also aligned with the S2 fabric direction (sample LID004, XPL). C: Elongate (augen) cordierite porphyroblast wrapped by the biotite fabric. Note that this fabric does not wrap the garnet porphyroblast (sample LCZ11-1, XPL). D: Cordierite porphyroblasts with inclusions of fibrolitic sillimanite, which show a crenulated fabric (sample LCZ11-1, PPL). E: K-feldspar with rounded inclusions of quartz and subidioblastic biotite (sample LID004, XPL). F: Irregular quartz grain with cuspate grain boundaries, interpreted as crystallised melt, in contrast to the polygonal quartz more common in the sample (sample LKR013, XPL). Mineral abbreviations after Kretz (1983).

Apart from the field evidence for anatexis of pelitic rocks, petrographic evidence for melting includes K-feldspar (Fig. 6.4E) and plagioclase feldspar that commonly contains rounded inclusions of quartz and biotite, and corroded plagioclase found included in quartz, both indicating that some K-feldspar and quartz may be the product of crystallised melt. Additionally, quartz grains with irregular shapes and cuspate edges (Fig. 6.4F) have very high dihedral angles (in contrast to the generally recrystallised nature of most quartz grains, which have polygonal shapes), which further suggests that these quartz grains are crystallised melt pools (see Sawyer, 2008). Field evidence (Fig. 6.2) indicates syn-D2 anatexis over the study area, although petrographic evidence for syn-deformational melting is scarce, and is restricted to local alignment of possible former melt pools with the S2 schistosity in the samples (Fig. 6.4B).

The petrography of the garnet-cordierite-biotite schists suggests that metamorphic mineral growth was generally coeval with deformation in the study area – fibrolitic sillimanite in the cores of cordierite porphyroblasts contains a fabric (possibly representing D1), and cordierite is both elongate with the S2 schistosity in the rocks, and is wrapped by this schistosity. Although some garnets are seen to truncate the fabric, garnet may also be wapped by the S2 fabric, indicating that garnet growth was syn-to immediately post-D2. Elsewhere orthopyroxene and sillimanite are seen to

grow in pressure shadows adjacent to garnet, and are aligned with the fabric. Textural relationships indicate that sillimanite formed early on the prograde path, and since it is commonly preserved in the cores of cordierite porphyroblasts, it predates cordierite. Garnet postdates cordierite – inclusions of pinitised cordierite are found in garnet, and garnet appears to have grown later in the deformation history than cordierite. A second phase of cordierite growth, associated with an orthopyroxene-producing melting reaction at the expense of garnet and biotite, appears to have occurred in some samples at the peak of metamorphism. These are the only samples in which orthopyroxene has been noted, and compositional controls on mineral growth are evaluated later in this chapter (see section 6.6.10). Field relationships indicate that anatexis was largely syn-tectonic.

6.5.2 Cordierite-biotite schists

Cordierite-biotite schists contain the assemblage cordierite-biotite-quartz-plagioclase -K-feldspar-ilmenite-magnetite in the groundmass. Cordierite occurs as large porphyroblasts with inclusions of dark green spinel (Fig. 6.5A) and ilmenite, and commonly forms a symplectic intergrowth with the spinel. Cordierite also typically contains inclusions of sillimanite needles (Fig. 6.5A). Spinel is not present in the groundmass of the rock, and only occurs intergrown with or included in cordierite. Sillimanite is also generally only found within cordierite, with the exception of a few small corroded sillimanite grains in the groundmass of sample LHA008 (Fig. 6.5B). In this sample andalusite, rather than sillimanite, is found as large inclusions within cordierite, along with coarse-grained (1-2 mm) biotite that is unaligned with the S2 fabric in the rock (Fig. 6.5C) and, in rare cases, coarse (1 mm) muscovite (Fig. 6.5D). The spinel and sillimanite (or andalusite) are rarely seen in contact with one another, and are generally separated by a moat of cordierite (Fig. 6.5E). The symplectic intergrowth of spinel and cordierite is locally seen occurring only on the outer edges of cordierite porphyroblasts (Fig. 6.5C). Cordierite porphyroblasts (with associated/included sillimanite/andalusite and spinel) are commonly surrounded by a biotite-free rim of quartz, plagioclase feldspar and K-feldspar (Fig. 6.5F).

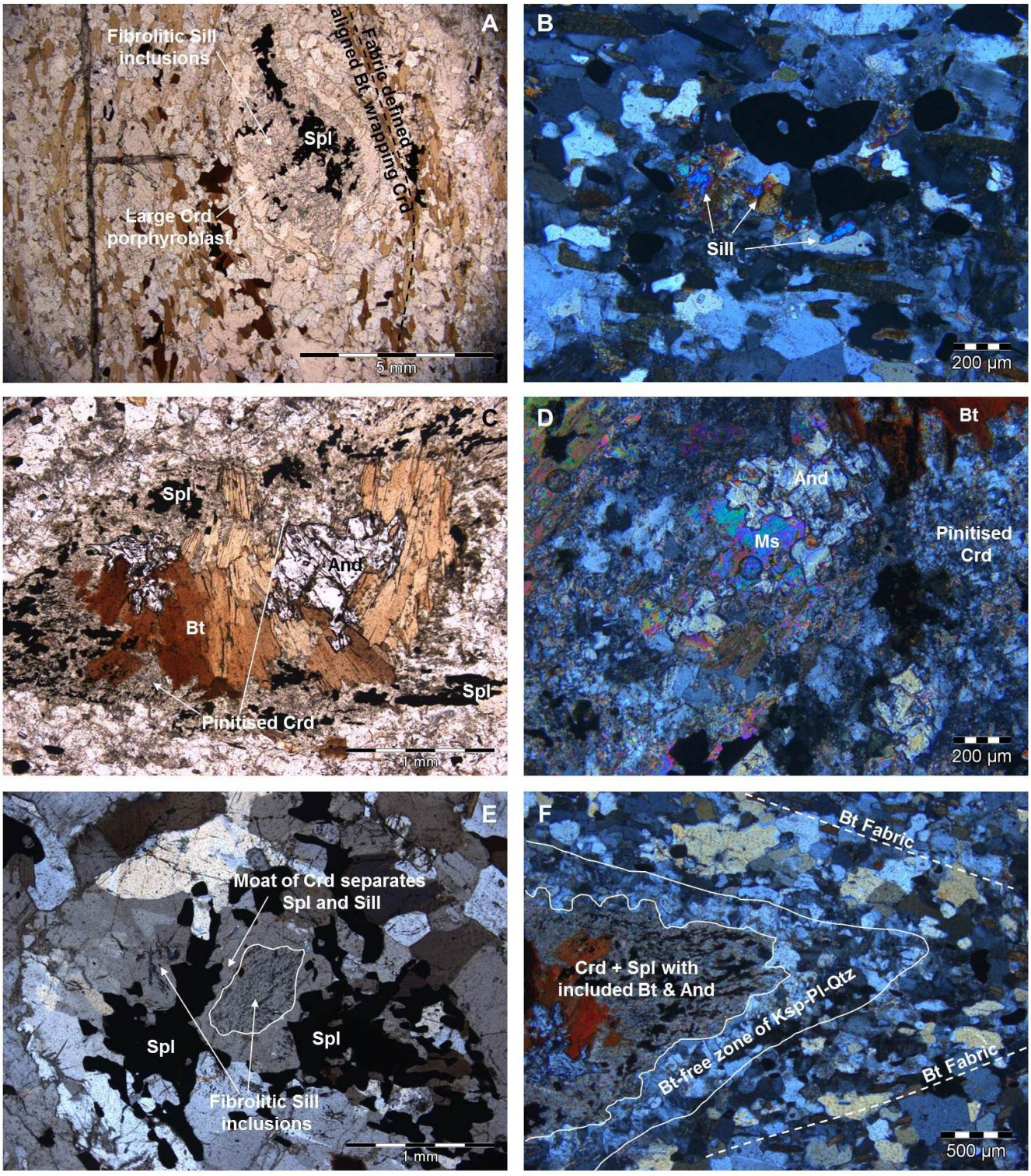
A
Fibrolitic Sill inclusions
Fabric defined by aligned Bt wrapping Crd
Spl
Large Crd porphyroblast
5 mm
B
Sill
200 µm
C
Spl
And
Bt
Spl
Pinitised Crd
1 mm
D
Bt
And
Ms
Pinitised Crd
200 µm
E
Moat of Crd separates Spl and Sill
Spl
Spl
Fibrolitic Sill inclusions
1 mm
F
Bt Fabric
Crd + Spl with included Bt & And
Bt-free zone of Ksp-Pl-Qtz
Bt Fabric
500 µm

Fig. 6.5 (previous page) – Photomicrographs of cordierite-biotite schists. A: Large, elongate cordierite porphyroblast with spinel inclusions, wrapped by the schistose S2 fabric. Note the inclusions of fibrolitic sillimanite in the cordierite, and the zone of inclusion-free cordierite at the outer edge of the porphyroblast (sample LHA006, PPL). B: Small grains of sillimanite found in the groundmass in sample LHA008. Note the corroded irregular shape of the grains, suggesting that sillimanite may have been unstable and in the process of reacting (XPL). C: Cordierite porphyroblast (pinitised) with a core of andalusite and coarse-grained, unaligned biotite, and an outer rim of symplectic cordierite-spinel intergrowth (sample LHA008, PPL). D: Relict muscovite grain, together with andalusite and coarse biotite, included in pinitised cordierite (sample LHA008, XPL). E: Cordierite with inclusions of fibrolitic sillimanite and symplectically intergrown with spinel. Note that spinel and sillimanite are separated by a moat of inclusion-free cordierite (sample LHA006, XPL). F: Biotite-free zone of K-feldspar, quartz and plagioclase feldspar surrounding a cordierite porphyroblast – note that the biotite fabric wraps the porphyroblast, but the felsic rim around cordierite is biotite-free (sample LHA008, XPL). Mineral abbreviations after Kretz (1983).

The absence of sillimanite or andalusite in the groundmass of the rock, and their presence exclusively in the cores of cordierite porphyroblasts, suggests that they were consumed in the reaction that formed the cordierite. Furthermore, the spinel-cordierite intergrowths surrounding sillimanite-bearing cordierite cores suggest that spinel + cordierite may be produced from a reaction consuming sillimanite/andalusite + biotite, such as:

biotite + plagioclase + andalusite/sillimanite = spinel + cordierite + ilmenite + K-feldspar + melt (Johnson *et al*., 2004).

The presence of felsic rims around cordierite-spinel porphyroblasts suggests that these felsic rims were the product of such a melting reaction, and the textures of these rims suggests the presence of former melt. The K-feldspar found in these felsic rims is irregular-shaped, with cuspate grain boundaries, and is commonly developed in narrow zones between quartz and plagioclase grains that appear corroded (Fig. 6.6A), indicating that this K-feldspar replaced pools and intergranular films of melt (Sawyer, 2001; 2008). Where K-feldspar forms larger masses, it includes rounded (corroded) quartz and plagioclase grains (Fig. 6.6A, B). Commonly, larger K-feldspar

grains, with inclusions of corroded K-feldspar and quartz, are observed in pressure shadows adjacent to large cordierite porphyroblasts (Fig. 6.6B). In sample LHA009, K-feldspar makes up 30% of the modal mineralogy of the sample, and occurs as large polygonal grains, with 120˚ triple junctions (Fig. 6.6C). However, some larger, subhedral grains are found, with inclusions of rounded quartz, plagioclase feldspar and biotite (Fig. 6.6C). These larger inclusion-filled grains may be interpreted as K-feldspar that crystallised from the melt, or as the product of a melt-producing reaction (Sawyer, 2008), and the rounded inclusions are partially corroded reactants. Additionally, thin films of albite are found adjacent to polygonal K-feldspar and biotite (Fig. 6.6C), and are interpreted as crystallised melt films (Sawyer, 2001; 2008). Quartz films along the edges of grains are common (Fig. 6.6D) and, in places, these films appear to coalesce to form larger, irregular quartz grains with cuspate grain edges and partially corroded inclusions of quartz and biotite (Fig. 6.6D). Plagioclase too is locally observed as irregular grains with cuspate boundaries (Fig. 6.6E). Garnet, although generally absent from these samples, is locally observed as small (*ca.* 0.1 mm) grains (Fig. 6.6F), and may be a peritectic phase. Both ilmenite and magnetite are present, and the samples contain variable amounts of plagioclase feldspar and K-feldspar (both microcline and orthoclase), with some samples containing up to 30 % K-feldspar, with lesser plagioclase feldspar, suggesting that not all K-feldspar has formed as part of a melting reaction.

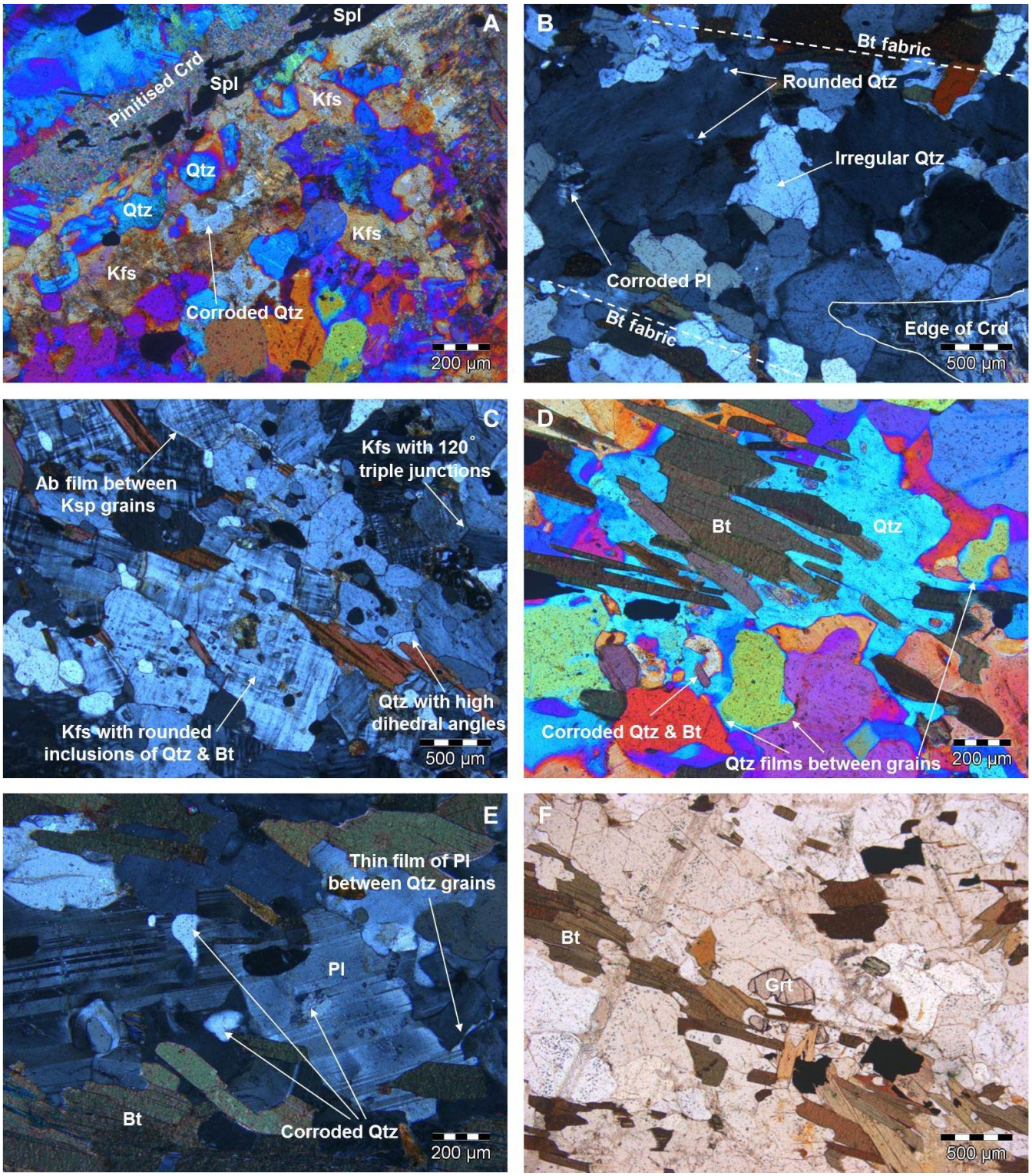
A
Spl
Pinitised Crd
Spl
Kfs
Qtz
Qtz
Kfs
Kfs
Corroded Qtz
200 µm
B
Bt fabric
Rounded Qtz
Irregular Qtz
Corroded Pl
Bt fabric
Edge of Crd
500 µm
C
Ab film between Ksp grains
Kfs with 120° triple junctions
Qtz with high dihedral angles
Kfs with rounded inclusions of Qtz & Bt
500 µm
D
Bt
Qtz
Corroded Qtz & Bt
Qtz films between grains
200 µm
E
Thin film of Pl between Qtz grains
Pl
Bt
Corroded Qtz
200 µm
F
Bt
Grt
500 µm

Fig. 6.6 (previous page) – Photomicrographs of cordierite-biotite schists. A: Irregular grain of K-feldspar including corroded quartz grains adjacent to a cordierite porphyroblasts with intergrown spinel (sample LHA008, XPL, 530 nm quartz accessory plate). B: Large (1 mm) K-feldspar grain with inclusions of rounded quartz and corroded plagioclase feldspar. This grain is found in a pressure shadow adjacent to a large elongate cordierite porphyroblast, and is interpreted as the product of a melt-forming reaction. Note the irregular shape of the adjacent quartz, with cuspate grain boundaries, suggesting that it is crystallised melt (sample LHA006, XPL). C: Large K-feldspar grain with numerous small inclusions of rounded quartz and biotite. Note that K-feldspar elsewhere in the sample is polygonal, with 120˚ triple junctions. Note the thin albite films between K-feldspar grains, and the small quartz grains with cuspate grain boundaries and high dihedral angles. D: Quartz grain with inclusions of corroded biotite and quartz. Note that the quartz continues as thin films between adjacent grains, indicating that this quartz represents crystallised melt (sample LHA006, XPL, 530 nm quartz accessory plate). E: Plagioclase grain with included corroded quartz, and an irregular grain shape. Note how the plagioclase forms a narrow film between adjacent quartz grains, indicating that it is crystallised melt (sample LHA006, XPL). F: Single tiny garnet grain in sample LHA006 (PPL). Mineral abbreviations are after Kretz (1983).

Cordierite porphyroblasts (with sillimanite-rich cores and intergrown with spinel as symplectites) form elongate lenses aligned with the S2 fabric in these rocks (Figs 6.5 A, F), defined by aligned biotite laths and elongate grains of quartz and plagioclase feldspar. These lenses are wrapped by the S2 schistosity, and spinel grains are aligned with this S2 fabric (Figs 6.5A, C, F), indicating that growth of both spinel and cordierite was syn-D2, and that D2 continued after cordierite growth. The presence of larger K-feldspar grains and irregular K-feldspar + quartz in pressure shadows adjacent to cordierite (Fig. 6.6B) suggests that both melting and K-feldspar growth was also syn-tectonic. The fabric in the aligned fibrolitic sillimanite inclusions preserved in the cordierite porphyroblasts is locally discordant to the S2 fabric in the host rocks and may represent an earlier D1 fabric.

These cordierite-spinel assemblages are similar to spinel-bearing samples described by Nex *et al*. (2001a), who noted elongate augen poikiloblasts with Fe-Ti oxide + spinel included in fibrolite mats, and surrounded by pinitised cordierite and a rim of antiperthitic plagioclase feldspar, or together with sillimanite in the cores of

cordierite porphyroblasts. However, Nex *et al*. (2001a) interpreted fibrolitic cores in cordierite porphyroblasts as due to the breakdown of cordierite, in contrast to the suggestion above that cordierite and spinel are the products of a reaction that consumed sillimanite. Nex *et al*. (2001) also suggest that unaligned fibrolite needles crossing grain boundaries between host quartz and cordierite indicate late-stage cordierite development, whereas this could be due to relict fibrolite needles included in the products of the reaction that consumed sillimanite. Although Nex *et al*. (2001) do note that spinel growth may be due to the reaction

biotite + sillimanite = cordierite + hercynitic spinel ± K-feldspar ± ilmenite + melt (Brown, 1998)

Nex *et al.* (2001) conclude that since this reaction takes place after garnet growth at temperatures in excess of 750 ˚C, it is incompatible with the observation that garnet forms late in the mineral paragenetic sequence. The biotite breakdown reaction

biotite + sillimanite + plagioclase +quartz = cordierite + spinel + melt

was suggested by Jung *et al*. (1998) for migmatites in the Southern Zone of the Damara Orogen. Such spinel producing reactions generally have fairly small ΔP/ΔV, and have been used as evidence for isothermal decompression (e.g. Johnson *et al*., 2004). The implications of these assemblages and reactions are further discussed in terms of quantitative and qualitative petrogenetic grids (see sections 6.7 and 6.10).

6.5.3 Garnet-sillimanite-cordierite schists

The two samples (CZRL19, CZRL20) of garnet-sillimanite-cordierite schist are both from the shear zone found near the basement-cover contact (in the Etusis Formation) adjacent to the Arcadia Syncline (Fig. 6.1) and are unique with respect to other pelitic samples in the large amount of sillimanite (>15%) that they contain. They contain the assemblage sillimanite-biotite-cordierite-garnet-K-feldspar-plagioclase-quartz-ilmenite-magnetite. Much of the sillimanite occurs as seams of fibrolite, which is

intergrown with dark red-brown biotite and appears to be replacing biotite (Fig. 6.7A). Cordierite, biotite and sillimanite form the schistose fabric in the shear zone (Fig. 6.7A), interpreted to be related to D2 deformation (see section 3.4.2), and although most sillimanite occurs as fibrolite, coarse (1 mm diameter, 30 mm length) crystals of euhedral sillimanite are locally found (Fig. 6.7B). Garnet occurs as large (>10 mm) anhedral porphyroblasts that are elongate and aligned with the S2 fabric (Fig. 6.7C), and similarly large (30 mm) lenses of cordierite are wrapped by the schistose fabric of fibrolite and biotite (Fig. 6.7D). The cordierite contains included quartz, euhedral biotite, patches of fibrolitic sillimanite and opaques (ilmenite and magnetite – Fig. 6.7D). Biotite is red-brown, but locally occurs as pale green-brown euhedral laths, although no textural relationships distinguish the two varieties. Although magnetite is present, ilmenite is the more abundant opaque mineral. Plagioclase and quartz generally occur in elongate ribbons that are aligned with the fabric between seams of fibrolite (Fig. 6.7E), and augen of plagioclase are observed to be wrapped by the fabric (Fig. 6.7F). Fibrolite inclusions are found in garnet, K-feldspar and quartz. K-feldspar commonly occurs as small irregular grains (Fig. 6.7G) with numerous inclusions, and quartz is observed as thin films adjacent to K-feldspar and cordierite (Fig. 6.7G). Quartz also occurs as irregular grains that may have numerous inclusions of sillimanite and rounded biotite and quartz, and cuspate grain boundaries (Fig. 6.7H). These irregular grains of quartz and feldspar, with numerous corroded inclusions and cuspate grain boundaries, are microtextural evidence for crystallised melt (Sawyer, 2001; 2008). Melt in these samples appears to be restricted to small pockets, indicating either that most of the melt has been extracted, or that only a small amount of melting occurred. The alignment of fibrolitic sillimanite and biotite to form the schistose fabric, which also wraps cordierite, indicates that sillimanite, cordierite and biotite all grew syn-tectonically during the D2 shearing which formed this shear zone. Inclusions of fibrolitic sillimanite in garnet and cordierite indicates that fibrolite predates both garnet and cordierite growth. The alignment of elongate garnet porphyroblasts with the fabric suggests syn-tectonic garnet growth, although garnet growth may have been mimetic, and has grown along the fabric post-shearing. The large garnet and cordierite porphyroblasts, and the

evidence for melt in these samples, suggests that garnet and cordierite may be the products of a melting reaction such as:

biotite + sillimanite + quartz = garnet + cordierite + K-feldspar + melt (Yardley, 1989).

The replacement of biotite by fibrolitic sillimanite (Fig. 6.7A) suggests that sillimanite may have been produced through an earlier biotite breakdown reaction such as:

muscovite + biotite + quartz + H_2O = sillimanite + melt (Yardley, 1989).

Since sillimanite is aligned with the fabric, such a reaction is likely to have occurred early in the D2 deformation history of the rock. Further possible reactions are discussed in sections 6.7 and 6.10.

Fig. 6.7 (following page) – Photomicrographs of garnet-sillimanite-cordierite schists. A: Intergrown biotite and sillimanite (with ilmenite) defining the S2 shear fabric (sample CZRL19, PPL). B: Large sillimanite crystals cross-cutting the S2 shear fabric (sample CZRL20, XPL). C: Elongate garnet porphyroblast aligned with the S2 fabric (sample CZRL19, PPL). D: Large cordierite porphyroblast containing inclusions of fibrolitic sillimanite, biotite and ilmenite, wrapped by the biotite-sillimanite S2 fabric (sample CZRL20, XPL). E: Band of quartz and plagioclase feldspar between the biotite-sillimanite S2 fabric. Note that the plagioclase and quartz are elongate along the fabric direction (sample CZRL19, XPL). F: Elongate plagioclase augen, aligned along the S2 shear fabric (sample CZRL19, XPL). G: Irregular K-feldspar grain, with associated films of quartz, adjacent to a cordierite porphyroblast. Note the cuspate grain boundary of the K-feldspar and quartz, and the inclusion of corroded quartz, indicating that this grain is crystallised melt (sample CZRL19, XPL). H: Quartz grain with numerous inclusions of sillimanite, corroded quartz and biotite. This grain is interpreted as crystallised melt (sample CZRL19, XPL). Mineral abbreviations after Kretz (1983).

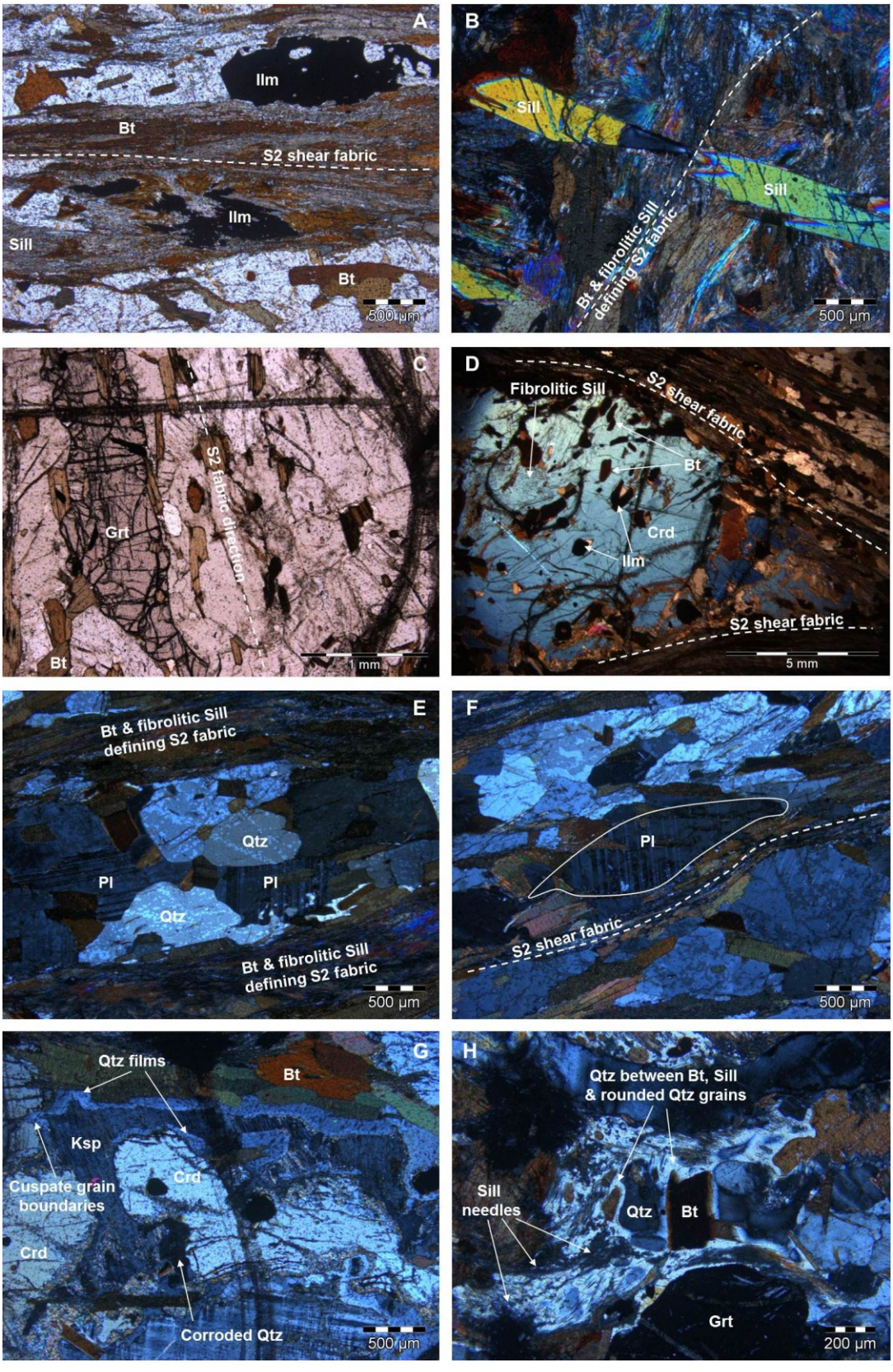
A
Ilm
Bt
S2 shear fabric
Ilm
Sill
Bt
500 µm
B
Sill
Sill
Bt & fibrolitic Sill defining S2 fabric
500 µm
C
S2 fabric direction
Grt
Bt
1 mm
D
Fibrolitic Sill
S2 shear fabric
Bt
Crd
Ilm
S2 shear fabric
5 mm
E
Bt & fibrolitic Sill defining S2 fabric
Qtz
Pl
Pl
Qtz
Bt & fibrolitic Sill defining S2 fabric
500 µm
F
Pl
S2 shear fabric
500 µm
G
Qtz films
Bt
Ksp
Cuspate grain boundaries
Crd
Crd
Corroded Qtz
500 µm
H
Qtz between Bt, Sill & rounded Qtz grains
Sill needles
Qtz
Bt
Grt
200 µm

6.5.4 Interpretation of petrographic results

The three sample groups described above contain a number of petrographic similarities, in spite of the differences in their mineral assemblages. All these pelitic samples contain cordierite, and most pelitic samples contain the assemblage garnet-cordierite-K-feldspar, in addition to fibrolitic sillimanite as inclusions within cordierite. In all samples, a progression of mineral growth is observable, and sillimanite seems generally to have grown early in the metamorphic history, as it is found only as inclusions within cordierite (and in some samples, garnet and K-feldspar). In sample LHA008, andalusite relicts are preserved within cordierite, indicating that these rocks passed through the andalusite stability field before moving into the sillimanite field, and suggesting a low-pressure prograde path. Samples CZRL19 and CZRL20 are exceptions, and contain abundant fibrolitic sillimanite, which along with aligned biotite forms the schistose fabric. The presence of orthopyroxene in samples LID004 and LID039 indicates that these rocks did indeed reach the granulite facies. Although garnet is generally late, and cordierite early, in this case orthopyroxene (and cordierite) appear to have grown at the expense of biotite and garnet late in the metamorphic history, suggesting a second phase of cordierite growth via a melt-producing reaction such as:

biotite + garnet + quartz = cordierite + orthopyroxene + K-feldspar + melt (Spear *et al*., 1999)

Symplectites of spinel and cordierite (with associated ilmenite) appear to be replacing sillimanite (or andalusite) and biotite. The reaction

biotite + plagioclase + andalusite/sillimanite = spinel + cordierite + ilmenite + K-feldspar + melt (Johnson *et al*., 2004)

has been suggested as a possible reaction which may form melt whilst producing spinel-cordierite symplectites, and may indicate decompression at the peak of metamophism. However, spinel is only associated with cordierite in certain samples

(LHA006, LHA008, LHA009), although most cordierites contain fibrolite inclusions. The inclusion of rounded (corroded) inclusions of quartz and biotite in many K-feldspar grains, and the association of cordierite with irregular grains of quartz and K-feldspar (crystallised melt) suggests that a more general melt-producing prograde reaction such as

biotite + sillimanite + quartz = K-feldspar + cordierite + melt (Yardley, 1989)

may be applicable for most samples. The presence of biotite-free zones adjacent to cordierite in some samples, which commonly have higher proportions of irregular K-feldspar and quartz with cuspate grain boundaries, confirms that K-feldspar and melt are also products of the cordierite-producing, biotite-consuming reaction. Spinel and sillimanite are rarely seen in contact, and are separated by a moat of cordierite. In almost all samples, garnet appears to have formed later than cordierite and sillimanite – pinitised inclusions of cordierite are locally found within garnet, and garnet also locally contains fibrolite inclusions (samples CZRL19, CZRL20). Garnet commonly has a core with rounded inclusions of biotite and quartz and may be surrounded by rims of coarse quartz with cuspate grain boundaries. This indication of multiple generations of garnet growth suggesting that garnet may have formed both on the prograde path and during a melt-producing reaction, such as

biotite + quartz + plagioclase + H_2O = melt + garnet + cordierite (Ward *et al*., 2008)

Whilst this is a the fluid-present reaction, the fluid-absent reaction

biotite + plagioclase + quartz = garnet + K-feldspar + melt (Vielzeuf & Montel, 1994)

may form melt and garnet without producing orthopyroxene (which is only locally observed in samples from this study). Evidence for anatexis of pelitic samples is common – numerous irregular grains of K-feldspar, quartz and plagioclase feldspar are found, with cuspate grain boundaries and inclusions of rounded, corroded quartz,

plagioclase and/or biotite, indicating that they are crystallised melt (Sawyer, 2008). These confirm migmatitic field textures, which indicate widespread anatexis of not only pelitic rocks, but also more quartzofeldspathic and calcareous lithologies. Field relationships suggest that anatexis was coeval with non-coaxial S- to SE-verging deformation in the study area (D2), and microtextures confirm the syn-tectonic nature of the metamorphic peak. Fibrolitic sillimanite inclusions in cordierite have fabrics that may be crenulated and are commonly oblique to the main S2 fabric, suggesting that they may be early-D2 (D2 was noncoaxial and progressive deformation means that younger fabrics may have overprinted older fabrics). Cordierite appears to have formed syntectonically – cordierite porphyroblasts are commonly elongate along the fabric direction, may occur as σ-shaped porphyroblasts, and are wrapped by biotite and sillimanite in the groundmass, which are aligned to form the S2 fabric in pelitic schists. Garnet commonly appears post-tectonic, although it is locally seen to be wrapped by the S2 fabric, and is likely to have formed during late-stage D2 deformation. Elongate garnet porphyroblasts in samples CZRL19 and CZRL20 may have formed by fabric-parallel mimetic growth. Anatexis also appears to be syn-tectonic – felsic rims (interpreted as crystallised melt) around elongate cordierite porphyroblasts are wrapped by the S2 fabric, and larger K-feldspar grains with inclusions of corroded quartz and plagioclase feldspar are found in pressure shadows adjacent to cordierite, and large pools of quartz with rounded plagioclase and euhedral biotite are elongate in the fabric direction. In the field, leucosomes are commonly found aligned with the fabric, and may form stromatic migmatites. Should garnet be the product of a melting reaction, it would suggest that some anatexis may have been late-tectonic. Thus, metamorphism in the study area generally appears to have a sequence of mineral growth with early fibrolitic sillimanite followed by cordierite, and late garnet growth. However, some samples do show differing sequences (e.g. late sillimanite in LID004 and CZRL20), and the mineral growth sequence of each sample must be evaluated individually (see section 6.10). Spinel growth in some samples appears to be associated with cordierite growth and sillimanite (+ biotite and plagioclase) consumption. There is no textural evidence for multiple metamorphic pulses; metamorphism and mineral growth appears to have

occurred progressively during D2 deformation, and continued post-tectonically. This is in agreement with Poli (1997), but contrasts with Nex *et al*. (2001) who suggested a two-stage metamorphic model. This is discussed in more detail later in the chapter (see section 6.11)

Based on the assemblages and textures described above (a summary of assemblages and textures is found in Table 6.3) these rocks appear to have reached lower-granulite facies conditions. The presence of orthopyroxene suggests the possibility of temperatures in excess of 800 ˚C (Vielzuef & Montel, 1994), and pressures in excess of 8 kbar, based on the KFMASH petrogenetic grid of Spear *et al*. (1999). Such pressures and temperatures are significantly higher (3-4 kbar and 50-100 ˚C) than most previous estimates for the Central Zone (e.g. Nex *et al*., 2001a; Ward *et al*., 2008), and care must be taken when using generalised petrogenetic grids, and the effects of compositional on phase stability must be taken into consideration (see section 6.10). However, this does appear to confirm the conclusion of Masberg *et al*. (1992) that granulite facies conditions were reached in the southwestern Central Zone. The widespread petrographic evidence for melting, such as small, corroded inclusions of biotite, plagioclase and quartz in larger quartz and K-feldspar grains, and the common occurrence of irregular quartz grains with cuspate edges corroborates field evidence for widespread anatexis. A number of suggestions have been made regarding the reactions that may have produced melt and restite minerals. Since no obvious tectonic boundaries are found across the study area, it may be assumed that metamorphic conditions over the study area were similar and, thus, that variations in the mineral assemblages are due to compositional differences between the samples. The validity of this assumption is discussed further in section 6.11. In order to evaluate mineral paragenesis and possible reactions, consideration must be given to bulk chemistry of the samples and their minerals. Mineral and whole-rock compositional data have been collected for all the samples listed in Tables 6.2 and 6.3, and these data are used below to infer possible prograde reactions. Mineral compositions have also been used to infer peak metamorphic temperatures, using conventional cation-exchange thermometry.

Table 6.3: Summary assemblages of samples collected, with comments on the textural features. Mineral abbreviations after Kretz (1983).

Sample	Biotite	Sillimanite/ Andalusite	Cordierite	Garnet	Spinel	K-Feldspar	Plagioclase	Quartz	Gedrite	Orthopyroxene	Ilmenite	Magnetite	Other
CZRL19	24% Red-brown Bt is intergrown with Sill, and aligned to form the fabric. Green Bt is perpendicular to the fabric	26 % (Sill) Fibrolitic, intergrown with biotite, forms the fabric. Inclusions in Crd, Kfs & Grt	12% Large (>30mm) lenses/augen, contains inclusions of Sill, idioblastic Bt and opaques, wrapped by the Bt-Sill schistose fabric	5% Large (>10 mm), elongate along the fabric direction, not wrapped by fabric		15% Rounded inclusions of Qtz and Bt	6% Elongate lenses aligned with the fabric, local Pl-Qtz myrmekites	8% Elongate 'ribbons' aligned with the fabric, may have inclusions of rounded Bt, local Pl-Qtz myrmekites			2%	1%	
CZRL20	38% Red-brown Bt is intergrown with Sill, and aligned to form the fabric. Green Bt is perpendicular to the fabric	15% (Sill) Fibrolitic, also coarser (*ca*. 3 mm) needles, inclusions in Crd, Kfs & Grt	26% Elongate augen, inclusions of Bt & Sill	14% Large porphyroblasts, elongate along fabric, inclusions of Sill & Zrn		4%	1%	2%			Trace	Trace	
LHA006	37% Defines the S2 shistosity, wraps Crd	8% (Sill) Aligned inclusions in Crd (fibrolite), also needles in Pl	19% Elongate along the S2 fabric direction, intergrown with Spl, contains inclusions of Sill	Trace Single 0.1 mm grain	5% Symplectic intergrowth with Crd	14% Inclusions of rounded, corroded Qtz & Bt & Pl, often irregular grain shapes - pools of melt	7% May be corroded, as inclusions in Kfs, also as thin films (melt)	10% Inclusions in Kfs, also in groundmass				Trace	
LHA008	18% Defines the S2 shistosity, also unaligned Bt as inclusions in Crd	2% (And) Corroded inclusions in Crd with Bt	8% Large augen, with inclusions of corroded And and unaligned, coarse Bt, and an outer rim symplectically intergrown with Spl		3% Symplectic intergrowth with Crd, or inclusions in Crd	34% Irregular grains with inclusions, formed at the margins of Crd-Spl porphyroblasts, also in the matrix	7% Common in matrix, may be corroded	9% Irregular cuspate edges (former melt?), also polygonal			Trace	Trace	Ms inclusions in Crd
LHA009	10% Defines S2 schistosity, inclusions in Ksp	5% (Sill) Aligned inclusions in Crd	30% Large porphyroblasts of Crd, wrapped by S2 fabric, also inclusions of Sill and spinel	Trace One single *ca*. 0.1 mm grain, as an inclusion in Qtz	2% Symplectic intergrowth with Crd, or inclusions in Crd	30% Or & Mc, contains inclusions of Qtz, Pl & Bt	6% Inclusions in Ksp	18% In groundmass, inclusions in Ksp			Trace	Trace	

Table 6.3 (continued): Summary assemblages of samples collected, with comments on the textural features. Mineral abbreviations after Kretz (1983).

Sample	Biotite	Sillimanite/ Andalusite	Cordierite	Garnet	Spinel	K-Feldspar	Plagioclase	Quartz	Gedrite	Orthopyroxene	Ilmenite	Magnetite	Other
LCZ11-1	24% Green-brown Bt aligned to form the fabric, inclusions in Grt & Ksp	11% (Sill) Fibrolitic inclusions in Crd, aligned with the fabric	23% Elongate lenses, aligned with the fabric	5% Small & subhedral, mostly inclusion-free, but some inclusions of Bt and Zrn	Trace	26% Contains rounded inclusions of Qtz & Bt	4%	6% Contains rounded/corroded inclusions of Pl & Bt, may be strained			Trace	1%	
LG003	38% Defining fabric, intergrown with Qtz		42%	15% Large, inclusion-free Grt		2%	Trace	2% Strained, in places intergrown with Bt			1% Associated with Bt	Trace	Rt associated with Bt & as inclusions in Grt
LID004	29% Defines fabric, inclusions in Grt	Trace (Sill)	3% Late Crd associated with Opx	5% Texturally zoned, inclusion-free rims & inclusions of Qtz & Bt in the core		10%	28%	23%	Trace	Trace	Trace Inclusions in Grt	Trace Inclusions in Grt	Rt
LID039	23% Reddish-brown, defining fabric, and as inclusions in Grt	Trace (Sill)	16% Pinitised Crd, in places retrogressed to Ms. Late Crd associated with Opx	3% 2-3 mm poikiloblastic Grt, texturally zoned with inclusion-rich core & inclusion-free rim		14%	25%	16%		Trace	Trace Ilm needles growing along Bt ceavage	2%	
LID042	22% Bt defines fabric		23% Rounded Qtz inclusions	15%		10%	9%	18%			Trace	3%	
LKR012	24% Bt defines fabric		22% Pinitised	16% Large, poikiloblastic, with inclusions of Qtz & Bt		13% Or	7%	17% Strained Qtz			Trace	1%	
LKR013	18% Red-brown Bt		9%	5% 0.5-1 mm poikiloblastic Grt with Zrn inclusions			30%	32%			Trace	2%	

6.6 Mineral and Whole-rock Chemical Data

Whole-rock and mineral chemical data have been collected for all the metapelitic samples listed in Table 6.2 and described above. Analytical procedures for whole-rock data, which were collected using XRF, can be found in Appendix 1C. Whole-rock and mineral chemical data for these samples, in addition to the procedures used in the collection of mineral chemical data, can be found in Appendix 3.

6.6.1 Garnet

Profiles across a number of garnet grains have been analysed in order to check for any prograde growth zoning, or evidence for any retrogression. These profiles show that almost all garnets have flat chemical profiles, with some retrograde decrease in Mg and increase in Mn contents towards the rims of the garnets (Fig. 6.8). With the exception of sample LID039 (Fig. 6.8AB), none of the samples analysed show any prograde garnet zoning. This is the case for a number of samples from both garnet-cordierite-biotite schists and garnet-sillimanite-cordierite schists, and is consistent with the observation of Poli (1997) that metamorphic minerals show a lack of growth zonation (although a number of the traverses do not necessarily go through the centre of garnet grains – Fig. 6.8). The lack of prograde zoning in and presence of retrograde rims in most samples indicates that diffusional re-equilibration of samples has occurred, and the compositions of the garnets analysed are unlikely to represent the compositions at peak conditions. Owing to this diffusional re-equilibration, the calculation of metamorphic temperatures through conventional cation-exchange (i.e garnet-biotite) thermometry in high-grade rocks is likely to be problematic (Harley, 1989; Spear, 1991).

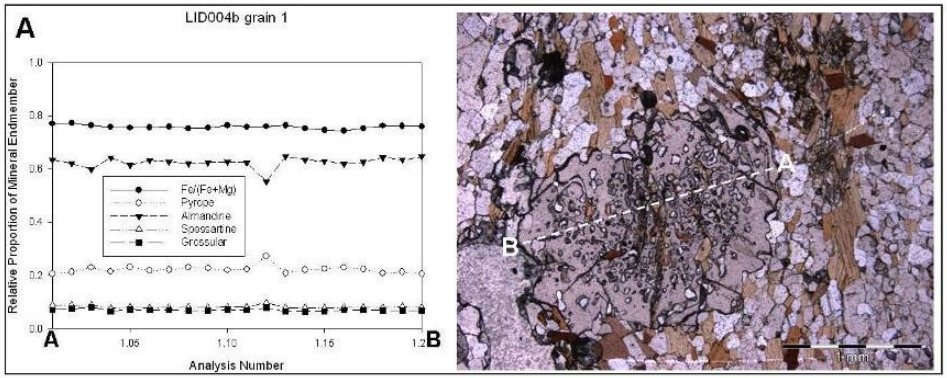
A
LID004b grain 1
Relative Proportion of Mineral Endmember
Fe/(Fe+Mg)
Pyrope
Almandine
Spessartine
Grossular
Analysis Number
A
B
1 mm

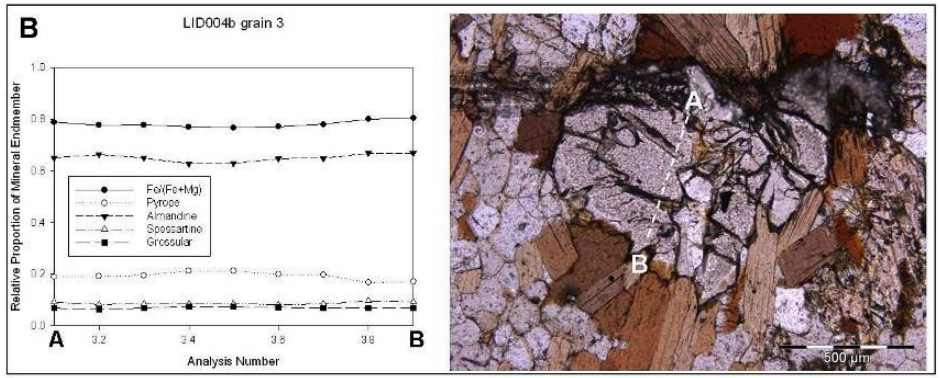
B
LID004b grain 3
Relative Proportion of Mineral Endmember
Fe/(Fe+Mg)
Pyrope
Almandine
Spessartine
Grossular
Analysis Number
A
B
500 µm

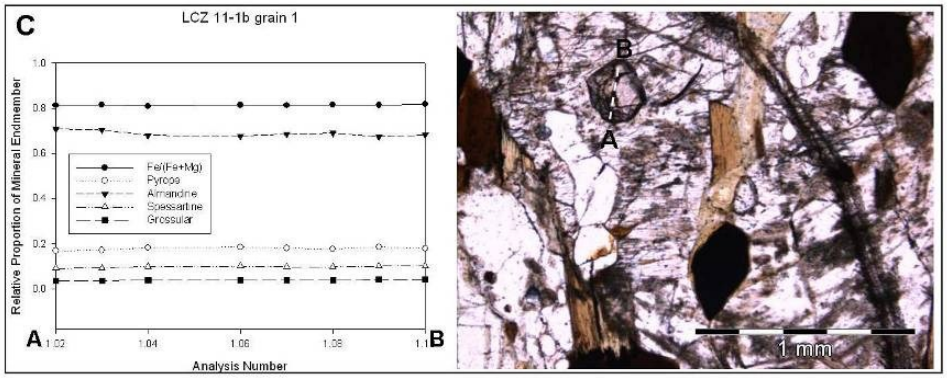
C
LCZ 11-1b grain 1
Relative Proportion of Mineral Endmember
Fe/(Fe+Mg)
Pyrope
Almandine
Spessartine
Grossular
Analysis Number
A
B
1 mm

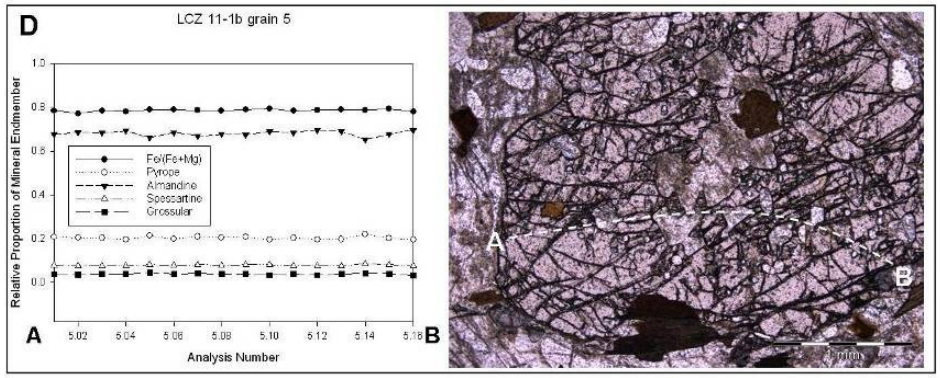
D
LCZ 11-1b grain 5
Relative Proportion of Mineral Endmember
Fe/(Fe+Mg)
Pyrope
Almandine
Spessartine
Grossular
Analysis Number
A
B

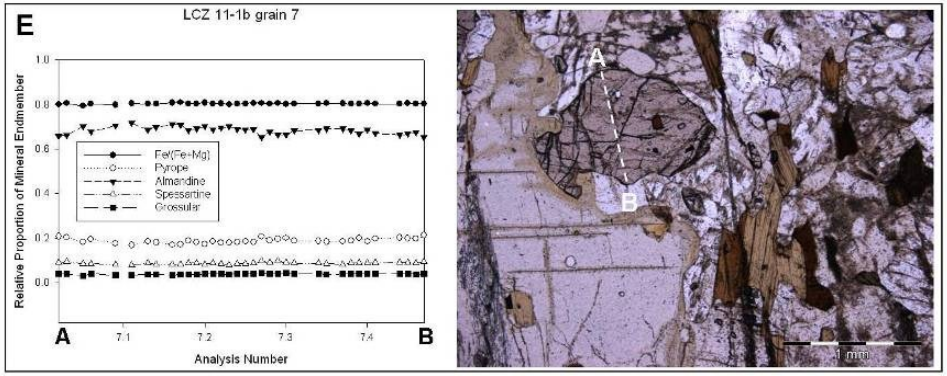
E
LCZ 11-1b grain 7
Relative Proportion of Mineral Endmember
Fe/(Fe+Mg)
Pyrope
Almandine
Spessartine
Grossular
Analysis Number
A
B
1 mm

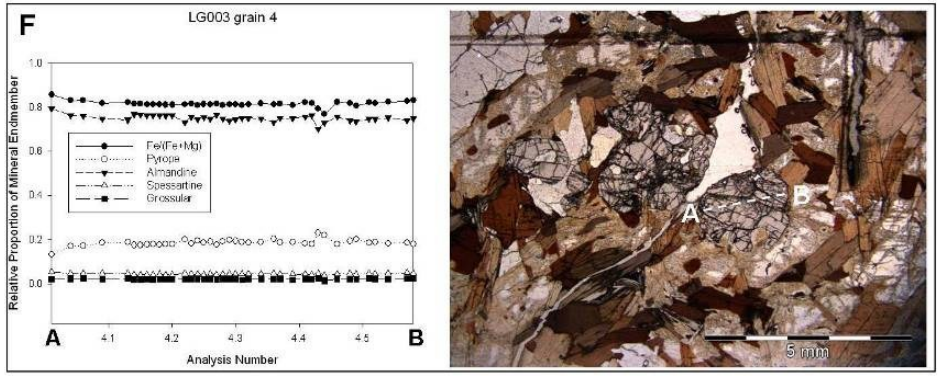
F
LG003 grain 4
Relative Proportion of Mineral Endmember
Fe/(Fe+Mg)
Pyrope
Almandine
Spessartine
Grossular
Analysis Number
A
B
5 mm

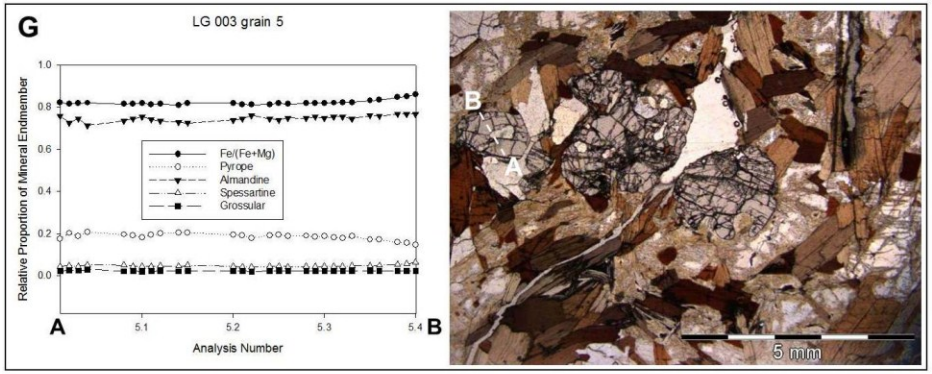
G
LG 003 grain 5
Relative Proportion of Mineral Endmember
Fe/(Fe+Mg)
Pyrope
Almandine
Spessartine
Grossular
Analysis Number
A
B
5 mm

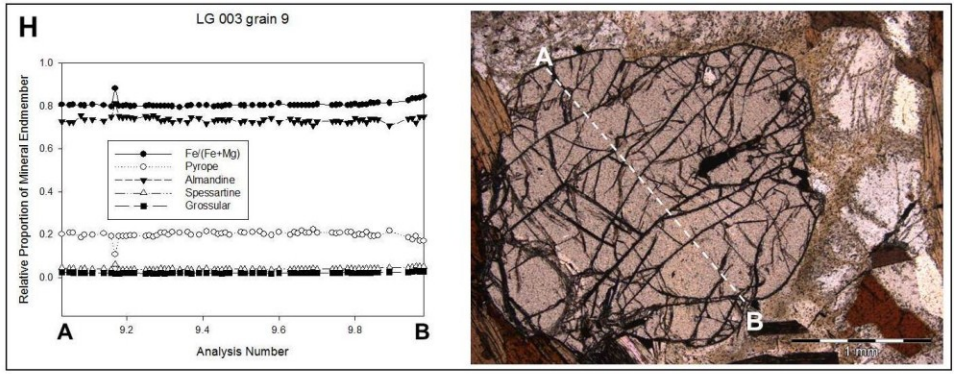
H
LG 003 grain 9
Relative Proportion of Mineral Endmember
Fe/(Fe+Mg)
Pyrope
Almandine
Spessartine
Grossular
Analysis Number
A
B
1 mm

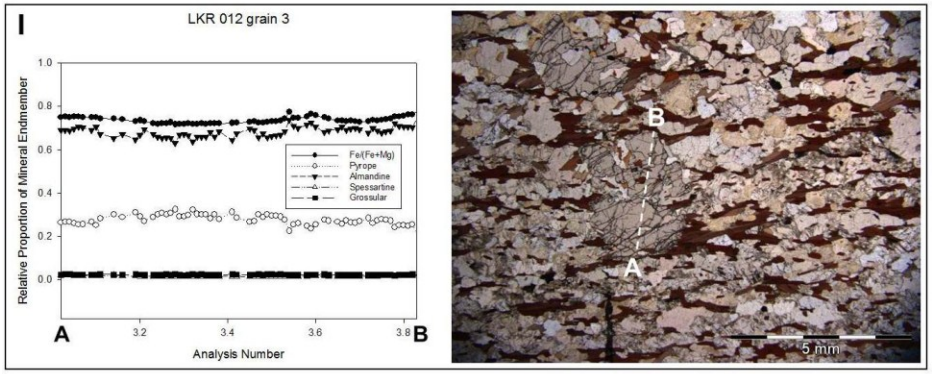
I
LKR 012 grain 3
Relative Proportion of Mineral Endmember
Fe/(Fe+Mg)
Pyrope
Almandine
Spessartine
Grossular
Analysis Number
A
B
5 mm

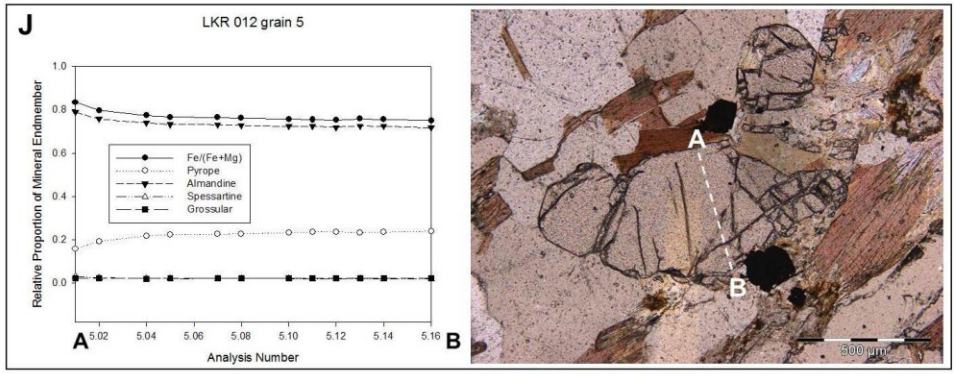
J
LKR 012 grain 5
Relative Proportion of Mineral Endmember
Fe/(Fe+Mg)
Pyrope
Almandine
Spessartine
Grossular
Analysis Number
A
B
500 µm

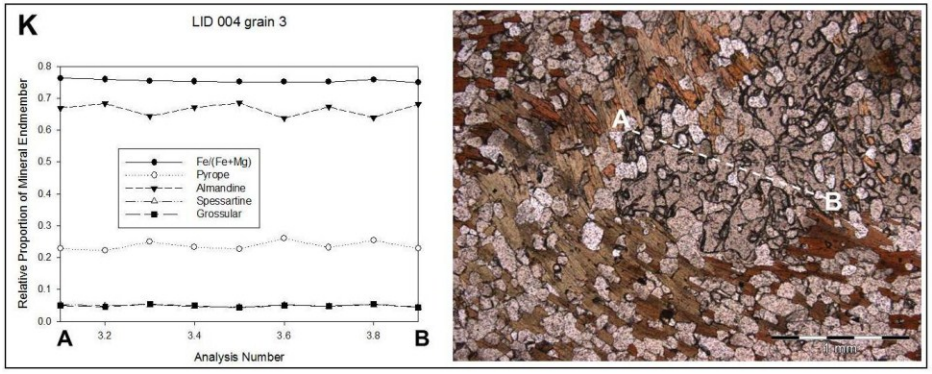
K
LID 004 grain 3
Relative Proportion of Mineral Endmember
Fe/(Fe+Mg)
Pyrope
Almandine
Spessartine
Grossular
Analysis Number
A
B
1 mm

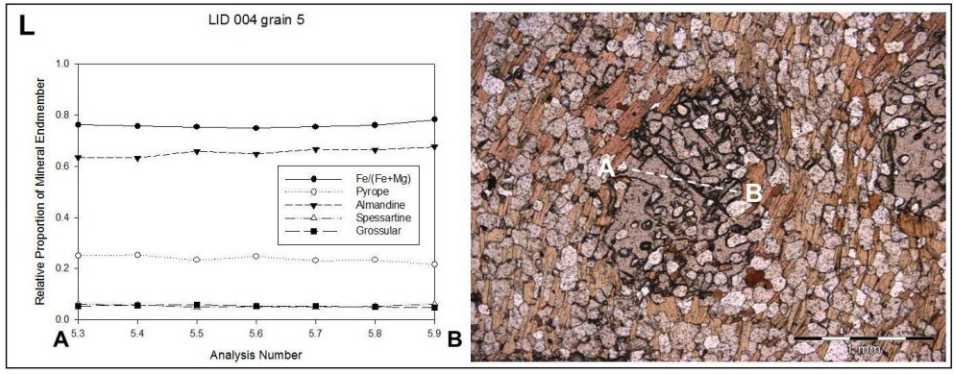
L
LID 004 grain 5
Relative Proportion of Mineral Endmember
Fe/(Fe+Mg)
Pyrope
Almandine
Spessartine
Grossular
Analysis Number
A
B
1 mm

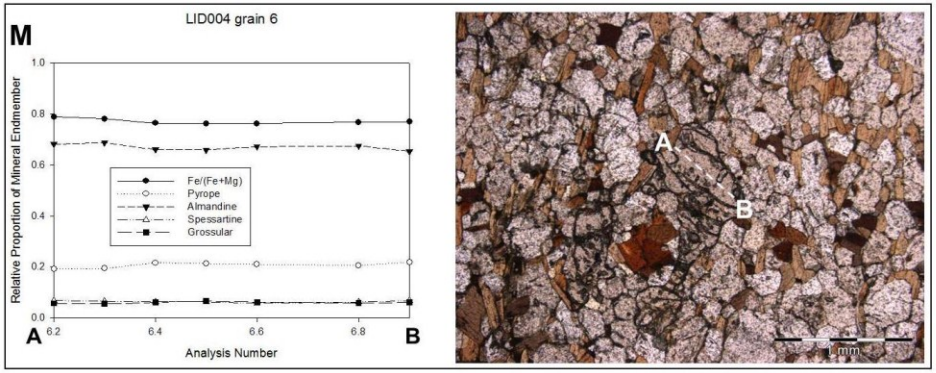
M
LID004 grain 6
Relative Proportion of Mineral Endmember
Fe/(Fe+Mg)
Pyrope
Almandine
Spessartine
Grossular
A
B
Analysis Number
1 mm

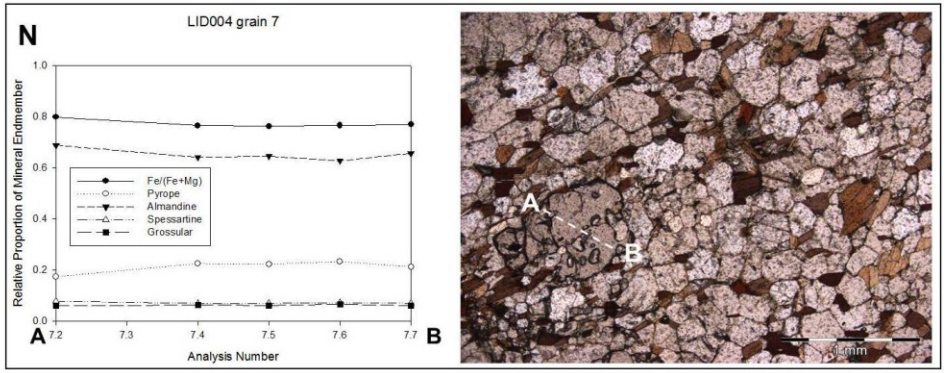
N
LID004 grain 7
Relative Proportion of Mineral Endmember
Fe/(Fe+Mg)
Pyrope
Almandine
Spessartine
Grossular
A
B
Analysis Number
1 mm

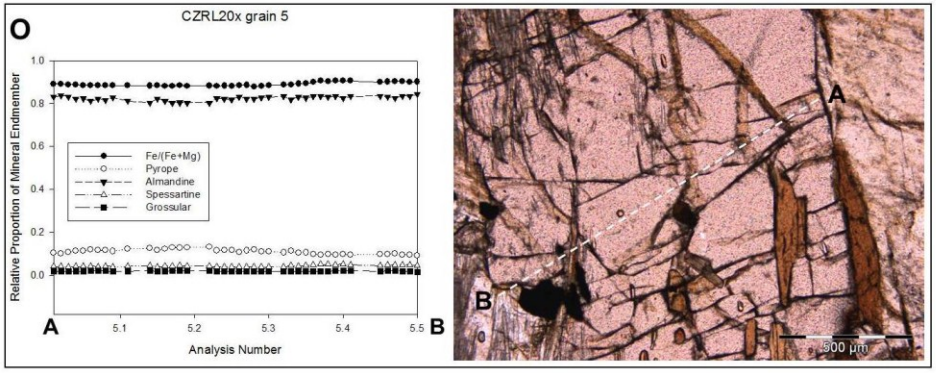
O
CZRL20x grain 5
Relative Proportion of Mineral Endmember
Fe/(Fe+Mg)
Pyrope
Almandine
Spessartine
Grossular
A
B
Analysis Number
500 µm

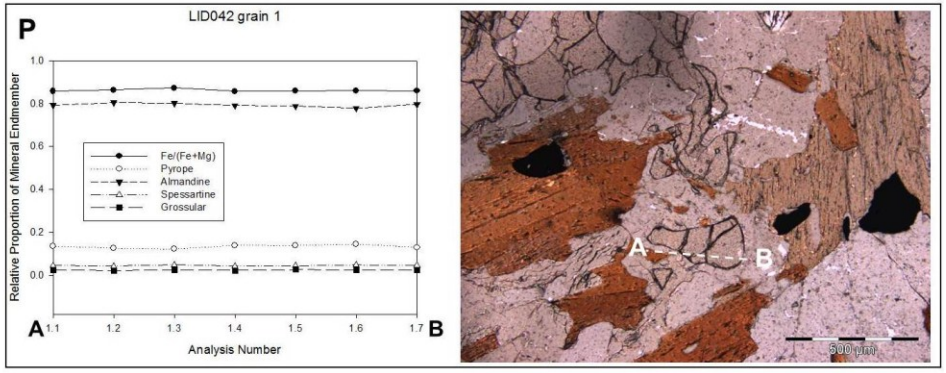
P
LID042 grain 1
Relative Proportion of Mineral Endmember
Fe/(Fe+Mg)
Pyrope
Almandine
Spessartine
Grossular
A
B
Analysis Number
500 µm

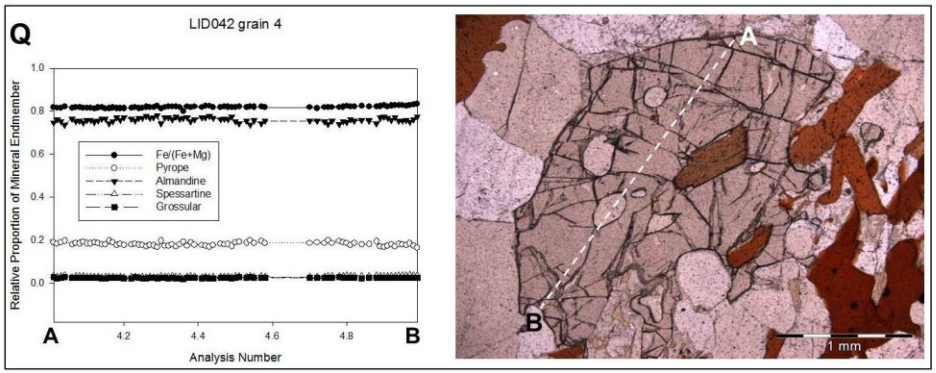
Q
LID042 grain 4
Relative Proportion of Mineral Endmember
Fe/(Fe+Mg)
Pyrope
Almandine
Spessartine
Grossular
A
B
Analysis Number
1 mm

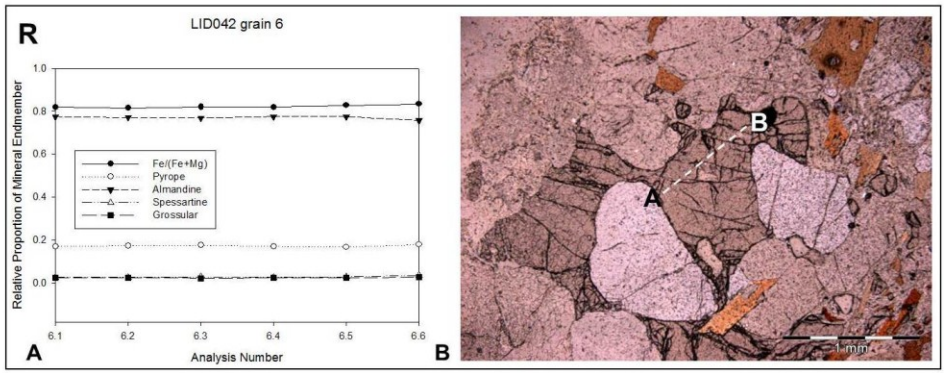
R
LID042 grain 6
Relative Proportion of Mineral Endmember
Fe/(Fe+Mg)
Pyrope
Almandine
Spessartine
Grossular
A
B
Analysis Number
1 mm

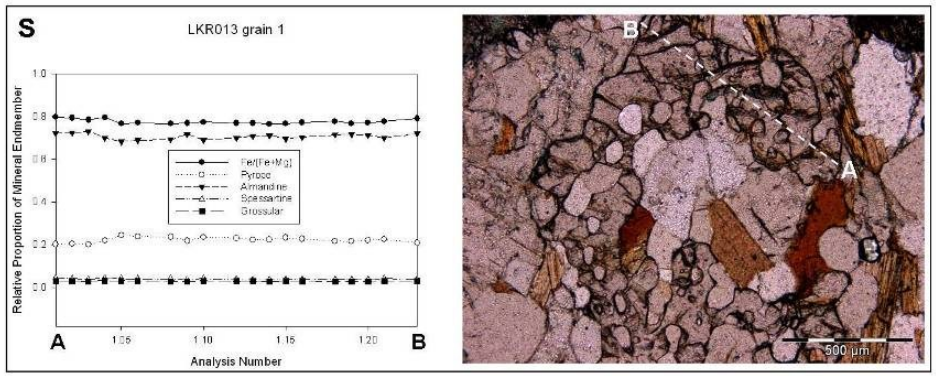
S
LKR013 grain 1
Relative Proportion of Mineral Endmember
Fe/(Fe+Mg)
Pyrope
Almandine
Spessartine
Grossular
A
B
Analysis Number
500 µm

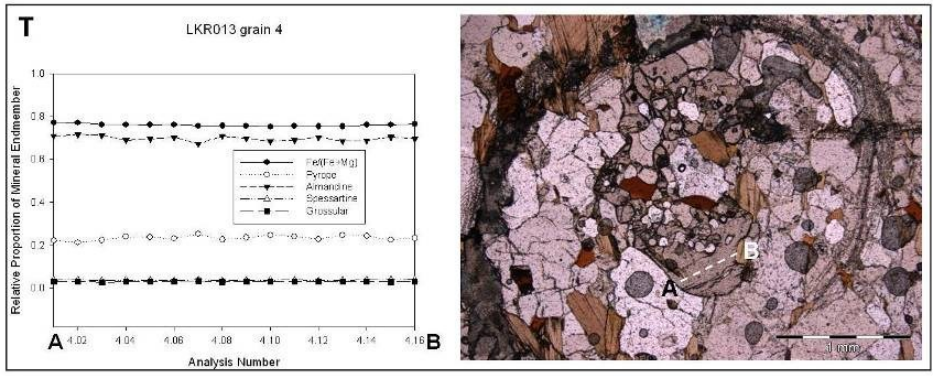
T
LKR013 grain 4
Relative Proportion of Mineral Endmember
Fe/(Fe+Mg)
Pyrope
Almandine
Spessartine
Grossular
A
B
Analysis Number
1 mm

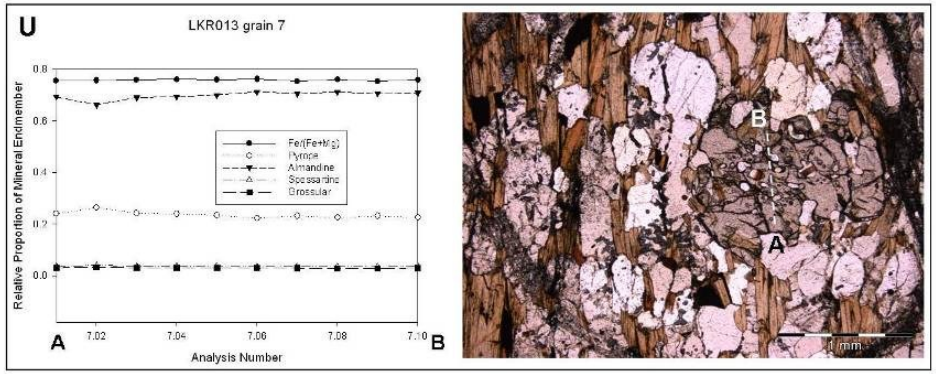
U
LKR013 grain 7
Relative Proportion of Mineral Endmember
Fe/(Fe+Mg)
Pyrope
Almandine
Spessartine
Grossular
A
B
Analysis Number
1 mm

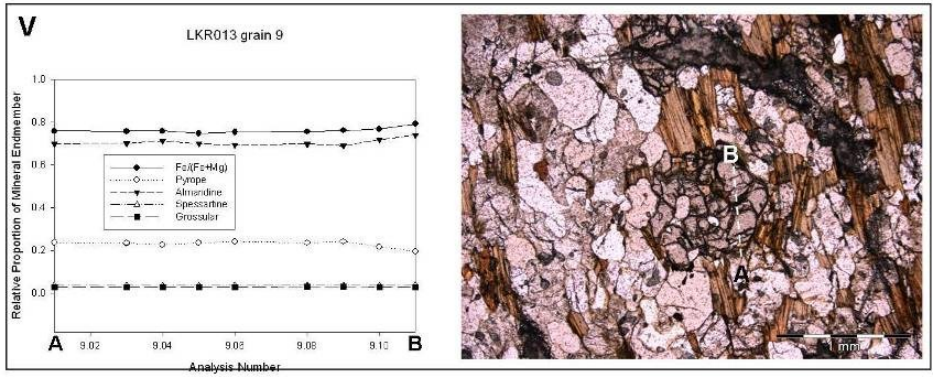
V
LKR013 grain 9
Relative Proportion of Mineral Endmember
Fe/(Fe+Mg)
Pyrope
Almandine
Spessartine
Grossular
A
B
Analysis Number
1 mm

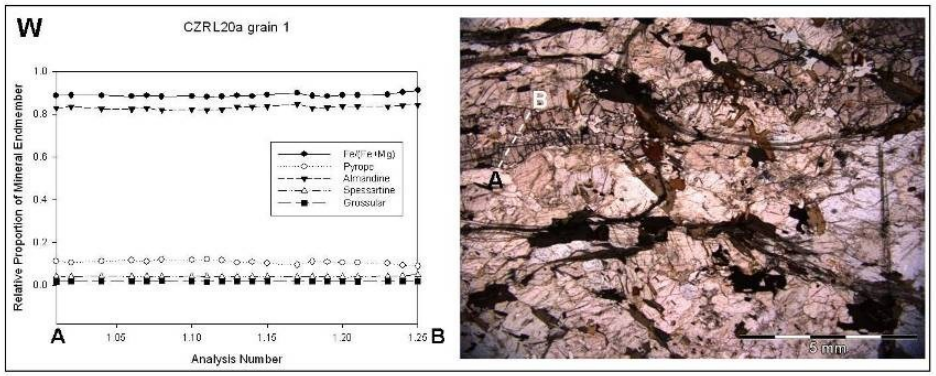
W
CZRL20a grain 1
Relative Proportion of Mineral Endmember
Fe/(Fe+Mg)
Pyrope
Almandine
Spessartine
Grossular
A
B
Analysis Number
5 mm

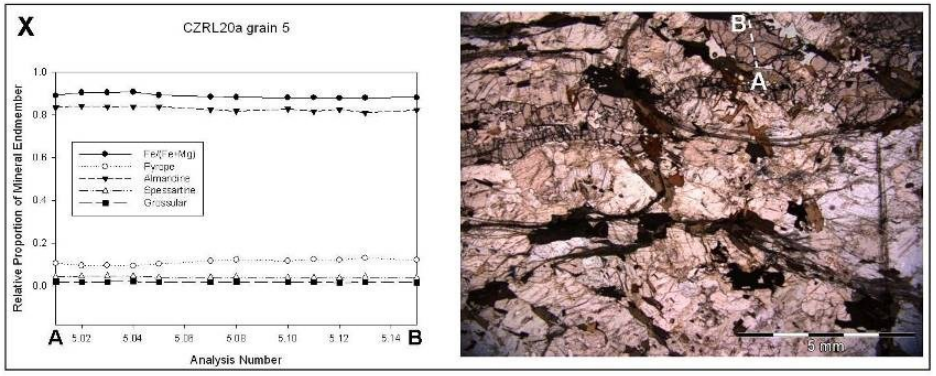
X
CZRL20a grain 5
Relative Proportion of Mineral Endmember
Fe/(Fe+Mg)
Pyrope
Almandine
Spessartine
Grossular
A
B
Analysis Number
5 mm

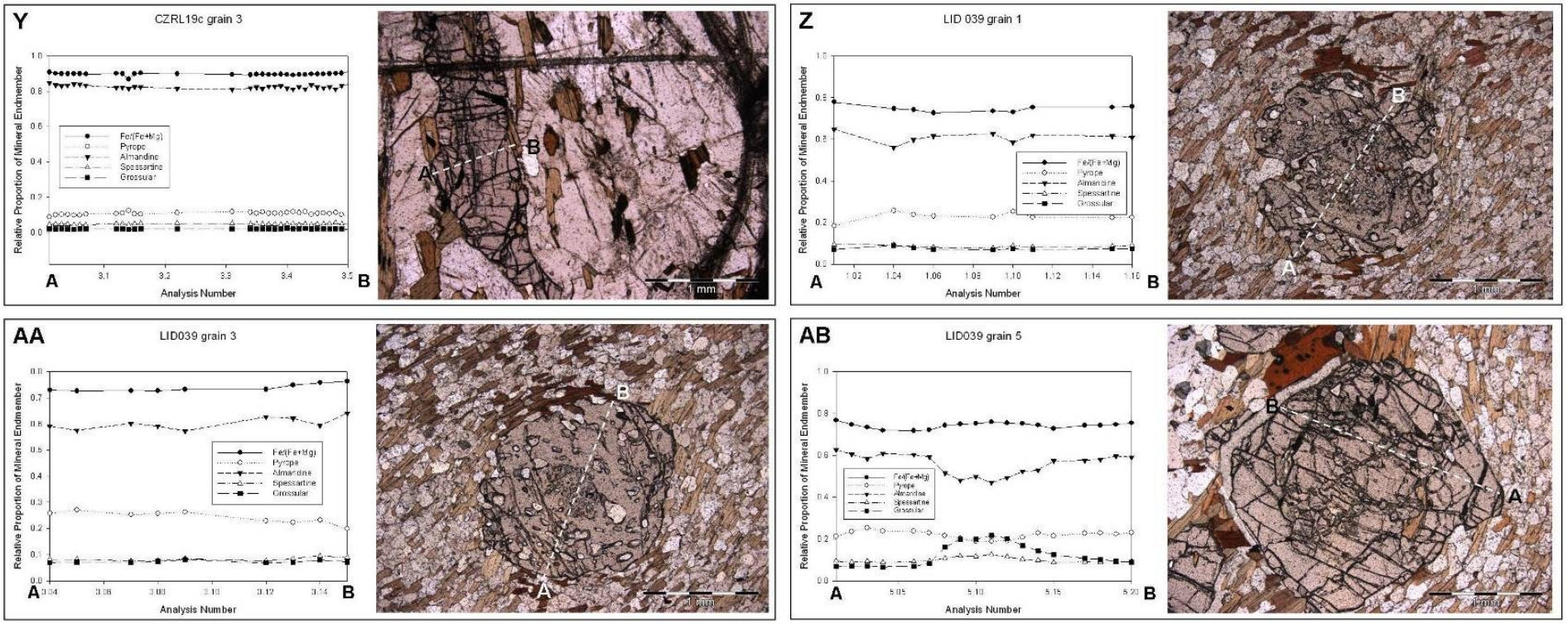

Fig. 6.8 (previous pages) – Chemical profiles across garnet grains, with relative proportions of mineral end members (pyrope, almandine, spessartine and grossular), in addition to Fe/(Fe + Mg) shown. Photomicrographs showing the locations of the profiles are also shown (all PPL). Sample numbers and grains analysed are labelled. Note that almost all profiles are flat, with retrograde changes near the margins of some grains (F – LG003 grain 4, G – LG003 grain 5, H – LG003 grain 9, I – LKR012 grain 3, J – LKR012 grain 5). Despite textural zoning of some garnets (e.g. A – LID004b grain 1, Z – LID039 grain 1, AA – LID039 grain 3), only a single sample shows possible prograde zonation (AB – LID039 grain 5).Data are contained in Appendix 3.

Sample LID039 contains a single texturally zoned garnet that also shows prograde chemical zoning (Fig. 6.8AB). The core of this garnet contains elevated grossular and spessartine components (i.e. elevated Ca and Mn), and lower almandine and pyrope components (i.e. lower Fe and Mg), a typical concentrically zoned prograde zoning pattern for garnet (Vernon, 2004). The Fe/(Fe + Mg) ratio changes from higher Fe/(Fe + Mg) values of up to 0.760 in the core, dropping to 0.718 in the zone around the core, and increasing again to 0.767 in the outer rim. Many garnets, although not compositionally zoned, show a textural zoning, with inclusion-rich cores and inclusion-free rims. The inclusions in the cores of these garnets are typically biotite and quartz, with zircon locally included, and rarely pinitised cordierite. Both biotite in the groundmass of samples and biotite included in other minerals have been analysed.

6.6.2 Biotite

Biotite is ubiquitous in all samples, and is generally aligned to form the S2 schistosity, which wraps cordierite, and in some cases, garnet. Additionally, biotite is also commonly found as small, rounded inclusions in the cores of garnet porphyroblasts, and also locally as inclusions in cordierite. In sample CZRL19, reddish-brown and greenish biotite is common and, together with fibrolitic sillimanite, forms the fabric. The compositions of all the biotites from the samples, which occur in a variety of textural locations, can be found in Appendix 3B. Generally, the Fe/(Fe+Mg) ratios of biotite are fairly uniform within individual samples (Fig. 6.9), although a range of compositions is found across all samples analysed. Variations in the proportions of Fe, Mg and Ti make up the compositional variability in biotites, with Fe/(Fe + Mg) varying between 0.35 and 0.70, and Ti ranging from 0.137 to 0.290 cations per 11 oxygen anions (2.47 to 5.08 wt %). Within individual samples, Fe/(Fe + Mg) ratios remain fairly constant, with the exception of biotite grains found as inclusions within garnet or cordierite. Biotite grains included within garnet (LID039 grain 8 – Fig. 6.9A, LCZ11-1b grain 6 – Fig. 6.9B, CZRL20x grains 7 and 9 – Fig. 6.9C, LID042 grain 5 – Fig. 6.9C, CZRL19c grains 3 and 7 – Fig. 6.9D, LKR013 grains 2 and 10 – Fig. 6.9F) have

lower Fe/(Fe + Mg) than biotite from the groundmass. Biotite included in cordierite (LHA008 grain 8 – Fig. 6.9A, CZRL19 grain 3 – Fig. 6.9D) may have higher Fe/(Fe + Mg) relative to groundmass biotite, although this difference may be small in some cases (Fig. 6.9D). These changes in Fe/(Fe + Mg) correspond to changes in Fe/Ti, although the Fe/Ti ratio is variable in cases where there is no apparent change in Fe/(Fe + Mg) (e.g. LG003 – Fig. 6.9B). Since Fe and Mg partitioning between garnet and biotite is temperature dependent (Ferry & Spear, 1978), and the Fe content of biotite increases with increasing temperature (Ferry & Spear, 1978) with a concomitant decrease in the Mg content of biotite, lower Fe/(Fe + Mg) biotite included in garnet are likely to have formed at lower temperature conditions than biotite in the groundmass, during prograde heating. The biotite included in cordierite in sample CZRL19 (Fig. 6.9F) has a marginally higher Fe/(Fe + Mg) than groundmass biotite in this sample, indicating that this biotite may have formed at peak temperatures, and that the composition of groundmass biotite (which has likely undergone retrograde diffusional re-equilibration and cation-exchange with garnet – see section 6.6.1) does not represent peak conditions. Sample LHA008 has large biotite laths included in cordierite (together with andalusite – Fig. 6.5C), and this included biotite has higher Fe/(Fe + Mg) than groundmass biotite (Fig. 6.9A), as opposed to other samples where biotite in the groundmass has higher Fe/(Fe + Mg) than biotite inclusions. Sample LHA008 does not contain garnet, and cordierite will increase in Fe/(Fe + Mg) with increasing temperature, with a concomitant decrease in Fe/(Fe + Mg) in biotite with increasing grade. Thus, higher Fe/(Fe+Mg) biotite preserved (together with andalusite) in the cores of cordierite porphyroblasts have compositions reflecting their formation along the prograde path at lower grades than biotite found in the groundmass. In sample CZRL19, changes in biotite colour from reddish-brown to greenish may be the result of changes in Fe/Ti ratios (Deer *et al*., 1971).

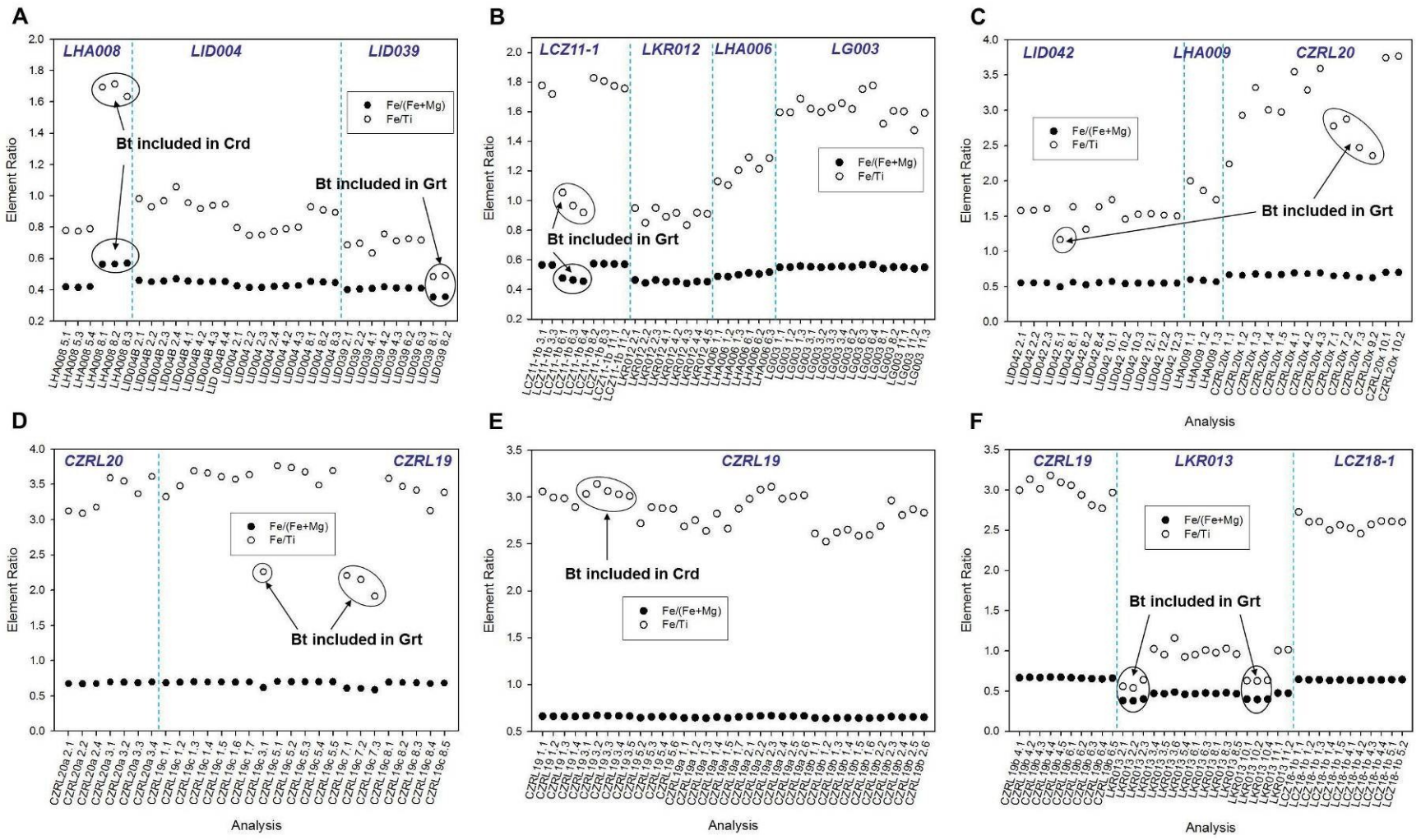
A
LHA008
LID004
LID039
Fe/(Fe+Mg)
Fe/Ti
Bt included in Crd
Bt included in Grt
Element Ratio
B
LCZ11-1
LKR012
LHA006
LG003
Fe/(Fe+Mg)
Fe/Ti
Bt included in Grt
Element Ratio
C
LID042
LHA009
CZRL20
Fe/(Fe+Mg)
Fe/Ti
Bt included in Grt
Element Ratio
Analysis
D
CZRL20
CZRL19
Fe/(Fe+Mg)
Fe/Ti
Bt included in Grt
Element Ratio
Analysis
E
CZRL19
Bt included in Crd
Fe/(Fe+Mg)
Fe/Ti
Element Ratio
Analysis
F
CZRL19
LKR013
LCZ18-1
Fe/(Fe+Mg)
Fe/Ti
Bt included in Grt
Element Ratio
Analysis

Fig. 6.9 (previous page) – Fe, Mg and Ti chemical data of biotites analysed, with both Fe/(Fe + Mg) and Fe/Ti ratios shown. Note that whilst Fe/(Fe + Mg) ratios remain fairly constant (except in cases where biotite is included in other minerals), the Fe/Ti ratios are variable within samples. Biotites included in cordierite or garnet are labelled. Mineral abbreviations after Kretz (1983). Data are contained in Appendix 3.

6.6.3 Cordierite

A variety of cordierite grains were analysed from the different sample types, including cordierite with fibrolitic sillimanite inclusions (LCZ11-1b), cordierite with inclusions of both fibrolite and spinel (LHA006, LHA009) and clear cordierite without inclusions of sillimanite or spinel (LG003, LID042). Cordierite grains analysed show a range of compositions between different samples (Fig. 6. 10), with ranges in Fe/(Fe + Mg) between 0.263 (LHA006 spot 4.13 – Fig. 6. 10B) and 0.484 (CZRL19b spot 3.9 – Fig. 6.10D), although within individual samples cordierite compositions remain fairly constant, and do not appear to be dependent on the inclusions within the cordierite (e.g. cordierites from LHA006 and LHA009 both have spinel and sillimanite inclusions – Figs. 6.10B, C) and profiles across single grains reveal no compositional zoning (e.g. LHA006 grain 10 – Figs. 6. 10B, C).

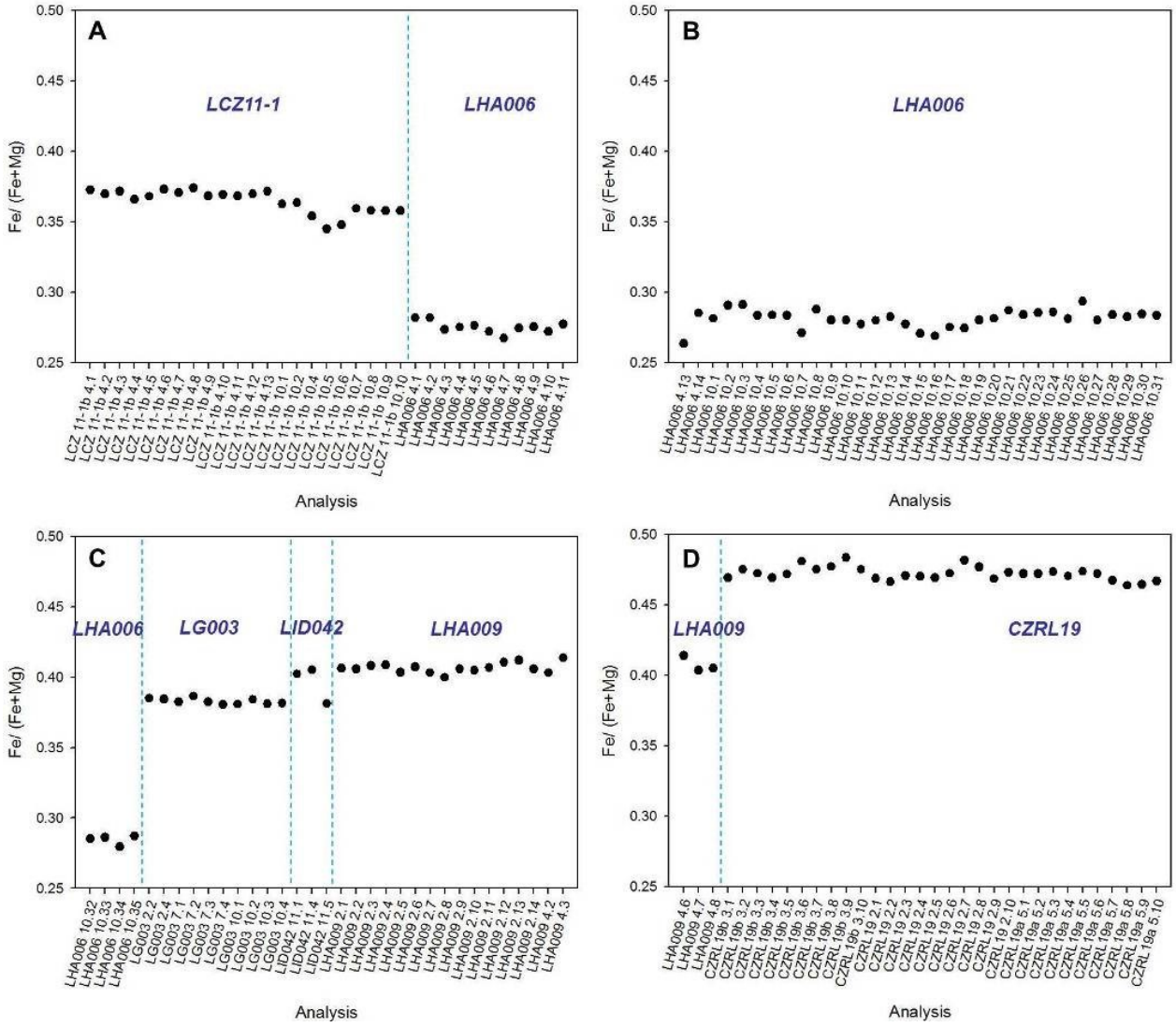

Fig. 6.10 – Fe/(Fe + Mg) values of cordierites analysed, showing variation between individual samples, but little intrasample variability in cordierite composition, and no compositional zoning in cordierite. Data are contained in Appendix 3D.

6.6.4 Spinel

In samples LHA006, LHA008 and LHA009, spinel is present as inclusions within large cordierite porphyroblasts, or as symplectic intergrowths with cordierite (Fig. 6.5). This spinel has a fairly constant hercynitic composition (Fig. 6.11), with some spinel component – i.e. spinels are Fe-rich. LHA009 has spinel compositions which are enriched in gahnite relative to

spinel (i.e. spinel in this sample is enriched in Zn relative to Mg). Spinel is also found in sample LCZ11-1, where the composition is also hercynitic (with the exception of a single spinel analysis that shows a composition that is slightly less hercynitic, but still is enriched in Fe relative to Mg).

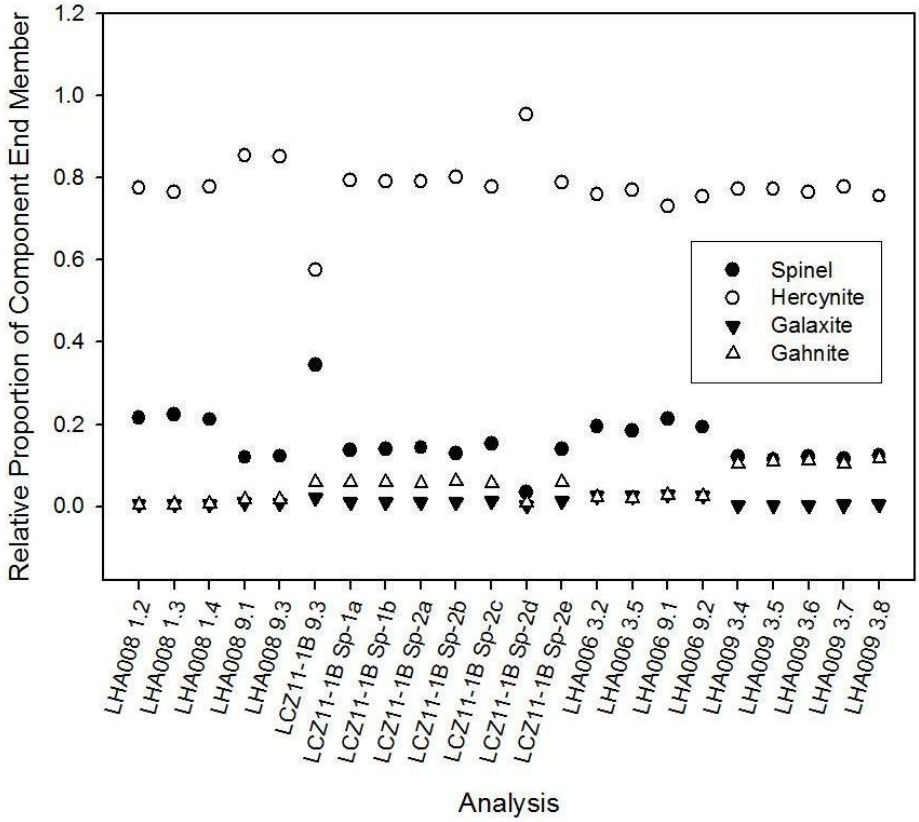

Fig. 6.11 – Chemical data of spinels analysed, showing the relative proportions of component end members. Data are contained in Appendix 3F.

6.6.5 Feldspars

Feldspars analysed show a range of compositions (Fig. 6.12), reflecting the fact that both K-feldspar and plagioclase are found in these samples. Plagioclase compositions within individual samples may vary considerably (e.g. An_{11} to An_{76} – LHA008), although the higher anorthite analyses in this sample are from inclusions in cordierite and are unlikely to be equilibrated with the matrix of the sample. The alkali feldspars also show a range of

compositions, and are not generally pure K-feldspar, but may have up to 60% albite component (LCZ18-1), or even pure albite (CZRL19, LHA009). This albite commonly forms as films adjacent to K-feldspars (Fig. 6.6C), and is interpreted as crystallised melt.

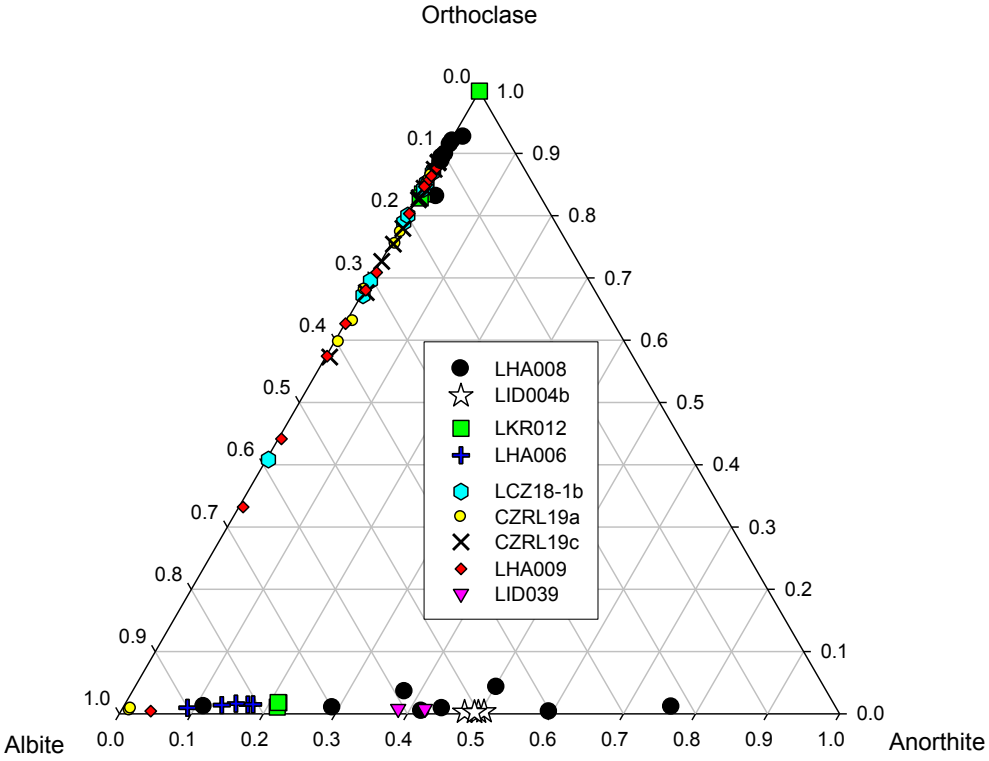

Fig. 6.12 – Chemical data of feldspars analysed, showing the relative proportions of albite, orthoclase and anorthite. Data are contained in Appendix 3.

6.6.6 Orthopyroxene and gedrite

Orthopyroxene and gedrite are only locally found – orthopyroxene is found in trace amounts in two samples – LID004 and LID039, both from a single outcrop. Gedrite is even rarer, found only in trace amounts in sample LID004. Due to this rarity, and difficulties in finding suitable grains for analysis, only two grains have been analysed. Orthopyroxene from LID039 shows ferro-hypersthene to hypersthene compositions (Fig. 6.13A), and the low Ca content of the analyses confirms that the mineral is indeed orthopyroxene (see data in

Appendix 3). Two grains of gedrite from LID004 were analysed. The first grain (analyses 1.1-1.4) shows low totals (85-90% - see data in Appendix 3), and these analyses are considered unreliable. The second grain (analyses 8.1-8.3) gives better totals, and shows that the amphiboles are fairly ferruginous, and have fairly high Al contents (Fig. 6.13B). The low Ca and Na contents (see data in Appendix 3) show that these are not calcium or alkali amphibolies, and the elevated Al contents relative to Si, Fe and Mg show that (Mg, Fe^{2+})Si has been substituted for AlAl (Deer *et al*., 1971), confirming that this is gedrite rather than anthophyllite.

Chemical data for a number of grains of magnetite and ilmenite have been collected. These data confirm petrographic observations of these as major opaque phases, but are not presented here for brevity. Data are contained in Appendix 3.

Whilst high-temperature diffusion appears to have led to compositional equilibrium in garnets from across the study area, metamorphic assemblages found are not necessarily equilibrium assemblages. On the contrary, a number of samples contain relict phases (such as fibrolite, spinel, or andalusite) in the cores of cordierite porphyroblasts that are not found in the groundmass of the sample. These relict phases indicate that full equilibrium of the entire bulk-rock volume has not taken place, and these relict phases may indicate some of the prograde P-T path.

The compositions of minerals are dependent on both temperature-dependent cation exchange reactions (e.g. Fe and Mg in garnet, biotite and cordierite), as well as on the bulk composition of individual samples. Hence, the chemistry of phases should be evaluated with respect to the compositions of rocks in which they are contained. This is done using ACF and AK'F diagrams, in addition to the AFM projection of Thompson (1957), to show the relationships between phases and bulk compositions, and to evaluate some possible prograde reactions.

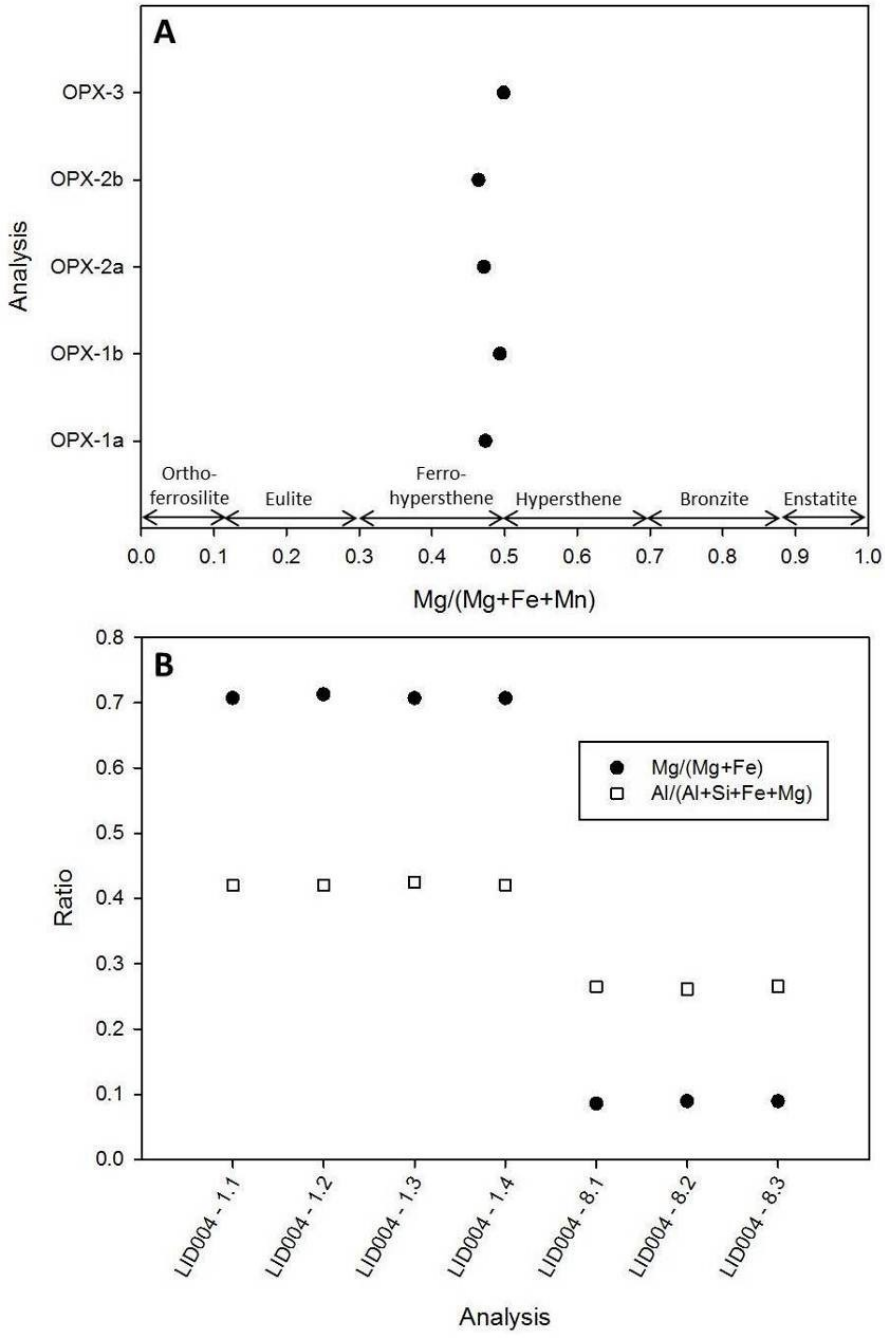

Fig. 6.13 – Chemical data of orthopyroxene and gedrite amphiboles analysed. A: Orthopyroxene, which has a ferro-hypersthene to hypersthene composition. B: Gedrite, which shows elevated Al contents, and low Mg/(Mg+Fe). Data are contained in Appendix 3.

6.6.7 Garnet-cordierite-biotite schists

Garnet-cordierite-biotite schists typically have the assemblage garnet-cordierite-biotite-K-feldspar-plagioclase-quartz-ilmenite-magnetite, and may contain inclusions of fibrolitic sillimanite in the cores of cordierite porphyroblasts. Orthopyroxene, gedrite and rutile are found locally. An ACF diagram (Fig. 6.14A), A'KF diagram (Fig. 6.14B) and AFM projection (Fig. 6.14C) illustrate that the compositions of garnet-cordierite-biotite schists are consistent with the assemblage cordierite-garnet-biotite-K-feldspar. The A'KF diagram (Fig. 6.14B) illustrates that sillimanite and biotite are unstable with an assemblage cordierite-garnet-K-feldspar, and that the sillimanite-biotite tie-line is crossed by the garnet-K-feldspar/cordierite-K-feldspar tie-lines, indicating that the reaction

sillimanite + biotite = garnet + cordierite + K-feldspar + melt

has taken place in these rocks. Similarly, an AFM projection (from K-feldspar) illustrates that the garnet + cordierite assemblage has been produced from a sillimanite + biotite consuming reaction. Petrographic evidence confirms that sillimanite + biotite is unstable – fibrolitic sillimanite needles are found exclusively in the cores of cordierite porphyroblasts, and never in the groundmass of these samples. However, sillimanite is not found as inclusions in garnet porphyroblasts in these samples, and cordierite is locally found as inclusions in garnet, indicating that cordierite growth and sillimanite consumption preceded garnet growth. This is confirmed by the syn-tectonic nature of cordierite, whilst garnet is seen to be late- to post-tectonic. Thus, it is possible that the initial sillimanite-consuming reaction was

sillimanite + biotite + quartz = cordierite + K-feldspar + melt (Yardley, 1989),

and that garnet growth occurred later, possibly owing to the reaction:

biotite + plagioclase + quartz = garnet + K-feldspar + melt (Vielzeuf & Montel, 1994).

Fig. 6.14 – Phase diagrams for garnet-cordierite-biotite schists. A: ACF diagram. B: A'KF diagram. C: AFM projection from K-feldspar (after Thompson, 1957). Schematic diagrams illustrating possible reactions are shown in B and C. Data are contained in Appendix 3.

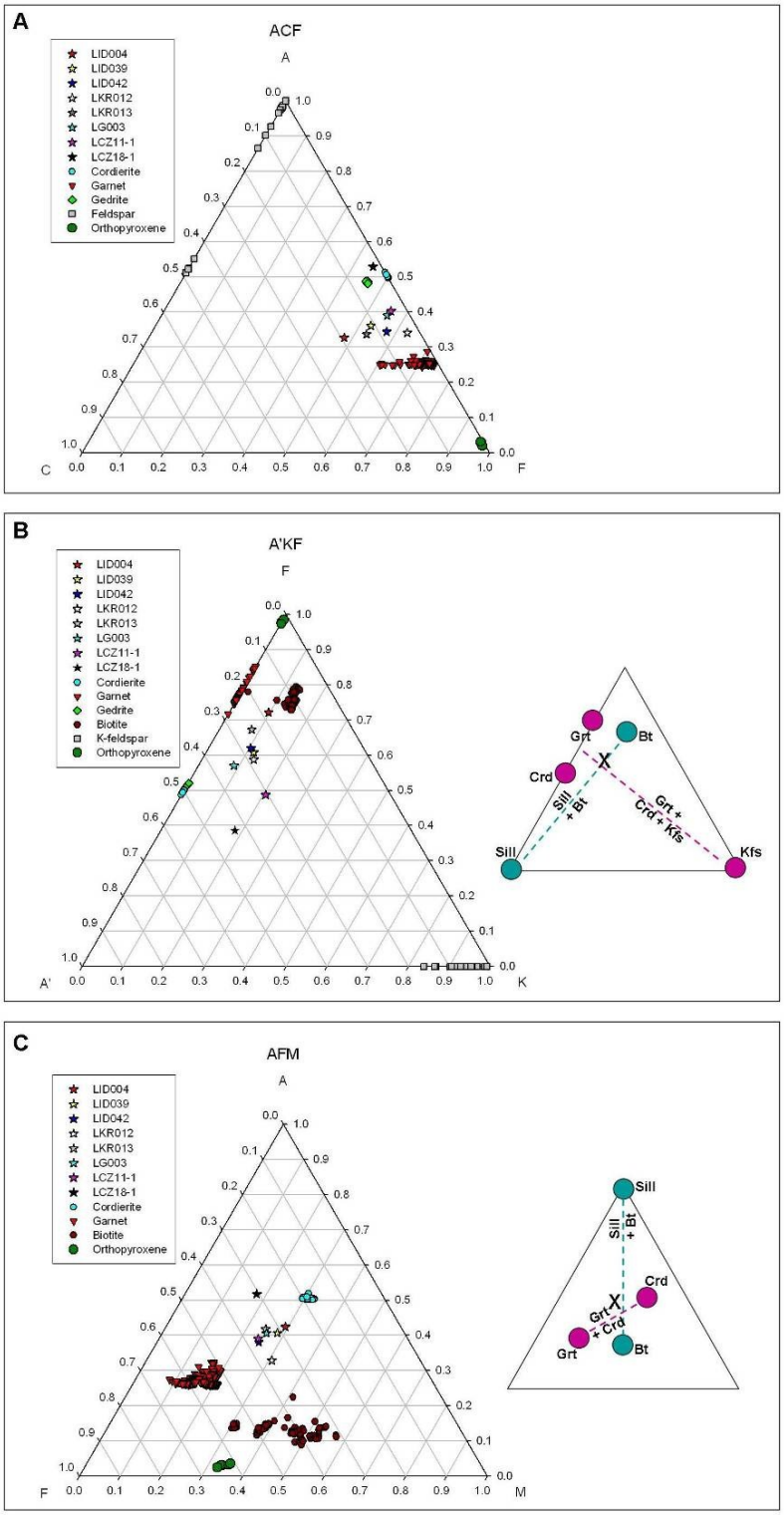

6.6.8 Cordierite-biotite schists

Cordierite-biotite schists are distinguished by the general lack of garnet (with the exception of one small grain in LHA006), and the presence of hercynitic spinel, which is found as inclusions in cordierite, or intergrown with cordierite as symplectites. These samples typically contain the assemblage cordierite-spinel-biotite-K-feldspar-plagioclase-quartz-ilmenite-magnetite, and sillimanite or andalusite is present as inclusions within cordierite porphyroblasts. The consumption of sillimanite (or andalusite) and biotite to produce cordierite and spinel is evident on an ACF diagram (Fig. 6.15A), an A'KF diagram (Fig. 6.15B) and an AFM projection (Fig. 6.15C), although the local preservation of corroded sillimanite in LHA006 indicates that this reaction did not go to completion. The reaction

biotite + sillimanite/andalusite + quartz = cordierite + spinel + melt (Jung *et al*., 1998)

may be responsible for the assemblages and textures observed, and has been suggested as a possible melt-producing reaction in the Donkerhuk contact aureole (Southern Zone). Jung *et al*. (1998) also suggested that the reaction

spinel + cordierite + quartz = garnet + sillimanite

occurred in the Donkerhuk aureole, thus consuming spinel and cordierite. However, although samples LHA006 and LHA009 do show rare minute garnet grains, and corroded sillimanite relicts were found in sample LHA008, there is no textural evidence for the consumption of cordierite and spinel to produce sillimanite and garnet. Assuming these samples experienced similar P-T paths to the garnet-cordierite-biotite schists, the differences in assemblages between these two assemblages are likely to be due to compositional differences between the samples. On an A'KF diagram, it is evident that cordierite-biotite schists (Fig. 6.15B) are more potassic and less ferromagnesian than garnet-cordierite-biotite schists (Fig. 6.14B). AFM projections also reveal that cordierite-biotite schists (Fig. 6.15C) are slightly more aluminous and less magnesian than garnet-cordierite-biotite schists.

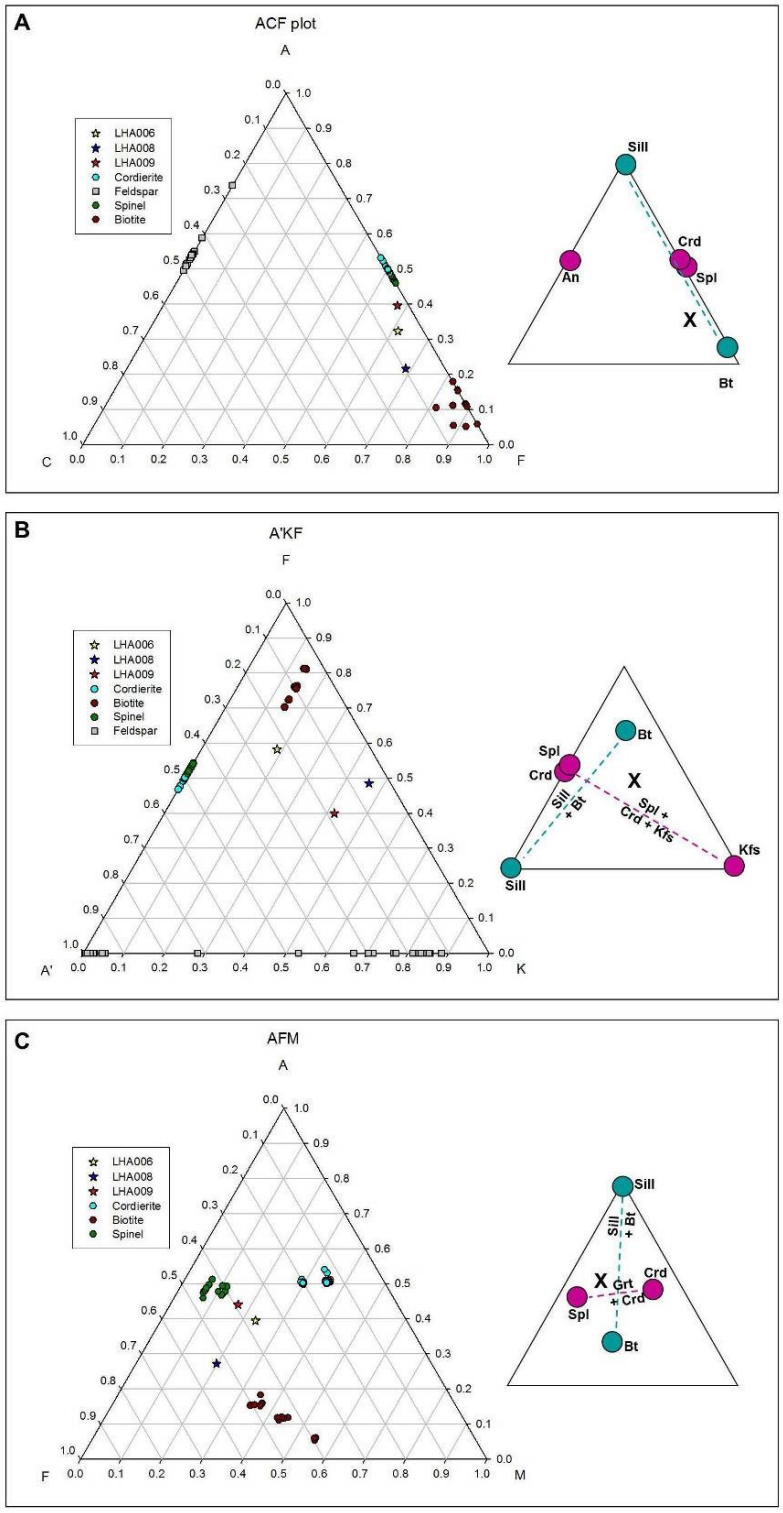

Fig. 6.15 – Phase diagrams for cordierite-biotite schists, with schematic diagrams illustrating reactions. A: ACF diagram. B: A'KF diagram. C: AFM projection from K-feldspar (after Thompson, 1957). Data are contained in Appendix 3.

6.6.9 Garnet-cordierite-sillimanite schists

Garnet-cordierite-sillimanite schists contain the assemblage garnet-cordierite-sillimanite-biotite-K-feldspar-plagioclase-quartz-ilmenite-magnetite, with no preserved reaction textures. Sillimanite appears to have formed early in the metamorphic history, as it is included in both garnet and cordierite, and together with biotite forms the S2 schistosity. Cordierite growth appears to be syn-tectonic, and was followed by post-tectonic mimetic garnet growth. As expected from the large volumes of sillimanite in the samples, these samples are more aluminous than garnet-cordierite-biotite schists or cordierite-biotite schists, and compositions of these samples are shown on an ACF diagram (Fig. 6.16A), an A'KF diagram (Fig. 6.16B) and an AFM projection (Fig. 6.16C), where they fall in the sillimanite-garnet-cordierite-K-feldspar field. Due to the high grades experienced (there is microtextural evidence for anatectic melt), it is likely that a sillimanite-consuming reaction such as

sillimanite + biotite + quartz = garnet + cordierite + K-feldspar + melt (Yardley, 1989)

may have taken place, but did not consume all sillimanite. Although sillimanite may have formed through a high-grade reaction such as

cordierite + K-feldspar = sillimanite + garnet + melt (Spear *et al*., 1999),

the clear syn-tectonic nature of sillimanite and late- to post-tectonic nature of garnet indicates that garnet grew later than cordierite, and may have consumed cordierite through a reaction such as

cordierite + biotite = garnet + K-feldspar + melt (Spear *et al*., 1999).

However, the lack of preserved reaction textures makes inferences regarding reactions somewhat speculative.

Fig. 6.16 – Phase diagrams for garnet-sillimanite-cordierite schists. A: ACF diagram. B: A'KF diagram. Dashed line indicates the assemblage garnet-biotite-K-feldspar-sillimanite-cordierite. C: AFM projection from K-feldspar (after Thompson, 1957). Dashed line indicates the assemblage garnet-biotite-sillimanite-cordierite. Data are contained in Appendix 3.

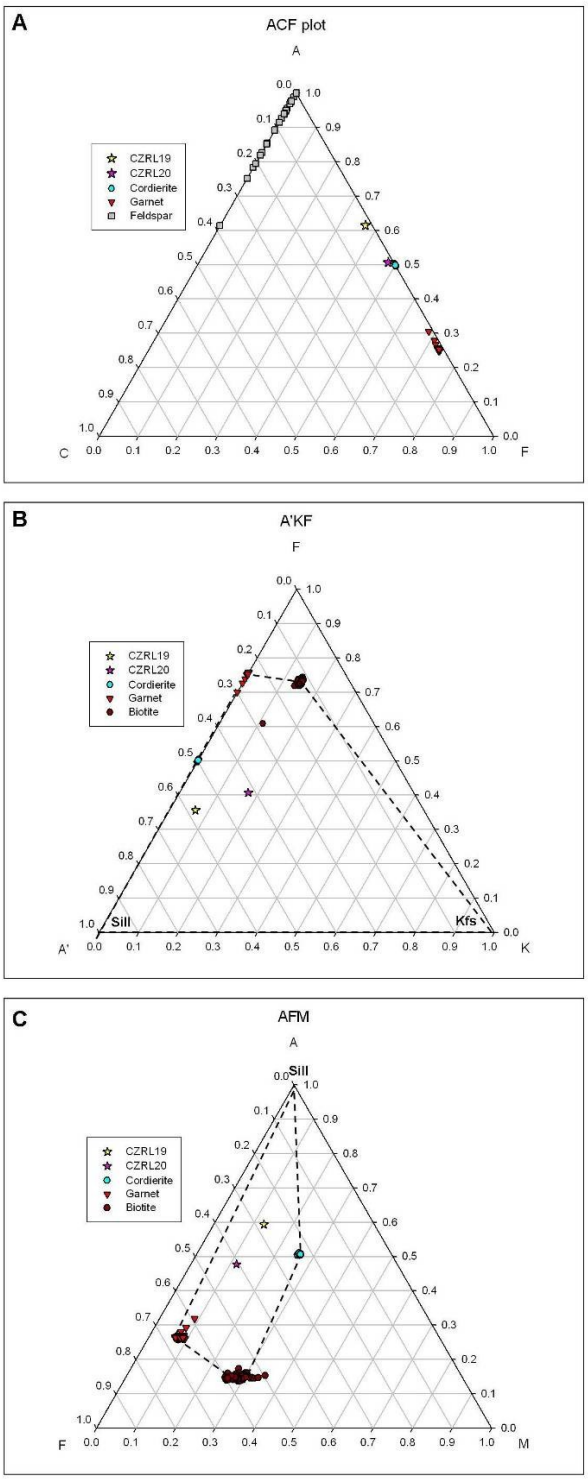

6.6.10 Compositional controls on mineral assemblages

Since no major tectonic boundaries appear to exist across the study area (see Chapter 3), it is assumed that all rocks have experienced fairly similar P-T conditions (upper-amphibolite to granulite facies). Although this is evaluated in more detail later in this chapter, one may assume that the major mineralogical variations between samples are due to compositional differences. Indeed, Harker diagrams for pelitic samples (Fig. 6.17) show that garnet-cordierite-biotite schists, cordierite-biotite schists and garnet-sillimanite-biotite schists can be distinguished geochemically. MgO/(MgO+FeO vs. Al_2O_3 (Fig. 6.17A) shows that garnet-cordierite-biotite schists have higher Mg/(Mg+Fe) ratios than other samples, and that garnet-cordierite-sillimanite schists have elevated Al_2O_3, consistent with the large volumes of sillimanite in these samples. Al_2O_3/(FeO+MgO) vs. K_2O+CaO+Na_2O (Fig. 6.17B) highlights the elevated Al_2O_3 of the garnet-cordierite-sillimanite schists, whilst illustrating that cordierite-biotite schists have both elevated Al_2O_3 relative to MgO+FeO, and elevated alkali contents. Since MnO stabilises garnet growth at lower temperatures and pressures, a plot of MnO vs. Al_2O_3/(FeO+MgO) (Fig. 6.17C) illustrates that cordierite-biotite schists have very low MnO contents, which may be a partial explanation for the lack of garnet in these samples. An exception is sample LHA006, which contains more elevated MnO, and has been noted to contain rare, minute garnet crystals. The plot of TiO_2 vs. Al_2O_3 (Fig. 6.17D) shows that cordierite-biotite schists have elevated TiO_2 relative to garnet-cordierite-biotite schists, but that garnet-cordierite-sillimanite schists have both elevated TiO_2 and Al_2O_3. Plots of SiO_2 vs. Al_2O_3/(FeO+MgO) (Fig. 6.17E) and of SiO_2 vs. MgO/(MgO+FeO) (Fig. 6.17F) show that garnet-cordierite-sillimanite schists have slightly lower SiO_2 than other samples, and that cordierite-biotite schists have slightly higher SiO_2 than other samples, with garnet-cordierite-biotite having median values of SiO_2.

Fig. 6.17 (following page) – Harker plots for pelitic samples. A: MgO/(MgO+FeO vs. Al_2O_3. B: Al_2O_3/(FeO+MgO) vs. K_2O+CaO+Na_2O. C: MnO vs. Al_2O_3/(FeO+MgO). LHA006 indicated. D: TiO_2 vs. Al_2O_3. E: SiO_2 vs. Al_2O_3/(FeO+MgO) F: SiO_2 vs. MgO/(MgO+FeO).

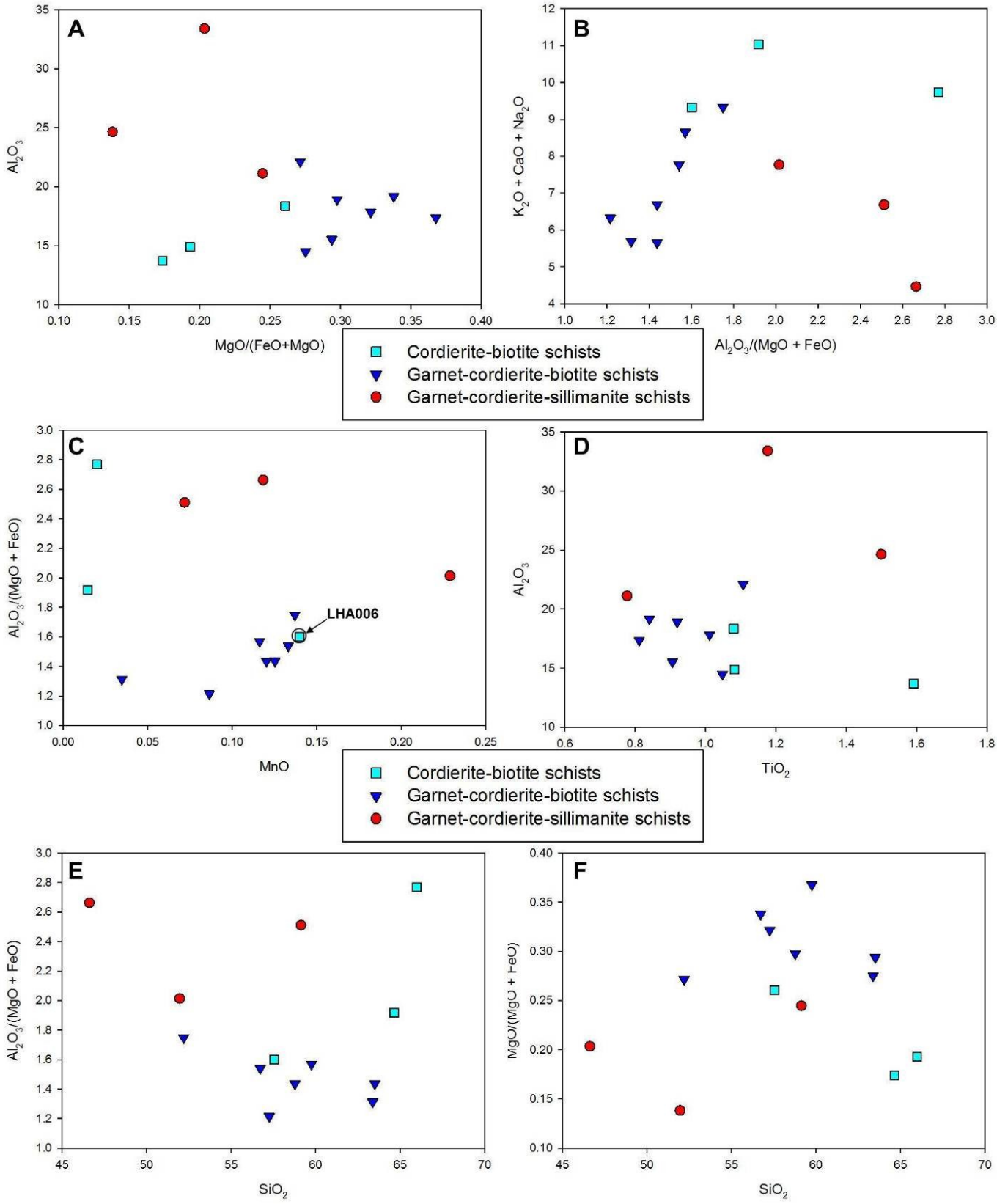
A
B
C
D
E
F
Al2O3
MgO/(FeO+MgO)
K2O + CaO + Na2O
Al2O3/(MgO + FeO)
MnO
LHA006
TiO2
SiO2
MgO/(MgO + FeO)
Cordierite-biotite schists
Garnet-cordierite-biotite schists
Garnet-cordierite-sillimanite schists

In summary, the principal difference between the garnet-cordierite-sillimanite schists and the garnet-cordierite-biotite schists is the presence or absence of sillimanite in the matrix, and is explained by the elevated Al_2O_3 contents of the garnet-cordierite-sillimanite schists, with a concomitant decrease in SiO_2. The MgO/(MgO+FeO) ratios of the garnet-cordierite-sillimanite schists are also lower. The cordierite-biotite schists, however, do not contain garnet, and also contain distinctive cordierite-spinel intergrowths. These samples have low MgO/(MgO+FeO) ratios and low total Al_2O_3 contents, but have elevated Al_2O_3/(FeO+MgO) and high K_2O+CaO+Na_2O, with low MnO values. The elevated Al_2O_3/(FeO+MgO) may explain the formation of spinel rather than garnet, as spinel is a more aluminous mineral than garnet. The principal chemical differences between the sample groups are shown in Table 6.4.

Table 6.4 – Summary of geochemical characteristics of pelitic samples.

Garnet-cordierite-biotite schists	Cordierite-biotite schists	Garnet-cordierite-sillimanite schists
High MgO/(MgO+FeO)	Low MgO/(MgO+FeO)	Low MgO/(MgO+FeO)
Low Al_2O_3	Low Al_2O_3	High Al_2O_3
Low TiO_2	High TiO_2	High TiO_2
Low Al_2O_3/(MgO+FeO)	High Al_2O_3/(MgO+FeO)	High Al_2O_3/(MgO+FeO)
	High SiO_2	Low SiO_2
	Low MnO	
	High K_2O+CaO+Na_2O	

6.7 Qualitative Petrogenetic Grids

A number of possible melt-forming reactions have been suggested for the pelitic samples described above, and these reactions have previously been constrained in P-T space using petrogenetic grids (e.g. Spear *et al*., 1999). These grids may be used to estimate the P-T conditions and P-T paths of the samples.

Petrographic evidence suggests that sillimanite (or andalusite) was consumed, in most cases to produce cordierite and garnet, and the reaction

sillimanite + biotite + quartz = cordierite + garnet + K-feldspar + melt

has been suggested. This reaction is fluid-absent, although the similar fluid-present melting reaction

sillimanite + biotite + quartz + H_2O = cordierite + garnet + melt

has been suggested by Ward *et al*. (2008). However, textural evidence indicates that cordierite growth preceded garnet growth, and thus the reaction

sillimanite + biotite + quartz = cordierite + K-feldspar + melt

is more likely to have occurred earlier in the thermal history. The growth of cordierite in preference to garnet early in the P-T history may indicate that low-pressure conditions were experienced. Indeed, in sample LHA008, andalusite relicts are preserved in the cores of cordierite porphyroblasts, indicating that the rocks passed through the andalusite field before reaching peak conditions in the sillimanite field, and did not reach pressures required for kyanite stability. The lack of preserved kyanite implies that peak pressures in the Central Zone were not particularly high (the aluminosilicate triple point is between 3.5 and 5.5 kbar and between 500 and 650 ˚C. (Richardson *et al*., 1969; Holdaway, 1971). Cordierite growth was followed by garnet growth, which occurred later in the thermal history. Garnet is locally seen to contain inclusions of cordierite, indicating that garnet may have grown at the expense of cordierite, possibly via a continuous melting reaction such as

cordierite + biotite = garnet + K-feldspar + melt (Spear *et al*., 1999),

rather than via a retrograde reaction such as

cordierite = garnet + sillimanite + quartz (Thomson, 2001),

as sillimanite generally does not appear late in the thermal history, and no textural evidence exists to indicate that garnet growth is retrograde. Locally developed orthopyroxene

indicates that temperatures in excess of 800 ˚C (Vielzeuf & Montel, 1994) may have been reached in the Central Zone, higher than previous estimates. A petrogenetic grid (Fig. 6.18A) illustrates that the reaction

sillimanite + biotite + quartz = cordierite + garnet + K-feldspar + melt

occurs at temperatures *ca*. 700-720 ˚C (at 3-4 kbar) and that orthopyroxene begins to form at temperatures *ca*. 770-800 ˚C (at 3-4 kbar). A clockwise P-T path has been suggested for the Central Zone (e.g. Nex *et al*., 2001a), and on the prograde path (Fig. 6.18A), this would result in the formation of sillimanite or andalusite through the reaction:

muscovite + albite + quartz = sillimanite/andalusite + K-feldspar + melt.

Whether sillimanite or andalusite is produced depends on the pressure at which this reaction occurs (Fig. 6.18A). In sample LHA008, muscovite and biotite are preserved together with andalusite in the cores of cordierite porphyroblasts, indicating that andalusite (rather than sillimanite) was produced, and suggesting that the reaction

muscovite + biotite + albite + quartz = andalusite + K-feldspar + melt

took place, and indicating that prograde heating may have occurred at low pressures (*ca*. 2-3 kbar). However, sillimanite is present in all other samples, indicating that pressures of at *ca*. 4 kbar must have been reached during prograde heating. Further evidence for generally low pressures is illustrated by the fact that that the reaction

biotite + sillimanite + quartz = spinel + cordierite + K-feldspar + melt

is likely to have occurred on the prograde path at conditions of *ca*. 720 ˚C and 3 kbar (Fig. 6.18B).

The local development of orthopyroxene suggests temperatures in excess of 800 ˚C

(Vielzeuf & Montel, 1994), but at low pressures, the grid of Spear *et al*. (1999) indicates that orthopyroxene growth may begin at temperatures as low as 750 ˚C (at 2 kbar – Fig. 6.18A). The fact that orthopyroxene is only locally developed further suggests that temperatures did not significantly exceed 800 ˚C.

The petrogenetic grids suggest that conditions of up to 800 ˚C and 4 kbar may have been reached in the Central Zone, slightly exceeding previous temperature estimates (Buhn *et al*., 1995; Nex *et al*., 2001a; Ward *et al*., 2008), but confirming the clockwise P-T paths, and low pressures (3-5 kbar) for the thermal peak suggested by previous workers (e.g. Nash, 1971; Buhn, 1995; Nex *et al*., 2001a). However, since the formation of the assemblages from which these inferences were made are demonstrably influenced by the bulk rock composition of the samples (see section 6.6.10), it is necessary to evaluate each sample individually, and to examine possible reactions and assemblages based on a specific bulk composition for each sample, using qualitative petrogenetic grids constructed with the program THERMOCALC (Powell & Holland, 1988). The results of conventional thermobarometry are first described, so that they may be compared to P-T estimates from qualitative petrogenetic grids, and for comparison with other previous P-T estimates made using similar methods.

Fig. 6.18 (following page) – Petrogenetic grids and possible P-T paths. A: NCKFMASH grid after Spear et al*. (1999) with a low-pressure clockwise P-T path shown, illustrating that the reaction muscovite + albite + quartz = aluminosilicate + K-feldspar + melt would occur in either the sillimanite or andalusite fields, resulting in sillimanite or andalusite growth, (depending on pressure) followed by consumption of sillimanite and biotite via the reaction sillimanite + biotite + quartz = cordierite + garnet + K-feldspar + melt, and growth of orthopyroxene at 770-800 ˚C. B: Grid after Jung* et al*. (1998), with a similar clockwise P-T path shown, illustrating that such a path would result in the reaction biotite + sillimanite (or metastable andalusite) + quartz = spinel + cordierite + K-feldspar + melt.*

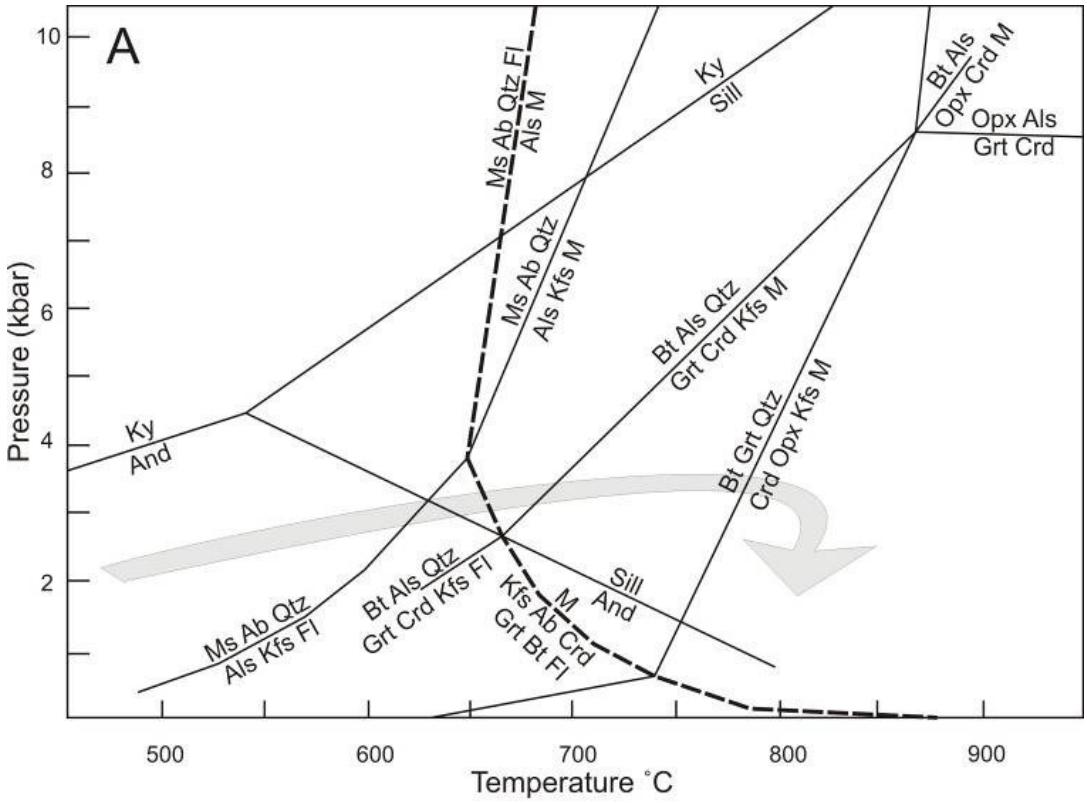
A
Pressure (kbar)
Temperature ˚C
10
8
6
4
2
500
600
700
800
900
Ky
Sill
Ms Ab Qtz Fl
Als M
Bt Als
Opx Crd M
Opx Als
Grt Crd
Ms Ab Qtz
Als Kfs M
Bt Als Qtz
Grt Crd Kfs M
Bt Grt Qtz
Crd Opx Kfs M
Ky
And
Sill
And
Ms Ab Qtz
Als Kfs Fl
Bt Als Qtz
Grt Crd Kfs Fl
Kfs Ab Crd
Grt Bt Fl
M

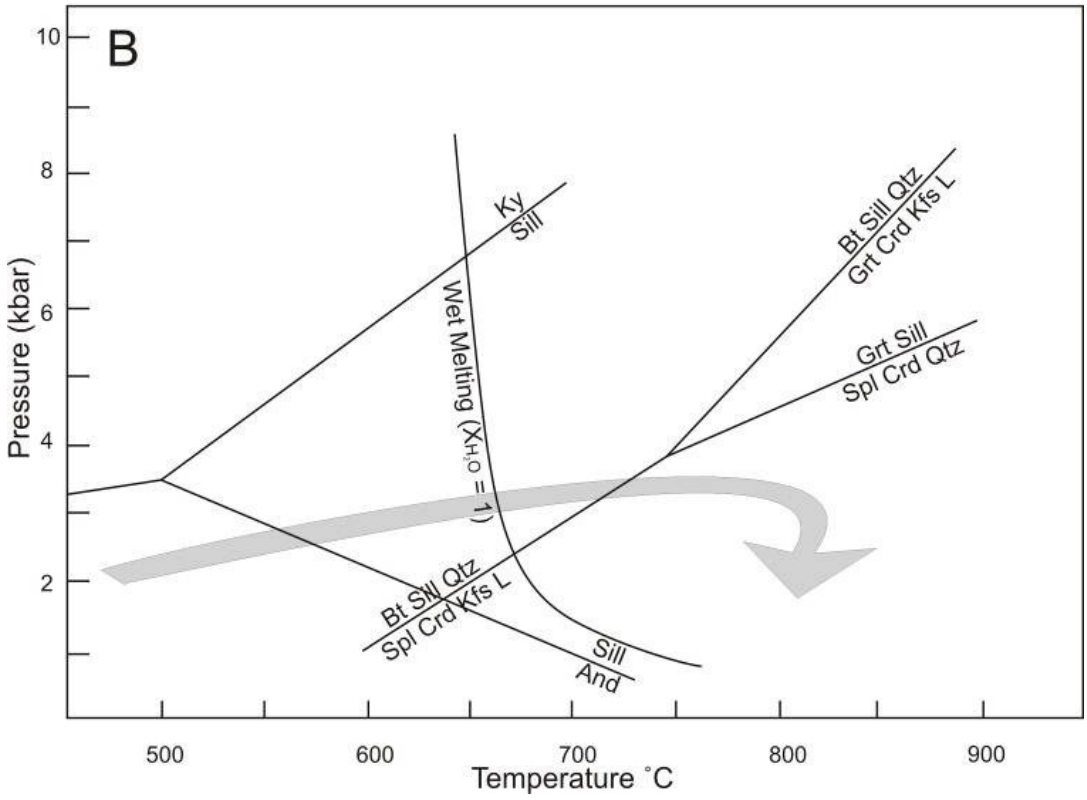
B
Pressure (kbar)
Temperature ˚C
10
8
6
4
2
500
600
700
800
900
Ky
Sill
Wet Melting (X_{H_2O} = 1)
Bt Sill Qtz
Grt Crd Kfs L
Grt Sill
Spl Crd Qtz
Bt Sill Qtz
Spl Crd Kfs L
Sill
And

6.8. Cation exchange thermometry

A number of samples contain assemblages with garnet + biotite, making them suitable for cation exchange thermometry. A variety of garnet-biotite cation exchange thermometers have been published and a number of these are used. Although more recent discussions of these calibrations exist (e.g. Kleemann & Reinhardt, 1994; Holdaway *et al*., 1997; Gessmann *et al*., 1997), the calibrations used here are those used by previous workers in the Central Zone (e.g. Poli, 1997; Nex *et al*., 2001a), and are thus useful for comparison with both previous work and with phase equilibria modeling. Here the following thermometers are used:

- Ferry & Spear (1978)

$T\ (^{\circ}C) = \mathbf{(}2089 + 9.56P\mathbf{/}0.782 - \ln K_D\mathbf{)} - 273$

Where $K_D = [Fe/Mg^{(biotite)}]/[Fe/Mg^{(garnet)}]$

- Perchuk & Lavrent'eva (1983)

$T\ (^{\circ}C) = \mathbf{(}7843.7+[\Delta V^{*}\{6-P\}]\mathbf{)/(}[1.987^{*}\ln(K_D)]+5.699\mathbf{)}-273$

Where $K_D = [Fe/Mg^{(garnet)}]/[Fe/Mg^{(biotite)}]$

- Dasgupta *et al.* (1991)

$T\ (^{\circ}C) = \mathbf{(}[4301 + 3000(X_{Ca})^{gt} + 1300(X_{Mn})^{gt} - 495(X_{Mg} - X_{Fe})^{gt} - 3595(X_{Al[VI]})^{bi} - 4423\ (X_{Ti})^{bi} + 1073(X_{Mg} - X_{Fe})^{bi} + 0.0246P]\mathbf{/}[1.85 - R\ln K_D]\mathbf{)} - 273$

Where $K_D = [Fe/Mg^{(garnet)}]/[Fe/Mg^{(biotite)}]$ and $R = 1.987207$ cal/(mol.K)

For garnet:

$X_{Ca} = Ca/(Ca + Fe^{2+} + Mg + Mn)$

$X_{Mn} = Mn/(Ca + Fe^{2+} + Mg + Mn)$

$X_{Mg} = Mg/(Ca + Fe^{2+} + Mg + Mn)$

$X_{Fe} = Fe/(Ca + Fe^{2+} + Mg + Mn)$

For biotite

$X_{Mg} = Mg/(Fe + Mg + Ti + Al^{VI})$

$X_{Fe} = Fe/(Fe + Mg + Ti + Al^{VI})$

$X_{Ti} = Ti/(Fe + Mg + Ti + Al^{VI})$

$X_{Al[VI]} = \sum Al - (Si + Al^{VI})$ where Si + Al[VI] = 3 per formula unit

- Bhattacharya *et al*. (1992)

$T\ (^{\circ}C) = \big([20286 + 0.0193P - \{2080(X^{gt}_{Mg})^2 - 6350(X^{gt}_{Fe})^2 - 13807(X^{gt}_{Ca})(1 - X^{gt}_{Mn}) + 8540(X^{gt}_{Fe})(X^{gt}_{Mg})(1 - X^{gt}_{Mn}) + 4215(X^{gt}_{Ca})(X^{gt}_{Mg} - X^{gt}_{Fe})\} + 4441(2X^{bt}_{Mg} - 1)]/[13.138 + 8.3143 Ln K_D + 6.276(X^{gt}_{Ca})(1-X^{gt}_{Mn})]\big) - 273$

Using the almandine-pyrope mixing parameters of Hackler & Wood (1984), and where $K_D = [Fe/Mg^{(garnet)}]/[Fe/Mg^{(biotite)}]$

and where:

$X^{gt}_{Ca} = Ca/(Ca + Fe^{2+} + Mg + Mn)$

$X^{gt}_{Mn} = Mn/(Ca + Fe^{2+} + Mg + Mn)$

$X^{gt}_{Mg} = Mg/(Ca + Fe^{2+} + Mg + Mn)$

$X^{gt}_{Fe} = Fe/(Ca + Fe^{2+} + Mg + Mn)$

$X^{bt}_{Mg} = Mg/(Fe + Mg + Ti + Al^{VI})$

The equation of Ferry & Spear (1978) assumes that garnets are simple binary mixtures of pyrope and almandine, although K_D is a function of the Ca and Mn contents of garnet, and the Ti and Al^{VI} contents of biotite. The equation is suggested by Ferry & Spear (1978) to be applicable to rocks where garnets have (Ca + Mn)/(Ca + Mn + Fe + Mg) ≤ 0.2 and biotites have $(Al^{VI} + Ti)/(Al^{VI} + Ti + Fe + Mg) \leq 0.15$. Almost all garnets analysed have (Ca + Mn)/(Ca + Mn + Fe + Mg) less than 0.2, with the exception of analyses 5.8-5.15 on sample LID039 and the small garnet grain (Grt-1) found in LHA006 (see data in Appendix 3C). However, biotites analysed are all fairly titaniferous, with $(Al^{VI} + Ti)/(Al^{VI} + Ti + Fe + Mg)$ exceeding 0.15 in almost all cases (see Appendix 3B).

The equation of Perchuk & Lavrent'eva (1983) is also based purely on Fe-Mg exchange between garnet and biotite, and ignores the effects of Ca and Mn. Both Ca and Mn in garnet

as well as Ti and Al^{VI} in biotite have been included in the equations of Dasgupta *et al*. (1991) and Bhattacharya *et al*. (1992), and these expressions may be expected to give more accurate results, particularly in samples with elevated levels of Ti in biotite. Since profiles across garnet grains suggest that garnet compositions are uniform (Fig. 6.8), and biotites appear to be of fairly uniform composition within individual samples (Fig. 6.9), averages of garnet grains and biotite grains have been used for these calculations. In the rare case where a zoned garnet has been found (LID039 grain 5 – Fig. 6.8AB), the core of the garnet has been treated separately from the rim of the garnet. Some biotite grains included in garnet or cordierite have compositions that differ from matrix biotite, and temperatures calculated from these grains are discussed below.

A histogram of temperatures obtained using the various methods (Fig. 6.19) shows that the calibration of Ferry & Spear (1978) gives higher temperatures than other calibrations, with a number of garnet-biotite pairs giving temperatures over 800 ˚C, with an average temperature of 756 ± 70 ˚C (9.26 % standard deviation). However, this calibration also gives a wide spread of data, and does not show a typical Gaussian distribution curve. The calibrations of Perchuk & Lavrent'eva (1983) and Bhattacharya *et al*. (1992) give the best Gaussian distributions, with the highest frequency temperatures calculated between 650 ˚C and 700 ˚C (at 4 kbar). The calibration of Perchuk & Lavrent'eva gives 670 ± 32 ˚C (4.78 % standard deviation) and that of Bhattacharya *et al*. (1992) gives 651 ± 34 ˚C (5.22 % standard deviation). The calibration of Dasgupta *et al*. (1991) incorporates the effects of Mn and Ca in garnet and Ti and Al^{VI} in biotite, and does not show a Gaussian distribution, but rather shows peaks at 620-640 ˚C, at 680-700 ˚C and at 740-760 ˚C (Fig. 6.19), with an average of 668 ± 69 ˚C (10.33 % standard deviation). This may reflect the preservation of a more complex thermal history than indicated by the Gaussian distributions of the Perchuk & Lavrent'eva (1983) and Bhattacharya *et al*. (1992) calibrations. Additionally, this simple histogram comparison assumes a single temperature and pressure across the entire study area. This assumption is evaluated in more detail later in this chapter.

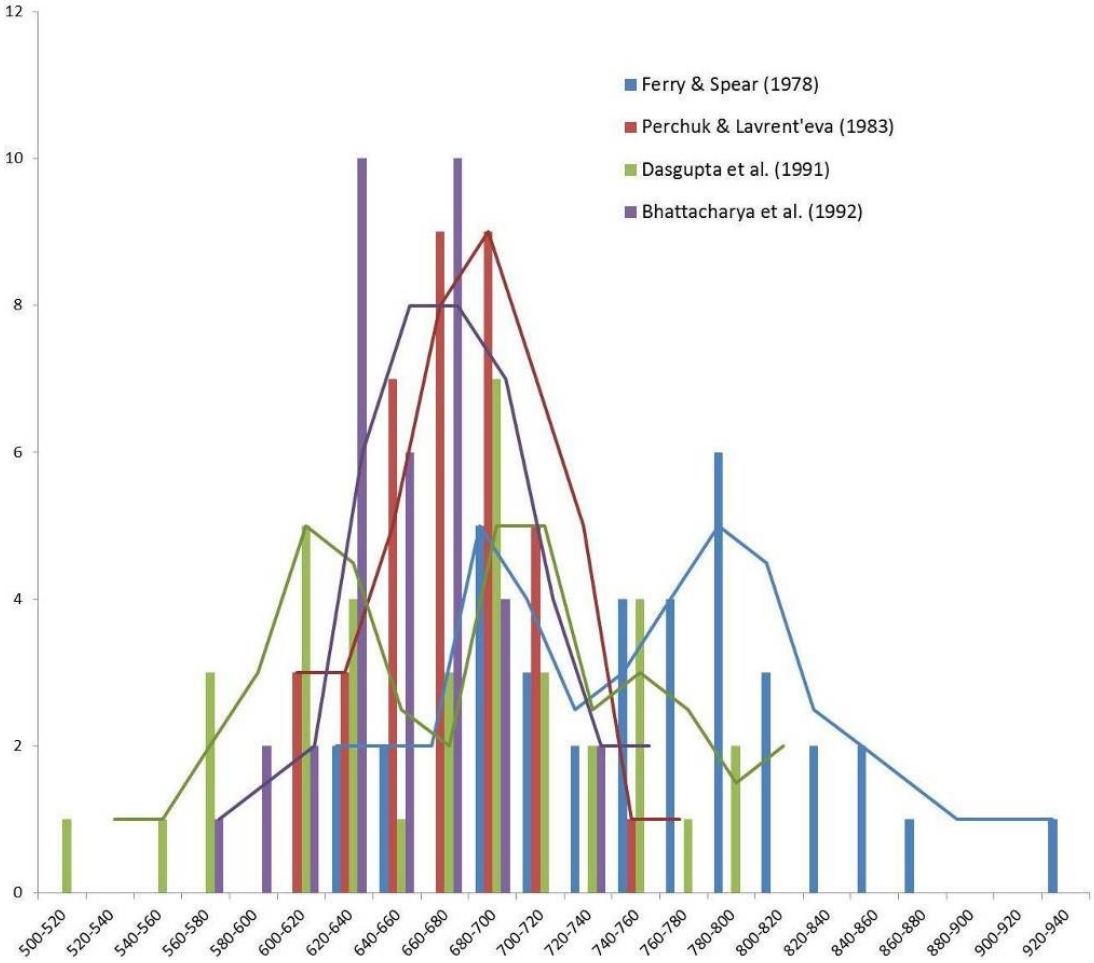

Figure 6.19 – Histogram showing the frequency of temperatures calculated using the calibrations of Ferry & Spear (1978), Perchuk & Lavrent'eva (1983), Dasgupta et al*. (1991) and Bhattacharya* et al*. (1992) at 4 kbar. Data are presented in Appendix 4a.*

However, although most garnet profiles show uniform compositions, LID039 grain 5 shows a typical prograde zoning profile (Fig. 6.8AB) and, thus, core temperatures may differ from rim compositions in this sample. Additionally, a number of biotite inclusions within garnet and cordierite have compositions which differ from matrix biotites (Fig. 6.9). When a comparison is made between temperatures calculated from included biotite versus matrix biotite (Table 6.5), it is clear that the temperatures calculated from biotite inclusions are consistently lower than the temperatures calculated from matrix biotites (Fig. 6.20), regardless of the calibration used.

Table 6.5 – Comparison of temperatures obtained through various calibrations for included biotite and matrix biotite. Individual grains analysed are labelled. Data are presented in Appendices 3B and 3C.

SAMPLE	CALIBRATION	GRAINS ANALYSED AND CALCULATED TEMPERATURE		GRAINS ANALYSED AND CALCULATED TEMPERATURE					
		Included Biotite		Matrix Biotite					
LCZ11-1b		Grains 5 & 6		Grains 1 & 3	Grains 7 & 8				Average
	Ferry & Spear (1978)	725.99		864.01	923.89				893.95
	Perchuk & Lavrent'eva (1983)	657.55		718.33	742.35				730.34
	Dasgupta *et al* (1991)	672.72		749.41	787.53				768.47
	Bhattacharya *et al* (1992)	632.16		694.88	722.82				708.85
LID039		Grains 5 (core) & 8		Grains 1 & 2	Grains 3 & 4	Grains 5 (rim) & 6			
	Ferry & Spear (1978)	652.57		713.87	765.83	742.34			740.68
	Perchuk & Lavrent'eva (1983)	621.70		651.81	675.93	665.18			664.31
	Dasgupta *et al* (1991)	755.42		735.86	744.46	763.47			747.93
	Bhattacharya *et al* (1992)	629.56		639.18	656.39	654.66			650.08
CZRL20x		Grains 5 & 7		Grains 1 & 2	Grains 3 & 4				
	Ferry & Spear (1978)	696.45		683.81	835.04				759.42
	Perchuk & Lavrent'eva (1983)	643.44		637.28	706.22				671.75
	Dasgupta *et al* (1991)	564.02		516.22	647.92				582.07
	Bhattacharya *et al* (1992)	621.99		608.26	690.26				649.26
LID042		Grains 4 & 5		Grains 1 & 2	Grains 2 & 4	Grains 6 & 8	Grains 6 & 10	Grains 6 & 12	
	Ferry & Spear (1978)	682.77		633.30	789.45	749.43	762.20	751.39	733.60
	Perchuk & Lavrent'eva (1983)	636.76		611.84	686.50	668.45	674.28	669.35	660.27
	Dasgupta *et al* (1991)	608.52		549.02	667.12	625.38	632.34	624.36	618.46
	Bhattacharya *et al* (1992)	616.36		589.55	667.79	647.93	653.84	648.26	639.78
LKR013		Grains 1 & 2	Grains 9 & 10	Grains 1 & 3	Grains 4 & 5	Grains 7 & 8	Grains 9 & 10	Grains 9& 11	
	Ferry & Spear (1978)	613.65	642.93	770.16	771.58	797.74	642.93	785.68	745.60
	Perchuk & Lavrent'eva (1983)	601.57	616.79	677.88	678.52	690.15	616.79	684.82	665.84
	Dasgupta *et al* (1991)	577.35	603.94	660.14	687.07	702.85	603.94	694.90	663.50
	Bhattacharya *et al* (1992)	526.54	590.44	652.58	653.53	666.18	590.44	661.59	640.68

Once again, the calibrations of Perchuk & Lavrent'eva (1983) and Bhattacharya *et al*. (1992) give results with smaller standard deviations than the calibrations of Ferry & Spear (1978) and Dasgupta *et al*. (1991). Lower temperatures obtained from included biotites suggest that these biotites grew on the prograde path, rather than at peak temperatures, and that peak temperatures may be best estimated from matrix biotites.

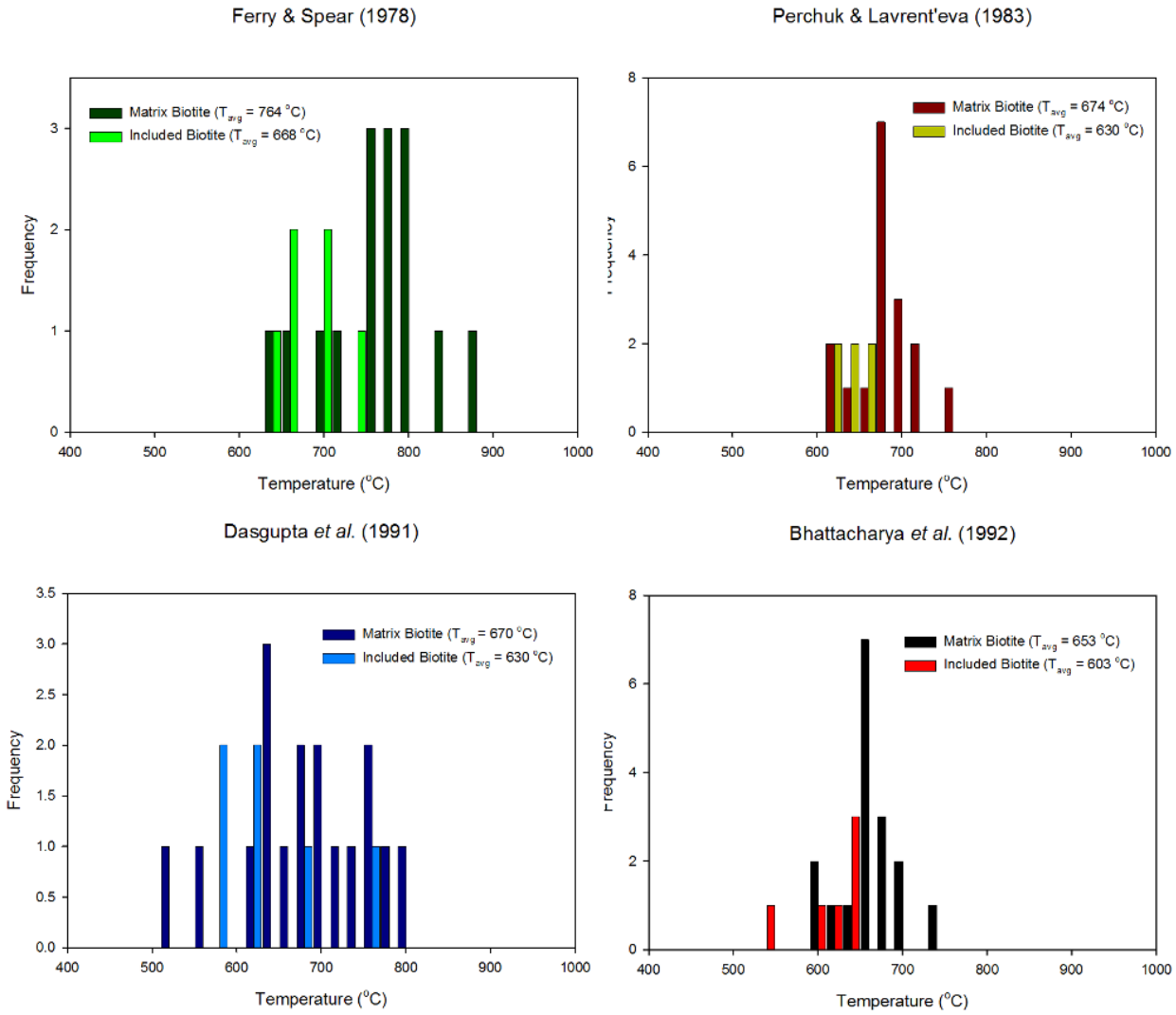

Fig. 6.20 – Histograms showing the differences in temperatures (at 4 kbar) calculated using biotite inclusions in garnet compared to matrix biotites, for four calibrations. Note that inclusion temperatures are consistently lower than matrix temperatures. Data are contained in Table 6.5.

The temperatures discussed above were all obtained at 4 kbar using the various calibrations (Fig. 6.19). The averages of these temperatures given above, which range from 651 ˚C (Bhattacharya *et al*., 1992) to 756 ˚C (Ferry & Spear, 1978), also include temperatures obtained from included biotites. Since it has been shown that biotite inclusions give temperatures on the prograde path, rather than peak temperatures (Fig. 6.20), temperatures obtained using included biotites should be disregarded when averaging peak

temperature estimates (i.e. excluding LCZ11-1b grains 5-6, LID039 grains 5(core)-8, CZRL20x grains 5-7, LID042 grains 4-5, and LKR013 grains 1-2 and 9-10). Furthermore, since only temperatures at 4 kbar have been considered, higher pressures should also be evaluated. Table 6.6 shows the average temperatures estimated for each sample for each calibration, at a range of pressures, in addition to the overall average temperature incorporating all samples. As seen previously (Fig. 6.19), the calibration of Ferry & Spear (1978) gives the highest average temperature estimates of 777-796 ˚C, close to the >800 ˚C temperatures suggested by the presence of orthopyroxene (although temperatures in excess of 900 ˚C have been calculated using this calibration). The other calibrations give significantly lower temperature estimates, with no average temperature estimates over 700 ˚C. On the basis of the phases present (including orthopyroxene) as well as on the basis of petrographic evidence for significant melting via the general reaction

sillimanite + biotite + quartz = cordierite + garnet + K-feldspar + melt

temperatures at the peak of metamorphism may have exceeded 800 ˚C, and the estimates from conventional thermobarometry may be underestimates. The flat garnet profiles (Fig. 6.8), indicating retrograde re-equilibration via cation diffusion, are further evidence that cation-exchange thermometers may not give the peak temperatures reached during metamorphism, and it appears possible that previous temperature estimates for the Central Zone of *ca*. 650-750 ˚C (Buhn *et al*., 1995; Poli, 1997; Nex *et al*., 2001a; Ward *et al*., 2008) may be underestimates. These previous estimates were obtained using a variety of techniques, including phase relationships, O-isotope thermometry (Buhn *et al*., 1995), and various computer programs based on cation exchange reactions (Poli, 1997; Nex *et al*., 2001a; Ward *et al*., 2008). Traditional cation exchange calculation used the same calibrations as used here (Ferry & Spear, 1978; Perchuk & Lavrent'eva, 1983; Bhattacharya *et al*., 1992; Dasgupta *et al*., 1992), in addition to some older calibrations (Thompson, 1976; Holdaway & Lee, 1977). Conditions estimated by conventional thermobarometry in this study are similar to those from previous studies, and are thus useful as a comparison with pseudosection modelling (see section 6.10).

Table 6.6 – Average temperatures for each sample for various calibrations, at a range of pressures from 2 to 6 kbar. The overall average of all samples is shown in bold type.

	LID004	LID039	LCZ11-1b	LKR012	LG003	CZRL20x	LID042	LKR013	CZRL19c	CZRL20a	Average	Std Dev
P (kbar)	T(˚C)	T(˚C)	T(˚C)	T(˚C)	T(˚C)	T(˚C)	T(˚C)	T(˚C)	T(˚C)	T(˚C)	T(˚C)	T(˚C)
Ferry & Spear (1978)												
2	715	732	883	845	820	750	728	786	757	757	**777**	55
3	720	736	889	850	825	755	733	791	762	762	**782**	56
4	724	741	894	855	830	759	737	795	766	766	**787**	56
5	729	745	899	860	835	764	742	800	771	771	**792**	56
6	733	750	904	865	840	769	746	805	776	776	**796**	56
Perchuk & Lavrent'eva (1983)												
2	650	658	724	708	698	666	656	682	669	669	**678**	24
3	653	661	727	712	701	669	659	685	672	672	**681**	25
4	656	664	730	715	704	672	662	688	675	675	**684**	25
5	659	667	734	718	707	675	665	691	678	678	**687**	25
6	662	670	737	721	710	678	668	694	681	681	**690**	25
Dasgupta et al. (1991)												
2	702	737	756	744	689	571	609	653	631	631	**672**	63
3	707	742	762	750	695	576	614	659	637	637	**678**	63
4	713	748	768	756	701	582	620	665	642	642	**684**	63
5	718	753	775	762	707	588	625	671	648	648	**689**	63
6	723	759	781	768	713	593	631	676	653	653	**695**	63
Bhattacharya et al. (1992)												
2	639	649	707	724	682	648	640	673	657	657	**668**	29
3	640	649	708	725	683	648	641	674	657	657	**668**	29
4	641	650	709	726	684	649	641	675	658	658	**669**	29
5	641	651	710	727	685	650	642	676	659	659	**670**	29
6	642	652	711	727	685	651	643	677	660	660	**671**	29

6.9 Average P-T calculations using THERMOCALC

The peak temperatures calculated using a variety of calibrations for the garnet-biotite thermometer at a number of pressures (Table 6.6 – generally between 650 ˚C and 800 ˚C) are similar to previous estimates, although the range of temperatures is large, and (with the exception of the calibration of Ferry & Spear, 1978) too low to explain the local presence of orthopyroxene in some samples. Using the average P-T function of the program THERMOCALC version 3.33 (Powell *et al.*, 1998), it is possible to use the compositions of both the garnet and biotite, in addition to other minerals analysed in the samples, to estimate peak P-T conditions. All calculations were carried out in the 'average P-T' mode of THERMOCALC, using the internally consistent dataset of Holland & Powell (1988) and subsequent updates. For these calculations, the compositions of garnet, biotite, cordierite,

amphibole, and orthopyroxene for each sample were calculated by averaging all the analyses for each mineral in each sample, since mineral compositions show little variation within individual samples, and profiles across minerals are flat (Figs. 6.8, 6.9, 6.10, 6.11, 6.13). However, where biotite inclusions in garnet or cordierite have different compositions from matrix biotites, these biotite inclusions were excluded from the average. Additionally, the core of the garnet in sample LID039 (grain 5) which showed prograde zoning, was also excluded from the garnet average for this sample. For feldspars, which show a range of compositions within an individual sample (Fig. 6.12), averages were only taken of feldspars with similar compositions. Using the averaged mineral compositional data, end-member activities were calculated using the program AX (Powell *et al*., 1998) at 4 kbar and 750 ˚C. Tables of the mineral compositions and corresponding end-member activities used for each sample can be found in Appendix 4b. Since temperatures of greater than 700 ˚C at 4-5 kbar were estimated by previous workers (Nex *et al*., 2001a; Ward *et al*., 2008), the rocks may be expected to lie above the albite + K-feldspar + quartz + H_2O = melt curve of Luth *et al*. (1964) and, thus, no water-rich free fluid would be present at the peak of metamorphism. Hence, average P-T calculations were carried out under fluid-absent conditions. Biotite incongruent melting at these temperatures is likely to buffer water activity at between 0.3 and 0.6 (Clemens & Watkins, 2001) and, hence, water activity is estimated at 0.5.

Table 6.7 – Results of average P-T calculations using THERMOCALC. P-T calculations were carried out assuming fluid-absent conditions, with water activity = 0.5. Compositional and AX data used are contained in Appendix 4b.

Sample	Temperature (˚C)	±	Pressure (kbar)	±
CZRL19 (garnet-cordierite-sillimanite schist)	674	74	4.2	1.2
CZRL20 (garnet-cordierite-sillimanite schist)	679	77	4.2	1.2
LG003 (garnet-cordierite-biotite schist)	681	50	5.8	0.7
LCZ11-1 (garnet-cordierite-biotite schist)	751	56	3.5	1.1
LID042 (garnet-cordierite-biotite schist)	729	56	4.6	1.0
LKR012 (garnet-cordierite-biotite schist)	813	57	5.3	1.2
LKR013 (garnet-cordierite-biotite schist)	802	58	4.5	1.2
LID039 (garnet-cordierite-biotite schist)	798	40	6.5	1.2
LID004 (garnet-cordierite-biotite schist)	787	41	5.2	1.2
LHA006 (cordierite-biotite schist)	673	53	4.4	0.9
LHA008 (cordierite-biotite schist)	685	97	4.6	1.2
LHA009 (cordierite-biotite schist)	664	61	3.8	1.0

When the results of the average P-T calculations are plotted and compared to qualitative petrogenetic grids (Fig. 6.21) it is clear that the majority of garnet-cordierite schists plot in the field garnet-cordierite-K-feldspar-melt, and two of these samples appear to lie on the reaction line for the reaction:

biotite + garnet + quartz = cordierite + orthopyroxene + K-feldspar + melt

However, no samples plot entirely within the orthopyroxene stability field, and the samples with the highest calculated temperatures are garnet-cordierite-biotite schists without orthopyroxene (LKR012 and LKR013 – Table 6.7), rather than LID004 or LID039, where orthopyroxene is noted (and can be seen consuming biotite and garnet). This suggests that orthopyroxene growth may be affected by the composition of the sample rather than simply the P-T conditions, and this is more carefully evaluated with phase equilibrium modelling below (section 6.10). Cordierite-biotite schists and garnet-cordierite-sillimanite schists plot at lower temperatures than garnet-biotite schists, but cordierite-biotite schists have calculated pressures that are higher than the pressures for the spinel stability field, despite the fact that spinel is observed as the product of a reaction consuming sillimanite and biotite (Fig. 6.5).

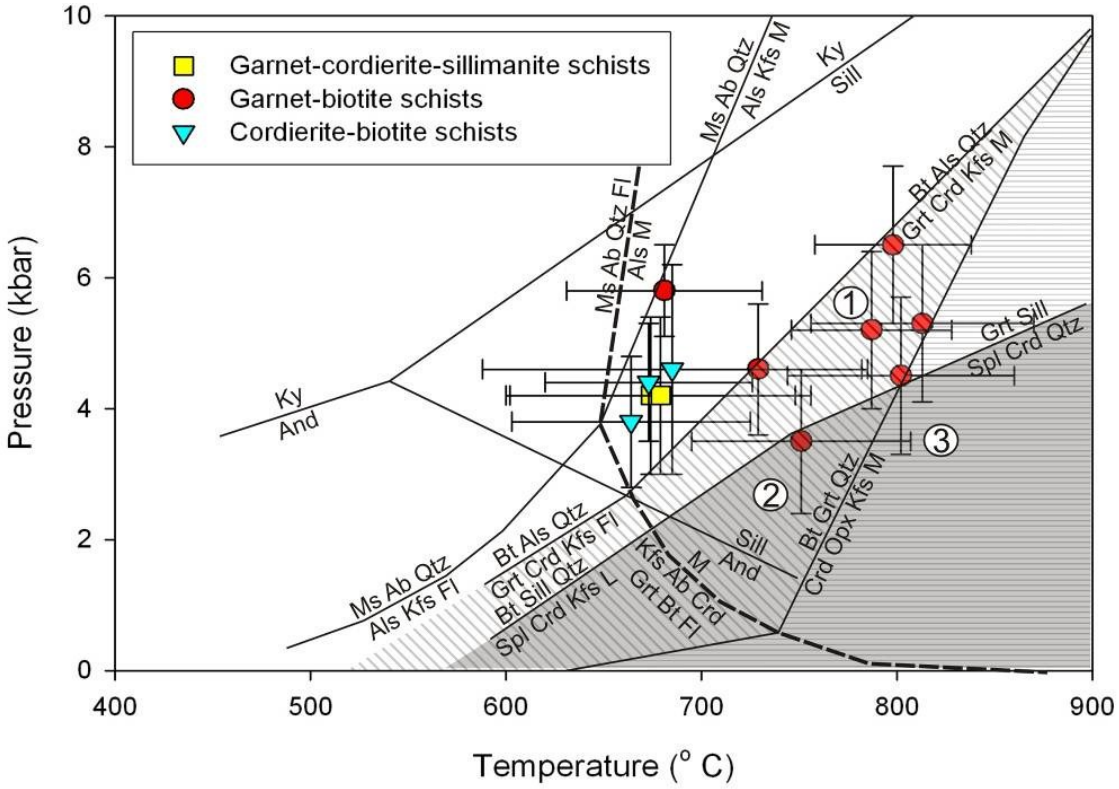

Fig. 6.21 – Results of average P-T calculations using THERMOCALC, plotted on a petrogenetic grid, modified after Spear et al*. (1999) and Jung* et al*. (1998). Shaded fields for 1: garnet + cordierite + K-feldspar + melt, 2: spinel + cordierite and 3: cordierite + orthopyroxene are shown. Note that cordierite-biotite schists and garnet-cordierite-sillimanite schists plot at lower grades than garnet-biotite schists.*

However, although sillimanite (or andalusite – sample LHA008) is present in the cordierite-biotite schists, it is only found in the cores of cordierite (± spinel) porphyroblasts. No sillimanite is found in the matrix of the samples, and it appears that sillimanite has been consumed via the reaction

biotite + sillimanite + quartz = spinel + cordierite + K-feldspar + melt

Thus, sillimanite (or andalusite) does not form part of the equilibrium assemblage in these samples, but is a relict phase. Initial average P-T calculations on cordierite-biotite schists (Table 6.7) included sillimanite in the assemblage (see Appendix 4b). If sillimanite is

excluded, and the calculations are repeated using identical conditions (fluid-absent, H_2O activity = 0.5, cordierite CO_2 activity = 0.1 and H_2O activity = 1), lower pressures and higher temperatures are calculated than the initial calculations with sillimanite (Table 6.8), although with large errors.

Table 6.8 – Results of average P-T calculations using THERMOCALC for cordierite-biotite schists, comparing calculations run with sillimanite or without sillimanite. P-T calculations were carried out assuming fluid-absent conditions, with water activity = 0.5. Compositional and AX data used are contained in Appendix 4b.

SAMPLE	Temperature (˚C)	±	Pressure (kbar)	±
LHA006	673	53	4.4	0.9
LHA008	685	97	4.6	1.6
LHA009	664	61	3.8	1
LHA006 (no sill)	693	77	3.8	1.6
LHA008 (no sill)	787	147	1.6	3.1
LHA009 (no sill)	715	79	2.3	1.7

It is apparent that excluding sillimanite from the calculations gives results that are consistent with the observation that spinel + cordierite is present in these samples, and the lower pressures (at higher temperatures) fall within the spinel stability field of Jung *et al*. (1998) (Fig. 6.22). The pressures predicted are lower than the 3.5-6.5 kbar estimated for garnet-biotite schists, but any explanation for this (i.e. a possible decompression path) is unclear. A possible decompression path (Path 1 – Fig. 6.22) from the conditions predicted for cordierite-biotite schists with sillimanite (*ca*. 670 ˚C and 4 kbar) to those within the spinel + cordierite stability field (*ca*. 750 ˚C and 2 kbar) would involve decompression with simultaneous heating. However, an alternative option (Path 2 – Fig. 6.22), is that cordierite-biotite schists with spinel-cordierite intergrowths were formed through isothermal decompression from the peak conditions recorded by garnet-biotite schists (*ca*. 790 ˚C and 5 kbar to *ca*. 750 ˚C and 2 kbar). However, such a decompression path would cross the reaction line

garnet + sillimanite = spinel + cordierite + quartz

rather than the reaction

biotite + sillimanite + quartz = spinel + cordierite + K-feldspar + melt

which is the reaction suggested here from textural evidence, and would not be compatible with the generally late growth of garnet.

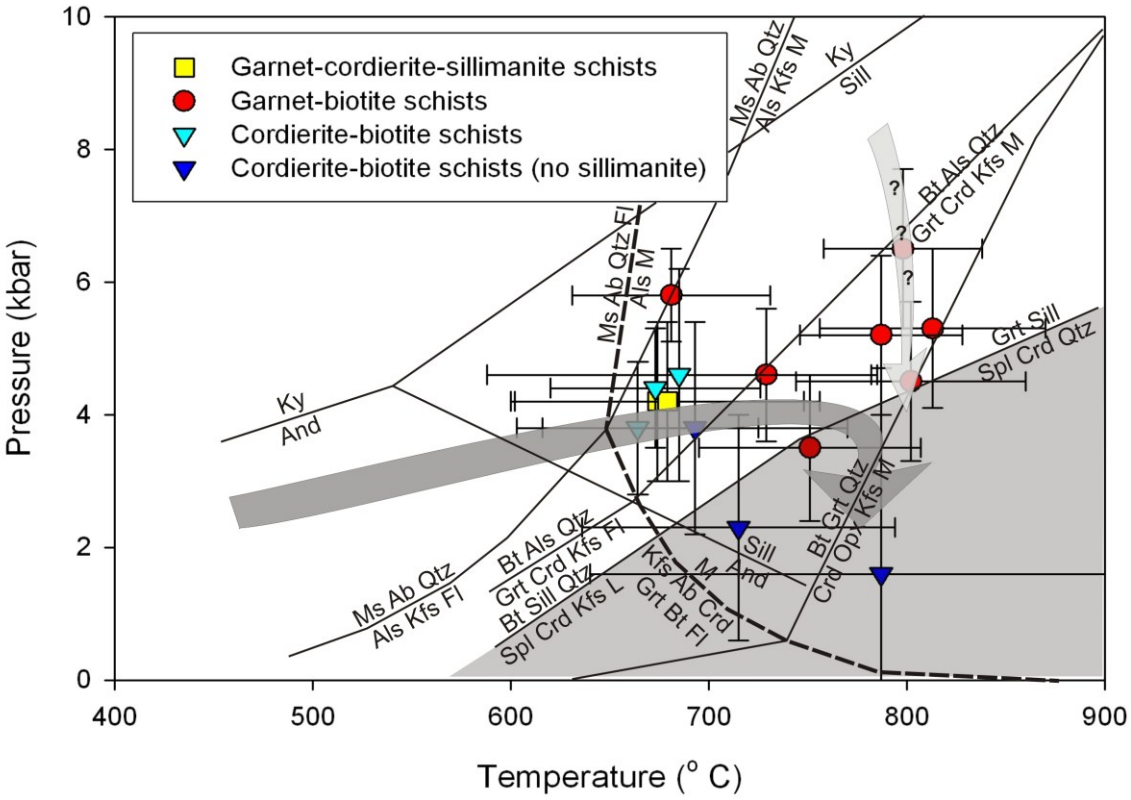

Fig. 6.22 – Results of average P-T calculations using THERMOCALC, plotted on a petrogenetic grid, modified after Spear et al*. (1999) and Jung* et al*. (1998). Shaded field indicates spinel + cordierite stability. Note that cordierite-biotite schists calculated without sillimanite plot at lower pressures and higher temperatures than those with sillimanite included in the calculations. Although a tentative decompression path may be applicable (indicated by faint arrow with question marks), the preservation of andalusite rather than kyanite suggests that a near-isobaric heating path with slight decompression at the thermal peak (darker arrow) could be more applicable. Both paths would cross the biotite + sillimanite + quartz = spinel + cordierite + K-feldspar + melt reaction line.*

The problem with inferring P-T paths from two groups of samples with different assemblages is that there is a compositional control on the different assemblages of the cordierite-biotite vs. garnet-biotite schists (see section 6.6.10). Additionally, although all samples have been assumed to have experienced similar P-T conditions, without any tectonic boundaries existing across the study area, this assumption has not yet been tested. In order to evaluate P-T paths more rigorously, quantitative petrogenetic grids (i.e. pseudosections) need to be constructed for individual bulk compositions. Such grids, constructed using THERMOCALC 3.33 (Powell *et al*., 1998), should allow both a more careful reconstruction of the P-T paths followed by each sample, as well as better constraints on the peak conditions reached, as quantitative grids for fixed bulk compositions eliminate the problems associated with diffusional re-equilibration of mineral compositions during cooling.

6.10 Pseudosection Modelling (Quantitative Petrogenetic Grids) using THERMOCALC

In order for conventional thermobarometry to be accurate, two assumptions must be correct – that the mineral assemblages preserved represent the equilibrium mineral assemblages for the part of the P-T path for which P-T conditions are being estimated (usually the peak conditions) and that the compositions of the minerals represent equilibrium compositions – i.e. the equilibrium compositions for a small part of the P-T path of the rock have been preserved. Additionally, it is typically assumed that this small part of the P-T path represents the peak conditions reached during metamorphism. The average P-T function of the program THERMOCALC (Powell & Holland, 1988; 2008) has advantages over conventional thermobarometry, in that it uses internally-consistent thermodynamic datasets and activity-composition relationships that can handle the multi-component phases and order-disorder relationships, rather than assuming simple binary end-member exchange (e.g. Ferry & Spear, 1978). However, the assumptions that equilibrium mineral assemblages and compositions are preserved, and that these represent peak conditions, must be true in order for the average P-T calculations to be accurate. Mineral compositional profiles (section 6.6) indicate that the rocks experienced diffusional re-equilibration on

cooling. Thus, the assumption that peak equilibrium compositions have been preserved is likely to be invalid for these samples. Secondly, the results of average P-T calculations differ according to sample type, with cordierite-biotite schists indicating significantly lower pressures than garnet-biotite schists. Although the results for average P-T calculations (section 6.9) suggest higher-grade conditions for the Central Zone (possibly up to 800 ˚C and 6 kbar) than conventional thermobarometry and previous estimates (which generally give conditions of less than 700 ˚C and pressures of *ca*. 4 kbar – Buhn *et al*., 1995; Poli, 1997; Nex *et al*., 2001a), many samples do give similar conditions to these previous estimates (e.g. Fig. 6.22). This raises the question of the P-T path – what part of this path has been preserved in each sample, and have all samples experienced similar P-T paths? The pseudosection approach of Powell & Holland (1988; 2008) involves forward modelling of mineral equilibria for a given rock composition to calculate a P-T phase diagram for that specific composition. Once such a diagram (pseudosection) has been constructed, it is possible to relate mineral assemblages, mineral proportions and mineral compositions to this diagram, thereby identifying areas in P-T space that correspond to the observed assemblages, and narrowing this field using mineral compositions and proportions, to arrive at a P-T estimate using far more information than conventional thermobarometry (Powell & Holland, 2008). In addition, pseudosections may be used to deduce a portion of the P-T path experienced by the rock, should prograde or retrograde phases (which are not part of the peak equilibrium assemblage) be preserved. For this study, pseudosections have been constructed for a number of samples, from all three sample types. Samples CZRL19 (garnet-sillimanite-cordierite schist), LID039, LKR013 (garnet-biotite schists) and LHA006 (cordierite-biotite schist) have been investigated. Initially, pseudosections were constructed in the system Na_2O-CaO-K_2O-FeO-MgO-Al_2O_3-SiO_2-H_2O (NCKFMASH), in order to obtain initial estimates on the phase relationships and approximate P-T conditions. Following this, pseudosections were constructed in the system Na_2O-CaO-K_2O-FeO-MgO-Al_2O_3-SiO_2-H_2O-TiO_2-fO_2 (NCKFMASHTO) to include the effects of TiO_2 and oxygen fugacity (fO_2) on the phase relationships. Finally the effects of possible melt-loss on peak assemblages (e.g. White & Powell, 2002) were investigated using the melt-reintegration procedure of White *et al*. (2004). Note that mineral abbreviations used in this section follow the convention of Powell & Holland (1988, 2008) and differ from those used previously (after Kretz, 1983). Mineral

abbreviations for section 6.10 are tabulated below. (Table 6.9)

Table 6.9 – Mineral abbreviations used for pseudosection modelling.

Symbol	Phase	Symbol	Phase	Symbol	Phase
H2O	water	sill	sillimanite	opx	orthopyroxene
mu	muscovite	ky	kyanite	sp	spinel
bi	biotite	pl	plagioclase	mt	magnetite
cd	cordierite	q	quartz	ilm	ilmenite
g	garnet	ksp	K-feldspar	liq	melt
and	andalusite	ged	gedrite		

6.10.1 Pseudosections in the system NCKFMASH

6.10.1.1 Sample CZRL19 (sillimanite-cordierite schist)

Sample CZRL19 has a highly aluminous composition relative to garnet-biotite schists and cordierite-biotite schists (section 6.6.9). The composition obtained by XRF (in wt% - Appendix 3) has been converted to mol. % (Fig. 6.23). Sample CZRL19 contains both garnet and cordierite, in addition to abundant sillimanite. Petrographic evidence (Fig. 6.7) suggests that the sample has melted and is, thus, above the solidus. When comparing the observed assemblage biotite-sillimanite-cordierite-garnet-quartz-K-feldspar-plagioclase with the P-T pseudosection (Fig. 6.23) it is clear that the sample must lie above the solidus, at pressures above the garnet-in line, but below the cordierite-out line. The presence of quartz appears to constrain temperatures to below the quartz-out line, and since the sample contains both plagioclase feldspar and K-feldspar, the narrow divariant field biotite-cordierite-garnet-sillimanite-plagioclase-quartz-K-feldspar-liquid appears appropriate, with temperatures between 720 ˚C and 770 ˚C, and pressures between 3.9 and 6.4 kbar. These are higher-grade conditions than the 670-680 ˚C and 4.2 kbar predicted from the average P-T calculations for this sample (Table 6.7). Petrographic evidence for the early growth of sillimanite is compatible with the ubiquitous presence of the aluminosilicates due to the highly aluminous nature of the sample.

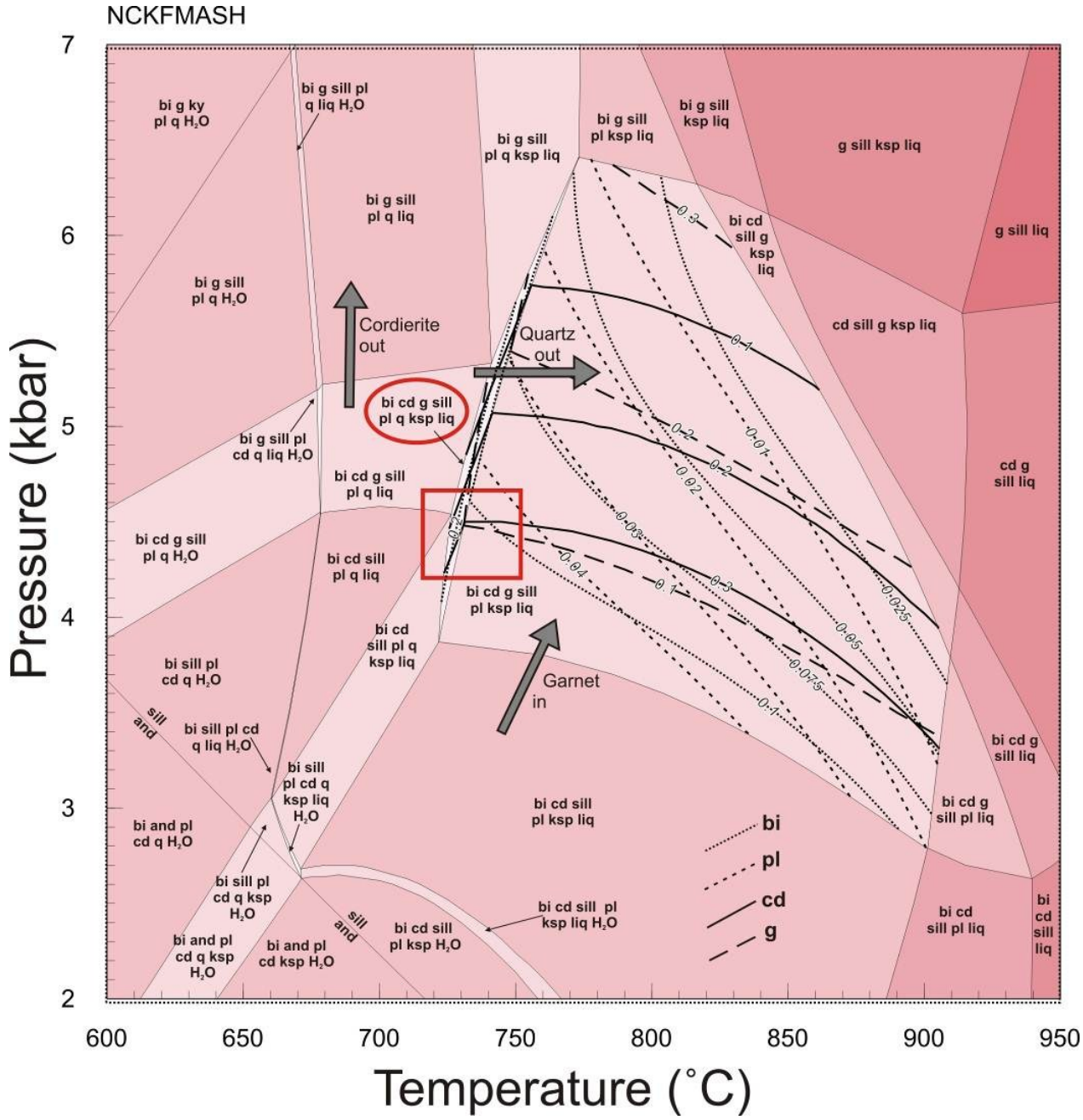

Fig. 6.23 – P-T pseudosection for sample CZRL19 in the system NCKFMASH. Note the field bi-cd-g-sill-pl-q-ksp-liq (circled in red), which initially appears to be the peak assemblage. Modal proportions confirm the peak assemblage, and the area shown by the red rectangle is likely to represent the peak conditions. See text for details. Composition used (mol. %):

H_2O	SiO_2	Al_2O_3	CaO	MgO	FeO	K_2O	Na_2O
5.56	53.24	22.48	0.61	4.34	9.54	2.25	0.98

However, although minor amounts of quartz are present, this quartz commonly has rounded inclusions of biotite and may form myrmekites, as well as occurring as thin films. This suggests that much (possibly all) quartz may represent crystallised melt, and that quartz may not in fact form a separate phase in the assemblage. However, when comparing the modal proportions of biotite, garnet, cordierite and plagioclase from point counting (Table 6.3) with the calculated modal proportions, the intersection of the 10% cordierite, 5% garnet, 4% plagioclase and 20% biotite isopleths (representing the observed modal proportions) does occur in the divariant field biotite-cordierite-garnet-sillimanite-plagioclase-quartz-K-feldspar-liquid, and further constrains P-T conditions to *ca*. 730 ˚C and 4.7 kbar (Fig. 6.23).

6.10.1.2 Sample LID039 (garnet-biotite schist)

Sample LID039 is one of two samples in which orthopyroxene was observed, clearly placing it in the granulite facies. Both garnet and cordierite are found in this sample. Cordierite is partially pinitised, and garnet locally contains small rounded inclusions of pinitised cordierite, indicating that cordierite growth preceded garnet growth. Although sillimanite is not present in the matrix of the sample, small needles of fibrolitic sillimanite are locally found as inclusions within cordierite, indicating that sillimanite was present at some stage on the P-T path. Garnet grains have inclusion-filled cores, which contain rounded quartz and biotite inclusions (in addition to pinitised cordierite), and inclusion-free rims. A single compositional profile (Fig. 6.8AB) indicates prograde growth zoning for a garnet from sample LID039. The strong D2 biotite fabric in this schist wraps garnet porphyroblasts, indicating that D2 deformation outlasted garnet growth. Both field and petrographic evidence indicates anatexis of the sample – the sample is a stromatic migmatite and thin bands of leucosome are aligned with the D2 fabric, and these contain plagioclase, K-feldspar and quartz. Microstructures confirm the presence of former melt, with a thin film of quartz present along grain boundaries, and quartz grains in the leucosome having cuspate grain boundaries. Since the sample clearly contains both orthopyroxene and biotite, temperatures are constrained between the orthopyroxene-in and biotite-out lines (Fig. 6.24). Additionally, the presence of both garnet and cordierite indicates that the sample

must lie at pressures above the garnet-in line and, thus, the sample lies in the narrow divariant field cordierite-garnet-K-feldspar-plagioclase-biotite-quartz-orthopyroxene-liquid (Fig. 6.24), constraining conditions to 770-820 ˚C and 4.2-7 kbar, in agreement with the average P-T calculation of 800 ˚C and 6.5 kbar.

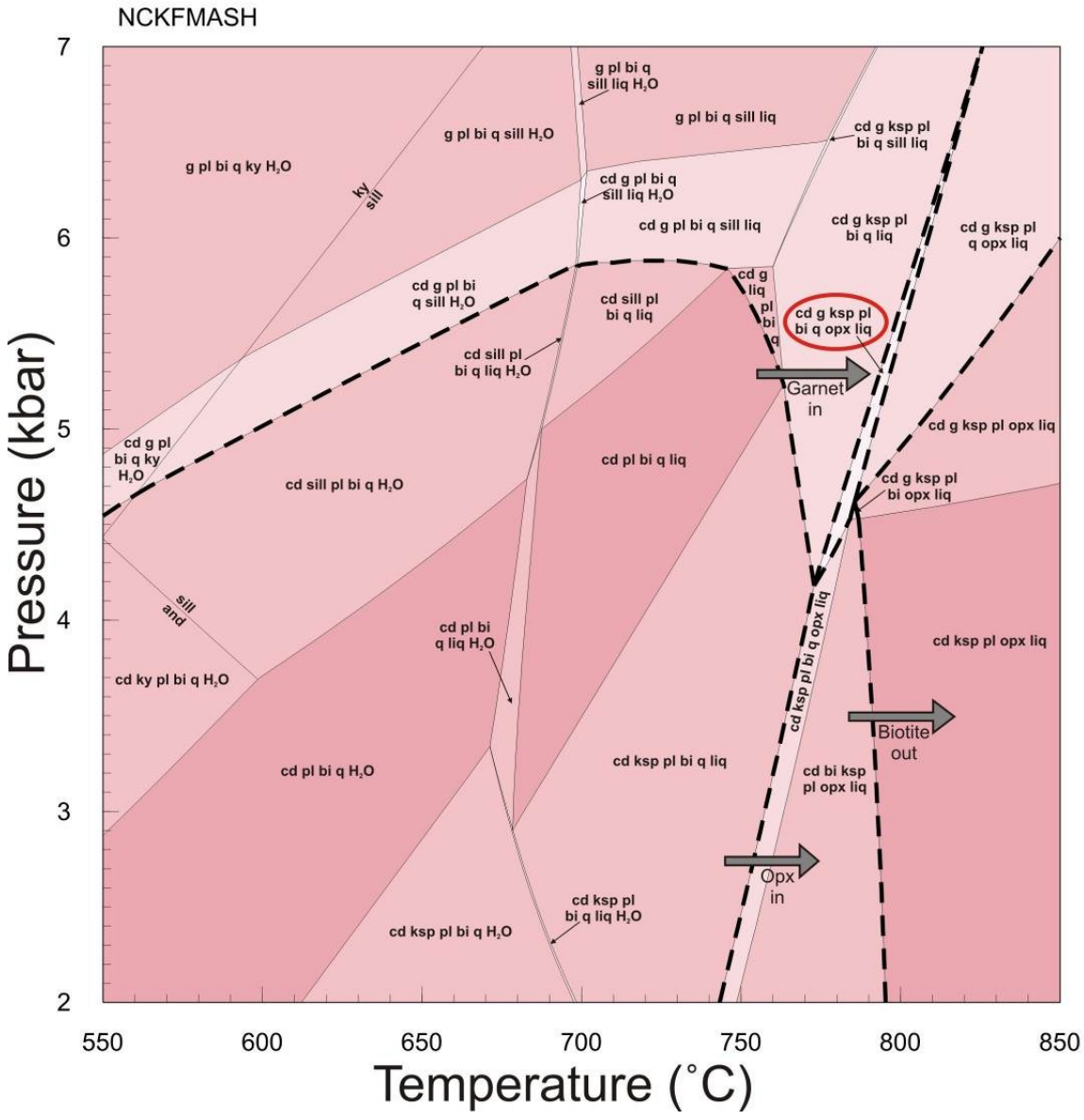

Fig. 6.24 – P-T pseudosection for sample LID039 in the system NCKFMASH. Note the field cd-g-ksp-pl-bi-q-opx-liq (circled in red), interpreted to be the peak assemblage. Composition used (mol. %):

H_2O	SiO_2	Al_2O_3	CaO	MgO	FeO	K_2O	Na_2O
5.94	60.78	12.13	2.94	6.71	7.38	2.45	1.66

However, using the modal proportions from point counting of the sample (garnet = 3%, plagioclase = 25%, cordierite = 16%, biotite = 25%; Table 6.3), together with calculated modal isopleths (Fig. 6.24) it is possible to further constrain the P-T conditions. These modal proportions give conditions of 770-780 ˚C and 4.4-4.6 kbar (Fig. 6.25), at the lower-grade end of this divariant field. Modal proportions of biotite should decrease to zero over a narrow temperature range with the growth of orthopyroxene (Fig. 6.25), and the large amounts of biotite remaining in the sample, together with the observation that only trace amounts of orthopyroxene are found, indicates that orthopyroxene was at the incipient stages of growth.

The local presence of fibrolitic sillimanite within cordierite porphyroblasts indicates that the rock must have contained sillimanite in the assemblage at some stage. Additionally, cordierite inclusions in garnet indicate that cordierite must have been present prior to garnet growth. Therefore, a clockwise P-T path is suggested, with the rock passing through the field cordierite-sillimanite-plagioclase-biotite-quartz-liquid. The lack of sillimanite inclusions in garnet suggests that all sillimanite was reacted out prior to garnet growth – i.e. the rock passed through the field cordierite-plagioclase-biotite-quartz-liquid prior to moving into the garnet stability field. Some near-isothermal decompression must have then taken place to reach the peak conditions recorded by the modal proportions in the assemblage. However, since this sample is migmatitic, it is likely to have experienced melt-loss, and the effects of this on the peak assemblages have not been accounted for. Melt re-integration will be addressed later (see section 6.10.2).

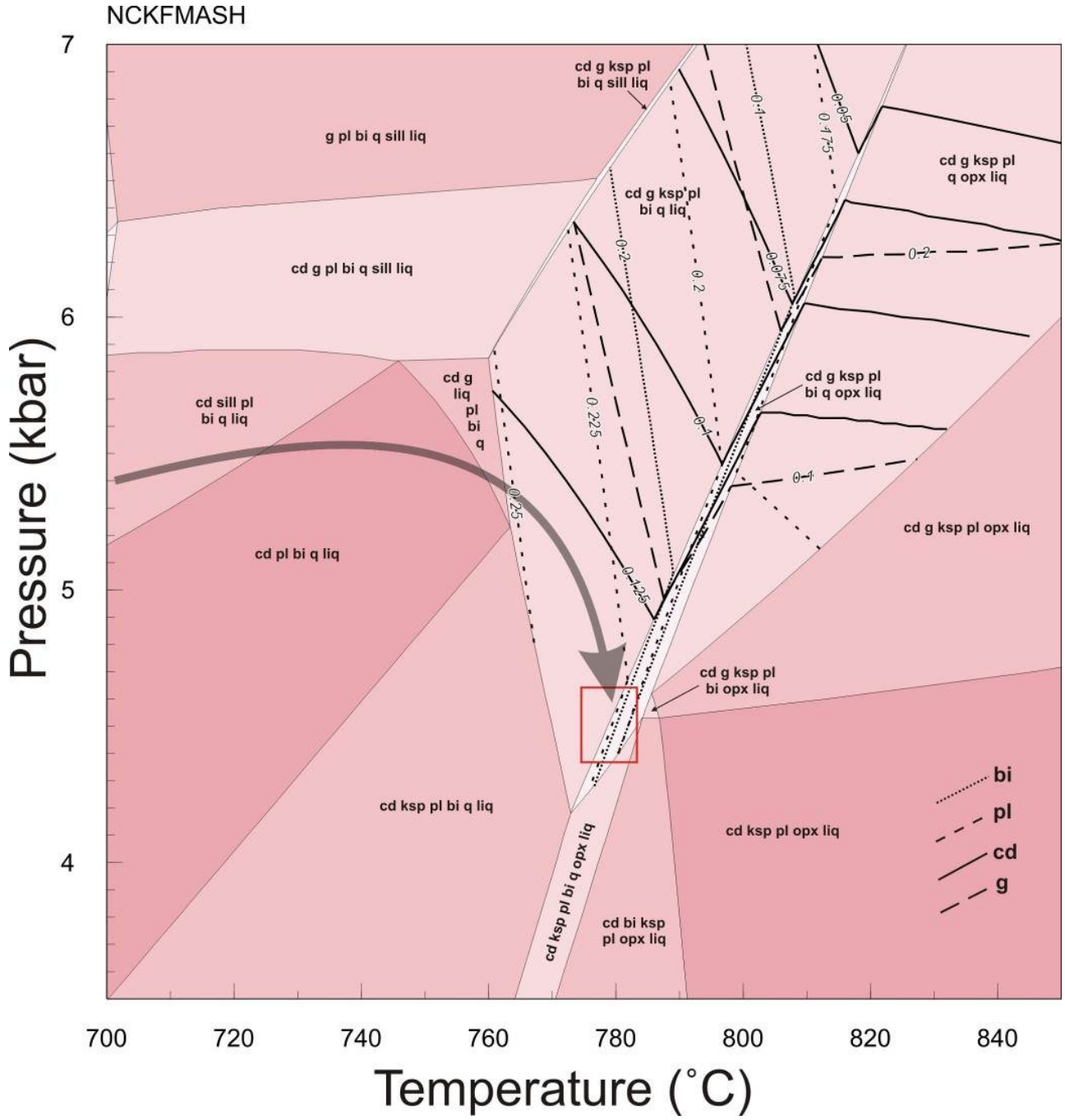

Fig. 6.25 – P-T pseudosection for sample LID039 in the system NCKFMASH, showing modal isopleths for garnet, cordierite, plagioclase and biotite. Note the red rectangle, where calculated modal proportions match those observed, and hence interpreted as the peak conditions. The likely P-T path is shown by the grey arrow (see text for details).

6.10.1.3 Sample LKR013 (garnet-biotite schist)

Although no orthopyroxene was found in LKR013, average P-T calculations gave conditions of 800 ˚C and 4.5 kbar (Table 6.7), and microtextures indicate that this sample has experienced partial melting – areas with larger quartz grains, which contain inclusions of rounded/corroded plagioclase feldspar and biotite, and smaller interstitial quartz crystals with cuspate edges are clues to the former presence of melt in this sample. However, the rock does not display a typical migmatitic appearance in hand sample, and the presence of leucosome exclusively along grain margins suggests that this sample may have experienced only incipient melting, without segregation of the melt. The rock is clearly above the liquidus, placing it in excess of 700 ˚C on the P-T pseudosection (Fig. 6.26). Throughout much of the pseudosection (Fig. 6.26), gedrite amphibole is modelled as a stable phase, which is likely to be due to the higher amounts of MgO (relative to Al_2O_3 and K_2O) in this sample compared to a 'typical metapelite'. The amount of MgO is too great to be incorporated into biotite, and must therefore be incorporated into gedrite amphibole at temperatures lower than those required for orthopyroxene stability. Both garnet and cordierite are present, along with quartz and plagioclase feldspar – no K-feldspar is observed. The absence of observed gedrite amphibole or orthopyroxene places this rock between the gedrite-in and orthopyroxene-in lines, in the field biotite-cordierite-garnet-plagioclase-quartz-liquid, with a fairly wide P-T range of 700-780 ˚C and 5.5-6.9 kbar, which are slightly lower temperatures and higher pressures than the 800 ˚C and 4.5 kbar calculated using the average P-T function of THERMOCALC. Modal proportions are addressed in the system NCKFMASH (section 6.10.2).

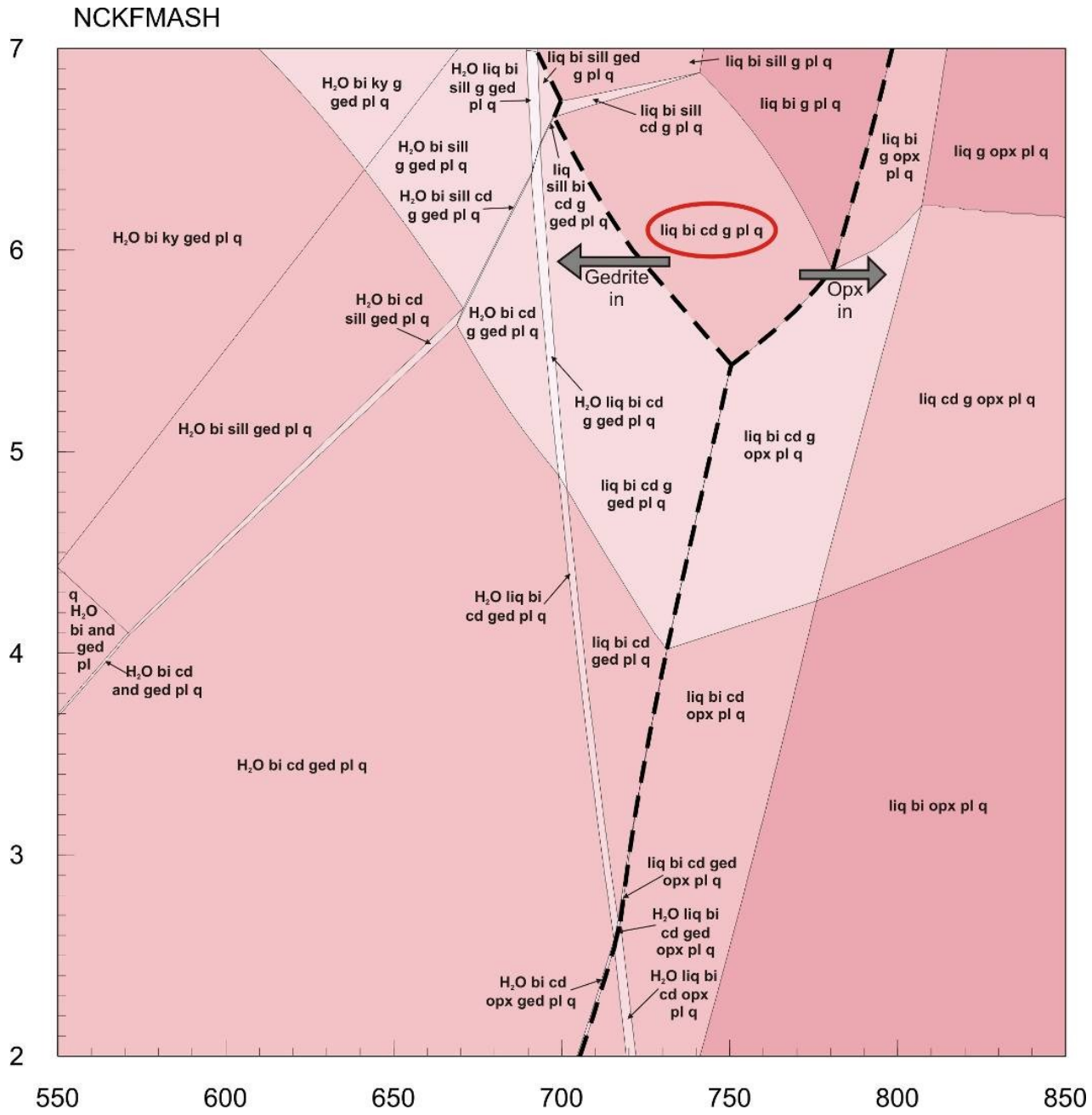

Fig. 6.26 – P-T pseudosection for sample LKR013 in the system NCKFMASH. Note the field liq-bi-cd-g-pl-q (circled in red), interpreted to be the peak assemblage, between the orthopyroxene-in and gedrite-in lines. See text for details.
Composition used (mol. %):

H_2O	SiO_2	Al_2O_3	CaO	MgO	FeO	K_2O	Na_2O
4.73	67.25	9.67	2.83	5.05	6.76	1.24	2.46

6.10.1.4 Sample LHA006 (cordierite-biotite schist)

This sample contains the assemblage cordierite-biotite-quartz-plagioclase-K-feldspar-ilmenite-magnetite in the groundmass, and a distinctive reaction texture of cordierite-spinel symplectites containing a core with fibrolitic sillimanite (± biotite), with no sillimanite present in the matrix. Large cordierite porphyroblasts contain symplectic intergrowths with spinel, and inclusions of sillimanite needles are also common in the cores of cordierite porphyroblasts. A single small garnet grain has been noted, and no orthopyroxene is found in LHA006. In the pseudeosection calculated in NCKFMASH for LHA006 (Fig. 6.27), spinel is only calculated as stable in a small field at low pressures (<4 kbar) and at temperatures in excess of 830 ˚C, and orthopyroxene is modelled as stable above 750 ˚C, despite no orthopyroxene being observed. Sillimanite and cordierite are modelled as essentially mutually exclusive, with a possible isobaric heating path at 4 kbar explaining the loss of sillimanite to produce cordierite, with maximum temperatures of *ca*. 840 ˚C reached in the spinel stability field (Fig. 6.27). Similarly, the assemblage spinel + quartz is unstable, consistent with observations that these two phases are never in contact. However, whilst there is a general agreement between petrographic observations and modelled phase equilibria, there are a number of inconsistencies, the most notable of which is the modelled presence of orthopyroxene. Additionally, whilst textures found in sample LHA006 indicate sillimanite consumption to produce spinel + cordierite, the pseudosection indicates a sillimanite-consuming, cordierite-producing reaction without spinel, which is not modelled as stable until quartz is consumed at temperatures above those required for orthopyroxene stability. Although there is a possibility that orthopyroxene may not have been observed in the thin sections prepared, the modelled modal proportions for orthopyroxene in the spinel stability field (>15%) suggest that this is unlikely. It therefore appears that the mineral stability fields calculated for this bulk composition appear somewhat inconsistent with petrographic observations.

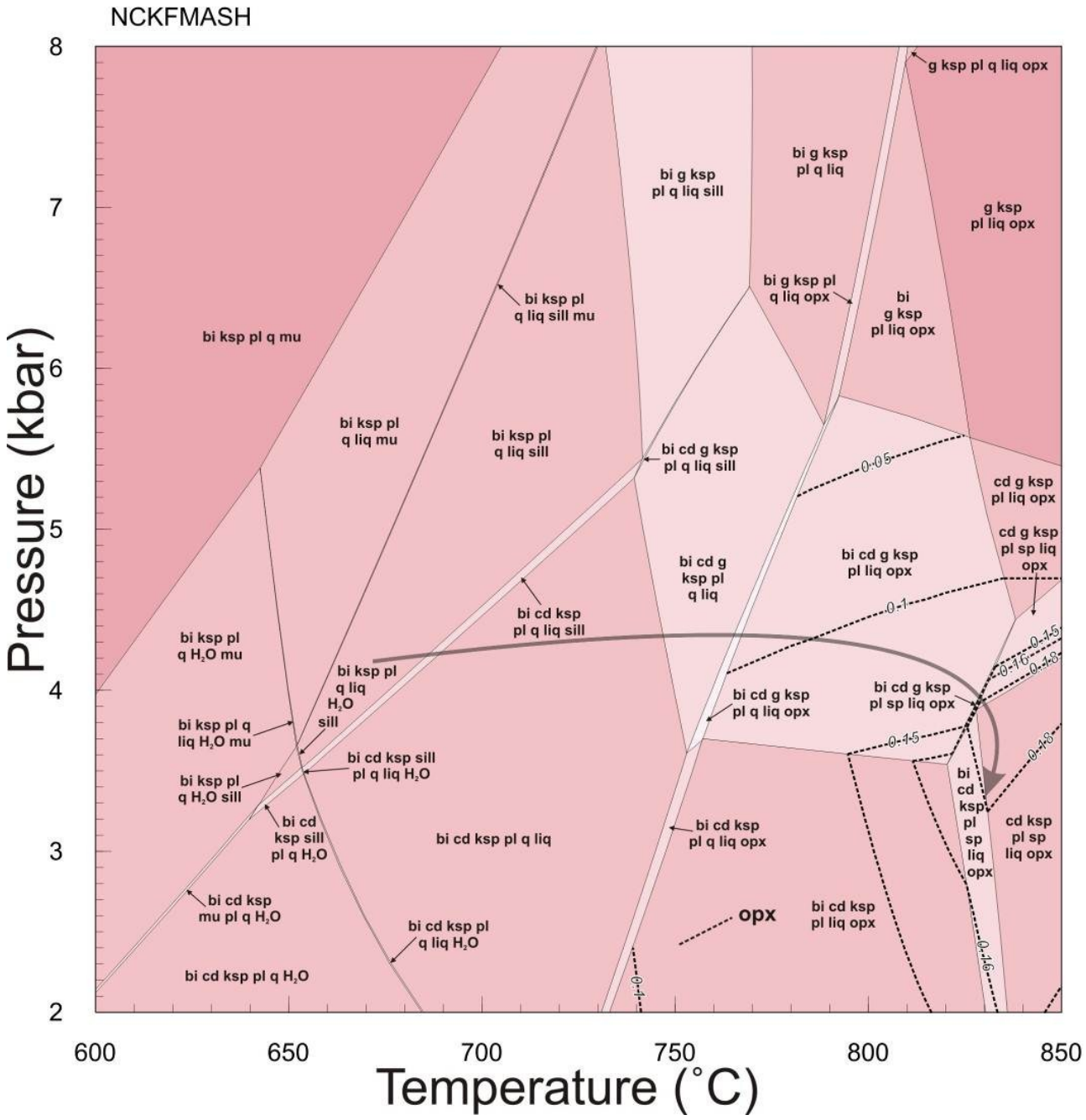

Fig. 6.27 – P-T pseudosection for sample LHA006 in the system NCKFMASH. A possible isobaric heating P-T path is shown by the grey arrow (see text for details). Composition used (mol. %):

H_2O	SiO_2	Al_2O_3	CaO	MgO	FeO	K_2O	Na_2O
6.50	63.98	12.00	1.48	4.98	7.88	3.66	3.13

The reason for this error may be that the equilibration volume is smaller than the volume analysed by XRF for the bulk rock composition. Indeed, the relict sillimanite in the cores of cordierite-spinel symplectites suggests probable domainal equilibrium. Additionally, since this rock is a migmatite, melt-loss may have affected the bulk composition of the sample, and this may represent a restitic composition – i.e. the restite:leucosome ratio observed may not reflect the ratio at the time of melting. Whilst the pseudosection in NCKFMASH does not address the effects of Zn on spinel stability (e.g. Johnson, 1998; Tajčmanová *et al*., 2009), spinel analyses (section 6.6.4) show that these spinels from LHA006 have very low Zn contents. Furthermore, the fact that spinel and quartz are observed to be mutually exclusive (i.e. spinel crystallised under silica-undersaturated conditions suggests that Zn did not play a significant role in stabilising spinel (Tajčmanová *et al*., 2009)).

A possible explanation for the inconsistency between pseudosection modelling and petrographic observations may be the isolation of Al_2SiO_5 in the cores of cordierite-spinel porphyroblasts. This isolation only occurred after cordierite growth. The presence of sillimanite solely within porphyroblasts means that this sillimanite is not 'seen' by the matrix of the sample – i.e., the effective Al_2SiO_5 content of the matrix is lower than the overall Al_2SiO_5 content obtained through XRF analysis of the entire sample (Fig. 6.28A). However, the isolation of Al_2SiO_5 within cordierite-spinel porphyroblasts also means that these porphyroblasts represent areas enriched in Al_2SiO_5 relative to the bulk composition obtained from XRF (Fig. 6.28B). It is also possible that localised increases in Al_2SiO_5 content during prograde metamorphism (caused by sillimanite porphyroblasts) set up the local chemical potential gradients that drove the initial sillimanite-consuming reactions to produce the spinel-cordierite porphyroblasts (Fig. 6.28B). In other words, the spinel-cordierite symplectites may have formed due to localised increases in Al_2SiO_5 content within the rock.

Point counting of minerals in sample LHA006 (Table 6.3) indicates that *ca.* 8% of the sample is made up of sillimanite in the cores of cordierite-spinel porphyroblasts. This means that *ca*. 8 vol. % of sample LHA006 may be made up of Al_2SiO_5 that is isolated from the matrix, resulting in a bulk rock composition for the matrix that overestimates SiO_2 and Al_2O_3.

However, the cordierite + spinel assemblages are likely to have formed in areas that were exposed to at least *ca*. 8 vol. % *more* Al_2SiO_5 than the overall bulk rock composition. Essentially, composition of the equilibration volume for the observed texture (spinel-cordierite porphyroblast surrounding sillimanite cores) differs in Al_2SiO_5 content from the bulk XRF composition of the sample. It is possible to examine the effects of variable Al_2SiO_5 content on the modelled assemblages using a T-X pseudosection at constant pressure.

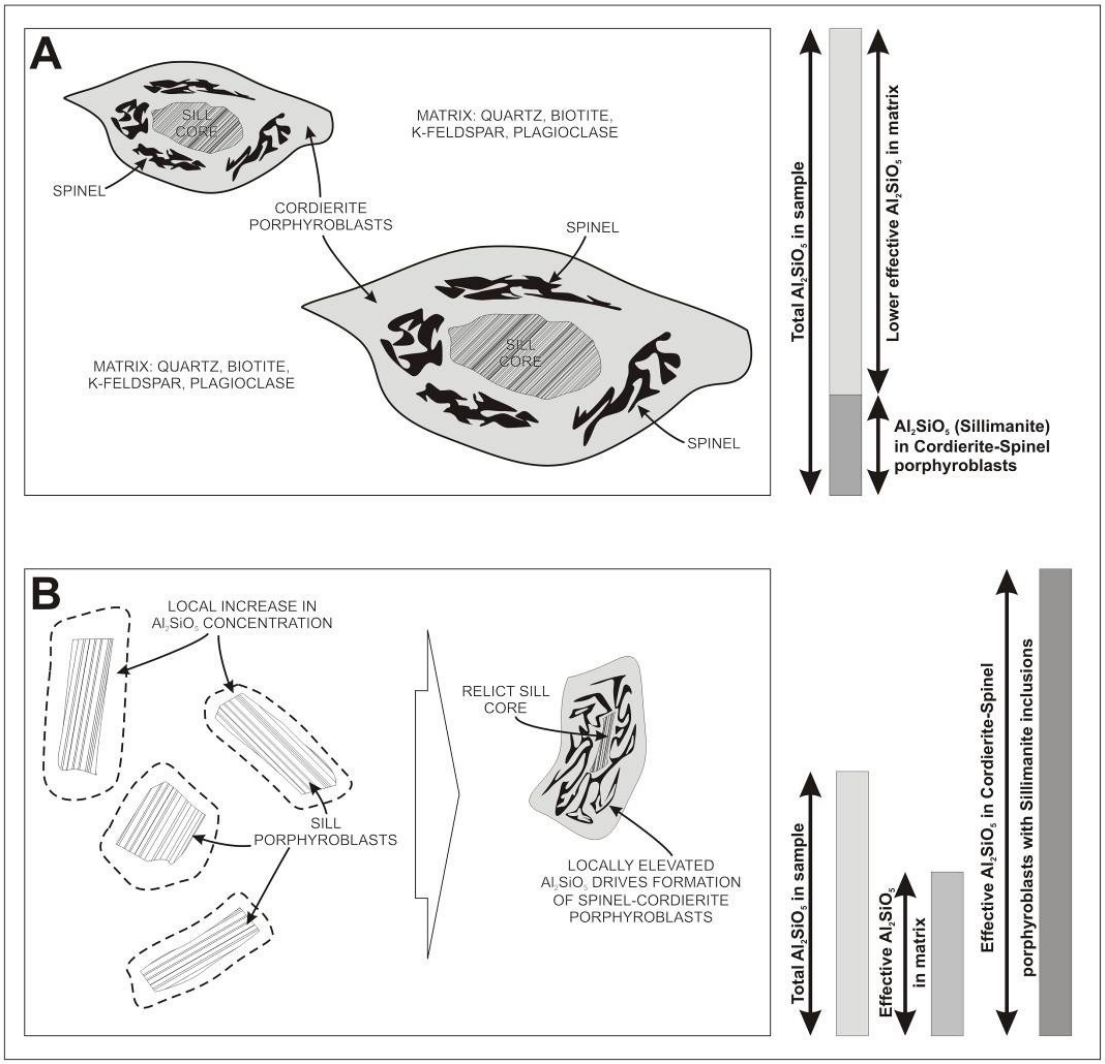

Fig. 6.28 – Schematic diagrams illustrating the effects of the inclusion of sillimanite within spinel-cordierite porphyroblasts. A: Sillimanite inclusions are isolated from the matrix of the sample, thereby effectively lowering the Al_2SiO_5 content of the matrix. B: Initial locally elevated Al_2SiO_5 around sillimanite porphyroblasts may have set up sites for the formation of spinel-cordierite porphyroblasts. Whilst this effectively lowers the Al_2SiO_5 content of the matrix, the effective Al_2SiO_5 content in spinel-cordierite porphyroblasts is higher than the bulk Al_2SiO_5 obtained from XRF analysis.

Examining the effects of addition and subtraction of Al_2SiO_5 has been done using a T-X pseudosection at 4 kbar, where Al_2O_3 content is varied between 18.00 mol. % to 6.00 mol. % and SiO_2 content from 70.00 mol. % to 58.00 mol. % (Fig. 6.29), whilst keeping other compositional variables the same, effectively adding (X=0) or subtracting (X=1) 6 mol. % Al_2SiO_5 from the original bulk composition of LHA006. From this pseudosection, it is evident that increasing the Al_2SiO_5 content of the sample results in the stabilisation of garnet and spinel to lower temperatures, and the stabilisation of sillimanite to higher temperatures. Increasing the Al_2SiO_5 content also results in orthopyroxene only becoming stable at higher temperatures (above 800 ˚C). In contrast, lowering of the Al_2SiO_5 content of the sample results in destabilisation of cordierite, garnet and spinel whilst increasing orthopyroxene stability to temperatures below 750 ˚C. Since the texture of interest is the cordierite-spinel porphyroblasts with sillimanite cores, a composition that increases the stability of these phases should be used. Conversely, in the matrix of the sample, the inclusion of sillimanite within cordierite + spinel porphyroblasts has resulted in the lowering of the effective Al_2O_3 content after cordierite + spinel production. However, although the T-X pseudosection (Fig. 6.29) illustrates the effects of effective Al_2O_3 on spinel stability, it is not possible to accurately model the phase relationships and P-T path associated with the reaction of sillimanite to produce cordierite + spinel using the bulk XRF composition. Nonetheless, the phases and textures observed in sample LHA006 do indicate similar P-T conditions (*ca*. 800 ˚C and 4 kbar) to those calculated from other samples, and the spinel-cordierite porphyroblasts do suggest decompression (as was suggested by Nex *et al*., 2001a based on similar textures), although this decompression appears to have been at the thermal peak, rather than preceding an isobaric heating event (as was suggested by Nex *et al*., 2001a).

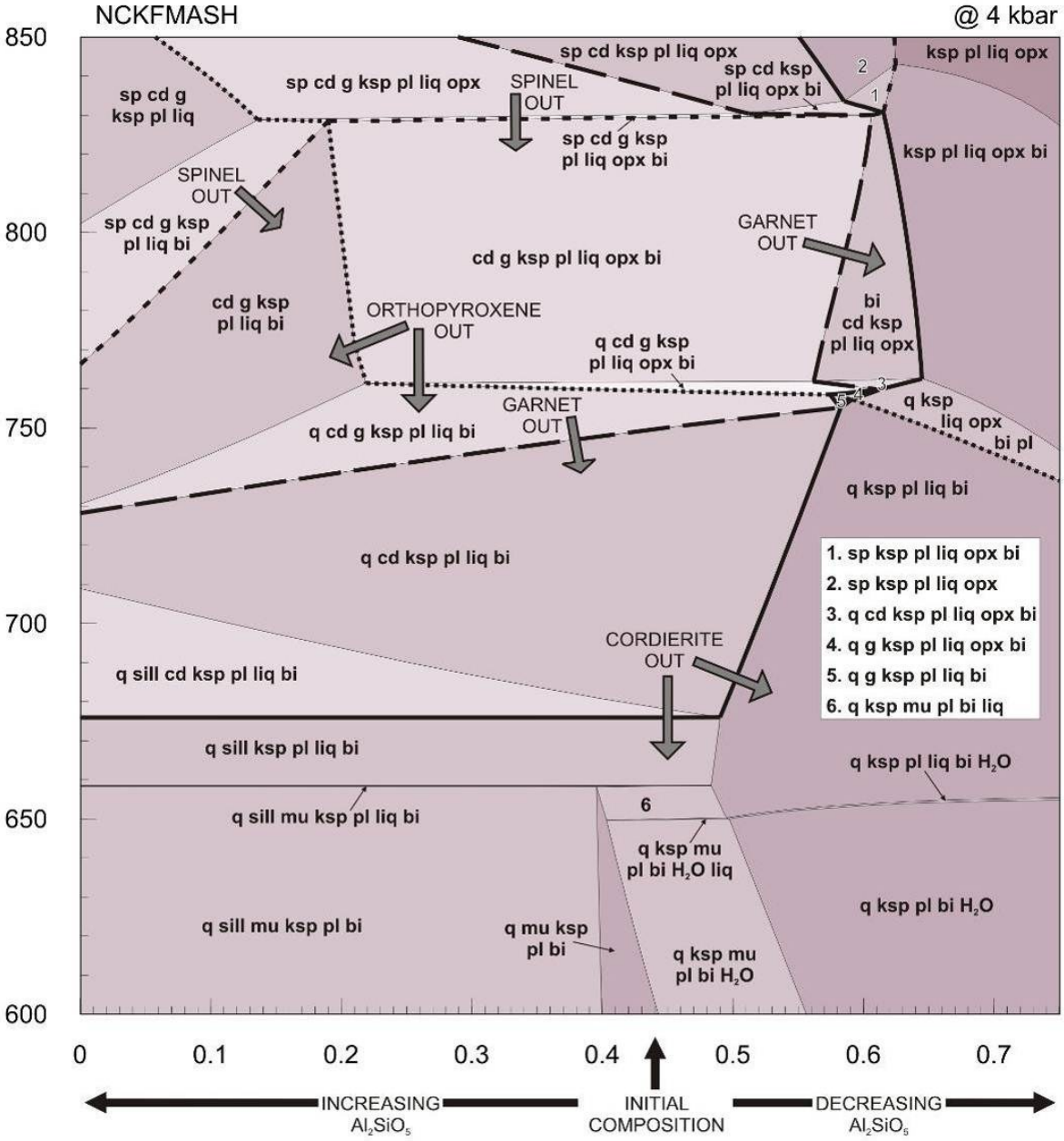

Fig. 6.29 – T-X (Al_2SiO_5) pseudosection for sample LHA006 in the system NCKFMASH at 4 kbar. Note that increasing Al_2SiO_5 content stabilises spinel and garnet to lower temperatures, but raises the stability field for orthopyroxene to higher temperatures. In contrast, decreasing Al_2SiO_5 content results in cordierite, garnet and spinel becoming unstable. The composition used in Fig. 6.27 lies at X = 0.44.
Composition used (mol. %):

	H_2O	SiO_2	Al_2O_3	CaO	MgO	FeO	K_2O	Na_2O
X=0	7.00	70.00	18.00	1.48	4.98	7.88	3.66	3.13
X=1	7.00	58.00	6.00	1.48	4.98	7.88	3.66	3.13

Pseudosection modelling in the system NCKFMASH has revealed peak temperatures similar to or slightly higher than those previously suggested for the Central Zone (700-780 ˚C), at low pressures (4-5kbar) similar to previous estimates. Peak temperatures appear to have been reached through near-isobaric heating, and there may have been some decompression at peak temperatures, indicating a clockwise P-T path. However, the effects of TiO_2 and fO_2 on the stability of many phases have not been accounted for in this system. Fe^{3+} content (i.e. fO_2) affects the stability of ferromagnesian phases – garnet and orthopyroxene are stable for reduced compositions, whilst the stability of cordierite increases to lower temperatures with increasing Fe^{3+} (Diener & Powell, 2010). TiO_2 affects the stability of biotite and spinel (White *et al*. 2007), and modelling in the system NCKFMASHTO (i.e. incorporating TiO_2 and Fe^{3+}) allows for phase relationships involving magnetite, ilmenite, rutile and haematite to be investigated. Hence, modelling of samples CZRL19, LID039 and LKR013 has been carried out in the system NCKFMASHTO to include these effects, and to increase the accuracy of the estimated peak conditions and P-T path. Due to the domainal equilibrium observed in LHA006, this sample has not been modelled in NCKFMASHTO.

6.10.2 Pseudosections in the system NCKFMASHTO

The more complete system NCKFMASHTO includes the effects of TiO_2 and fO_2 (oxygen fugacity) on the phase equilibria initially calculated. Whilst TiO_2 content is based on the XRF analysis of the sample, the oxygen fugacity (i.e. the ratio $FeO:Fe_2O_3$) needs to be estimated, as ferric iron is not determined through routine analytical methods such as XRF. Solid mineral buffers, such as the hematite-magnetite (H-M) or quartz-fayalite-magnetite (Q-F-M) buffers have been typically used to fix the aO_2 during experimental studies, but in nature the oxygen fugacity is controlled by multivariant equilibria between silicates, oxides and melt (Frost, 1991). Whilst most igneous rocks have fairly narrow ranges of fO_2, metamorphic rocks can have a much wider range of fO_2, and the ratio of FeO to Fe_2O_3 can significantly affect phase relationships (Diener & Powell, 2010), particularly for the amphiboles. The effect of fO_2 (as XFe^{3+}) has been investigated for greenschist- to granulite-grade metamorphism of pelites by Diener & Powell (2010), who showed that whilst some phase

equilibria are unaffected by $X\mathrm{Fe}^{3+}$, garnet, staurolite and orthopyroxene are only stable at fairly low oxygen fugacitities ($X\mathrm{Fe}^{3+}$<0.45). Since garnet is common in garnet-biotite schists and in garnet-sillimanite-cordierite schists, $X\mathrm{Fe}^{3+}$ must be fairly low for these rock types (i.e they must be fairly reducing). Additionally, no hematite is observed in any of the samples, and they generally contain magnetite and ilmenite. The stability field for ilmenite according to the phase diagram of Diener & Powell (2010) is fairly narrow ($X\mathrm{Fe}^{3+}$ <0.32), up to temperatures of 740˚C, where the closure of the ilmenite-hematite solvus occurs (Diener & Powell, 2010). Given that most samples contain garnet and ilmenite, and that two samples contain orthopyroxene, it is reasonable to assume fairly low fO_2 values for these samples. Hence, samples CZRL19, LID039 and LKR013 have initially been assumed to have $X\mathrm{Fe}^{3+}$values of between 0.2 and 0.4.

6.10.2.1 Sample CZRL19 (sillimanite-cordierite schist)

The pseudosection for sample CZRL19 in NCKFMASHTO (Fig. 6.30) displays similar phase stabilities to that modelled in NCKFMASH (Fig. 6.23) for the major phases. However, additional patterns are revealed regarding the stabilities of spinel and magnetite. Spinel is stable at low pressures and high temperatures, and magnetite has a fairly narrow stability window (Fig. 6.30). A spinel-magnetite solvus has resulted in a univariant line with the assemblage biotite-cordierite-garnet-quartz-sillimanite-plagioclase-K-feldspar-liquid-spinel-magnetite, around which a number of divariant fields exist (inset, Fig. 6.30). Sample CZRL19 contains the assemblage biotite-cordierite-garnet-sillimanite-plagioclase-K-feldspar-quartz-ilmenite-magnetite. Although magnetite is observed, ilmenite is the more abundant opaque mineral. No spinel is found. Thus, the field that matches the assemblage observed is found at *ca*. 770-790 ˚C and 4.6-5.2 kbar (Fig. 6.30). Owing to the incorporation of magnetite into calculations, this field is narrower, with more well-constrained P-T conditions than in the system NCKFMASH (Fig. 6.23), and the conditions calculated indicate higher grades than the 670-680 ˚C and 4.2 kbar predicted from the average P-T calculations.

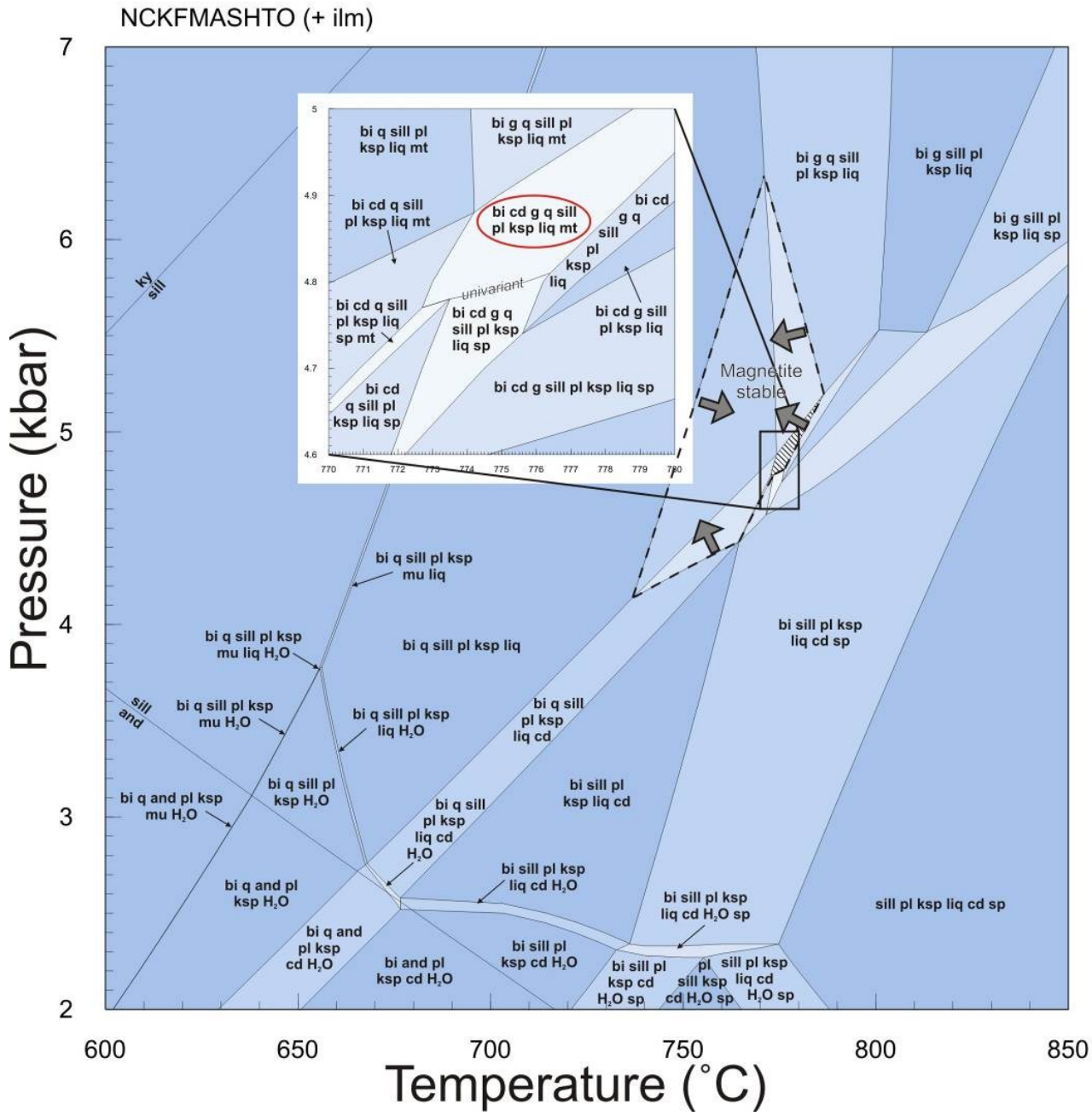

Fig. 6.30 – P-T pseudosection for sample CZRL19 in the system NCKFMASHTO. Note the small stability field for magnetite (indicated). The assemblage biotite-cordierite-quartz-sillimanite-plagioclase-K feldspar-liquid-magnetite (circled in inset) matches the observed assemblage, and is shown by the hatched field in the pseudosection. The inset shows details around the univariant line caused by the spinel-magnetite solvus. Composition used (mol. %):

H_2O	SiO_2	Al_2O_3	CaO	MgO	FeO	K_2O	Na_2O	TiO_2	O
5.47	52.33	22.10	0.602	4.35	9.38	3.78	0.98	0.996	0.3

However, since petrographic evidence indicates that sample CZRL19 experienced anatexis, the rock is likely to have experienced loss of melt. In order to account for effect of melt-loss on the bulk composition of the rock, it is possible to re-integrate melt back into the sample, using the procedure outlined by White *et al*. (2004). This procedure involves a number of steps, the first being reducing the H_2O content of the bulk rock composition from the XRF-calculated content to the point where the observed high-grade assemblage (in this case bi-cd-g-q-sill-pl-ksp-liq-mt) is calculated at the water-undersaturated solidus. This occurs when H_2O is reduced from 5.47 to 4.77 mol. % at a constant pressure of 4.5 kbar (the estimated pressure for the sample). Following recalculation of the H_2O content so that the peak assemblage biotite-cordierite-quartz-sillimanite-plagioclase-K-feldspar-liquid-magnetite lies immediately above the solidus (i.e. there is a liquid-out boundary from the peak assemblage), the proportion of melt in this field is increased to the point where melt persists below the cordierite-out boundary, essentially re-integrating melt of the appropriate composition into the bulk composition in the proportion appropriate for these temperature conditions (White *et al*., 2004). When melt is reintegrated into the bulk composition, the appropriate P-T path is important, as an incorrect path may result in the incorrect amount of melt being reintegrated. Since modelled phase relationships for a number of samples in NCKFMASH indicate a near-isobaric heating path at 4-5 kbar (CZRL19 – Fig. 6.23; LID039 – Figs. 6.24, 6.25), a more appropriate P-T path would be isobaric heating at 4.8 kbar. As phase boundaries are crossed on this path, the appropriate phases need to be removed from the peak assemblage (i.e. the assemblage experiencing melting).

Adding melt along an isobaric heating path at 4.8 kbar, garnet goes to zero with the addition of 3.1% liquid, and the solidus is at 772 ˚C. Thus, the assemblage cordierite-biotite-quartz-sillimanite-plagioclase-K-feldspar-liquid-magnetite is then used for the reintegration of melt, as melt produced from a garnet-free assemblage will differ in composition from that produced from a garnet-bearing assemblage. Cordierite goes to zero with the further addition of only 0.69% liquid to the garnet-free assemblage (solidus at 769 ˚C). Further addition of 0.5% liquid to the assemblage biotite-quartz-sillimanite-plagioclase-K-feldspar-liquid-magnetite results in magnetite going to zero at 749 ˚C. Following removal of magnetite from the assemblage, the addition of 0.8% liquid at lowers the liquid-out point to

665 ˚C. This large drop in the solidus temperature suggests the addition of muscovite to the assemblage, and the assemblage muscovite-biotite-quartz-sillimanite-plagioclase-K feldspar-liquid gives a solidus temperature of 674 ˚C. Adding 11.9% liquid to the assemblage muscovite-biotite-quartz-sillimanite-plagioclase-K feldspar-liquid results in K-feldspar going to zero at a solidus temperature of 672 ˚C. Addition of a further 3.5 % liquid to the K-feldspar free assemblage results in the stabilisation of a wet solidus at 657 ˚C, and this wet solidus is stable over the entire pressure range 2-7 kbar. The melt reintegrated pseudosection is shown in Fig. 6.31.

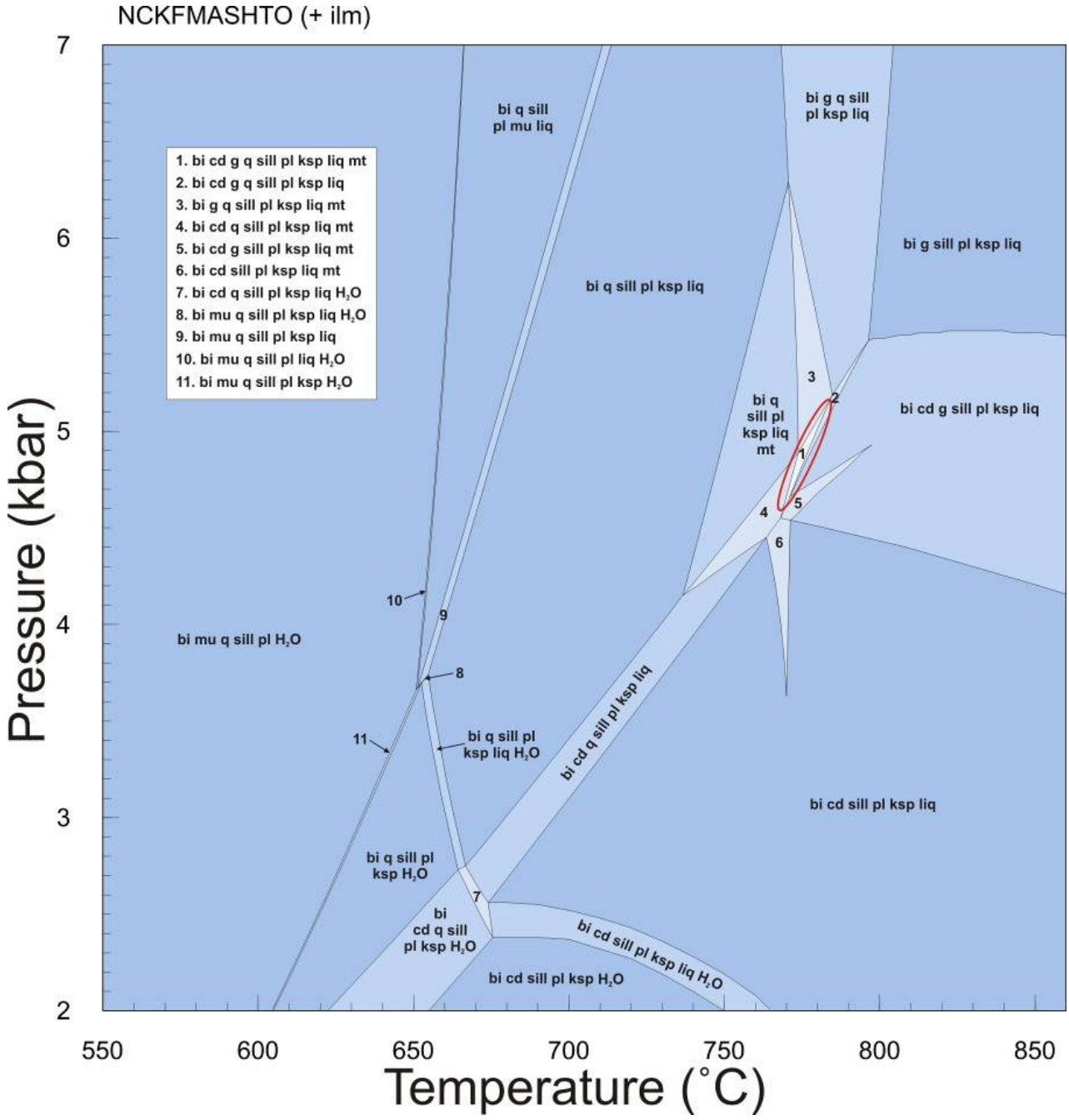

Fig. 6.31 – P-T pseudosection for sample CZRL19 in the system NCKFMASHTO, with a melt-reintegrated composition. The peak assemblage biotite-cordierite-garnet-quartz-sillimanite-plagioclase-K feldspar-liquid-magnetite is shown by hatching, and is circled in inset. Composition used (mol. %):

H_2O	SiO_2	Al_2O_3	CaO	MgO	FeO	K_2O	Na_2O	TiO_2	O
7.607	54.760	19.584	0.539	3.617	7.813	3.661	1.343	0.827	0.249

Whilst the overall stability of most phases in the P-T pseudosection for CZRL19 following melt reintegration has not significantly changed, spinel is no longer modelled as a stable phase in the pseudosection. The peak assemblage biotite-cordierite-garnet-quartz-sillimanite-plagioclase-K-feldspar-liquid-magnetite (Fig. 6.31) falls in a narrow field with P-T conditions of *ca*. 770-780 ˚C and 4.5-5.2 kbar. Calculation of modal isopleths for garnet, cordierite and biotite (Fig. 6.32) confirms that modelled proportions match with observed proportions calculated through point counting. Peak conditions are thus *ca*. 775 ˚C and 4.75 kbar.

Fig. 6.32 (following page) – Detail of area in melt-reintegrated pseudosection for sample CZRL19 in the system NCKFMASHTO, showing modal isopleths for garnet, cordierite and biotite. Peak conditions (shown by the red rectangle) are ca*. 775 ˚C and 4.75 kbar.*

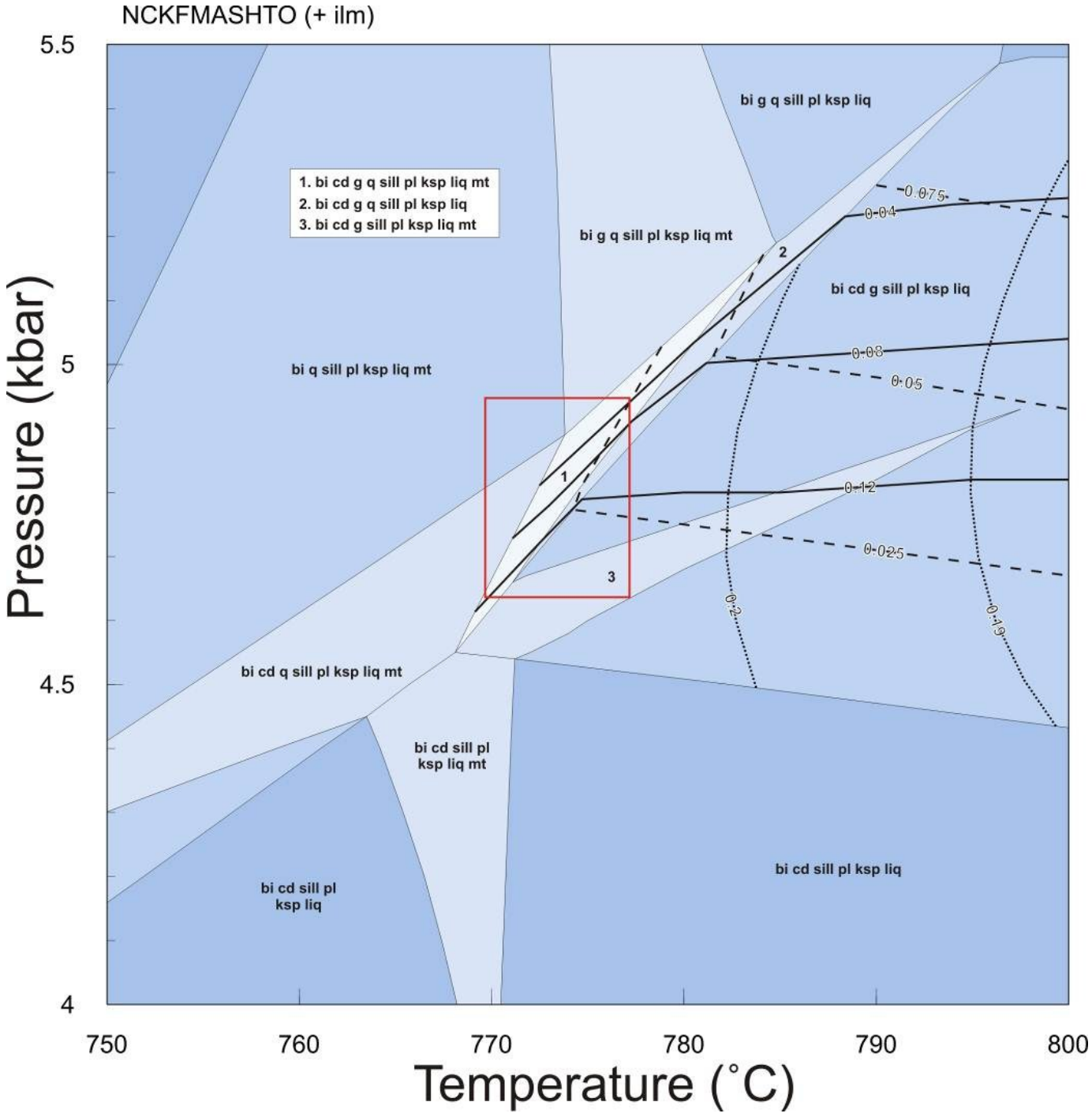
NCKFMASHTO (+ ilm)
1. bi cd g q sill pl ksp liq mt
2. bi cd g q sill pl ksp liq
3. bi cd g sill pl ksp liq mt
bi g q sill pl ksp liq
bi g q sill pl ksp liq mt
bi cd g sill pl ksp liq
bi q sill pl ksp liq mt
bi cd q sill pl ksp liq mt
bi cd sill pl ksp liq mt
bi cd sill pl ksp liq
bi cd sill pl ksp liq
0.075
0.04
0.08
0.05
0.12
0.025
0.2
0.19
1
2
3
Pressure (kbar)
Temperature (˚C)
5.5
5
4.5
4
750
760
770
780
790
800

6.10.2.2 Sample LID039 – garnet cordierite schist

The peak assemblage biotite-garnet-cordierite-quartz-orthopyroxene-plagioclase-K feldspar-liquid was modelled as occurring at conditions of 770-820 ˚C and 4.2-7 kbar in the system NCKFMASH (Fig. 6.24). However, LID039 also contains magnetite and ilmenite in the peak assemblage, as well as relict needles of fibrolitic sillimanite in the cores of cordierite porphyroblasts. Modelling the bulk XRF composition in the system NCKFMASHTO (Fig. 6.33), the peak assemblage biotite-garnet-cordierite-quartz-orthopyroxene-plagioclase-K feldspar-liquid-magnetite-ilmenite occurs at conditions of 830-870 ˚C and 4.5-6.3 kbar. Although this narrow divariant field contains no sillimanite, the sillimanite recorded as inclusions in cordierite suggests cordierite growth at the expense of sillimanite. Fibrolitic sillimanite is not found within garnet porphyroblasts, indicating that sillimanite was consumed (likely by a cordierite-producing reaction) prior to garnet growth. Cordierite inclusions in garnet also indicate that cordierite growth preceded garnet growth. Such a sequence of mineral growth and consumption is consistent with a near-isobaric heating path at 4-5 kbar (Fig. 6.33).

The high grade conditions experienced by this sample are likely to have led to melting, as confirmed by petrographic evidence, and thus melt-loss is likely. In order to check the effects of melt-loss, melt-reintegration has been carried out.

Fig. 6.33 (following page) – P-T pseudosection for sample LID039 in the system NCKFMASHTO, showing the peak assemblage cd-g-kfs-pl-bt-q-opx-liq-mt (circled), and a possible decompression path from a cordierite-absent, sillimanite-present field at pressures of ca. *7 kbar.*
Composition used (mol. %):

H_2O	SiO_2	Al_2O_3	CaO	MgO	FeO	K_2O	Na_2O	TiO_2	O
5.90	60.38	12.05	2.92	6.67	7.33	2.43	1.65	0.67	0.39

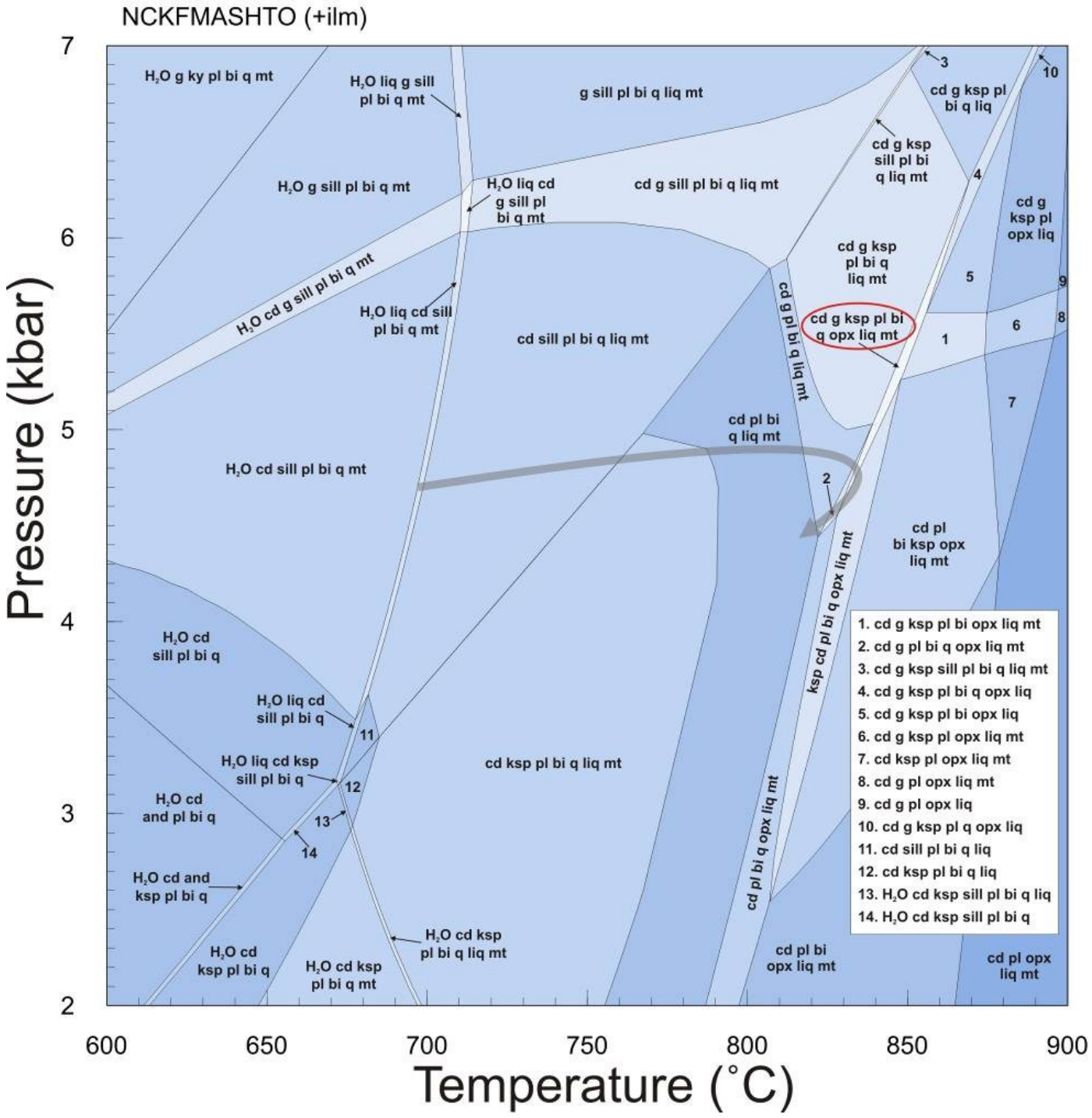
NCKFMASHTO (+ilm)
Pressure (kbar)
Temperature (˚C)
7
6
5
4
3
2
600
650
700
750
800
850
900
H2O g ky pl bi q mt
H2O liq g sill pl bi q mt
g sill pl bi q liq mt
H2O g sill pl bi q mt
H2O liq cd g sill pl bi q mt
cd g sill pl bi q liq mt
H2O cd g sill pl bi q mt
H2O liq cd sill pl bi q mt
cd sill pl bi q liq mt
H2O cd sill pl bi q mt
H2O cd sill pl bi q
H2O liq cd sill pl bi q
H2O liq cd ksp sill pl bi q
cd ksp pl bi q liq mt
H2O cd and pl bi q
H2O cd and ksp pl bi q
H2O cd ksp pl bi q
H2O cd ksp pl bi q mt
H2O cd ksp pl bi q liq mt
cd g ksp pl bi q liq
cd g ksp sill pl bi q liq mt
cd g ksp pl bi q liq mt
cd g ksp pl opx liq
cd g pl bi q liq mt
cd g ksp pl bi q opx liq mt
cd pl bi q liq mt
ksp cd pl bi q opx liq mt
cd pl bi q opx liq mt
cd pl bi ksp opx liq mt
cd pl bi opx liq mt
cd pl opx liq mt
1. cd g ksp pl bi opx liq mt
2. cd g pl bi q opx liq mt
3. cd g ksp sill pl bi q liq mt
4. cd g ksp pl bi q opx liq
5. cd g ksp pl bi opx liq
6. cd g ksp pl opx liq mt
7. cd ksp pl opx liq mt
8. cd g pl opx liq mt
9. cd g pl opx liq
10. cd g ksp pl q opx liq
11. cd sill pl bi q liq
12. cd ksp pl bi q liq
13. H2O cd ksp sill pl bi q liq
14. H2O cd ksp sill pl bi q

Initially, the H_2O content is adjusted so that the peak assemblage occurs just above the solidus, reducing the water content from 5.90 mol. % (estimated from the XRF analysis) to 3.10 mol %. This results in a liquid-out line from the peak assemblage biotite-garnet-cordierite-quartz-orthopyroxene-plagioclase-K-feldspar-liquid-magnetite-ilmenite. Since orthopyroxene is the highest-temperature phase present in the sample, and is only present in small amounts, a small amount of liquid needs to be added. Since modelling of this composition in the system NCKFMASH indicated near-isobaric heating at *ca*. 5 kbar, it is assumed here that isobaric heating took place at 4.7 kbar. After adding 1% liquid at 4.7 kbar, orthopyroxene becomes unstable and is no longer found in the assemblage. From this point melt is added into an orthopyroxene-free assemblage at 4.7 kbar until garnet becomes unstable at a solidus of 816 ˚C after adding 5.46% melt. An additional 6.7% liquid is then added to a garnet-free, orthopyroxene-free assemblage at until magnetite becomes unstable at 722 ˚C. Adding a further 1% melt to this assemblage results in the stabilisation of muscovite, and the further lowering of the solidus to 699 ˚C. Melt is now added to the assemblage biotite-muscovite-cordierite-quartz-plagioclase-K-feldspar-liquid-ilmenite, and addition of 4% melt results in K-feldspar going to zero at 697 ˚C. Adding 0.8% melt to a K-feldspar-free assemblage results in stabilisation of H_2O at 676 ˚C. Adding an additional 2% melt to the assemblage biotite-muscovite-cordierite-quartz-plagioclase-H_2O-liquid-ilmenite stabilises the solidus over the pressure range 2-8 kbar, and this is the final melt-reintegrated composition.

The melt-reintegrated pseudosection (Fig. 6.34) again shows that the peak assemblage biotite-garnet-cordierite-quartz-orthopyroxene-plagioclase-K-feldspar-liquid-magnetite-ilmenite occurs at conditions of 820-865 ˚C and 4.4-6.3 kbar. Additionally, the assumed isobaric heating P-T path followed to reach the peak (orthopyroxene-bearing) conditions is apparent; textural evidence indicates that cordierite growth preceded garnet growth, and that cordierite growth was at the expense of sillimanite, which is now present only as inclusions in cordierite. For this to occur, the P-T path shown (Fig. 6.34) must have been followed, allowing for cordierite to grow before garnet. In contrast, an isothermal decompression path would have resulted in garnet growth preceding cordierite growth.

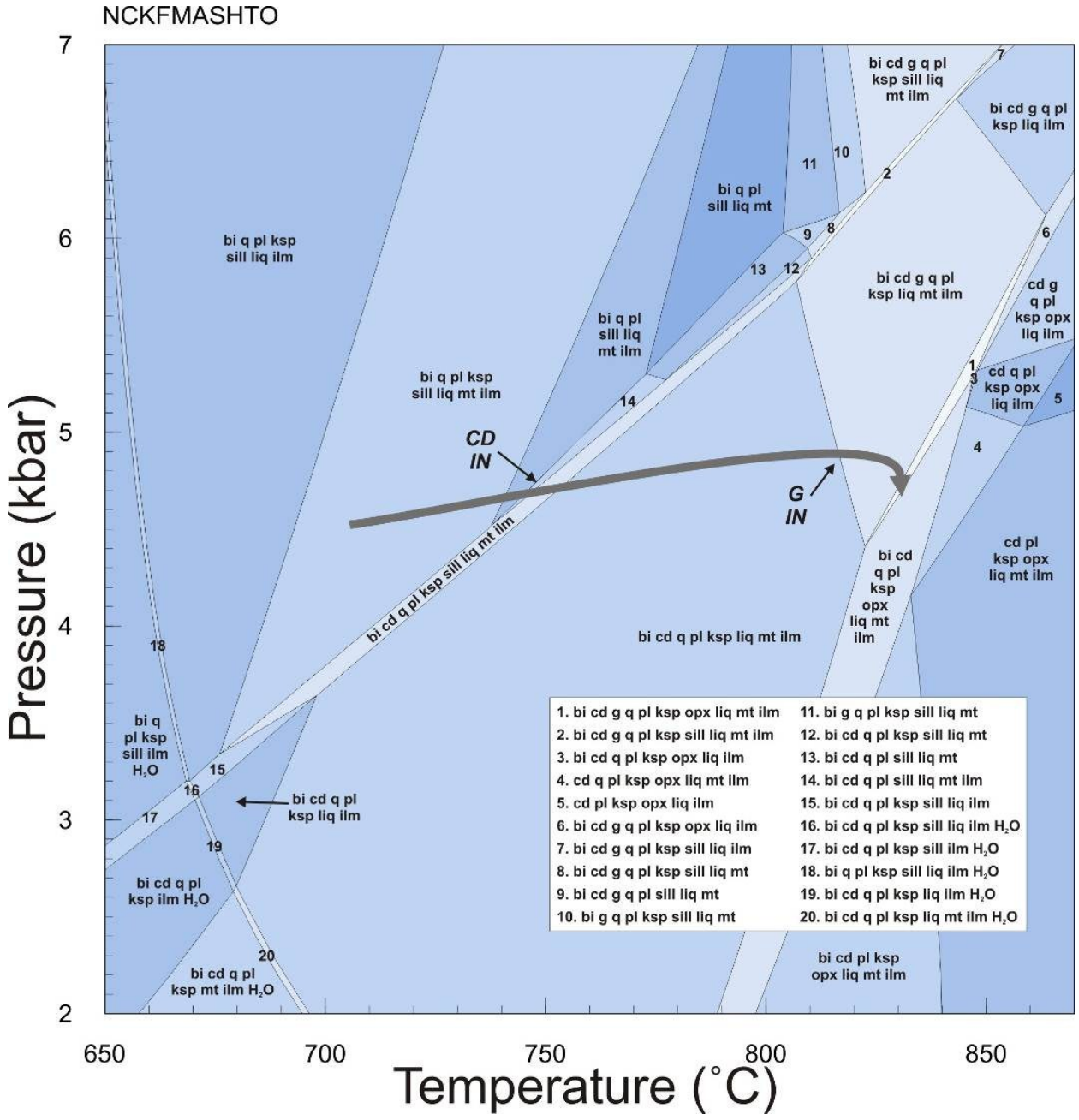

Fig. 6.34 – Melt-reintegrated P-T pseudosection for sample LID039 in the system NCKFMASHTO, showing the peak assemblage cd-g-kfs-pl-bt-q-opx-liq-mt, and the suggested P-T path, which would result in cordierite growth before garnet growth (as evidenced by petrographic textures), whereas isothermal decompression) would result in garnet growing before cordierite.

Composition used (mol. %):

H_2O	SiO_2	Al_2O_3	CaO	MgO	FeO	K_2O	Na_2O	TiO_2	O
5.771	62.979	11.456	2.523	5.612	6.266	2.686	1.788	0.599	0.326

Checking the observed modal proportions of phases (from point counting – Table 6.3) with modelled isopleths for biotite, cordierite, garnet and orthopyroxene (Fig. 6.35) confirms the peak assemblage and further constrains the P-T conditions. Orthopyroxene proportions increase rapidly as temperature is increased, but only traces of orthopyroxene have been noted in this sample. This indicates that only incipient growth of orthopyroxene took place in this sample, and that P-T conditions were not sufficiently high for significant orthopyroxene growth. Modal proportions constrain P-T conditions to *ca*. 825 ˚C and 4.6 kbar (Fig. 6.35). It should also be noted that cordierite proportions increase up-temperature in the orthopyroxene stability field, whilst biotite proportions decrease, confirming petrographic observations that that orthopyroxene + cordierite are the products of a melt-producing biotite breakdown reaction.

Fig. 6.35 (following page) – Detail of the peak conditions for the melt-reintegrated P-T pseudosection of sample LID039 in the system NCKFMASHTO. Modal proportions from point-counting match the modelled modal proportions, constraining the P-T conditions to ca*. 825* ˚C *and 4.6 kbar (indicated by red rectangle).*

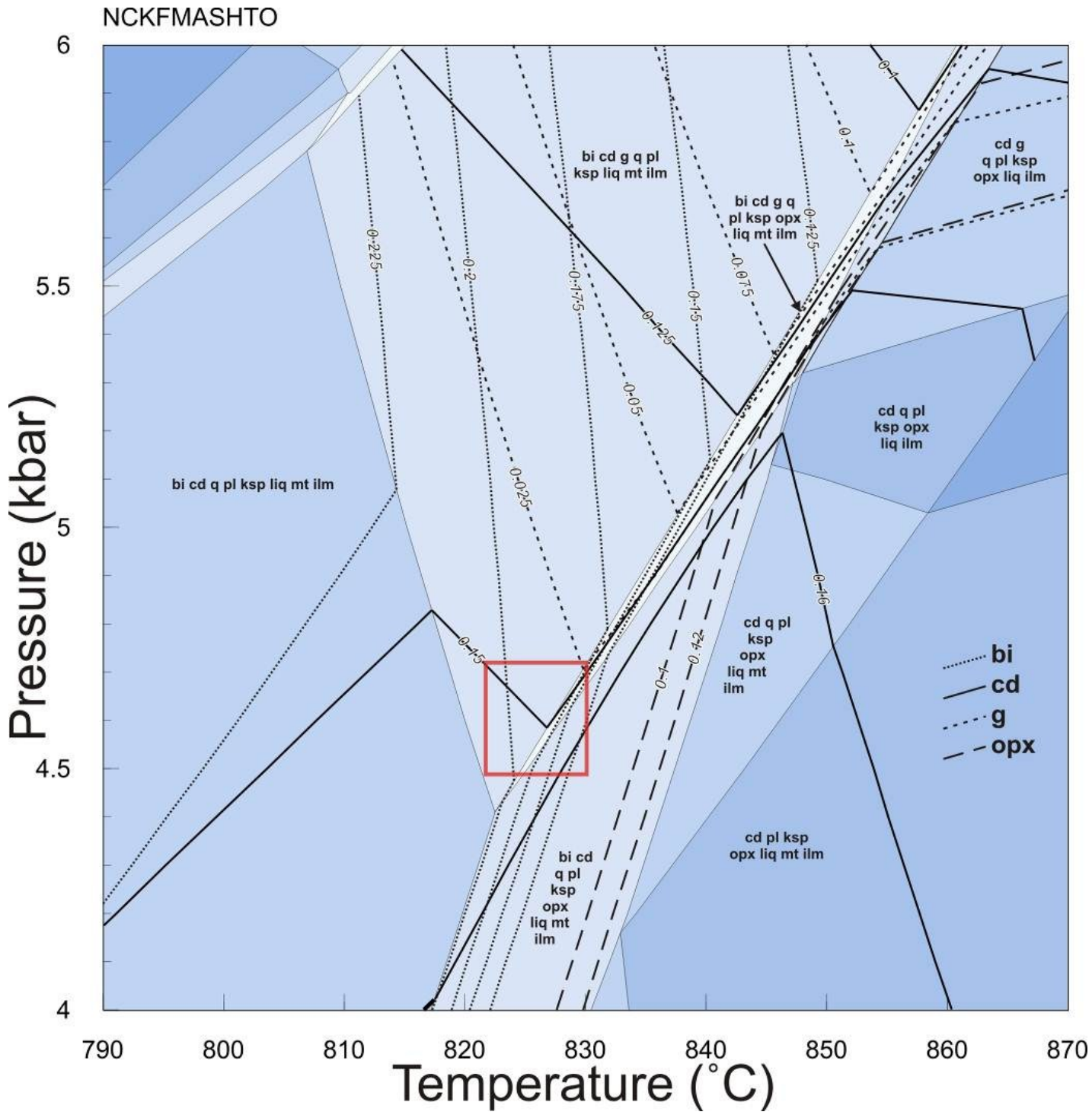
NCKFMASHTO
Pressure (kbar)
Temperature (˚C)
6
5.5
5
4.5
4
790
800
810
820
830
840
850
860
870
bi cd g q pl ksp liq mt ilm
bi cd g q pl ksp opx liq mt ilm
cd g q pl ksp opx liq ilm
cd q pl ksp opx liq ilm
bi cd q pl ksp liq mt ilm
cd q pl ksp opx liq mt ilm
bi cd q pl ksp opx liq mt ilm
cd pl ksp opx liq mt ilm
bi
cd
g
opx

6.10.2.3 Sample LKR013 – garnet cordierite schist

No orthopyroxene, gedrite, sillimanite or K-feldspar is noted in LKR013, and this appears to be consistent with the assemblage biotite-cordierite-garnet-quartz-plagioclase-liquid-ilmenite. This assemblage forms a large field that falls on the original P-T pseudosection in NCKFMASHTO at conditions of >715 ˚C and >5.2 kbar (Fig. 6.36). However, these conditions suggest pressures higher than those modelled for other samples from this study, which typically had pressures of <5 kbar. Furthermore, magnetite is not modelled as stable in the field biotite-cordierite-garnet-quartz-plagioclase-liquid-ilmenite, but has been observed petrographically. Much of the pseudosection (including areas of magnetite stability) shows either gedrite amphibole or orthopyroxene as stable phases. Although neither of these has been noted petrographically, modal isopleths of orthopyroxene in the field biotite-cordierite-garnet-quartz-plagioclase-liquid-magnetite-ilmenite-orthopyroxene indicate that orthopyroxene did not reach significant proportions, and may have been missed owing to thin section preparation. Based on the presence of magnetite, and the possibility that orthopyroxene may have been missed owing to thin section preparation, the likely peak assemblage appears to be biotite-cordierite-garnet-quartz-plagioclase-liquid-magnetite-ilmenite-orthopyroxene. Since the rock is above the solidus, some melt-loss may have occurred, and melt-reintegration needs to conducted.

Assuming that biotite-cordierite-garnet-quartz-plagioclase-liquid-magnetite-ilmenite-orthopyroxene is the peak assemblage, reducing the H_2O content from 4.70 mol. % to 2.45 mol. % results in the stabilisation of this assemblage just above the solidus. In this case, melting is assumed to have taken place along an isobaric heating path at 4.7 kbar. At 4.7 kbar, the solidus for the peak assemblage occurs at 783 ˚C. Adding 0.6% melt stabilises gedrite, and the solidus for the assemblage biotite-cordierite-garnet-quartz-plagioclase-liquid-magnetite-ilmenite-orthopyroxene-gedrite occurs at 762 ˚C. Adding just a further 0.2% melt results in orthopyroxene going to zero, also at 762 ˚C.

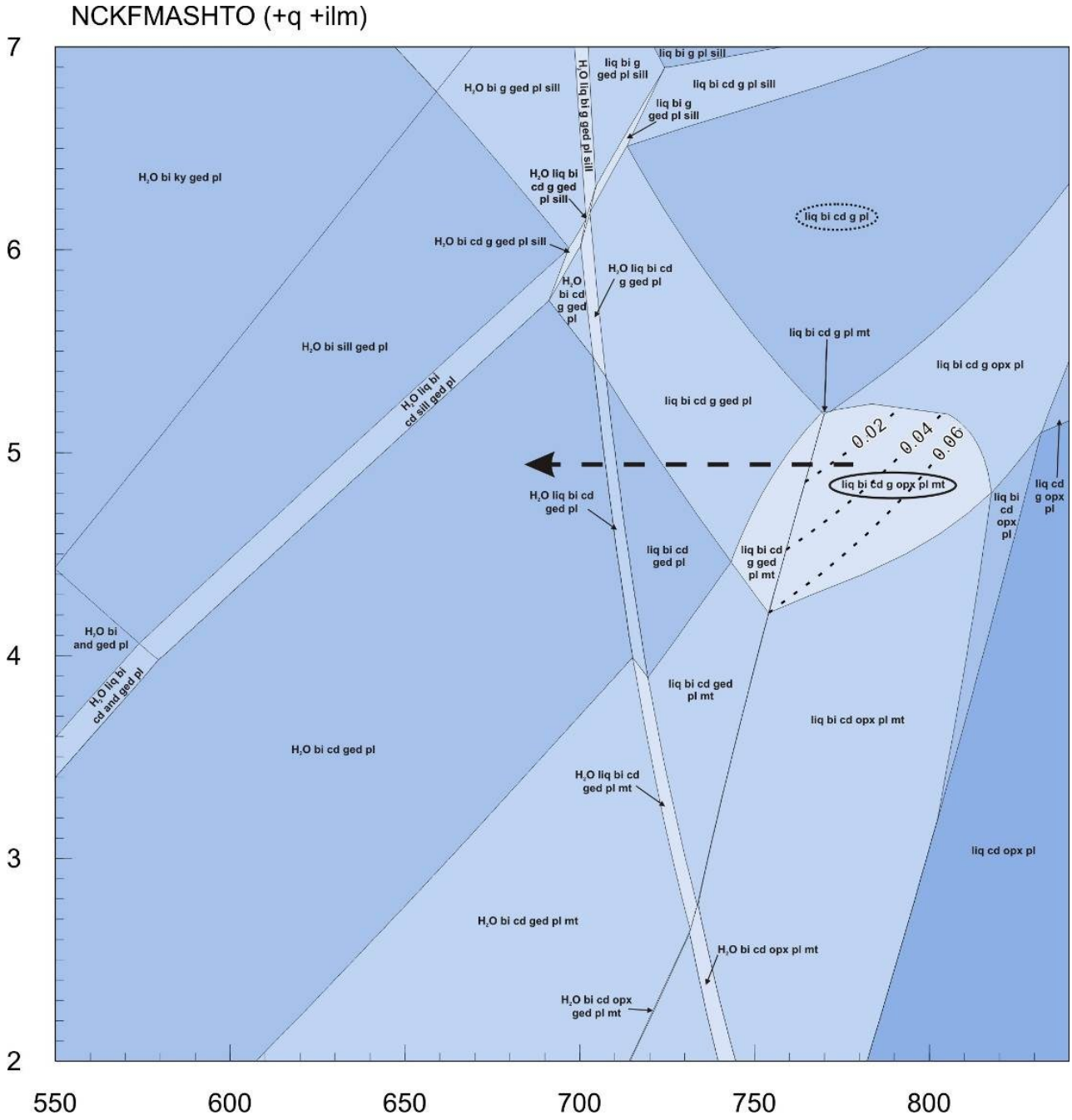

Fig. 6.36 – P-T pseudosection for sample LKR013 in the system NCKFMASHTO. Note that whilst orthopyroxene is not observed in the sample, it may occur in low modal proportions and was missed during thin section preparation. As isobaric heating path at 4.7 kbar is assumed for this sample.

Composition used (mol. %):

H_2O	SiO_2	Al_2O_3	CaO	MgO	FeO	K_2O	Na_2O	TiO_2	O
4.70	66.77	9.60	2.81	5.02	6.71	1.23	2.45	0.72	0.3

Adding 2.5% melt to the assemblage biotite-cordierite-garnet-quartz-plagioclase-liquid-magnetite-ilmenite-gedrite results in magnetite going to zero, and the magnetite-free solidus now occurs at 735 ˚C. Adding just 0.2% melt results in garnet going to zero, and the garnet-free, solidus (i.e. for the assemblage biotite-cordierite- quartz-plagioclase-liquid-ilmenite-gedrite) occurs at 740 ˚C. Adding just 0.1% melt results in the stabilisation of sillimanite and the lowering of the solidus to 608 ˚C. Adding a further 0.31% melt to the assemblage biotite-cordierite- quartz-plagioclase-liquid-ilmenite-gedrite-sillimanite results in sillimanite going to zero, and the sillimanite-free solidus is at 616 ˚C. At this point water is stabilised without adding and further melt – the assemblage biotite-cordierite-quartz-plagioclase-liquid-ilmenite-gedrite-H_2O has a solidus at 707 ˚C, and this wet solidus is stable over the entire pressure range of 2-8 kbar.

The melt-reintegrated P-T pseudosection for sample LKR013 (Fig. 6.37) does not differ significantly from the non-melt reintegrated pseudosection, and the peak assemblage biotite-cordierite-garnet-quartz-plagioclase-liquid-magnetite-ilmenite-orthopyroxene falls into a field with temperatures in of 750-820 ˚C and pressures of 4.1-5.4 kbar. Since orthopyroxene has not been observed, it is likely to have occurred only in trace amounts. Modal isopleths for biotite, cordierite and garnet agree with estimates from point counting, and suggest that P-T conditions were 760-780 ˚C and 4.4-4.9 kbar. In this region, modal isopleths for orthopyroxene and gedrite, approach zero, and the best estimate for peak conditions is *ca.* 760 ˚C and 4.9 kbar. These are slightly lower temperatures and higher pressures than the 802 ˚C and 4.5 kbar obtained from average P-T calculations (Table 6.7).

Fig. 6.37 (following page) – Melt-reintegrated P-T pseudosection for sample LKR013 in the system NCKFMASHTO. The field bi-cd-g-pl-q-liq-ilm(-opx) represents the peak assemblage. Point counting and modal isopleths of cordierite, garnet and biotite constrain the peak conditions to ca. *760 ˚C and 4.9 kbar.*
Composition used (mol. %):

H_2O	SiO_2	Al_2O_3	CaO	MgO	FeO	K_2O	Na_2O	TiO_2	O
3.311	67.884	9.667	2.767	4.932	6.615	1.265	2.560	0.706	0.294

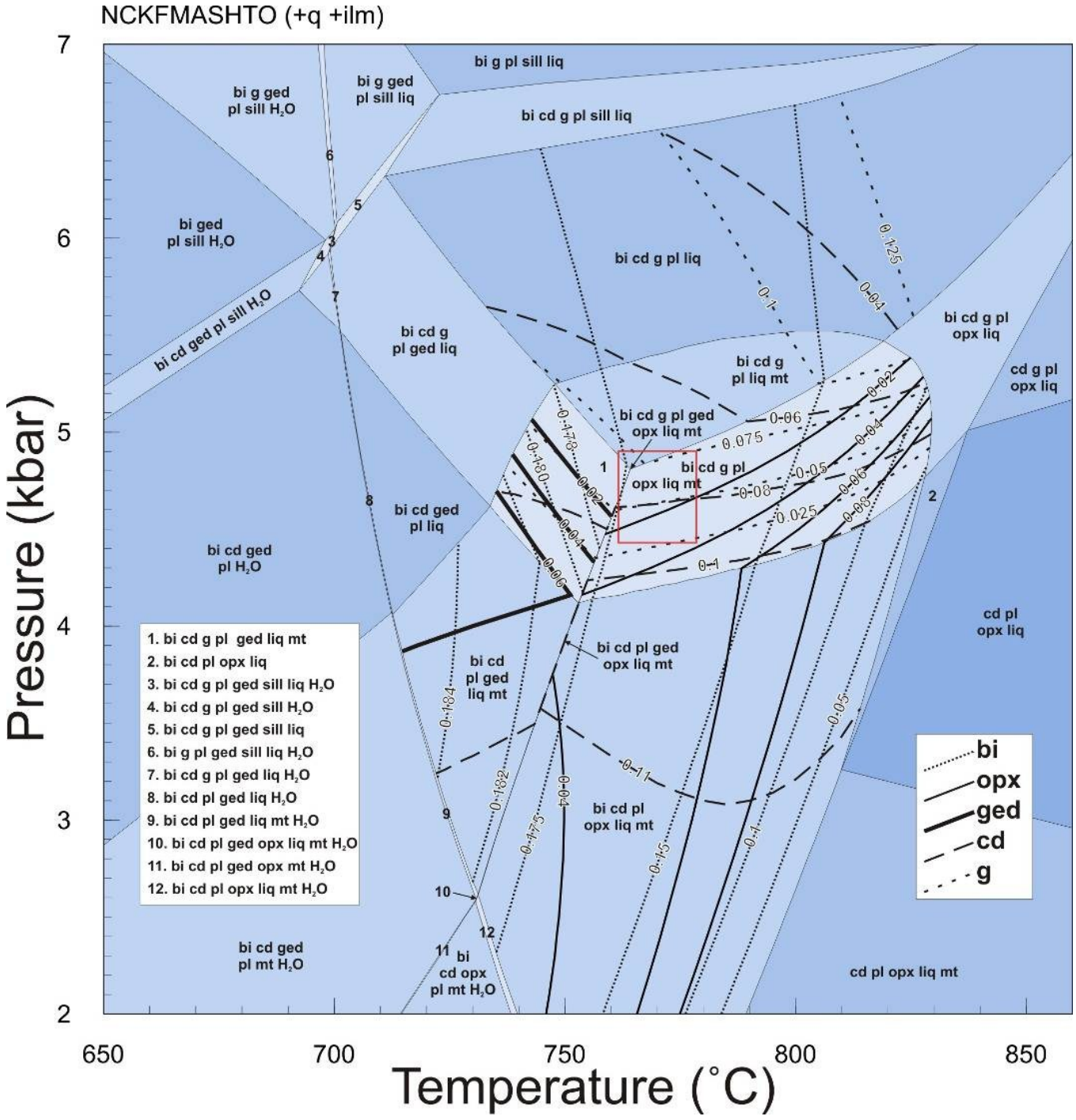
NCKFMASHTO (+q +ilm)
Pressure (kbar)
Temperature (˚C)
7
6
5
4
3
2
650
700
750
800
850
bi g pl sill liq
bi g ged pl sill H2O
bi g ged pl sill liq
bi cd g pl sill liq
bi ged pl sill H2O
bi cd g pl liq
bi cd g pl opx liq
bi cd ged pl sill H2O
bi cd g pl ged liq
bi cd g pl liq mt
cd g pl opx liq
bi cd g pl ged opx liq mt
bi cd g pl opx liq mt
bi cd ged pl liq
bi cd ged pl H2O
cd pl opx liq
bi cd pl ged opx liq mt
bi cd pl ged liq mt
bi cd pl opx liq mt
bi cd ged pl mt H2O
bi cd opx pl mt H2O
cd pl opx liq mt
1. bi cd g pl ged liq mt
2. bi cd pl opx liq
3. bi cd g pl ged sill liq H2O
4. bi cd g pl ged sill H2O
5. bi cd g pl ged sill liq
6. bi g pl ged sill liq H2O
7. bi cd g pl ged liq H2O
8. bi cd pl ged liq H2O
9. bi cd pl ged liq mt H2O
10. bi cd pl ged opx liq mt H2O
11. bi cd pl ged opx mt H2O
12. bi cd pl opx liq mt H2O
bi
opx
ged
cd
g

6.11 Discussion

Having evaluated the metamorphic history of a number of samples using both conventional thermobarometry and phase equilibria modelling, the questions posed at the beginning of the chapter can be answered. These include evaluating the peak metamorphic conditions in the study area, and any evidence for more than one phase of metamorphism, the overall P-T-t path for the study area, the heat source for metamorphism, and the relationships between metamorphism in the study area to the geodynamics of the Central Zone and the Damara Orogen.

6.11.1 Overall P-T path

Textural relationships between metamorphic minerals from a variety of sample types show a number of similarities, including the early growth of sillimanite, consumption of sillimanite to produce cordierite, and the late development of garnet. When these relationships are examined together with the P-T pseudosections constructed for various samples, it is evident that rocks in the study area experienced a near-isobaric heating P-T path, reaching upper-amphibolite to lower-granulite facies conditions (750-850 ˚C). This heating look place at fairly low pressures of 4.5-5 kbar. The local preservation of andalusite in the cores of cordierite porphyroblasts, the lack of relict kyanite in any samples, and the fact that cordierite growth preceded garnet growth all suggest such a low-pressure heating path. Summarising the peak conditions obtained from pseudosection modelling, and comparing them with those obtained from previous workers (Fig. 6.38) shows that temperatures in the Central Zone may in fact be slightly greater than those previously estimated using conventional cation exchange thermobarometry (Buhn *et al*., 1995; Poli, 1997; Nex *et al*., 2001) or using the average P-T function of THERMOCALC (Ward *et al*., 2008), but pressure estimates by previous workers are similar to those obtained by pseudosection modelling. The near-isobaric heating P-T path suggested above is compatible with most previous P-T estimates. Spinel-cordierite symplectites suggest that some decompression may have occurred at the thermal peak, indicating a clockwise P-T path. As discussed earlier, peak temperatures calculated using Fe-Mg garnet-biotite exchange thermometry may be lower

than the actual peak temperatures attained (Spear, 1991), as high cation diffusion rates in high-grade rocks easily destroy rim compositions of garnet during cooling (Spear, 1991; Harley, 1989). An alternative possibility is that rocks in the study area reached higher-grade conditions than elsewhere in the Central Zone. However, a number of the previous P-T estimates for the Central Zone come from areas immediately adjacent to the study area (e.g. Goanikontes – Nex *et al*., 2001a; the Nose Structure – Poli, 1997; the Khan River gorge – Ward *et al*., 2008), and such a scenario seems unlikely.

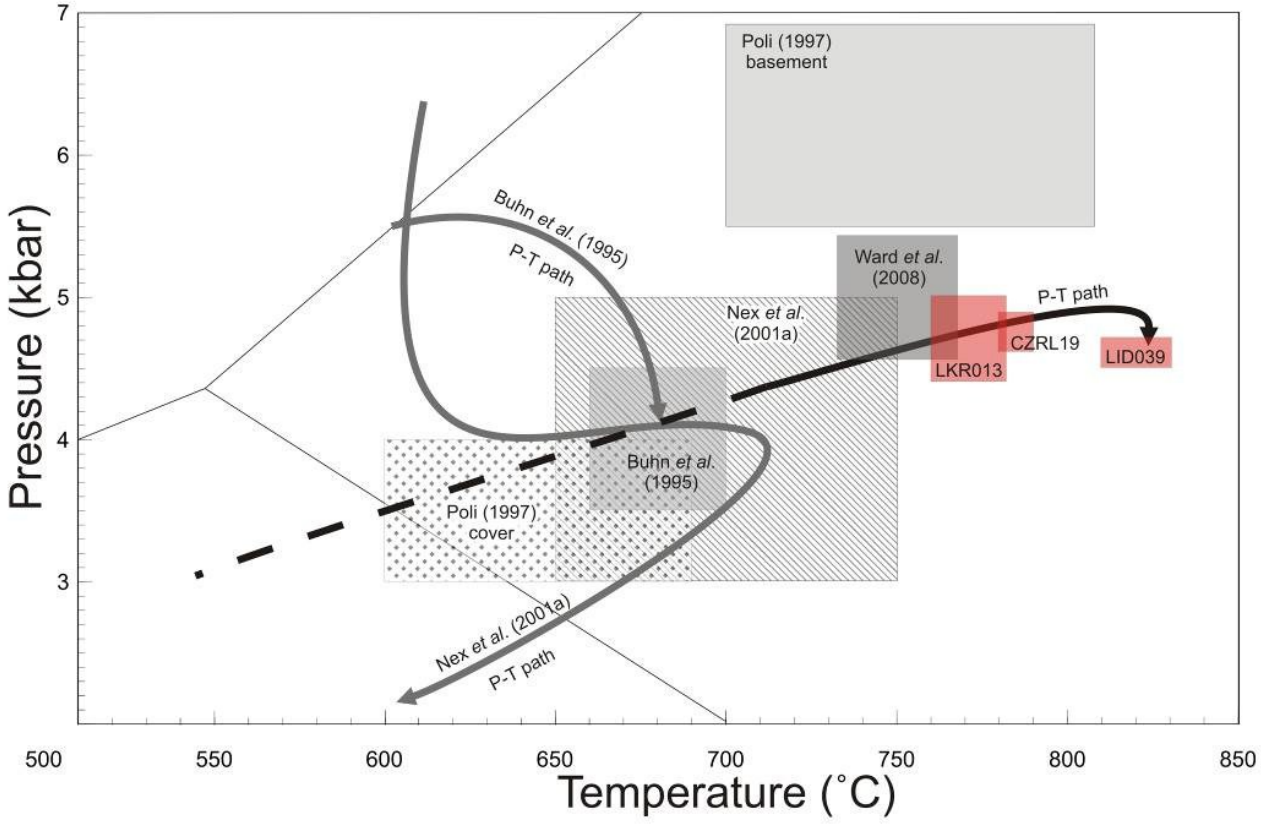

Fig. 6.38 – Peak conditions and P-T paths estimated from phase equilibria modelling, compared to previous P-T estimates for the Central Zone. Note that whilst the range of pressures previously estimated matches the pressure conditions from this study, temperatures may have previously been slightly underestimated. Note that the suggested P-T path lies in the andalusite and sillimanite stability fields, and passes through most previous P-T estimates.

The fact that samples with a wide geographic range from within the study area show similar conditions and lie on the same P-T path, corroborates the observation that no major tectonic boundaries exist across the study area. Whilst the small temperature differences between the various samples (LID039 shows a *ca*. 50 ˚C greater temperature than LKR013 and CZRL19) may be due to small temperature variations across the study area, this difference may also be due to cessation of reactions at slightly different points on the P-T path.

6.11.2 Evidence for polymetamorphism?

A number of previous workers have suggested two metamorphic episodes in the Central Zone (e.g. Kasch, 1981; Next *et al*., 2001a; Miller, 2008), with earlier M1 event preceding the M2 metamorphism that has resulted in the widespread anatexis evident in the Central Zone. The P-T path evident from mineral textures and pseudosection modelling indicates only a single episode of metamorphism, with a clockwise P-T path involving near isobaric heating to *ca.* 800 ˚C at 4.5-5 kbar, and slight decompression at the thermal peak (Fig. 6.38). In contrast to the P-T history of Buhn *et al*. (1995) and Nex *et al*. (2001a), who suggested an initial high-pressure M1 metamorphism (6-7 kbar and 600 ˚C) followed by decompression and heating to M2 metamorphism (4 kbar and 700 ˚C), there is no evidence for an earlier episode of metamorphism in any samples examined in this study. However, the early phase of higher-pressure metamorphism suggested by Nex *et al*. (2001a) was based on earlier estimates, and the geothermobarometry of Nex *et al*. (2001a) suggested a near-isobaric heating path, similar to that shown by this study. Nex *et al*. (2001a) attributed this heating to regional contact metamorphism owing to emplacement of voluminous granitoids. Whilst no petrographic evidence is found to suggest a separate M1 event distinguishable from the overall P-T path of the study area, dating of anatectic leucosomes produced during the peak of metamorphism indicates an age of 520-510 Ma for the thermal peak of metamorphism (Chapter 5). This is younger than some metamorphic ages of 540-535 Ma for the Central Zone (Jung & Mezger, 2003a, b), and is younger than anatectic red granites, which have been dated at 539-536 Ma (Briqueu *et al*., 1980; this study). These anatectic red granites are regarded as the product of melting of the Abbabis Complex during M2 metamorphism

(Miller, 2008), but since they are significantly older than M2 anatectic leucosomes (this study), they may in fact be related to an earlier M1 metamorphism. Thus, geochronological results suggest that an earlier metamorphic event may have taken place, despite their being no petrographic evidence confirming this.

6.11.3 The relationship between melting and deformation, timing of metamorphism and the P-T-d-t path of the Central Zone

Both field and petrographic evidence show that both metamorphic mineral growth and anatexis were syn-tectonic with respect to D2 deformation. Fibrolitic sillimanite inclusions in cordierite show strong fabrics, and all samples show a schistose fabric. The schistose fabric in the samples typically wraps cordierite or cordierite-spinel porphyroblasts, which may have elongate shapes, indicating that deformation lasted throughout most of the prograde heating path. Garnet, which appears to postdate cordierite and formed near the thermal peak, commonly appears to be late-tectonic to post-tectonic, and may locally truncate the schistose fabric. However, in the highest-grade sample (LID039) orthopyroxene growth and melting is seen to be roughly fabric-parallel, suggesting that deformation only ceased at or near peak conditions. Thus, S- to SE-verging D2 deformation was coeval with M2 metamorphism, in contrast to the assertion of Miller (2008) that M2 metamorphism in the Central Zone was post-tectonic.

The thermal peak of metamorphism and corresponding anatexis in the study area is dated at 520-510 Ma. This timing for metamorphism is similar to the U-Pb monazite and Sm-Nd garnet results of Jung & Mezger (2003a,b), who suggested that peak metamorphic conditions along the Khan River (adjacent to the study area) were reached between 525 Ma and 504 Ma. These ages are also similar to the 515-525 Ma ages determined for the S-type Donkerhuk Granite and the associated migmatites in its aureole (Blaxland *et al*., 1979; Haack & Gohn, 1988; Kukla, 1993). The Donkerhuk Granite is thought to have been emplaced along the Okahandja Lineament (the boundary between the Central Zone and Southern Zone) shortly after the peak of regional metamorphism. These 520-510 Ma ages for metamorphism are considerably younger than the suggested age of 535 Ma for M2

metamorphism in the Central Zone (Miller, 2008). However, metamorphic ages of 540-530 Ma have been noted for the Central Zone (Jung & Mezger, 2003a), and this age for metamorphism may correspond to a cryptic M1 metamorphism (not evident petrographically), rather than to the M2 metamorphism. In the area surrounding Karibib, Kisters *et al.* (2004) have noted NW-verging fold and thrust structures, constrained to between 560-540 Ma by the syn-tectonic mafic to granodioritic magmatism of the Goas Intrusive Suite (Jacob *et al*., 2000; De Kock *et al*., 2000; Johnson *et al.,* 2006). These structures contrast to the SE-verging structures and NE-SW extension further to the southwest, as documented in this study. In the Karibib area (approximately 100 km northeast of the study area), the 539 Ma Rotekuppe homogeneous red granite is clearly seen to be post-tectonic, whereas 536-539 Ma Red Granites dated for this study clearly have a D2 gneissic fabric and thus are pre-D2. This implies that intrusives which are post-tectonic near Karibib are pre-tectonic in the study area, and that 'post-tectonic' metamorphism dated at 535 Ma around Karibib may in fact be pre-tectonic in the study area – i.e. post-tectonic, 535 Ma metamorphism near Karibib may predate the syn-tectonic 520-510 Ma metamorphism further to the southwest. Whilst the 536-539 Ma anatectic red granites are the only record preserved in the field for a possible M1 anatectic event, a number of garnet-bearing leucogranite sheets and leucosomes were generated during the 520-510 Ma M2 event through anatexis of pelitic rocks of the Damara Supergroup. The 535 Ma metamorphic event may be related to the emplacement of the mafic to granodioritic magmas of the Goas Intrusive Suite and the Salem-type Granites at 560-540 Ma (Jacob *et al*., 2000; De Kock *et al*., 2000; Johnson *et al*., 2006). Thus, metamorphism cannot be considered uniformly pre-, syn or post-tectonic along the entire Central Zone, as clearly the timing of deformation varies along strike. The variability in the timing of deformation and metamorphism does not necessarily reflect actual differences in the timing of collision along strike, but may rather reflect preservation of different parts of the orogenic history of the Central Zone along strike. The southwestern Central Zone (i.e. the area in which this study has been conducted) is likely to have recorded the late stages of the orogen, with SE-verging deformation and NE-SW extension at 520-510 Ma coeval with low-pressure near-isobaric heating. In contrast, the area round Karibib appears to record an earlier history, with NW-verging folding and thrusting at 560-540 Ma (Kisters *et al*., 2004) recording crustal

thickening during construction of the orogen. M1 metamorphism took place at this time and led to the anatexis of the Abbabis Complex basement and formation of anatectic red granites. A summary of the P-T-t path for the Central Zone is shown in Fig. 6.39. Much of the evidence for the timing of the metamorphic history is based on geochronology and field relationships, and a combination of petrography and pseudosection modelling has provided the detailed P-T path, as well as confirming the syn-tectonic timing of M2.

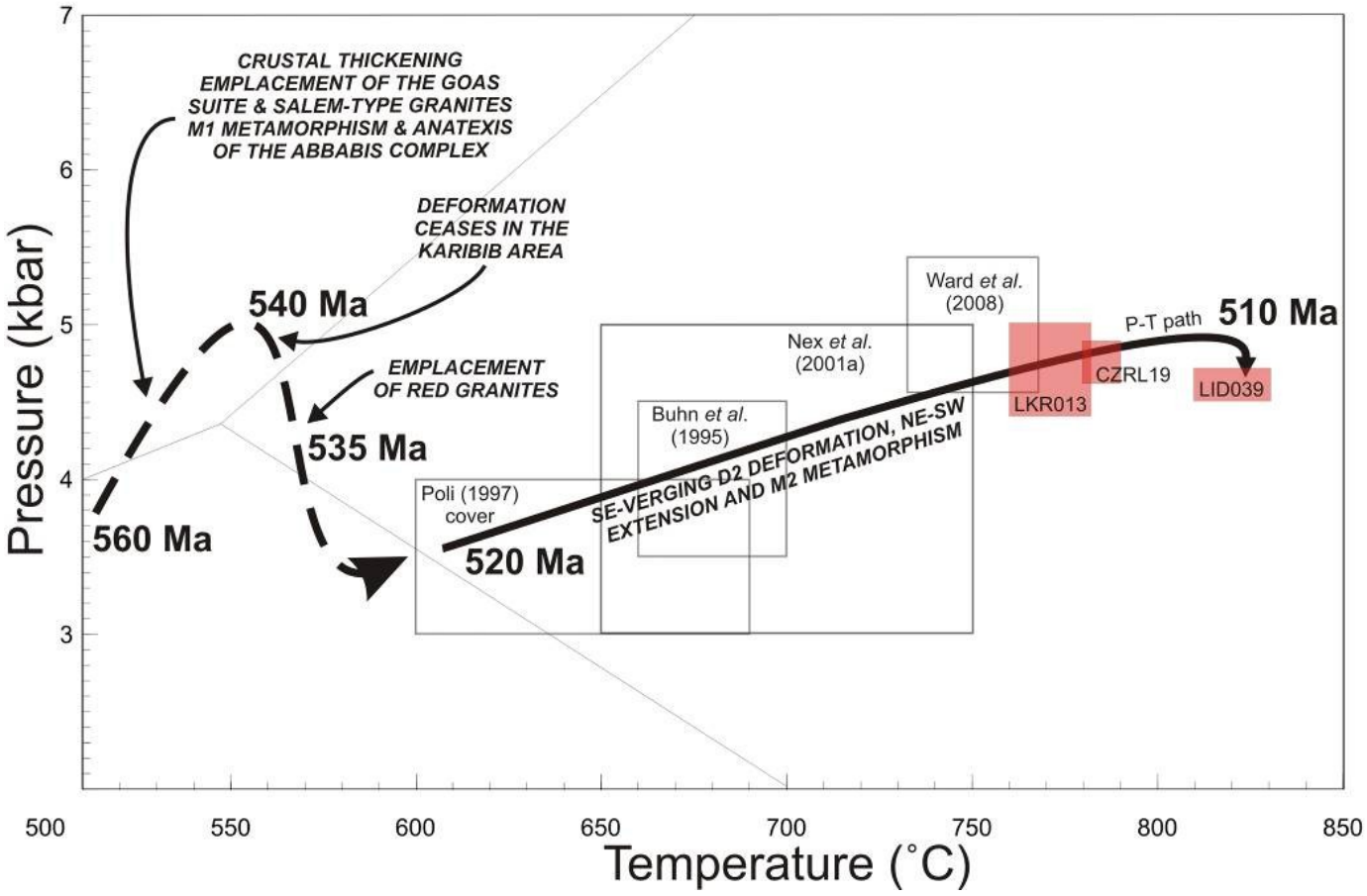

Fig. 6.39 – Summary of the P-T-path for the Central Zone. Note that although there is no petrographic evidence for M1 in the study area, geochronology suggests an early M1 metamorphic event. The early history (560-535 Ma) of the Central Zone is inferred from geochronology and the results of previous workers. Only M2 metamorphism is evident in samples from this study.

The possible preservation of an earlier phase of metamorphism at shallower crustal levels near Karibib may explain the metamorphic zoning of the Central Zone (Fig. 6.40), where metamorphic grade increases towards the southwest along the strike of the orogen (e.g. Puhan, 1983; Goscombe, 2004). The higher metamorphic grades found in the southwestern portions of the Central Zone may be the product of 520-510 Ma upper-amphibolite to granulite facies M2 metamorphism, whereas the lower grades found inland may be the result of older (*ca*. 540 Ma) lower- to mid-amphibolite facies M1 metamorphism. Changes in metamorphic grade as the result preservation of different stages of the metamorphic history in different areas could also explain the high grades recorded by Buhn *et al*. (1995) in the northeastern parts of the Central Zone. These high grades are at odds with the simple model of Puhan (1983) where metamorphic grade increases to the southwest. However, the change in temperatures along strike is shown to be gradational (Fig. 6.40) and no discrete zones of change in metamorphic grade have yet been identified.

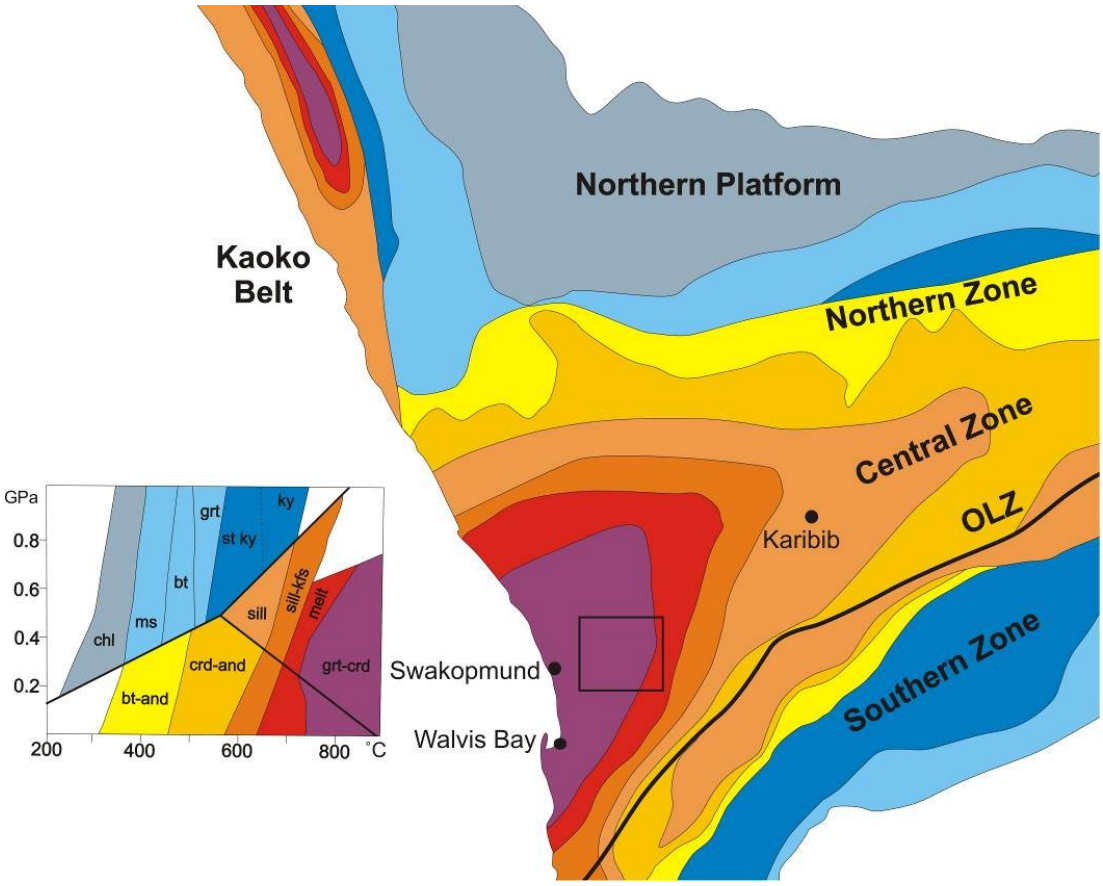

Fig. 6.40 - Simplified map of peak metamorphic assemblages in the Damara Orogen (Modified after Puhan, 1983 and Goscombe, 2004). Note the increase in peak conditions towards the southwest in the Central Zone. The change in temperature along strike in the Central Zone may be due to preservation of lower-grade (earlier) M1 metamorphism inland (near Karibib) and higher grade (younger) metamorphism towards the coast (in the study area east of Swakopmund).

6.11.4 Implications for partial melting in the Central Zone

Although it is widely established that both pelitic rocks of the Damara Supergroup as well as felsic gneisses of the Abbabis Complex experienced anatexis during Damaran metamorphism (Miller, 2008; Ward *et al*., 2008; Kisters *et al*., 2009), the nature of this melting is dependent on the peak conditions reached. Temperatures of below 750 ˚C calculated previously for the Central Zone (Poli, 1997; Nex *et al*., 2001a; Ward *et al*., 2008)

are inconsistent with the large volumes of anatectic melt evident in the Central Zone, as fluid-absent biotite-dehydration melting occurs only at temperatures in excess of 800 ˚C (Vielzeuf & Montel, 1994; Patiño Douce & Harris, 1998). This discrepancy led Ward *et al*. (2008) to propose fluid-present biotite melting to account for such large melt volumes at low temperatures. The low porosity of high-grade metamorphic rocks means that, whilst some fluid-present melting is likely to occur at the wet solidus to absorb the water-rich grain boundary fluids (Stevens *et al*., 1995), this process is unlikely to produce significant volumes of melt. In order for significant volumes of fluid-present melting to occur, large-scale fluid ingress must take place, a process that is unlikely in high-grade terranes. Indeed, the oxygen-isotopic studies of Hoernes & Hoffer (1985) suggest that no large-scale fluid ingress is evident in the migmatites and metapelites of the Central Zone, and that only locally derived fluids could result in fluid-present anatexis. Ward *et al*. (2008) suggested that local dilational sites (D2 extensional sites – Kisters *et al*., 2009) concentrated fluids and resulted in structurally localised fluid-present biotite melting. This process may be responsible for localised melting, particularly in the Kuiseb Formation metapelites that were studied by Ward *et al*. (2008), but is unlikely to account for the massive volumes of anatectic melt throughout the Central Zone. Rather, the P-T conditions seen to correspond to the observed mineral assemblages, as determined by phase equilibria modelling, indicate that temperatures of 750-850 ˚C were reached in the Central Zone. These temperatures are sufficiently high for fluid-absent biotite dehydration melting to have taken place, thereby accounting for the large volumes of melt in the Central Zone without needing to invoke fluid ingress.

6.11.5 Possible heat sources for metamorphism

The emplacement of the Goas Intrusive Suite and Salem-type Granites at 560-540 Ma, and the emplacement shortly thereafter of red granites derived from the melting of the Abbabis Complex basement, suggests that the melting of the basement may be related to the emplacement of the Goas Intrusive Suite and Salem-type Granites. It is possible that M1 metamorphism was the result of heating owing to the emplacement of these igneous rocks, in conjunction with crustal thickening (as evidenced by the NE-verging folds and thrusts

found near Karibib; Kisters *et al*., 2004). However, an alternative may be that both M1 metamorphism and the Goas Intrusive Suite and Salem-type Granites are the products of a major thermal and magmatic event which affected the crust in the Central Zone between 560 and 540 Ma.

Similarly, the emplacement of voluminous granitoids has been considered as the heat source for M2 metamorphism by Nex *et al*. (2001a). However, if crustal heating occurred early in the history of the Central Zone, M2 metamorphism may be the thermal relaxation and heating of the mid-crust following such thickening. In this case, it is possible that the voluminous granitoid magmatism which characterises the Central Zone is a product of widespread anatexis of the mid- to lower-crust as a consequence of high-grade metamorphism, rather than being the cause of this metamorphism. These ideas are discussed further in Chapter 7.

6.11.6 The relationship between metamorphism in the study area and the geodynamics of the Central Zone and the Damara Orogen.

The deformation history in the study area records SE-verging folding and non-coaxial extensional shear zones together with coaxial NE-SW extension in the southwestern Central Zone. High-grade metamorphism and anatexis of both Damaran supracrustals and pre-Damaran basement is clearly temporally associated with this extensional deformation (Ward *et al*., 2008; Kisters *et al*., 2009), and thus dating of anatectic leucosomes has constrained both high-grade metamorphism and extensional deformation to between 520 Ma and 510 Ma. P-T paths deduced from phase equilibria modelling and preserved reaction textures in metapelites indicate slight decompression at the peak of metamorphism associated with this 520-510 Ma extensional event. This is in contrast to NW-trending fold and thrust deformation in the Karibib area, which records an earlier crustal thickening event constrained by the syn-tectonic Goas Intrusive Suite and Salem-type Granites to between 560 and 540 Ma. The emplacement of the Goas Suite also appears to have caused heating of the mid-crust to produce anatectic red granites, dated at 539-536 Ma.

Thus, the thermal history of the southwestern Central Zone can be related to the overall evolution of the Central Zone, in which a record of crustal thickening, magmatism and exhumation is preserved. In order to understand the Damara Orogen as a whole, the crustal thickening and exhumation recorded in the Central Zone must be related to the other zones of the Damara Orogen, and to the Pan-African Orogeny as a whole. This will be discussed in the final chapter.

CHAPTER 7 – DISCUSSION AND CONCLUSIONS

7.1 Introduction

The aim of this thesis has been to gain a holistic understanding of the Central Zone of the Damara Orogen, and to place this understanding within the context of the Damara Orogen and the Pan-African Orogeny. Specifically, the nature, evolution and timing of deformation, metamorphism and granitoid emplacement in the Central Zone have been evaluated. In this chapter, the results of the thesis are incorporated into a revised tectonic model for the Damara Orogen, which is discussed in the context of the Pan-African Orogeny and other orogenic belts, and in the context of current thinking regarding orogenic processes. The results of this study, in conjunction with the work of various other authors, suggest a more complex tectonic history for the Central Zone than previously described. Over *ca*. 50 Myr, between 560 Ma and 510 Ma, the southern Central Zone of the Damara Orogen experienced crustal thickening and early magmatic and metamorphic events, which were followed by recumbent folding, extensional deformation and granulite-facies metamorphism in the mid-crust of the southwestern Central Zone.

In the study area, S- to SE- verging D2 folding (Chapter 3) resulted in infolding of Damara Supergroup metasediments into the Abbabis Complex, and a number of these infolds are found in the Palmenhorst Dome, an area previously considered to be exclusively underlain by Abbabis Complex gneisses. The development of a number of shear zones, and NE-SW extensional deformation also occurred during D2 deformation, which was coeval with the peak of metamorphism. U-Pb dating of granites and anatectic leucosomes (Chapter 5) showing syn-D2 relationships indicate that this deformation and (M2) metamorphism took place at *ca*. 520-510 Ma, contrary to the generally held notion that peak M2 occurred at *ca*. 535 Ma (Miller, 2008).

The southerly to south-easterly vergence for structures formed during D2 deformation in the study area is in contrast to previous suggestions that deformation in the southwestern Central Zone was SW-verging (Downing & Coward, 1981; Coward, 1983; Oliver, 1994, 1995;

Miller, 2008). Principal stress directions deduced from a conjugate set of extensional shear bands (Chapter 3 – section 3.4.3) show that σ_1 was S- to SE-plunging, and that σ_3 was near-horizontal and NE-SW trending. This NE-SW extension direction is consistent with the widely noted shallow NE-plunging mineral stretching lineation in the southwestern Central Zone (Downing & Coward, 1981; Coward, 1983; Oliver, 1994, 1995; Poli, 1997; Poli & Oliver, 2001). Rather than explaining the occurrence of SE-closing folds and a NE-SW stretching lineation through a SW-verging sheath-folding model for the Central Zone (Downing & Coward, 1981; Coward, 1983), where hinge lines of folds were rotated into parallelism with the stretching lineation, a model is suggested in which orogen-parallel extensional deformation occurred as a result of pure shear, with a S- to SE-verging component of simple shear involved in producing orogen-oblique to orogen-perpendicular deformation (Fig. 3.14). Shallow NE-plunging, upright D3 deformation followed this S- to SE-verging folding, and type-2 fold interference between km-scale recumbent to shallow N- to NW-dipping D2 folds and km-scale upright, NE-trending D3 folds has resulted in domes (which are commonly basement-cored). These domes are therefore not considered to be the result of diapirism (e.g. Kröner, 1984), km-scale sheath folds (e.g. Coward, 1983), or a single phase of progressive deformation in a constrictional field (e.g. Poli, 1997).

A number of granitoid types are found in the study area (Chapter 4); the emplacement of these show contemporaneity with D2 and D3 deformation – dating of grey granites and anatectic garnet-bearing granites constrains D2 folding to between 520 Ma and 515 Ma (Chapter 5 – sections 5.1.4, 5.1.6). Younger anatectic leucosomes are controlled by D2 shear zones and extensional structures, and date extensional deformation at *ca*. 510 Ma (Chapter 5). Thus, D2 deformation (and the M2 metamorphic peak) is dated at 520-510 Ma, and it is suggested that there may be a progression from slightly older folding through to younger shearing and extension within this time period. This age for deformation is significantly younger than the 560-550 Ma previously suggested for D2 deformation in the Central Zone (Miller, 2008). The emplacement of uraniferous leucogranites was controlled by upright D3 folding (Chapter 4 – section 4.4.3). Whilst the high-U zircons found in these uraniferous leucogranites give unreliable SHRIMP zircon ages, they (and hence D3 deformation) are

suggested to be 508 Ma in age (Briqueu *et al*., 1980), indicating that D3 followed closely on D2.

In an area *ca*. 100 km to the northeast of the study area, near Karibib, Kisters *et al*. (2004) noted NW-verging folding and thrusting, coeval with the emplacement of mafic to granitic magmas at 560-540 Ma (the Goas Intrusive Suite and the Salem-type granites). This deformation took place at lower-amphibolite facies conditions, and was suggested by Kisters *et al*. (2004) to be evidence for shallow-crustal tectonic thickening during Damaran collision. The M1 metamorphic event is suggested to have occurred at this time, and the heat source for this metamorphic event may be related to the 560-540 Ma magmatic event (see section 6.11.5). Whilst crustal thickening at shallow-crustal levels was suggested by Kisters *et al*. (2004) to be coeval with orogen-parallel extension in the mid-crust, the 520-510 Ma age for deformation in the southwestern Central Zone indicates that extension postdates 560-540 Ma crustal thickening.

Field and petrographic relationships confirm that D2 deformation in the study area was coeval with the peak of M2 metamorphism, and modelling of phase equilibria in peak metamorphic assemblages (Chapter 6) shows that rocks in the southwestern Central Zone experienced a clockwise P-T path, reaching lower granulite facies conditions (*ca*. 750-850 ˚C and 4.5-5 kbar), with a low-pressure (*ca*. 4 kbar) near-isobaric heating path for M2, and some decompression possibly occurring at the thermal peak. These temperatures exceed previous temperature estimates of 650-750 ˚C based on conventional cation exchange thermobarometry, and are sufficiently high for fluid-absent biotite melting, explaining the large volumes of anatectic melt in the southwestern Central Zone without invoking fluid-present melting (which would require large amounts of fluid ingress). The facts that pressures never exceeded 5 kbar (i.e. depths of 15-20 km) and that only minor evidence for decompression is recorded in metamorphic assemblages suggests that the rocks in the southwestern Central Zone were not buried to significant depths, and were not rapidly exhumed. D2 folding was coeval with the 520-510 Ma prograde heating path and metamorphic peak. This was followed by upright, NE-trending folding (D3 in this study) as the result of the final phases of convergence between the Congo and Kalahari Cratons at

510-505 Ma. However, this final (D3) compression does not appear to have thickened the crust – only large-scale open folding (without any evidence for thrusting) is observed, and no thermal response to such thickening is apparent. The near-contemporaneous nature of the sequential D2 and D3 deformation events may have led Poli (1997) and Poli & Oliver (2001) to see them as a single phase of progressive deformation (see discussion in Chapter 5), and the emplacement of the variety of sheeted leucogranites found in the Central Zone (e.g. Nex & Kinnaird, 1995) were emplaced largely syn-tectonically during both D2 and D3. D3 deformation was followed by the emplacement of 496-486 Ma post-tectonic A-type granitoids (McDermott *et al*., 2000), and cooling of the Central Zone to *ca*. 300 ˚C at 480-460 Ma (Gray *et al*., 2006).

7.2 A tectonic model for the Central Zone, and the evolution of the Damara Orogen

A tectonic model is presented here which details a multi-stage evolution for the Central Zone, involving subduction, continent-continent collision, crustal thickening, slab breakoff, magmatism, granulite-facies metamorphism, and exhumation of the mid-crust. The proposed model explains the multiple ages for deformation and metamorphism in the Central Zone, as well as taking into account geochemical evidence for the source of the intrusive rocks therein, and placing the Central Zone within the context of other zones of the Damara Orogen.

The earliest major deformation event recorded in the Central Zone is the NW-vergent folding and thrusting event (i.e. crustal thickening) recorded by Kisters *et al*. (2004) near Karibib, which is constrained to between 560 Ma and 540 Ma by the syn-tectonic Salem-type granites and Goas Intrusive Suite (Jacob *et al*., 2000; De Kock *et al*., 2000; Johnson *et al*., 2006). This age for folding and thrusting is similar to the widely quoted age of 555 Ma for D2 (the main phase of deformation in the Central Zone – Miller, 2008). Whilst poorly preserved or absent in the study area, the bedding-parallel D1 fabric and associated intrafolial folds locally found may be evidence for this early event.

The Goas Intrusive Suite, whilst voluminously minor, is suggested to represent a calc-alkaline, active margin plutonic suite in the Central Zone (Miller, 2008), and the mafic to ultramafic rocks have been suggested to have formed in a volcanic arc setting (De Kock, 1991). The Goas Suite is thus the only suggested record of subduction-related magmatism in the Central Zone. However, local gabbroic intrusions within this suite are suggested to be mantle-derived (Miller, 2008), and the Goas Suite is coeval with the far more voluminous Salem-type granitoids, the most abundant rock in the Damaran plutonic suite (Miller, 2008). These granitoids have field relationships which suggest that they are related to the Goas Suite (Ameglio *et al*., 2000; Jacob *et al*., 2000), and this is confirmed by the similar ages of 560-540 Ma for both the Goas Suite and Salem-type granites (Jacob *et al*., 2000; De Kock *et al*., 2000; Johnson *et al*., 2006). The Salem-type granites are considered to be crustal-melt granitoids (McDermott, 1986). Therefore, between 560 and 540 Ma, an event must have occurred which resulted minor calc-alkaline and mantle-derived mafic magmas, as well as in heating and melting of the lower crust to generate the voluminous Salem-type granites. McDermott (1986) suggested that replacement of lithosphere with hot asthenosphere may have promoted melting of the lower crust, producing calc-alkaline diorites and Salem-type granites. Whilst such upwelling of hot asthenosphere is commonly associated with back-arcs to subduction zones (e.g. Hyndman *et al*., 2005), the association of the Goas Suite and Salem-type granites with crustal thickening is contrary to the extension typically associated with back-arc regions. Furthermore, subduction in the Damara Orogen is suggested to have occurred between 595 and 575 Ma (Miller, 2008), prior to the emplacement of the Goas Suite and Salem-type granites. It is therefore suggested here that the Goas Suite and Salem-type granites are the products of asthenospheric upwelling owing to slab breakoff. This slab breakoff is likely related to the collision of the Congo and Kalahari Cratons– coeval NW-verging shallow-crustal folding and thrusting in the Central Zone was suggested by Kisters *et al*. (2004) to be related to this collision (Fig. 7.1), and this constrains collision in the Damara Belt at 560-540 Ma. However, although subduction of oceanic crust below the Congo Craton during closure of the Khomas Sea is believed to have occurred (Barnes & Sawyer, 1980), there is no record of whiteschists or eclogitic rocks in the Damara Orogen, such as are found in Pan-African rocks of the Zambezi Belt (John *et al*., 2003, 2004), *ca*. 2000 km along strike. This period of subduction is believed to have been brief (<30 Myr – Miller, 2008), and did

not result in the development of a long-lived Andean-type margin (with a >100 Ma history of subduction – Ramos, 2008), possibly explaining the paucity of subduction-related calc-alkaline magmatism in the Central Zone.

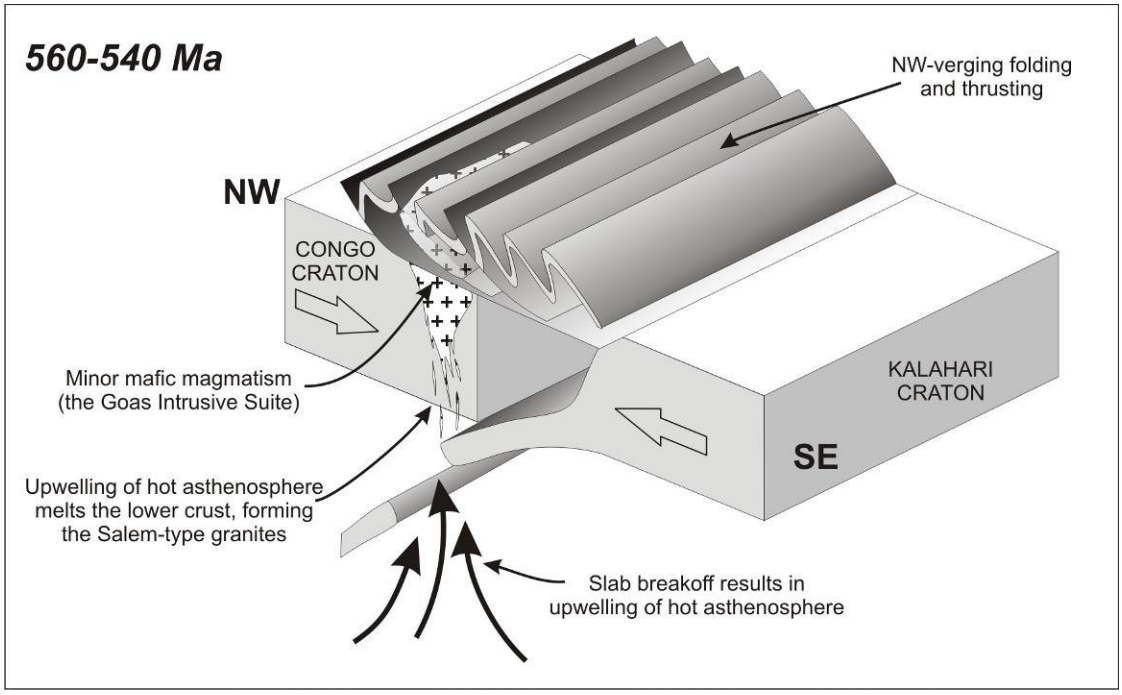

Fig. 7.1 – Schematic illustration of the early tectonic history of the Central Zone. Following a brief period of subduction, collision of the Congo and Kalahari Cratons between 560 and 540 Ma led to slab breakoff, asthenosphere upwelling and the generation of the Goas Suite, melting of the lower crust and generation of the voluminous Salem-type granites.

The *ca*. 540 Ma age suggested by Miller (2008) for collision of the Congo and Kalahari Cratons and associated closure of the Khomas Sea represents the end of the main 560-540 Ma collisional phase. In the Karibib area, the *ca*. 540 Ma Rotekuppe Granite (Jacob *et al*., 2000) cuts fabrics related to NW-verging deformation, and thus provides an age constraint on the end of this deformation (Kisters *et al*., 2004). Whilst the Rotekuppe Granite is post-tectonic, this homogeneous red granite has similar ages to red granites in the southwestern Central Zone, which have been dated at 539-535 Ma (this study; Briqueu *et al*., 1980). These red granites have a D2 gneissic fabric, indicating that they predate D2 deformation in the southwestern Central Zone. Thus, 560-540 Ma NW-verging deformation near Karibib

predates the red granites, which were later affected by 520-510 Ma D2 deformation in the southwestern Central Zone. Miller (2008) considered these red granites to be the product of near total in-situ melting, a hypothesis which has been shown to be highly unlikely (see section 4.2), although the peraluminous composition of these red granites, together with numerous xenoliths of sillimanite gneiss, suggests that the red granites are derived from anatexis of metasedimentary material. Inherited zircons in these red granites indicate that they are sourced from partial melting of a *ca*. 1 Ga protolith (see Chapter 5). Whilst this source could be the Abbabis Complex basement (1-1.1 Ga ages obtained by Kröner *et al*., 1991), most workers have shown that the Abbabis Complex is consistently *ca*. 2 Ga in age (this study; Jacob *et al*., 1978, 2000; Tack *et al*., 2002), and is thus too old to be a source for the red granites. Similarly, zircons in 520 Ma grey granites have *ca*. 2 Ga Hf-isotope model ages, whilst zircons in the Abbabis Complex have *ca*. 3 Ga model ages, indicating that grey granites are unlikely to be sourced from melting of Abbabis Complex material. Mesoproterozoic to Neoproterozoic Kalahari Craton crust, subducted/underthrust below the Congo Craton and heated to high grades during Damaran collision (Fig. 7.2), is suggested as a possible alternative source for many of the Damaran granitoids, including the red granites and the grey granites. However, the isotopic signatures of many of the Damaran granitoids may be mixtures of both older and younger source material, and are not conclusive (Chapter 5).

Whilst Miller (2008) considered the peak of M2 metamorphism (and associated anatexis) in the Central Zone to be post-tectonic and constrained at 535 Ma by the red granites, the coeval relationship between peak metamorphism and D2 deformation in the southwestern Central Zone has been recognised by other workers (e.g. Ward *et al*., 2008; Kisters *et al*., 2009), and the timing of the peak of metamorphism has been previously constrained to between 525 Ma and 505 Ma (Jung & Mezger, 2003a, 2003b). Such ages for metamorphism ages that are similar to the 520-510 Ma suggested here for syn-D2 M2 metamorphism in the study area. It is therefore suggested that 540-535 Ma represents the age of M1 metamorphism in the Central Zone, and that the anatectic red granites are the product of this metamorphic event. Upwelling of hot asthenosphere following slab breakoff is suggested as a possible heat source for M1, and thus the Goas Suite, Salem-type granites

and red granites are all the products of this major thermal event early in the history of the Central Zone.

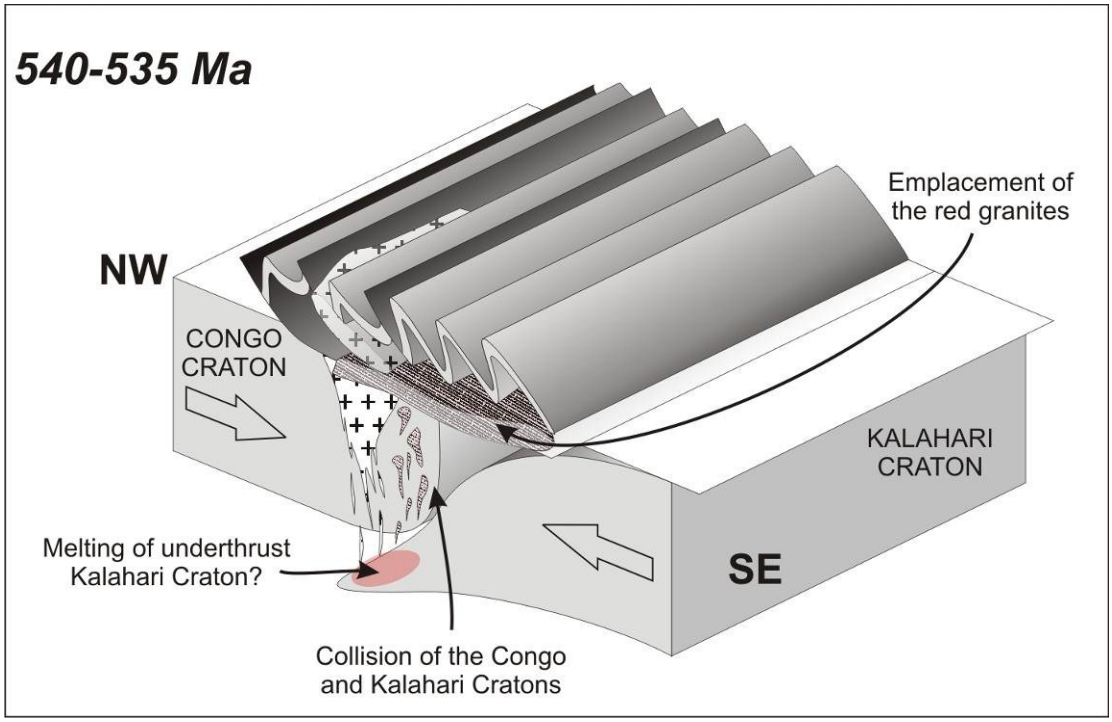

Fig. 7.2 – Schematic illustration of the collision between the Congo and Kalahari Cratons. During collision, Kalahari Craton material is underthrust below the Congo Craton. Anatectic red granites emplaced at the contact between the Abbabis Complex and Damara Supergroup are formed from melting of this underthrust material. Anatexis may have resulted from residual heat following asthenosphere upwelling between 560 and 540 Ma.

In contrast to shallow-crustal deformation and amphibolite-facies metamorphism near Karibib, which occurred between 560 and 540 Ma, D2 (the main phase of deformation) in the southwestern Central Zone took place at lower granulite-facies conditions between 520 and 510 Ma. S- to SE-verging non-coaxial D2 deformation led to the development of km-scale recumbent folds, ductile shear zones were formed during D2 at or near the interface between the Abbabis Complex and the Damara Supergroup, and NE-SW extension was also associated with D2. Field relationships indicate that grey granites and garnet-bearing leucogranites were emplaced during SE-verging D2 folding, and they have U-Pb zircon and monazite ages of 520-514 Ma. Anatectic leucosomes found in D2 shear zones and extensional shear bands constrain the timing of D2 shearing and extension in the

southwestern Central Zone to *ca*. 510 Ma, indicating a progression from folding to shearing and extension during D2. Phase equilibrium modelling (see Chapter 6) shows that the Central Zone experienced a prograde heating path at low pressures of 4.5-5 kbar, and possible slight decompression at the peak of metamorphism (temperatures of *ca*. 800 °C. However, the lack of large-scale extensional structures related to D2 deformation and the generally recumbent nature of deformation, combined with only minimal evidence for decompression indicates that no rapid extensional exhumation took place in the Central Zone. Maximum pressures of 5 kbar suggest that the Central Zone was not buried to greater than mid-crustal depths (15-20 km). However, >20 km of uplift of the Central Zone relative to the Southern Zone (Miller, 1979; Corner, 1983) may indicate that, during collision of the Congo and Kalahari Cratons, the crust in the Central Zone was thickened by *ca*. 20 km (the amount of uplift is generally similar to the amount of thickening in an orogenic belt – England & Thompson, 1984). Since collision (and hence crustal thickening) in the Damara Orogen appears to have occurred at *ca*. 560-540 Ma, heating of the mid-crust (with associated 520-510 Ma granulite-facies metamorphism, S- to SE-verging deformation and NE-SW extension) in the Central Zone appears to have postdated this thickening by at least 20 Myr (Fig. 7.3). Note that, although exhumation may be expected during this time period, and NE-SW extension is associated with this, the NW-SE convergence between the Congo and Kalahari Cratons had not yet ceased. Indeed, convergent plate motion need not have stopped immediately following collision; in the Himalayan Orogeny, the Indian Plate continued to move towards the Asian Plate *ca*. 50 Myr after the onset of collision (Paul *et al*., 2000). Whilst deformation and prograde metamorphism are likely to have occurred in the southwestern Central Zone in the interval between 540 and 520 Ma, the lack of associated granitoids, the subsequent metamorphic peak, and the progressive nature of D2 deformation means there is little record of this. During the metamorphic peak, anatectic garnet-bearing granites were generated from localised anatexis of metapelitic lithologies, whilst grey granites were likely to have a deeper source, possibly from Kalahari Craton material underthrust/subducted below the Congo Craton and heated. The wide variety of sheeted leucogranites and pegmatites found in the Central Zone also appear to have been generated during or immediately post D2 and the peak of metamorphism between 520 and 510 Ma, with uraniferous leucogranites emplaced slightly after the thermal peak. The low-

pressure prograde P-T path suggests that crustal thickening and burial of the Central Zone was not significant, and that there must be an additional heat source to explain the granulite-facies metamorphism.

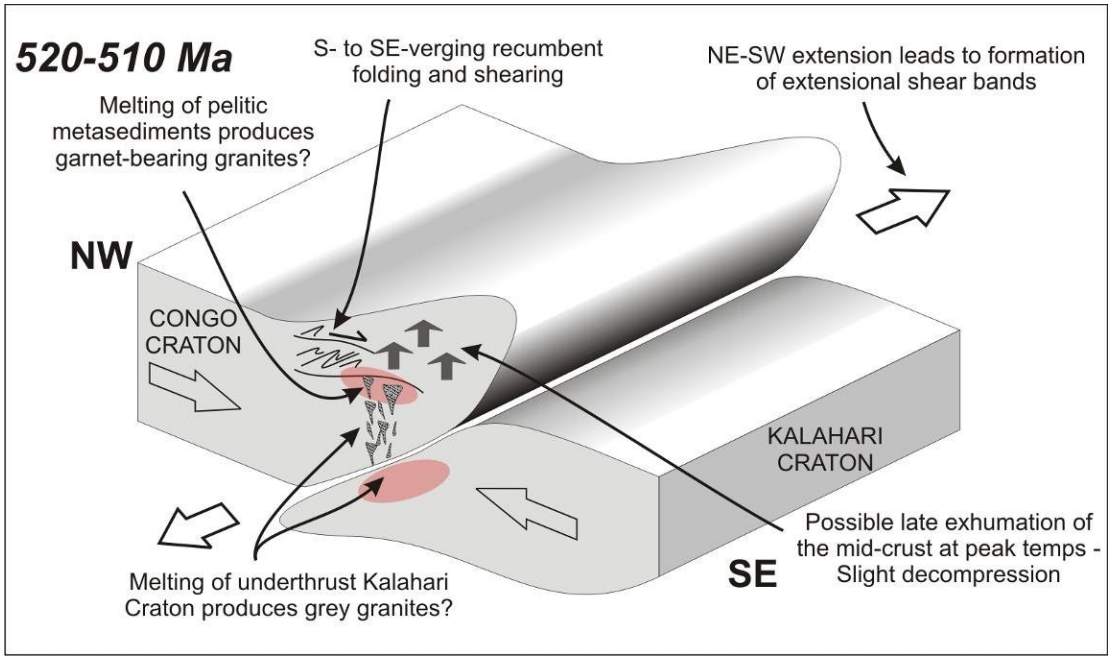

Fig. 7.3 – Schematic illustration of the mid-crust in the Central Zone. Following collision and ca*. 20 km of crustal thickening, the mid-crust is heated to granulite facies conditions, producing anatectic garnet-bearing granites. Melting of the Kalahari Craton at greater depths produces the grey granites. S- to SE-verging folding and shearing, and NE-SW extension may be related to exhumation.*

Following the SE-verging deformation, NE-SW extension (D2) and granulite-facies metamorphism in the southwestern Central Zone was an episode of NE-trending upright folding (D3). In contrast to the strong vergence noted for D2 deformation, only minor southeasterly vergence is noted for upright D3 structures, and D3 deformation is considered here to be largely coaxial relative to D2. The orientation of principal stress directions during D2 deformation indicates that SE-verging deformation and NE-SW extension occurred in a stress field with a subhorizontal σ_3 extension direction, and a moderately-plunging σ_1 extension direction. This has been shown to be inconsistent with the upright folding developed during D3, where a subhorizontal, orogen-perpendicular σ_1 compression and a

subvertical σ_3 are the likely stress directions (see Chapter 3). The large-scale upright folds produced during D3 thus occurred in a horizontally compressive tectonic regime (Fig. 7.4), during the final phases of convergence between the Congo and Kalahari Cratons. Geochronology of uraniferous leucogranites, which are seen to be either post-tectonic (Miller, 2008) or controlled by D3 deformation and are thus syn-D3 (this study), indicates that these granites were emplaced at *ca*. 508 Ma (Briqueu *et al*., 1980). This means that recumbent D2 deformation, which occurred between 520 Ma and 510 Ma, was immediately followed by upright D3 folding, which had taken place by 508 Ma. The cause of such a switch in principal stress directions is unclear. Removal of 10-20 km of material by erosion during exhumation may have affected the stress field by reducing vertical stress by between 0.3 and 0.6 GPa, (following which σ_1 would be subhorizontal, and owing to stresses from the final stages of convergence between the Congo and Kalahari Cratons, σ_3 would be then be subvertical) leading to the upright D3 folding observed (Fig. 7.4). However, although >20km of uplift of the Central Zone relative to the Southern Zone has previously been suggested (Miller, 1979; Corner, 1983), only minor decompression at the thermal peak has been noted (Chapter 6), and cooling of the Central Zone or a change in boundary conditions related to regional tectonics (the effect of collision in the Gariep belt) may have contributed to the observed change in stress directions between D2 and D3. An additional possibility is that during the thermal event which resulted in M2 metamorphism, the entire crust was weakened, allowing for extensional collapse of the orogen and the formation of subhorizontal structures. Upon cooling, the crust would have returned to a more rigid state, resulting in upright D3 structures. Although field relationships illustrate that D2 and D3 were distinct deformation events in terms of overprinting relationships and styles of deformation, the timing of upright D3 folding does appear to be nearly coeval with the late stages of D2 deformation (at *ca*. 510 Ma).

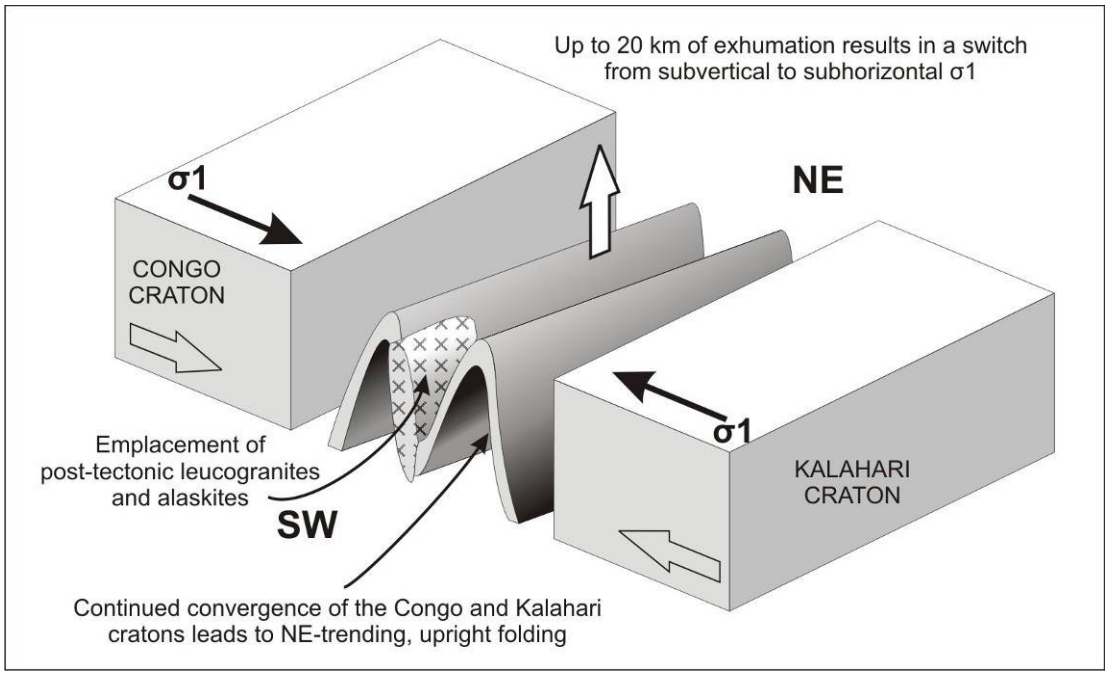

Fig. 7.4 – Following 10 km of exhumation in the Central Zone, a shift in stress directions to subvertical σ_3 and subhorizontal σ_1 would result in orogen-parallel upright D3 folding. However, there is no evidence for rapid exhumation between D2 and D3, and the cause of this shift in stress directions is unclear.

Following upright D3 folding, an episode of dextral (Blaine, 1977; Steven *et al*., 2008) brittle strike-slip movement is locally recorded in the Central Zone, which is suggested to have occurred late in the tectonic history of the Damara Orogen (Blaine, 1977; Basson & Greenway, 2004; Steven *et al*., 2008), and is termed D4. Much of this strike-slip movement took place along major lineaments (Blaine, 1977; Steven, 1993) and is possibly associated with a rotation of the subhorizontal σ_1 from NW-SE during D3 to WNW-ESE during D4 (Steven *et al*., 2008). Late-tectonic movement along D4 lineaments is thought to be an important mineralising process (Basson & Greenway, 2004; Corner, 2008). In the vicinity of the Rössing Dome, D4 deformation appears to have controlled the emplacement of uraniferous granitoids (Basson & Greenway, 2004), indicating that it may have occurred very shortly after or was coeval with upright D3 deformation. This suggests a change in the rheology of the crust from ductile (associated with D2 and D3 deformation) to brittle (associated with strike-slip D4 movement) shortly after 510 Ma (due to cooling of the mid-

crust during exhumation of the Central Zone), and cooling ages of 500-460 Ma have been obtained for the Central Zone (Blaxland *et al.*, 1979; Hawkesworth *et al.*, 1983; Kukla, 1993; Gray *et al*., 2006; Miller, 2008), similar to 500-493 Ma age for titanites from this study (see section 5.1.2) and from the Navachab Mine near Karibib (Jacob *et al.*, 2000). These 500-493 Ma ages are interpreted as the age for hydrothermal alteration and Au-mineralisation in the Central Zone (Miller, 2008), which is also related to late-orogenic strike-slip movement (Steven, 1993; Dirks, 2000), and thus D4 strike-slip deformation generally appears to post-date D3 deformation by *ca*. 10 Myr.

Whilst late strike-slip movement along the Omaruru and Okahandja lineaments is thought to be dextral (Blaine, 1977; Steven, 1993), sinistral strike-slip movement has been noted along the NNE-trending Welwitschia Lineament, and has been considered transtensional (Basson & Greenway, 2004). Steven *et al*. (2008) suggested that dextral strike-slip movement was related to a change in the σ_1 direction from NW-SE to WNW-SSE (Fig. 7.5), and NNE-trending structures (e.g. the Welwitschia Lineament) may be second-order structures, along which sinistral movement took place (Fig. 7.5).

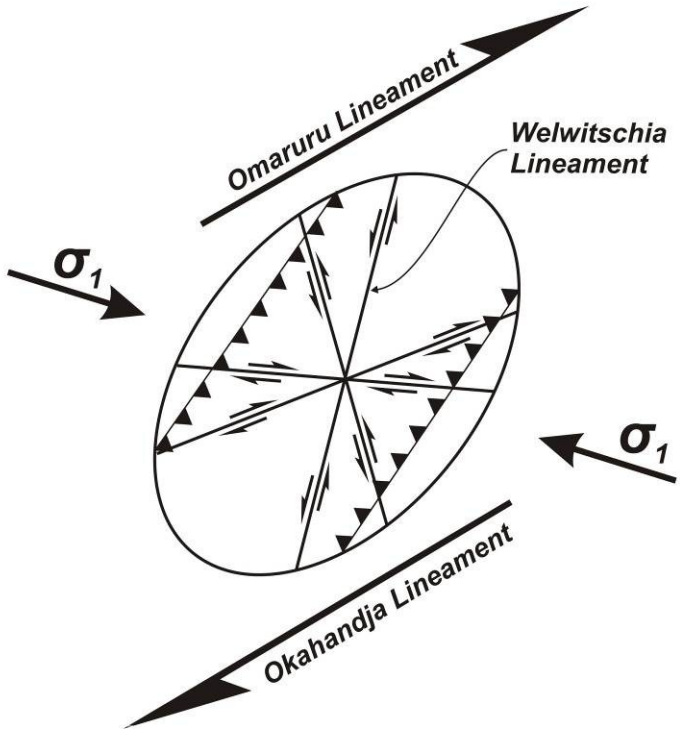

Fig. 7.5 – Schematic diagram illustrating the relationship between σ_1, dextral movement along the Omaruru & Okahandja Lineaments, and sinistral movement along the NNE-trending Welwitschia Lineament (modified after Steven et al*., 2008).*

A P-T-t path for the Central Zone (Fig. 7.6) shows the clockwise evolution typical of a collisional orogen with thickened crust (e.g. Harley, 1989). However, the pressures (4.5-5 kbar) for prograde heating (as recorded by metamorphic assemblages) indicate that although the crust in the Central Zone was thickened, the rocks exposed at in the study area do not appear to have been buried to depths greater than 20 km. Many granulite terrains elsewhere are characterised by horizontal structures formed at or near the thermal peak, followed by slow cooling without any evidence for rapid exhumation (Sandiford, 1989). The presence of recumbent (D2) structures associated with peak M2 metamorphism, and the lack of major decompression in the Central Zone appears analogous to this general situation. Sandiford (1989) ascribes such horizontal prograde structures to bulk crustal thinning during extensional collapse. Whilst the details of the early P-T history of the Central Zone (related to slab breakoff and the onset of collision) are still unclear, the timing of D2 deformation and granulite-facies M2 metamorphism is clearly recorded in the study area, and these postdate 560-540 Ma crustal thickening, and are suggested to be related to exhumation. However, the heat sources for granulite facies metamorphism need to be more carefully investigated.

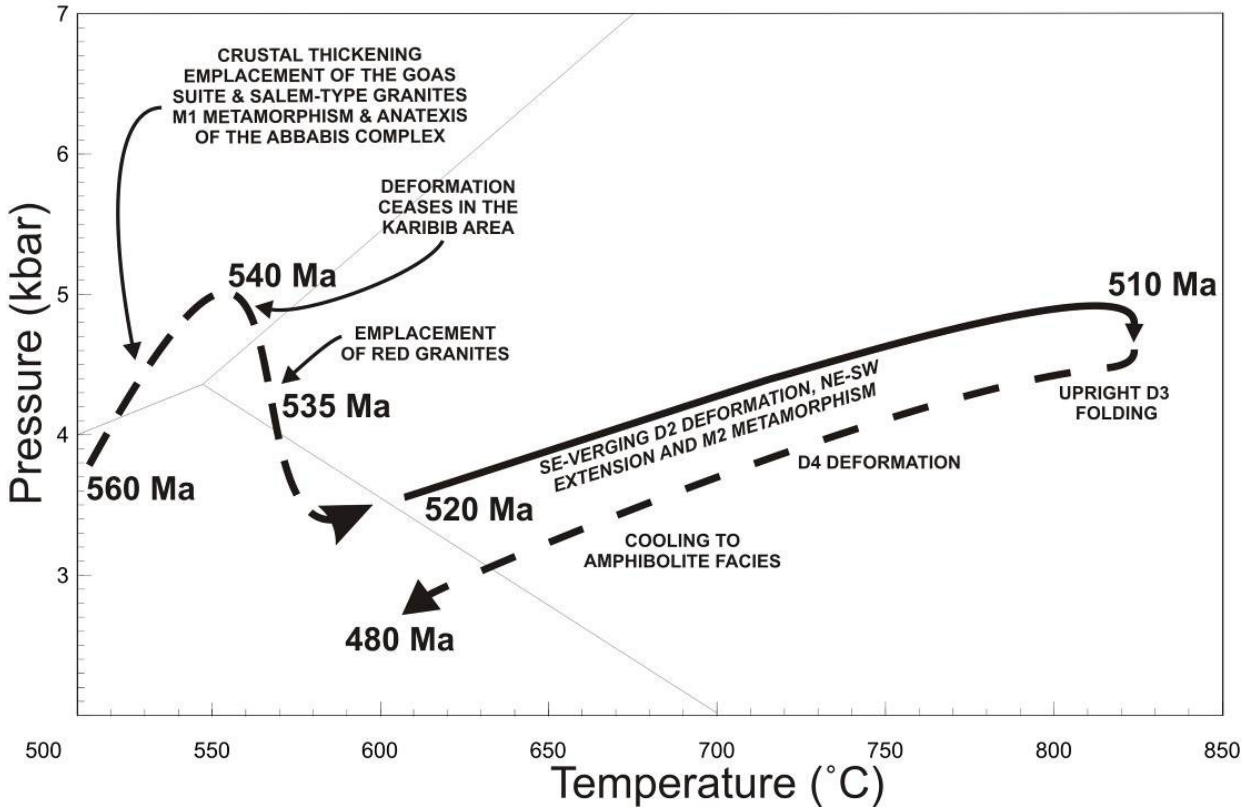

Fig. 7.6 – A proposed P-T-t path for the Central Zone, involving an early subduction-related episode (for which detailed P-T-t relationships have not yet been established) followed by recumbent folding and heating to lower granulite-facies conditions. Continued D3 compression may have prevented rapid exhumation. Although cooling ages constrain the timing of cooling in the Central Zone, the amount and timing of uplift (i.e decompression) is poorly defined.

7.2.1 Heat sources for metamorphism

In the proposed model, a brief period of subduction preceded collision between the Congo and Kalahari Cratons between 560 and 540 Ma. M1 metamorphism and the generation and emplacement of minor mafic to calc-alkaline intrusive rocks and more voluminous granitic magmas in the Central Zone occurred during this period. Replacement of lithosphere with hot asthenosphere is suggested as a heat source for this early event, with consequent heating and melting of the lower crust providing a source for the Salem-type granites. The low pressure P-T path for M2 suggests that crustal thickening was not significant, and deep

burial appears an unlikely explanation for M2. However, the fact that the metamorphic peak occurred *ca*. 20 Myr after thickening at 540 Ma is consistent with estimates for the delay between crustal thickening and the onset of erosion and exhumation (Richardson & England, 1979; England & Thompson, 1984). Typically, 35 km of crustal thickening is required for granulite-facies metamorphism without invoking additional heat sources (England & Thompson, 1984). However, the suggested P-T path for the southwestern Central Zone, with only *ca*. 20 km of crustal thickening (Fig. 7.7), shows that an additional heat source may be required for the upper-amphibolite- to granulite-facies conditions to have been reached at much lower pressures (i.e. depths) than average granulites (Bohlen, 1987; Harley, 1989), or those predicted by theoretical models for the heating of the crust due to thermal relaxation (England & Thompson, 1984).

The addition of mafic magma to the lower crust is a commonly invoked source of additional heat (Harley, 1989), and various mechanisms include thinned continental crust recently underplated by basaltic magma, magmatic areas accreted onto the continental margin, or syn-to post-thickening accretion of mantle-derived magmas (Harley, 1989). Whilst addition of mafic magma to the crust is associated with M1, this (the Goas Suite) is voluminously minor, and is suggested to be the product of slab breakoff. In the Central Zone, there are no mafic rocks emplaced younger than *ca*. 550 Ma, and all the intrusions younger than 540 Ma are crustal-melt granitoids (McDermott, 1986). Thus, it appears unlikely that mafic magmatism is a viable heat source for M2 metamorphism. Nex *et al*. (2001a) suggested that the heat source for regional M2 metamorphism in the Central Zone was the numerous granitoids emplaced at this time. However, none of the granitoids in the study area show contact metamorphic aureoles, suggesting that magmas forming the granites did not move very far upward after melting, and these granites are likely to be an effect of the metamorphism, rather than its cause (e.g. Chamberlain & Sonder, 1990). Therefore, a heat source is required for the Central Zone that does not involve the addition of magma.

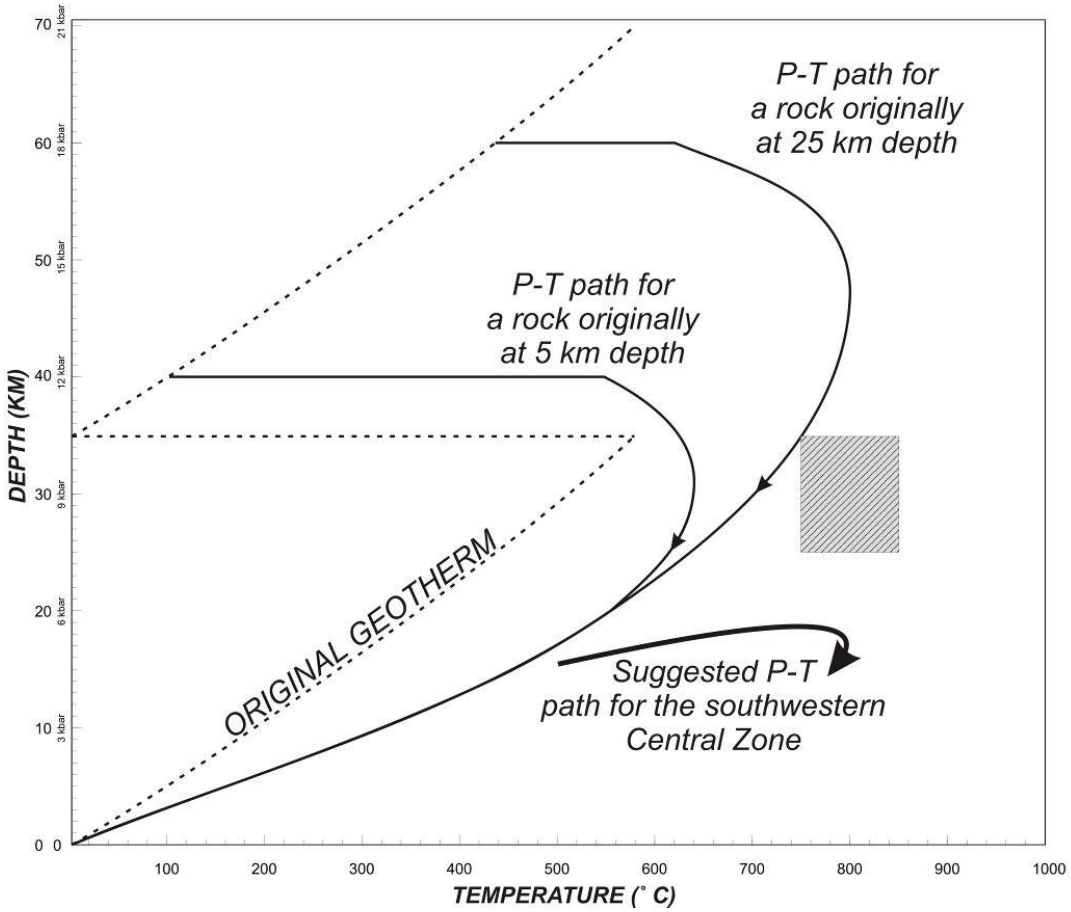

Fig. 7.7 – Depth vs. temperature diagram illustrating the suggested P-T path for the Central Zone in comparison with the model of England & Thompson (1984), and the average granulite field (shaded rectangle) of Bohlen (1987). Pressure estimates are based on assuming 3.33 km/kbar.

Jamieson *et al*. (1998) suggested that tectonic redistribution of high-heat-producing material during collision (i.e. subduction of crustal rocks) can generate temperatures high enough for granulite facies metamorphism. The model ages for Damaran granites suggest that they may have been sourced from subducted Kalahari Craton material, and the mechanism of Jamieson *et al*. (1998) may be applicable in the case of the Damara Orogen. A related possibility is that the crust that was thickened during collision was more radioactive (and thus higher heat-producing) than typical continental crust. The idea that the thickening of crust enriched in heat-producing elements may result in granulite-facies

metamorphism and crustal melting, without invoking the addition of mafic magma to the crust, has been suggested for the Acadian orogeny (Chamberlain & Sonder, 1990), and for the Mount Painter Province (McLaren *et al*., 2002, 2006). Typical estimates for heat production in the upper continental crust range from 1.5 μWm^{-3} to 3 μWm^{-3} (England & Thompson, 1984; Jamieson *et al*., 1998; Perry *et al*., 2006), whereas the Mount Painter Province has heat production values of up to 16 μWm^{-3} (McLaren *et al*., 2002, 2006). Rather than addition of magmatic heat, the thermal energy generated by the thickened U- and Th-rich crust produced the high-grade rocks and anatectic granites observed in these areas (Chamberlain & Sonder, 1990; McLaren *et al*., 2002, 2006). It is possible to calculate heat flow for Abbabis Complex rocks in the study area by using analyses of these rocks (Appendix 1). Since only the decay series of ^{238}U, ^{235}U, ^{232}Th and ^{40}K contribute significantly to heat production, and radiogenic heat production of a rock can be expressed according to the equation of Rybach (1976):

$$H(\mu W.m^{-3}) = 10^{-5}\rho(9.52c_U + 2.56c_{Th} + 3.48c_K)$$

Where ρ is density (2650 $kg.m^{-3}$ for granite), c_U and c_{Th} are in ppm, and c_K is in wt %. Table 7.1 shows heat production for a number of samples of Abbabis Complex rocks and Damaran granitoids from the study area. Average heat production values of 2.83 $\mu W.m^{-3}$ are calculated for Abbabis Complex gneisses, with values of up to 5.75 $\mu W.m^{-3}$. These values are within the range of heat production values for typical upper continental crust (England & Thompson, 1984). However, Damaran granitoids all show elevated average heat production values of between 5.13 $\mu W.m^{-3}$ (red granites) and 25.66 $\mu W.m^{-3}$ (uraniferous leucogranites), with one uraniferous leucogranite samples reaching up to 56.15 $\mu W.m^{-3}$. Similarly, previous work on the basement rocks in the Central Zone shows that they have heat production rates of 2.6 $\mu W.m^{-3}$ to 3.7 $\mu W.m^{-3}$ (Haack *et al*., 1983), and basement lithologies on the Kalahari Craton have rates of 2.9 $\mu W.m^{-3}$ to 3.4 $\mu W.m^{-3}$, whereas some Damaran granitoids show high rates of heat production: Salem-type granites give up to 19.7 $\mu W.m^{-3}$ and red granites up to 31 $\mu W.m^{-3}$ (Haack *et al*., 1983).

The high heat production values for Damaran granitoids have been previously suggested to be a major contributor to the high-grade metamorphism in the Central Zone (Haack *et al*., 1983). However, it should be noted that basement rocks do not appear to have significantly elevated heat production values, and any additional heat producing elements were therefore emplaced in the crust with the granitoids. In particular, the granites emplaced early in the tectonic history of the Central Zone (the Salem-type and red granites) would have had significant time periods over which to generate heat, whereas younger granites would have been emplaced into rocks which were already hot. It is suggested here that addition of heat-producing elements to a slightly thickening of crust may have contributed to the low-pressure granulite facies metamorphism observed in the Central Zone. Possible alternatives to this which do not require addition of mafic magma to the lower crust include the thinning of the crust and sub-continental lithosphere owing to orogenic collapse following crustal thickening, or localised asthenospheric upwelling related to the position of the southwestern Central Zone near a major oroclinal bend. Thinning of the crust related to orogenic collapse is a mechanism that has been invoked to explain granulite facies metamorphism, particularly where no rapid exhumation is apparent (Sandiford, 1989). Delamination of the sub-continental lithospheric mantle related to the formation of the Iberian-Armorican orocline has been suggested as a heat source for the post-tectonic magmatism and metamorphism that characterises the high-grade portion of this orogen (the Iberian Massif - Gutiérrez-Alonso *et al*., 2011, and asthenospheric upwelling related to slab breakoff has already been suggested as a heat source for M1 metamorphism). It is possible that, following collision of the Congo and Kalahari cratons, detachment of the Congo Craton subcontinental lithosphere may have occurred, and subsequent upwelling of the asthenosphere contributed to heating of the mid-crust. Indeed, seismeic tomography (Begg *et al*., 2009) shows that in the upper 200 km of the earth, S-wave velocities are lower beneath the crust of northern Nambia and southern Angola (i.e. the Congo Craton) than that in southern Nambia and northwest South Africa (i.e. the Kalahari Craton) which may imply that the sub-continental lithospheric mantle below the Congo Craton has been thinned or removed.

Table 7.1 – Heat production values for rocks from this study

Sample	Rock type	U (ppm)	Th (ppm)	K_2O (wt %)	HPU (μWm^{-3})
LKR002	Red granite	11.7	65.7	7.10	8.06
LKR003	Red granite	3.31	53.0	7.56	5.13
LKR010	Red granite	3.30	29.2	8.49	3.59
LKR017	Red granite	2.00	39.8	7.17	3.86
LKR018	Red granite	2.88	55.4	7.76	5.20
LCZ11-2	Red granite	5.29	70.2	8.48	6.88
CZRL14	Red granite	5.34	52.8	6.54	5.53
CZRL15	Red granite	1.63	24.0	8.06	2.78
	Average red granite				**5.13**
LID010	Grey granite	4.65	28.0	2.43	3.30
LID011	Grey granite	6.88	71.27	4.28	6.97
LID015	Grey granite	1.65	27.2	3.84	2.61
LID017	Grey granite	2.13	37.17	4.63	3.49
LID019	Grey granite	1.66	24.80	6.00	2.65
LID020	Grey granite	3.72	25.52	4.00	3.04
LID029	Grey granite	5.32	64.9	5.49	6.25
LID030	Grey granite	4.74	70.54	4.85	6.43
LID031	Grey granite	4.37	41.97	5.43	4.45
LHA002	Grey granite	9.71	168	5.62	14.38
LHA003	Grey granite	5.27	13.9	2.11	2.47
LHA004	Grey granite	3.42	33.6	3.35	3.45
LHA005	Grey granite	2.20	11.8	2.00	1.54
LHA010	Grey granite	4.34	16.9	3.05	2.52
LHA011	Grey granite	4.20	24.1	3.66	3.03
LHA012	Grey granite	22.5	75.1	7.27	11.44
LKR005	Grey granite	4.04	143	5.79	11.23
LKR006	Grey granite	6.73	32.0	5.70	4.39
LKR007	Grey granite	1.48	24.5	3.06	2.32
LKR015	Grey granite	2.12	26.0	6.11	2.86
LKR020	Grey granite	10.5	341	5.95	26.35
LCZ2-2	Grey granite	2.34	18.9	3.10	2.16
LCZ2-3	Grey granite	5.36	38.8	7.09	4.63
LCZ6-2	Grey granite	7.46	155	5.84	12.92
LZC6-4	Grey granite	4.03	111	6.52	9.16
LCZ8-1	Grey granite	1.72	6.74	1.41	1.02
LCZ13-2	Grey granite	1.91	130	7.29	9.96
LCZ15-1	Grey granite	1.95	33.3	5.13	3.22
CZRL5	Grey granite	1.81	137	6.55	10.39
CZRL12	Grey granite	3.21	56.7	7.84	5.37
LCZ7-2	Grey granite	3.99	4.07	3.98	1.65
	Average grey granite				**5.99**
LRV001	Uraniferous leucogranite	105	10.6	7.48	27.83
LCZ7-1	Uraniferous leucogranite	41.0	11.8	1.42	11.28
LCZ14-1	Uraniferous leucogranite	210	41.2	5.03	56.15
LVA-1	Uraniferous leucogranite	15.1	45.3	5.50	7.38
	Average uraniferous leucogranite				**25.66**
LID024	Garnet-bearing leucogranite			5.08	0.47
LID038	Garnet-bearing leucogranite	3.69	8.20	5.34	1.98
	Average garnet-bearing leucogranite				**1.22**
LCZF-1	Pink pegmatitic granite	9.20	57.1	10.89	7.20
LCZF-2	Pink pegmatitic granite	55.3	15.5	4.18	15.39
	Average pink pegmatitic granite				**11.29**
LID012	Abbabis Complex gneiss	1.41	20.95	5.32	2.27
LID016	Abbabis Complex gneiss	2.80	21.60	1.92	2.35
LID036	Abbabis Complex gneiss	2.39	16.65	1.77	1.89
LID041	Abbabis Complex gneiss	7.73	26.82	2.05	3.96
LID045	Abbabis Complex gneiss	2.56	20.00	1.94	2.18
LKR008	Abbabis Complex gneiss	4.07	61.7	5.74	5.75
LKR023	Abbabis Complex gneiss	1.45	16.8	4.45	1.92
CZRL28	Abbabis Complex gneiss	2.34	18.6	5.07	2.32
	Average Abbabis Complex gneiss				**2.83**

The formation of the Kaoko-Damara-Gariep orocline is related to the timing of collisional events in the Pan-African Orogeny, an issue about which there remains considerable contention (see section 7.5 below). These heat sources are suggested as possibilities at this stage, and the resolution of which (if any) is most applicable to the Central Zone remains to be tested through more detailed thermal modelling of the Central Zone, and further work on the timing and nature of Pan-African collision. Nonetheless, the low-pressures recorded in the Central Zone do indicate that the low-pressure, high-temperature metamorphic grades observed cannot be explained through simple crustal thickening and thermal relaxation, and additional heat is required.

7.2.2 Preservation of different domains in the Central Zone

The discrepancy initially apparent between the 555 Ma D2 and 535 Ma post-tectonic M2 metamorphism suggested by Miller (2008), and the 520-510 Ma D2 and syn-tectonic M2 suggested here (but supported by the data of Jung & Mezger, 2003a, 2003b; Ward *et al*., 2008 and Kisters *et al*., 2009) appears to be related to the preservation of different portions of the orogenic history in different geographic areas within the Central Zone. In the area around Karibib, the early (560-540 Ma) history of the Central Zone is preserved, whilst the late (520-510 Ma) history of exhumation of the mid-crust is preserved in the study area and elsewhere in the southwestern Central Zone. Whilst it has been widely recognised that deeper crustal levels are exposed closer to the Atlantic coastline in the southwestern Central Zone, and shallower crustal levels further inland near Karibib (e.g. Kisters *et al*., 2004), the diachroneity of deformation, metamorphism and magmatism between these areas has not been previously recognised, and Kisters *et al*. (2004) considered shallower-crustal orogen-perpendicular shortening in the Karibib area to have been accommodated by coeval orogen-parallel ductile flow of rock at mid-crustal levels. So-called 'post-collisional' granites from the Ida Dome dated by Tack *et al*. (2002) at 542 ± 6 Ma were considered as evidence that deformation was contemporaneous across the Central Zone at both mid-crustal and shallow crustal levels, at 560-540 Ma (Kisters *et al*., 2004). However, these granites were noted to have a fabric parallel to the main tectonic fabric (Tack & Bowden, 1999) and, thus, are not conclusively post-tectonic. They were considered by Tack &

Bowden (1999) as potentially analogous to 535 Ma red granites at Goanikontes, which are considered here to predate D2 deformation in the study area.

Whilst it is evident that various tectonic events with different ages and characteristics are preserved in different areas in the Central Zone, what is unclear is how these areas relate to one another. As no major tectonic boundaries are evident between the study area and Karibib, it is not apparent whether earlier deformation is preserved only in a localised klippen, or whether younger deformation progressively overprints older deformation as one moves from the shallow crust (near Karibib) through to the mid-crust (in the study area). Resolution of this issue will require more detailed mapping, metamorphic petrology and geochronology along strike in the Central Zone.

7.3 The Timing of Events in the Other Zones of the Damara Orogen

The history suggested above is the product of orogenic processes not restricted to the Central Zone, and which should be reflected in other zones of the Damara Orogen (Fig. 7.8). On the Northern Platform, NW-trending structures along the western margin and doubly-plunging anticlines along the southern margin are related to late-stage compressional deformation in the Kaoko Belt (Goscombe *et al*., 2003a; Miller, 2008), and are likely to be older than *ca*. 550 Ma (Miller, 2008). Younger ENE-trending crenulations and upright, E- to ESE-trending km-scale cylindrical folds with horizontal axes are attributed to the high-angle convergence of the Congo and Kalahari Cratons after the cessation of the main phase of deformation in the Kaoko Belt (Goscombe *et al*., 2003a).

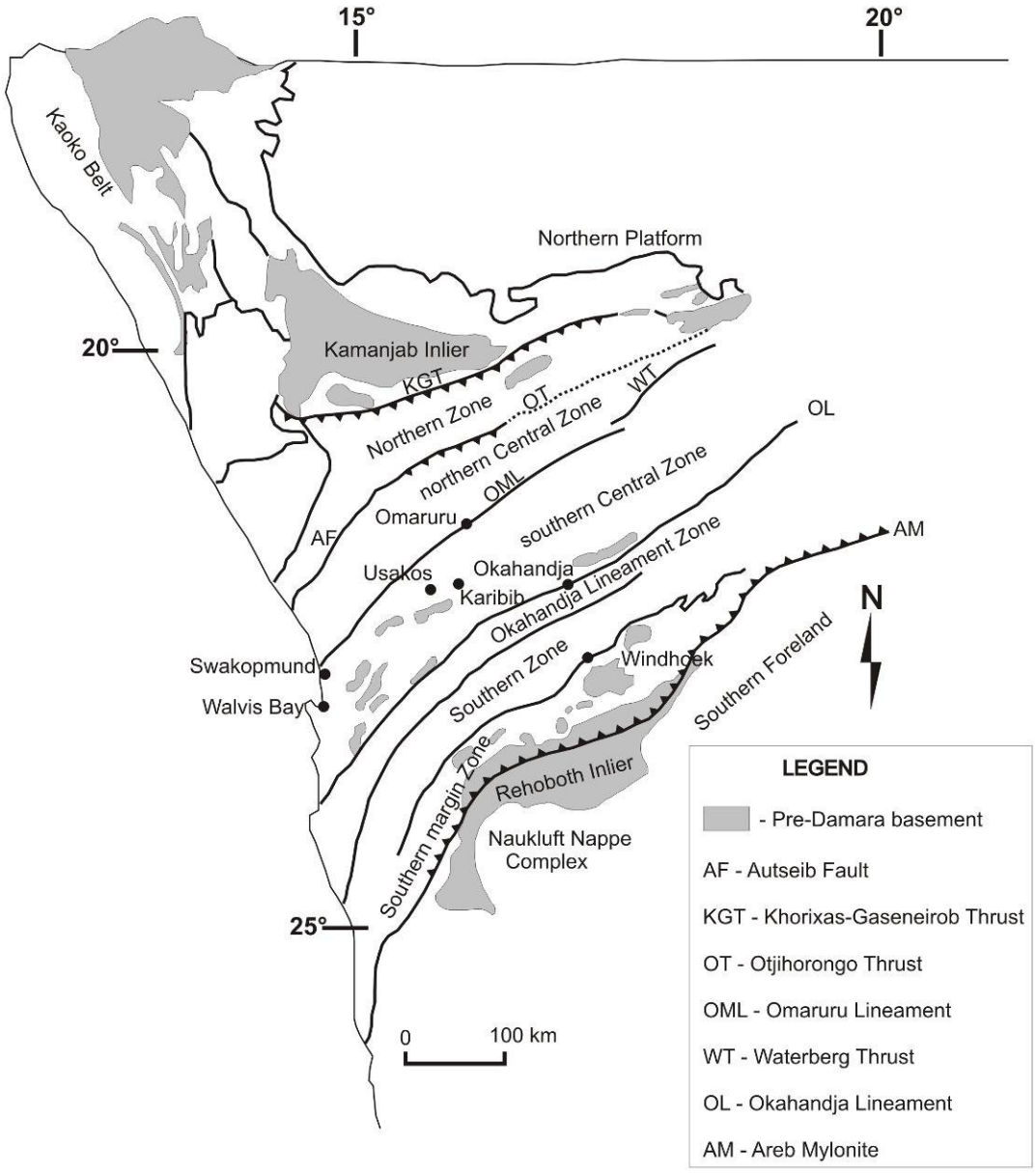

Fig. 7.8 – Map of zones of the Damara Orogen, with major thrusts and lineaments shown. Modified after Miller (1983) and Miller (2008).

In contrast, the Northern Zone does not appear to have any major (N-S trending) structures related to collision in the Kaoko Belt (between the Congo and Rio de la Plata Cratons), and E-W trending structures here are thought to be related to collision of the Congo and

Kalahari Cratons (i.e. to the Inland or Damara Belt – Goscombe *et al*., 2003a). A 535-530 Ma age has been suggested for deformation in the Northern Zone (Goscombe *et al*., 2004), based on a 530 ± 3 Ma date for the syn-tectonic Footspoor Pluton (Seth *et al*., 2000), although there is a paucity of other zircon age data for the Northern Zone (Goscombe *et al*., 2004). Since deformation in the Northern Zone has been related to N-S directed shortening (Passchier *et al*., 2002; Goscombe *et al*., 2003a, b), and there is no record of extension, it is suggested here that structures may be related to the onset of collision and crustal thickening in the Damara Belt (dated elsewhere at 560-540 Ma in the Damara Belt), rather than 520-510 Ma exhumation. The validity of this hypothesis may be tested by better constraints on the ages of pre-, syn- and post-tectonic intrusions in the Northern Zone.

The northern Central Zone differs from the southern Central Zone in the level of exposure; whilst Abbabis Complex and Nosib Group rocks are exposed in the southern Central Zone, only upper Swakop Group rocks are exposed in the northern Central Zone, which is dominated by the schists of the Kuiseb Formation (Miller, 2008). However, the deformation history for the northern Central Zone appears similar to that for the southern Central Zone; a 560-550 Ma (Haack *et al*., 1980; Miller, 2008) D1 event produced isoclinal, intrafolial folds and a regional fabric (Klein, 1980), and was largely overprinted by 514 ± 11 Ma (Haack *et al*., 1980) recumbent folding and thrusting during D2 deformation (Klein, 1980; Miller, 2008). This was followed by lateral shortening and the formation of domes during D3 deformation (Klein, 1980). As with the southern Central Zone, D2 was coeval with the peak of regional metamorphism (Klein, 1980; Haack *et al*., 1980), and the formation of anatectic leucogranites. However, although the nature and timing of deformation in the northern Central Zone has been described in detail, there is no mention made as to the vergence or general orientation of structures in this area (see Klein, 1980 and Miller, 2008), and this could form the focus for future work.

Both the Southern and Southern Margin Zones are characterised by 560 to 550 Ma (Miller, 2008) SE-verging thrusts, tight to isoclinal asymmetric folds and a NW-dipping regional penetrative fabric (Sawyer, 1981; Hoffmann, 1983; Kukla, 1992), coeval with low-temperature, high-pressure metamorphism (Sawyer, 1981; Kasch, 1981). A decrease in the

intensity of fabrics upwards in the stratigraphy of the Southern Zone (Sawyer, 1981; Kasch, 1988; Kukla, 1992) has led to an interpretation of the Southern Zone as a forearc trench, with deposition occurring during subduction, and ongoing deformation during deposition leading to more intense, complex deformation at lower stratigraphic levels (Miller, 2008). Folding and thrusting of pre-Damaran basement with Damaran metasediments in the Southern Margin Zone indicates crustal shortening (Hoffmann, 1983). The preservation of kyanite in the Southern Zone (Miller, 2008) indicates higher-pressure, lower-temperature conditions than in the Central Zone, and syn-tectonic (Sawyer, 1981; Kukla, 1992) peak metamorphic conditions of 7-10 kbar and 550-600 ˚C (Sawyer, 1981; Kasch, 1981) are recorded in the Southern Zone.

However, in contrast to the Central Zone, there is no record of 520-510 Ma deformation in the Southern and Southern Margin Zones, and the 525-505 Ma (Blaxland *et al*., 1979, Haack & Gohn, 1988; Kukla, 1993) Donkerhuk Granite is considered post-tectonic (Miller, 2008). The growth of andalusite and sillimanite in the aureole to this granite (Hoffer, 1977) indicates post-tectonic metamorphic conditions of up to 700 ˚C at 4.5 kbar (Sawyer, 1981), lower than pressures for earlier metamorphism, and indicating exhumation of the Southern Zone between 550 and 525 Ma. However, the precise timing of this exhumation is unclear.

The Nama Group (Fig. 7.9), deposited on an extensive peneplain on the Southern Foreland of the Damara Orogen, comprises over 3 km of distal orogenic flysch (the lower Kuibis Subgroup and overlying Schwarzrand Subgroup) and molasse (the upper Fish River Subgroup) sediments. Sediments were derived from the uplifted Damara Orogen to the north and from the Gariep Orogen to the west (Grotzinger & Miller, 2008). Deposition in the Nama basin began between 555 and 550 Ma (Miller, 2008), coeval with the onset of collision in the Damara Orogen, whilst the uppermost ash layer dated in the Nama Group (539.4 ± 1 Ma – Grotzinger *et al*., 1995) is coeval with the end of collision and crustal thickening. This ash layer lies near the top of the Schwarzrand Subgroup flysch, indicating that deposition of the upper molasse portion of the Nama Group (i.e. the Fish River Subgroup) must have occurred after *ca*. 540 Ma, and is likely related to erosion and exhumation of the uplifted orogen. The Nama Group succession was deformed by Damaran

deformation along the northwestern and western margins of the basin (Gresse & Germs, 1993; Grotzinger & Miller, 2008), and was affected by *ca*. 530 Ma regional metamorphism, (Ahrendt *et al*., 1977; Horstmann *et al*., 1990).

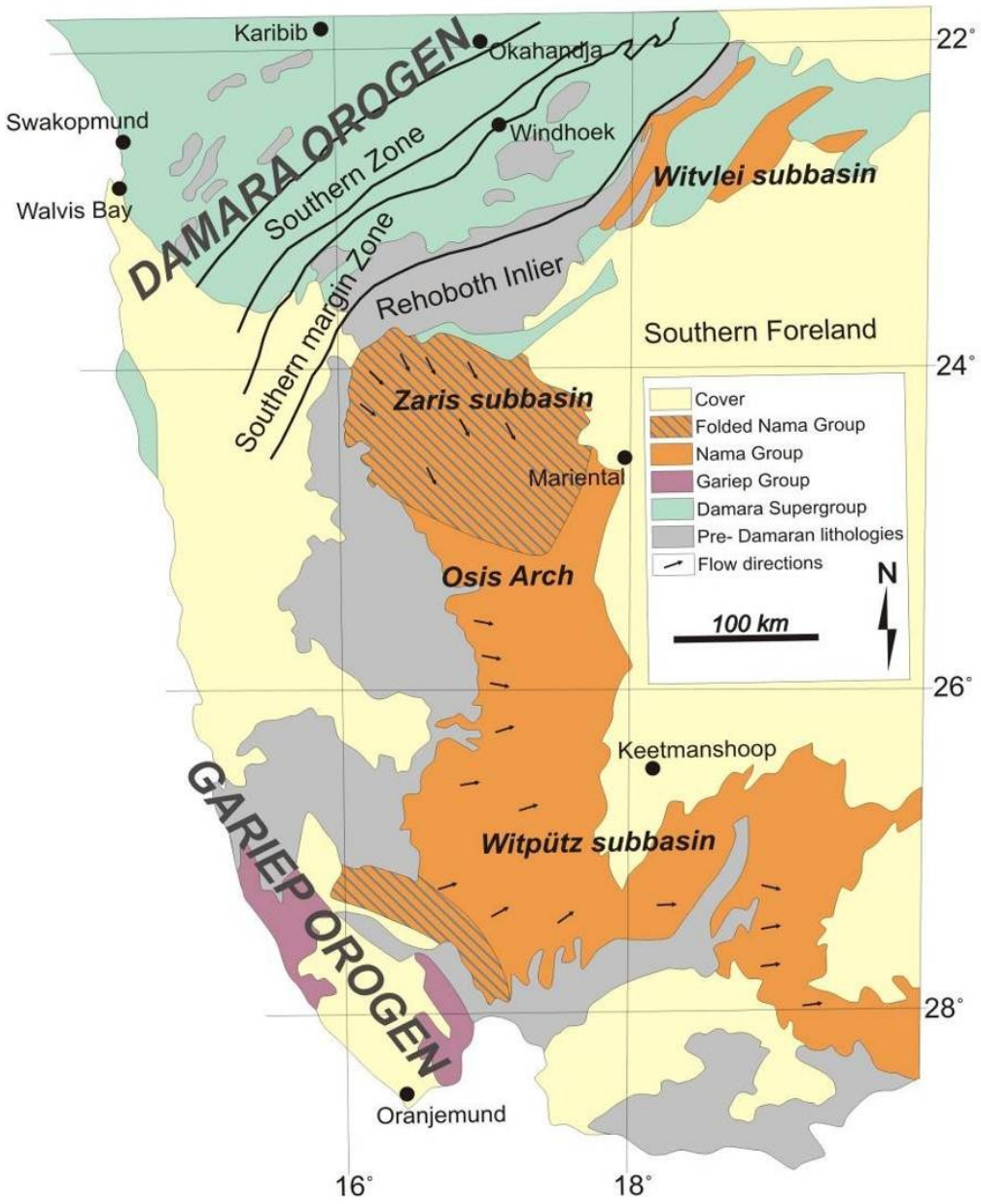

Fig. 7.9 – Location of the Nama Foreland basin, the Zaris, Witvlei and Witpütz subbasins, and their relationships to the Damara Orogen in the north and Gariep Orogen in the west. Note that flow directions indicate that sediments in the Zaris subbasin were derived from the north whilst those in the Witpütz subbasin were derived from the west. Modified after Grotzinger & Miller (2008) and Germs (1983).

The Naukluft Nappe Complex is a thin-skinned allochonous nappe complex comprising seven units, and its development is linked to the structural evolution of the Southern Margin Zone and the deposition of the Nama Group (Miller, 2008). Two formations (the Zebra River and Klipbok River Formations) make up the stratigraphy of the Naukluft Nappe Complex, and are considered correlatives of the lower Nama Group (Hoffmann, 1989). Thrusting and imbrication of nappes in the Naukluft Nappe Complex is thought to have begun at the same time as D1 thrusting in the Southern Margin Zone, and is suggested to have occurred between 550 and 540 Ma (Miller, 2008), with metamorphism and development of a slaty cleavage dated at 547-532 Ma (Ahrendt *et al*., 1977), coeval with M1 metamorphism (which Miller, 2008 considers post-tectonic M2 metamorphism). The timing of nappe formation in the Naukluft Nappe Complex links it to crustal thickening and the collision between the Congo and Kalahari Cratons. However, final emplacement of the Naukluft Nappe Complex over a distance of >80 km (Hartnady, 1978) only took place at 495 Ma (Ahrendt *et al*., 1977; Miller, 2008), and may be related to extension and exhumation of the orogen.

Thus, the effects of collision and exhumation in the Damara Orogen between 560 and 500 Ma are not simply preserved in the Central Zone, but are apparent across the entire orogen and its flanks. Deposition of flysch sediments in the Southern Zone (Hureb Formation) and Southern Foreland (lower Nama Group) took place from *ca*. 560 Ma, related to the onset of collision (Fig. 7.10A). Crustal thickening is evident at this time in the Central Zone, coeval with slab breakoff, melting of the lower crust and emplacement of the Goas Suite and Salem-type granites. Following collision of the Congo and Kalahari Cratons, the uplifted Central and Southern Zones were eroded, and deposited as molasse in the Nama Group (Fig. 7.10B). The leading edge of the Kalahari Craton was subducted and melted, and the red granites were emplaced in the Central Zone. Between 520 and 510 Ma, a thermal event led to granulite-facies metamorphism in the Central Zone, which was exhumed at this time (Fig. 7.10C). Anatexis led to the generation of the 525-505 Ma S-type Donkerhuk granite, which was emplaced post-tectonically in the Southern Zone, following *ca*. 12 km of exhumation, but was coeval with extensional D2 deformation, granulite facies metamorphism and

widespread crustal melting in the southwestern Central Zone (Fig. 7.10C). This S-type granite may be the result of melting deeper in the crust associated with high-grade metamorphism in the Central Zone (Fig. 7.10C). During the final stages of convergence between the Congo and Kalahari Cratons between 510 and 490 Ma, upright D3 deformation took place in the northern and southern Central Zone, with thrusting along the bounding faults to the northern Central Zone (Fig. 7.10D). Post-tectonic pegmatites in the northern Central Zone have been dated at 492 ± 11 Ma (Steven *et al*., 1993), indicating that D3 may have been coeval throughout the Central Zone, although younger ages of 480-460 Ma have been suggested for D3 deformation in the northern Central Zone (Haack *et al*., 1980). The emplacement of uraniferous leucogranites (sourced from melting of U-enriched Congo or Kalahari Craton) also occurred at this time in the southern Central Zone.

Fig. 7.10 (following page) – Schematic diagram illustrating the evolution of the Damara Orogen, with major events in each of the zones of the orogen. A: Subduction of the Kalahari Craton below the Congo Craton, NW-verging folding and thrusting in the Central Zone coeval with asthenosphere upwelling, melting of the lower crust and emplacement of the Goas Suite and Salem-type granites. Syn-sedimentary SE-verging deformation in the Southern Zone and SE-verging thrusting in the Southern Margin Zone occurred at this time, as did deposition of the lower Nama Group. B: Collision of the Congo and Kalahari Cratons at 540 Ma led to subduction and melting of the leading edge of the Kalahari Craton to form the red granites. Uplift and exhumation of the Southern Zone occurred at this time, and led to deposition of the upper Nama Group between 540 and 530 Ma. C: Thermal relaxation in the Central Zone from 530 Ma led to granulite-facies metamorphism of the mid-crust between 520 and 510 Ma. The S-type Donkerhuk Granite was emplaced into the Southern Zone, leading to contact metamorphism. The northern Central Zone may have been downfaulted relative to the southern Central Zone at this time. D: The final stages of convergence led to upright folding in the Central Zone and thrusting along the bounding faults to the northern Central Zone, and strike-slip deformation along major structures occurred at this time. Uraniferous granites were emplaced in the southern Central Zone (and may be derived from melting of uranium-enriched Kalahari or Congo Craton.

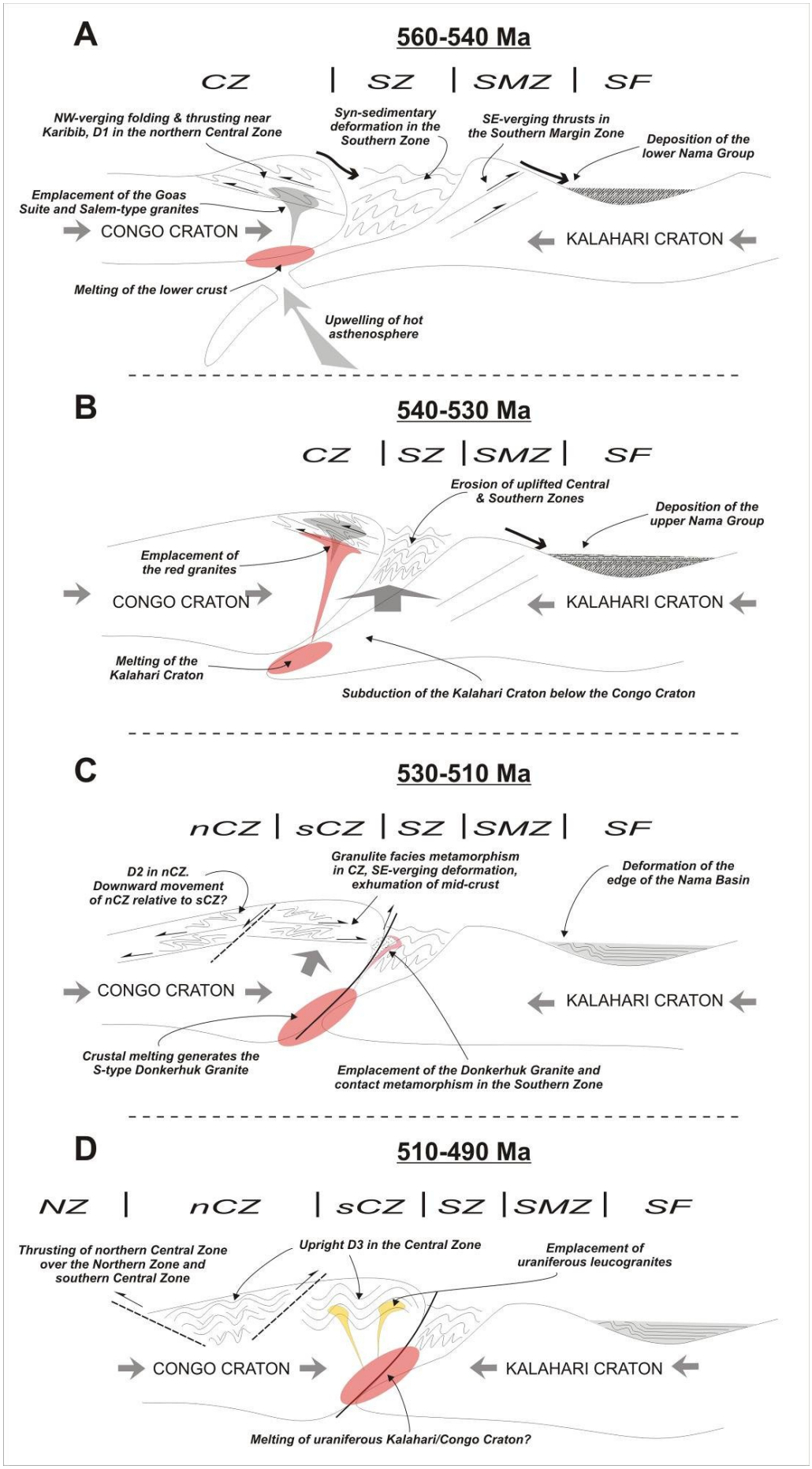
A
560-540 Ma
CZ | SZ | SMZ | SF
NW-verging folding & thrusting near Karibib, D1 in the northern Central Zone
Syn-sedimentary deformation in the Southern Zone
SE-verging thrusts in the Southern Margin Zone
Deposition of the lower Nama Group
Emplacement of the Goas Suite and Salem-type granites
CONGO CRATON
KALAHARI CRATON
Melting of the lower crust
Upwelling of hot asthenosphere
B
540-530 Ma
CZ | SZ | SMZ | SF
Erosion of uplifted Central & Southern Zones
Deposition of the upper Nama Group
Emplacement of the red granites
CONGO CRATON
KALAHARI CRATON
Melting of the Kalahari Craton
Subduction of the Kalahari Craton below the Congo Craton
C
530-510 Ma
nCZ | sCZ | SZ | SMZ | SF
D2 in nCZ. Downward movement of nCZ relative to sCZ?
Granulite facies metamorphism in CZ, SE-verging deformation, exhumation of mid-crust
Deformation of the edge of the Nama Basin
CONGO CRATON
KALAHARI CRATON
Crustal melting generates the S-type Donkerhuk Granite
Emplacement of the Donkerhuk Granite and contact metamorphism in the Southern Zone
D
510-490 Ma
NZ | nCZ | sCZ | SZ | SMZ | SF
Thrusting of northern Central Zone over the Northern Zone and southern Central Zone
Upright D3 in the Central Zone
Emplacement of uraniferous leucogranites
CONGO CRATON
KALAHARI CRATON
Melting of uraniferous Kalahari/Congo Craton?

The sequence of events described above give a detailed chronology of events in the Damara Belt, and allow for comparisons with other Pan-African mobile belts (see section 7.4 below) However, whilst general correlation of events across the orogen appears possible, a number of questions remain regarding the specific timing of some of these events . For example, the northern Central Zone is thought to be a pop-up structure (Miller, 2008), bounded to the north by the Otjohorongo Thrust, and separated from the southern Central Zone by the Omaruru Lineament and Waterberg Thrust (Fig. 7.8). Uplift of the northern Central Zone along these structures is suggested to have occurred due to continued compressive stresses late in the tectonic history of the Damara Belt, during D3 (Miller, 2008). However, metamorphic grades in the northern Central Zone (greenschist to lower-amphibolite facies – Miller, 2008) are lower than in the southern Central Zone, and this juxtaposition of shallower crustal levels (lower grades) in the northern Central Zone with deeper crustal levels (higher grades) in the southern Central Zone means that there must have been significant upward movement of the southern Central Zone relative to the northern Central Zone. Miller (2008) ascribes this to the northern Central Zone being a down-faulted back-arc basin, formed between 490 Ma and 460 Ma (i.e. post-dating thrusting along the Otjohorongo Thrust and Omaruru Lineament). However, an alternative hypothesis may be that exhumation of the southern Central Zone between 520 and 510 Ma resulted in uplift of the southern Central Zone relative to the northern Central Zone, and explains the absence of any preserved back-arc sediments in the northern Central Zone, which should be expected in the of case back-arc extension (Miller, 2008). Additionally, geophysical imaging of the Omaruru Lineament (Ritter *et al*., 2003) suggests that it was a thrust fault, at least for the later stages of its movement, and that back-arc extension late in the orogenic history of the Central Zone is unlikely. However, the validity of these hypothetical models remains to be tested, especially as no rapid decompression is recorded by metamorphic P-T paths. Evidence for extensional deformation along the Omaruru Lineament and Waterberg Fault should be expected – this extension should be post-thrusting (490-460 Ma) for the back-arc extension model of Miller (2008) to be valid, but should down-faulting of the northern Central Zone relative to the southern Central Zone be related to exhumation of the southern Central Zone, normal movement along the Omaruru Lineament and Waterberg Fault would be geochronologically constrained to 520-510 Ma. Key evidence on the nature

and timing of both deformation and metamorphism in the poorly studied northern Central Zone is missing, and future work on this should help to clarify the tectonic history of the Damara Belt.

7.4 The Damara Orogen in the Context of the Pan-African Orogeny

The events outlined above for the Damara Belt form only a small part of the Pan-African orogeny, which assembled the Gondwana Supercontinent (Kennedy, 1964). Understanding the assembly of Gondwana requires a detailed understanding of the timing of deformation, metamorphism and magmatism across this entire orogen. The Damara Belt lies along strike from the Zambezi Belt and Lufilian Arc, and adjacent to the Gariep and Kaoko belts (Fig. 7.11). The timing of events in these areas of the Pan African must be reviewed before placing them in the context of the assembly of Gondwana.

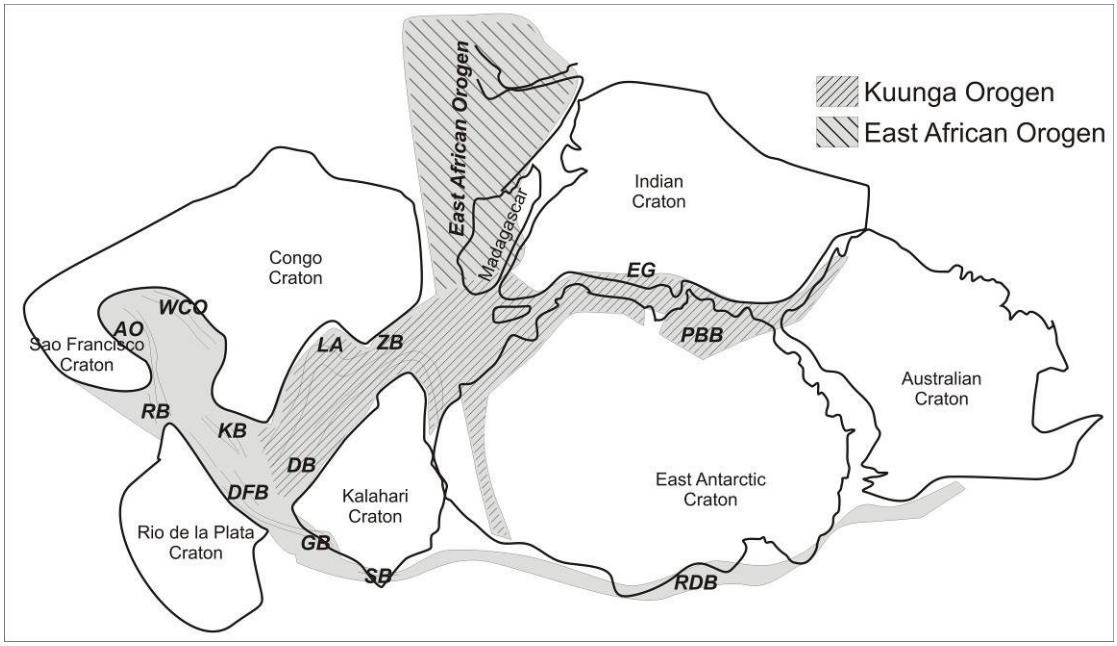

Fig. 7.11 – Map of Pan-African mobile belts relative to cratonic blocks involved in the assembly of Gondwana. AO = Araquai Orogen, DB = Damara Belt, DFB = Dom Feliciano Belt, EG = Eastern Ghats, GB = Gariep Belt, KB = Kaoko Belt, LA = Laurentian Arc, PBB = Prydz Bay Belt, RDB = Ross Delamerian Belt, SB = Saldanian Belt, WCO = West Congo Orogen, ZB = Zambezi Belt. Note that the East African Orogen is suggested to predate the Kuunga Orogen (Modified after Meert, 2003 and Gray et al.*, 2008).*

7.4.1 The Kaoko Belt

The NNW-trending Kaoko Belt (Figs. 7.8, 7.11, 7.12) contains a record of sinistral transpression (Goscombe *et al*., 2003a, b), the result of collision between the Congo Craton and Rio de la Plata Craton following westward-dipping (Germs, 1995; Frimmel *et al*., 1996; Masberg *et al*., 2005; Miller, 2008) or eastward-dipping (Frimmel, 2008; Goscombe & Gray, 2007) subduction. An early 'thermal phase' (Goscombe *et al*., 2003a, b) took place in the Western Kaoko Zone (Fig. 7.12) from 656 Ma (Goscombe *et al*., 2003a, b). This early thermal event is thought to pre-date the collision of the Congo and Rio de la Plata cratons, and is preserved only in the exotic Coastal Terrane (Fig. 7.12) of the Western Kaoko Zone. The collision of the Congo and Rio de la Plata cratons, and the associated sinistral transpression in the Kaoko Belt occurred between 580 Ma and 550 Ma (Seth *et al*., 1998; Goscombe *et al*., 2005a, 2005b; Goscombe & Gray, 2009). During this collision, intense wrench-style deformation in the Orogen Core (Fig. 7. 12) was coeval with large-scale nappes and folds, verging east to northeast outwards from the core of the orogen towards the foreland margin in the Escape Zone and Eastern Kaoko Zone (Goscombe *et al*., 2005a). This was followed by a phase of NNW-SSE directed coaxial shortening (Goscombe *et al*., 2005a), which occurred at 535-505 Ma (Goscombe *et al*., 2005b).

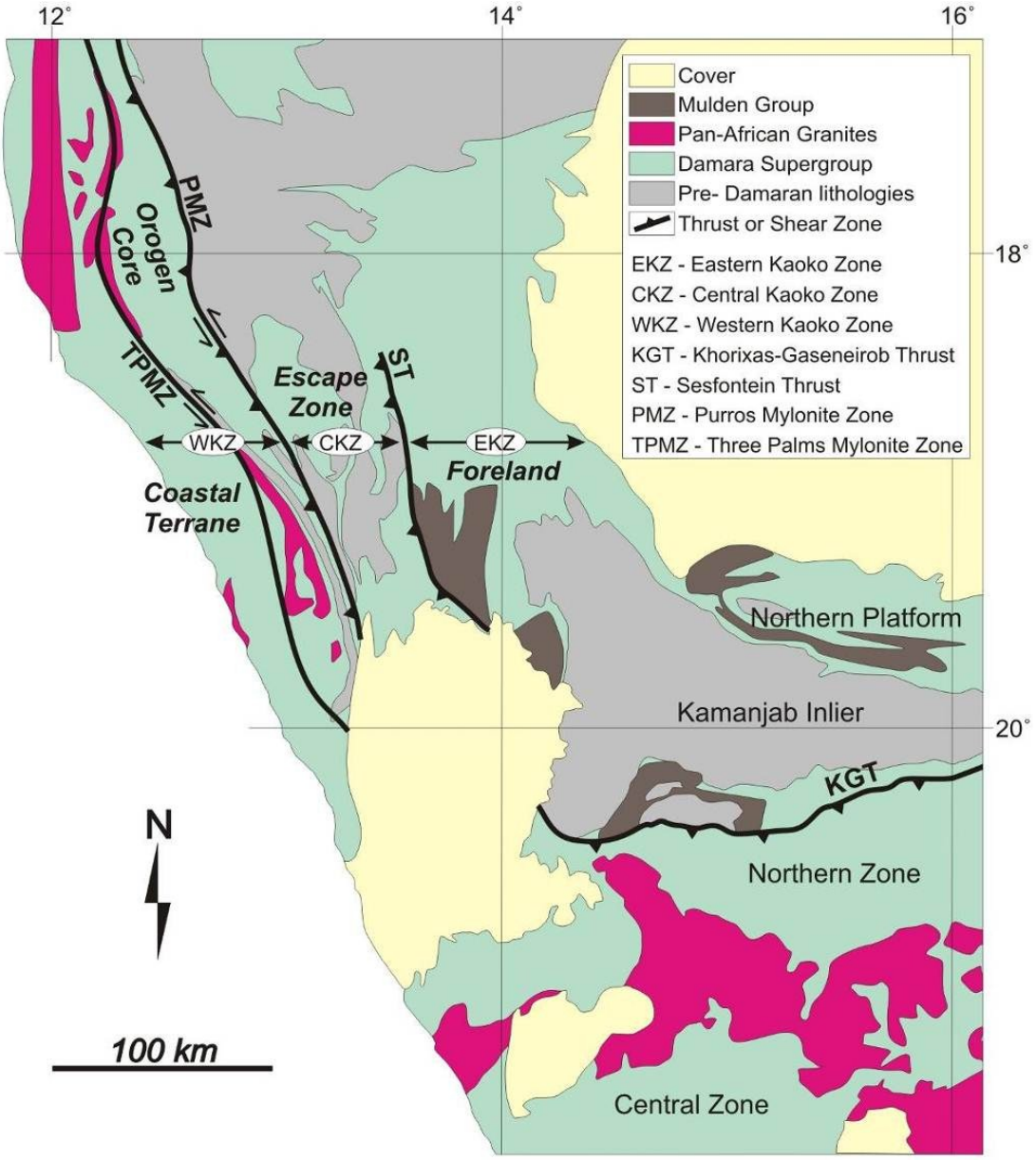

Fig. 7.12 – Geological map of the Kaoko Belt and northwestern Damara Belt, illustrating major sinistral structures in the Kaoko Belt, the tectonostratigraphic subdivision of the Kaoko Belt, and the distribution of the Mulden Group. Modified after Goscombe et al*. (2003a; 2005a) and Miller (2008).*

Uplift and erosion in the Kaoko Belt, associated with deformation and metamorphism at the onset of collision between the Congo and Rio de la Plata cratons, provided the source for molasse sediments of the Mulden Group, deposited adjacent to the Kaoko Belt from 575 Ma

to 555 Ma (Miller, 2008). Mulden Group sediments in the Eastern Kaoko Zone were overthrust by the Central Kaoko Zone along the Sesfontein Thrust (Fig. 7.12). This thrusting is considered by Goscombe *et al*. (2003a) to have occurred late in the history of the Kaoko Belt, at the same time as E-verging compressional deformation in the Eastern Kaoko Zone also produced deformation in the Mulden Group molasse (Goscombe *et al*., 2003a), and deformation had ceased by *ca*. 530 Ma (Goscombe *et al*., 2005b).

These ages for deposition of the Mulden Group indicate that molasse sediments deposited on the Northern Platform predate the main phase of crustal thickening in the Central Zone at 560-540 Ma, and the final phases of compressional deformation in the Kaoko Belt. According to Goscombe *et al*. (2005b), NNE-SSW shortening in the Kaoko Belt, associated with collision of the Congo and Kalahari Cratons, only took place between 535 Ma and 505 Ma, by which time the molasse deposits of the Mulden Group had already been deposited and deformed by compressional deformation. In contrast, Miller (2008) states that NE-trending F2 structures in the Northern Margin Zone are unconformably overlain by Mulden Group rocks, which were subsequently also deformed by D2. This apparently contradictory scenario requires D2 deformation in the Northern Margin Zone to have begun prior to deposition of the Mulden Group and continued throughout the *ca*. 20 Myr deposition of the Mulden Group, as well as post-deposition. This seems unlikely, especially given the fact that Swakop Group rocks of the Northern Zone were thrust over Mulden Group along the D2 Khorixas-Gaseneirob Thrust (Fig. 7.11). The so-called F2 folds below the Mulden Group (Miller, 2008) are thus more likely to be related to deformation in the Kaoko Belt than to deformation in the Damara Belt. These discrepancies highlight the problem with correlating deformation events across three orogenic belts (the Kaoko, Gariep and Damara Belts), and the need for more careful geochronology of specific deformation events in specific areas.

7.4.2 The Gariep Belt

In the Gariep Belt, sinistral transpression (similar to the Kaoko Belt) is recorded, with the main episode of deformation suggested to be younger than in the Kaoko Belt (Gray *et al*., 2008). Largely transpressive contractional deformation in the Gariep Orogen led to a fold

and thrust belt with a steep orogenic front, associated with SE-directed deformation and sinistral movement along the eastern margin, and this deformation was accompanied by low- to medium-grade metamorphism (Frimmel, 2008). The low-grade conditions and the lack of any syn-orogenic magmatism in the Gariep Orogen (Frimmel, 2008) contrast with the granulite facies conditions and voluminous magmatism found in the Central Zone of the Damara Orogen. The timing of collision and metamorphism in the Gariep Orogen is between 550 and 545 Ma (Frimmel, 2008), similar to 560-540 Ma collisional ages for the Damara Belt (Miller, 2008; this study). The slightly earlier onset of subsidence and deposition of Nama Group rocks in the Witpütz subbasin relative to the Zaris subbasin (Fig. 7.9) indicates that collision in the Gariep Orogen may have slightly preceded that in the Damara Belt. Collision and uplift in the Gariep Orogen is still further preceded by tectonic events in the Kaoko Belt. Both the Gariep and Kaoko Belts are suggested to have formed through the closure of the Adamastor Ocean (Stanistreet *et al.*, 1991). However, Stanistreet *et al*. (1991) suggested that closure of the Khomas Sea to form the Damara Belt preceded closure of the Adamastor Ocean, whereas Prave (1996) suggested, based on sedimentological evidence, that closure of the Adamastor Ocean preceded that of the Khomas Sea, and this is consistent with geochronological evidence that collision in the Kaoko Belt preceded collision in the Damara Belt (Goscombe *et al*., 2005b; Gray *et al*, 2008; this study). However, although deposition in the Witpütz subbasin may have slightly preceded that in the Zaris subbasin, collisional events in the Gariep and Damara Belts may have been fairly similar in age.

7.4.3 The Zambezi Belt

The Damara Belt lies along strike from the Zambezi Belt and Lufilian Arc (Fig. 7.11), which have shared a similar history since the breakup of Rodinia at *ca*. 750 Ma (Master, 2009). Syenites, rhyolites and granites in the Damara Belt are dated at between 765 and 747 Ma (Hoffman *et al*., 1996; Sanz, 2008), similar to syenites, volcanics and granites in Malawi and Zamibia, which are dated at 765 to 730 Ma (Key *et al*., 2001; Ashwal *et al*., 2007; Sanz, 2008). These deformed alkaline rocks and carbonatites in the Damara-Zambezi-Lufilian belts are thought to record the rifting of Rodinia, and indicate that rifting and spreading was fairly uniform along over 2000 km of strike on the southern margin of the Congo Craton (Master,

2009). Similarly, ages for subduction and collision in the Damara-Zambezi-Lufilian belt are similar. In the Zambezi Belt, eclogite-facies metamorphism related to N-directed subduction below the Congo Craton is dated at 595 ± 10 Ma (John *et al*., 2003) or 592 ± 22 Ma (Rainaud *et al*., 2005b), whilst 595-575 Ma ages are suggested by Miller (2008) for NW-directed subduction below the Congo Craton. Ages of 560-510 Ma have also been recorded for continent-continent collision, magmatism and granulite-facies metamorphism in the Zambezi Belt in northern Zimbabwe (Hanson *et al*., 1993; Goscombe *et al*., 1998; Rainaud *et al*., 2005b), and appear similar to the history of collision, magmatism and metamorphism in the Damara Belt, which occurred from *ca*. 560 Ma to 510 Ma, and the final stages of collision of the Congo and Kalahari Cratons have been dated at *ca.* 530-510 Ma in the Zambezi Belt (John *et al*., 2004; Rainaud *et al*., 2005b). Since details such as a P-T-d-t path for the Zambezi Belt are not yet available, and individual events (such as crustal thickening or the emplacement of characteristic intrusive rock types) cannot yet be correlated between the Zambezi Belt and the Damara Belt, any correlation across the entire Kuunga Orogeny must remain general at this time. Nonetheless, the Zambezi and Damara Belts appear to have experienced similar sequences of events, and the similar ages for subduction, collision and associated high-grade metamorphism along *ca*. 2000 km of strike length suggests that collision between the Congo and Kalahari Cratons was essentially contemporaneous along strike. This uniformity in the ages of collision along the strike of the Damara-Zambezi-Lufilian belt confirms the high angle of convergence between the Congo and Kalahari Cratons (Gray *et al*., 2008), and is at odds with suggestions of the Damara being a transpressional belt (e.g. Miller, 2008), as any strike-slip movement in the Damara was late, brittle, and relatively minor, with no evidence for large-scale strike-parallel movement, in contrast to the major crustal-scale transcurrent shears noted in the Kaoko Belt (Goscombe *et al*., 2003a).

7.5 The Damara Orogen and the Assembly of Gondwana

The Damara Orogen occupies a key area within the Pan African mobile belts that formed during the assembly of Gondwana, as it lies at the junction between east and west Gondwana. During the assembly of eastern Gondwana, at least two major orogenic events can be identified (Meert, 2003). The earliest of these, the East African Orogen (Stern, 1994; Meert, 2003), resulted in the collision between eastern Africa, parts of Madagascar, Sri Lanka, the Seychelles, India and East Antarctica between 750 Ma and 620 Ma (Fig. 7.11; Meert, 2003). This was followed by the so-called Kuunga Orogeny at 570-530 Ma (Meert *et al*., 1995; Meert 2003; Boger & Miller, 2004), resulting in the final collision of the Kalahari Craton, Congo Craton, Madagascar, India, Sri Lanka, the East Antarctic Craton, and the Australian Craton to form eastern Gondwana (Fig. 7.11). The Damara Belt is considered to be part of the latter orogeny. The NNE-tending Kaoko Belt adjacent to the Damara Belt lies along strike from the West Congo/Aracuai Orogens and the Gariep Orogen (Fig. 7.11), and formed during the assembly of western Gondwana. Whilst ages for collision are similar along the Damara-Zambezi-Lufilian belt (see 7.4.3 above), the 580-560 Ma timing for collision and transpression in the Kaoko Belt (Goscombe *et al*., 2003a) precedes the 550-545 Ma collision in the Gariep Belt (Frimmel, 2008) by 20-30 Myr. Further along strike to the south, ages of 550-510 Ma are found for granites of the Cape Granite Suite (Scheepers & Armstrong, 2002; Scheepers & Poujol, 2002) in the Saldania Belt, the earliest of which are syn-tectonic. North of the Kaoko Belt, peak metamorphism and collision in the Aracuai Orogen and Ribiera Belt has been dated at 585-560 Ma (Heilbron & Machado, 2003; Heilbron *et al*., 2004; Gray *et al*., 2008). Older ages for collision in the Kaoko and Ribiera Belts relative to the Gariep and Saldania Belts have led to suggestions that closure of the Adamastor Ocean was oblique, with subduction-related closure beginning in the north and progressing to the south (Gray *et al*., 2008). It has also been suggested that anticlockwise rotation of the Sao Francisco Craton relative to the Congo Craton occurred as a result (Alkmim *et al*., 2006).

This relatively simplistic model has recently been challenged by Rapela *et al*. (2011), who suggested that closure of the northern Adamastor Ocean (beginning at *ca*. 680 Ma – Gray *et*

al., 2006) involved sinistral collision and oblique displacement of the Paranapanema block (Fig. 7.13) relative to the Angola block (Congo Craton) between 640 and 600 Ma, with deformation recorded in the Kaoko and Dom Feliciano belts. Subsequent to collision, sinistral transpression is recorded in major shear zones in these belts between 580 and 550 Ma. Later closure of the southern Adamastor Ocean constituted a different orogeny (Rapela *et al*., 2011), beginning with the formation of the Gariep belt at *ca*. 545 Ma. Closure of this ocean was progressive, migrating southward into the Saldanian belt until *ca*. 520 Ma (Rapela *et al*., 2011).

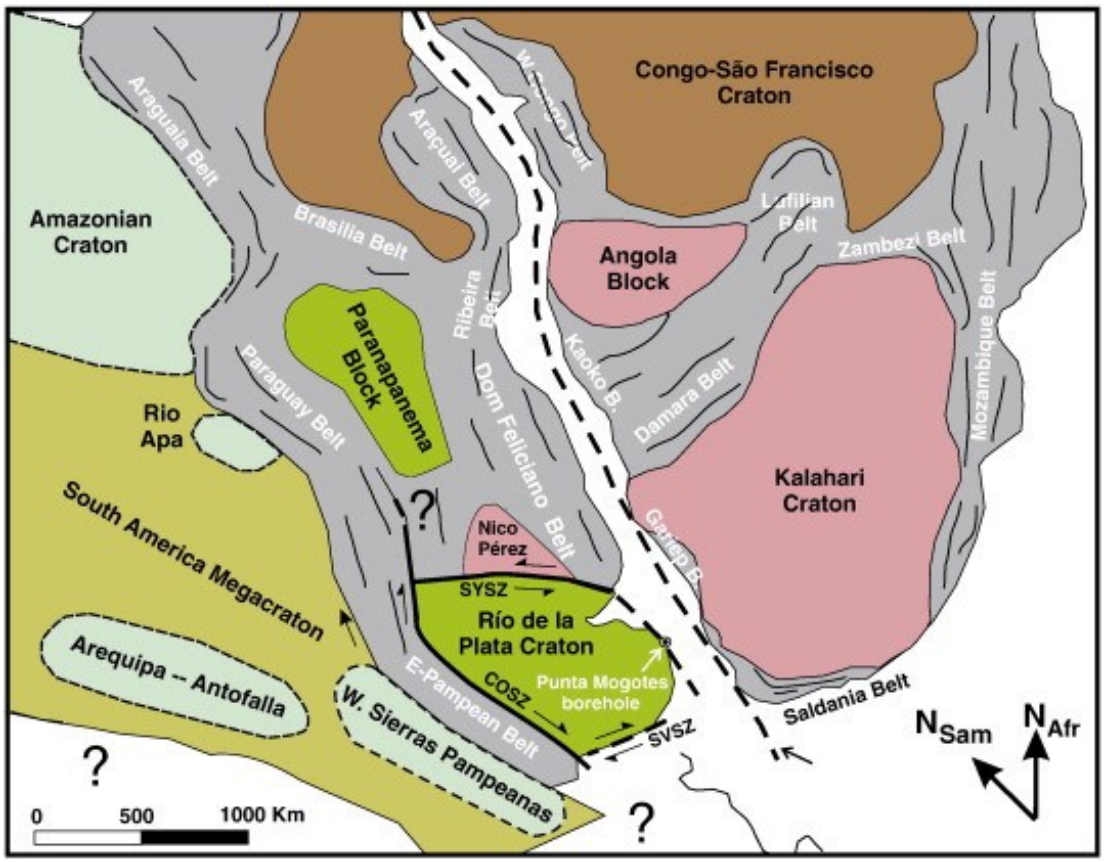

Fig. 7.13 – Cratonic blocks and collisional belts of southwestern Gondwana (Modified after Rapela et al*., 2011).*

This timing is confirmed by recent data from Oyhantçabal *et al*. (2011) that confirms the relationship between the Kaoko Belt and the Dom Feliciano Belt, with subsequent collision

of both belts with the Kalahari Craton. The model of Rapela *et al*. (2011) raises questions about the overall sequence of events in the assembly of Gondwana – in this new model, the Kaoko and Gariep belts are no longer regarded as the result of the progressive closure of the Adamastor Ocean, but as two separate events. The similarity in the timing of collision in the Damara and Gariep belts suggests that they may represent part of the same orogeny, and are younger collisional events than the Kaoko-Dom Feliciano Belts, i.e., the Gariep Belt should be considered part of the Kuunga Orogeny. The near-coeval deposition of sediments derived from these orogens in the Nama Basin further confirms this relationship. It may be that the Kalahari Craton was involved in simultaneous collision along its (present day) western and northern margins, forming the Gariep and Damara belts, respectively. This would suggest that the Gariep-Damara belts form a major orocline, and that this orocline formed after the Kaoko-Dom Feliciano Belts. The model of Rapelo *et al*. (2011) also considers the Rio de la Plata Craton to be derived from the west, and tectonically emplaced against the Kalahari Craton to form the Gariep-Saldania Belts. This differs from Frimmel *et al*. (2011), who considered the Rio de la Plata and Kalahari Cratons to be united prior to the breakup of Rodinia. The Kalahari Craton thus appears to be the central piece in the puzzle of the assembly of Gondwana, with Pan-African belts along all margins. Whilst the assembly of western Gondwana has been the matter of much recent debate (e.g. Siegesmund *et al*., 2011 and references therein) and it is beyond the scope of this thesis to attempt to resolve the matter, the more detailed tectonic history outlined in this chapter should provide the basis for correlating the Damara Belt with other Pan-African belts in southwest Gondwana.

7.6 Comparison with Other Collisional Orogens

Originally, the Damara Belt was considered to be an intracratonic fold belt formed in an ensialic aulacogen (Martin, 1965; Martin & Porada, 1977a, b; Kröner, 1977), before a plate-tectonic model involving subduction of ocean crust and subsequent continent-continent collision was proposed by Barnes & Sawyer (1980). The geodynamics of the Central Zone have also been reinterpreted a number of times, as progress is made on the understanding of collisional orogens in general. The early plate-tectonic classification of orogenic belts by

Dewey & Bird (1970) recognised that orogens can form through subduction at continental margins, intra-oceanic subduction (i.e. oceanic island arcs), ophiolite obduction, collision between continents and island arcs, or continent-continent collision. Clearly, the Damara Belt formed through continent-continent collision, but it is less clear how the details of this collision compare to other collisional orogens globally. Although subduction is thought to have preceded this collision, there is a lack of high-pressure rocks in the Damara Belt, and no record of long-lived continental arc magmatism, suggesting that this period of subduction was not particularly long-lived. Additionally, the lack of early island arc magmatism precludes arc-continent collision in the history of the Damara Belt. The Alps and Himalayas represent the two areas where continent-continent collision is currently ongoing, and the tectonics of these regions should provide useful comparisons for the Damara.

7.6.1 A comparison with Himalayan-type and Alpine-type orogens

Sengör (1990) refined the classification of orogens formed through continent-continent collision into two 'superfamilies' in which the architecture of the orogen is the result of its pre-orogenic history. Whilst generalisations, these highlight the underlying common structure in collisional orogenic belts. Orogens formed through continent-continent collision were classed by Sengör (1990) as continental override-type (Alpine-type) or non-continental override-type (Himalayan-type) orogens (Figs. 7.14A, B). In both these 'superfamilies' of orogens, pre-orogenic continental crust belonging to colliding continents is apposed across a narrow suture, and continental growth from the associated orogeny is thought to be negligible (Sengör & Natal'in, 1996). Subsequently, Turkic-type orogens were defined as an additional class of collisional orogen (Sengör & Okuroğullari, 1991; Sengör & Natal'in, 1996), owing to the fact that in north-central Asia, vast subduction-accretion complexes are seen separating the preorogenic crustal rafts of the colliding continents, and no narrow sutures are evident (Fig. 7.14C; Sengör & Natal'in, 1996).

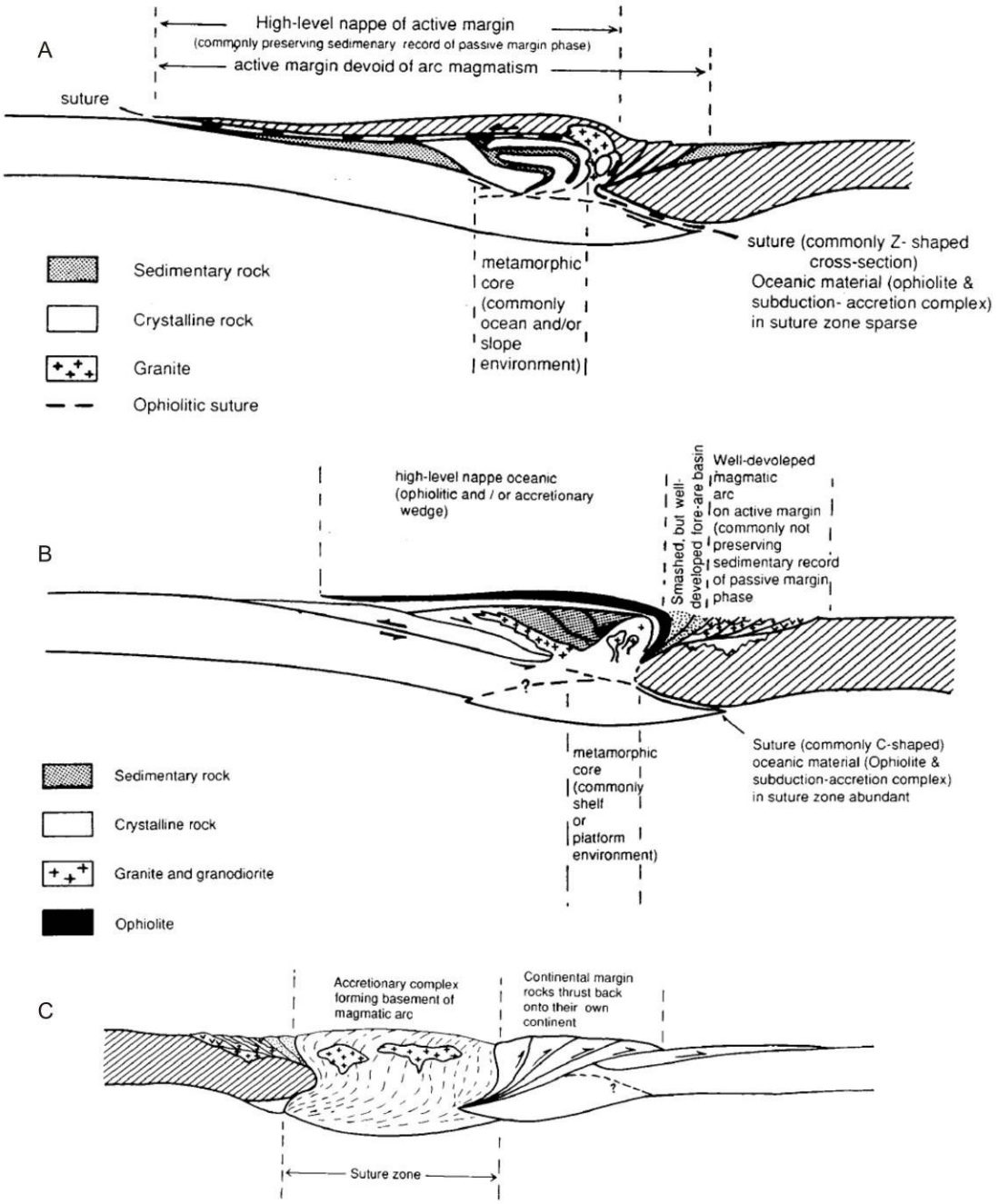

Fig. 7.14 – Superfamilies of collisional orogenic belts (from Sengör & Natal'in, 1996). (A) Alpine-type with an allochthon of continental material overriding the lower plate for considerable distances at shallow levels, indicating loss of a small ocean. (B) Himalayan-type with no high continental allochthon and a well-developed magmatic arc and accretionary wedge. (C) Turkic-type, a modified Himalayan-type without a well-defined, narrow suture, owing to very large subduction-accretion complexes.

The Okahandja Lineament is commonly regarded as the (fairly narrow) zone of suture between the colliding Congo and Kalahari Cratons (Miller, 2008), and thus the model of a Turkic-type orogen (with vast accretionary complexes separating the two colliding cratons) is not applicable to the Damara Orogen, which must rather share the characteristics of Alpine-type or Himalayan-type orogens. Continental override-type (Alpine-type) orogens are characterised by large thrust sheets of continental material overriding the other continent at upper-crustal levels (Sengör, 1990), and are typified by the Alpine Orogeny. In contrast, the Himalayas do not contain such large shallow-crustal thrust sheets, and orogens of this type are thus classed as non-continental override-type (Himalayan-type) collisional orogens. The origin of this difference is thought to be related to the presence or absence of a well-developed subduction-accretion complex and magmatic arc prior to collision (Sengör, 1990). Accretionary prisms and associated magmatic arcs may deform internally and thicken, forming 'cushions' between the two converging continental masses (Sengör, 1990). In the absence of this 'cushioning' of the colliding continents, much of the force of the collision is taken up through thrusting and imbrication of the upper crust, forming large-scale nappes of material from the overriding continent being thrust over the underlying continent during collision. For this reason, Alpine-type orogens typically have poorly developed magmatic arcs, a lack of ophiolitic melanges belonging to former subduction-accretion complexes or large pre-collisionally obducted ophiolite slabs, sparse post-collisional magmatism, and a metamorphic core consisting of former continental and oceanic sediments and their basement (Sengör, 1990). Alpine-type orogens are commonly associated with the closure of small (<1000 km) oceans. In contrast, Himalayan-type orogens are commonly associated with the closure of large (>1000 km) oceans, have more abundant ophiolitic melanges, and commonly have pre-collisionally obducted giant ophiolite nappes. They have well-developed magmatic arcs, abundant post-collisional magmatism and metamorphic cores of former shelf/platform basement with its sediments sheared off into decollement sheets (Sengör, 1990).

The Damara Belt can be compared with these generalised orogen types on the basis of their main characteristics (Table 7.2). The mafic to dioritic Goas Intrusive Suite is thought to

represent arc magmatism preceding collision of the Congo and Kalahari Cratons (De Kock, 1991), or may be related to slab breakoff (this study). Nonetheless, it is voluminously minor, similar to Alpine-type orogens. Similarly, no large ophiolite slabs are seen to have been obducted onto during collision, suggesting an Alpine-type affinity. However, the ocean separating the Congo and Kalahari Cratons (the Khomas Sea) is thought to have been between 1500 and 2000 km wide (Miller, 2008), and post-collisional magmatism is widespread throughout the Damara Orogen (including the Donkerhuk Granite in the Southern Zone, numerous leucogranites of the Central Zone and large granite bodies in the Northern Zone – Miller, 2008), indicating a similarity to Himalayan-type orogens. Similarly, sediments which make up the high-grade core of the Damara orogen (i.e. the Central Zone) are the rift-related sediments of the Nosib Group, and the continental shelf sediments of the Swakop Group, including the shelf carbonates of the Karibib Formation (Miller, 2008). Himalayan-type orogens typically have continental shelf or platform sediments making up their high-grade core (e.g. the Neoproterozoic to early Paleozoic Gondwanan continental margin succession of the Greater Himalaya Sequence - Myrow *et al*. 2003; Jamieson *et al*., 2006), whereas continental rise or oceanic sediments making up the lower-grade core in Alpine-type orogens (e.g. the Penninic Nappes), and thus the Damara appears to have a Himalayan affinity in this regard.

One of the important differences highlighted by Sengör (1990) between Alpine-type and Himalayan-type orogens is the nature of the highest allochthon. In the Alps, this is a *ca*. 10-15 km thick continental wedge formed from a stack of nappes, and is the result of collision of the southern continental margin with the attenuated European margin, imbricating it into a ‘sandwich’ of nappes which then overrode the southern continent (Sengör, 1990). This material was metamorphosed to upper-amphibolite conditions. In contrast, the continental margin of the Asian Craton was a well-developed magmatic arc, which could not be imbricated on collision with the Indian Shield. As a result, the ophiolitic basement of the Transhimalayan fore-arc and the subduction-accretion complex that accumulated in front of it forms the highest allochthon (Sengör, 1990), which was thrusted and imbricated upon collision.

Table 7.2 – Comparison of the major features of Alpine-type and Himalayan-type orogens (after Sengör, 1990) with the Damara Orogen.

Feature	**Alpine-type (collisional override type)**	**Himalayan-type (non-collisional override type)**	**Damara Orogen**	**Similar to?**
Magmatic arc?	Minor	Well developed	Minor (Goas Intrusive Suite)	Alpine-type
Ophiolite melange/subduction-accretion complex?	None	Well developed	Yes - Matchless belt & Khomas schists	Himalayan-type
Obducted ophiolite slabs?	None	Common	No	Alpine-type
Sediments of metamorphic core?	Continental rise & oceanic sediments & their basement	Shelf/platform basement and sediments	Rift & continental rise sediments	Himalayan-type
Large/small ocean?	Small	Large	Large	Himalayan-type
Post-collisional magmatism?	Poorly developed	Well developed	Well developed	Himalayan-type
Highest allochthon?	Continental material from overriding continent	Ophiolite/ accretionary complex	Accretionary wedge	Himalayan-type

Thus, should the Damara Orogen represent an Alpine-type orogen, one should expect a number of stacked nappes of continental material, thrust southwards over the Kalahari Craton. The Naukluft Nappe Complex may represent one such set of stacked nappes, with multiple stages of nappe emplacement evident (Hartnady, 1978). The lithostratigraphy of this nappe complex has been correlated with the flysch sediments of the Damara Orogen (the Hakos, Witvlei and lower Nama Groups – Miller, 2008), which have been emplaced *ca*. 80 km over the molasses sediments of the upper Nama Group (Hartnady, 1978). The Naukluft Nappe Complex may thus be similar to the Helvetic Nappes in the Alps, which were thrust over molasse sediments north of the Alps (Hsü, 1979; Sengör, 1990). The numerous

thrusts and km-scale recumbent folds and nappes recorded in the Southern Margin Zone (the Samara-Dagbreek, Tesbris, Lichtenstein-Auas and Rostock nappe complexes – Hoffmann, 1981; 1983; Miller, 2008) may be Damaran correlatives of the Penninic nappes of the Alps. The Penninic nappes (lying south of the Helvetic nappes, and closer to the Alpine orogenic suture of the Insubric Line) contain hemipelagic sedimentary rocks interlayered with basaltic volcanic rocks and shreds of ultramafics and flysch deformed into large recumbent folds with a characteristic axial plane schistosity, in addition to large recumbent basement nappes, (Sengör, 1990). Similarly, the numerous nappe complexes of the Southern Margin Zone also include slivers of basement rocks and flysch sediments of the Hakos Group (Miller, 2008), along with serpentinites which have an Alpine-type chemistry (Barnes, 1982). However, the schists of the Southern Zone are generally regarded as an accretionary prism or subduction-accretion complex (Kukla & Stanistreet, 1991), more consistent with a Himalayan-type orogen. Additionally, the high-grade metamorphism that characterises the Central Zone makes a comparison with the generally shallow-crustal Alps problematic. No analogous zone of mid-crustal ductile deformation is found in the Alps and, whilst large-scale recumbent folding is evident in the study area (see Chapter 3), it does not appear similar to the nappes typical of the Alpine Orogeny. Furthermore, the high-grade Central Zone may show a number of other similarities to the high-grade core of the Himalayan Orogen (the Greater Himalaya Sequence), where recent studies have proposed that a combination of gravitational loading and focused erosion on the orogenic front may result in the ductile flow and extrusion of a channel of high-grade rocks in collisional orogens (Beaumont *et al*., 2001; Grujic *et al*., 2002; Godin *et al*., 2006; Grujic *et al*., 2006).

7.6.2 Channel flow as a potential mechanism for the exhumation of the Central Zone

In the model of channel flow and ductile extrusion (Beaumont *et al*., 2001; Long & McQuarrie, 2010), high-grade metamorphic rocks of the Greater Himalaya (GH) are separated from low-grade rocks by two shear zones (Fig. 7.15). The basal shear zone, the Main Central Thrust (MCT), shows top-to-the-S movement, whilst the upper boundary of the GH is the top-to-the-N-verging South Tibetan Detachment (STD). Hundreds of kilometres of coeval movement is noted along both of these major structures. It is postulated that a

pressure gradient formed due to gravitational loading of the orogen has caused less viscous high-grade metamorphic rocks of the GH to flow from the lower crust towards the orogenic front. This movement is accentuated by focused erosion along the Himalayan front. Evidence for this is the opposite vergence of the shear zones bounding the GH (top-N in the upper STD, top-S in the lower MCT), synchronous movement on the MCT and STD between 22 Ma and 15 Ma, and the isothermal decompression of rocks of the GH from peak pressures of 8-12 kbar at 750-800 °C to *ca.* 5 kbar at 600-750 °C. The presence of melt owing to anatexis provides the requisite decrease in rock strength required for this mechanism to take place. In the Himalaya, this ductile, low-viscosity channel is inclined northwards and is linked with a partially melted body that has been detected at depth by geophysical methods as part of the INDEPTH program (Nelson *et al*., 1996). Channel flow is characterised by early stage flow and ductile shearing, with syntectonic metamorphism and magmatism, and with weakened flow activity and more localised deformation at a later stage.

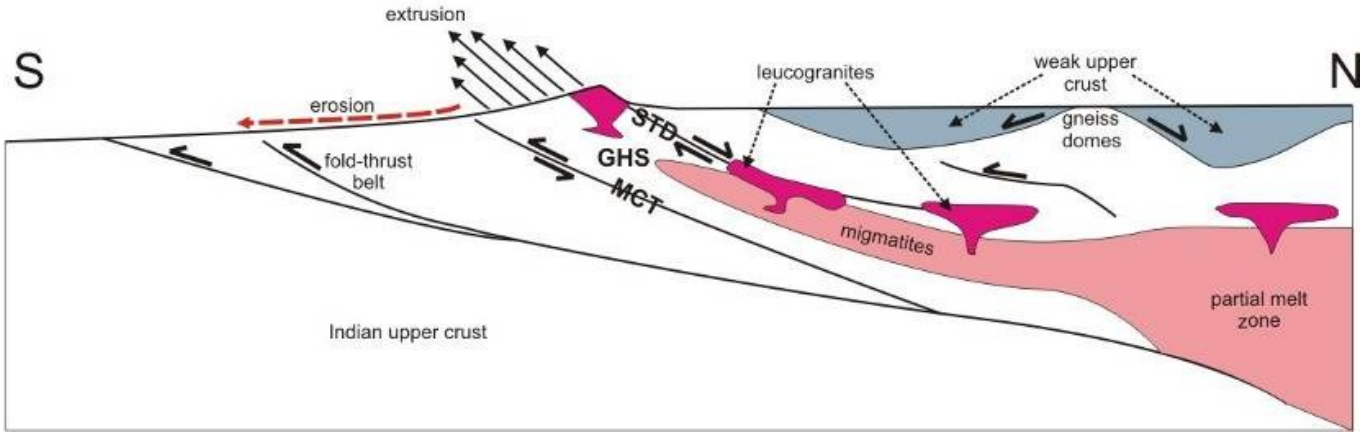

Fig. 7.15 – General tectonic features of the Himalaya. GHS: Greater Himalayan Sequence. STD: South Tibetan Detachment. MCT: Main Central Thrust. Note the opposite sense of shear on the STD and MCT, the migmatites and leucogranites of the GHS, and the presence of a foreland fold-thrust belt. Modified after Beaumont et al*. (2001).*

Although the Central Zone appears as a zone of high-grade metamorphism and ductile deformation, there does not appear to be any evidence for isothermal decompression in the study area (see Chapter 6). Additionally, the high-grade orogenic core of the Greater

Himalaya Sequence (thought to represent flow of ductile material from the mid- to lower-crust) is characterised by a number of specific geological features (Godin *et al*., 2006), including:

- A crustal package of lower viscosity material bounded by higher viscosity rocks.
- Inverted and right-way-up metamorphic sequences at the base and top of the extruding channel, respectively.
- Pervasive shearing throughout the channel and extruded crustal block, although strain is predicted to be concentrated along its boundaries.
- An incubation period of up to 10-20 My is necessary between crustal thickening and the commencement of channel flow.
- Melts (leucosomes) coeval with ductile channel flow must be younger than shortening structures in the upper crust.
- When active, the channel is predicted to be 10-20 km thick.

A number of these key geological characteristics may be apparent in the Central Zone. The granulite-facies southern Central Zone contains evidence for widespread anatexis and numerous leucogranites, indicating that it was of lower viscosity than the adjacent Southern Zone and northern Central Zone, which experienced amphibolite-facies metamorphism. The drop in metamorphic grade away from the southern Central Zone to the northern Central Zone represents a right-way up metamorphic sequence, pervasive deformation is documented throughout the southern Central Zone, and the delay between continent-continent collision at *ca*. 540 Ma (Miller, 2008) and the 520 Ma onset of extension and exhumation of the southern Central Zone is consistent with the *ca*. 10-20 My incubation period required for channel flow to initiate. The ages of leucosomes related to exhumation of the southern Central Zone are younger than structures related to crustal thickening/shortening, the 60 km width (plan view) for the southern Central Zone equates to a 20 km thick channel, assuming a dip of 20˚ for the channel (Fig. 7.16). However, there are a number of problems with channel flow as a model for the Central Zone - the actual dip of the bounding structures to the southern Central Zone appears to be steeper than this, and it may be thicker than 20 km and, whilst the juxtaposition of granulite facies rocks of the southern Central Zone with amphibolite facies rocks of the Southern Zone appears to

represents an inverted metamorphic sequence, this would be the case only if the metamorphism in both areas was coeval. M2 granulite facies metamorphism in the Central Zone is dated at 520-510 Ma (this study), whilst the Southern and Southern Margin Zones are characterised by 560 and 550 Ma deformation and metamorphism (Miller, 2008). Additionally, although deformation is noted to be concentrated along the Okahandja and Omaruru Lineaments, much of this deformation appears to be late-stage and the relationships between high-grade metamorphism in the Central Zone and movement along these lineaments is unclear.

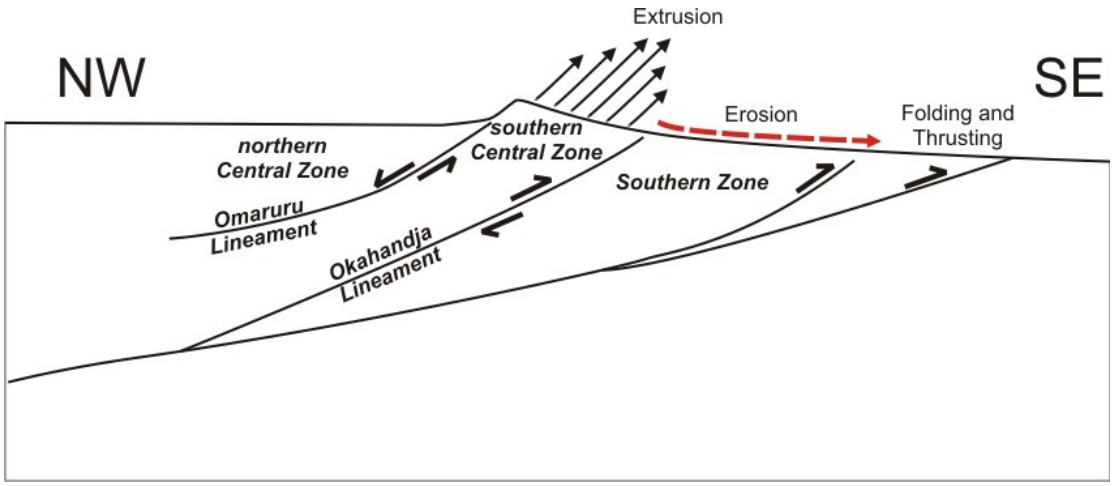

Fig. 7.16 – Schematic representation of the southern Central Zone as a Himalayan-style ductile channel. In this scenario, granulite-facies metamorphism deformation in the southern Central Zone would need to be coeval with normal movement along the Omaruru Lineament and thrusting along the Okahandja Lineament.

One of the key characteristics of the channel flow model is that normal movement of the upper bounding structure (the STD for the GHS or the Omaruru Lineament for the southern Central Zone) must be coeval with thrusting along the lower bounding structure (the MCT for the GHS or the Okahandja Lineament for the southern Central Zone – Fig. 7.16), and evidence for opposite-sense shear zones bounding the southern Central Zone is not obvious. The southern Central Zone is bounded to the north by the Omaruru Lineament and Waterberg Fault, which are thought to be thrust faults along which there was uplift of the northern Central Zone relative to the southern Central Zone during D3 deformation (Ritter

et al., 2003). The southern boundary of the Central Zone is the Okahandja Lineament, along which the Central Zone is suggested to have been uplifted relative to the Southern Zone, although Barnes & Sawyer (1980) suggested that *ca*. 10 km uplift of the Southern Zone relative to the Central Zone occurred at the late stages of collision in the Damara Orogen. In order for a channel flow model to be applicable for the southern Central Zone, there needs to be evidence of coeval normal movement along the Omaruru Lineament and thrusting along the Okahandja Lineament. Whilst the level of exposure in the northern Central Zone could suggest downfaulting relative to the southern Central Zone along the Omaruru Lineament prior to late (D3) thrusting, this could also be due to differential thickening and exhumation between these two areas, and there is as yet no evidence that any such normal movement occurred, and was coeval with thrusting along the Okahandja Lineament. Thus, there is little evidence for ductile extrusion and channel flow in the southern Central Zone as the result of Himalayan-style collision, although neither the nature nor timing of deformation along the bounding structures to the southern Central Zone are particularly well resolved. At this stage a channel flow model for the Central Zone remains speculative, and alternative mechanisms for the exhumation of high-grade rocks of the mid-crust have been proposed for the Central Zone (Oliver, 1994; 1995; Poli, 1997; Poli & Oliver, 2001).

Although the Damara Orogen is the result of continent-continent collision, and thus most comparable to other such recent orogens (i.e. the Alpine and Himalayan orogens), the processes of crustal exhumation in subduction-related orogens may be applicable to the Central Zone. Once such process that has already been applied to the Central Zone is the concept of a metamorphic core complex (Oliver, 1994, 1995), originally developed to explain features of the North American Cordillera (Coney & Harms, 1984; Lister & Davis, 1989). Metamorphic core complexes develop in extensional tectonic settings, and the interpretation of the Central Zone as a deep extensional metamorphic core complex (Oliver, 1994; 1995) was based on extensional deformation observed in the southwestern Central Zone, and that the basement and cover are typically separated by ductile shear zones, interpreted as regional detachments by Oliver (1994; 1995). Typically, the extension associated with core-complex development may be attributed to vertical extrusion due to topographic collapse or back-arc extension due to slab rollback (Bendick & Baldwin, 2009).

Since subduction is thought to have been relatively short-lived prior to Damaran collision (Miller, 2008), and since exhumation of the mid-crust in the Central Zone occurred late in the orogenic history, any extension and vertical extrusion would likely be related to topographic collapse of the Damara Belt rather than slab rollback. Like the models of channel flow recently applied to exhumation of the mid-crust in the Himalaya, metamorphic core complexes share a set of common characteristics (Bendick & Baldwin, 2009), including:

- Association of crustal exhumation with brittle normal faulting.
- Localisation of exhumation at the edge of a craton.
- Localisation of exhumation associated with a thick crustal welt.
- Exhumation follows crustal thickening, and lasts for 10-15 Myr.

Whilst the Central Zone of the Damara Orogen shows most of these characteristics, exhumation does not appear to be associated with brittle normal faulting. Oliver (1994, 1995) suggested deeper crustal level core complex development to explain this, with a low-angle detachment at the base of the Damara Supergroup. Whilst this has been shown (Chapter 3) to be a high-strain zone in the study area, no single detachment is found at the basement-cover contact, nor is it associated with a change in metamorphic grade (see Chapter 6), as is typical of core complexes (Brun & Van Den Driessche, 1994). Although ductile shear zones are noted near basement-cover contacts throughout the study area, similar shear zones are found both in the basement and in the cover. Additionally, field evidence from this study has shown that, rather than forming two distinct entities, the basement of the Abbabis Complex and the Damaran Supergroup cover have been interfolded during D2, and infolds of Damaran metasediments are found within the basement through the Palmenhorst Dome. This is contrary to any suggestion of a separate basement and cover.

One of the essential geodynamic differences between the development of a channel-flow vs. core-complex style of mid-crustal exhumation is the fact that large viscosity contrasts exist across distinct boundaries in the former case. In other words, channels of weak (partially molten), viscous material develop between stiffer channel walls and result in

channel flow, whereas areas of localised vertical flow (core-complex development) occur in the absence of more rigid channel boundaries (Bendick & Baldwin, 2009). The granulite-facies Central Zone (with widespread anatectic melt and granite) may have represented a zone of weakness, bounded by the lower grade (stiffer) northern Central Zone and Southern Zone. It appears that the southwestern Central Zone may not represent a metamorphic core complex. However, there is also little evidence for channel-flow as a model for the development of the southwestern Central Zone, and the Damara Orogen appears to share characteristics with both Himalayan-type and Alpine-type orogens.

Although the Damara Orogen may be analogous to the Himalayas and the Alps, older, well-studied orogens (such as the Caledonian and Variscan Orogens) may also be compared with the Damara. Whilst no two orogens are likely to be identical, the evolving sets of processes that occur in orogens are likely to be comparable. The Variscan and Caledonian orogen models are useful as the processes of lithospheric delamination (in the Variscan) and slab breakoff (in the Caledonian) have been well characterised (Gutiérrez-Alonso *et al*., 2011; Oliver *et al*, 2008), and these key processes may be tested with regard to the Damara Orogen.

7.6.3 Comparison with the Variscan and Caledonian Orogens

The Variscan Orogen formed from continent-continent collision between *ca*. 350 and 280 Ma (Fernández-Sáurez *et al*., 2000; Bea *et al*., 2006). Whilst much of the Variscan has been subsequently overprinted by the younger Alpine Orogeny, it is exposed in a number of massifs across Europe, the largest of these being the Iberian Massif (Fig. 7.14; Pérez-Estaún & Bea, 2004). The Iberian Massif is also one of the best studied areas of the Variscan of Western Europe (Fernández-Sáurez *et al*., 2000) and, like the Damara Orogen, consists of several zones with different stratigraphic, structural, magmatic and metamorphic characteristics (Bea *et al*., 2006). This includes a high-grade orogenic core (the Variscan Autochthon of the Central Iberian Zone and West Asturian Leonese Zone), which, like the Central Zone of the Damara Orogen, is characterised by large-scale recumbent folding (Simancas *et al*., 2001), numerous domal structures (Martinez *et al*., 1988) and the

emplacement of voluminous granitoids (Bea *et al*., 2006). However, the Variscan is known to have a more complex history than the Damara Orogen, involving the collision of a number of smaller fragments (Ziegler, 1984; Stampfli *et al*., 2002), rather than simply between two large cratonic blocks (as in the Damara). However, one of the characteristic features of the Variscan Orogen in Western Europe is the bending of the orogen into the Iberian-Armorican orocline (Fig. 7.17; Gutiérrez-Alonso *et al*., 2011), and although the Damara Belt is markedly linear (Fig. 7.8), the southwestern Central Zone does appear to lie near a major oroclinal bend between the Damara Belt, the Gariep Belt and the Kaoko Belt (Fig. 7.8).

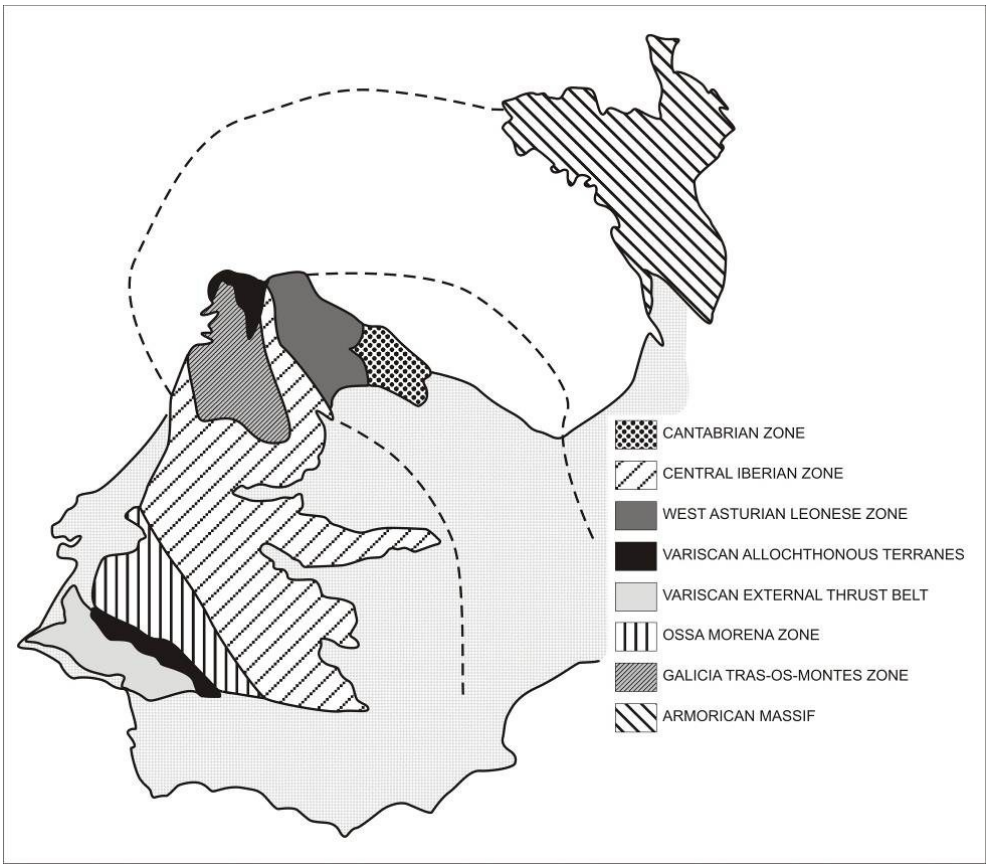

Fig. 7.17 – Simplified map of the Variscan Orogen in southwestern Europe, showing the various zones of the orogen. Note the oroclinal curvature of the orogeny, as indicated by the dashed lines. Modified after Fernández-Sáurez et al. *(2000) and Simancas* et al*. (2001).*

Multiple episodes of magmatism have been identified in the high-grade portions of the Iberian Massif – for example, in the West Asturian Leonese Zone, tonalite-granodiorite-monzogranite intrusions were emplaced syntectonically during the main phase of crustal deformation at *ca*. 325 Ma (Fernández-Sáurez *et al*. (2000). Leucogranitic magmatism is associated with later extension at 320-310 Ma, and this was followed by post-tectonic tonalite-granodiorite-monzogranite (with minor mafic-intermediate) magmatism (Fernández-Sáurez *et al*., 2000). It has been suggested that much of the post-tectonic magmatism that characterises the Iberian Massif is the result of delamination of the sub-continental lithospheric mantle following the formation of this orocline (Gutiérrez-Alonso *et al*., 2011).

In contrast to mantle lithosphere delamination, voluminous granitoid magmatism in the older Caledonian Orogen is suggested to be the result of slab breakoff (Oliver *et al*., 2008). Like the Variscan, the Caledonian represents another older, well-studied orogeny, and encompasses areas of the British Isles, Eastern Greenland, and Scandinavia. The Caledonian Orogeny formed from microplate accretion and collision of Laurentia, Baltica and Avalonia (Soper & Hutton, 1984; Hutton & Dewey, 1986) between *ca*. 550 and 400 Ma during the closure of the Iapetus Ocean (McKerrow *et al*., 2000; Oliver *et al*., 2008). The history of this orogeny involves an extended history of subduction, arc-continent collision, and continent-continent collision (Van Staal *et al*., 1998; Cocks & Torsvik, 2006; Oliver *et al*., 2008), and continues as the Appalachian Orogen on the North American Continent (Williams & Hatcher, 1982). The British Caledonides represent a particularly well-studied portion of this orogenic system, where a number of tectonic episodes have been recognised (Armstrong & Owen, 2001; Oliver *et al*., 2008). Detailed geochronological studies of intrusive rocks in this portion of the orogen, in conjunction with studies of field relationships of these intrusions (Oliver *et al*., 2008 and references therein) have enabled recognition of two major collisional events. The first of these events in the British Caledonides (termed the Grampian), involved collision of an island arc terrane (the Midlands Valley island arc) with Laurentia at *ca*. 475 Ma (Oliver, 2001). This was followed by the collision of Avalonia and Baltica with Laurentia during the Scandian event (the second collisional event) at *ca*. 430 Ma (Oliver *et al*., 2008). Although the history of microcontinent collision and arc accretion in the Caledonian

Orogeny appears more complicated than the relative simplicity of the Damara Belt, and may be more comparable with the Kaoko Belt (which also shows a record of terrane accretion; Goscombe & Gray, 2007) the detailed record of slab breakoff described by Oliver *et al*. (2008) provides a useful comparison with the Damara. One of the key features of the British Caledonides is the record of multiple slab break-off events over the history of the orogen. During the Grampian, collision of the Midland Valley island arc with Laurentia resulted in slab breakoff and associated mantle upwelling. The effect of this rising hot asthenosphere was to induce lower crustal melting and thereby generate S-type granites, in addition to producing low-pressure, high-temperature metamorphism (Oliver *et al*., 2008). Subsequently, collision of Avalonia and Baltica with Laurentia during the Scandian event resulted in a second episode of slab breakoff and rising asthenosphere, with more S-type granites. The temperatures generated in the lower crust following the second slab breakoff event were high enough to generate I-type magmas in addition to S-types.

Thus, in the Variscan and Caledonian Orogens, the processes of delamination of the subcontinental lithospheric mantle and slab breakoff, respectively, are well recorded, and their characteristics may be summarised for comparison with the Damara.

7.6.3.1 Slab breakoff vs. lithospheric delamination in the Damara

Detachment of the sub-continental lithospheric mantle in collisional orogens is a commonly invoked cause for widespread post-tectonic magmatism (Bird, 1979; Gutiérrez-Alonso *et al*., 2011), and active lithospheric delamination may be characterised in several modern settings by clustered subcrustal seismicity not aligned along a subduction-associated dipping Wadati-Benioff Zone (Knapp *et al*., 2005). In addition to subcrustal seismicity, the effects of delamination include regional uplift, elevated heat flow, postorogenic extensional collapse and deep-seated alkaline magmatism (Knapp *et al*., 2005). Whilst demonstrating lithospheric delamination in older orogens is more difficult (Gutiérrez-Alonso *et al*., 2011), in the Variscan there appears to be a transition in the isotopic characteristics of mafic magmas over tens of millions of years from “older” lithospheric mantle to “young” asthenospheric mantle (Manthei *et al*., 2010; Gutiérrez-Alonso *et al*., 2011; Ducea, 2011). In the Damara

Orogen, there is a paucity of mafic magmatism, and no post-tectonic mafic magmas are noted, possibly argueing against the likelyhood for lithospheric delamination to have occurred following collision in the Damara. However, the paucity of Sm-Nd data and accurate U-Pb dating for intrusive rocks in the Damara means that geochemical tracing as a means of identifying this process is not yet possible in the Damara.

Slab breakoff is a more commonly invoked process in collisional orogens (e.g. Sperner *et al*., 2001; Vos *et al*., 2007; Replumaz *et al*., 2010), and is thought to be responsible for widespread mafic to granitic syn- to post-collisional magmatism, melting of the lower crust, and exhumation of eclogitic crust (Davies & von Blanckenburg, 1995). In the Caledonian, slab breakoff during the Grampian event is thought to have generated syn-metamorphic S-type granites and coeval gabbroic rocks (Oliver *et al*., 2008), whilst during the Scandian event, both S-type and I-type granites were thought to be the result of slab breakoff, with the presence of I-type granites indicative of melting of igneous protoliths in the lower crust at temperatures in excess of 850 ˚C (Oliver *et al*., 2008). Significantly for the thermal history of orogens, slab breakoff is thought to produce fast regional tectonometamorphism, without the delay observed for the onset of metamorphism following crustal thickening (England & Thompson, 1984).

Slab break-off has been suggested by Miller (2008) to have occurred late in the tectonic history of the Damara Belt, between 480 and 460 Ma. In the model outlined by Miller (2008), the breakoff of the subducting slab resulted in back-arc extension in the northern Central Zone and down-faulting of the northern Central Zone relative to the southern Central Zone. However, apart from a single Rb-Sr date by Haack *et al*. (1980), there is little evidence for widespread metamorphism and magmatism in the Damara at this time, and the two main thermal and magmatic episodes in the Damara Belt occurred at 560-540 Ma and at 520-510 Ma. Slab breakoff and the upwelling of hot asthenosphere have been suggested as the heat source for the 560-540 Ma thermal event (section 7.2). Minor mafic magmatism (the Goas Intrusive Suite) was coeval with voluminous crustal melting to produce the Salem-type granites (McDermott, 1986) at this time. This is in contrast to the model of Miller (2008), where slab breakoff is suggested to have been much later. It should

be noted that mantle upwelling may occur in the back-arc region of an orogen without slab breakoff being involved (e.g. Hyndman *et al*., 2005) and that, should the Central Zone have been such a back-arc region early in the collisional history, it would not be necessary to invoke slab break-off for the Damara orogen. However, the folding and thrusting seen to be coeval with 560-540 Ma magmatism in the Central Zone (Kisters *et al*., 2004) and suggests a compressional rather than extensional stress regime, contrary to that expected in an extending back-arc region (e.g. Karig, 1971; Barker & Hill, 1980). Thus, it is proposed that slab breakoff occurred between 560 and 540 Ma, and consequent upwelling of hot asthenosphere resulted in the generation of the mafic Goas Suite magmas, and melting of the crust to produce the Salem-type granites.

One feature that may be associated with slab breakoff, and which is not noted in the Damara, is the preservation of eclogites. Once subducted continental crust (at the eclogite facies) is detached from the (dense) downgoing slab, it may be rapidly exhumed (Davies & von Blanckenburg, 1995). However, whilst slab breakoff is a mechanism for the exhumation of eclogites, the preservation of eclogite is not necessary for slab breakoff to be invoked, and no eclogites are preserved in the British Caledonides (Oliver *et al*., 2008). However, along strike from the Damara Belt, eclogitic rocks are preserved elsewhere in the Pan-African belts (John *et al*., 2003; 2004).

7.6.4 The exhumation of the Central Zone

The S- to SE-verging deformation, high-grade metamorphism and magmatism in the Central Zone has been characterised in detail in this study, and age constraints have distinguished this 520-510 Ma event from an earlier episode of crustal thickening. Geodynamically, this deformation and metamorphism is thought to be related to orogenic collapse and exhumation of the Central Zone, as it occurred after the main episode of crustal thickening, shows possible decompression, and is associated with a number of extensional features noted by previous workers (e.g. Oliver, 1994; Kisters *et al*., 2009). Having reviewed the regional geology of the Damara and other Pan-African belts, and the geodynamic processes of analogous orogenic belts, the details of this exhumation and orogenic collapse can now

be discussed. The elevated topography found in collisional orogens drives exhumation of the orogen core by removal of uplifted material through two processes: erosion and gravitational collapse (Dewey, 1988; Jadamec *et al*., 2007). Typically, sediments derived from eroded material are deposited in basins adjacent to the orogen (e.g. Clift *et al*., 2004). In the case of the Damara Belt, sedimentation in the Nama Basin began at *ca*. 550 Ma (Grotzinger & Miller, 2008), forming the flysch deposits of the Kuibis and Schwarzrand Subgroups). Erosion of the uplifted orogen to form the Fish River Subgroup began slightly after 540 Ma (Grotzinger *et al*., 1995 – see section 7.3). However, gravitational collapse of thickened crust and the exhumation of high-grade rocks is typically characterised by low-angle extensional faulting (Dalmayrac & Molnar, 1981; Dewey *et al*., 1993; Clift *et al*., 2004; Kapp *et al*., 2008). This extensional faulting may be coeval with thrusting (Dalmayrac & Molnar, 1981) or may postdate the main crustal thickening phase (Kapp *et al*., 2008),and may also be orogen-perpendicular (e.g. Dalmayrac & Molnar, 1981) or orogen-parallel (e.g. Kapp *et al*., 2008). In the Damara Belt, the emplacement of the Naukluft Nappe Complex at 495 Ma may be the result of this final gravitational collapse. However, this nappe emplacement is younger than high-grade metamorphism and deformation in the Central Zone. Constrained to 520-510 Ma, this event in the Central Zone cannot be related to crustal thickening, and is likely due to collapse of thickened crust. As discussed earlier (section 7.2.1) the heat for the low-pressure 520-510 Ma metamorphism in the study area may be either from asthenosphere upwelling related to the collision of the Congo and Kalahari cratons or the position of the southwestern Central Zone relative to a major orocline, or to thickening of crust enriched in heat-producing elements. The ductile nature of deformation is likely to be the result of the high temperature of the crust, and although folding is commonly associated with compression, high-grade rocks can be folded in extensional settings (Harris *et al*., 2002). Additionally, whilst stretching lineations suggest orogen-parallel extension (see Chapter 3), the overall vergence for deformation in the study area suggests orogen-oblique to orogen-perpendicular movement. Such synchronous extension in differing directions has previously been noted (e.g. Sawyer & Barnes, 1994), and it is possible to have stretching both-orogen parallel and orogen-perpendicular during orogenic collapse (Harris *et al*., 2002). The origin of the recumbent folding in the study area can be

ascribed to the Central Zone representing a zone of ductile extension in the mid- to shallow-crust (Harris *et al*., 2002), owing to orogen-perpendicular gravitational collapse (Fig. 7.18).

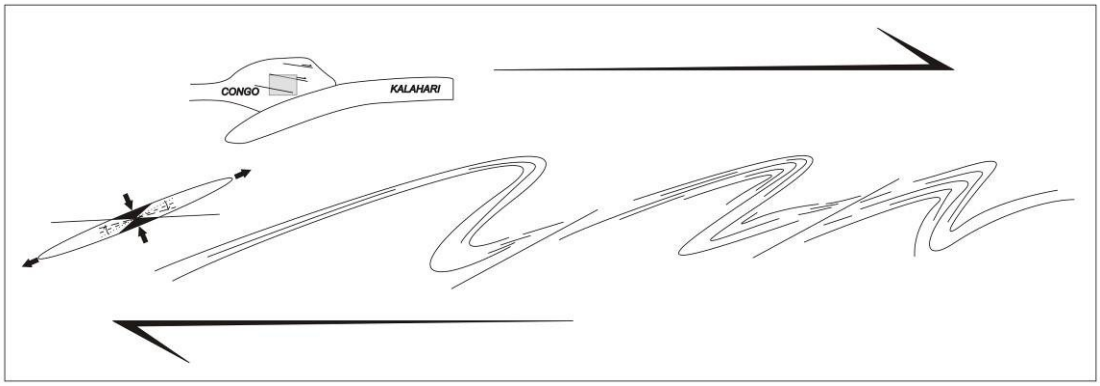

Fig. 7.18 – Schematic diagram after Harris et al*. (2002) illustrating the relationships between gravitational collapse of thickened crust in the Damara Belt and recumbent folding in the southwestern Central Zone.*

7.7 Conclusions and Recommendations for Future Studies of the Damara Orogen

The structural, geochronological and metamorphic evidence gathered in previous chapters, in conjunction with previous workers' results, has led to the identification of two major tectonic events in the Central Zone. A 560-540 Ma crustal thickening event is preserved in the Central Zone in the area around Karibib (*ca*. 100 km northeast of the study area), and is related to collision between the Congo and Kalahari Cratons. Owing to this collision, slab breakoff and asthenosphere upwelling led to crustal melting, evidenced by the emplacement of minor (mantle-derived – McDermott, 1986) mafic magmas (the Goas Intrusive Suite), and the Salem-type granites. The anatectic red granites were also produced during this thermal event. This deformation is also thought to be coeval with the main phase of SE-verging D2 deformation in the Southern Zone. Deposition of the Mulden Group was largely complete by the time of collision in the Damara Belt, which produced large-scale, upright, open E-W trending folds in the Kaoko Belt, and also deformed the Mulden Group. The timing of the onset of collision in the Gariep Belt is suggested to have been very

similar, between 550 and 545 Ma (Frimmel, 2008), and collision in both the Gariep and Damara Belts led to the formation of the Nama basin on the Southern Foreland (Grotzinger & Miller, 2008).

Subsequently, orogenic collapse and exhumation of the mid-crust look place in the Central Zone. Granulite facies metamorphism was coeval with SE-verging deformation and NE-SW extension, and minor decompression may have occurred at the metamorphic peak. The peak of deformation and metamorphism took place between 520 Ma and 510 Ma, although deformation may have begun as early as 530 Ma. This deformation and metamorphism is suggested to be related to orogenic collapse. Ages of 530-510 Ma for N-S compression in the Kaoko Belt (Goscombe *et al*., 2003a) and 530 Ma for deformation in the Northern Zone (Kamona *et al*., 1999; Seth *et al*., 2000; Goscombe *et al*., 2004) suggest that much of the N-verging structures in the Northern Zone, and Northern Platform may be related to orogenic collapse in the Damara Belt, rather than to the onset of collision. Following exhumation of the Central Zone, a switch in stress directions led to the formation of upright, NE-trending folds and the coeval emplacement of late- to post-tectonic granitoids (e.g. the uraniferous leucogranites) at 510-505 Ma, and an anticlockwise rotation of the σ_1 stress direction resulted in D4 dextral shearing along major structures. A summary of deformation in various parts of the Kaoko, Gariep and Damara belts is shown in Fig. 7.19.

A channel flow model recently developed to explain the general features of the Himalaya may be applicable to the exhumation of the mid-crust in the Central Zone, but there are a number of features have yet to be identified in the Damara and more detailed studies of the nature and timing of deformation along the bounding structures of the Central Zone are needed for a full evaluation of this model. The tectonic history presented here for the Damara Orogen is related to the timing of collision between continental fragments during the assembly of Gondwana, and hence is related to the timing of major tectonometamorphic events in other belts in the Pan-African Orogen. The similarity in the timing of events between the Damara and Gariep Belts (see sections 7.4, 7.5) suggests that they may be part of the same orogenic event (Rapela *et al*., 2011), in contrast to previous

suggestions (Alkmim *et al*., 2006, Gray *et al*., 2008) that the Kaoko Belt and Gariep Belt were related, and predated the Damara Belt.

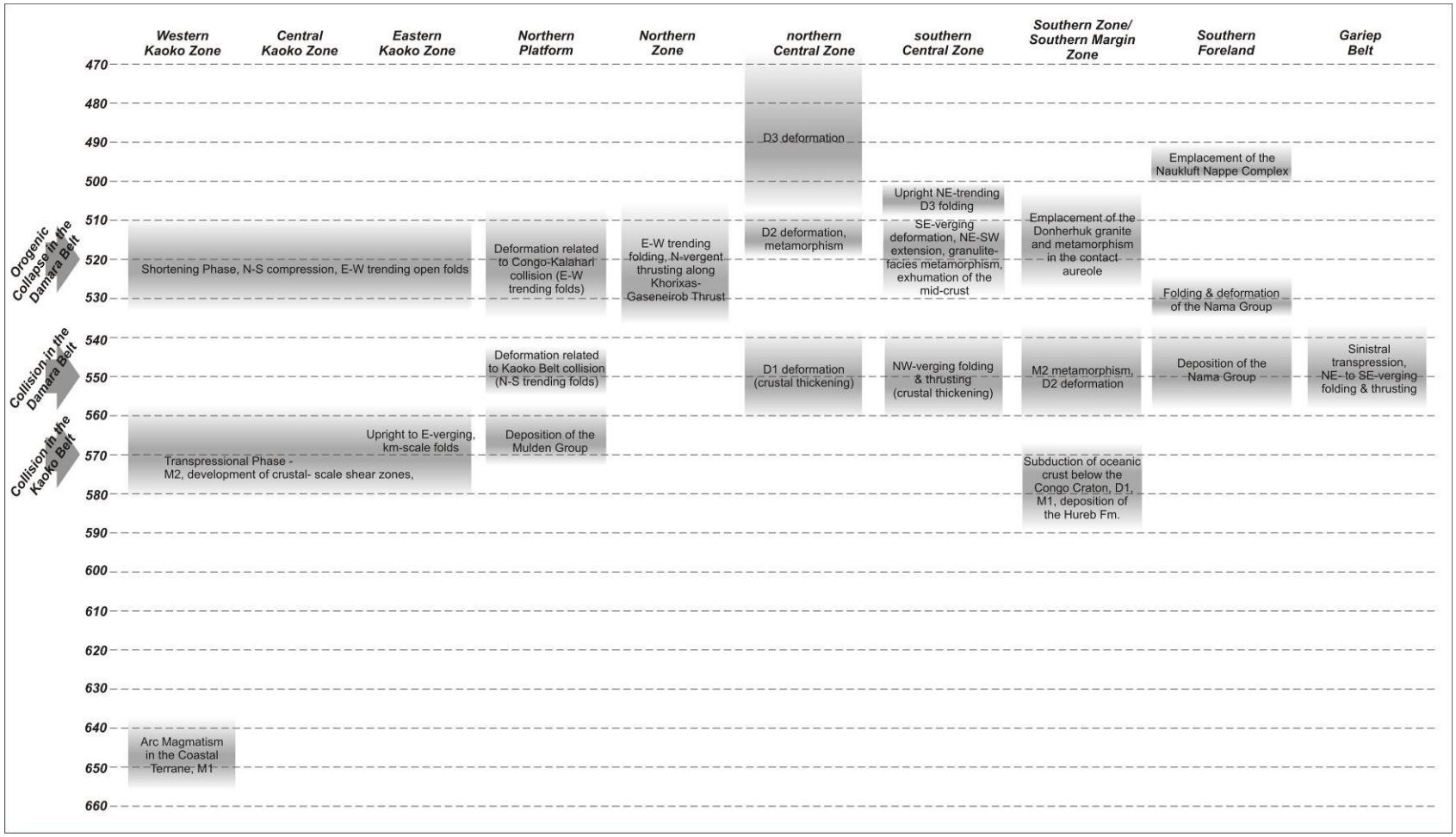

Fig. 7.19 – Summary of the timing of events across the Kaoko, Gariep and Damara belts, based on this and other studies (see text for details).

The detailed structural, geochronological and metamorphic study presented here has revealed a history of crustal thickening and orogenic collapse not previously identified in the Central Zone. However, the vast majority of the intrusive rocks in the Damara Orogen have not yet been precisely dated, and there is a lack of up-to date metamorphic studies across the orogen. Improved geochronology and metamorphic petrology may result in the further refinement of the model presented here. Suggestions for future work include:

- Using in-situ ion-microprobe geochronology of zircon or monazite in metamorphic assemblages to obtain detailed P-T-t paths for the Central and Southern Zones. One of the conclusions of this study is that deformation and metamorphism are not coeval across the entire Damara Orogen, and the timing of events needs to be carefully evaluated in detail within each zone.
- Accurate U-Pb dating of more granitoids within the Damara Orogen, and careful constraints on the structural relationships of these granites – this will aid in constraining the timing of deformation more accurately.
- Isotopic studies on zircons from Damaran Granitoids – Hf isotopes have revealed that grey granites are sourced from the Kalahari Craton, which was subducted beneath the Congo Craton. A similar source has been suggested for uraniferous leucogranites, but Nd isotopes (McDermott, 1986) are inconclusive. The sources of more of the granitoid varieties within the Damara Orogen can be better constrained with this technique.
- Detailed structural and geochronological studies of the lineaments bounding the southern Central Zone, which may represent a zone of ductile channel flow in a Himalayan-type setting. Accurate constraints on the nature, vergence and timing of movement along the Omaruru and Okanhandja lineaments are needed to confirm or disprove this hypothesis.
- Updated thermobarometry throughout the Damara Belt using phase equilibrium modelling of mineral assemblages. Current P-T estimates based on conventional thermobarometry are inaccurate, and are insufficient for understanding the P-T-t evolution of the Damara Belt.

- Careful structural studies and detailed mapping of the southern Central Zone, in order to distinguish structures related to crustal thickening from those related to extension and exhumation. Since both of these events are recorded in the southern Central Zone, their extent and influence needs to be evaluated.

These are some general suggestions which may help to advance the understanding of the tectonic evolution of the Damara Orogen and constrain the timing of events more carefully. One of the fundamental findings of this study is that tectonometamorphic events cannot necessarily be correlated across the entire orogen, and that the nature and timing of deformation must be evaluated for each area and zone before broad correlations are made. This approach must be taken before the tectonometamorphic evolution of the entire Damara Orogen can be understood.

REFERENCES

Ahrendt, H., Hunziker, J. C. & Weber, K. (1977). Age and degree of metamorphism and time of nappe emplacement along the southern margin of the Damara Orogen/Namibia (SW-Africa). *Geologische Rundschau* **67**, 719-742.

Ahrendt, H, Behr, H. J., Clauer, N., Porada, H. & Weber, K. (1983). K/Ar age determinations of the northern Damara Branch and their implications for the structural and metamorphic evolution of the Damara Orogen, South West Africa/Namibia. *In*: Miller, R. McG. (Ed.) *Evolution of the Damara Orogen*. Special Publications of the Geological Society of South Africa, **11**, 281-287.

Alkmim, F. F., Marshak, S., Pedrosa-Soares, A. C., Peres, G. G., Cruz, S. C. P. & Whittington, A. (2006). Kinematic evolution of the Araçuaí-West Congo orogen in Brazil and Africa: Nutcracker tectonics during the Neoproterozoic assembly of Gondwana. *Precambrian Research*, **149**, 43-64

Allsopp, H. L., Barton, E. S., Kröner, A., Welke, H. J. & Burger, A. J. (1983). Emplacement versus inherited isotopic age patterns: a Rb-Sr and U-Pb study of Salem-type granites in the central Damara Belt. *In*: Miller, R. McG. (Ed.) *Evolution of the Damara Orogen*. Special Publications of the Geological Society of South Africa, **11**, 281-287.

Ameglio, L., Page, P. & Jacob, R. E. (2000). 3D-geometry of the Mon-Repos granodiorite (Goas diorite suite, Damara Belt, Namibia) inferred from gravity data. *Journal of African Earth Sciences*, **31**, 1A.

Anders, E. & Grevesse, N. (1989). Abundances of the elements: Meteoritic and solar. *Geochimica et Cosmochimica Acta,* **53**, 197-214.

Armstrong, H. A. & Owen, A. W. (2001). Terrane evolution of the paratectonic Caledonides of northern Britain. *Journal of the Geological Society, London*, **158**, 475-486.

Ashwal, L. D., Armstrong, R. A., Roberts, J., Schmitz, M. D., Corfu, F., Hetherington, C. J., Burke, K. and Gerber, M. (2007). Geochronology of zircon megacrysts from nepheline-bearing

gneisses as constraints on tectonic setting: implications for resetting of the U-Pb and Lu-Hf isotopic systems. *Contributions to Mineralogy and Petrology*, **153**, 389-403.

Badenhorst, F. P. (1986). 'n Voorlopige petrografiese studie van die granitiese gesteentes van Gebied 2115B in die noordelike Sentrale Sone van die Damara-orogeen. *Communications of the Geological Survey of Namibia*, **2**, 13-26.

Badenhorst, F. P. (1988). The lithostratigraphy of the Chuos mixtite in part of the southern Central Zone of the Damara Orogen, South West Africa. *Communications of the Geological Survey of Namibia*, **4**, 103-110.

Badenhorst, F. P. (1992). *The lithostratigraphy of area 2115B and D in the Central Zone of the Damara Orogen in Namibia: with emphasis on facies changes and correlation*. MSc Thesis (unpublished), University of Port Elizabeth, 124 pp.

Barker, P. F. & Hill, I. A. (1980). Asymmetric spreading in back-arc basins. *Nature*, **285**, 652-654.

Barnes, J. F. H. (1981). *Some aspects of the Tectonic History of the Khan-Swakop region of the Damara Belt, Namibia*. PhD Thesis (unpublished), University of Leeds, Leeds, 466 pp.

Barnes, J. F. H. & Downing, K. H. (1979). Origin of domes in the central Damaran belt, Namibia. *Revue de Géologie Dynamique et de Géographie Physique*, **21**, 383-386.

Barnes, S. –J. (1982). *Serpentinites in central South West Africa/Namibia – a reconnaissance study*. Memoirs of the Geological Survey of South West Africa, **8**.

Barnes, S. -J. & Sawyer, E. W. (1980). An alternative model for the Damara Mobile Belt. Ocean crust subduction and continental convergence. *Precambrian Research*, **13**, 297-336.

Basson, I. J. & Greenway, G. (2004). The Rössing Uranium Deposit: a product of late-kinematic localization of uraniferous granites in the Central Zone of the Damara Orogen, Namibia. *Journal of African Earth Sciences*, **38**, 413-435.

Bea, F., Montero, P. G., Gonzalez-Lodeiro, F., Talavera, C., Molina, J. F., Scarrow, J. H., Whitehouse, M. J. & Zinger, T. (2006). Zircon thermometry and U–Pb ion-microprobe dating of the gabbros and associated migmatites of the Variscan Toledo Anatectic Complex, Central Iberia. *Journal of the Geological Society, London*, **163**, 847-855.

Beaumont, C., Jamieson, R. A., Nguyen, M. H. & Lee, B. (2001). Himalayan tectonics explained by extrusion of a low-viscosity crustal channel coupled to focused surface denudation. *Nature*, **414**, 738-742.

Becker, T., Hansen, B. T., Weber, K., Wiegand, B. (1996). U-Pb and Rb-Sr isotopic data of the Mooirivier Complex, the Weener Igneous Suite, and the Gaub Valley Formation (Rehoboth Sequence), Nauchas area and their significance for the Paleoproterozoic evolution of Namibia. *Communications of the Geological Survey of Namibia*, **11**, 31-46.

Becker, T., Hansen, B. T, Weber K., Wiegand, B. (2004). Isotope systematics (Sm/Nd, Rb/Sr, U/Pb) of the Elim Fm, the Alberta Complex, and the Weener Igneous Complex – probable genetic links between magmatic rocks of the Paleoproterozoic Rehoboth Basement Inlier/Namibia. *Communications of the Geological Survey of Namibia*, **13**, 75-84.

Begg, G. C., Griffin, W. L., Natapov, L. M., O'Reilly, S. Y., Grand, S. P., O'Neill, C. J., Hronsky, J. M. A., Djomani, Y. P., Swain, C. J., Deen, T. & Bowden, P. (2009). The lithospheric architecture of Africa: Seismic tomography, mantle petrology, and tectonic evolution. *Geosphere*, **5**, 23-50.

Bendick, R. & Baldwin, J. (2009). Dynamic models for metamorphic core complex formation and scaling: the role of unchannelized collapse of thickened continental crust. *Tectonophysics*, **477**, 93-101.

Berning, J. (1986). The Rössing Uranium Deposit, South West Africa/Namibia. *In*: Annhausser, C. R., Maske, S. (Eds.), *Mineral Deposits of Southern Africa*. Geological Society of South Africa, **II**, 1819-1832.

Berning, J., Cooke, R., Heimstra, S. A. & Hoffman, U. (1976). The Rössing Uranium Deposit, South West Africa. *Economic Geology*, **71**, 351-368.

Bhattacharya, A. Mohanty, L., Maji, A., Sen, S. K. & Raith, M. (1992). Non-ideal mixing in the phlogopite-annite binary: constraints from experimental data on Mg-Fe partitioning and a reformulation of the biotite-garnet geothermometer. *Contributions to Mineralogy and Petrology*, **111**, 87-93.

Bird, P. (1979). Continental delamination and the Colorado Plateau. *Journal of Geophysical Research*, **84**, 7561-7571.

Black, L. P., Kamo, S. L., Allen, C. M., Davis, D. W., Aleinikoff, J. N., Valley, J. W., Mundil, R., Campell, I. H., Korsch, R. J., Williams, I. S. & Foudoulis, C. (2004). Improved 206-Pb/U-218 microprobe geochronology by the monitoring of a trace-element related matrix effect; SHRIMP, ID-TIMS, ELA-ICP-MS and oxygen isotope documentation for a series of zircon standards. *Chemical Geology*, **205**, 115-140.

Blaine, J. L. (1977). Tectonic evolution of the Waldau Ridge structure and the Okahandja Lineament in part of the Central Damara Orogen, west of Okahandja, South West Africa. *Bulletin of the Precambrian Research Unit, University of Cape Town*, **21,** 99 pp.

Blaxland, A., Gohn, E., Haack, U. & Hoffer, E. (1979). Rb/Sr ages of late-tectonic granites in the Damara Orogen, Southwest Africa/Namibia. *Neues Jahrbuch fur Mineralogie, Monatshefte*, **11**, 498-508.

Blichert-Toft, J. & Albarede, F. (1997). The Lu-Hf isotope geochemistry of chondrites and the evolution of the mantle-crust system. *Earth and Planetary Science Letters*, **148**, 243-258.

Boger, S. D. & Miller J. McL. (2004). Terminal suturing of Gondwana and the onset of the Ross-Delamerian Orogeny: the cause and effect of an Early Cambrian reconfiguration of plate motions. *Earth and Planetary Science Letters*, **219**, 35-48.

Bohlen, S. R. (1987). Pressure-temperature-time paths and a tectonic model for the evolution of granulites. *Journal of Geology*, **95**, 617-632.

Bowden, P., Herd, D. & Kinnaird, J. A. (1995). The significance of uranium and thorium concentrations in pegmatitic leucogranites (alaskites), Rössing Mine, Swakopmund, Namibia. *Communications of the Geological Survey of Namibia*, **10**, 43-49.

Brandt, R. (1985). Preliminary report on the stratigraphy of the Damara Sequence and the geology and geochemistry of the Damaran granites in an area between Walvis Bay and Karibib. *Communications of the Geological Survey of Namibia*, **1**, 31-43.

Brandt, R. (1987). A revised stratigraphy for the Abbabis Complex in the Abbabis Inlier, Namibia. *South African Journal of Geology*, **90**, 314-323.

Breitkopf, J. H. & Maiden, K. J. (1986). A volcanogenic exhalative iron formation in the Southern Margin Zone of the Damara Orogen. *Communications of the Geological Survey of South West Africa/Namibia*, **2**, 131-143.

Briqueu, L., Lancelot, J. P., Valois, J. P. & Walgenwitz, F. (1980). Géochronologie U-Pb et gènese d'un type de minéralisation uranifère: les alaskites de Goanikontes (Namibie) et leur encaissant. *Bulletin des Centre de. Récherches Exploration-production Elf-Aquitaine*, **4**, 759-811.

Brown, M. (1994). The generation, segregation, ascent and emplacement of granite magma: the migmatites-to-crustally derived granite connection in thickened orogens. *Earth Science Reviews*, **36**, 83-130.

Brun, J. -P. & Van Den Driessche, J. (1994). Extensional gneiss domes and detachment fault systems: structures and kinematics. *Bulletin of the Geological Society of France*, **165**, 519-530.

Buhn, B., Häussinger, H., Kramm, U., Kukla, C., Kukla, P. A. & Stanistreet, I. G., (1994). Tectonometamorphic patterns developed during Pan-African continental collision in the Damara inland belt, Namibia. *Chemie der Erde*, **54**, 329-354.

Buhn, B., Okrusch, M., Woermann, E., Lehnert, K. & Hoernes, S. (1995). Metamorphic evolution of Neoproterozoic manganese formations and their country rocks at Otjosondu, Namibia. *Journal of Petrology*, **36**, 463-496.

Bunting, F. J. L. (1977). *Geology of part of the central Damara belt around the Tumas River, east of Swakopmund, South West Africa*. MSc Thesis (Unpublished), Rhodes University, Grahamstown.

Cahen, L., Snelling, N. J., Delhal, J., Vail, J. R., Bonhomme, M. & Ledent, D. (1984). *The Geochronology and Evolution of Africa*. Clarendon Press, Oxford, 512 pp.

Carey, J. W., Rice, J. M. & Grover, T. W. (1992). Petrology of aluminous schists in the Boehls Butte region of northern Idaho: Geologic history and aluminium-silicate phase relations. A*merican Journal of Science*, **292**, 455-473.

Chamberlain, C. P. & Sonder, L. J. (1990). Heat-Producing Elements and the Thermal and Baric Patterns of Metamorphic Belts. *Science*, **250**, 763-769.

Cherniak, D. J., Watson, E. B. (2000). Pb diffusion in zircon. *Chemical Geology*, **172**, 5-24.

Clemens, J. D. & Watkins, J. M. (2001). The fluid regime of high-temperature metamorphism during granitoid magma genesis. *Contributions to Mineralogy and Petrology*, **140**, 600-606.

Clifford, T. N. (2008). The geology of the Neoproterozoic Swakop-Otavi transition zone in the Outjo District, northern Damara Orogen, Namibia. *South African Journal of Geology*, **111**, 117-140.

Clift, P. D., Dewey, J. F. Draut, A. E., Chew, D. M., Mange, M. & Ryan, P. D. (2004). Rapid tectonic exhumation, detachment faulting and orogenic collapse in the Caledonides of western Ireland. *Tectonophysics*, **384**, 91-113.

Cocks, L. R. M. & Torsvik, T. H. (2006). European geography in a global context from the Vendian to the end of the Palaeozoic. *In*: Gee, D. G. & Stephenson, R. A. (Eds). *European Lithosphere Dynamics*. Geological Society, London, Memoirs, 32, 83-95.

Compston, W., Williams, I. S. & Kirschvink, J. L. (1992). Zircon U-Pb ages for the Early Cambrian time-scale. *Journal of the Geological Society, London*, **149**, 171–184.

Cumming, G. L. & Richards, J. R. (1975). Ore lead isotope ratios in a continuously changing earth. *Earth and Planetary Science Letters*, **28**, 155-171.

Coney, P. J. & Harms, T. A. (1984) Cordilleran metamorphic core complexes: Cenozoic extensional relics of Mesozoic compression. *Geology*, **12**, 550-554.

Corner, B. (1983). An interpretation of the aeromagnetic data covering the western portion of the Damara Orogen in South West Africa/Namibia. *In*: Miller, R. McG. (Ed.), *Evolution of the Damara Orogen of South West Africa/Namibia*. Special Publications of the Geological Society of South Africa, **11**, 339-354.

Corner, B. (2008). The Crustal Framework of Namibia Derived from an Integrated Interpretation of Geophysical and Geological Data. *In*: Miller, R. McG. *The Geology of Namibia. Volume 1: Archaean to Mesoproterozoic*. Geological Survey of Namibia, 2-1 – 2-19.

Corner, B. & Henthorn, D. I. (1978). *Results of a Palaeomagnetic survey undertaken in the Damara Mobile Belt, South West Africa, with special reference to the magnetisation of the uraniferous pegmatitic granites*. South African Atomic Energy Board Report PEL-260.

Coward, M. P. (1981). The junction between Pan African mobile belts in Namibia: its structural history. *Tectonophysics*, **76**, 59-73.

Coward, M. P. (1983). The tectonic history of the Damaran belt. *In*: Miller, R. McG. (Ed) *Evolution of the Damara Orogen in South West Africa/Namibia*. Special Publications of the Geological Society of South Africa, **11**, 409-421.

Dalmayrac, B. & Molnar, P. (1981). Parallel normal and thrust faulting in peru, and constraints on the state of stress. *Earth and Planetary Science Letters*, **55**, 473-481.

Dasgupta, S., Sengupta, P., Guha, D. & Fukuoka, M. (1991). A refined garnet- biotite Fe- Mg exchange geothermometer and its application in amphibolites and granulites. *Contributions to Mineralogy and Petrology*, **109**, 130-137.

Dasgupta, S., Sanyal, S., Sengupta, P. & Fukuoka, M. (1994). Petrology of granulites from Anakapalle – evidence for Proterozoic decompression in the Eastern Ghats, India. *Journal of Petrology*, **35**, 433-459.

Davies, J. H. & von Blanckenburg, F. (1995). Slab breakoff: A model of lithosphere detachment and its test in the magmatism and deformation of collisional orogens. *Earth and Planetary Science Letters*, **129**, 85-102.

Davidson, A. (1998). An overview of Grenville Province geology, Canadian Shield: Chapter 3. *In*: Lucas, S. B. & St-Onge, M. R. (Eds) *Geology of the Precambrian Superior and Grenville provinces and Precambrian fossils in North America*. Geological Survey of Canada, Geology of Canada, **7**, 205-270.

De Kock, G. S. (1989). *'n geotektoniese studie van die Damara-orogeen in 'n gebied suidoos van Karibib, Suidwes-Afrika.* PhD Thesis (unpublished), University of the Orange Free State, Bloemfontein, 438 pp.

De Kock, G. S. (1991). The mafic Audawib Suite in the Central Damara orogeny of Namibia: geochemical evidence for volcanic arc volcanism. *Journal of African Earth Sciences,* **12**, 593-599.

De Kock, G. S. (2001). A reappraisal of the Namibian Damara stratigraphy in part of the Southern Swakop Terrane and its implications to basin evolution. *South African Journal of Geology*, **104**, 115-136.

De Kock, G. S. & Botha, B. J. V. (1988). Basin development in the Damara orogen during the deposition of the Okomis and Omusema Formations at the base of the Swakop Group, in the region southeast of Karibib, South West Africa/Namibia. *South African Journal of Geology*, **91**, 83-96.

De Kock, G. S. & Botha, B. J. V. (1988). Komontwikkeling in die Damara-orogeen gedurende die afsetting van die Okomis-en Omusemaformasies aan die basis van die Swakopgroep, in die gebied suid-oos van Karibib, Namibia. *South African Journal of Geology*, **91**, 83-96.

De Kock, G. S., Eglington, B., Armstrong, R. A., Harmer, R. E. & Walraven, F. (2000). U-Pb and Pb-Pb ages of the Naauwpoort rhyolite, Kawaeup leptite and Okongava diorite: implications for the onset of rifting and orogenesis in the Damara belt, Namibia. *Communication of the Geological Survey of Namibia*, **12**, 81-88.

De Kock, G. S. (2001). A reappraisal of the Namibian Damara stratigraphy in part of the Southern Swakop Terrane and its implications to basin evolution. *South African Journal of Geology*; **104**, 115-136.

Deer, W. A., Howie, R. A. & Zussman, J. (1971). *An Introduction to the Rock-Forming Minerals*. Longman, London, 528 pp.

Delhal, J. & Ledent, D. (1973). Ĺ âge du complexe métasédimentaire de Luiza, region du Kasai (Zaire). *Annales de la Société Géologique de Belgique*, **94**, 211-221.

Delhal, J., Ledent, D. & Torquato, J. R. (1976). Nouvelles données géochronologiques reatives au complexe gabbro-noritique et charnockitique du bouclier du Kasai et à son prolongement en Angola. *Annales de la Société Géologique de Belgique*, **99**, 211-226.

Dewey, J. F. (1988). Extensional collapse of orogens. *Tectonics*, **7**, 1123-1139

Dewey, J. F. & Bird, J. M. (1970). Mountain belts and the new global tectonics. *Journal of Geophysical Research*, **75**, 2625-2647.

Dewey, J. F., Ryan, P. D. & Andersen, T. B. (1993). Orogenic uplift and collapse, crustal thickness, fabrics and metamorphic phase changes: the role of eclogites. *Geological Society, London, Special Publications*, **76**, 325-343.

Dewey, J. F., Holdsworth, R. E. & Strachan, R. A. (1998). Transpression and transtension zones. *In*: Holdsworth, R. E., Strachan, R. A. & Dewey, J. F. (Eds) *Continental Transpressional and Transtensional Tectonics*. Geological Society, London, Special Publications, **135**, 1-14.

DiBenedetto, S. & Grotzinger, J. P. (2005). Geomorphic evolution of a storm-dominated carbonate ramp (*ca*. 549 Ma), Nama Group, Namibia. *Geological Magazine*, **142**, 583-604.

Diener, J. F. A. & Powell, R. (2010). Influence of ferric iron on the stability of mineral assemblages. *Journal of Metamorphic Geology*, **28**, 599-613.

Dirks, P. H. G. M. (2000). *An assessment of the structural controls on gold mineralisation at Navachab Mine and related Au occurrences; implications for regional exploration*. Report compiled for Anglogold Ltd.

Downing, K. N. & Coward, M. P. (1981). The Okahandja lineament and its significance for Damaran tectonics in Namibia. *Geologische Rundschau* **70**, 972-1003.

Downing, K. N. (1982). *The evolution of the Okahandja Lineament and its significance for Damara tectonics in Namibia.* Ph.D. Thesis (unpublished), University of Leeds, Leeds.

Droop, G. T. R (1987). A general equation for estimating Fe^{3+} concentrations in ferromagnesian silicates and oxides from microprobe analyses, using stochiometric criteria. *Mineralogical Magazine*, **51**, 431-435.

Ducea, M. N. (2011). Fingerprinting orogenic delamination. *Geology*, **39**, 191-192.

England, P. C. & Thompson, A. B. (1984). Pressure-temperature-time paths of regional metamorphism I. Heat transfer during the evolution of regions of thickened continental crust. *Journal of Petrology*, **25**, 894-928.

Eskola, P. E. (1949). The problem of mantled gneiss domes. *Quarterly Journal of the Geological Society of London*, **104**, 461-476.

Fermor, P. R. & Price, R. A. (1987). Multiduplex structures along the base of the Lewis thrust sheet in the southern Canadian Rockies. *Bulletin of Canadian Petroleum Geology*, **35**, 159-185.

Fernández-Suárez, J., Dunning, G. R., Jenner, G. A., & Gutiérrez-Alonso, G. (2000). Variscan collisional magmatism and deformation in NW Iberia: Constraints from U-Pb geochronology of granitoids: *Geological Society of London Journal*, **157**, 565-576.

Ferry, J. M. & Spear, F. S (1978). Experimental calibration of the partitioning of Fe and Mg between biotite and garnet. *Contributions to Mineralogy and Petrology*, **66**, 113-117.

Fletcher, J. M. & Bartley, J. M. (1994). Constrictional strain in a noncoaxial shear zone; implications for fold and rock fabric development, central Mojave Metamorphic Core complex, California. *Journal of Structural Geology*, **16**, 555-570.

Fletcher, J. M., Bartley, J. M., Martin, M. W., Glazner, A. F. & Walker, J. D. (1995). Large magnitude continental extension – an example from the central Mojave metamorphic core complex. *Geological Society of America Bulletin*, **107**, 1468-1483.

Fletcher, R. C. (1991). 3-dimensional folding of an embedded viscous layer in pure shear. *Journal of Structural Geology*, **13**, 87-96.

Fletcher, R. C. (1995). 3-dimensional folding and necking of a power-law layer: Are folds cylindrical, and if so, do we understand why? *Tectonophysics*, **247**, 65-83.

Fossen, H. & Tikoff, B. (1998). Extended models of transpression and transtension, and application to tectonic settings. *In*: Holdsworth, R. E., Strachan, R. A. & Dewey, J. F. (Eds) *Continental Transpressional and Transtensional Tectonics*. Geological Society, London, Special Publications, **135**, 1-14.

Fowler, T. J. & Osman, A. F. (2001). Gneiss-cored interference dome associated with two phases of late Pan-African thrusting in the Central Eastern Desert, Egypt. *Precambrian Research*, **108**, 17-43.

Frimmel, H. E. (2008). Neoproterozoic Gariep Orogen. *In*: Miller, R. McG (Ed). *The Geology of Namibia. Volume 2: Neoproterozoic to Lower Palaeozoic*. Geological Survey of Namibia, p14-1–14-39.

Frimmel, H. E., Harnady, C. J. H. & Koller, F. (1996). Geochemistry and tectonic setting of magmatic unites in the Pan-African Gariep Belt, Namibia. *Chemical Geology*, **130**, 101-121.

Frimmel, H. E. & Frank, W. (1998). Neoproterozoic tectono-thermal evolution of the Gariep Belt and its basement, Namibia and South Africa. *Precambrian Research,* **90**, 1-28.

Frimmel, H. E. Basei, M. S. & Gaucher, C. (2011). Neoproterozoic geodynamic evolution of SW-Gondwana: a southern African perspective. *International Journal of Earth Science*, **100**, 323-354.

Frost, R. B. (1991). Introduction to oxygen fugacity and its petrologic importance. *Reviews in Mineralogy and Geochemistry*, **25**, 1-9.

Gapais, D., Pecher, A., Gilbert, E. & Ballevre, M. (1992). Syn-convergence spreading of the main central sheet, Ladakh Himalaya. *Tectonics*, **11**, 1045-1056.

Gessman, C. K., Spiering, B. & Raith, M. (1997). Experimental study of the Fe-Mg exchange between garnet and biotite: Constraints on the mixing behavior and analysis of the cation-exchange mechanisms. *American Mineralogist*, **82**, 1225-1240.

Germs, G. J. B. (1972). The stratigraphy and palaeontology of the lower Nama Group, South West Africa. *Bulletin of the Precambrian Research. Unit, University of Cape Town*, **12**.

Germs, G. J. B. (1983). Implications of a sedimentary facies and depositional environment analysis of the Nama Group in South West Africa/Namibia. *In*: Miller, R. McG. (Ed) *Evolution of the Damara Orogen in South West Africa/Namibia*. Special Publications of the Geological Society of South Africa, **11**, 89-114.

Germs, G. J. B. (1995). The Neoproterozoic of southwestern Africa, with emphasis on platform stratigraphy and palaeontology. *Precambrian Research*, **73**, 137-151.

Germs, G. J. B & Gresse, P. G (1991). The foreland basin of the Damara and Gariep orogens in Namaqualand and southern Namibia: stratigraphic correlations and basin dynamics. *South African Journal of Geology*, **94**, 159-169.

Gervais, F., Nadeau, L., & Malo, M. (2004). Migmatitic structures and solid-state diapirism in orthogneiss domes, Eastern Grenville Province, Canada. *In*: Whitney, D. L., Teyssier, C. &

Siddoway, C. S. *Gneiss Domes in Orogeny*. Geological Society of America Special Paper, **380**, 359-378.

Ghosh, S. K., Khan, D. & Sengupta, S. (1995). Interfering folds in constrictional deformation. *Journal of Structural Geology*, **17**, 1361-1373.

Godin, L., Grujic, D., Searle, M. & Law, R. D. (2006). Channel flow, extrusion, and exhumation in continental collision zones: an introduction. *In*: Law, R. D., Searle, M., Godin, L. (Eds.) *Channel Flow, Extrusion and Exhumation of Lower-mid Crust in Continental Collision Zones*. Geological Society, London, Special Publications, **268**, 1-23.

Goodge, J. W. & Vervoort, J. D. (2006). Origin of Mesoproterozoic A-type granites in Laurentia: Hf isotope evidence. *Earth and Planetary Science Letters*, **243**, 711-731.

Goscombe, B., Armstrong, R. & Barton, J. M. (1998). Tectonometamorphic Evolution of the Chewore Inliers: Partial Re-equilibration of High-grade Basement during the Pan-African Orogeny. *Journal of Petrology*, **39**, 1347-1384.

Goscombe, B. & Gray, D. R. (2007). The Coastal Terrane of the Kaoko Belt, Namibia: Outboard arc-terrane and tectonic significance. *Precambrian Research*, **155**, 139-158.

Goscombe, B. & Gray, D. R. (2009). Metamorphic response in orogens of different obliquity, scale and geometry. *Gondwana Research*, **15**, 151-167.

Goscombe, B., Gray, D. & Hand, M. (2004). Variation in metamorphic style along the Northern Margin of the Damara Orogen, Namibia. *Journal of Petrology*, **45**, 1261-1295.

Goscombe, B., Gray, D. & Hand, M. (2005a). Extrusion tectonics in the core of a transpressional orogen; the Kaoko Belt, Namibia. *Journal of Petrology*, **46**, 1203-1241.

Goscombe, B., Gray, D. R., Armstrong, R., Foster, D. A. & Vogl, J. (2005b). Event geochronology of the Pan-African Kaoko Belt, Namibia. *Precambrian Research*, **140**, 1-41.

Goscombe, B., Hand, M. & Gray, D. R. (2003a). Structure of the Kaoko Belt, Namibia: progressive evolution of a classic transpressional orogen. *Journal of Structural Geology*, **25**, 1049-1081.

Goscombe, B. D., Hand, M., Gray, D. & Mawby, J. (2003b). The metamorphic architecture of a transpressional orogen: the Kaoko Belt, Namibia. *Journal of Petrology*, **44**, 676–711.

Gray, D. R., Foster, D. A., Goscombe, B. D., Passchier, C. W. & Trouw, R. A. J. (2006). $^{40}Ar/^{39}Ar$ thermochronology of the Pan-African Damara orogen, Namibia, with implications for tectonothermal and geodynamic evolution. *Precambrian Research*, **150**, 49-72.

Gray, D. R., Foster, D. A., Meert, J. G., Goscombe, B. D., Armstrong, R., Trouw, R. A. J., & Passchier, C. W. (2008). A Damara orogen perspective on the assembly of southwestern Gondwana. *In:* Pankhurst, R. J., Trouw, R. A. J., Brito Neves, B. B. & De Wit, M. J. (Eds) *West Gondwana: Pre-Cenozoic Correlations Across the South Atlantic Region.* Geological Society, London, Special Publications, **294**, 257-278.

Greenfield, J. E., Clargke, G. L. & White, R. W. (1998). A sequence of partial melting reactions at Mt Stafford, central Australia. *Journal of Metamorphic Geology*, **16**, 363-378.

Gresse, P. G. & Germs, G. J. B. (1993). The Nama foreland basin: sedimentation, major unconformity bounded sequences and multisided active margin advance. *Precambrian Research,* **63**, 247-272.

Grotzinger, J. P., Bowring, S. A., Saylor, B. Z. & Kaufman, A. J. (1995). Biostratigraphic and geochronologic constraints on early animal evolution. *Science*, **270**, 598-604.

Grotzinger, J. P. & Miller, R. McG. (2008). Nama Group. *In*: Miller, R. McG (Ed). *The Geology of Namibia. Volume 2: Neoproterozoic to Lower Palaeozoic*. Geological Survey of Namibia, p13-229–13-272.

Grujic, D., Hollister, L. S. & Parrish, R. R. (2002). Himalayan metamorphic sequence as an orogenic channel: insight from Bhutan. *Earth and Planetary Science Letters*, **198**, 177–191.

Grujic, D., Coutand, I., Bookhagen, B., Bonnet, S., Blythe, A., Duncan, C. (2006). Climatic forcing of erosion, landscape, and tectonics in the Bhutan Himalayas. *Geology*, **34**, 801-804.

Guidotti, C. V. (1970). The mineralogy and petrology of the transition from the lower to upper sillimanite zone in the Oquossoc area, Maine. *Journal of Petrology*, **11**, 277-336.

Guiraud, M., Powell, R. & Rebay, G. (2001). H_2O in metamorphism and unexpected behaviour in the preservation of metamorphic mineral assemblages. *Journal of Metamorphic Geology*, **19**, 181-192.

Gutiérrez-Alonso, G., Murphy, J. B., Fernández-Suárez, J., Weil, A. B., Franco, M. P., & Gonzalo, J. P. (2011). Lithospheric delamination in the core of Pangea: Sm-Nd insights from the Iberian mantle. *Geology*, **39**, 155-158.

Haack, U., Hoffer, E., (1976). K/Ar ages of biotites from the Damara orogen, South West Africa. *Transaction of the Geological Society of South Africa*, **79**, 213-216.

Haack, U., Gohn, E. and Klein, J. A. (1980). Rb/Sr ages of granitic rocks along the middle reaches of the Omaruru River and the timing of orogenetic events in the Damara Belt (Namibia). *Contributions to Mineralogy and Petrology*, **74**, 349-360.

Haack, U., Hoers, J. & Gohn, E. (1982). Constraints on the Origin of Damaran Granites by Rb/Sr and $\delta^{18}O$ Data. *Contributions to Mineralogy and Petrology*, **79**, 279-289.

Haack, U. (1983). Reconstruction of the Cooling History of the Damara Orogen by Correlation of Radiometric Ages with Geography and Altitude. *In*: Martin, H. & Eder, F. W. (Eds) *Intracontinental Fold Belts*. Springer Verlag, Berlin, 873-884.

Haack, U. & Martin, H. (1983). Geochronology of the Damara Orogen – A Review. *In*: Martin, H. & Eder, F. W. (Eds) *Intracontinental Fold Belts*. Springer Verlag, Berlin, 839-846.

Haack, U., Gohn, E. & Hartmann, O. (1983). Heat generation in Damaran Rocks. *In*: Miller, R. McG. (Ed.) *Evolution of the Damara Orogen*. Special Publications of the Geological Society of South Africa, **11**, 225-231

Haack, U. & Gohn, E. (1988). Rb–Sr data on some pegmatites in the Damara Orogen, Namibia. *Communications of the Geological Survey of South West Africa/Namibia*, **4**, 13–17.

Haack U., Gohn E., Brandt R. & Feldmann, H. (1988). Rb-Sr data on the Otjimbingwe Alkali complex in the Damara orogen, South West Africa, Namibia. *Chemie der Erde*, **48**, 131-140.

Hackler R. T. & Wood B. J. (1989). Experimental determination of Fe and Mg exchange between garnet and olivine and estimation of Fe-Mg garnet mixing properties. *American Mineralogist*, **74**, 994-999.

Hanson, R. E., Wardlaw, M. S., Wilson, T. J. & Mwale, G. (1993). U-Pb zircon ages from the Hook granite massif and Mwembeshi dislocation: constraints on Pan-African deformation, plutonism, and transcurrent shearing in central Zambia. *Precambrian Research*, **63**, 189-209.

Harley, S. L. (1989). The origins of granulites: a metamorphic perspective. *Geological Magazine*, **126**, 215-247.

Harris, L. B., Koyi, H. A. & Fossen, H. (2002). Mechanisms for folding of high-grade rocks in extensional tectonic settings. *Earth Science Reviews*, **59**, 163-210.

Hartmann, O., Hoffer, E. & Haack, U. (1983). Regional metamorphism in the Damara Orogen: Interaction of crustal motion and heat transfer. *In*: Miller, R. McG. (Ed.) *Evolution of the Damara Orogen*. Special Publications of the Geological Society of South Africa, **11**, 233-241.

Hartnady, C. J. (1978). *The structural geology of the Naukluft Nappe Complex and its relationship to the Damara Orogenic Belt, South West Africa*. PhD Thesis (unpublished), University of Cape Town.

Hartnady, C. J., Joubert, P. & Stowe, C. (1985). Proterozoic crustal evolution of southwestern Africa. *Episodes*, **8**, 236-244.

Hawkesworth, C. J., Gledhill, A. R., Roddick, J. C., Miller, R. McG. & Kröner, A. (1983). Rb-Sr and $^{40}Ar/^{39}Ar$ studies bearing on models for the thermal evolution of the Damara Belt, Namibia. *In*:

Miller, R. McG. (Ed.) *Evolution of the Damara Orogen*. Special Publications of the Geological Society of South Africa, **11**, 323-338.

Heilbron, M. & Machado, N. (2003). Timing of terrane accretion in the Neoproterozoic–Eopaleozoic Ribeira orogen (SE Brazil) Precambrian Research, **125**, 87-112.

Heilbron, M., Pedrosa-Soares, A. C., Campos Neto, M., Silva, L. C., Trouw, R. A. J. & Janasi, V. (2004). Província Mantiqueira. *In*: Mantesso-Neto, V., Bartorelli, A., Carneiro, C. D. R. & Brito Neves, B. B. (Eds.), *Geologia do Continente Sul-Americano: Evolução da Obra de Fernando Flávio Marques de Almeida. Beca, São Paulo*. 203-234.

Henry, G. (1992). *The sedimentary evolution of the Damara Sequence in the lower Khan River valley, Namibia*. PhD Thesis (unpublished), University of the Witwatersrand, Johannesburg.

Henry, G., Stanistreet, I. G. & Maiden, K. J. (1986). Preliminary results of a sedimentological study of the Chuos Formation in the Central Zone of the Damara orogen: evidence for mass flow processes and glacial activity. *Communications of the Geological Survey of Namibia*, **2**, 75-92.

Hill, R. S. (1975). Geological map 2315 BD – Rostock, scale 1:50 000. *Geological Survey of Namibia* (unpublished).

Hoal, K. O., Hoal, B. G., Griffin, W. L. & Armstrong, R. A. (2000). Characterization of the age and nature of the lithosphere in the Tsumkwe region, Namibia. *In*: Miller, R. McG. (Ed.), *Special Issue: Henno Martin Commemorative Volume.* Communications of the Geological Survey of Namibia, **12**, 21-28.

Hodges, K. V. & Applegate, J. D. (1993). Age of Tertiary extension in Bitterroot metamorphic core complex, Montana and Idaho. *Geology*, **21**, 161-164.

Hoernes, S. & Hoffer, E. (1979). Equilibrium relations of prograde metamorphic mineral assemblages. A stable isotope study of rocks of the Damara Orogen, from Namibia. *Contributions to Mineralogy and Petrology*, **68**, 377-389.

Hoernes, S. & Hoffer, E. (1985). Stable isotope evidence for fluid-present and fluid absent metamorphism in metapelites from the Damara Orogen, Namibia. *Contributions to Mineralogy and Petrology*, **90**, 322-330.

Hoffer, E. (1977). *Petrologische Untersuchungen zur Regionalmetamorphose Al-reicher Metapelite im südluchen Damara-Orogen*. Habilitationsschrift (unpublished), University of Göttingen, Göttingen.

Hoffman, P. F. (2005). On Cryogenian (Neoproterozoic) ice-sheet dynamics and the limitations of the glacial sedimentary record. *South African Journal of Geology*, **108**, 557-577.

Hoffman, P. F., Hawkins, D. P., Isachsen, C. E. & Bowring, S. A. (1996). Precise U-Pb zircon ages for early Damaran magmatism in the Summas Mountains and Welwischia Inlier, northern Damara belt, Namibia. *Communications of the Geological Survey of Namibia*, **11**, 47-52.

Hoffmann, C. (1976). Granites and migmatities of the Damara belt, South West Africa. Petrography and melting experiments. *Geologische Rundschau*, **65**, 939-966.

Hoffman, K. H. (1981). Structural and stratigraphic relationships of overthrust basement rocks in the Oamites area, southern Damara margin, South West Africa/Namibia. *Abstract Volume of the Geological Society of South Africa Geocongress 1981*.

Hoffmann, K. H., (1983). Lithostratigraphy and facies of the Swakop Group of the Southern Damara Belt, S W A/Namibia. *In*: Miller, R. McG. (Ed.) *Evolution of the Damara Orogen*. Special Publications of the Geological Society of South Africa, **11**, 11-43.

Hoffmann, K. H. (1989). New aspects of lithostratigraphic subdivision and correlation of late Proterozoic to early Cambrian rocks of the southern Damara Belt and their correlation with the central and northern Damara Belt and the Gariep Belt. *Communications of the Geological Survey of Namibia*, **5**, 59-67.

Hoffmann, K. H., Condon, D. J., Bowring, S. A. & Crowley, J. L. (2004). U-Pb zircon date from the Neoproterozoic Ghaub Formation, Namibia: Constraints on Marinoan glaciation. *Geology*, **32**, 817-820.

Holdaway, M. J. (1971). Stability of andalusite and the aluminium silicate phase diagrams. *American Journal of Science*, **271**, 97-131.

Holdaway, M.J., & Lee, S. M. (1977). Fe-Mg cordierite stability in high grade pelitic rocks based on experimental, theoretical and natural observations. *Contributions to Mineralogy and Petrology*, **63**, 175-198.

Holdaway, M. J., Mukhopadhyay, B., Dyar, M. D., Guidotti, C. V. & Dutrow, B. L. (1997). Garnet-biotite geothermometry revisited: New Margules parameters and a natural specimen data set from Maine. *American Mineralogist*, **82**, 582-595.

Horstmann, U. E., Ahrendt, H., Clauer, N. & Porada, H. (1990). The metamorphic history of the Damara Orogen based on K/Ar data of detrital white micas from the Nama Group, Namibia. *Precambrian Research*, **48**, 41-61.

Hsü, K. J. (1979). Thin skinned plate tectonics during Neo-Alpine orogenesis. *American Journal of Science*, **279**, 353-366.

Hutton, D. H. W. & Dewey, J. F. (1986). Palaeozoic terrane accretion in the western Irish Caledonides. *Tectonics*, **5**, 1115-1124.

Hyndman, R. D., Currie, C. A. & Mazzotti, S. P. (2005). Subduction zone backarcs, mobile belts, and orogenic heat. *GSA Today*, **15**, 5-10.

Ickert, R. B., Hiess, J., Williams, I. S., Holden, P. Ireland, T. R., Lane, P., Schram, N., Foster, J. J. and Clement, S. W. (2008). Determining high precision, in-situ, oxygen isotope ratios with a SHRIMP II: Analyses of MPI-DING silicate-glass reference materials and zircon from contrasting granites. *Chemical Geology*, **257**, 114-128.

Jacob, R.E. (1974). *Geology and metamorphic petrology of part of the Damara Orogen along the lower Swakop River, South West Africa*. Bulletin of the Precambrian Research Unit, University of Cape Town **17**, 184 pp.

Jacob, R. E., Kröner, A. & Burger, A. J. (1978). Areal extent and first U-Pb age of the Pre-Damaran Abbabis complex in the central Damara belt of South West Africa (Namibia). *International Journal of Earth Sciences*, **67**, 706-718.

Jacob, R.E., Snowden, P.A. & Bunting, F.J.L. (1983). Geology and structural development of the Tumas basement dome and its cover rocks. *In*: Miller, R. McG. (Ed.) *Evolution of the Damara Orogen*. Special Publications of the Geological Society of South Africa, **11**, 157-172.

Jacob, R. E., Corner, B., & Brynard, H. J. (1986). The Regional Geological and Structural Setting of the Uraniferous Granitic Provinces of Southern Africa. *In*: Anhaeusser, C.R. & Maske, E. (Eds). *Mineral Deposits of Southern Africa*, **II**, Geological Society of South Africa Special Publication, 1807-1818.

Jacob, R. E., Moore, J. M. & Armstrong, R. A. (2000). Zircon and Titanite age determination from igneous rocks in the Karibib District, Namibia: implications for Navachab vein-style gold mineralization. *Communication of the Geological Survey of Namibia*, **12**, 157-166.

Jadamec, M. A., Turcotte, D. L. & Howell, P. D. (2007). Two-Dimensional analytic models for orogenic collapse. *Tectonophysics*, **435**, 1-12.

Jamieson, R. A., Beaumont, C., Fullsack, P. & Lee, B. (1998). Barrovian regional metamorphism: Where's the heat? *In*: Treloar, P. J. & O'Brien, P. J**.** (Eds) *What Drives Metamorphism and Metamorphic Reactions?* Geological Society, London, Special Publications, **138,** 23-51.

Jamieson, R. A., Beaumont, C., Nguyen, M. H. & Grujic, D. (2006). Provenance of the Greater Himalayan Sequence and associated rocks: Predictions of channel flow models. *In*: Law, R., Searle, M. P. & Godin, L. (Eds). *Channel flow, ductile extrusion, and exhumation in continental collision zones*. Geological Society, London, Special Publications*,* **268**, 165-182

John, B. E. (1987). Geometry and evolution of a midcrustal extensional fault system: Chemehuevi Mountains, southeastern California. *Geological Society Special Publication*, **28**, 313-335.

John, T., Schenk, V., Haase, K., Scherer, R. & Tembo, F. (2003). Evidence for a Neoproterozoic ocean in South-central Africa from mid-oceanic ridge- type geochemical signatures and pressure–temperature estimates of Zambian eclogites. *Geology*, **31**, 243-246.

John, T., Schenk, V., Mezger, K. & Tembo, F. (2004). Timing and PT evolution of whiteschist metamorphism in the Lufilian arc-Zambezi belt orogen (Zambia): implications for the assembly of Gondwana. *The Journal of Geology*, **112**, 71-90.

Johnson, A. M. (1998). *Textural and Chemical Relations Among Spinel-Saphirrine-Garnet-Orthopyroxene, Salt-Hill Emery Mine, Cortlandt Complex, N. Y.* MSc Thesis (unpublished), Virginia Polytechnic Institute and State University, Blacksburg, Virginia.

Johnson, T., Brown, M., Gibson, R. & Wing, B. (2004). Spinel-cordierite symplectites replacing andalusite: evidence for melt-assisted diapirism in the Bushveld Complex, South Africa. *Journal of Metamorphic Geology*, **22**, 529-545.

Johnson, S. D., Poujol, M. & Kisters, A. F. M. (2006). Constraining the timing and migration of collisional tectonics in the Damara Belt, Namibia: U-Pb zircon ages for the syntectonic Salem-type Stinkbank granite. *South African Journal of Geology*, **109**, 611-624.

Jones, R. R., Holdsworth, R. E. & Bailey, W. (1997). Lateral extrusion in transpression zones: the importance of boundary conditions. *Journal of Structural Geology*, **19**, 1201-1218.

Jung, S. (2000). High-temperature, low/medium pressure clockwise P-T paths and melting in the development of regional migmatities: the role of crustal thickening and repeated plutonism. *Geological Journal*, **35**, 345-359.

Jung, S. & Mezger, K. (2003a). Petrology of basement-dominated terranes: I. regional metamorphic T-t path and geochronological constraints on Pan-African high-grade metamorphism (central Damara orogen, Namibia). *Chemical Geology*, **198**, 223-247.

Jung, S. & Mezger, K. (2003b). U-Pb garnet chronometry in high-grade rocks—case studies from the central Damara orogen (Namibia) and implications for the interpretation of Sm-Nd

garnet ages and the role of high U-Th inclusions. *Contributions to Mineralogy and Petrology*, **146**, 382-396.

Jung, S., Mezger, K., Masberg, P., Hoffer, E. & Hoernes, S. (1998). Petrology of an intrusion-related high-grade migmatites: implications for partial melting of metasedimentary rocks and leucosome-forming processes. *Journal of Metamorphic Geology*, **16**, 425-445.

Jung, S., Mezger, K. & Hoernes, S. (2001). Trace element and isotopic (Sr, Nd, Pb, O) arguments for a mid-crustal origin of Pan-African garnet-bearing S-type granites from the Damara orogen (Namibia). *Precambrian Research*, **110**, 325-355.

Jung, S., Hoernes, S. & Mezger, K. (2002). Synorogenic melting of mafic lower crust: constraints from geochronology, petrology and Sr, Nd, Pb and O isotope geochemistry of quartz diorites (Damara orogen, Namibia). *Contributions to Mineralogy and Petrology*, **143**, 551-566.

Kamona, A.F., Leveque, J., Friedrich, G. & Haack, U. (1999). Lead isotopes of the carbonate-hosted Kabwe, Tsumeb and Kipushi Pb-Zn-Cu sulphide deposits in relation to Pan African orogenesis in the Damaran-Lufilian Fold Belt of Central Africa. *Mineralium Deposita*, **34**, 273-283.

Kapp, P., Taylor, M., Stockli, D. & Ding, L. (2008). Development of active low-angle normal fault systems during orogenic collapse: Insight from Tibet. *Geology*, **36**, 7-10.

Karig, D. E. (1971). Origin and development of marginal basins in the western pacific. *Journal of Geophysical Research*, **76**, 2542-2561.

Kasch, K. W. (1978). Recognition of a major shear zone in the southern Damara Belt, SWA/Namibia. *Transactions of the Geological Society of South Africa*, **81**, 205-209.

Kasch, K. W. (1981). *The structural geology, metamorphic petrology and tectonothermal evolution of the southern Damara belt around Omitara, SWA/Namibia*. Bulletin of the Precambrian Research Unit, University of Cape Town, **27**, 333 pp.

Kasch, K. W. (1983a). Regional P-T variations in the Damara Orogen with particular reference to early high-pressure metamorphism along the Southern Margin. *In*: Miller, R. McG. (Ed.) *Evolution of the Damara Orogen*. Special Publications of the Geological Society of South Africa, **11,** 243-253.

Kasch, K. (1988). Lithostratigraphy and structural geology of the upper Swakop River area east of Okahandja South West Africa/Namibia. *Communications of the Geological Survey of South West Africa/Namibia*, **4**, 59-66.

Kennedy, W. Q. (1964). The structural differentiation of Africa in the Pan African (± 500 Ma) tectonic episode. *8th Annual Report of the Research Institute for African Geology*, University of Leeds, 48-49.

Key R. M., Liyungu A. K., Njamu F. M., Somwe V., Banda J., Mosley P. N., Armstrong R. A. (2001). The western arm of the Lufilian Arc in NW Zambia and its potential for copper mineralization. *Journal of African Earth Sciences*, **33**, 503-528.

Kinnaird, J. A. & Nex, P. A. M. (2007). A review of geological controls on uranium mineralisation in sheeted leucogranites within the Damara Orogen, Namibia. *Applied Earth Science*, **116**, 69-85.

Kinny, P. D., McNaughton, N. J., Fanning, C. M. & Maas, R. (1994). 518 Ma sphene (titanite) from the Khan pegmatite, Namibia, southwest Africa: a potential ion-microprobe standard. *Abstracts of the eighth International Conference on Geochronology, Cosmochronology, and Isotope Geology*. U. S. Geological Survey Circular **1107**.

Kisters, A. F. M., Jordaan, L. S. & Neumaier, K. (2004). Thrust-related dome structures in the Karibib district and the origin of orthogonal fabric domains in the south Central Zone of the Pan-African Damara belt, Namibia. *Precambrian Research*, **133**, 283-303.

Kisters, A. F. M., Ward, R. A., Anthonissen, C. J. & Vietze, M. E. (2009). Melt segregation and far-field melt transfer in the mid-crust. *Journal of the Geological Society, London,* **166**, 905-918.

Klein, J. (1980). Evolution of first generation folds in a marble unit (Damara Orogenic Belt, Namibia). *Geologische Rundschau*, **69**, 770-800.

Kleemann, U. & Reinhardt, J. (1994). Garnet-biotite thermometry revisited: The effect of Al^{VI} and Ti in biotite. *European Journal of Mineralogy*, **6**, 925-941.

Knapp, J. H., Knapp, C. C., Raileanu, V., Matenco, L., Mocanu, V. & Dinu, C. (2005). Crustal constraints on the origin of mantle seismicity in the Vrancea zone, Romania: The case for active continental lithospheric delamination. *Tectonophysics*, **410**, 311-323.

Konopásek, J., Kröner, S., Kitt, S. L., Passchier, C. W. & Kröner, A. (2005). Oblique collision and evolution of large-scale transcurrent shear zones in the Kaoko belt, NW Namibia. *Precambrian Research*, **136**, 139-157.

Konopásek, J., Košler, J., Tajčmanová, L., Ulrich, S. & Kitt, S. L. (2008). Neoproterozoic igneous complex emplaced along major tectonic boundary in the Kaoko Belt (NW Namibia): ion probe and LA-ICP-MS dating of magmatic and metamorphic zircons. *Journal of the Geological Society, London*, **165,** 153-165.

Korn, H. & Martin, H (1959). Gravity tectonics in the Naukluft Mountains of South West Africa. *Bulletin of the Geological Society of America*, **70**, 1047-1078.

Kretz, R. (1983). Symbols for rock-forming minerals. *American Mineralogist*, **68**, 277-279.

Kröner, A. (1977). Precambrian mobile belts in southern and eastern Africa—ancient sutures or sites of ensialic mobility. A case for crustal evolution towards plate tectonics. *Tectonophysics*, **40**, 101-135.

Kröner, A. (1982). Rb-Sr geochronology and tectonic evolution of the Pan-African Damara belt of Namibia, south-western Africa. *American Journal of Science,* **282**, 1471-1507.

Kröner, A. (1984). Dome structures and basement reactivation in the Pan-African Damara belt of Namibia. In: A.G. Kröner, R. Stuttgart, Nagele u. Obermiller. *Precambrian Tectonics Illustrated*, 191-206.

Kröner, A., Retief, E. A., Compston, W., Jacob, R. E. & Burger., A. J. (1991). Single-Age and conventional zircon dating of remobilised basement gneisses in the central Damara belt of Namibia. *South African Journal of Geology*, **94**, 379-387.

Kukla, C. (1993). Strontium isotope heterogeneities in amphibolite facies, banded metasediments – a case study from the Late Proterozoic Kuiseb Formation of the southern Damara Orogen, Central Namibia. *Memoirs of the Geological Survey of Namibia*, **15**, 139pp.

Kukla, P. A. (1992). Tectonics and sedimentation of a Late Proterozoic Damaran Convergent Continental Margin, Khomas Hochland, Central Namibia. *Geological Survey of Namibia Memoirs*, **12**.

Kukla, P. A. & Stanistreet, I. A. (1991). Record of the Damaran Khomas Hochland accretionary prism in central Namibia: Refutation of an "ensialic" origin of a Late Proterozoic orogenic belt. *Geology*, **19**, 473-476.

Kuno, H. (1968). Differentiation of basalt magmas. *In*: Hess, H. H. & Poldervaart, A. (Eds*) Basalts: The Poldervaart treatise on rocks of basaltic composition*, Vol. 2, Interscience, New York, 623-688.

Lehtonen, M. I., Manninen, T. E. T. & Schreiber, U. M. (1995). *The geology of the area between the Khan river and the Coast, and in the vicinity of Omdel Dam*. Mapping Report and geochemical study, Finnish-Namibian Geological mapping and maps project. Map 2215A.

Lehtonen, M. I., Manninen, T. E. T. & Schreiber, U. M. (1996). Report on the lithostratigraphy of the area between the Swakop, Khan and lower Omaruru Rivers, Namib Desert. *Communications of the Geological Survey of Namibia*, **11**, 65-75.

Lister, G. S. & Williams, P. F. (1983). The partitioning of deformation in flowing rock masses. *Tectonophysics*, **92**, 1-33.

Lister, G. S. & Davis, G. A. (1989). The origin of metamorphic core complexes and detachment faults formed during Tertiary continental extension in the northern Colorado River region, USA. *Journal of Structural Geology*, **11**, 65-94.

Long, S. & McQuarrie, N. (2010). Placing limits on channel flow: Insights from the Bhutan Himalaya. *Earth and Planetary Science Letters*, **290**, 375-390.

Ludwig, K. R. (2000). *Squid 1.02. A Geochronological Toolkit for Microsoft Excel*. Berkeley Geochronology Center Special Publication **2**.

Ludwig, K. R. (2003). *Isoplot 3.00. A Geochronological Toolkit for Microsoft Excel*. Berkeley Geochronology Center Special Publication **4**.

Luth, W. D., Jahns, R. H. & Tuttle, O. F. (1964). The granite system at pressures of 4 to 10 kilobars. *Journal of Geophysical Research*, **69**, 659-773.

MacDonald, G. A. (1968). Composition and origin of Hawaiian lavas. *In*: Coats, R. R., Hay, R. L. & Anderson, C. A. (Eds). *Studies in volcanology: a memoir in honour of Howel Williams*. Geological Society of America Memoirs, **116**, 477-522.

Manthei, C. D., Ducea, M. N., Girardi, J. D., Patchett, P. J., & Gehrels, G. E. (2010). Isotopic and geochemical evidence for a recent transition in mantle chemistry beneath the western Canadian Cordillera. *Journal of Geophysical Research, Solid Earth*, **115**, B02204.

Marlow, A. G. M. (1981). *Remobilisation and Primary Uranium Genesis in the Damaran Orogenic Belt*. PhD Thesis (unpublished), University of Leeds, Leeds, 247 pp.

Martin, H. (1965). *The Precambrian Geology of South West Africa and Namaqualand.* Precambrian Research Unit, University of Cape Town, 159 pp.

Martin, H. & Porada, H. (1977a). The Intracratonic Branch of the Damara Orogen in South West Africa I. Discussion of Geodynamic Models. *Precambrian Research*, **5**, 311-338.

Martin, H. & Porada, H. (1977b). The Intracratonic Branch of the Damara Orogen in South West Africa II. Discussion of relationships with the Pan-African mobile belt system. *Precambrian Research*, **5**, 339-357.

Martinez, F. J., Julivert, M., Sebastian, A., Arboleya, M. L. & Gilibarguchi, J. I. (1988). Structural and thermal evolution of high-grade areas in the northwestern parts of the Iberian Massif. *American Journal of Science*, **288**, 969-996.

Masberg, H. P., Hoffer, E. & Hoernes, S. (1992). Microfabrics indicating granulite-facies metamorphism in the low-pressure central Damara Orogen, Namibia. *Precambrian Research*, **55**, 243-257.

Masberg, P., Mihm, D. & Jung, S. (2005). Major and trace element and isotopic (Sr, Nd, O) constraints for Pan-African crustally contaminated grey granite gneisses from the southern Kaoko belt, Namibia. *Lithos*, **84**, 25-50.

Master, S. (2009). Neoproterozoic DARCs in the Damara-Lufilian-Zambezi and Ubendian belts and the Western Rift Rise- relics of Rodinia fragmentation at 750 ± 50 Ma. *Abstract Volume: Out of Africa Conference, Wits University of the Witwatersrand, Johannesburg, South Africa*.

McDermott, P. F. (1986). *Granite Petrogenesis and Crustal Evolution Studies in the Damara Pan-African Orogenic Belt, Namibia*. PhD Thesis (Unpublished), Open University, 302 pp.

McDermott, F., Harris, N. B. W. & Hawkesworth, C. J. (1989). Crustal reworking in southern Africa: constraints from Sr-Nd isotope studies in Archaean to Pan-African terrains. *Tectonophysics*, **161**, 257-270.

McDermott, F., Harris, N. B. W. & Hawkesworth, C. J. (1996). Geochemical constraints on crustal anatexis: a case study from the Pan-African Damara granitoids of Namibia. *Contributions to Mineralogy and Petrology*, **123**, 406-423.

McKerrow, W. S., MacNiocaill, M. & Dewey, J. F. (2000). The Caledonian Orogeny redefined. *Journal of the Geological Society, London*, **157**, 1149-1154.

McLaren, S., W. James Dunlap, W. J., Sandiford, M. & McDougall, I. (2002). Thermochronology of high heat-producing crust at Mount Painter, South Australia: Implications for tectonic reactivation of continental interiors. *Tectonics*, **21**, 2.1-2.17.

McLaren, S., W. J., Sandiford, M., Powell, R., Neumann, N. & Woodhead, J. (2006). Palaeozoic Intraplate Crustal Anatexis in the Mount Painter Province, South Australia: Timing, Thermal Budgets and the Role of Crustal Heat Production. *Journal of Petrology*, **47**, 2281-2302.

McQuarrie, N., Robinson, D., Long, S., Tobgay, T., Grujic, D., Gehrels, G. & Ducea, M. (2008). Preliminary stratigraphic and structural architecture of Bhutan: Implications for the along strike architecture of the Himalayan system. *Earth and Planetary Science Letters*, **272**, 105-117.

Meert, J. G. (2003). A synopsis of events related to the assembly of eastern Gondwana. *Tectonophysics*, **362**, 1-40.

Meert, J. G., Van der Voo, R. & Ayub, S. (1995). Paleomagnetic investigation of the Neoproterozoic Gagwe lavas and Mbozi Complex, Tanzania and the assembly of Gondwana. *Precambrian Research*, **74**, 225-244.

Miller, R.McG. (1973). *The Salem granite suite, South West Africa: genesis by partial melting of the Khomas schist*. Memoir of the Geological Survey of South Africa **64**, 97 pp.

Miller, R. McG. (1979). The Okahandja Lineament, a fundamental tectonic boundary in the Damara Orogen of South West Africa/Namibia. *Transactions of the Geological Society of South Africa*, **82**, 349-361.

Miller, R. McG. (1980). Geology of a Portion of Central Damaraland, South West Africa/Namibia. *Memoirs of the Geological Survey of South Africa, SWA Series*, **6**, 1-78.

Miller, R. M. (1983). The Pan-African Damara Orogen of South West Africa/Namibia. *In*: Miller, R. McG. (Ed.) *Evolution of the Damara Orogen*. Special Publications of the Geological Society of South Africa, **11,** 431-515.

Miller, R. McG. (2008). *The Geology of Namibia. Volume 2: Neoproterozoic to Lower Palaeozoic*. Geological Survey of Namibia, Windhoek.

Miller, R. McG & Burger, A. J. (1983). U-Pb zircon ages of members of the Salem Granitic Suite along the northern edge of the central Damara Granite Belt. *In*: Miller, R. McG. (Ed.) *Evolution of the Damara Orogen*. Special Publications of the Geological Society of South Africa, **11,** 273-280.

Mouillac, J. L., Valois, J. -P. & Walgenwitz, F. (1986). The Goanikontes uranium occurrence in southwest Africa/Namibia. *In*: Anhaeusser, C. R. & Maske, S. (Eds). *Mineral deposits of southern Africa, Vol. 2*. Geological Society of South Africa, Johannesburg, 1833-1843.

Myrow, P. M., Hughes, N. C., Paulsen, T. S., Williams, I. S., Parcha, S. K., Thompson, K. R., Bowring, S. A., Peng, S -C. & Ahluwalia, A. D. (2003). Integrated tectonostratigraphic analysis of the Himalaya and implications for its tectonic reconstruction, *Earth and Planetary Science Letters*, **212**, 433-441.

Nagel, R. (1999). *Eine Milliarde Jahre geologischer Entwicklung am NW-Rand des Kalahari Kratons*. Dr. rer. Nat. thesis, Univ. Göttingen, Göttingen.

Nash, C. R. (1971). *Metamorphic petrology of the SJ Area, Swakopmund District, South West Africa*. Bulletin of the Precambrian Research Unit, University of Cape Town **9**, 77 pp.

Nelson, K. D., Zhao, W., Brown, L. D. Kuo, J., Che, J., Liu, X., Klemperer, S. L., Makovsky, Y, Meissner, R., Mechie, J., Kind, R., Wenzel, F., Ni, J., Nabelek, J., Leshou, C., Tan, H., Wei, W., Jones, A. G., Booker, J., Unsworth, M., Kidd, W. S. F., Hauck, M., Alsdorf, D., Ross, A., Cogan, M., Wu, C., Sandvol, E. & Edwards, M. Partially Molten Middle Crust Beneath Southern Tibet: Synthesis of Project INDEPTH Results. *Science*, **274**, 1684-1688.

Nex, P. A. M. (1997). *Tectono-metamorphic setting and evolution of granitic sheets in the Goanikontes area, Namibia*. PhD Thesis (Unpublished) Department of Geology, National University of Ireland, Cork, 322 pp.

Nex, P. A. M. & Kinnaird, J. A. (1995). Granites and their mineralisation in the Swakop River area around Goanikontes, Namibia. *Communications of the Geological Survey of Namibia*, **10**, 51-56.

Nex, P. A. M., Oliver, G. J. H. & Kinnaird, J. A. (2001a). Spinel-bearing assemblages and P-T-t evolution of the Central Zone of the Damara Orogen, Namibia. *Journal of African Earth Sciences* **32**, 471-498.

Nex, P. A. M., Kinnaird, J. A. & Oliver, G.J.H. (2001b). Petrology, geochemistry and uranium mineralisation of post-collisional magmatism around Goanikontes, southern Central Zone, Damaran Orogen, Namibia. *Journal of African Earth Sciences* **33**, 481-502.

Oliver, G. J. H. (1994). Mid-crustal detachment and domes in the central zone of the Damara orogen, Namibia. *Journal of African Earth Science*, **19**, 331-344.

Oliver, G. J. H. (1995). The Central Zone of the Damara Orogen, Namibia, as a deep metamorphic core complex. *Communications of the Geological Survey, Namibia*, **10**, 33-41.

Oliver, G. J. H. (2001). Reconstruction of the Grampian episode in Scotland: its place in the Caledonian Orogeny. *Tectonophysics*, **33**2, 23–49.

Oliver, G. J. H. & Kinnaird, J. A. (1996). The Rössing-SJ Dome, Central Zone, Damara Belt, Namibia: an example of mid-crustal extensional ramping. *Communications of the Geological Survey, Namibia*, **11**, 53-64.

Oliver, G. J. H., Wilde, S. A. & Wan, Y. (2008). Geochronology and geodynamics of Scottish granitoids from the late Neoproterozoic break-up of Rodinia to Palaeozoic collision. *Journal of the Geological Society*, **165**, 661-674.

Oyhantçabal, P., Siegesmund, S., Wemmer, K. & Passchier, C. W. (2011). The transpressional connection between Dom Feliciano and Kaoko Belts at 580-550 Ma. *International Journal of Earth Sciences*, **100**, 379-390.

Passchier, C. W., Trouw, R. A. J., Ribeiro, A. & Paciulo, F. (2002). Tectonic evolution of the southern Kaoko belt, Namibia. *Journal of African Earth Sciences*, **35**, 61-75.

Passchier, C. W. & Trouw, R. A. J. (2005). *Microtectonics*. Springer-Verlag, Heidelberg, Germany, 228 pp.

Patiño Douce, A. E. & Harris, N. (1998). Experimental constraints on Himalayan anatexis. *Journal of Petrology*, **39**, 689-710.

Paul, J., Bürgmann, R., Gaur, V. K., Bilham, R. Larson, K. M., Ananda, M. B., Jade, S., Mukal, M., Anupama, T. S., Satyal, G. & Kumar, D. (2001). The motion and active deformation of India. *Geophysical Research Letters*, **28**, 647-651.

Pearce, J. A. (1983). Role of the sub-continental lithosphere in magma genesis at active tectonic margins. *In*: Hawkesworth, C. J. & Norry, M. J. (Eds). *Continental basalts and mantle xenoliths*. Shiva, Nantwich, 230-249.

Pearce, J. A. & Cann, J. R. (1973). Tectonic setting of basic volcanic rocks determined using trace element analyses. *Earth and Planetary Science Letters*, **12**, 339-349.

Pearce, J. A. & Norry, M. J. (1979). Petrogenetic implications of Ti, Zr, Y, and Nb variations in volcanic rocks. *Contributions to Mineralogy and Petrology*, **69**, 33-47.

Perchuk, L. L. & Lavrent'eva I. V. (1983). Experimental investigation of exchange equilibria in the system cordierite garnet-biotite. *Advances in Physical Geochemistry*, **3**, 199-239.

Pérez-Estaún, A. & Bea, F. (2004). Macizo Ibérico. *In:* Vera, J. A. (Ed.) *Geología de España*. SGE-IGME, Madrid, 19–230.

Perry, H. K. C., Jaupart, C., Mareschal, J. C. & Bienfait, G. (2006). Crustal heat production in the Superior Province, Canadian Shield, and in North America inferred from heat flow data. *Journal of Geophysical Research*, **111**, B04401

Pfurr, N., Wissmann, K., Ahrendt, H., Hill, R. S. & Weber, K. (1987). Alpinotype thrust tectonics and basement-cover relationships in the Southern Margin Zone of the Pan-African Damara Orogen, Rostock area. *Communications of the Geological Survey of Namibia*, **3**, 129-136.

Poli, L. C. (1997). *Mid-crustal geodynamics of the Southern Central Zone, Damara Orogen, Namibia*. PhD Thesis (unpublished). University of St Andrews, Scotland, 233 pp.

Poli, L. C. & Oliver, G. J. H. (2001). Constrictional deformation in the Central Zone of the Damara Orogen, Namibia. *Journal of African Earth Sciences*, **33**, 303-321.

Porada, H. (1979). The Damara-Ribeiro Orogen of the Pan-African Brasiliano cycle in Namibia (Southwest Africa) and Brazil interpreted in terms of continental collision. *Tectonophysics*, **57**, 237-265.

Porada, H., Ahrendt, H., Behr, H. -J., & Weber, K. (1983). The join of the coastal and intracontinental branches of the Damara Orogen, Namibia, South West Africa. *In*: Martin, H. & Eder, F. W. (Eds*) Intracontinental Fold Belts*, Springer Verlag, Berlin, 901-912.

Powell, R. & Holland, T. J. B. (1988). An internally consistent thermodynamic dataset with uncertainties and correlations: 3. Applications to geobarometry, worked examples and a computer program. *Journal of Metamorphic Geology*, **6**, 173-204.

Powell, R. & Holland, T. J. B. (2008). On thermobarometry. *Journal of Metamorphic Geology*, **26**, 155-179.

Powell, R., Holland, T. J. B. & Worley, B. (1998). Calculating phase diagrams involving solid solutions via non-linear equations, with examples using THERMOCALC. *Journal of Metamorphic Geology*, **16**, 577-588.

Prave, A. R. (1996). Tale of three cratons: tectonostratigraphic anatomy of the Damara Orogen in northwestern Namibia and the assembly of Gondwana. *Geology* **24**, 1115-1118.

Puhan, D. (1979). *Petrologische und thermometrische Untersuchungen an Dolomit-Calcit-Marmoren des zentralen Damara-Orogens*. Habilitationsschrift, Gottingen.

Puhan, D. (1983). Temperature and Pressure of metamorphism in the Central Damara Orogen. *In*: Miller, R. McG. (Ed.) *Evolution of the Damara Orogen*. Special Publications of the Geological Society of South Africa, **11,** 219-223.

Ramberg, H. (1980). Diapirism and gravity collapse of the Scandinavian Caledonides. *Journal of Geological Society, London*, **137**, 261-270.

Rainaud, C., Master, S., Armstrong, R. A. & Robb, L. J. (2005a). Geochronology and nature of the Palaeoproterozoic basement in the Central African Copperbelt (Zambia and the Democratic Republic of Congo), with regional implications. *Journal of African Earth Sciences*, 42, 1-31.

Rainaud, C., Master, S., Armstrong, R. A., Phillips, D. & Robb, L. J. (2005b). Monazite U–Pb dating and 40Ar–39Ar thermochronology of metamorphic events in the Central African Copperbelt during the Pan-African Lufilian Orogeny. *Journal of African Earth Sciences*, **42**, 183-199.

Ramos, V. A. (2009). Anatomy and global context of the Andes: Main geologic features and the Andean orogenic cycle. *GSA Memoirs*, **204**, 31-65.

Ramsay, J. G. (1967). *Folding and Fracturing of Rocks*. McGraw-Hill, New York, 568 pp.

Ramsay, J. G. & Huber, M. I. (1987) *The Techniques of Modern Structural Geology*. Academic Press, London, 393 pp.

Rapela, C. W., Fanning, C. M., Casquet, C., Pankhurst, R. J., Spalletti, L., Poiré, D. & Baldo, E. G. (2011). The Rio de la Plata craton and the adjoining Pan-African/brasiliano terranes: Their origins and incorporation into south-west Gondwana. *Gondwana Research*, **20**, 673-690.

Reid, D. L. (1997). Sm-Nd age and REE geochemistry of Proterozoic arc-related igneous rocks in the Richtersveld Subprovince, Namaqua Mobile Belt, southern Africa. *Journal of African Earth Sciences*, **24**, 621-633.

Renne, P. R., Ernesto, M., Pacca, I. G., Coe, R. S., Glen, J. M., Prévot, M. & Perrin, M. (1992). The age of Paraná flood volcanism, rifting of Gondwanaland, and the Jurassic-Cretaceous boundary. *Science*, **258**, 975-979.

Replumaz, A., Negredo, A. M., Antonio Villaseñor, A. & Guillot, S. (2010). Indian continental subduction and slab break-off during Tertiary collision. *Terra Nova*, **22**, 290-296.

Richardson, S. W., Gilbert, M. C. & Bell, P. M. (1969). Experimental determination of kyanite-andalusite and andalusite-sillimanite equilibrium; the aluminium silicate triple point. *American Journal of Science*, **267**, 259-272.

Richardson, S. W. & England, P. C. (1979). Metamorphic consequences of crustal eclogite production in overthrust orogenic zones. *Earth and Planetary Science Letters*, **42**, 183-190.

Ritter, O., Weckmann, U., Vietor, T. & Haak, V. (2003). A magnetotelluric study of the Damara Belt in Namibia 1. Regional scale conductivity anomalies. *Physics of the Earth and Planetary Interiors*, **138**, 71-90.

Rollinson, H. R. (1993). *Using Geochemical Data: Evaluation, Presentation, Interpretation*. Longman, UK, 352 pp.

Rumvegeri, B. T. (1991). Tectonic significance of Kibaran structures in Central and eastern Africa. *Journal of African Earth Sciences*, **13**, 267-276.

Sajeev, K & Osanai, Y. (2004). Ultrahigh-temperature metamorphism (1150 ˚C and 12kbar) and Multistage evolution of Mg-, Al-rich granulites from Central Highland Complex, Sri Lanka. *Journal of Petrology*, **45**, 1821-1844.

Sajeev, K, Osanai, Y., Connolly, J. A. D., Suzuki, S., Ishioka, J., Kagami, H. & Rino, S. (2007). Extreme crustal metamorphism during a Neoproterozoic event in Sri Lanka: a case study of dry mafic granulites. *Journal of Geology*, **115**, 563-582.

Sandiford, M. (1989). Horizontal structures in granulite terrains: A record of mountain building or mountain collapse? *Geology*, **17**, 449-452.

Sanz, A. L. -G. (2008). *Pre- and post-Katangan granitoids of the Greater Lufilian Arc - geology, geochemistry, geochronology and metallogenic significance*. PhD Thesis (unpublished). University of the Witwatersrand, Johannesburg.

Saunders, A. D. & Tarney, J. (1984). Geochemical characteristics of basaltic volcanism within back-arc basins. *In*: Kokelaar, B. P. & Howells, M. F. (Eds). *Marginal basin geology*. Special Publications of the Geological Society, London, **16**, 59-76.

Sawyer, E. W. (1976). *The geology of an area south-east of Walvis Bay: Lithology, sedimentation and field relationships*. Geological Survey of Namibia Regional Geology Reports, **3**.

Sawyer, E. W. (1981) Damaran structural and metamorphic geology of an area south-east of Walvis Bay, South West Africa/Namibia. *Memoir of the Geological Survey of South West Africa*, **7**, 94 pp.

Sawyer, E. W. (2001). Melt segregation in the continental crust: distribution and movement of melt in anatectic rocks. *Journal of Metamorphic Geology*, **19**, 291-309.

Sawyer, E. W. (2008). *Atlas of Migmatites*. The Canadian Mineralogist, Special Publication 9, NRC Research Press, Ottawa, Canada, 371 pp.

Sawyer, E. W., Barnes, S. J. (1994). Thrusting, magma intraplating, and metamorphic core complex development in the Archaean Belleterre –Angliers greenstone belt, Superior Province, Quebec, Canada. *Precambrian Research*, **68**, 183-200.

Scheepers, R & Armstrong, R. (2002). New U-Pb SHRIMP zircon ages of the Cape Granite Suite: Implications for the magmatic evolution of the Saldania Belt. *South African Journal of Geology*, **105**, 241-256.

Scheepers, R. & Poujol, M. (2002). U-Pb zircon age of Cape Granite Suite ignimbrites: characteristics of the last phases of the Saldanian magmatism. *South African Journal of Geology*, **105**, 163-178.

Sengör, A. M. C. (1990). Plate tectonics and orogenic research after 25 years: a Tethyan perspective. *Earth Science Reviews*, **27**, 1-201.

Sengör, A. M. C. & Natal'in, B. A. (1996). Turkic-type orogeny and its role in the making of the continental crust. *Annual Reviews in Earth and Planetary Science*, **24**, 263-337.

Sengör, A. M. C. & Okuroğullari, A. H. (1991). The role of accretionary wedges in the growth of continents: Asiatic examples from Argand to plate tectonics. *Eclogae Geologicae Helvetiae,* **84**, 535-597.

Seth, B. (1999). *Crustal evolution of the Kaoko belt, NW Namibia*. PhD Thesis (Unpublished) Bayerischen Julius-Maximilians-Universität, Würzburg, 135 pp.

Seth, B., Kröner, A., Mezger, K., Nemchin, A. A., Pidgeon, R. T. & Okrusch, M. (1998). Archaean to Neoproterozoic magmatic events in the Kaoko belt of NW Namibia and their geodynamic significance. *Precambrian Research*, **92**, 341-363.

Seth, B., Okrusch, M., Wilde, M. & Hoffmann, K-H. (2000). The Voetspoor Intrusion, Southern Kaoko Zone, Namibia: mineralogical, geochemical and isotopic constraints for the origin of a syenitic magma. *Communications of the Geological Survey of Namibia*, **12**, 125–137.

Siegesmund, S, Basei, M. & Oyhantçabal, P. (2011). Multi-accretional tectonics at the Rio de la Plata Craton margins: preface. *International Journal of Earth Sciences*, **100**, 197-200.

Simancas, J. F., Martínez Poyatos, D., Expósito, I., Azor, A. & González Lodeiro, F. (2001). The structure of a major suture zone in the SW Iberian Massif: the Ossa-Morena/Central Iberian contact. *Tectonophysics*, **332**, 295-308.

Singletary, S. J., Hanson, R. E., Martin, M. W., Crowley, J. L., Bowring, S. A., Key, R. M., Ramokate, L. V., Direng, B. B. and Krol, M. A. (2003). Geochronology of basement rocks in the Kalahari Desert, Botswana, and implications for regional Proterozoic tectonics. *Precambrian Research*, **121**, 47-71.

Smith, D. A. M. (1965). *The geology of the area around the Khan and Swakop Rivers in South West Africa*. Memoir of the Geological Survey of South Africa, **3**, 107 pp.

Smith H. A. & Giletti B. J. (1997). Lead diffusion in monazite. *Geochimica et Cosmochimica Acta*, **61**, 1047-1055.

Söderlund U., Patchett P. J., Vervoort J. D. & C. E. Isachsen (2004). The ^{176}Lu decay constant determined by Lu-Hf and U-Pb isotope systematics of Precambrian mafic intrusions. *Earth and Planetary Science Letters*, **219**, 311-324.

Soper, N. J. & Hutton, D. H. W. (1984). Late Caledonian sinistral displacements in Britain: Implications for a three-plate collision model. *Tectonics*, **3**, 781-794.

South African Committee for Stratigraphy (SACS) (1980) Stratigraphy of South Africa, I. (Compiler L.E. Kent). *Lithostratigraphy of the Republic of South Africa, South West Africa/Namibia, and Republics of Bophutshatswana, Transkei and Venda*. Geological Survey of South Africa, Handbook **8**.

Spear, F. S. (1991). On the interpretation of peak metamorphic temperatures in light of garnet diffusion during cooling. *Journal of Metamorphic Geology*, **9**, 379-388.

Spear, F. S. & Parrish, R. R. (1996). Petrology and Cooling Rates of the Valhalla Complex, British Columbia, Canada. *Journal of Petrology*, **37**, 733-765.

Spear, F. S., Kohn, M. J. & Cheney, J. T. (1999). P -T paths from anatectic pelites. *Contributions to Mineralogy and Petrology*, **134**, 17-32.

Sperner, B., Lorenz, F., Bonjer, K., Hettel, S., Müller, B. & Wenzel, F. (2001). Slab break-off – abrupt cut or gradual detachment? New insights from the Vrancea Region (SE Carpathians, Romania). *Terra Nova*, **13**, 172-179.

Stampfli, G. M., von Raumer, J. F. & Borel, G. D. (2002). *Paleozoic evolution of pre-Variscan terranes: From Gondwana to the Variscan collision.* Geological Society of America Special Paper **364**.

Stanistreet, I. G., Kukla, P. A. & Henry, G. (1991). Sedimentary basinal response to a late Precambrian Wilson cycle: the Damara Orogen and Nama Foreland, Namibia. *Journal of African Earth Sciences*, **13**, 141-156.

Stern, R. J. (1994). Arc assembly and continental collision in the Neoproterozoic East Africa Orogen: implications of the consolidation of Gondwanaland. *Annual Reviews in Earth and Planetary Science*, **22**, 319-351.

Steven, N. M. (1993). *A study of epigenetic mineralisation in the Central Zone of the Damara Orogen, Namibia, with special reference to gold, tungsten, tin and rare-earth elements.* Memoirs of the Geological Survey of Namibia, **16**.

Steven, N. M. (1994). Note: Mafic dykes in the pre-Damara basement, southeast of Usakos, central Namibia. *Communications of the Geological Survey of Namibia*, **9**, 92-95.

Steven, N. M., Badenhorst, F., Kitt, S. & Wulff, K. (2008). The Navachab Gold Mine, Namibia: the largest non-Witwatersrand-type gold deposit in southern Africa. *Abstract Volume: Africa Uncovered GSSA-SEG conference.*

Stevens, G., Clemens, J. D. & Droop, G. T. R. (1995). Hydrous Cordierite in granulites and crustal magma production. *Geology*, **23**, 925-928

Stevens, G. Clemens, J. D & Droop, G. T. R. (1997). Melt production during granulite-facies anatexis: experimental data from ``primitive'' metasedimentary protoliths. *Contributions to Mineralogy and Petrology*, **128**, 352-370.

Sun, S. S. (1980). Lead isotopic study of young volcanic rocks from mid-ocean ridges, ocean islands and island arcs. *Philosophical Transaction of the Royal Society*, **A297**, 409-445.

Tack, L., Boven, A., Bowden, P. & Oliver, G. J. H. (1995). The significance of $^{40}Ar/^{39}Ar$ ages on a mylonitic cover gneiss from the contact shear zone of the Ida Dome, Central Damaran Belt, western Namibia. *Musee Royal de l'Afrique centrale, Tervuren (Belgique). Department Geologie Mineralogie, Rapport Annual 1993-1994*, 159-172.

Tack, L. & Bowden, P. (1999). Post-collisional granite magmatism in the central Damaran (Pan-African) Orogenic Belt, western Namibia. *Journal of African Earth Sciences,* **28**, 653-674.

Tack, L., Williams, I. & Bowden, P. (2002). SHRIMP consraints on early post-collisional granitoids of the Ida Dome, central Damara (Pan-African) Belt, western Namibia. *Abstracts of the 11th IAGOD Quadrennial Symposium and Geocongress, Windhoek, Namibia.*

Tajčmanová, L., Konopásek, J. & Košler, J. (2009). Distribution of zinc and its role in the stabilization of spinel in high-grade felsic rocks of the Moldanubian domain (Bohemian Massif). *European Journal of Mineralogy*, **21**, 407-418.

Teyssier, C. & Whitney, D. L. (2002). Gneiss domes and orogeny. *Geology*, **30**, 1139-1142.

Thompson, A.B. (1975). Mineral reactions in pelitic rocks: II. Calculation of some P-T-X (Fe-Mg) phase relations. *American Journal of Science*, **276**, 425-454.

Thompson, A. B. (1999). Some time-space relationships for crustal melting and granitic intrusion at various depths. *In*: Castro, A., Fernandez, C. & Vigneresse, J. L. (Eds) *Understanding Granites: Integrating New and Classical Techniques*. Geological Society, London, Special Publications, **168**, 7-25.

Thompson, J. B. (1957). The graphical analysis of mineral assemblages in pelitic schists. *American Mineralogist*, **42**, 842-858.

Thomson, J. A. (2001). A counterclockwise P-T path for anatectic pelites, south-central Massachusetts. *Contributions to Mineralogy and Petrology*, **141**, 623-641.

Trumbull, R. B., Emmermann, R., Buhn, B., Gerstenberger, H., Mingram, B., Schmitt, A. & Volker, F. (2000). Insights on the genesis of the Cretaceous Damaraland igneous complexes in Namibia from a Nd- and Sr-isotopic perspective. *Communications of the Geological Survey of Namibia*, **12**, 313-324.

Unrug, R. (1992). The supercontinent cycle and Gondwanaland assembly – component cratons and the timing of suturing events. *Journal of Geodynamics* **16**, 215-240.

Valley, J. W., Kinny, P. D., Schulze, D. J. and Spicuzza, M. J. (1998). Zircon megacrysts from kimberlite: oxygen isotope variability among mantle melts. *Contributions to Mineralogy and Petrology*, **133**, 1-11.

Van Staal, C. R., Dewey, J. F.,MacNiocaill, C. & McKerrow, W. S. (1998). The Cambrian-Silurian tectonic evolution of the northern Appalachians and British Caledonides: history of a complex, west and southwest Pacific-type segment of Iapetus. *In*: Blundell, D. J. & Scott, A. C. (Eds) *Lyell: The Past is the Key to the Present*. Geological Society, London, Special Publications, **143**, 197-242.

Vernon, R. H. (2004). *A practical guide to rock microstructure*. Cambridge University Press, Cambridge, 594 pp.

Vervoort, J. D. and Blichert-Toft, J. (1999). Evolution of the depleted mantle: Hf isotope evidence from juvenile rocks through time. *Geochimica et Cosmochimica acta*, **63**, 533-556.

Vielzeuf D. & Holloway J. R. (1988). Experimental determination of the fluid-absent melting relations in the pelitic system. *Contributions to Mineralogy and Petrology*, **98**, 257-276.

Vielzuef, D. & Montel, J. (1994). Partial melting of metagreywackes Part I. Fluid-absent experiments and phase relationships. *Contributions to Mineralogy and Petrology*, **117**, 375-393.

Vigneresse, J. -L., Barbey, P. & Cuney, M. (1996). Rheological transitions during partial melting and crystallization with application to felsic magma segregation and transfer. *Journal of Petrology*, **37**, 1597-1600.

Vos, I. M. A., Bierlein, F. P. & Heithersay, P. S. (2007). A crucial role for slab break-off in the generation of major mineral deposits: insights from central and eastern Australia. *Mineralium Deposita*, **42**, 515-522.

Wall, F., Niku-Paavola, V. N., Storey, C., Müller, A. & Jeffries, T. (2008). Xenotime-(Y) from carbonatite dykes at Lofdal, Namibia; unusually low LREE/HREE ratio in carbonatite, and the first dating of xenotime overgrowths on zircon. *Canadian Mineralogist*, **46**, 861-877.

Ward, R., Stevens, G. & Kisters, A. (2008). Fluid and deformation induced partial melting and melt volumes in low-temperature granulite-facies metasediments, Damara Belt, Namibia. *Lithos*, **105**, 253-271.

Whitney, D. L., Teyssier, C. & Vanderhaeghe, O. (2004). Gneiss domes and crustal flow. *In*: Whitney, D. L., Teyssier, C & Siddoway, C. S. (Eds). *Gneiss Domes in Orogeny*. Geological Society of America Special Paper, **380**, 15-33.

White, R. W. & Powell, R. (2002). Melt loss and the preservation of granulite facies mineral assemblages. *Journal of Metamorphic Geology*, **20**, 621-632.

White, R. W., Powell, R. & Halpin, J. A. (2004). Spatially-focussed melt formation in aluminous metapelites from Broken Hill, Australia. *Journal of Metamorphic Geology*, **22**, 825-845.

White, R. W., Powell, R. & Holland, J. T. B. (2007). Progress relating to calculation of partial melting equilibria for metapelites. *Journal of Metamorphic Geology*, **25**, 511-527.

Wigand, M., Schmitt, A. K., Trumbull, R. B., Villa, I. M. & Emmermann, R. (2003). Short-lived magmatic activity in an anorogenic subvolcanic complex: $^{40}Ar/^{39}Ar$ and ion microprobe U-Pb zircon dating of the Erongo, Damaraland, Namibia. *Journal of Volcanology and Geothermal Research* **2715**, 1-21.

Williams, I. S. (1998). U-Th-Pb Geochronology by Ion Microprobe. *In*: McKibben, M. A., Shanks III, W. C. & Ridley, W. I. (Eds). *Applications of microanalytical techniques to understanding mineralizing processes*. Reviews in Economic Geology **7**, 1-35.

Williams, H. & Hatcher, R. D. (1982). Suspect terranes and accretionary history of the Appalachian orogen. *Geology*, **10**, 530-536.

Williams, I. S. & Claesson, S. (1987). Isotopic evidence for the provenance and Caledonian metamorphism of high grade paragneisses from the Seve Nappes, Scandianavian Calledonides: ion microprobe zircon U-Th-Pb. *Contributions to Mineralogy and Petrology*, **97**, 205-217.

Yardley, B. W. D. (1989). *An Introduction to Metamorphic Petrology*. Longman, New York, 248 pp.

Yin, A. (1991). Mechanisms for the formation of domal and basinal detachment faults – a 3-dimensional analysis. *Journal of Geophysical Research*, **96**, 14577-14594.

Yin, A. (2004). Gneiss domes and gneiss dome systems. *In*: Whitney, D. L., Teyssier, C & Siddoway, C. S. (Eds). *Gneiss Domes in Orogeny*. Geological Society of America Special Paper, **380**, 1-14.

Yin, A. & Dunn, J. F. (1992). Structural and stratigraphic development of the Whipple-Chemehuevi detachment fault system, southeastern California – implications for the geometrical evolution of domal and basinal low-angle normal faults. *Geological Society of America Bulletin*, **104**, 659-674.

Yin, A. & Kelty, T. K. (1991) Structural evolution of the Lewis plate in Glacier National Park, Montana: Implications for regional tectonic development. *Geological Society of America Bulletin*, **103**, 1073-1089.

Zeh, A. (2001). Inference of a detailed P-T path from P-T pseudosections using metapelitic rocks of variable composition from a single outcrop, Shackleton Range, Antarctica. *Journal of Metamorphic Geology*, **19**, 329–350.

Ziegler, U. R. F. & Stoessel, G. F. U. (1993). *Age determinations in the Rehoboth Basement Inlier*. Namibia Geological Survey of Namibia, Memoir **14**.

Ziegler, P. A. (1984). Caledonian and Hercynian crustal consolidation of Western and Central Europe – A working hypothesis. *Geologie en Mijnbouw*, **63**, 93-108.

LIST OF APPENDICES

Appendix 1A: XRF Data	APPENDICES PAGE 1
Appendix 1B: ICP-MS Data	APPENDICES PAGE 3
Appendix 1C: Procedure for Whole Rock Geochemistry	APPENDICES PAGE 5
Appendix 2A: U-Pb Zircon, Monazite and Titanite Data	APPENDICES PAGE 6
Appendix 2B: Lu-Hf Isotopic Data	APPENDICES PAGE 15
Appendix 2C: Oxygen Isotopic Data	APPENDICES PAGE 16
Appendix 2D: Procedure for Geochronology	APPENDICES PAGE 17
Appendix 2E: Procedure for Oxygen an Hafnium Isotopic Data	APPENDICES PAGE 19
Appendix 3A: Pelite XRF Data	APPENDICES PAGE 20
Appendix 3B: Biotite Analyses	APPENDICES PAGE 21
Appendix 3C: Garnet Analyses	APPENDICES PAGE 27
Appendix 3D: Cordierite Analyses	APPENDICES PAGE 43
Appendix 3E: Feldspar Analyses	APPENDICES PAGE 47
Appendix 3F: Ilmenite Analyses	APPENDICES PAGE 50
Appendix 3G: Clinopyroxene Analyses	APPENDICES PAGE 51
Appendix 3H: Amphibole Analyses	APPENDICES PAGE 52
Appendix 3I: Electron Microprobe Analyses Methodology	APPENDICES PAGE 52
Appendix 4A: Thermometry calculations	APPENDICES PAGE 53
Appendix 4B: Compositional averages and AX data used for average P-T calculations	APPENDICES PAGE 63